Université de Paris

Ecole doctorale
Astronomie et Astrophysique d'Île-de-France ED127

Laboratoire AIM, Service d'Astrophysique CEA-Saclay

The nature and role of starbursting galaxies in the distant universe

par
Antonello Calabrò

Thèse de doctorat de Astronomie et Astrophysique

Dirigée par Emanuele Daddi

Présentée et soutenue publiquement le 24 Septembre 2019
devant un jury composé de :

Isabelle Grenier	Professeur	DAp CEA-Saclay (LEPCHE)	Président
Daniela Calzetti	Professeur	University of Massachusetts	Rapporteur
Johan Richard	Professeur	CRAL - Observatoire de Lyon	Rapporteur
Veronique Buat	Professeur	LAM Marseille	Examinatrice
Luis Colina	Astronome	CAB/INTA Madrid	Examinateur
Mathieu Puech	Astronome	GEPI – Observatoire de Paris	Examinateur
Emanuele Daddi	Astronome	DAp CEA-Saclay (LCEG)	Directeur de thèse

Except where otherwise noted, this work is licensed under
https://creativecommons.org/licenses/by-nd/3.0/fr/

La nature et le rôle des galaxies à flambée d'étoiles dans l'univers lointain

Résumé court : Cette thèse étudie la morphologie, les propriétés physiques et les mécanismes de déclenchement des galaxies à flambée d'étoiles à redshift intermédiaire. Les Starbursts (SB) sont des galaxies avec un taux de formation d'étoiles (SFR) bien supérieur à la population moyenne située sur la séquence de corrélation principale SFR - masse stellaire. À haut redshift, on pense que les SB sont les progéniteurs des elliptiques passifs que l'on trouve dans l'univers local. Cependant, leur nature et leur rôle sont encore débattues: ces systèmes sont les plus lumineux et les plus faciles à détecter et à étudier (par exemple dans l'infrarouge), mais nous ne savons pas s'ils sont représentatifs de la majorité de l'activité de formation d'étoiles. De plus, nous ne savons pas si elles sont déclenchées par des fusions ou s'il s'agit simplement des systèmes isolés riches en gaz ayant eu un afflux de gaz anormal. L'atténuation de la poussière et la métallicité sont des quantités cruciales pour tester l'hypothèse de fusion, mais, pour mieux les contraindre, il est fondamental d'observer les galaxies à des longueurs d'ondes de l'infrarouge proche au repos, qui peuvent pénétrer plus profondément à travers la poussière par rapport aux diagnostics optiques. Dans cet objectif, j'ai observé, réduit et analysé les spectres infrarouges d'un échantillon de 25 SB à $0.5 < z < 0.9$. En comparant les raies de Paschen β et Hα aux luminosités infrarouges totales, j'ai trouvé que les starbursts hébergent des noyaux optiquement épais et très obscurcis, qui peuvent être expliqués seulement par des fusions (Calabro et al. 2018, ApJ Letters). De plus, les observations indiquent que la poussière et les jeunes étoiles sont mélangées de manière homogène et que le modèle géométrique à écran de poussière n'est pas valable. J'ai également constaté que l'atténuation des galaxies est corrélée à d'autres propriétés physiques, telles que la taille en radio, le rapport de raies [NII]/Hα, la largeur des raies d'émission et la largeur équivalente des raies de Balmer et de Paschen. J'ai interprété ces corrélations comme une séquence de différentes étapes temporelles de fusion (Calabro et al. 2019, A&A). Curieusement, des émissions de rayons X n'ont été détectées que dans 6 galaxies en phases tardives de fusion, suggérant des AGN émergents qui pouvent conduire finalement à un quasar lumineux. La similarité entre l'atténuation des rayons X et celle déduite de l'infrarouge suggère également une distribution particulière de la poussière et du gaz, où la plus grande partie de l'obscurcissement affectant l'émission AGN est produite dans le milieu interstellaire de la galaxie hôte, à des échelles de 10^2-10^3 pc, plutôt que dans le tore de l'AGN. De plus, en regardant les images HST dans la bande i, les galaxies starburst au même redshift sont dominés (par rapport aux disques normaux isolés) par des régions de formation stellaire très lumineuses (appelé 'clumps'), situé dehors de la région nucléaire centrale. Ces clumps sont généralement attribués à des instabilités gravitationnelles violentes produit dans des disques turbulents riches en gaz. Mon étude toutefois suggére que les fusions, en plus que déclencher l'activité de formation stellaire starburst, constituent des canaux importants et compétitifs même pour la formation des clumps.

Mots clefs : évolution des galaxies, galaxies à flambée d'étoiles, extinction, poussière, atténuation de la poussière, clumps, formation des galaxies, formation d'étoiles, AGN, fusions des galaxies, interaction des galaxies, trous noirs supermassifs, galaxies infrarouges lumineuses, spectre infrarouge proche, Magellan FIRE

The nature and role of starbursting galaxies in the distant universe

Short abstract : The thesis investigates the morphology, the physical properties and triggering mechanisms of starburst galaxies at intermediate redshifts z. Starbursts (SB) are galaxies with a star-formation rate (SFR) much higher than the average population lying on the SFR - stellar mass main correlation sequence. At high-z, SBs are thought to be the progenitors of passive ellipticals that we find in the local Universe. However, there is still a hot debate on their nature and role: they are the most luminous systems and easiest to detect and study (e.g., in the infrared), but we do not know whether they are representative of the bulk of the SFR activity. Moreover, we do not know whether they are triggered by major mergers or they are simply gas-rich isolated systems experiencing anomalous gas accretion events. The dust attenuation and metallicity are crucial quantities to test the merger hypothesis, but, for better constraining them, it is fundamental to observe the galaxies at near infrared rest-frame wavelengths, which can penetrate deeper through the dust compared to optical diagnostics. To this aim, I observed, reduced and analyzed the near-IR spectra of a representative sample of 25 SBs at $0.5 < z < 0.9$, using the Magellan-FIRE spectrograph. Comparing the Paschen β and Hα lines to the bolometric infrared luminosities, I found that starbursts host extremely compact optically thick star-forming cores, which can be only explained by assuming they are triggered by major mergers events (Calabro et al. 2018, ApJ Letters). Additionally, the observations indicate that at high obscurations the dust and young stars are homogeneously mixed, and the dust-screen geometry model does not hold anymore. I also found that the attenuation of the galaxies correlates with other physical properties, such as the size in radio, the [NII]/Hα ratio, the line velocity width and the equivalent width of Balmer and Paschen lines, all of which correlations are interpreted as a sequence of different time-evolutionary merger stages (Calabro et al. 2019, A&A). Intriguingly, X-ray emission was detected for six mergers only in the late phases, suggesting emergent AGNs possibly leading to a final bright quasar for these systems. The qualitative agreement between the X-ray attenuation and that inferred from the infrared also suggests a peculiar dust/gas distribution, where most of the obscuration affecting the AGN emission is produced in the host galaxy ISM, on scales of 10^2-10^3 pc, rather than in the AGN torus. Furthermore, looking at HST i-band images, starbursts at the same redshift have a morphology that is systematically more clumpy compared to normal star-forming isolated disks with matching stellar masses. Indeed, SBs are statistically more dominated by off-nuclear bright patches of stellar emission, contributing up to 20% to the total emission at those wavelengths. While most studies explain such clumps through violent gravitational instabilities in gas-rich turbulent disks, my result indicates that mergers are also a powerful and competitive channel for clumps formation.

Keywords : galaxy evolution, starburst, extinction, dust attenuation, clumps, galaxy formation, star formation, AGN, merger, galaxy interaction, supermassive black holes, luminous infrared galaxies, near infrared spectrum, Magellan FIRE

Résumé

Les galaxies à flambée d'étoiles (aussi appelé *starburst*, SB) et très lumineuses dans l'infrarouge, représentent une fraction mineure des galaxies (2 - 4%) à toutes les epoques cosmiques, avec un taux de formation d'étoiles (SFR) bien supérieur à la population moyenne située sur la corrélation principale (aussi dit 'Main Sequence', MS) entre la masse stellaire et la SFR. Malgré cela, ils peuvent être la clé pour comprendre un mystère de longue date de l'évolution des galaxies: la formation des elliptiques massives à partir des collisions de galaxies spirales et à disque. Dans l'univers local, en effet, les observations et simulations montrent que les galaxies ultra-lumineuses dans l'infrarouge (ULIRG) sont crées par des collisions, appelées aussi 'fusions' (mergers). En conséquence du processus de fusion (révélé, par example, par des coquilles, des queues de marée étendues ou des perturbations), toutes hébergent des noyaux compacts, fortement obscurcis par la poussière, et des AGN obscurcis.

Malgré la relation claire qui existe localement, la situation n'est toujours pas claire lorsque nous passons à des décalages vers le rouge plus élevés. La nature des galaxies à flambée d'étoiles à $z > 0$ est en effet trés débattue: bien que les SB les plus lumineux puissent être déclenchés par des fusions, d'autres études affirment qu'il ne s'agit que de galaxies riches en gaz ayant eu un afflux de gaz anormal. Ceci est corroboré par le fait que les fusions ne peuvent pas augmenter facilement le taux de formation d'étoiles à z élevé, selon des simulations numériques. La raison de ce débat est que les galaxies *starburst* sont les systèmes les plus lumineux et les plus faciles à détecter et à étudier (par exemple, dans l'infrarouge), mais nous ne savons pas s'ils sont représentatifs de la majorité de l'activité de formation d'étoiles.

Cette thèse étudie la nature des galaxies *starburst* au-delà de l'univers local, en évaluant les mécanismes de déclenchement de leur activité violente de formation d'étoiles. Des travaux précédents ont tenté de mesurer par des raies d'emission dans l'optique leur atténuation et métallicité à 'redshift' élevé, deux paramètres cruciaux pour comprendre l'histoire et l'activité en cours de ces systèmes. Cependant, il était clair que seules des limites inférieures pouvaient être fixées sur l'atténuation totale, alors que toutes les propriétés physiques dérivées de leurs spectres optiques ne tracent que de petites lignes de visée non atténuées par la poussière, et ne peuvent donc pas être utilisées pour caractériser l'ensemble du système.

Il est donc urgent de disposer d'observations à des longueurs d'onde plus grandes, principalement parce qu'elles sont moins affectées par l'atténuation de la poussière et peuvent sonder des profondeurs optiques plus grandes. Par exemple, Paβ (la deuxième raie la plus brillante de la série de Paschen à 1.281μm) peut être ~ 10 fois moins atténuée que les raies de Balmer dans des conditions de fort obscurcissement. Malheureusement, à ce jour, nos

connaissances sur les propriétés des spectres des galaxies dans le proche infrarouge au repos sont extrêmement limitées. Ceci est en partie lié à la difficulté de la réduction spectrale à ces longueurs d'onde (en raison des raies denses et lumineuses du ciel), mais également au bruit instrumental et à la présence des régions opaques de transmission atmosphérique.

Dans cet objectif, j'ai observé avec Magellan-FIRE un échantillon de 25 galaxies à flambée d'étoiles dans le champ COSMOS à $0.5 < z < 0.9$, qui est le seule intervalle permettant de détecter à la fois Paβ dans la bande K et Hα dans la bande Y ou J. En comparant Hα, Paβ et les luminosités bolométriques infrarouge, j'ai trouvé que les étoiles ne suivaient pas une loi d'atténuation standard de Calzetti ou Cardelli (c'est-à-dire une géométrie à écran de poussières, mais forment une séquence en accord avec les prédictions d'un modèle mixte, dont le paramètre caractéristique $A_{V,tot}$ (c'est-à-dire l'atténuation intégrée vers le centre) peut être mesuré directement. Bien qu'elles couvrent un large éventail de valeurs ($1 < A_{V,tot} < 30$), ces galaxies ont une valeur moyenne $A_{V,tot}$ de 9 magnitudes, ce qui implique que leur noyau interne est optiquement épais, même à des longueurs d'onde proches de l'infrarouge.

Étant donné que les fusions sont les seuls mécanismes viables permettant d'expliquer de tels obscurcissements extrêmes, j'ai conclu que la plupart des galaxies à flambée d'étoiles à $z0 < 0.9$ devraient être déclenchés par une collision. En effet, la morphologie optique n'est pas totalement efficace pour identifier les collisions de galaxies à haut redshift (en particulier les systèmes déjà coalescés), à cause de la faible résolution et la diminution de la luminosité de surface.

Dans la seconde partie de la thèse, pour comprendre l'origine de la séquence d'atténuation trouvée précédemment, j'ai analysé d'autres propriétés physiques des 25 galaxies *starburst*, en trouvant pour la première fois des corrélations très fortes entre l'atténuation, la taille des galaxies en radio, la largeur des raies d'émission et la largeur équivalente (EW) des raies de Balmer et de Paschen. J'ai interprété ces corrélations de la manière physique la plus simple comme une séquence évolutive d'étapes de fusion, dans laquelle tous les paramètres susmentionnés évoluent avec le temps et constituent donc de bons traceurs temporels du phénomène de fusion.

Curieusement, des émissions de rayons X n'ont été détectées que dans 6 galaxies en phases tardives de fusion, suggérant des AGN émergents qui pouvent conduire finalement à un *quasar* lumineux. La similarité entre l'atténuation des rayons X et celle déduite de l'infrarouge suggère également une distribution particulière de la poussière et du gaz, où la plus grande partie de l'obscurcissement affectant l'émission AGN est produite dans le milieu interstellaire de la galaxie hôte, à des échelles de 10^2-10^3 pc, plutôt que dans le tore de l'AGN. De plus, par analogie avec les conclusions d'autres études récentes, la taille des galaxies en radio (qui trace les régions de formation des étoiles) apparaît extrêmement petite, beaucoup plus petite que les disques et les galaxies passives (ETG) au même redshift et masses stellaires. Leur extension est au contraire similaire à celle des bulbes présents au centre des

galaxies spirales et lenticulaires, qui pourraient donc être les descendantes naturelles des noyaux des galaxies à flambée d'étoiles à $z \sim 0.7$.

La dernière partie de la thèse est dédiée à une étude détaillée des effets des collisions sur la morphologie des galaxies à des échelles plus petites. En examinant visuellement des images à haut résolution *HST-ACS* en bande i (sensibles à la masse stellaire et moins affectées par la poussière que le régime UV), je me suis rendu compte que les galaxies à flambée d'étoiles ont en moyenne une structure plus 'granuleuse' que les galaxies normales (MS). En effet, beaucoup de SB sont dominées (jusqu'à 20%) par des régions de formation stellaire très lumineuses (appelé 'clumps'), situées en dehors de la région nucléaire centrale. On pense que ces clumps stellaires ont un impact important sur la dynamique et la stabilité de toute la galaxie, contribuant probablement à la croissance du bulbe stellaire au centre. Autrement, ils pourraient être à l'origine de galaxies naines satellites ou des amas globulaires.

Les clumps identifiés dans les galaxies à haut redshift sont généralement attribués à des instabilités gravitationnelles violentes, qui sont fortement favorisées par le teneur en gaz plus élevée par rapport aux disques locaux. Notre inspection visuelle a toutefois suggéré que les fusions, en plus de déclencher la puissante activité de formation stellaire nucléaire, peuvent constituer des canaux compétitifs même pour la formation des clumps. Cette possibilité a déjà été suggérée par des travaux antérieurs basés sur de petits échantillons de galaxies (ayant une gamme précise de masses stellaires et de décalage vers le rouge), mais elle n'a toujours pas été étudiée systématiquement et avec des observations et des simulations.

Pour vérifier cette hypothèse, j'ai quantifié et comparé le paramètre 'clumpiness' entre des échantillons représentatifs de galaxies SB et MS (isolées), de systèmes merger et non merger, et j'ai également utilisé des nouvelles simulations de collisions des disques avec des conditions physiques typiques de cette epoque à $z \sim 0.7$. Tous les résultats indiquent une augmentation statistiquement significative de la 'clumpiness' dans les galaxies *starburst* (et les mergers en général). J'ai donc conclu qu'un lien de causalité entre les fusions des galaxies et la formation des clumps stellaires doit exister et qu'il est physiquement solide.

Le travail entamé dans cette thèse sera développé encore plus profondément grâce à d'autres observations qui ont été obtenues dans le cadre de propositions des temps d'observation acceptées que j'ai menées comme PI, ou auxquelles j'ai participé en tant que co-investigateur. Le premier objectif est de tester l'interprétation du modèle mixte et la corrélation entre l'attenuation et la taille radio des galaxies *starburst*, en utilisant des observations de l'émission de poussières et des raies du CO avec l'interferomètre IRAM/NOEMA. Ensuite, je ferai de nouveaux tests pour mieux caractériser la population des *starbursts* et vérifier leur lien avec les collisions. À cette fin, j'élargirai l'échantillon de 25 *starburst* avec plus de 100 galaxies MS observées par VLT/KMOS et Subaru/MOIRCS. J'analyserai àpres leur spectre

infrarouge proche au repos, y compris les raies d'émission émis par des éléments métalliques.

Les nombreuses données disponibles pour les galaxies normales permettront de vérifier la validité de la loi d'atténuation de Calzetti pour ces systèmes, puis de calibrer la métallicité avec des raies de l'infrarouge proche, afin de l'appliquer ultérieurement à l'ensemble de l'échantillon. La découverte d'une quelconque signature d'augmentation de la métallicité vers le coeur des galaxies *starburst* pourrait confirmer leur déclenchement par des fusions et leur efficacité supérieure de formation stellaire attendue dans ce scénario. En outre, des signatures de contribution de chocs dans le milieu interstellaire pourraient être observées, en particulier pour les phases de merger plus tardives.

Globalement, ces données auraient un héritage important pour les enquêtes futures comme JWST, qui atteindront des niveaux de sensibilité plus élevés et détecteront les raies du proche infrarouge jusqu'à l'époque de la réionisation pour des centaines d'objets. Enfin, les installations actuelles et futures (par exemple, ALMA, HST et VLT/MOONS ou ERIS) permettront d'étudier le phénomène de *starburst* de manière spatialement résolue, en approfondissant de manière plus détaillée la dynamique, la répartition de l'atténuation de la poussière et le mécanismes de rétroaction régulant (et éventuellement éteignant) l'activité de formation d'étoiles dans ces systèmes (par exemple, par des éjections de gaz). Dans le même temps, ils permettront de mieux caractériser les propriétés des clumps, y compris leur masse stellaire, leur âge et leur stabilité, ce qui est nécessaire non seulement pour confirmer leur origine, mais également pour comprendre leur sort final.

Abstract

Infrared luminous starbursts (SB) represent a minor fraction of star-forming galaxies (2-4%), with a star-formation rate (SFR) much higher than the average population lying on the SFR - stellar mass main sequence correlation (MS). Despite this, they might be key to understand a long standing mistery of galaxy evolution: the transformation of spiral/disk star-forming galaxies into massive, passive ellipticals through merger episodes. In the local Universe, indeed, there is a well established connection between Ultra-luminous infrared galaxies (ULIRGs) and mergers, supported by both simulations and observations. As a consequence of the collision (revealed, e.g., through extended tidal tails and bridges), all of them host compact, highly dust obscured starburst cores, and obscured AGNs. Despite the clear relation locally, the picture is still unclear when we go to higher redshifts. The nature of high redshift starbursts is indeed hotly debated: while the most luminous might still be merger triggered, other studies claim they are just gas rich galaxies experiencing anomalous gas accretion events. This is supported by the evidence that mergers may not enhance the star-formation rate in an easy way at high-z, according to numerical simulations. The reason for the hot debate is that starbursts are the most luminous systems and easiest to detect and study (e.g., in the infrared), but we do not know whether they are representative of the bulk of the SFR activity.

This thesis investigates the nature of starburst galaxies beyond the local Universe, assessing the triggering mechanisms of their violent star-formation activity. Previous works have attempted at measuring through optical lines the attenuation and metallicity of high redshift starbursts, both of which are crucial parameters to understand the history and ongoing activity of these systems. However, it appeared clear that only lower limits could be put on the total attenuation, while all physical properties derived from their optical spectra trace just small unattenuated lines of sight, hence cannot be used to conclude on the whole system. Therefore, longer wavelength observations are urgely needed, primarily because they are less affected by dust attenuation and can probe larger optical depths. For example, Paβ (the second brightest Paschen line at $1.281\mu m$) can be ~ 10 times less attenuated than Balmer lines in strong obscuration conditions. Unfortunately, up to this moment, our knowledge of the near-IR rest-frame properties of galaxies is extremely limited. This is in part related to the difficulty of the spectral reduction at these wavelengths (for the dense and brigth sky lines), but also to the instrumental noise and the presence of opaque regions of atmospheric transmission.

With this aim, I followed-up with Magellan-FIRE a sample of 25 starbursts in the COSMOS field at $0.5 < z < 0.9$, which is the only range allowing to detect both Paβ in K band and Hα in Y/J bands. Comparing Hα, Paβ

and the IR bolometric luminosities, I found that starbursts do not follow a standard Calzetti/Cardelli attenuation law (i.e., a dust screen geometry), but form an attenuation sequence that is in qualitative agreement with the predictions of a mixed model, whose characteristic parameter $A_{V,tot}$ (i.e., the integrated attenuation towards the center) can be directly measured. While spanning a broad range of values (ranging $1 < A_{V,tot} < 30$), these starbursts have on average an $A_{V,tot}$ of 9 magnitudes, which implies that their inner core is optically thick even at near-IR wavelengths. Since, according to our knowledge, mergers are the only viable mechanisms to explain such extreme obscurations, I concluded that most starbursts at $z < 0.9$ should be merger triggered. The optical morphology is indeed not fully efficient at indentifying galaxy collisions (especially already coalesced systems), given the lower resolution and surface brigthness dimming at higher z.

In the second part of the thesis, to understand the origin of the attenuation sequence previously found, I analyzed other physical properties of the Magellan starbursts, finding for the first time tight correlations among the attenuation, the radio size, the line velocity width and the equivalent width (EW) of Balmer and Paschen lines. I interpreted these correlations in the most simple physical way as an evolutionary sequence of merger stages, where all the above parameters evolve with time and are thus good time tracers of the merger phenomenon. Intriguingly, X-ray emission was detected for six mergers only in the late phases, suggesting emergent AGNs possibly leading to a final bright QSO for these systems. The qualitative agreement between the X-ray attenuation and that inferred from the infrared also suggests a peculiar dust/gas distribution, where most of the obscuration affecting the AGN emission is produced in the host galaxy ISM, on scales of 10^2-10^3 pc, rather than in the AGN torus. Furthermore, in analogy with findings of other recent studies, the radio sizes of the starbursts (tracing the star-formation) appear extremely small, much smaller than both star-forming disks and passive early-type galaxies (ETG) at the same redshifts and stellar masses. Their extension is instead similar to bulges present in the center of spiral and lenticular galaxies, which could then be the natural descendant of intermediate-z starburst cores.

The last part of the thesis is dedicated to a detailed study of the effects of mergers on the morphology of galaxies at smaller scales. From a visual inspection of high resolution HST-ACS i-band images (sensitive to the stellar mass and less affected by dust compared to the UV regime), I realized that starbursts have on average more clumpy structures compared to normal MS galaxies. Indeed, many of them are dominated up to 20% by off-nuclear bright patches of stellar emission emerging from a smoother luminosity profile. Stellar clumps are thought to have a great impact on the dynamics and stability of the whole galaxy, possibly contributing to the stellar bulge growth. In alternative, they could originate tidal dwarf galaxies or globular clusters. Clumps identified in high redshift galaxies are usually attributed to

violent gravitational instabilities, which are strongly favoured by their typically higher gas content with respect to local disks. However, our inspection suggested that mergers, in addition to triggering nuclear starbursts, might be powerful and competitive channels even for the formation of clumps. This possibility has been already suggested by some previous works based on small samples of galaxies with particular stellar mass and redshift ranges, but it is still largely uninvestigated with both observations and simulations. To verify this hypothesys, I quantified and compared the 'clumpiness' parameter for representative samples of SB and MS (isolated) galaxies, visual mergers and not mergers, and also performed new simulations of disks collisions with physical conditions typical of $z \sim 0.7$. All the results pointed toward a (statistically) significant clumpiness enhancement in starbursts (and mergers in general). I thus concluded that a causal connection between mergers and newly formed stellar clumps is physically plausible and strongly favoured.

The work started in this thesis will be further developed thanks to other observations taken as part of accepted proposals that I led as PI or participate as co-I. On the one hand, the first goal is to test the interpretation of the mixed model and the radio-size correlation of SBs, using ongoing IRAM/NOEMA observations of CO lines and dust continuum. On the other hand, I will perform new tests to further characterize the SB population and verify their connection with mergers. To this aim, I will complement the 25 Magellan starbursts with more than 100 MS galaxies observed with VLT/KMOS and Subaru/MOIRCS. I will then analyze their full spectral range in the near-infrared rest-frame (including emission lines coming from metal elements). The large statistics available for normal galaxies will allow to verify the validity of the Calzetti attenuation law for these systems, and then calibrate the metallicity with near-infrared lines, in order to be applied afterwards to the whole sample. Finding any signature of metallicity enhancement towards the core of starburst galaxies would corroborate the merger triggering and the higher star-formation efficiency that we expect in this scenario. In addition, signatures of increasing shock contribution could be checked, especially for later stage mergers. All in all, these data would have a great legacy value for future surveys like JWST, which will reach deeper sensitivity levels and detect near-IR lines up to the reionization epoch for hundreds of objects. Finally, current and new facilities (e.g., respectively, ALMA, HST and VLT/MOONS or ERIS) will allow to study the starburst phenomenon in a spatially resolved way, probing with more detail the dynamics, the distribution of dust attenuation, and the feedback mechanisms regulating (and possibly quenching) the star-formation activity in those systems (e.g., through outflows). At the same time, they will enable a better characterization of clumps in starbursts, including their stellar mass, age and stability, which is necessary not only to confirm their origin, but also to understand their final destiny.

Contents

List of Abbreviations

ACS	**A**dvanced **C**amera for **S**urveys
AGN	**A**ctive **G**alactic **N**ucleus
ALMA	**A**tacama **L**arge **M**illimeter/submillimeter **A**rray
CANDELS	**C**osmic **A**ssembly **N**ear-infrared **D**eep **E**xtragalactic **L**egacy **S**urvey
CFHT	**C**anada **F**rance **H**awaii **T**elescope
CGM	**C**ircum**g**alactic **M**edium
COSMOS	**COSMO**logical Evolution **S**urvey
ERIS	**E**nhanced **R**esolution **I**mager and **S**pectrograph
ESO	**E**uropean **S**outhern **O**bservatory
ETG	**E**arly **T**ype **G**alaxy
EW	**E**quivalent **W**idth
FIRE	**F**olded-port **I**nf**red** **E**chellette
FWHM	**F**ull **W**idth at **H**alf **M**aximum
HST	**H**ubble **S**pace **T**elescope
ID	**ID**entification number
IMF	**I**nitial **M**ass **F**unction
IR	**I**nfra**r**ed
IRAM	**I**nstitut de **R**adio**a**stronomie **M**illimétrique
IRAS	**I**nfra**r**ed **A**stronomical **S**atellite
ISM	**I**nter**s**tellar **M**edium
JWST	**J**ames **W**ebb **S**pace **T**elescope
KMOS	**K**-band **M**ulty **O**bject **S**pectrograph
LIRG	**L**uminous **I**nfrared **G**alaxies
LMC	**L**arge **M**agellanic **C**loud
LTG	**L**ate **T**ype **G**alaxy
MOONS	**M**ulty **O**bject **O**ptical and **N**ear-infrared **S**pectrograph
MS	**M**ain **S**equence
MW	**M**ilky **W**ay
PAH	**P**olycyclic **A**romatic **H**ydrocarbons
PDF	**P**robability **D**istribution **F**unction
QSO	**Q**uasi **S**tellar **O**bject
S/N	**S**ignal to **N**oise
SB	**S**tar**b**urst
SDSS	**S**loan **D**igital **S**ky **S**urvey
SED	**S**pectral **E**nergy **D**istribution
SF	**S**tar **F**ormation/**F**orming
SFE	**S**tar **F**ormation **E**fficiency
SFH	**S**tar **F**ormation **H**istory

SFR	**S**tar **F**ormation **R**ate
SSFR	**S**pecific **S**tar **F**ormation **R**ate
SMC	**S**mall **M**agellanic **C**loud
SMG	**S**ub**m**illimeter **G**alaxy
SN	**S**uper**n**ova
ULIRG	**U**ltra **L**uminous **I**nfrared **G**alaxies
UltraVISTA	**Ultra**-deep Survey with the **VISTA** telescope
UV	**U**ltra**v**iolet
VLA	**V**ery **L**arge **A**rray
VLT	**V**ery **L**arge **T**elescope
WFPC	**W**ide **F**ield **P**lanetary **C**amera

Chapter 1

Introduction

Starbursts (SB) are galaxies that form stars at significantly higher rates than the average population. They might be key to understand a long-standing mystery in galaxy formation and evolution: the transition from gas rich disks to massive, gas poor and passively evolving ellipticals. Indeed, according to a popular scenario (e.g., Di Matteo, Springel, and Hernquist, 2005; Hopkins et al., 2010), this transition is attributed to major mergers producing strong bursts of star formation in very dense cores and triggering obscured black hole accretion, which can both remove the remaining gas and dust from the galaxy, leaving a passive system.

Local ultra luminous infrared galaxies (or ULIRGs) are showcase examples of merger induced starbursts, showing compact cores and obscured AGN activity (e.g., Soifer et al., 2000; Juneau et al., 2009), in agreement with the above scenario. Hydrodynamical simulations with local conditions permit to follow the whole merger sequence, which happens in different phases, well represented by the so-called Toomre sequence (Toomre and Toomre, 1972). These numerical codes indicate that the final morphology of merger remnants is consistent with that of early type galaxies or spheroidal gar-poor systems (Barnes and Hernquist, 1991; Mihos and Hernquist, 1994; Mihos and Hernquist, 1996).

Despite the clear starburst-merger connection at $z = 0$, the nature and evolution of this type of strongly star-forming galaxies in the distant Universe is still hotly debated. While they might still be prevalently major merger events (Elbaz and Cesarsky, 2003), there are also claims that they might be instead very gas rich galaxies (e.g., Scoville et al., 2016), possibly due to exceptionally strong gas accretion events. This is supported by ideas that at higher redshifts, with higher gas fractions, major mergers might only rarely result in strong SFR enhancements (Fensch et al., 2017). Similarly, the connection between mergers and AGNs is still debated. Even though it may still hold for the most luminous cases (Combes, 2003), some studies (focused especially on optical wavelengths) do not find systematic differences in merger fraction and galaxy distortions between active and non-active systems (Cisternas et al., 2011; Kocevski et al., 2012), and not all AGNs are triggered by mergers, according to, for example, Draper and Ballantyne (2012) and Ellison, Patton, and Hickox (2015).

The solution to these long-standing problems is further complicated due to the intrinsic faintness of interacting features (e.g., tidal tales, bridges) and the elevated attenuations of the cores, which hamper their physical characterization using the widely adopted, well calibrated optical lines. A possible solution to study the properties of the dusty starburst population at high redshift is to observe them at longer wavelengths, targeting near-infrared rest-frame lines, such as the Paschen line series of hydrogen. For example, Paβ, the second brightest Paschen recombination line, is accessible from current ground-based spectrographs in K band up to a redshift of ~ 0.9. This constituted the underlying idea of my PhD.

In this beginning chapter, I present the global astrophysical context of my PhD work. I start in Section 1.1 with a description of the different types of galaxies in the local Universe. In Section 1.2, I summarize our knowledge about the connection among mergers, starburst galaxies and AGNs. Afterwards, I focus on the important role of dust, which is discussed first in a general astrophysical context (Section 1.3), and then applied specifically to starburst galaxies (Section 1.4). Finally, Section 1.5 explains the main motivations of this thesis and summarizes its content.

1.1 Galaxies

Galaxies are gravitationally bound systems of stars, gas and dust, immersed in a dark matter halo. In the current cosmological framework, their formation and assembly is tightly connected to the evolution of their parent dark matter structures. First, following the Universe expansion and cooling, the baryonic matter started to accumulate as dense and cold gas in protogalaxies at the center of their halo gravitational potential wells. While the halos were growing hierarchically from the initial density fluctuations, assembling bigger and more massive structures from smaller ones, if the progenitors contained central galaxies, these also merged, producing another galaxy at the end of the process. The different steps of galaxy formation are summarized in Fig. 1.1.

This flowchart is able to explain qualitatively the existence of the fundamental galaxy morphological types that we find in the Universe: ellipticals and spirals. Spiral galaxies typically consist of a thin disk (supported by rotation) made of spiral arms, a central bulge and sometimes a bar. The relative contribution of the disk and the bulge to the total galaxy surface brightness can also vary significantly among the whole population. The tightness of the spiral arms and the presence or absence of a bar were firstly used to classify spirals by Hubble in 1926. A more recent version of the Hubble sequence, made by de Vaucouleurs (1948), takes into account also the luminosity ratio between bulge and disk, adding more subclasses to the original ones. A recent and detailed description of the different galaxy morphological types is included in Table 1.1, from Baillard et al. (2011), while Fig. 1.2 shows the variety of morphologies of local galaxies as an example.

élément sous droit, diffusion non autorisée.

Figure 1.1: Representative flowchart of galaxy formation, showing all the possible channels leading to the assembling of ellipticals and spiral-disk galaxies. Note that the various steps do not always happen in the same order. For example, the cold gas could not have time to form a gaseous disk before a major merger takes place. Credits: Mo, van den Bosch, and White (2010).

The different galaxy luminosity profiles can be quantified by fitting a combination of Sersic analytic functions (with different weights) as (Sérsic, 1963):

$$I(R) = I_e \times exp\left[-\beta_n \left\{\left(\frac{R}{R_e}\right)^{1/n} - 1\right\}\right], \tag{1.1}$$

where $\beta(n)$ is chosen so that r_e, the effective radius, includes half of the light and $I_e = I(r_e)$. The disk component typically has a Sersic index $n = 1$ (exponential profile), while the bulge component has a Sersic index $n = 4$, known as the de Vaucouleurs profile (de Vaucouleurs, 1948). In the Hubble scheme, S0 spirals are bulge dominated, while Sc are disk dominated.

Class	Stage	Literal type	Description
Ellipticals			Ellipse or sphere. Structureless, smooth intensity distribution with relatively steep gradient.
Elliptical	Compact	cE	Compact elliptical.
Elliptical	0-6	E	More or less elongated.
Elliptical	cD	cD	Giant elliptical. Sharp central profile and very extended low surface brightness halo.
Lenticulars			Spheroidal bulge and disk but no visible spiral arms in the disk.
Lenticular	Early	$S0^-$	Dominant bulge, no sign of structure in disk nor dust.
Lenticular	Intermediate	$S0^0$	Some structure in disk but no arms, low amounts of dust.
Lenticular	Late	$S0^+$	Clear structure in disk but no arms, thin dust lanes.
Spirals			Central bulge and disk with spiral arms. May harbour a bar.
Spiral	0/a	S0/a	Very tightly wound arms, very prominent bulge, low amounts of dust
Spiral	a	Sa	Tightly wound arms, very prominent bulge, low amounts of dust
Spiral	ab	Sab	Quite tightly wound arms, prominent bulge, low amounts of dust
Spiral	b	Sb	Quite tightly wound arms, prominent bulge, strong dust lanes
Spiral	bc	Sbc	Quite loosely wound arms, medium bulge, dust lanes
Spiral	c	Sc	Grand design spiral, fairly weak bulge, dust lanes
Spiral	cd	Scd	Loosely wound and weak arms, weak bulge, scattered dust
Spiral	d	Sd	Loosely wound and very weak arms, weak bulge, scattered dust
Spiral	dm	Sdm	Very loosely wound arms, very weak bulge, low amounts of dust
Spiral	m	Sm	Some indication of spiral arms, very weak bulge, low amounts of dust
Irregular	Magellanic	Im	No arms, no bulge. Irregular profile. Low surface brightness. May host a bar.
Dwarf	Dwarf spheroid elliptical	dE	Regular low surface brightness profile, no arms. May contain a tight nucleus.

Table 1.1: A modern version of Hubble Sequence, from Baillard et al. (2011). The left column lists the class (elliptical, lenticular, spiral, irregular, Dwarf) and the second column the intermediate stage within each class. The third column gives instead the literal type, following de Vaucouleurs (1948). The last column briefly describes the class.

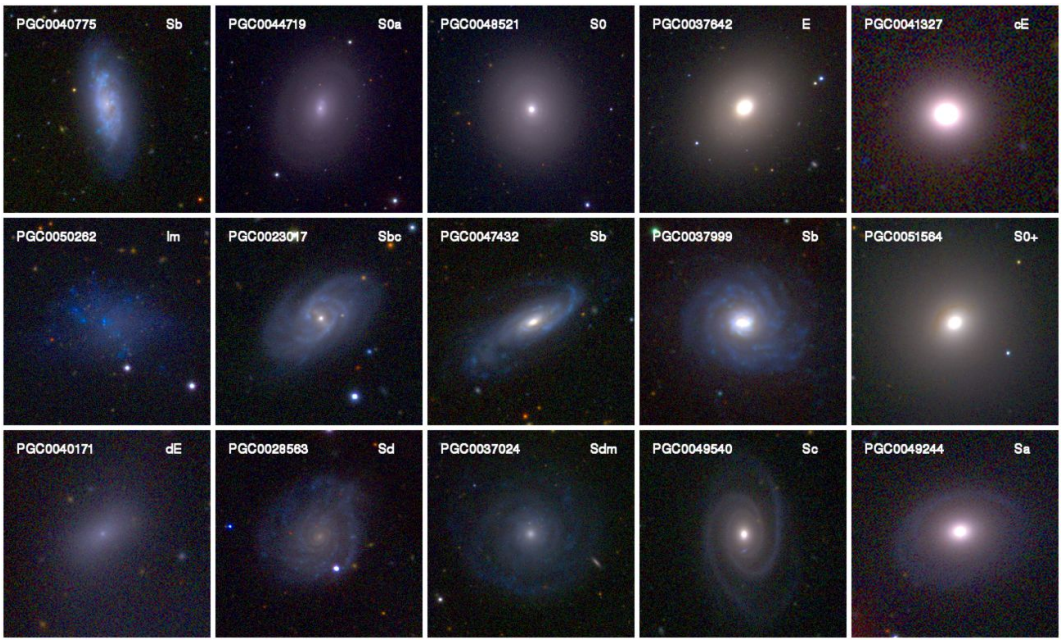

Figure 1.2: *irg* colour images of nearby galaxies with different morphological classes (cf. Table 1.1) and different Bulge/Disk luminosity ratios (increasing toward the right), from the EFIGI catalog ("Extraction de Formes Idéalisées de Galaxies en Imagerie") of Baillard et al. (2011).

On the other hand, elliptical galaxies are supported by random motions of their stars and have smooth, elliptical surface brightness distributions, with Sersic index of 4, similar to the bulge-dominated spiral galaxies. According to their apparent ellipticity, which essentially depends on the viewing angle of the observer, they are grouped in 7 classes in the Hubble classification, from E0 to E7. Despite their simple axisymmetric structure, they can have small deviations from it, identified in the two main categories of disky and boxy ellipticals. The first have peaked isophotes and typically low Sersic indexes, while in the latter the profile is box-shaped and the Sersic index is higher ($n > 4$) (Bender, Doebereiner, and Moellenhoff, 1988; Kormendy et al., 2009). These two main galaxy groups of ellipsoid-dominated and disk-dominated galaxies are historically referred as early-type and late-type galaxies, respectively, because spirals were supposed to be later evolutionary stages of elliptical galaxies, even though today we know this picture is not correct.

Apart from the different surface brightness profiles, these two main classes of galaxies also occupy distinct regions in the color-magnitude diagram (Strateva et al., 2001; Baldry et al., 2004; Baldry et al., 2006; Schawinski et al., 2014): the blue cloud and the red sequence (Fig. 1.3). The blue cloud in the bottom part is occupied by late-type galaxies, which are gas-rich and star forming, while the red sequence in the upper region includes gas poor early-type galaxies (ETGs) with old red stars and currently passive (Trager et al., 2000). This bimodality holds at least up to $z \lesssim 2.5$ (Franzetti et al., 2007;

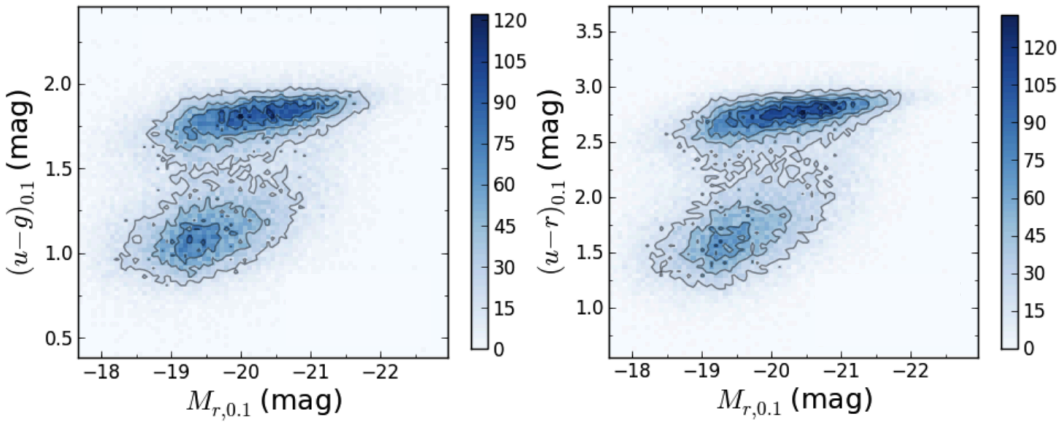

Figure 1.3: Color-magnitude diagrams built for a sample of $\sim$ 70k galaxies selected from the SDSS DR7, and reported to a common redshift of 0.1. Colors and contours represent the number density of galaxies. The x-axis contains the absolute magnitude in r band, while in the y-axis are displayed the colors $u - g$ and $u - r$. The red sequence is in the upper part, while the blue cloud has a larger dispersion and is located in the bottom part of the diagrams. The space between the two most populated regions is often called the 'green valley', and typically hosts galaxies transiting from the blue cloud to the red sequence (i.e., on the way of passivisation). This figure with explicative purposes comes from Jin et al. (2014).

Brammer et al., 2009). However, the number of galaxies and the stellar mass density in the red sequence increased by a factor of 2 from $z = 1$ to $z = 0$, while for blue galaxies they remained roughly constant (Arnouts et al., 2007). This evolution of the color-magnitude diagram implies that, across cosmic time, a fraction of galaxies should quench star-formation and migrate from the blue cloud to the red sequence (Bell et al., 2007; Walcher et al., 2008).

A phenomenon that has been invoked to explain this galaxy transformation and the formation of early-type galaxies (at least with low mass of 10^{10}-10^{11} M_{sun}) is the collision of two gas rich disks (Dasyra et al., 2006; Schawinski et al., 2014), also called a wet merger. Afterwards, the ETGs can grow in mass through dry merger episodes (i.e., a collision with another ETG) producing the most massive ellipticals, which have typically a boxy shape and slow rotation, and cannot be explained by a simple disk-disk collision (Cox et al., 2006; Naab, Khochfar, and Burkert, 2006; Burkert et al., 2008). In the next Section, I will discuss more in detail about the wet merger mechanism.

1.2 Mergers, starbursts, and AGNs

Wet mergers are thought to be responsible for triggering starburst and AGN activity inside galaxies. Numerical simulations of gas-rich disks show indeed that tidal perturbations induced by the interaction cause the disks to

become globally unstable, arising complex velocity fields in the system and distorsions in the stellar/gas distribution (e.g., tidal tails). In the meanwhile, gravitational torques can effectively remove angular momentum from the gas, which then starts to flow toward the coalescing center of the system. Here it forms a compact gas core of 1 kpc size or less, which is several orders of magnitude denser than the center of normal isolated galaxies (Combes et al., 1990; Mihos and Hernquist, 1996). A simple application of the Schmidt-Kennicut relation implies that this core should be also highly star-forming, with specific SFRs that are significantly higher (by factors of 5-10) than in average spirals. For this reason, they are also called starbursts, and their activity typically lasts for $\sim$ 200 Myr.

Because of their large SFRs, they usually produce also large amounts of dust in their central cores, which makes them completely obscured at UV and optical wavelengths. Indeed, in contrast with blue starbursts, which are relatively unobscured, they absorb the majority of UV photons produced by young OB stars and re-emit this energy in the far infrared, appearing as (Ultra) Luminous Infrared Galaxies ((U)LIRG). These are defined by having a bolometric IR luminosity L_{IR} higher than 10^{11} and 10^{12} L_{sun} (Soifer et al., 1984), for LIRGs and ULIRGs respectively.

During the starburst phase, if some of the gas continues to lose angular momentum, it may form and fuel a central black hole (eventually in addition to those of progenitor galaxies), giving rise to powerful AGN activity (Hernquist, 1989; Barnes and Hernquist, 1991). Feedback processes, such as the energy and momentum released by supernovae explosions and by the black hole can disperse the remaining gas and dust in a blowout episode, leading to a bright QSO phase.

Later, star formation and AGN luminosity rapidly decrease due to lack of fuel removed by the blowout, and the merger remnant becomes increasingly dominated by older stars with no or faint emission lines, showing a post-starburst spectral energy distribution (K+A or E+A, Poggianti and Wu (2000)). Finally, the system relaxes and evolves into a passive elliptical with no star formation, rapidly moving from the blue cloud to the red sequence in the galaxy color-magnitude diagram. The whole merger process is also defined as the Toomre sequence, from the pioneering work of Toomre and Toomre (1972), but a more recent version has also been summarized by Hopkins et al. (2008a), as shown in Fig. 1.4.

This theoretical connection between starbursts, mergers and AGNs is well supported by observations in the local Universe. Infrared luminous galaxies were first discovered in the 1980s with the Infrared Astronomical Satellite (IRAS), and it soon became clear that almost all of them show signs of recent or ongoing interactions, such as shells, tidal tails and complex kinematics (Joseph and Wright, 1985; Sanders and Mirabel, 1996). In addition, many ULIRGs show dominant either non-thermal optical emission lines, a mid-IR dusty torus component in the SED, or X-ray/radio luminosity in excess to that produced by star-formation, all of which reveal the presence of an

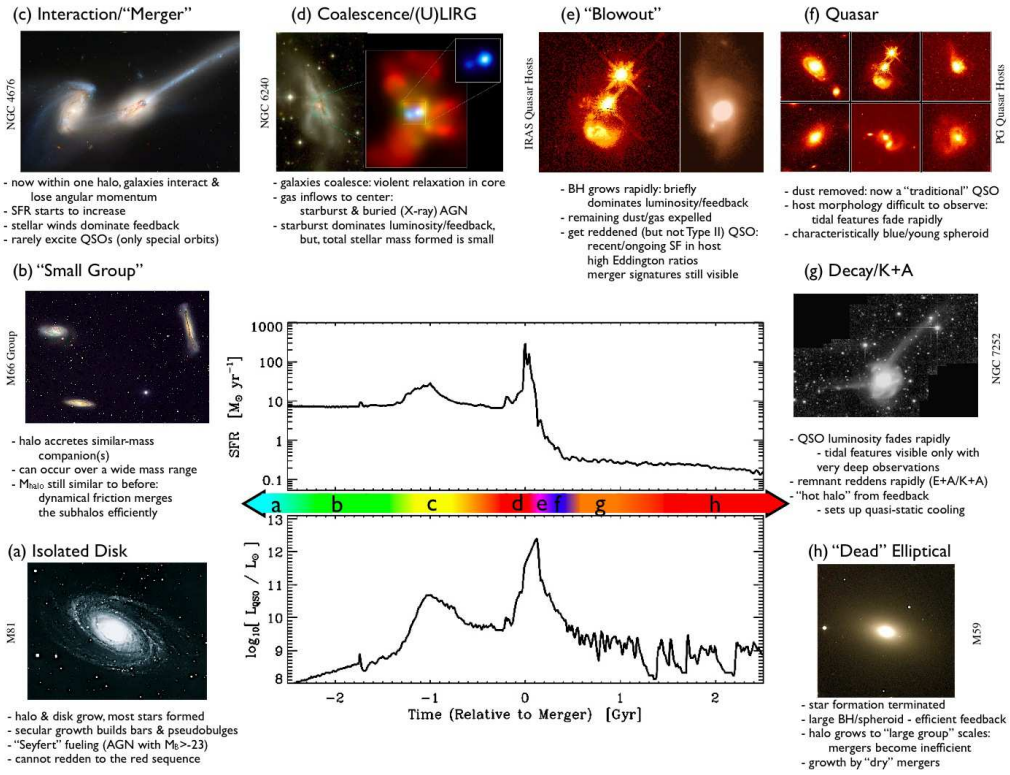

Figure 1.4: A schematic representation of the different phases of a gas-rich major merger event, from Hopkins et al. (2008a).

embedded active galactic nucleus (Sanders et al., 1988).

Despite this observational evidence, many details are still poorly understood, especially when we look at earlier cosmic times. How many of present-day early type galaxies formed through merger triggered starbursts ? Does the starburst - merger connection hold at all epochs ? Are most luminous AGNs induced by mergers and do all mergers trigger AGNs ? What is the role of feedback and how it affects the host galaxy ? These and many other questions are still open and will represent a hot topic in this research field during the next decade.

1.3 Dust extinction

In addition to the gaseous content, dust represents another important component of the interstellar medium (ISM) in galaxies. In the astrophysical context, it refers to a mixture of particles of different sizes, typically ranging 0.001-1 μm, and various composition, including silicates, carbonaceous grains (e.g., graphite) and 'Polycyclic Aromatic Hydrocarbons' (PAH). Their constituting metal elements (e.g., O, C, Si, N) are formed in stars, and are spread in the surrounding interstellar medium (ISM) at different stages of stellar evolution

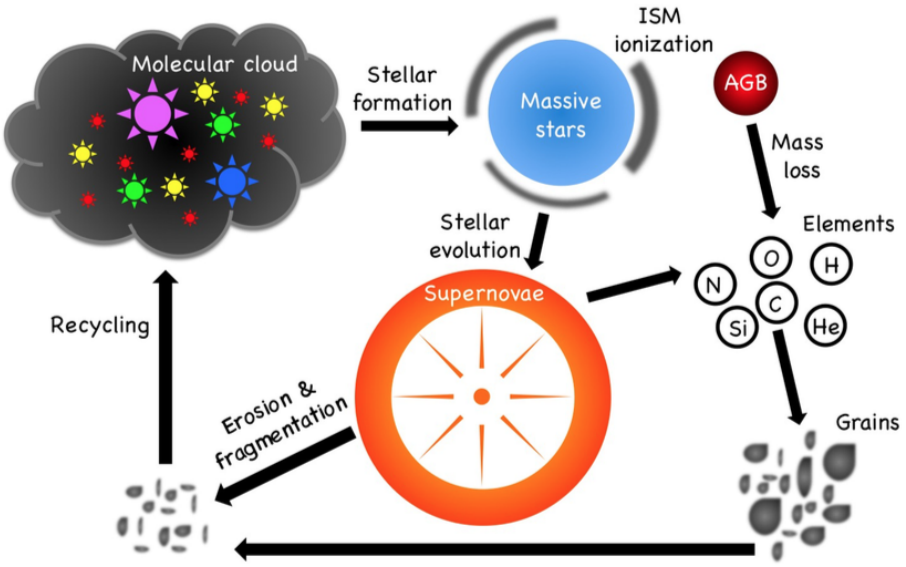

Figure 1.5: A schematic representation of the lifecycle of dust grains, with all the main processes responsible for their formation, destruction and then recycling. Credits: F. Galliano.

through winds or supernova explosions. In the ISM, the dust grains can assemble, grow, be destroyed, or even pollute neighbouring molecular clouds, from which a new generation of stars can form. This highly dynamic process is schematized in Fig. 1.5.

Despite representing a minor fraction of the ISM in mass ($\sim$ 1%), the dust has a major impact on the propagation of starlight and on the outcome spectrum of any system, due to photon absorption and scattering, whose combination is called interstellar extinction. These physical mechanisms increase the dust temperature and absorb up to $\sim$ 99% of the energy from stellar light, which then is re-emitted in the infrared wavelength range as greybody radiation. Figure 1.6 shows an example of how the intrinsic spectrum of a source (blue and red lines) is modified and how the energy stored by the dust is released at infrared wavelengths (pink curve).

The effects of dust can be described quantitatively under specific assumptions of its distribution with respect to the gas and stars in the galaxy. I will discuss in the following sections two opposite configurations that are the most considered in the literature: a foreground dust geometry and a mixed distribution of dust and stars. They are shown in Fig. 1.7, which also highlights the huge impact of the two different geometries on the emergent radiation spectrum. I remark however that these two configurations are not exaustive, as some intermediate situations (e.g., a clumpy structure) can be also be possible (see, e.g., Section 4 of Calzetti, Kinney, and Storchi-Bergmann (1994) for a review of all principal geometries).

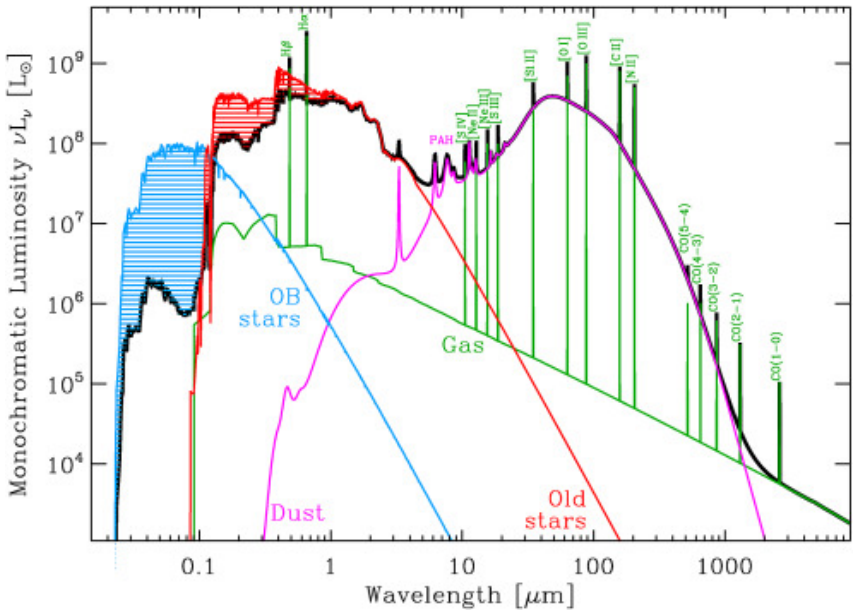

Figure 1.6: Figure showing a typical SED of a star-forming galaxy (in black). The hashed area is energy (ionizing in blue and not ionizing in red) absorbed by the gas and dust particles. In particular, the dust will re-emit the absorbed radiation at longer wavelengths in the infrared (pink curve). Credits: F. Galliano.

1.3.1 The dust screen geometry

The simplest model is a dust screen: it consists of starlight radiation (typically from a young star-forming region) crossing a dust cloud with a given, wavelength dependent, optical depth $\tau(\lambda)$, which is sensitive to the dust column density N_{dust} (the amount of dust along the line of sight). The monochromatic flux received by the observer can be related to the intrinsic emitted flux through the following definition:

$$f_{obs}(\lambda) = f_{int}(\lambda) \times e^{-\tau(\lambda)} = f_{int}(\lambda) \times 10^{-0.4A(\lambda)} \tag{1.2}$$

where the last term of the equation is expressed in magnitudes. We deduce from Eq. 1.2 that $A(\lambda) = 1.086 \times \tau(\lambda)$.

The extinction $A(\lambda)$ at a wavelength λ can be written as a product of two different components as:

$$A_\lambda = k(\lambda) \times E(B\text{-}V), \tag{1.3}$$

where $k(\lambda)$ is the reddening curve (also called the total-to-selective extinction), which encodes the wavelength dependence of the extinction, depending only on the physics of the dust grains. E(B-V) is instead the color excess ($=A_B$-A_V[1]), which measures the total amount of extinction ($\propto N_{dust}$) and

[1] B and V are broadband optical bands centered at 440 and 560 nm, respectively. However, the color excess can be also applied to different wavelengths and bands, as in general we have $E(\lambda\text{-}\lambda_0) = A_\lambda$-$A_{\lambda_0}$.

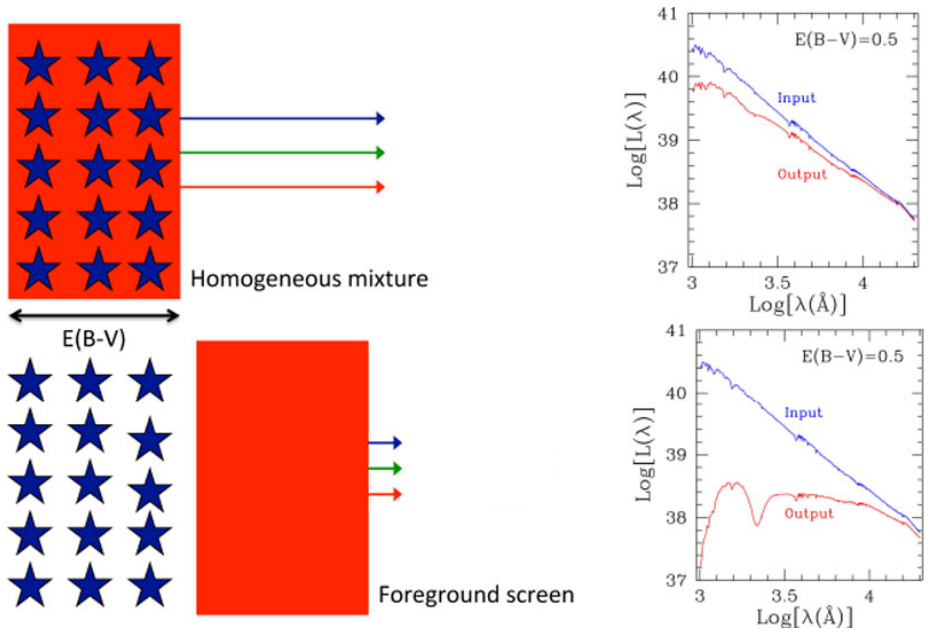

Figure 1.7: Cartoon representations of the foreground dust and mixed model configurations (top and bottom, respectively). In both panels, the stars have the same characteristics, and the dust obeys the Milky Way extinction curve (which has a prominent absorption feature at 2175Å) with a thickness of E(B - V) = 0.5. The panels to the right display the input stellar SED, which is the same for the two cases (blue; top spectrum), and the output SED (red; bottom spectrum). This exercise demonstrates that just the geometric relation between dust and stars has a huge effect on the final emerging spectrum of a source. Credits: Daniela Calzetti.

does not depend on the extinction function. Indeed, the different laws are normalized to k(B)−k(V)= 1.

Another important quantity is the total-to-selective extinction at V, that is, $R_V = A_V/E(B\text{-}V)$. This parameter, which can be estimated from the IR slope of the extinction curve, characterizes the different dust environments along the line of sight. It depends indeed on the size distribution of the dust grains and is typically higher in denser regions, where larger grains can form. Also, extinction curves with smaller R_V are steeper toward shorter wavelengths.

The figure 1.8 shows different extinction curves that are commonly adopted in the literature: three derived for the Milky Way (MW) with different R_V values, and two derived for the Small and Large Magellanic Clouds (SMC, LMC). As a common behaviour, the ISM is more transparent at longer wavelengths (toward the IR), for which reason the dust has also the effect of "reddening" the spectra of astrophysical sources. However, we can see that LMC and SMC curves are significantly different from those observed in the Milky Way. In particular, they have different slopes in the far-Ultraviolet (steeper in the SMC case). This has been attributed to a lower metallicity in the Clouds, which causes the molecular clouds to be more diffuse (Pak

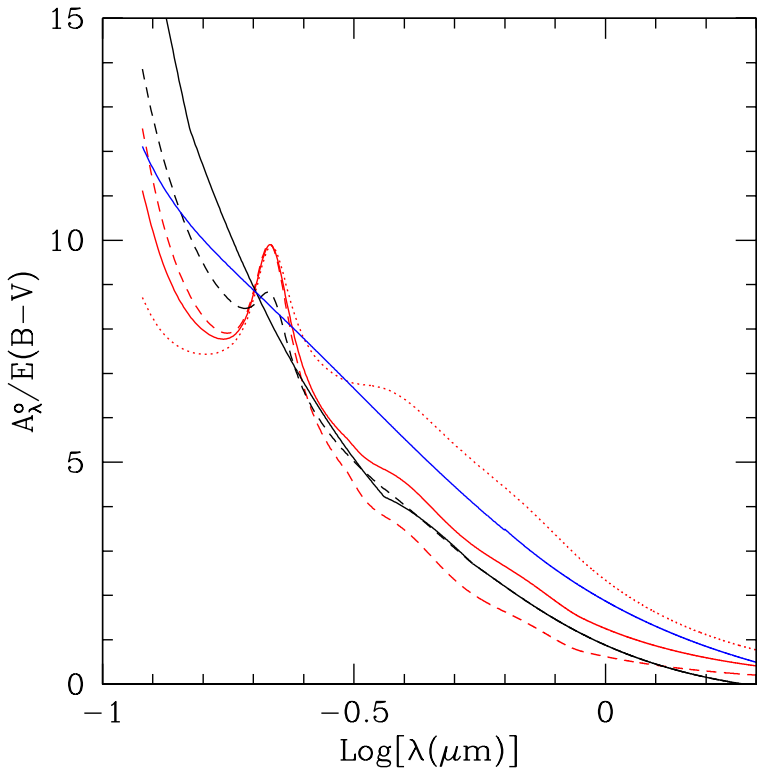

Figure 1.8: Examples of extinction curves in local galaxies. The MW extinction curve is shown for three different values of R(V), 3.1 (solid red line), 5.0 (dashed red line), and 2.0 (dotted red line) (Cardelli, Clayton, and Mathis, 1989; Fitzpatrick, 1999). The extinction curves of the Large Magellanic Cloud's 30 Doradus region (dashed black line) and of the Small Magellanic Cloud's bar (solid black line) are reported for R(V) = 2.7 (Gordon and Clayton, 1998; Misselt, Clayton, and Gordon, 1999). The starburst obscuration curve (Calzetti et al., 2000) (blue line) is shown here for a purely illustrative comparison because it refers to the dust obscuration of galaxies which is conceptually different from the dust extinction of stars. This curve will be discussed in Section 1.4. Credits: Calzetti (2001a).

et al., 1998) and, possibly, to produce on average smaller dust grains (Misselt, Clayton, and Gordon, 1999). Furthermore, the small UV-bump at $\sim$ 2175 seen through the MW (produced by the absorption of small graphite grains) is much less visible when looking at our satellite galaxies, possibly related to the different ongoing star formation activity (Fitzpatrick, 1986; Gordon and Clayton, 1998; Misselt, Clayton, and Gordon, 1999).

1.3.2 The mixed model

The mixed model reflects the presence of dust between the ionizing stars. Quantitatively, it has a different formulation from the dust screen geometry

(Eq. 1.2). The emergent radiation can be written in this case as:

$$f_{obs}(\lambda) = f_{int}(\lambda) \times \frac{1 - e^{-\tau'(\lambda)}}{\tau'(\lambda)}, \tag{1.4}$$

where τ' is in general different from that in Eq. 1.2 and needs a local extinction law to be assumed. In contrast with the dust screen model, in a mixed model the line ratios tend to saturate at a specific, wavelengths dependent value at increasing opacity. In Chapter 3, I will derive an analytic formula for the mixed model to calculate the observed flux as a function of the total integrated extinction, and the asymptotic value reached by emission line ratios at decreasing optical depths. I will also show how to derive an equivalent $k(\lambda, \tau)$, which allows to use a similar expression of the dust-screen formalism (Eq. 1.2) even with a mixed dust-stars geometry.

In general, a foreground dust screen produces the largest reddening and dimming among all possible configurations, at fixed E(B-V). On the other hand, a homogeneous mixture of dust and stars produces a SED with a similar shape of the intrinsic one, but dimmer (Fig. 1.7). Thus, in order to discriminate between the dust-free and the mixed models, we need indirect measurements of the total unobscured luminosity, such as that measured in the infrared.

1.4 Dust in starbursts

When we consider more distant objects such as galaxies, the situation is in general more complex than in the Milky Way and its neighbours, because single stellar complexes and HII regions can no longer be resolved.

The galaxy integrated dust properties are also generally referred with the term attenuation, which includes all possible mechanisms affecting the light propagation in the system (e.g., absorption, scattering towards the line of sight), and describes the global relation between the intrinsic and observed emission. Compared to the extinction, the attenuation accounts for the effects of geometrical distribution and mixing of different star-forming regions in the whole galaxy.

Despite the variety of extragalactic systems, we can classify their dust properties into few categories: (1) normal star-forming galaxies are characterized by widespread star-formation distributed across the disk with relatively low SFR surface density; (2) UV-bright starbursts are systems with a centrally concentrated star-formation activity in the inner 1-2 kpc, implying high SFR surface densities (SFR/area > 1 $M_\odot$ yr^{-1} kpc^{-2}), and with significant emission in the UV spectral range; (3) LIRGs and ULIRGs have instead equal or more compact star-formation, but they emit almost all the energy (90% or more) in the infrared rest-frame.

UV-bright starbursts have been studied since 30 years ago, and they appear to have a regular attenuation behavior. In particular, they behave

as if the dust is located in a shell surrounding the starburst region (Calzetti, Kinney, and Storchi-Bergmann, 1994; Calzetti et al., 2000; Calzetti, 2001), hence they can be treated with a foreground dust screen model. The analytic formula of the attenuation curve k(λ) is described by Calzetti, Kinney, and Storchi-Bergmann (1994) as:

$$\begin{aligned} k(\lambda) &= 2.659(-1.857 + 1.040/\lambda) + R_{\mathrm{V}} \\ &\qquad (0.63\mu\mathrm{m} \leq \lambda \leq 2.20\mu\mathrm{m}) \\ &= 2.659(-2.156 + 1.509/\lambda - 0.198/\lambda^2 + 0.011/\lambda^3) + R_V \\ &\qquad (0.12\mu\mathrm{m} \leq \lambda < 0.63\mu\mathrm{m}) \end{aligned} \tag{1.5}$$

and $R_{\mathrm{V}} = A_{\mathrm{V}}/E(B-V) = 4.05$.

The main features of this attenuation law are the absence of the $0.2175\mu m$ 'bump' (typical of regions in our Galaxy) and the grayer slope compared to the MW and LMC extinction laws (black curve in Fig. 1.8).

This curve was initially calibrated on a sample of 39 nearby UV-bright starbursts, but today it is also applied to correct UV/optical emission for dust in spatially integrated observations of high redshift galaxies. In particular, it is widely adopted in SED-fitting codes to reconstruct the intrinsic stellar SED of a galaxy (Ilbert et al., 2006; da Cunha, Charlot, and Elbaz, 2008; Noll et al., 2009; Bolzonella, Miralles, and Pelló, 2000). However, its universal validity is still debated. For example, Johnson et al. (2007) and Reddy et al. (2015) find good agreement with the local starburst attenuation curve, while Buat et al. (2012) report variations in the attenuation curve slope up to $\sim$ 40%. These variations however, seem to be mostly related to variations between individual galaxies. The usage of this curve seems to be still appropriate to large samples, at least in local galaxies (Battisti, Calzetti, and Chary, 2017).

Moreover, Calzetti, Kinney, and Storchi-Bergmann (1994) found that the stellar radiation is subject to almost half of the attenuation affecting the emission lines, which trace the ionized gas and recent star formation. This can be written as:

$$E(B-V)_{\mathrm{stars}} = 0.44 \times E(B-V)_{\mathrm{gas}} \tag{1.6}$$

The origin of this correlation has been explained by Calzetti (2001) as due to geometrical effects, together with the physics of star-forming regions and the aging of stellar populations. In particular, as the newly formed stellar population evolves, the inside of the native star-forming region becomes depleted of dust, because of dust grain destruction by supernovae shocks, hot star winds and supernovae-driven outflows. The expelled dust will act then as a foreground-like distribution for both the gas and the central stars (see Fig. 8 of Calzetti, Kinney, and Storchi-Bergmann (1996)). However, we have to consider two additional effects. On the one hand, because of its closer

spatial association with dust (Calzetti, 1997), the ionized gas will be more obscured than the stars. On the other hand, the long-lived, non-ionizing stars from previous generations have time to *diffuse* into regions of lower dust density (Calzetti, Kinney, and Storchi-Bergmann, 1994; Charlot and Fall, 2000; Granato et al., 2000), since their native clusters are disrupted by evaporation or by the host galaxy's gravitational field (Leisawitz and Hauser, 1988; Kim et al., 1999; Tremonti et al., 2001). For example, cooler stars in the LMC have been observed to be less embedded in dust compared to hotter stellar populations (Zaritsky, 1999).

To measure E(B-V) (or, equivalently, A_V) of the ionized gas, we can consider multiple hydrogen recombination lines, covering as much spectral range as possible, in order to probe different dust optical depths. In the simplest case, the brightest lines of the Balmer series (i.e., Hα and Hβ) are adopted. The amount of extinction is then found solving the following equation (Calzetti, Kinney, and Storchi-Bergmann, 1996):

$$E(B-V)_{H\alpha/H\beta} = \frac{log_{10}(R_{obs}/R_{int})}{0.4[k(H\alpha)-k(H\beta)]}, \tag{1.7}$$

where R_{obs} and R_{int} are the observed and intrinsic Hα/Hβ ratios, respectively.

As an alternative, in the absence of spectral information, we can derive $E(B-V)_{stars}$ from fitting synthetic stellar population models to the photometry, and then applying Equation 1.6 to infer the attenuation of the ionized gas.

1.4.1 The A_{IRX}-β relation

An important discovery for UV-bright starbursts is that their color excess E(B-V) (or their A_V) is tightly correlated with the slope of their UV spectra expressed in f_λ in the range 1300-2600 Å rest-frame, also called β-slope. According to this relation, more attenuated objects have redder UV spectra (Calzetti, Kinney, and Storchi-Bergmann, 1994). Similarly, a relation exists between β and the infrared excess A_{IRX}, as derived by Meurer, Heckman, and Calzetti (1999):

$$\begin{aligned} A_{IRX} &= 4.43 + 1.99 \times \beta \\ A_{IRX} &= 2.5 \times log_{10}\left(\frac{L_{IR}}{L_{UV}} + 1\right), \end{aligned} \tag{1.8}$$

where L_{UV} (and thus A_{IRX}) are calculated at 1600 Å in the original Meurer, Heckman, and Calzetti (1999) work, while β is the spectral slope in f_λ, derived between 1250 and 1950 Å. This formula is very useful to infer the total SFR in high-redshift UV-bright starbursts using just the near-IR/optical spectrum or color, when the far-IR photometry, tracing dust emission, is not available.

A modern version of the Meurer, Heckman, and Calzetti (1999) relation is shown in Fig. 1.9. In this diagram, we can also recognize the distribution of other types of galaxies. Normal star-forming systems with lower SFR are

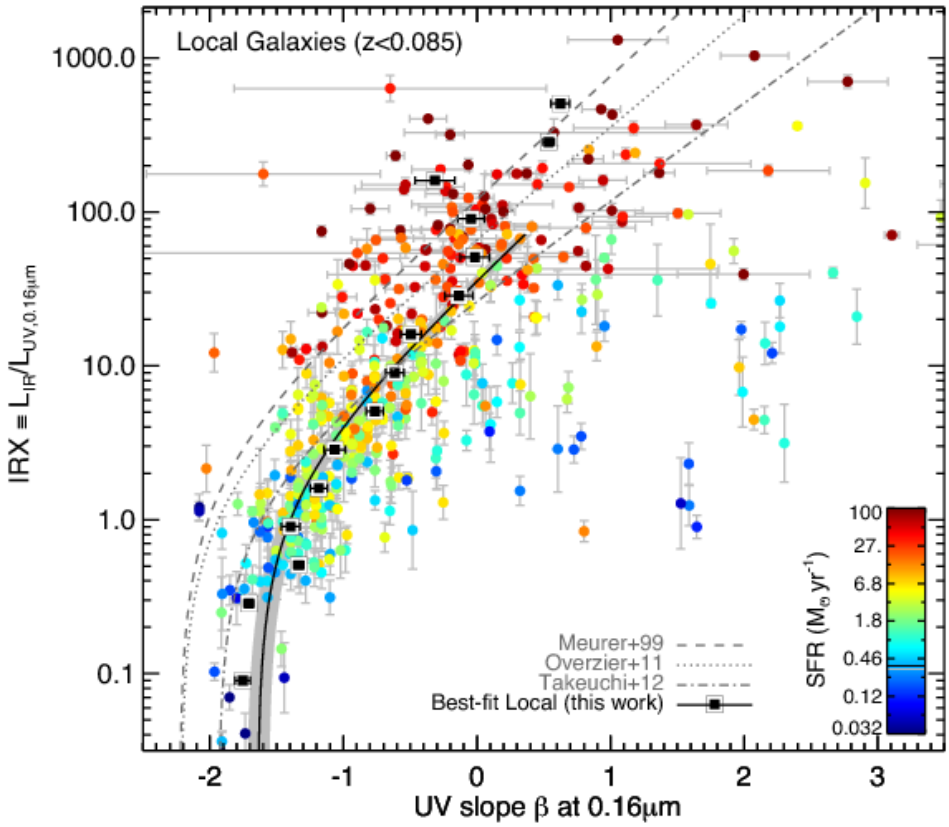

Figure 1.9: A_{IRX} - β relation for local galaxies (solid black curve with gray uncertainty envelope), color coded according to their SFR, from Casey, Narayanan, and Cooray (2014). Black squares denote the median UV slope in fixed IRX bins. The colored points comprise a representative sample of all galaxies in the local volume, including 1034 nearby galaxies described by Gil de Paz et al. (2007) and 135 local (U)LIRGs from Howell et al. (2010). For comparison purposes, the original relation from Meurer, Heckman, and Calzetti (1999) for blue compact starbursts is highlighted with a dashed gray line, the local Lyman-break analog (LBA) relation determined in Overzier et al. (2011) is shown with a dotted gray line. The revised relation (including aperture corrections) to the Meurer, Heckman, and Calzetti (1999) from Takeuchi et al. (2012) is also drawn with a dotted-dashed line.

generally located below bright UV-starbursts. However, they have a large scatter ($\sim$ 10 times larger than SBs) (Buat et al., 2002; Buat et al., 2005; Calzetti et al., 2005; Boquien et al., 2009; Boquien et al., 2012), explained as a combined effect of different ages of the underlying O-B stellar population, together with scatter and spatial variations in the dust geometry and composition.

On the other hand, local and some distant LIRGs and ULIRGs (which have the highest L_{IR} and SFR) lie above the Meurer A_{IRX}-β relation (see also Goldader et al. (2002) at $z \sim 0$ and Reddy et al. (2010) at $z \sim 2$), meaning that it is not possible to recover the total infrared luminosity of the system from the UV slope. Indeed, Goldader et al. (2002) showed that the global UV emission of a sample of 7 local ULIRGs, even after correction for dust

reddening, fail to account for the total bolometric luminosities by factors of 3 to 75. This result indicates that LIRGs and ULIRGs may follow in general different dust-star geometries, as already suggested by Calzetti (2001).

1.5 Thesis motivation

Beyond the local Universe, the properties, nature and future evolution of infrared luminous starbursts are not yet fully understood. These systems, in contrast with UV-bright starbursts, are typically defined by having a SFR (inferred from their infrared luminosity) significantly higher than the average level of the whole star-forming galaxy population at fixed stellar mass M_* and redshift. In other words, they are typically selected as being a factor of 3 or 4 above the Main Sequence (MS), the correlation between M_* and SFR observed for the majority of star-forming galaxies (Noeske et al., 2007; Daddi et al., 2007; Elbaz et al., 2007). While all of them typically have $L_{IR} > 10^{11}$ $L_\odot$, they do not always exceed $L_{IR} > 10^{12}$, depending on their stellar mass.

The origin of this classification comes from the idea that two main star-forming modes exist in the Universe: a secular evolution typical of spiral galaxy disks, and an enhanced efficiency star-forming mode likely triggered by merger interactions. If we analyze the SSFR (or distance from the MS) the two populations present two distinct normal distributions, with starbursts located at higher values (Fig. 1.10).

Recently, in Puglisi et al. (2017), we studied the optical rest-frame spectra of a sample of 12 IR-luminous, Herschel-detected starbursts at $z \sim 1.6$ and average SFR a factor of 8 above the MS, with the final goal of inferring their attenuation pattern and their intrinsic metallicity. We found that the attenuation derived from the Balmer decrement ($A_{H\alpha,BD}$) is orders of magnitudes lower than calculated from the IRX method ($A_{H\alpha,IRX}$, comparing Hα to the bolometric IR SFR). We initially explained this discrepancy by assuming a two component model for the galaxy: an inner core very obscured (optically thick) and an external, optically thin envelope. In this dust-stars configuration, it is possible to put constraints on the SFR and dust attenuation of the two components, making some assumptions.

In the first case, we can assume that the inner part has an infinite attenuation ($A_{H\alpha,thick} = \infty$). With this hypothesis, the core would be unobservable in the optical, despite containing almost all of the total SFR of the system ($\sim$ 89%). The skin is therefore entirely responsible for the emission lines observed, and the Balmer decrement allows to infer its optical depth. On the other hand, if we consider a dust-free thin component ($A_{H\alpha,thin} = 0$), it would be possible to infer a lower limit on the attenuation of the thick component as $A_{H\alpha,thick} = 4.5$ mag. In this limiting situation, the core would give its maximum possible contribution to the optical emission lines of $\sim$ 33%, while contributing $\sim$ 94% to the SFR_{tot}.

An important consequence of this study is that from optical lines only (e.g., Hα, [NII]λ6583, [SII]$\lambda\lambda$6719-6731) it is basically impossible to infer

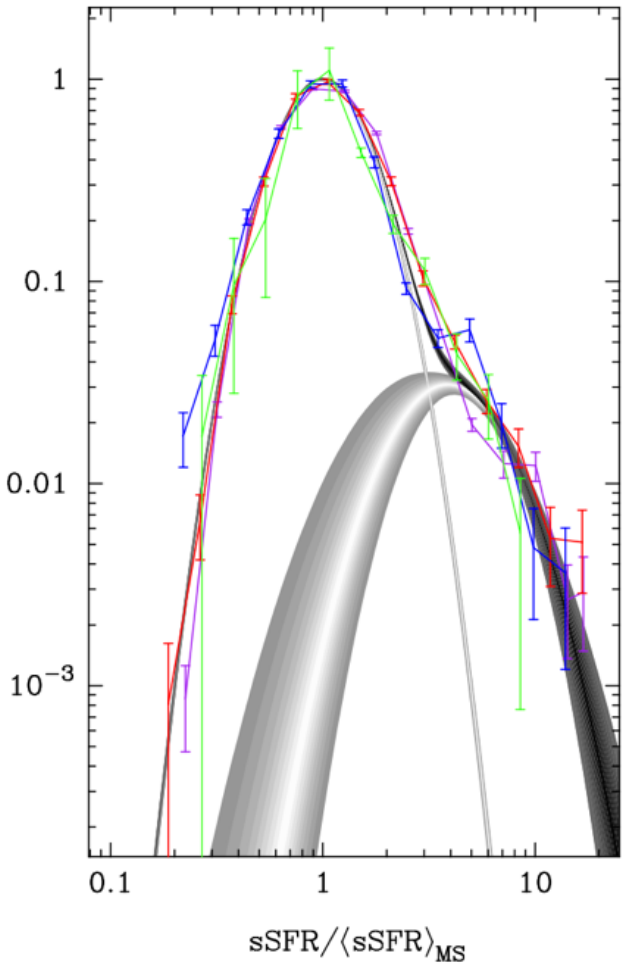

Figure 1.10: Double gaussian sSFR distribution for main sequence and starburst galaxies at $z \sim 2$ with $M_* > 10^{10}$ $M_\odot$, peaking at lower and higher sSFR, respectively. Gray bands indicate the 95% confidence regions, while the black line traces the total (main-sequence + starburst) distribution. From Sargent et al. (2012).

the metallicity, ionization and density of the whole ISM, since the lines are representative of small unattenuated regions. It is thus evident that, if we want to really characterize those objects, we need to penetrate deeper into the dust and probe larger optical depths, which would be possible only by observing them at longer wavelengths. For example, already in the near-infrared rest-frame, the Paβ and [FeII]λ1.257-1.321μm lines, accessible in K band from the ground up to $z \sim 0.9$, can be 20 times less attenuated than Hα in the case of strong attenuation conditions expected for these systems. With Paα and Brγ, the improvement would be even higher.

Additionally, probing systematically near-IR rest-frame lines in the dusty star-forming population to study their stellar and gas properties has a particular and compelling interest nowadays. First of all, very soon JWST will be able to detect them at very faint levels during the cosmic noon ($1 < z < 3$), when most of the SFR density of the Universe resided in dusty galaxies, and

even at earlier cosmic epochs up to reionization. Despite this clear opportunity, only few studies in the local Universe have exploited this spectral range for limited classes of galaxies (Mason et al., 2015; Martins et al., 2013).

Now appear thus clear the benefits that more near-infrared rest-frame spectral observations will apport to the astrophysics research, and why this study could and had to be undertaken at this time. My thesis tries to cover this missing knowledge in preparation for future surveys, while simultaneously characterizing the properties of high-redshift infrared luminous starbursts. To fulfil these goals, this project was built on near-IR rest-frame observations of representative starbursts at intermediate z, and then continued with complementary spectra taken for normal star-forming galaxies and an analysis of the morphology of both MS and SB systems.

In particular, during the first year I followed up a sample of 25 starbursts at $0.5 < z < 0.9$ with FIRE, a near-IR spectrograph mounted at the Magellan telescope in Chile, in order to probe the $0.6 < \lambda < 1.3$ Å rest-frame spectral range and primarily constrain their attenuation properties (hence their nature). This sample was selected in COSMOS field to be representative of starburst galaxies above a stellar mass of 10^{10} $M_{\odot}$. Along the way, these unique data offered the opportunity to investigate and physically characterize the different phases of the starburst and merger phenomena, similarly to what can be seen in simulations.

Finally, the clumpy morphology observed with HST (i-band) for many starbursts and merging systems in the original parent sample in COSMOS prompted us toward a deeper investigation of the physical properties and formation mechanisms of clumps. Even though they are typically associated to violent disk instabilities in highly turbulent gas rich disks, our data suggest on visual inspection that mergers could be at least competitive mechanisms of clumps formation at all redshifts, as tentatively suggested by other works for specific redshift and galaxy stellar mass regimes (e.g., Puech, 2010). Even though this represents a secondary topic of my PhD project, the clump formation mechanism is still important to understand the distribution of star-formation during a merger, and possibly explain the variety of extragalactic systems and morphologies observed in the present-day Universe.

The thesis is organized in 7 Chapters, each dedicated to a specific topic as explained below:

- **Chapter 2:** This chapter summarizes the methodology of my work. In particular, I show how the main galaxy properties are derived, such as the stellar mass, the SFR and the size of star-forming regions in radio. I also describe the sample selection, the spectroscopic observations (with Magellan-FIRE) and data reduction for a subset of 25 starbursts in the COSMOS field.

- **Chapter 3:** Here I present the first observational results on the attenuation of the Magellan starbursts. This is the most important parameter

to investigate the nature of distant starbursts, as it will remain the reference quantity throughout the whole thesis.

- **Chapter 4:** I study the origin and physical interpretation of the attenuation sequence found in chapter 3. To this aim, I compare and correlate the attenuation to other physical properties of the systems, namely the radio (3 GHz) sizes, the [NII]6583Å/Hα emission line ratios, the line velocity widths and the equivalent widths (EW) of Balmer and Paschen lines. Finally, I explain the different evolutionary phases of a merger, which I interpret as the most likely responsible for the observed correlation sequence.

- **Chapter 5:** Here I analyze in a more quantitative way the morphological properties (i.e., merger signatures, clumpy structure) for all the starbursts in COSMOS field and for a representative subset of normal star-forming Main Sequence galaxies. In particular, I define the clumpiness parameter and describe the clumps identification procedure from i-band (F814W) HST images, which will be used for the last main topic of this thesis.

- **Chapter 6:** I compare the quantitative merger diagnostics and the clumpiness of starburst galaxies to those of main sequence systems. The aim is to verify a connection between mergers and the formation (or the enhancement) of clumpy structures in the galaxies. In the same chapter, I will also present novel hydrodynamical simulations of colliding galaxies with typical conditions (i.e., gas fractions) of $z \sim 0.7$ disks, which are then compared to observational results.

- **Chapter 7:** This final part contains a summary of the main results and conclusions of my thesis, followed by perspectives and ideas to develop in the future after the PhD.

Chapter 2

Sample selection and observations

In this chapter I present the original sample that I used to study the properties of distant galaxies. In the first part, I will describe the basic multi-wavelength informations that are already available from previous surveys, and the main physical properties derived for all the objects, including redshift (z), stellar masses (M_*), star-formation rates (SFR) and radio sizes. In the second part I will present instead new spectroscopic observations with Magellan-FIRE for a subset of starbursts, followed by a detailed description of data reduction and emission line measurements. All this information will be used systematically for deriving the main results of this thesis in subsequent chapters.

2.1 The COSMOS field

The Cosmic Evolution Survey (COSMOS) is a large program to study the galaxy properties, their environment and evolution with cosmic time. It surveys a wide region in the sky, dubbed COSMOS, centered at RA$= +150.11917$ and DEC$= +2.20583$ degrees (J2000 reference system), extended over an area of approximately 2 square degrees, ~ 16 times the size of the full moon. This part of the sky was chosen because of the presence of a few stars and the lower galactic extinction, reducing dust contamination and allowing to observe fainter sources in the extra-galactic Universe.

COSMOS is the perfect field for the goals of this thesis, because of the multi-wavelength data available for hundreds of thousands of galaxies. Given the rare fraction of starbursts, which represent 2-4% of the whole star-forming population at all redshifts (Schreiber et al., 2015), the large area of COSMOS allows then to select a sizeable, statistical subset of this kind of objects, with uniform observational coverage, photometric properties and physical parameters estimations.

This field has been observed at all accessible wavelengths from X-rays to radio at different depths, in narrow, intermediate and broad-band filters, using both space (Hubble, Spitzer, GALEX, XMM, Chandra, Herschel) and ground-based telescopes (Keck, Subaru, Canada France Hawaii Telescope (CFHT), Very Large Array (VLA), ESO Very Large Telescope (VLT)). In the X-rays, COSMOS has been observed by both XMM-Newton and Chandra in the energy range 0.5-2 keV (X-ray soft) and 2-10 keV (X-ray hard) (Marchesi

et al., 2016; Civano et al., 2016). GALEX has imaged the field in the near and far Ultraviolet, at $\sim$ 2310 Åand $\sim$ 1530 Å, respectively, down to magnitudes of $m_{AB} = 25.5$ (Zamojski et al., 2007).

In the optical range, 590 HST orbits were allocated to observe 1.7 square degrees of the COSMOS field in F814W at a resolution of $0.095''$ and depth of 27.2 AB magnitude (for a point source at 10σ) (Koekemoer et al., 2007). Smaller areas were also covered with other filters: 88 HST orbits were used in the CANDELS project (Koekemoer et al., 2011) to obtain images within an area of 0.05 square degree in four broad-band filters (F160W, F814W, F125W and F160W) at resolutions of $0.08''$, $0.09''$, $0.12''$ and $0.18''$, respectively. More recently, the COSMOS-DASH program (PI: van Dokkum, Momcheva et al. (2016)) has observed in 57 orbits a larger area of 0.6 square degrees with the WFC3/IR camera, producing high-resolution ($0.2''$) images in H(F160W) band to a magnitude limit of 25. From the ground, extensive imaging observations were carried out with the Subaru Suprime-Cam in BVgriz broad-bands by Taniguchi et al. (2007) down to iAB $\sim$ 26.5 mag, as well as with CFHT Megacam in the u-band by Boulade et al. (2003).

At longer wavelengths, UltraVISTA has mapped ~ 1.8 deg^2 of COSMOS in YJHKs, plus half that area in the NB118 narrow-band filter at $1.19\mu m$ (Milvang-Jensen et al., 2013). UltraVISTA consists of two main parts: a deep survey reaching Ks $= 23.7$ AB mag (5σ) over the full area, and an ultra-deep survey reaching Ks $\simeq 25.3$ and H $\simeq 25.7$ AB mag (both 5σ) over four stripes covering a total of ~ 0.8 deg^2 in the final data release (McCracken et al., 2012). The Spitzer space telescope observed COSMOS in the mid-IR through several different programs. In particular, deep images are taken with the infrared camera array (IRAC) at $3.6\mu m$, $4.5\mu m$, $5.8\mu m$, and $8.0\mu m$ (respectively, channels 1, 2, 3, and 4), as part of the SPLASH (PI: P. Capak) and S-COSMOS (Sanders et al., 2007) programs. The magnitude limits (3σ depth, $3''$ aperture) are 25.5 AB mag for 3.6 and $4.5\mu m$ data, and 23 mag for IRAC channel 3 and 4. Moreover, Le Floc'h et al. (2009) presented images at $24\mu m$, taken with the Multiband Imaging Photometer for Spitzer (MIPS) instrument, reaching a sensitivity of 80μJy.

In the far-infrared, COSMOS has been observed by the Herschel telescope at 100 and $160\mu m$ with the PACS instrument, and at 250, 350, and $500\mu m$ with SPIRE. In the first case, maps are available from the PEP (PI: D. Lutz; Lutz et al. (2011)) and CANDELS-Herschel (PI: M. Dickinson) programs, while SPIRE data come from the Herschel Multi-tiered Extragalactic Survey (HerMES; PI: S. Oliver). The 3*sigma* depths for a point source are, in order of increasing wavelength, 5, 10.2, 8.1, 10.7 and 15.4 mJy, with angular resolutions ranging 5-$37''$. Bolometer observations are then available in the sub-mm range. In particular, we will use SCUBA2 $850\mu m$ images from the S2CLS program (Cowie et al., 2017; Geach et al., 2017), AzTEC $1.1mm$ nested maps from Aretxaga et al. (2011), and MAMBO $1.2mm$ images from Bertoldi et al. (2007). Finally, radio observations complete the multi-wavelength dataset images used for our analysis. The VLA-COSMOS 1.4 GHz (20 cm) surveys

(Schinnerer et al., 2007; Schinnerer et al., 2010) represent the largest radio deep field so far, at a depth *rms* of 7-15 μJy/beam over the 2 square degrees, and angular resolution $\sim 1.5''$. Similarly, 3 GHz (10 cm) radio images are available from VLA-COSMOS 3GHz large project (Smolčić et al., 2017), with a sensitivity $\sigma = 2.3\mu$Jy and FWHM $\sim 0.75''$.

All this broad imaging dataset was used to build large catalogs containing photometric and physical informations for thousands of sources in the whole COSMOS field. The catalog of Muzzin et al. (2013) presents PSF matched photometry in 30 photometric bands for a sample of $\sim$ 260k Ks-selected sources reaching $m_{AB} = 23.4$ mag over a portion of 1.62 deg^2. More recently, Laigle et al. (2016) presented the COSMOS2015 catalog, which contains photometric data from Ultraviolet to Spitzer IRAC bands for more than half a million objects in the whole 2 square degree field, including deeper, updated ULTRAVista YJHKs images, and deriving from them accurate photometric redshifts and stellar masses. On the other hand, Jin et al. (2018) published the "super-deblended" far-infrared (FIR) to (sub)mm catalog, containing the photometry of $\sim$ 194k mass-selected galaxies (including 88000 MIPS 24μm or radio-VLA detected priors) in the 2 deg^2 COSMOS field. With these data, ranging from 24μm to 1.4 GHz, they derived infrared star-formation rates (SFR_{IR}) and dust properties for a large sample of infrared detected (S/N_{IR}) galaxies, and upper/lower limits for the remaining sample. We will see in more detail the derivation of the above mentioned properties in the following subsections.

2.2 Redshifts and stellar masses

The photometric redshifts and stellar masses of all the galaxies were computed by Laigle et al. (2016) with the code LePhare (Arnouts et al., 1999). As far as the redshift calculation is concerned, they applied the methodology described in Ilbert et al. (2013). In practice, they considered a set of templates of spiral and elliptical galaxies from Silva et al. (1998) and Polletta et al. (2007), and of young star-forming galaxies from Bruzual and Charlot (2003). The extinction was set as a free parameter, and could follow a Calzetti et al. (2000) law, a Prevot et al. (1984) law, or a modified version of the Calzetti including a "bump" at 2175Å (Fitzpatrick, 1986). The contribution of the emission lines to the spectra is also taken into account, following an empirical relation between the UV light and the emission line fluxes as in Ilbert et al. (2009). The code is based on a χ^2 procedure, according to which, at different redshift steps, the fluxes predicted in every band by each template are compared to the galaxy observed fluxes, calculating a χ^2 in each case. After producing the redshift Probability Distribution Function (PDF) from the list of χ^2, the photometric redshift is defined as the median of this distribution, while 1σ uncertainties were calculated as the range including 68% of the PDF area around the median. Through a comparison with the zCOSMOS-bright

spectroscopic redshifts, the photometric redshift precision was found to be $\sigma_{\Delta z/(1+z_s)} = 0.007$, with a catastrophic failure fraction of 0.5%.

In a similar way, the stellar masses are derived at the photometric redshifts with the same code LEPHARE, following the methodology of Ilbert et al. (2015). They used the library of Bruzual and Charlot (2003)synthetic spectra, assuming a Chabrier (2003) Initial Mass Function (IMF), a combination of exponentially declining and delayed SFH ($\tau^{-2}te^{-t/\tau}$), and two metallicities (solar and half solar). Emission lines were included as before, and two attenuation curves were implemented: the starburst curve of Calzetti et al. (2000) and a curve with a slope of $\lambda^{0.9}$ (Appendix A of Arnouts et al. (2013)). The extinctions $E(B-V)$ could take values up to 0.7. Finally, the stellar masses and corresponding uncertainties were defined, respectively, as the median of the marginalized probability distribution function (PDF) and the neighbouring range enclosing 68% of its area. I remark that, for a subset of galaxies, the spectroscopic redshifts are available from private or public optical surveys. However, considering these redshifts does not significantly affect the final values of stellar masses, since the two estimates for the parent sample are in agreement within a 1σ scatter of 0.11 dex, compatible with the uncertainties reported by Laigle et al. (2016). Only when the real redshift is very different from the photometric estimate, as in the case of catastrophic failures, this would yield a significantly different stellar mass. We will consider these isolated cases on a single basis when it happens, and adopt the new measurements for each of them.

2.3 Star-formation rates and dust properties

For a reliable selection of starburst galaxy candidates, we need accurate measurements of the star-formation rates for all the sample. Since starbursts are typically very dusty galaxies, most of the ultraviolet radiation coming from young O and B stars (which trace recent star-formation on a timescale of 100 Myr) is absorbed by dust, and then re-emitted at infrared wavelengths. Only a small part of the UV stellar radiation is able to escape the galaxy without being blocked by the intervening dust. Therefore, if I want to recover the total SFRs, I have to add the obscured and unobscured components. The first ($\mathrm{SFR_{IR}}$) can be estimated from the dust infrared emission, while the unobscured, UV-based part ($\mathrm{SFR_{UV,unobscured}}$) can be calculated from the u-band magnitudes (Laigle et al., 2016), which probes the UV rest-frame at redshift $0.5 < z < 1$, following Heinis et al. (2014). However, for starburst galaxies, the contribution of the UV-unobscured SFR to the total value is on average small (1%).

Before calculating the $\mathrm{SFR_{IR}}$, I need to properly model the emission of the dust heated by young stars (hence attributed to recent SF), and separate it from the stellar SED peaking in the near-infrared rest-frame and from warmer dust emission heated by a harder photo-ionizing source, such as an AGN. To model the dust emission due to SF, I considered the Draine

and Li (2007) library. They describe the total dust emission as originating from two components: one located in the diffuse interstellar medium (ISM) and heated by a stellar radiation field with constant intensity $U = U_{min}$, and the other exposed to a radiation field generated by photo-dissociation regions (PDRs), parametrized by a power-law U^{α}, over a range of intensities $U_{min} < U < U_{max}$, with $U_{max} \gg U_{min}$. U can be used to infer $L_{IR}/Mdust$ and the metallicity-weighted star formation efficiency (i.e., SFE/Z), according to Magdis et al. (2012). Moreover, given that it is directly proportional to the dust temperature T_{dust}, this means that a large range of T_{dust} is present.

For simplification, usually the dust is modeled with a single, or at most two representative temperatures, which define a cold and a warm component, at 18–31 K and 45-70 K, respectively. Each of them is described by a gray-body spectrum, which, summed together, yields this final dust model:

$$L_{\nu,tot} = A_1 \nu^{\beta} B(\nu, T_{cold}) + A_2 \nu^{\beta} B(\nu, T_{warm}) \tag{2.1}$$

where ν is the frequency, A_1 and A_2 are normalization factors for each gray-body, β is the dust emissivity index (assumed equal for both components)[1], while $B(\nu, T_{cold})$ and $B(\nu, T_{warm})$ are the Planck functions for the cold and warm dust components, respectively.

This warm+cold dust templates from Draine and Li (2007) were then used together with a stellar Bruzual and Charlot (2003) SED (with age 200 Myr, constant star-formation history, solar metallicity $Z_{\odot}$, Chabrier IMF and Calzetti attenuation law) and a mid-infrared AGN dusty torus SED from Mullaney et al. (2011) to fit the observed photometry from IRAC to radio 1.4 GHz, following the χ^2-based methodology described by Jin et al. (2018) and Liu et al. (2018). I show the four-components fits for all the galaxies observed at Magellan in the Appendix 2.B at the end of this chapter. The IR contribution of the AGN is typically small compared to that coming from star formation, and represents on average 3% for the starburst sample analyzed in this work.

Finally, from the best-fit dust emission SED, decontaminated from the contribution of AGN, I derived the SFR_{IR}, U_{min} of the warm and cold dust components, and the total dust masses. SFRs are computed from the integrated L_{IR} assuming a Chabrier (2003) IMF and the relation (Daddi et al., 2010):

$$\mathrm{SFR} = L_{\mathrm{IR}} / \left(1 \times 10^{10}\, L_{\odot}\right)\ \mathrm{M}_{\odot}\ \mathrm{yr}^{-1} \tag{2.2}$$

L_{IR} here was calculated integrating the best-fit dust SED from 8 to 1000 μm as:

$$L = \int_{8\mu m}^{1000\mu m} L_{\nu}(\lambda) \times \frac{c}{\lambda^2} \left[L_{\odot}\right]\ d\lambda \tag{2.3}$$

[1]The spectral index (commonly referred as α) of the dust emission in the Raleigh-Jeans (RJ) limit is $2+\beta$.

For main sequence galaxies that are undetected in the $100\mu m$ - $850\mu m$ bands (including Herschel and SCUBA2 photometry) at $S/N_{IR} < 5$, the SFRs were computed from their $24\mu m$ fluxes as explained in Jin et al. (2018). Finally, the total SFRs are calculated as $SFR_{TOT}=SFR_{IR}+SFR_{UV,unobscured}$.

Instead, the dust masses were calculated according to the two temperature dust model from Dunne and Eales (2001):

$$M_{dust} = \frac{S_{850} D_L^2}{\kappa_{850}} \times \left[\frac{N_{cold}}{B(850, T_{cold})} + \frac{N_{warm}}{B(850, T_{warm})} \right] \tag{2.4}$$

where S_{850}, κ_{850}, and $B(850, T)$ are the observed flux, the dust emissivity and the black body emission at $850\mu m$, respectively, T_{cold} and T_{warm} are the dust temperatures of the cold and warm components, and N_{cold} and N_w are the relative masses of the cold and warm dust components. The dust emissivity was set to $\kappa_{850} = 0.0383\ m^2 kg^{-1}$ (Draine, 2003).

Finally, I remark that for sources with reliable spectroscopic redshifts, the SED fitting was performed at fixed redshift, while a variation within $\pm 10\% \times (1 + z_{phot})$ was allowed for sources with an optical/near-IR photometric redshift, which procedure finally yielded an updated redshift value.

2.4 Main Sequence and Starburst classification

The SFRs derived in the previous section can be used in combination with the stellar masses and redshifts to distinguish between the population of galaxies residing in the so-called star-forming Main Sequence (Noeske et al., 2007; Daddi et al., 2007; Elbaz et al., 2007), and outlier systems in the starburst regime, owing much higher levels of star-formation for their stellar mass and redshift. In this thesis, I adopt well defined criteria to classify starburst galaxies, and that are summarized as follows.

Firstly, the starburst candidates were selected in the COSMOS field from the IR+(sub)mm catalog of (Jin et al., 2018), by requiring the spectroscopic or photometric redshift to be in the range between 0.5 and 0.9. This is the range where we can follow up these galaxies with current near-infrared spectrographs from ground-based telescopes, and detect at least Paβ and Hα lines within Y and K band.

Secondly, following Rodighiero et al. (2011), I required the SFRs to be more than a factor of 4 higher compared to the star-forming main sequence, at the same stellar mass and redshift of the galaxy. The MS was derived independently for the parent sample through a running median on 10 stellar mass bins from 10^{10} to 10^{12} $M_\odot$, however I found that it is well in agreement with that derived by Schreiber et al. (2015). Therefore, the latter MS relation (evolving with redshift) is taken as a reference throughout all the work. A useful quantity that can be derived for each galaxy is the distance from the

MS ($\mathrm{dist_{MS}}$), defined as:

$$\mathrm{dist_{MS}} = log_{10}(SFR_{\mathrm{tot}}/SFR_{\mathrm{MS}}) \tag{2.5}$$

As a third last requirement, I asked the starbursts to be Herschel detected ($\mathrm{S/N_{IR}} > 5$) and their stellar masses $\mathrm{M_*}$ to be greater than 10^{10} $\mathrm{M_\odot}$. This condition ensures that, within the mass and redshift constraints adopted in this thesis, I have a SFR complete sample of SBs with infrared-detection at $> 5\sigma$, considering the current sensitivity level (cf. Fig. 13 in Jin et al. (2018)).

This criteria finally yielded a subset of 118 Herschel-detected starbursts, which represent $\sim$ 2% of the whole star-forming population in the same mass range and redshift, in agreement with Sargent et al. (2012) and Sargent et al. (2014) and Schreiber et al. (2015).

2.5 Spectroscopic observations

In addition to photometric data, spectroscopic observations can reveal fundamental properties of the galaxies that are otherwise unaccessible, such as the dust obscuration, the level of ionization and the metallicity, as well as the kinematic properties of the gas. However, as mentioned in the introduction, starburst systems can suffer from huge dust attenuations, which hampers their physical characterization and the discovery of their real nature. For example, Puglisi et al. (2017) selected a sample of starbursts ($\times$4 above the MS) at z $\sim$ 1.6, showing that optical lines, including Hα, [NII], [SII] and Hβ, only probe the external, nearly-unattenuated component of the galaxies, accounting for $\sim$ 10% of the total $\mathrm{SFR_{IR}}$. As a result, the inferred dust obscuration, gas density and metallicity are not representative of the whole system, but only of a small outer region.

A possible solution to study the properties of the dusty starburst population at high redshift is to observe them at longer wavelengths, targeting near-infrared rest-frame lines, such as the Paschen line series of hydrogen. Current ground-based spectrographs can observe Paβ (the second brightest Paschen recombination line) in K band up to a redshift of $\sim$ 0.9. Motivated by this idea, I followed-up a sample of 25 SBs at $0.5 < z < 0.9$ with FIRE, a single slit, near-IR spectrograph mounted at the Magellan telescope, which allows to detect optical/near-IR lines ranging $0.83 < \lambda < 2.4$ μm. The total number of starbursts was the largest possible that we could observe in four nights of observations (one in 2017 and the second in 2018), that I considered the minimum telescope time request for assembling a representative sample (in statistical terms) of this type of galaxies. In the following sections, I will present the FIRE spectrograph, and then describe in detail the choice of the starbursts to observe and the two observing runs at the Magellan telescope.

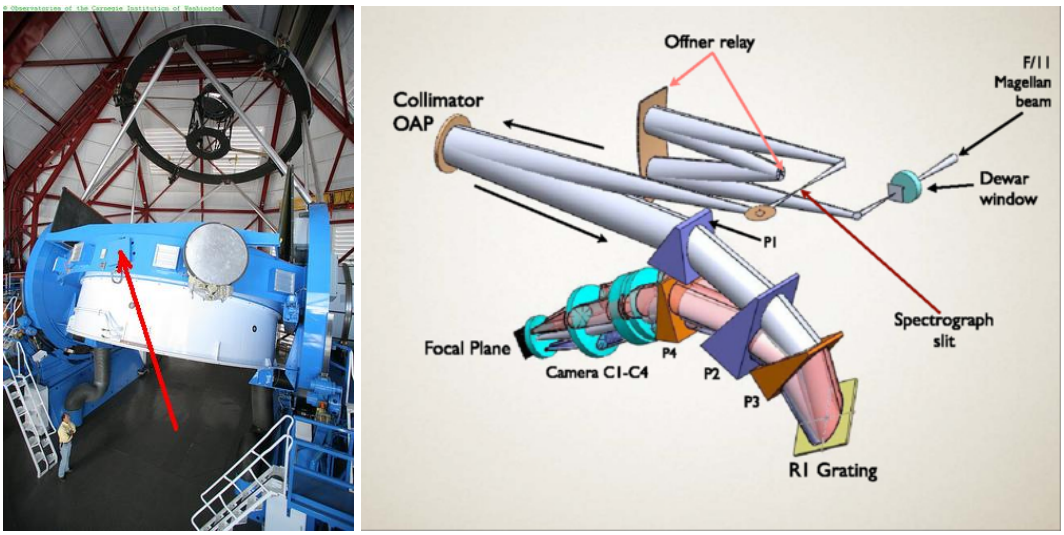

Figure 2.1: *Left:* View of the Magellan Baade telescope, where the arrow indicates the position of FIRE. *Right:* Optical layout of FIRE, showing 1:1 pre-slit Offner relay, reflecting collimator, cross-dispersing prism array, reflective diffraction grating, and four-element camera. (R. Bernstein)

2.5.1 The Magellan-FIRE spectrograph

FIRE (Folded-port InfraRed Echellette) is an infrared spectrometer mounted at the Magellan 6.5 m Baade Telescope at Las Campanas Observatory, in Chile. Its main operative mode consists of the use of a diffraction grating to produce cross dispersed echelle spectra covering the wavelength range between 0.82 and $\sim 2.4\mu m$ in a single exposure.

It is located at one of the Magellan's f/11 Nasmyth ports, also defined as "folded ports", which are addressed by rotating a flat tertiary mirror to the middle point between the two telescope's elevation bearings (Fig. 2.1), between the primary and secondary mirrors (corresponding to the telescope exit pupil). The whole spectrometer has a compact and low-complexity structure, and it is enclosed in a 77K vacuum cryogenic dewar, cooled by a closed cycle helium refrigerator. Its optical layout is visible in Fig. 2.1. In the upper right part, an Offner relay re-images the telescope focal plane into the spectrograph slit and blocks thermal emission from the telescope support structure. At the same time, off-axis light reflected from the back of the slit will be directed toward a small infrared acquisition camera, which is used for object finding and telescope guiding. The slit has a length of $6''$ and can have an aperture of $1''$, $0.6''$, or $0.45''$, which yields a final spectral resolution R of 3000, 6000 or 8000, respectively. After passing through the slit, the telescope's f/11 beam is collimated and directed toward the dispersion elements, which are constituted by a series of ZnSe and Infrasil prisms, and an echelle grating (the primary component). In particular, the prisms have the effect of magnifying the beam and sorting the 11 different spectral orders from the diffraction grating, in order of central wavelength down the

detector. Finally, a four-elements camera produces the 2D spectral images (> 90%EE within one pixel) on the focal plane, where a HAWAII-2RG detector is placed. This is made of a 2000 × 2000 pixel array, probing a spatial scale of 0.18″/pixel.

The slit-viewing camera is made of a 300 × 300 pixel HAWAII-2RG detector, and images a 1 × 1 arcminute field of the Offner relay, at a scale of 0.147″/pixel, in J band, in order to minimize the sky background. In median Magellan seeing conditions, its sensitivity is comparable to that of the spectrograph for long integrations, and is able to identify objects at J = 19-20 in 20-30s exposures. For a more detailed technical description of the instrument, I refer to Simcoe et al. (2013).

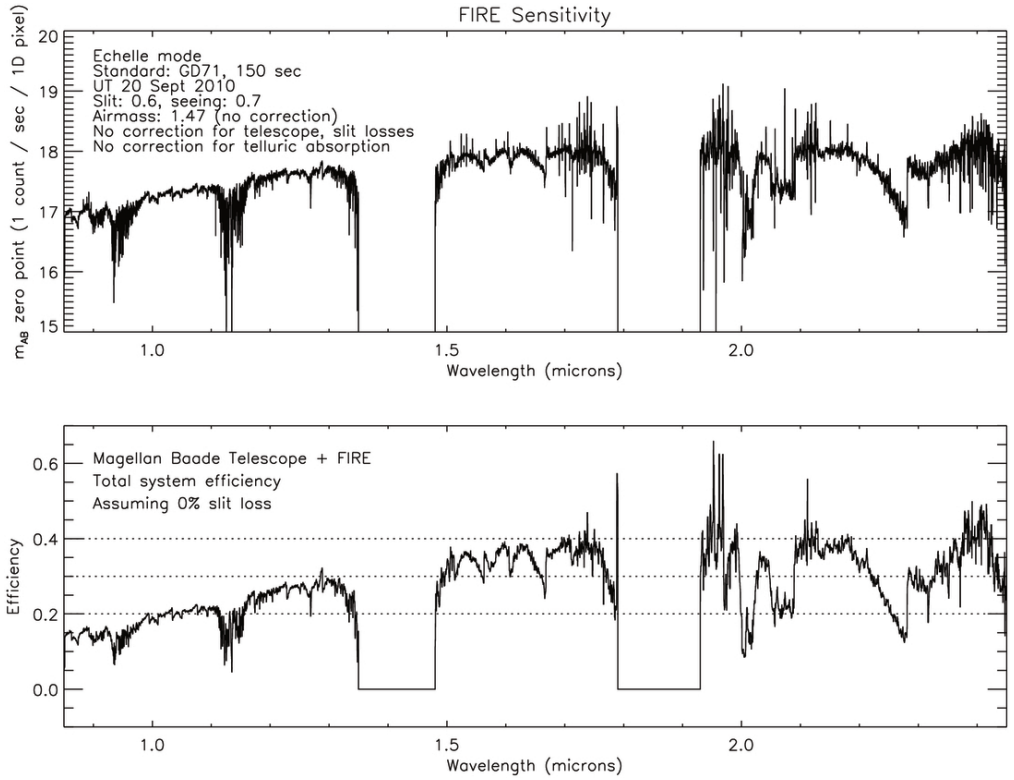

Figure 2.2: *Top:* FIRE sensitivity, obtained with R = 6000 echelle mode. No correction for slit loss, telescope loss, or airmass are included here. The zero point is defined as the AB magnitude delivering 1 count/s/pixel in the final extracted 1D spectrum. *Bottom:* FIRE + Magellan Baade telescope total throughput, with no telluric or atmospheric corrections included. A flux attenuation of 33% has been considered instead for slit losses, in 0.6″ FWHM seeing conditions. The figure comes from Simcoe et al. (2013).

The spectrograph sensitivity is displayed in Fig. 2.2. It is useful to constrain the allowed redshift ranges for the galaxies in order to avoid opaque atmospheric regions, bright sky lines, or the increased instrumental thermal noise at the longest wavelengths $\lambda > 2.2\mu m$. For the integration times, we also have to consider the saturation level of the detector, of the order of 20-25k ADU in the high-gain mode (1.34 e^-/DN).

2.5.2 FIRE observations of 25 starbursts

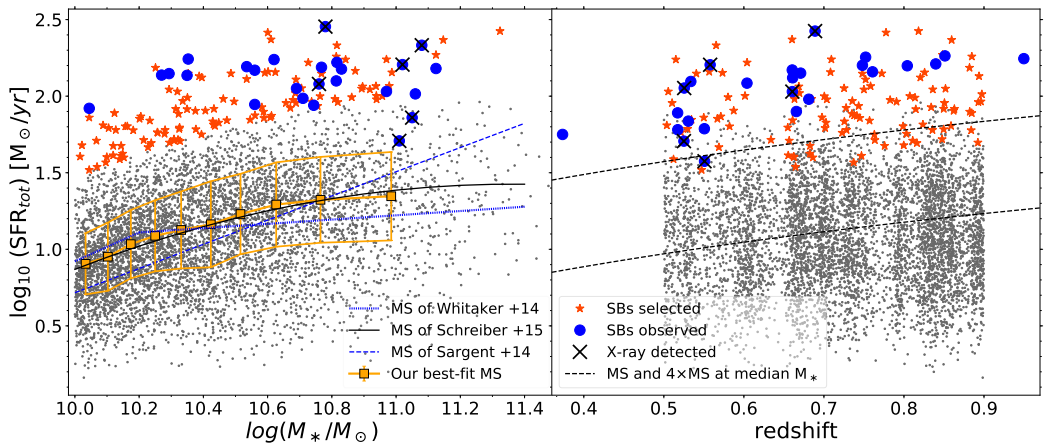

Figure 2.3: *Left:* SFR-M_* diagram for galaxies in our parent sample ($0.5 < z < 0.9$), where SFRtot is defined as $SFR_{UV,obs}$+SFR_{IR}, and is normalized to their median redshift (0.73) using the evolving trend from Sargent et al. (2014). For sources detected only at 24μm, we estimated the SFR from their 24μm flux using Magdis et al. (2012) templates. *Right:* SFR_{tot} vs. redshift for the same sample.

Among the sample of starburst candidates selected in Section 2.3, I observed with FIRE a subset of 25 galaxies during 4 nights: 17-18/03/2017 and 22-23/03/2018. The observations were conducted with my thesis Director E. Daddi, and the P.I. of the two runs, Dr. P.Cassata and Dr. R.Gobat, respectively. The final subset of starbursts was chosen from the pre-selected SB sample according to a priority list. We preferentially observed sources close to bright stars (J < 19-20 mag), so as to facilitate target acquisition, although we eventually avoided blind offsets, since our galaxies are already sufficiently bright (peak magnitudes $<$ 19 mag) to be detected in $\sim$ 20-60 s in good seeing conditions. In addition, we targeted intrinsically brighter sources first, maximizing SFR/D_L^2(z) ratio (D_L is the luminosity distance), and assuming no prior knowledge about the dust attenuation of the system, which was set to 0 in all cases. This introduces a small bias in our selection toward the more massive objects. However, our galaxies span the full range of stellar masses above $10^{10} M_\odot$. Within these limits, they can be considered as representatives of starburst galaxies at $0.5 < z < 0.9$. I remark that no preference has been given to a particular morphological type.

The observed SB sample can be seen in the M_*-SFR diagram in Fig. 2.3 with blue circles. To build this figure, I normalized the total SFRs to the median redshift of the sample (0.73) using the evolution of Sargent et al. (2014):

$$SFR_{\rm norm} = (SFR_{\rm IR} + SFR_{\rm UV,unobs}) \times \left(\frac{1+0.73}{1+z}\right)^{2.8}, \qquad (2.6)$$

while $SFR_{MS,z=0.73}$ is the SFR of the Main Sequence at redshift 0.73 from Schreiber et al. (2015).

Two starbursts that I have previously selected and observed turned out to have slightly lower SFRs than the $\times 4$ limit, because of subsequent updates of the photometric catalog. However, they are still highly star-forming with SFRs at least 3 times above the MS, thus well above the dispersion of 0.2 dex of that relation. Moreover, I discovered that existing spectroscopic redshifts were incorrect for two galaxies, with the new redshifts placing them outside of our selection range (Fig. 2.3-right). As in the previous case, I kept them in the final sample for the analysis as they satisfy the other selection criteria. I will show also that they share similar properties of the other starbursts in terms of, for example, merger signatures and dust obscuration.

In the FIRE observing setup, I chose a slit width of $1''$, (yielding a spectral resolution of R$=$ 3000) to minimize slit losses (the average intrinsic FWHM angular size in Ks-band for our sample is $\sim 0.6''$) and reduce the impact of OH sky emission. In all the cases, the slits were oriented along the semi-major axis of each galaxy, as determined from HST i-band images. Additionally, we benefited from good seeing conditions over all the four nights, with an average of $0.7''$ and a minimum of $0.45''$.

The majority of the starbursts were observed in AB sequence, with single exposure times of 15-20 minutes. I chose single frame integrations of 20 minutes during the first run and 15 minutes in the second run, which significantly reduces saturation of OH lines in K band, thus helping spectral reduction in that band. We decided to double the integration times (completing the ABBA sequence) for galaxies with a lower S/N of the Hα+[NII] complex (based on real-time reduction), to improve the detection of fainter lines. In practice, doing an AB sequence is irrelevant for the spectral reduction, as the pipeline reduces each frame separately (See Section 2.5.3), though it allows us to easily derive 2D emission line maps with the standard IRAF tasks IMARITH and IMCOMBINE.

2.5.3 Spectroscopic reduction

The spectra were fully reduced using the publicly available IDL-based FIRE-HOSE pipeline [2]. For each exposure, I used internal quartz lamps (one for each observing session) to trace the 21 orders of the echelle spectra and to apply the flat field correction. Then, the wavelength calibration was performed by fitting a low (1-5) order polynomial (depending on the spectral order) to ThAr lines of lamp exposures (taken close in time to the corresponding science frames). I checked that the residuals of the fitted lines to the best-fit wavelength solution are less than 1 pixel in all the cases, and is < 0.1 pixel for the majority of the orders. This translates into an average wavelength accuracy of $\Delta\lambda/\lambda \simeq 5 \times 10^{-5}$, nearly constant across the entire spectral

[2]Jonathan Gagné, Erini Lambrides, Jacqueline K. Faherty, Robert Simcoe. FireHose_v2: Firehose v2.0. Zenodo ; 2015

range. Finally, the sky subtraction was applied independently for each single frame following the method of Kelson (2003). In this step, the OH lines in the spectra are used to refine the wavelength calibration.

The 1-D spectra are extracted from the 2-D frames using an optimal extraction method (Horne, 1986). However, this procedure cannot be applied when there is a rapidly varying spatial profile of the object flux (Horne, 1986), as in the presence of spatially extended and tilted emission lines. I used in these cases a boxcar extraction procedure, with a sufficiently large extraction aperture (always $> 1.3''$) in order to include all the line emission from the 2-D exposure. I adopted the boxcar extraction for 3 galaxies in our sample, which are the IDs 245158, 493881 and 470239. Given the agreement within the uncertainties between the fluxes measured with the two approaches for the remaining galaxies, the use of the boxcar procedure does not appear to introduce a systematic flux bias.

After the spectral extraction, I applied the flux calibration to each 1-D extracted spectrum, using telluric spectra derived from the observations of A0V stars. Before dividing the object and telluric spectra in the pipeline, I could interactively refine the wavelength matching between the two by minimizing the *rms* of the product. However, at infrared wavelengths slightly different times and/or airmasses between science and standard star observations can produce non-negligible telluric line residuals, affecting the subsequent analysis. I found that this problem was more relevant in K-band, where strong telluric features are present in the observed wavelength ranges 19950-20250 Å and 20450-20800 Å. The residuals in these regions can produce artificial variations of the real flux up to a factor of 2, while it is less significant at shorter wavelengths (Y to H). In order to remove these artifacts, I followed the procedure described in Mannucci et al. (2001): I first considered a standard star at an airmass of ~ 1.5 and calibrated it with two different stars observed at significantly lower and higher airmasses (e.g., 1.2 and 1.9). Then the two obtained spectra are divided, yielding a global correction function (which is different from 1 only in the regions of strong telluric features defined above) that applies to all the single-exposure spectra, each of them with a different multiplicative factor until the telluric line residuals disappear [3]. Finally, I combined (with a weighted-average) all the 1-D calibrated spectra of the same object.

The error on the flux density f_λ obtained from the FIRE pipeline was checked over all the spectral range, analyzing the continuum of each galaxy in spectral windows of 200 Å and steps of 100 Å, masking emission lines. In each window, I rescaled the rms noise so as to have the $\chi^2_{\rm reduced} = 1$ when fitting the continuum with a low-order ($\lesssim 1$) polynomial[4]. This criterion,

[3] I fitted a linear function in nearby regions free of telluric regions and emission lines, and then determined the correction function through minimizing the rms of the difference between the corrected spectrum and the afore-mentioned continuum fit

[4] A spline of order 1 spanning the whole wavelength range was used as a correction function

equivalently, ensures that the noise level matches the 1-σ dispersion of the object spectrum in each window. Typical corrections are within a factor of 2, variable across the spectral bands.

Due to slit losses, variable seeing conditions and the spatial extension of our objects, which are typically larger than the slit width ($1''$), part of the total flux of the galaxies is lost. In order to recover the total absolute flux, I matched the whole spectrum to the photometric SED. This was done by applying a 5σ clipping and error-weighted average to the Magellan spectrum inside z++, Y, J, H and K_s photometric bands, and comparing the obtained mean f_λ in each filter to the corresponding broad-band photometry (Laigle et al., 2016). Since the SED shapes derived from the spectra are generally in agreement with the photometric SED shapes, I rescaled the spectra with a constant factor, determined through a least squares minimization procedure. The aperture correction factors for my sample range between 0.8 and 3, with a median of 1.4. They are subject to multiple contributions, i.e., slit position with respect to the object, seeing conditions during the target and the standard stars observations. The few cases in which the aperture correction was lower than 1 could be due indeed to a much better seeing of the standard star compared to the target observation. I remind that this procedure assumes that lines and continuum are equally extended, which is clearly an approximation. Spatially resolved near-IR line maps (e.g., with SINFONI) would be required to test possible different gradients of the two emission components, and to derive better total flux corrections.

2.5.4 Complementary optical spectra

A subset of our Magellan sample also has publicly available optical spectra: 10 starbursts in our sample have been observed with the VIMOS spectrograph (Le Fèvre et al., 2003) by the zCOSMOS survey (Lilly et al., 2007), and their optical spectra are publicly available through the LAM website (`cesam.lam.fr/zCOSMOS`). They span the range $5550 < \lambda < 9650$ Å, which includes [OII]λ3727 Å, Hγ, Hβ and [OIII]λ5007 Å lines for our galaxies. The spectral resolution is on average $R = 600$, constant across the whole range, while the noise level increases from the blue to the red part of the spectrum, due to the increased OH sky emission at longer wavelengths. Due to the absence of the noise spectrum in the public zCOSMOS release, I used instead a sky spectrum at the same resolution of VIMOS, rescaled with a spline to match the flux standard deviation in spectral regions free of emission lines, similarly to what has been done before on the Magellan spectra. Even though it is a first approximation, this procedure allows to reproduce the increasing noise in correspondence of OH lines, i.e., where strong sky-subtraction residuals are expected, and take into account the higher average noise level of the red part of the spectrum. For one galaxy in our sample (ID 493881), I took its optical spectrum from SDSS-III DR9 (Ahn et al., 2012), which spans a wider wavelength range $3600 < \lambda < 10400$ Å at higher resolution (R$\sim$ 2000), thus

allowing a better sky subtraction and a higher SNR. In both cases, the spectra were already fully reduced, wavelength and flux calibrated, as described in the respective papers. I applied only an aperture correction by matching the observed spectrum to the photometric SED (Laigle et al., 2016) with the same methodology adopted for the Magellan spectra. However, I warn that there could be some mis-matches compared to our Magellan observations in the slit centering and orientation, as also in the seeing conditions, thus the spectra may not be exactly representative of the same regions.

2.5.5 Line measurements

I measured emission line fluxes, line widths and uncertainties on fully calibrated and aperture corrected spectra using the python anaconda distribution (Mark Rivers, 2002[5]) of the IDL routine MPFIT (Markwardt, 2009). Given the FWHM resolution of FIRE for $1''$ slit width ($= 100$ km/s), all the emission lines are resolved, owing to intrinsically higher velocity widths.

I fitted the lines with a single Gaussian on top of an underlying order-1 polynomial continuum. In each case, I required a statistical significance of the fit of 95%, as determined from the residual χ^2. When a single Gaussian does not satisfy the above condition, I used a double Gaussian (with varying flux ratio and same FWHM, in km/s, for the two components), which instead provides a better fit, placing its χ^2 within the asked confidence level. The flux uncertainties were derived by MPFIT itself, and they were always well behaved, with best-fit $\chi^2_{\rm reduced} \simeq 1$. For non detected lines (i.e., SNR < 2 in our case), I adopted a 2σ upper limit [6]. However, I highlight that the detected emission lines have always high S/N ratios: Hα, [NII]λ6584 and Paβ are identified on average at 9.3, 8.4 and 7.4 σ, respectively (lowest SNRs are 4, 5.3 and 3.3 for the same lines).

I fitted a double Gaussian for 12 galaxies in our sample. As we will see later in Section 4.2 by combining the informations of their 1D and 2D spectra, in 6 of them I interpreted the two Gaussians as coming from different merger components. For the remaining galaxies, in 2 cases the lines are consistent with global rotation, while for the last 4 we were not able to derive firm conclusions, even though we favour the contribution of multiple system parts to their emission. In the Appendix 2.C at the end of this Chapter, I show the 1D emission line fits for all the 25 Magellan SBs, and I discuss in more detail the origin of double Gaussians line components.

I applied the stellar absorption correction on Balmer and Paschen emission lines, rescaling upwards their fluxes. In order to determine the level of absorption for these lines, I adopted Bruzual and Charlot (2003) synthetic

[5]GitHub Repository: stsci.tools/lib/stsci/tools/nmpfit.py

[6]I remark that we are guided by the wavelength position, line width and flux ratio (for double line components) of Hα, which is always detected at $> 4\sigma$. The Gaussian amplitude remains thus the only variable to constrain the fit for the other lines.

spectra with solar metallicity and constant star-formation history for 200-300 Myr, which are the typical merger-triggered starburst timescales (Di Matteo et al., 2008). The current starburst activity imposed by my selection suggests that the final coalescence of the major merger occurred relatively recently, certainly within the last 200 Myr. Numerical simulations of major mergers with different masses and dynamical times indicate indeed that star formation stops within 100-200 Myr after the coalescence, even without AGN quenching (Springel, Di Matteo, and Hernquist, 2005; Bournaud et al., 2011a; Powell et al., 2013; Moreno et al., 2015). Averaging the results over this interval, I applied an EW_{abs} correction of 5, 2.5, 2.5 and 2 Å for Hβ, Hα, Paγ and Paβ, respectively[7]. In the same order, I estimated for these lines an average absorption correction of 35%, 7%, 26%, 13% of the total flux. If I allow an uncertainty of ± 1 Å on the EW^{abs} correction of either Paγ and Paβ, this will produce variations on the final fluxes that are 6% on median average, and thus it will not significantly affect my results.

All the lines in the Magellan spectra, either in emission or in absorption, were analyzed based on the following steps. Firstly, Hα and [NII]$\lambda\lambda$ 6548,6583, which are the lines with the highest S/N, were fitted together assuming a common linear continuum and a fixed ratio of the [NII] doublet of 3.05 (Storey and Hummer, 1988). From this fit I derived the redshift of the galaxy, the intrinsic FWHM of Hα (in terms of velocity), and the flux ratio of the two Hα components for double Gaussian fits. The instrinsic total line widths were obtained by subtracting in quadrature the FIRE resolution width (100 km/s) from the best-fit observed FWHM. For double Gaussians, I used the same FWHM for both components in the fit. The total FWHM was then calculated adding to the single FWHM the separation between the two component peaks, as this quantity is more representative of the whole system.

Then, the three parameters defined above were fixed and used to fit all other emission lines, including those in the optical zCOSMOS and SDSS spectra, after rescaling the FWHM to account for the different spectral resolutions. For the galaxies with the highest S/N of Paβ ($> 8\sigma$), I verified that even without fixing its FWHM a-priori, the fit yields a line velocity width consistent within the errors with the value found from Hα, indicating that my assumption is generally valid. Given the *rms* wavelength calibration accuracy (see Section 2.5.3), I allowed the line central wavelength to vary in the fit by 3σ, corresponding to 1.5 Å at 10000 Å, and 3 Å at 20000 Å. For each measured flux, I also added in quadrature an error due to the uncertainty of the absolute flux calibration. This additional uncertainty ranges between 5% and 10%, and is determined as the maximum residual difference between the average fluxes estimated from the photometry and from the aperture corrected spectra, among all the bands ranging from z++ to K_S. Finally, the equivalent widths of the lines were derived following

[7]The EW_{abs} of Hβ and Hα are consistent with those adopted in previous works (e.g. Valentino et al., 2015), while it was not possible to make comparisons for Paγ and Paβ.

its definition ($= \int F(\lambda)/F_{cont}(\lambda)$), where $F(\lambda)$ is the best-fit Gaussian flux distribution and F_{cont} is the fitted underlying continuum. I will use these measurements in the following chapters to study the physical properties of the sample. In next sections I will show instead the measurements of their sizes in radio, which will play a fundamental role in the interpretation of my results, the identification of AGNs with X-ray emission, and an analysis of galaxy morphologies.

2.6 Radio size measurements

The radio continuum emission has been used as a dust-free tracer of the SFR in galaxies in the absence of contamination from an AGN (e.g., Condon, 1992). Since all my galaxies do not show either radio jets or radio flux excess compared to that expected from the SFR only (as I will show in Section 2.7), I used 3 GHz VLA images for measuring the FWHM size of their starburst cores, where the bulk of star-formation is taking place. For each SB, I used GALFIT (Peng et al., 2010) to fit a 2D function, convolved with the VLA synthesized beam, to their radio emission. I tested several 2D profiles, which include a Gaussian, a Sérsic function and the VLA beam itself, requiring a significance of the fit (probed by the χ^2) of at least 95% confidence level, as for the emission line measurements. In addition to the χ^2 analysis, all the GALFIT residuals of the fit (original-model) were checked by eye inspection, and the excluded fittings have always worst residuals. The best-fit profiles obtained for my sample are summarized as follows.

Firstly, a single 2D Gaussian with varying FWHM, axis ratio and position angle provided the best fit for 13 starbursts. In one case (ID 470239), the required conditions were obtained only by fitting a single Sérsic profile with varying parameters, but its half light diameter (calculated as $2 \times r_e$, with r_e the effective radius) was only 3% different from the total FWHM of a single Gaussian fit, thus I assumed the latter as the final value. I also tried to fit a single and double Sérsic profile for all the other sources. However, given the larger number of parameters of this profile and the limited VLA resolution, I did not obtain convergence for the majority of them, or the resulting $\chi^2_{\rm reduced}$ were too high.

A double 2D Gaussian was required by three galaxies (ID 245158, 412250 and 519651), allowing to resolve them and measure single components FWHM and their relative separation.

As a third option, fitting the VLA synthesized beam yielded the best solution for six galaxies, which are then unresolved with current resolution ($0.75''$).

Finally, a single 2D Gaussian with fixed axis ratio and position angle (to 1 and 0, respectively) was used for two sources (ID 578239 and 685067). I remark that, in case the 95% significance level of the fit was satisfied with either this or the previous approach (as in the case of some very compact

sources), I adopted the Gaussian solution only if the associated χ^2 probability level was at least double compared to the fit with the VLA beam.

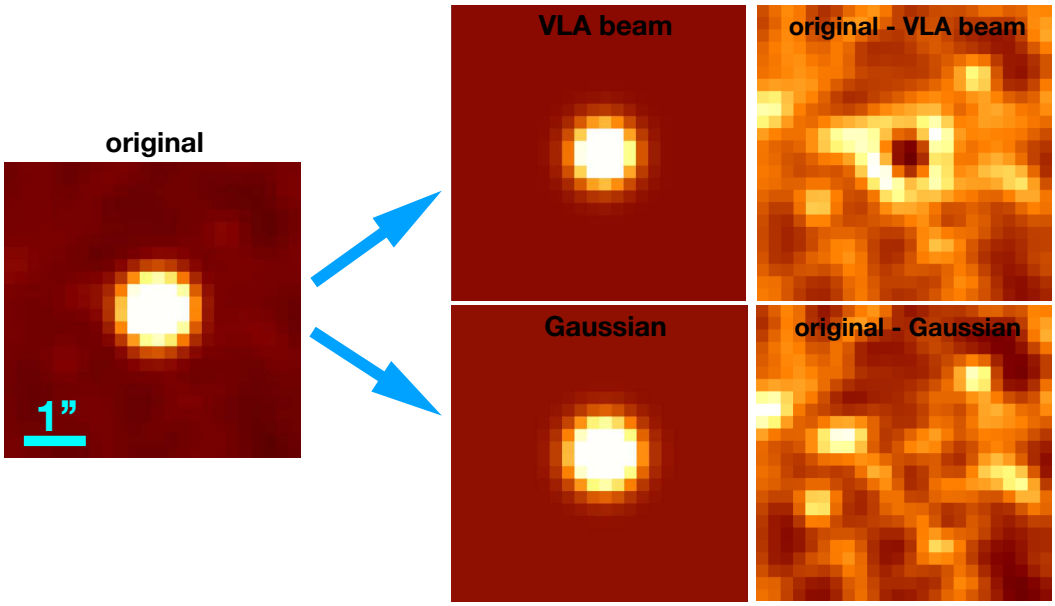

Figure 2.4: GALFIT fitting of the radio VLA image (3 GHz) of the galaxy ID 685067 ($z = 0.37$) with the VLA synthesized beam in the *upper* row and with a Gaussian profile (convolved with the beam) in the *bottom* row. In horizontal sequence are shown, from left to right, the original image, the fitted model and the residual (original-model). For this galaxy, I derived an angular size (FWHM of the Gaussian) of $0.20 \pm 0.04''$ (the pixel scale is $0.2''$/pixel), which corresponds to a physical size of 1.06 ± 0.19 kpc. I noticed that here GALFIT converges when fixing the position angle (PA) and axis ratio (q) parameters, to 0 and 1, respectively (Table 2 in the Appendix of this chapter). This example illustrates the possibility to reliably measure the radio sizes of my objects even when they are smaller than the FWHM resolution of VLA ($0.75''$). In this case, the difference between the two models is recognized by looking at the residual images (i.e., original-model).

As shown later, for a few galaxies I measured angular sizes that are much smaller than the synthesized beam FWHM ($\sim 0.75''$), down to $\sim 0.2''$ and to a physical scale of 1 kpc. To demonstrate that it is possible to reliably determine the sizes even for these extreme, compact sources, I show in Fig. 2.4 a comparison between the GALFIT residuals obtained when fitting the image with a Gaussian (convolved to the VLA beam) (upper row) and with the radio synthesized beam itself (bottom row). It is evident that a Gaussian profile provides a better fit of the original source profile and a cleaner residual compared to the VLA beam alone.

The uncertainties on the sizes were recalculated for all the starbursts from their radio S/N, using the fact that better detected radio sources also have the smallest radio size uncertainties, as shown for example in Coogan et al.

(2018). I used then the same formulation as:

$$FWHM_{err} \simeq 1 \times \frac{FWHM_{beam}}{S/N}, \tag{2.7}$$

where $FWHM_{beam}$ is the circularized FWHM of the VLA synthetized beam, and the multiplying coefficient was determined from simulations, following Coogan et al. (2018). All the size measurements with relative uncertainties and the method used for their determination are included in Table 2.

Since my galaxies are well detected in radio band (average S/N of 18) and the VLA synthetized beam is well known, I always obtained a good fit for the resolved sources. Among them, I was able to fit a double Gaussian for three objects. In these cases, their total FWHM (adopted throughout the paper) were determined as the sum of the average single FWHM sizes and the separation between the two components. However, I will also consider the single sizes in some cases, such as in Fig. 4.10. This finding suggests that also some other galaxies may represent double nuclei that are blended in $0.75''$ resolution VLA images. For the unresolved galaxies instead (i.e., those fitted with the VLA beam, as explained above), I adopted a 3σ upper limit on their FWHM. Within the most compact starbursts, some of them may be affected by pointlike emission from an AGN, which decreases artificially the observed size. However, I tend to discard this possibility since, as we will see later, none of our AGN candidates show a radio-excess compared to the radio emission due to their SFR.

2.7 AGN identification

I started searching for AGN components in the mid-IR. Through the multi component SED fitting of IR+(sub)mm photometry (described in Section 2.3) I detected at $> 3\sigma$ the dusty torus emission component for a subset of 12 SBs. The significance of the detection was derived from the ratio between the total best-fit dusty torus luminosity ($= L_{\rm AGN,IR}$) and its 1σ uncertainty, inferred as the luminosity range (symmetrized) yielding a variation of the $\chi^2_{red} \leq 1$ with respect to the minimum value of best-fit (Avni and Bahcall, 1976). More details about the torus estimation method are described in Liu et al. (2018) and Jin et al. (2018). Among the 12 mid-IR AGNs, I detected the dusty torus emission at high significance level ($> 5\sigma$) for 6 starbursts (ID 777034, 519651, 222723, 232171, 466112, 894779), while for the remaining objects I obtained a lower significance ranging $3\sigma < L_{AGN,IR} < 5\sigma$ (see Table 2).

Within the sample of IR-detected AGNs, 6 galaxies (ID 777034, 222723, 232171, 635862, 578239, 911723) are also detected in X-rays at more than 3σ by XMM-Newton, Chandra or NuStar (Cappelluti et al., 2009; Marchesi et al., 2016; Civano et al., 2015). Throughout the paper, I will consider the X-ray luminosities L_X measured by Lanzuisi et al. (2017), integrated over the energy range 2-10 keV. To estimate the contribution of star-formation to the

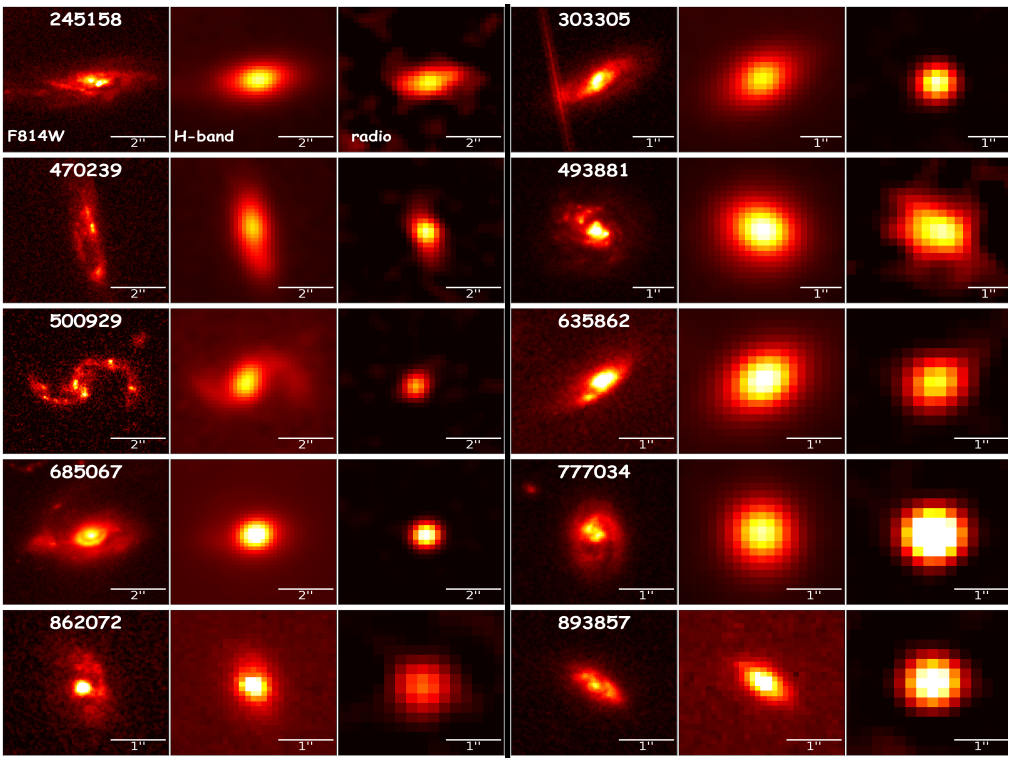

Figure 2.5: *Left:* HST-ACS F814W cutout images for 10 galaxies of our Magellan sample. Their FWHM resolution is 0.095″. *Center:* H-band UltraVISTA images with the same f.o.v. and with FWHM$_{res}$ $\sim$ 0.75″. *Right:* 3 GHz radio images from VLA-COSMOS 3GHz Large Project (Smolčić et al., 2017), FWHM$\sim$ 0.75″. For the galaxies 862072 and 893857, higher resolution (0.2″) H-band cutouts from the COSMOS-DASH program are shown (Momcheva et al., 2016).

total intrinsic L$_X$, I used the relation between SFR and L$_{X,SFR}$ of Mineo et al. (2014), rescaled to a Chabrier IMF and applying a correction factor of 0.6761 to convert the X-ray luminosity from the 0.5-8 keV to the 2-10 keV band.

I remind that the column densities N$_H$ inferred from their hardness ratios (Lanzuisi et al., 2017) are consistent with those derived from the dust attenuations (toward the centers) assuming a mixed model (Paper I), suggesting that also the X-ray emission is coming from the nucleus, where the AGN is expected to be located. Furthermore, all the starbursts do not show radio jets in VLA images, and do not have more significant radio excess than expected from their SFR, assuming a typical IR-radio correlation with q$_{IR}$ = 2.4, as in Ibar et al. (2008), Ivison et al. (2010) and Liu et al. (2018).

2.8 Morphological classification of Magellan starbursts

In addition to the analysis of radio and X-ray emission, optical imaging, despite it might be still affected by dust, allows us to investigate the global

structure of these systems thanks to the high resolutions offered by HST. It can be useful to recognize at first order which galaxies of my sample are clearly mergers. The morphology of 18 galaxies of the starburst sample has been already classified by Kartaltepe et al. (2010), revealing a merger origin for the majority of them, as shown in Fig. 2.5 and 2.6. Adopting the same criteria of Kartaltepe et al. (2010), I have classified visually the remaining 6 galaxies (one has no HST coverage), finding the following results: 61% of the total sample are major mergers, as revealed by their highly disturbed morphology, tidal tales and bridges, 23% are classified as minor mergers from the presence of only slightly perturbed structures (e.g., warped disks, asymmetric spiral arms, etc.) without large companions, 11% are classified as spheroidal/S0 galaxies and the remaining 5% as spirals. The major merger subset is additionally divided in five smaller classes according to their merger state (I: First approach, II: First contact, III: pre-merger, IV: Merger, V: Old-merger/merger remnant), following Kartaltepe et al. (2010).

However, I remind that the merger recognition and, even more, the merger stage classification from the optical morphology is very uncertain and more difficult at higher redshifts, due to lower resolution and to surface brightness dimming, which hampers the detection of faint tidal tails or interacting features, especially after the coalescence. The galaxy ID 245158 represents a show-case example of this uncertainty: it has been classified as spiral/minor merger from its global morphology, but it clearly shows a double nucleus in the central region of its i-band image, further confirmed by a double component Hα in the 2-D and 1-D spectrum, indicating rather an ongoing merger system.

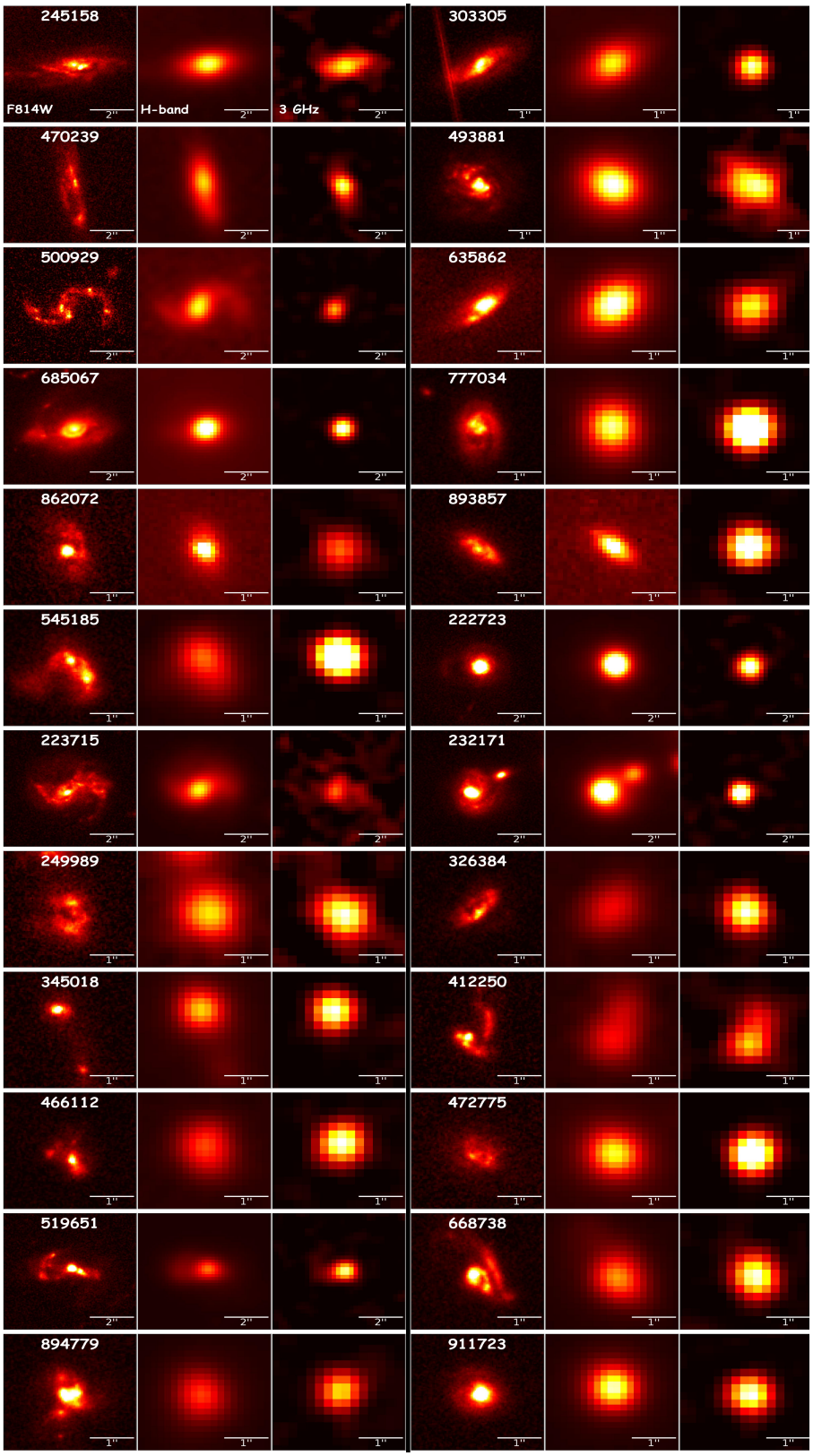

Figure 2.6: Same as Fig. 2.5, but for the remaining 14 galaxies in the Magellan sample with available HST F814W imaging (ID 578239 is not comprised).

2.A Tables

In this Appendix of Chapter 2, I present the main physical properties (derived above in the same Chapter) for the sample of 25 starbursts observed with Magellan FIRE. These properties include emission line measurements, stellar masses and total infrared luminosities, as well as the FWHM sizes in radio and morphological types.

ID	R.A. (deg)	Decl. (deg)	z_{spec}	$\log(M_*)$ ($M_\odot$)	$\log(LIR_{SFR})$ ($L_\odot$)	$H\alpha$ (10^{-17} $\frac{erg}{s\,cm^2}$)	$Pa\beta$ (10^{-17} $\frac{erg}{s\,cm^2}$)	$A_{V,tot}$ (mag)	$N_{H,X}$ (cm^{-2})	M_{type}
245158	150.18854	1.65498	0.5172	10.7	11.89 ± 0.07	249.6 ± 30.1	52.0 ± 5.6[a]	1.9 ± 0.1	...	S, m
493881	150.74967	2.04707	0.6039	10.8	12.09 ± 0.06	330.9 ± 30.2	53.3 ± 11.5	2.7 ± 0.2	...	...
223715	149.76537	1.61702	0.5174	10.7	11.78 ± 0.03	204.0 ± 20.8	28.5 ± 6.6	3.6 ± 0.2	...	m, S
249989	150.68540	1.66108	0.6656	10.6	11.90 ± 0.08	127.6 ± 15.9	19.0 ± 3.3	4.4 ± 0.2	...	MIII
894779	150.42710	2.65644	0.5506	10.0	11.79 ± 0.03	129.7 ± 19.3	22.0 ± 3.8	4.5 ± 0.2	...	MIV
466112	149.99928	2.00599	0.7607	10.3	12.16 ± 0.04	81.7 ± 6.2	20.9 ± 3.5	5.2 ± 0.3	...	MIII
470239	150.48155	2.01096	0.6609	10.6	12.12 ± 0.17	92.3 ± 9.5	23.0 ± 2.2	6.2 ± 0.2	...	...
500929	149.76844	2.05935	0.9498	10.8	12.25 ± 0.14	21.9 ± 5.3	<14.3[a]	>6.2	...	MIII
412250	150.74171	1.91764	0.8397	10.3	12.21 ± 0.04	118.6 ± 10.5	16.0 ± 4.7	6.7 ± 0.6	...	MIII
668738	150.21020	2.31168	0.7481	10.8	12.20 ± 0.04	81.4 ± 7.5	14.1 ± 1.4	6.7 ± 0.2	...	MIII
635862	149.69589	2.26450	0.5508	11.0	11.58 ± 0.10	59.7 ± 8.8	11.0 ± 2.7	6.8 ± 0.6	22.54 ± 0.14	...
862072	150.12329	2.60376	0.6811	11.1	11.98 ± 0.07	58.3 ± 6.0	14.3 ± 1.9	7.8 ± 0.4	...	m, S
222723	150.17321	1.61632	0.5254	11.0	12.05 ± 0.05	150.7 ± 11.1	24.4 ± 4.8	8.1 ± 0.5	<21.66	MV
519651	150.43020	2.08688	0.6709	10.5	12.15 ± 0.05	126.0 ± 10.5	19.5 ± 3.0	8.8 ± 0.5	...	MIV
911723	149.68134	2.68108	0.6606	10.8	12.03 ± 0.02	65.9 ± 7.2	16.2 ± 3.1	9.1 ± 0.6	21.98 ± 0.36	E
326384	149.51786	1.78357	0.8042	10.3	12.20 ± 0.07	68.8 ± 8.8	12.4 ± 3.8	9.8 ± 1.1	...	S
685067	149.74730	2.34574	0.3735	11.0	11.75 ± 0.01	136.9 ± 16.5	26.1 ± 1.2	10.9 ± 0.3	...	...
893857	150.15995	2.65434	0.8512	11.1	12.26 ± 0.09	27.4 ± 1.6	<11.5[a]	>11	...	E
578239	150.76543	2.18099	0.5578	11.1	12.21 ± 0.23	116.5 ± 10.4	26.1 ± 1.6	11.7 ± 0.3	22.36 ± 0.31	...
777034	150.15025	2.47517	0.6889	10.8	12.43 ± 0.08	114.0 ± 13.3	20.5 ± 1.8	12.0 ± 0.4	22.96 ± 0.04	MIV
303305	150.48305	1.74796	0.5306	10.7	11.84 ± 0.10	19.9 ± 3.6	<10.0[a]	>13.9	...	...
232171	150.06033	1.63269	0.5251	11.1	11.71 ± 0.02	60.1 ± 14.2	<8.5	>17.6	23.83 ± 0.1	MII
472775	150.48148	2.01362	0.6604	10.8	12.17 ± 0.06	44.3 ± 4.1	9.9 ± 1.6	18.0 ± 1.3	...	...
545185	149.52802	2.12725	0.5337	10.4	12.10 ± 0.06	49.8 ± 4.2	10.9 ± 0.9	22.5 ± 1.0	...	MIII
345018	149.72556	1.81069	0.7521	10.6	12.25 ± 0.06	37.0 ± 3.6	7.1 ± 2.1	23.7 ± 3.4	...	m, S

Figure 2.7: ID, RA, DEC (J2000) and M_* are from Laigle et al. (2016). The 1-σ error on M_* is 0.1 dex. Line fluxes are measured from aperture corrected spectra. Aperture correction errors ($\sim$ 0.04 dex) are included in the uncertainties. The infrared luminosities (integrated between 8-1000 μm), are AGN-torus decontaminated. Hα and Paβ are corrected for stellar absorption, assuming EW_{abs} = 2.5 and 2 Å, respectively. $A_{V,tot}$ is the total dust attenuation toward the center of the system. The morphological type (M_{type}) of Kartaltepe et al. (2010): E=Elliptical/S0; S=spiral/disc; m=Minor merger; M=Major merger (I:first approach, II:first contact, III:pre-merger, IV:Merger, V:Old merger/merger remnant). The galaxies are ordered with increasing $A_{V,tot}$. ‡: derived as Paβ = 2.2 × Paγ.

Main physical quantities derived for our Magellan sample of starbursts

ID	$\mathbf{z_{spec}}$	$\mathbf{A_{V,tot}}$ mag	$\mathbf{FWHM_{radio}}$ kpc	$\mathbf{FWHM_{line}}$ km/s	**EW(Hα)** Å	**EW(Paβ)** Å	**EW(Hδ)** Å	**[O III]5007** erg cm^{-2}s^{-1}	$\mathbf{H_\beta}$ erg cm^{-2}s^{-1}	$\mathbf{log_{10}(L_{bol,AGN})}$ $L_\odot$	$\boldsymbol{\sigma_{AGN,IR}}$	$\mathbf{M_{type}}$
(1)	(2)	(3)	(4)	(5)	(6)	(7)	(8)	(9)	(10)	(11)	(12)	(13)
245158	0.5172	1.9 ± 0.1	14.43 ± 0.24 ‡	378.1 ± 20.4	91.1 ± 11.3	33.1 ± 3.6	–	–	–	<11.59	<3	S, m*
470239	0.6609	6.2 ± 0.2	7.72 ± 0.26	372.0 ± 6.7	81.1 ± 8.6	24.5 ± 2.4	2.0 ± 1.6	17.7 ± 5.7	22.7 ± 2.3	<10.13	<3	MIII
493881	0.6039	2.7 ± 0.2	8.81 ± 0.26	347.4 ± 3.5	103.2 ± 9.6	44.4 ± 9.6	0.3 ± 1.3	23.1 ± 3.7	59.6 ± 2.6	<11.38	<3	S, m
578239	0.5578	11.7 ± 0.3	1.29 ± 0.24 †	514.0 ± 21.5	68.1 ± 6.3	14.8 ± 0.9	-2.6 ± 1.7	50.1 ± 5.9	13.5 ± 2.9	10.94 ± 0.14	3.0	no-HST
635862	0.5508	6.8 ± 0.6	3.43 ± 0.25	971.4 ± 32.6	31.2 ± 5.0	8.0 ± 1.9	-2.5 ± 2.3	15.0 ± 4.0	8.4 ± 1.8	11.22 ± 0.09	4.9	m
685067	0.3735	10.9 ± 0.3	1.06 ± 0.19 †	537.2 ± 35.7	12.1 ± 1.8	4.2 ± 0.2	-5.9 ± 0.5	8.8 ± 4.1	–	<10.76	<3	MV
777034	0.6889	12 ± 0.4	1.25 ± 0.26	641.7 ± 25.2	83.8 ± 10.0	20.3 ± 1.8	-4.2 ± 2.3	43.6 ± 4.9	21.7 ± 1.6	12.02 ± 0.04	9.7	MIV*
862072	0.6811	7.8 ± 0.4	2.98 ± 0.30	561.2 ± 15.2	55.8 ± 6.0	15.6 ± 2.1	-7.5 ± 1.2	–	3.7 ± 0.8	<10.91	<3	m, S*
545185	0.5337	22.5 ± 1.0	<0.70	345.6 ± 11.7	33.8 ± 4.8	20.5 ± 2.6	–	–	–	<10.56	<3	MIII*
222723	0.5254	8.1 ± 0.5	3.38 ± 0.23	168.3 ± 3.9	52.4 ± 4.0	13.5 ± 2.6	–	–	–	11.07 ± 0.07	5.8	MV*
223715	0.5174	3.6 ± 0.2	10.95 ± 0.28	237.0 ± 6.3	54.9 ± 6.0	16.3 ± 4.3	–	–	–	<11.47	<3	m, S*
249989	0.6656	4.4 ± 0.2	5.32 ± 0.30	261.2 ± 10.1	206.3 ± 26.0	38.5 ± 6.8	–	–	–	10.66 ± 0.13	3.3	MIII*
326384	0.8042	9.8 ± 1.1	2.78 ± 0.29	321.7 ± 7.8	174.2 ± 23.7	36.8 ± 11.4	–	–	–	<10.55	<3	S*
345018	0.7521	23.7 ± 3.4	<0.86	286.4 ± 11.9	82.3 ± 8.2	18.9 ± 5.5	-7.2 ± 1.1	16.7 ± 4.4	12.0 ± 1.8	<10.81	<3	m, S*
412250	0.8397	6.7 ± 0.6	8.84 ± 0.31 ‡	299.1 ± 6.5	244.7 ± 21.9	18.2 ± 5.4	–	–	–	11.14 ± 0.09	4.9	MIII*
466112	0.7607	5.2 ± 0.3	2.64 ± 0.28	298.1 ± 3.7	229.1 ± 17.6	57.8 ± 9.6	-3.9 ± 1.1	34.0 ± 4.0	9.0 ± 1.6	11.42 ± 0.06	7.3	MIII*
472775	0.6604	18.0 ± 1.3	<1.05	498.3 ± 27.9	65.7 ± 6.3	17.3 ± 2.7	–	–	–	<10.52	<3	MIII
519651	0.6709	8.8 ± 0.5	10.94 ± 0.26 ‡	191.1 ± 3.6	86.2 ± 7.4	32.0 ± 5.0	-2.9 ± 1.3	38.9 ± 7.1	27.3 ± 1.8	11.37 ± 0.06	7.3	MIV
668738	0.7481	6.7 ± 0.2	3.68 ± 0.28	484.2 ± 22.3	92.0 ± 13.3	24.0 ± 3.4	–	28.0 ± 4.4	11.3 ± 3.0	10.87 ± 0.13	3.3	MIII*
894779	0.5506	4.5 ± 0.2	2.41 ± 0.26	132.0 ± 10.5	140.8 ± 21.4	35.4 ± 6.2	–	–	–	10.66 ± 0.07	5.8	MIV*
911723	0.6606	9.1 ± 0.6	<0.88	440.8 ± 10.3	60.5 ± 6.8	23.9 ± 4.5	–	–	–	10.73 ± 0.12	3.7	E*
303305	0.5306	>13.9	<0.71	877.7 ± 85.1	11.0 ± 2.4	–	-9.3 ± 2.6	11.6 ± 1.3	–	<11.30	<3	E
500929	0.9498	>6.2	2.99 ± 0.32	547.6 ± 48.0	42.3 ± 10.8	–	–	–	–	<11.26	<3	MIII*
893857	0.8512	>11	<0.93	655.1 ± 29.6	39.6 ± 2.5	–	–	–	-	<11.08	<3	E*
232171	0.5251	>17.6	1.62 ± 0.23	374.4 ± 33.8	11.3 ± 3.3	–	–	–	–	11.54 ± 0.04	9.7	MII*

Table 2: Table columns: (1) Identification number from Laigle et al. (2016), as in Calabrò et al. (2018); (2) Spectroscopic redshift inferred from Magellan spectra; (3) Total attenuation $A_{V,tot}$ toward the center in a mixed model geometry, calculated in Calabrò et al. (2018) and explained in Section 2 ; (4) FWHM size in radio 3 GHz band (from VLA-COSMOS); †: fit with a single 2D gaussian but with fixed axis ratio and position angle (1 and 0); ‡: fit with a Double 2D gaussian, we give here the total FWHM (average of single component sizes + separation between the two); we put a 3σ upper limit for unresolved sources, while the remaining starbursts are fit with a single 2D gaussian and free parameters ; (5) line velocity width of emission lines, derived from fitting the Magellan spectra with MPFIT (for double gaussians, this quantity is the sum of the single gaussian FWHM and the separation in velocity between the two peaks); (6,7,8) Observed equivalent width of Hα,Paβ and Hδ, the latter coming from zCOSMOS or SDSS optical spectra; (9,10) Fluxes of [O III]λ5007Å and Hβ (in units of 10^{-17}) inferred from optical spectra. Hβ fluxes have been corrected for underlying absorption assuming EW_{abs} =5Å as determined from Bruzual & Charlot (2003) synthetic stellar spectra; (11) Bolometric AGN luminosity derived as $1.4\times L_{AGN,IR}$, the latter being the AGN luminosity in the infrared inferred from SED fitting (see Liu et al. (2018) and Jin et al. (2018) for the methodology); (12) Significance of mid-IR dusty-torus detection from SED fitting (< 3 means that it is not detected); (13) Morphological type following the visual criteria of Kartaltepe et al. (2010) (objects with a $*$ have been already classified in the same paper). We remind that the coordinates of our targets, their stellar masses, SFRs and Hα (Paβ) flux measurements can be retrieved from Calabrò et al. (2018).

2.B Infrared SED fitting

In this Appendix, I show in Fig. 2.8 the best-fit infrared to radio SED of all the 25 starbursts of the Magellan-FIRE sample, performed as explained in Section 2.3. The SED fitting procedure was performed by my collaborator Daizhong Liu, who is co-author of the first two papers written during my PhD.

The available photometric data from Spitzer MIPS 24μm to SCUBA-2 850μm were fitted with 5 components as:

- A Bruzual and Charlot (2003) stellar SED with Calzetti et al. (2000) attenuation law, age of 200 Myr, constant SFH, solar metallicity and Chabrier IMF. The only free parameter is the extinction E(B-V).
- A mid-infrared AGN SED based on observations, from Mullaney et al. (2011). In the fitting procedure, this component can be switched off if there is no substantial contribution from the AGN.
- A Draine and Li (2007) warm dust SED, where the free parameters are U_{min} and q_{PAH} of this dust component.
- A Draine and Li (2007) cold dust SED, where the free parameters are U_{min} and q_{PAH} of this dust component. While fitting, the U_{min} and q_{PAH} are locked to be the same as those in the previous component. I notice that the radio photometry (VLA 3GHz and 1.4 GHz) is not fitted in the procedure, in order to better constrain the infrared and (sub)mm spectral region, and avoid the fit to be affected by small variations of the IR-radio correlation. However, a typical radio SED with a power-law slope of -0.8 and flux normalization level determined by L_{IR}(8-1000μm) through the IR-radio correlation with $q_{IR} = 2.4$ is consistent with the observation for the large majority of starbursts .

The output parameters of the fit, whose values are found through minimizing their χ^2 distributions, are the following:

- The AGN luminosity $\log_{10}$ (L_{AGN}).
- The ambient interstellar radiation field strength U_{min} from the Draine and Li (2007) dust model, equal for the cold and warm dust components.
- The mass of the cold and warm dust component $\log_{10}$ (M_{dust}), in unit of solar masses.
- The fraction $\log_{10}$ δ_{PDR} of warm dust (coming from photon-dominated regions, PDRs) mass to the total (cold+warm) dust mass.
- The mean interstellar radiation field (ambient+PDR) strength (<U>) of the whole galaxy.

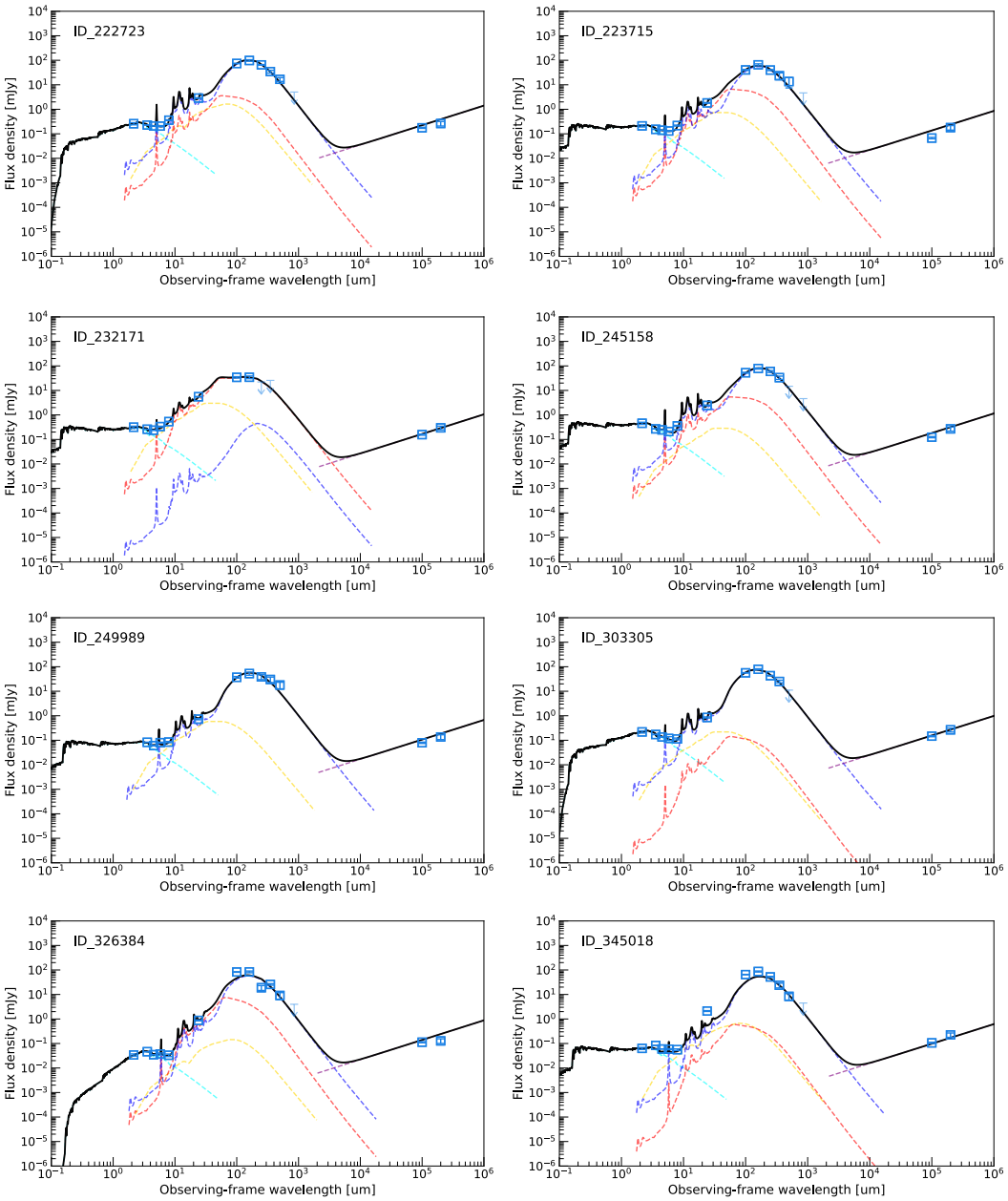

Figure 2.8: SED fitting of the 25 Magellan starbursts presented in this thesis. The photometric data and corresponding errors are shown with small blue boxes. Then, 5 components of the fits are displayed in different colors: (cyan) a stellar BC03 model; (yellow) the mid-IR AGN dusty torus emission from the templates of Mullaney et al. (2011); (red) a warm dust SED from Draine and Li (2007) models; (blue) a cold dust SED component from the same dust emission library as the warm component; (violet) the radio SED, which for our galaxies is fixed through the IR-radio correlation with $q_{IR} = 2.4$ and power-law slope of -0.8, thus is not a variable in the fit.

2.C Hα and Paβ line fitting

In this Appendix, I show in Fig.2.11, 2.12, 2.13, 2.14, the Hα+[NII]λ6583Å and Paβ emission lines (if detected) coming from the Magellan-FIRE spectra of the 25 starbursts sample investigated in this thesis, fit with single or double Gaussian profiles by using the tool MPFIT (see the Section 2.5.5 for the procedure). I show the best-fit Gaussians with red lines, superimposed on the fully reduced and calibrated spectra (black line). The noise spectrum in the same spectral range of the object is drawn in the lower panel for each cutout (green line), while the fit residuals (noise normalized, as described in Section 2.5.5) are displayed in the bottom panel with a black line.

For 12 galaxies in our sample, I fit their emission lines with a double Gaussian function (see Section 2.5.5). Among them, six are also precoalescence SBs (ID 245158, 493881, 470239, 223715, 545185, 668738) (see Section 4.2), and I interpret the two 1D Gaussians as coming from different merger components.

For the starbursts ID 862072 and 249989, the shape of the Hα line in the 2D spectra is consistent with global rotation, as they show a spatially extended Hα line with a single, uniform inclination. Additionally, their 1D line profiles are nearly symmetric, that is, the two Gaussian components have the same flux within the uncertainties. Even so, we cannot definitely exclude that these signatures are also produced by identical merging pairs rotating around the common barycenter with opposite relative velocities.

In four cases (ID 635862, 777034, 472775, 685067) I was not able to apply the two visual criteria presented in Section 4.2, because of the poor S/N of their sky-subtracted 2D spectra. However, I noticed that three of them have very asymmetric 1D emission line profiles, with fluxes of the two Gaussian components differing by $> 50\%$. Since they are less likely to be produced by a single rotating disk, I suggest they might be due to different merger components.

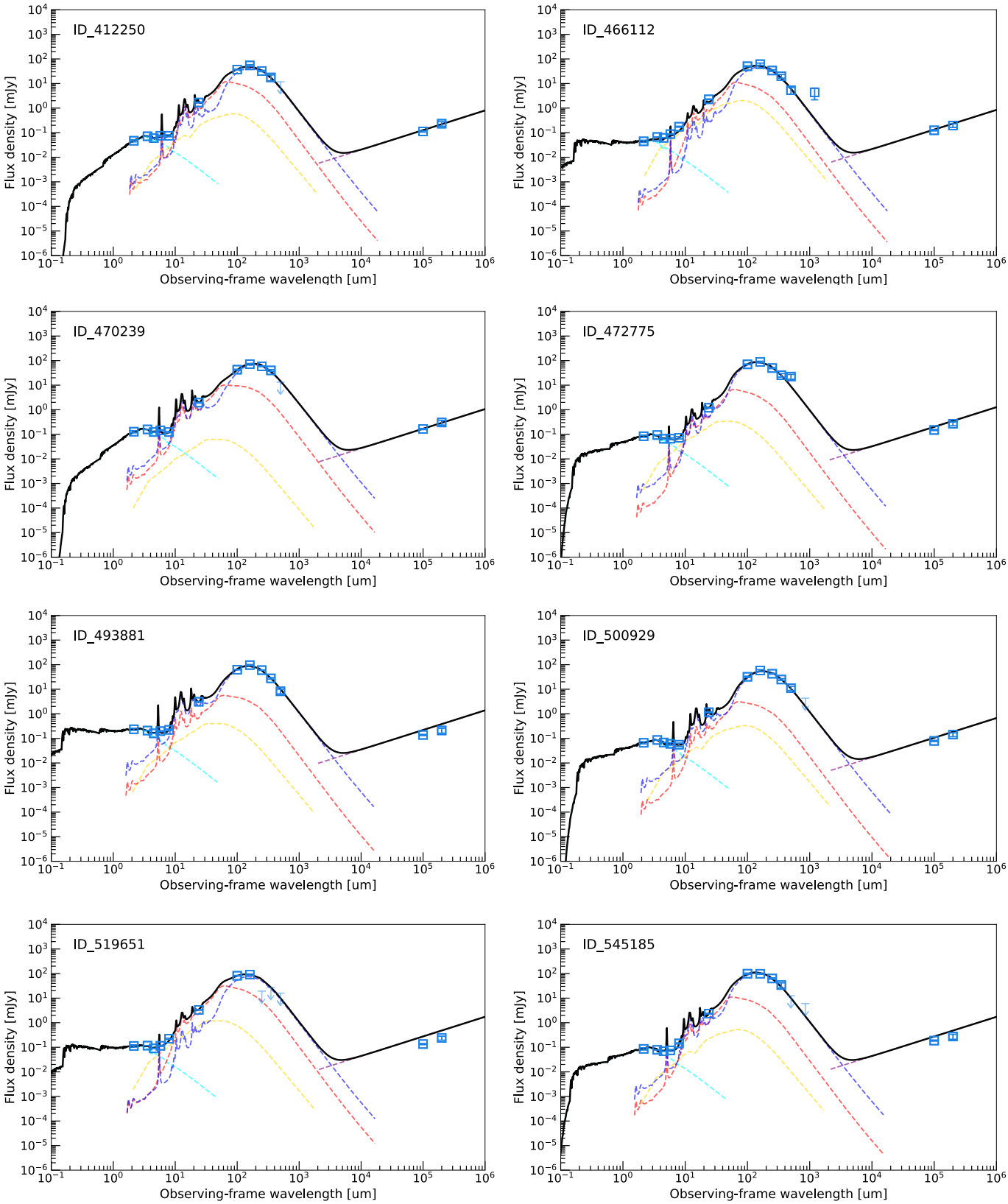

Figure 2.9: 2.8-continued.

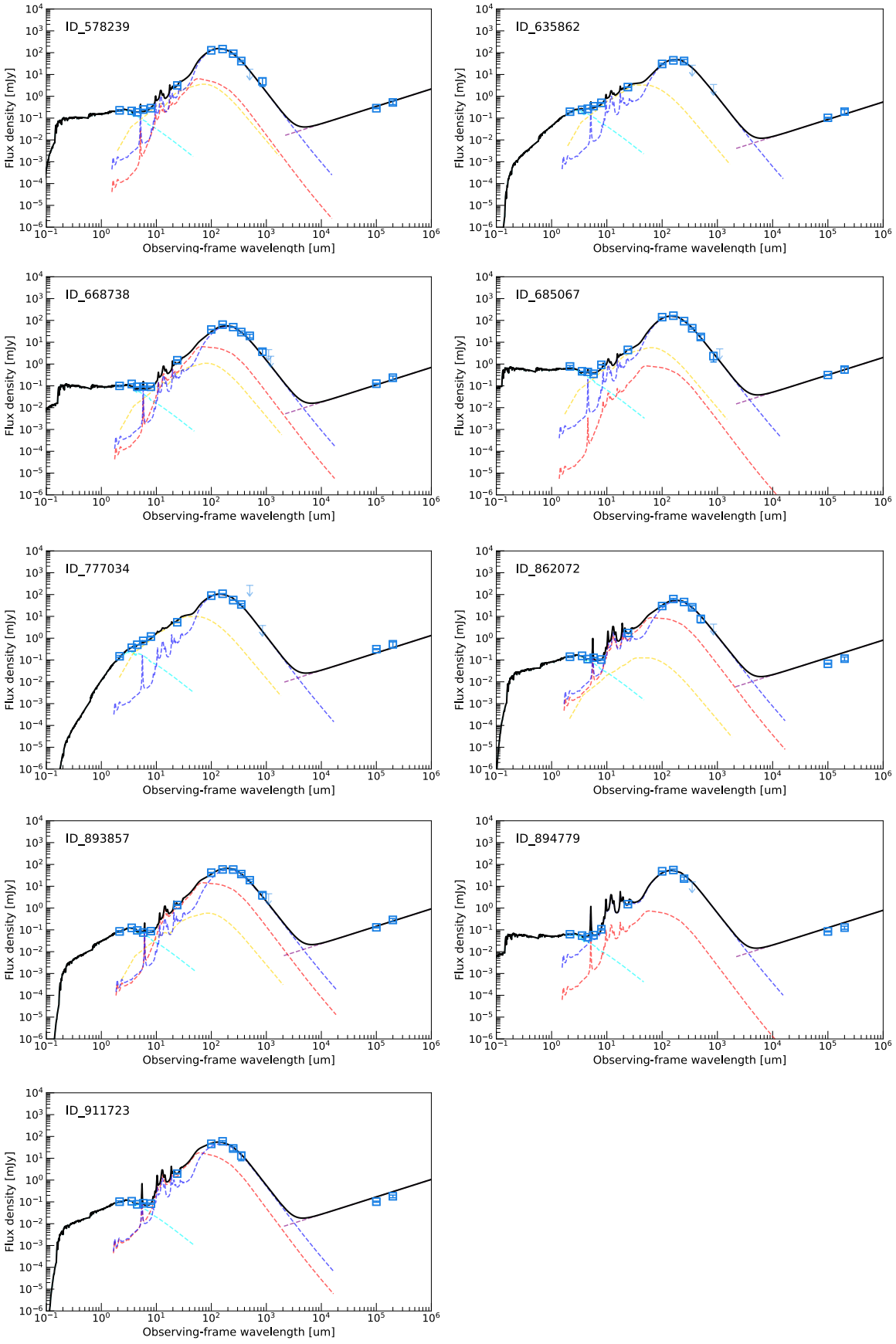

Figure 2.10: 2.8-continued.

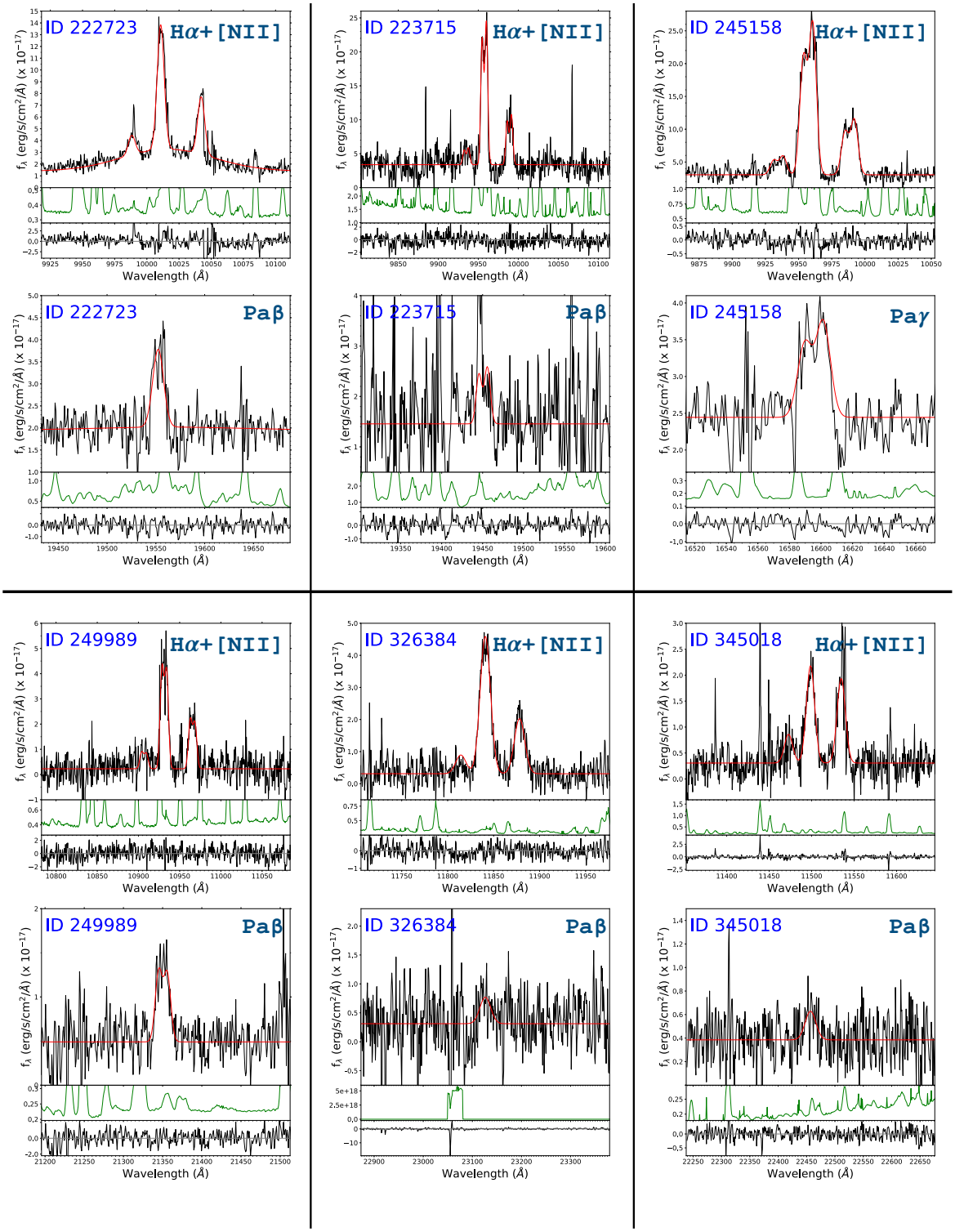

Figure 2.11: For each galaxy, I show in two contiguous panels (*Top* and *Bottom*) the Hα+[NII]λ6583Å and Paβ emission lines from the Magellan-FIRE spectrum (Paγ is shown for the galaxy ID 245158, since this line is used to infer the attenuation). Each panel is further divided into three sections: in the upper part is shown with a black line the 1-D portion of the spectrum (fully calibrated) close to Hα or Paβ line, along with the best-fit Gaussian superimposed (red line). In the second part below I display the noise spectrum for the same spectral range of the object (green line), while the fit residuals (noise normalized, as described in Section 2.5.5) are shown in the bottom section with a black line. The galaxies are presented in numerical order for double detections, while those with only Hα+[NII] detection are shown at the end.

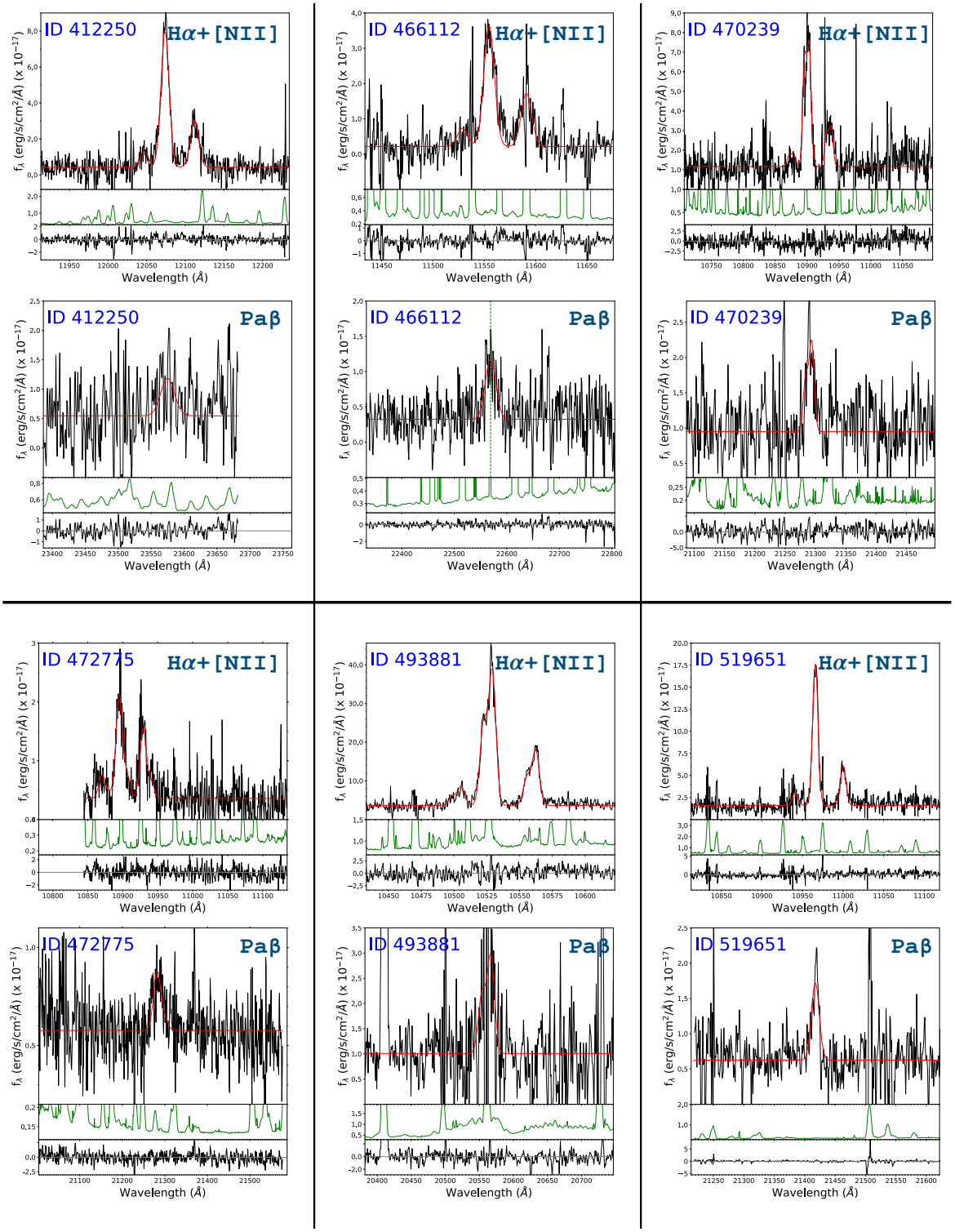

Figure 2.12: 2.11-continued.

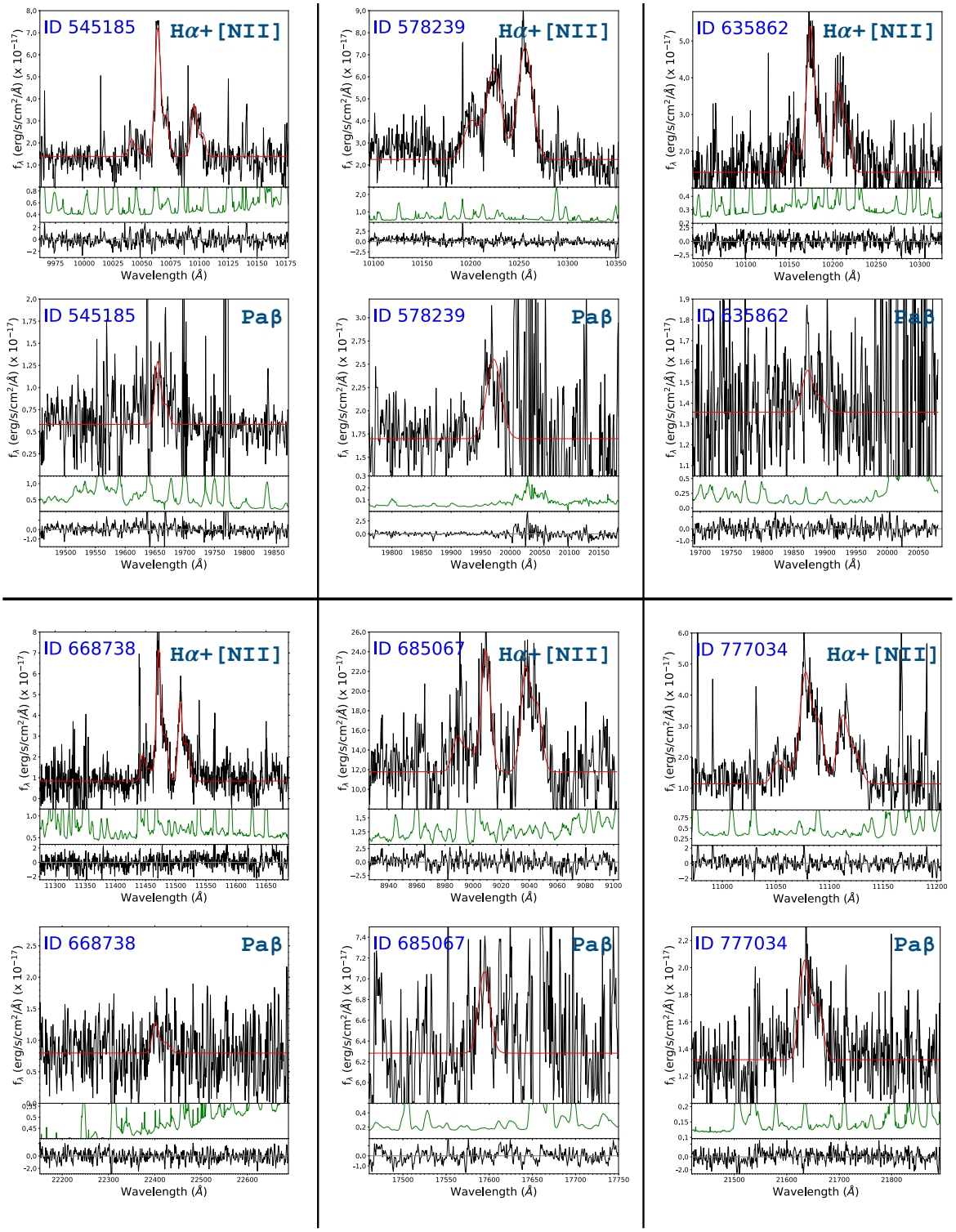

Figure 2.13: 2.11-continued.

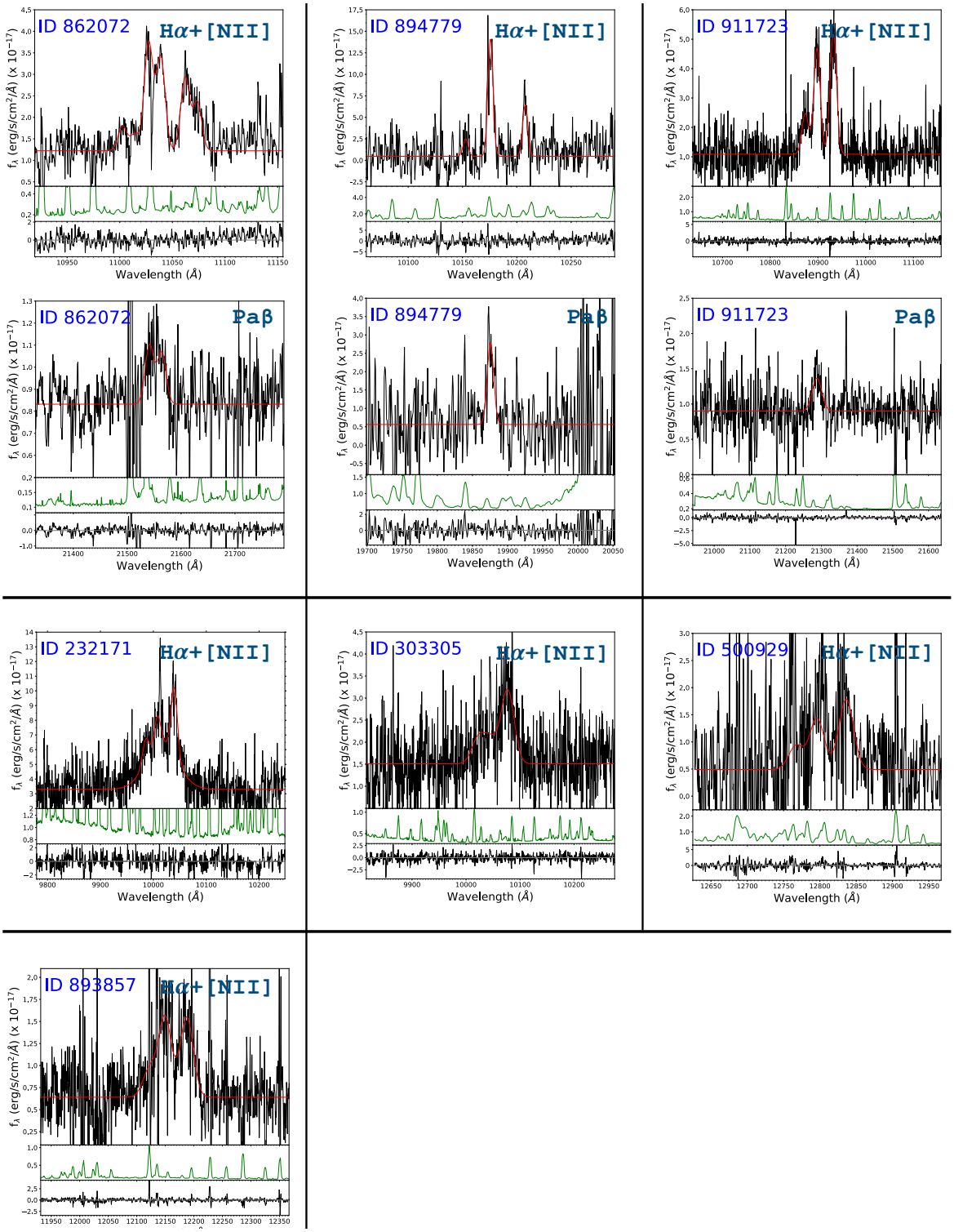

Figure 2.14: 2.11-continued.

Chapter 3

Discovery of a starburst sequence of extreme obscurations

As mentioned in Chapter 1, while locally there is a well-known connection between ultra-luminous infrared galaxies and mergers (Sanders and Mirabel, 1996; Murphy et al., 1996; Luo, Yang, and Zhang, 2014), in the distant Universe the nature and evolution of infrared luminous starbursts is still debated. Due to the enhanced gas fractions and disk instabilities of high redshift star-forming galaxies, mergers as a result might increase SFRs less dramatically (Fensch et al., 2017), and starburst galaxies may be triggered by anomalous gas accretion events (Scoville et al., 2016). However, other studies have shown that the most extreme starbursts are still merger-driven, displaying disturbed morphologies (Elbaz and Cesarsky, 2003) and increased star-formation efficiencies compared to MS galaxies (Sargent et al., 2014; Silverman et al., 2018a; Silverman et al., 2018b). In order to disentangle between the two possible scenarios, the dust attenuation is a crucial parameter to investigate, especially at higher redshifts, where interacting features (e.g., tidal tails and bridges) become difficult to identify. In particular, we know from simulations that merger events can produce a dramatic loss of angular momentum, funneling huge quantities of gas and dust particles toward their coalescing centers. This mechanism leads to the formation of very dense, compact and dust-enshrouded cores where violent, optically obscured, starburst activity is triggered, as observed in local ULIRGs, with typical sizes of the order of 1 kpc. The key point is that mergers are actually the only well known mechanism able to form such optically thick, compact, starbursting cores. Therefore, the degree of obscuration, derived by comparing dust-free and dust-affected SFRs, can provide fundamental clues on the real nature of starbursts and on their connection with local ULIRGs.

Optical lines are not enough to infer the dust properties of the whole system, as they probe very small unattenuated external regions, accounting for $\sim$ 10% of the total SFR_{IR} (Puglisi et al., 2017). We need instead a large spectral coverage extending from the optical to the near-infrared rest-frame regime (e.g., where the Paschen line series of hydrogen are present), where we can penetrate deeper in the dusty interstellar medium of these objects. This motivated the Magellan FIRE observations of 25 SBs that were described in previous Chapter 2. I remind that the redshift limit of $0.5 < z < 0.9$ is

currently the only possibility with ground-based spectrographs if we want to detect simultaneously Hα and Paβ, the second brightest Paschen recombination line. In this Chapter I present the first results of this effort (Section 3.1), and then discuss the implication on the nature of high redshift starbursts in Section 3.2. I adopt Chabrier (2003) IMF, AB magnitudes and standard cosmology ($H_0 = 70$ kms^{-1}Mpc^{-1}, $\Omega_{\rm m} = 0.3$, $\Omega_\Lambda = 0.7$). This Chapter is based on the article published in the Astrophysical Journal (Calabrò et al., 2018), in collaboration with several co-authors at CEA and foreign institutes.

3.1 Dust obscuration in distant starbursts

The first goal of this part of my thesis is to constrain the starburst attenuation properties and hence their nature from multi-wavelength diagnostics. This exploratory analysis, based on a unique sample of 25 starbursts, benefited from the wide spectral coverage of FIRE and the wealth of photometric data available for these targets (in addition to the emission lines and total infrared luminosity).

In Fig. 3.1-*top* I compare the ratio of Hα and Paβ (Paschen-Balmer decrement) to the ratio of SFRs derived from the observed Paβ and bolometric IR, that is:

$$A_{Pa\beta,\rm IRX} = 2.5 \times log_{10}(1 + \rm SFR_{IR}/SFR_{Pa\beta,obs}), \tag{3.1}$$

where $\rm SFR_{Pa\beta,obs}$ has been derived from the observed Paβ luminosity, adopting an intrinsic ratio Paβ/Hα $= 0.057$ and a standard Kennicutt, Tamblyn, and Congdon (1994) calibration, valid for case B recombination and $T_e = 10^4 K$. This plot can be considered equivalent to an IRX-β diagram (Meurer, Heckman, and Calzetti, 1999). I notice also that for three galaxies in my sample where Paβ falls in nearly opaque atmospheric spectral regions or out of FIRE coverage, I use Paγ line to infer the attenuation, estimating Paβ flux as 2.2$\times$ Paγ. Indeed, both in a mixed model and foreground dust-screen geometry, the expected observed ratio Paβ/Paγ ranges between 2.1 and 2.3, for all the attenuation values in my range.

I find that for the 25 starbursts, these two ratios, both independent measures of attenuation, do not generally scale as predicted by the Calzetti et al. (2000) and Cardelli, Clayton, and Mathis (1989) attenuation curves[1]. The value of Paβ/Hα rather saturates at ~ 0.18 (with a dispersion of ~ 0.08 dex), qualitatively consistent with an optically thick 'mixed model', in which different lines probe different optical depths.

As opposed to the foreground dust-screen, a mixed model is made of a uniform extended distribution of young stars and dust inside a volume, as already presented in Chapter 1. In the one-dimensional case, a simple analytic relation can be derived between the observed and intrinsic SFR by integrating along a segment the luminosity contribution from each differential volume element, subject to the extinction of the full optical depth in front

[1]The Cardelli relation is actually an extinction law.

of it. This yields:

$$\frac{SFR_{obs}(\lambda)}{SFR_{intr}(\lambda)} = \frac{L(\lambda)_{obs}}{L(\lambda)_{intr}} = \frac{log_{10}(e)}{0.4} \times \left(\frac{1 - 10^{-0.8 A_{\rm tot}(\lambda)}}{2 A_{\rm tot}(\lambda)} \right) \tag{3.2}$$

where L(λ) is the luminosity of a line at a wavelength λ and $A_{\rm tot}(\lambda)$ is the total absolute attenuation at λ towards the center defined as $k(\lambda)\mathrm{A_{V,tot}}/R_V$. In the last expression, $k(\lambda)$ and R_V correspond to the local extinction, for which I assumed two extreme cases of a Cardelli, Clayton, and Mathis (1989) and an SMC (Bouchet et al., 1985) law, yielding an asymptotic Paβ/Hα ratio of 0.17 and 0.2, respectively. The derivation of equation 3.2 and the calculation of the asymptotic line ratio in the limit of high attenuations is fully shown in the Appendix 3.A at the end of this chapter. Putting Eq. 3.2 (with $k(\lambda)$ calculated at Paβ) into Eq. 3.1, one can derive a relation (which is not linear) between $\mathrm{A}_{Pa\beta,\mathrm{IRX}}$ and $\mathrm{A_{V,tot}}$.

Using equation 3.2, which is similar to Eq. 19 derived by Calzetti, Kinney, and Storchi-Bergmann (1994) for a mixing geometry, we can predict the observed fluxes at all wavelengths as a function of a single parameter, $\mathrm{A_{V,tot}}$. For small values of $\mathrm{A_{V,tot}}$ this model coincides with the standard attenuation curves adopted. For large $\mathrm{A_{V,tot}}$, the local extinction inside the starburst core increases toward the center until the photons are not able to escape anymore from the galaxy, and are fully absorbed by the outer layers of dust. This leads us to depict heavily obscured starbursts as made of a central optically thick core, invisible to us, and a surrounding *skin*, producing the observed optical and near-IR nebular lines.

This picture naturally explains both the larger attenuation and SFR fraction that can be recovered by near-IR observations with respect to optical studies (Puglisi et al., 2017), as near-IR wavelengths allow us to penetrate deeper in the system. Because only the less attenuated light from the skin comes out, from Paβ we can recover, on average, 30% of the total IR SFR. However, inside the skin the optical depth becomes quickly large, with median $\mathrm{A}_{V,\mathrm{tot,\ mixed\ model}} = 9$, corresponding to a suppression of $\times$4000 of V-band light from the starburst core centers and up to extreme cases with $\mathrm{A}_{V,\mathrm{tot,mixed\ model}} \sim 30$ (10^{12} in linear scale). Hence, we cannot directly see the starburst cores in the optical/near-IR.

3.2 Discussion

Can we conclude that z $\sim$ 0.7 SBs contain extremely obscured cores that are well described by mixed stars/dust models? It is worth considering alternative explanations. It might be possible that the UV radiation from newly born massive stars is absorbed by dust within HII regions, before reaching to ionize HI outside. While strong stellar winds push the dust away to form a screen (Calzetti et al., 2000), a substantial amount of absorbing

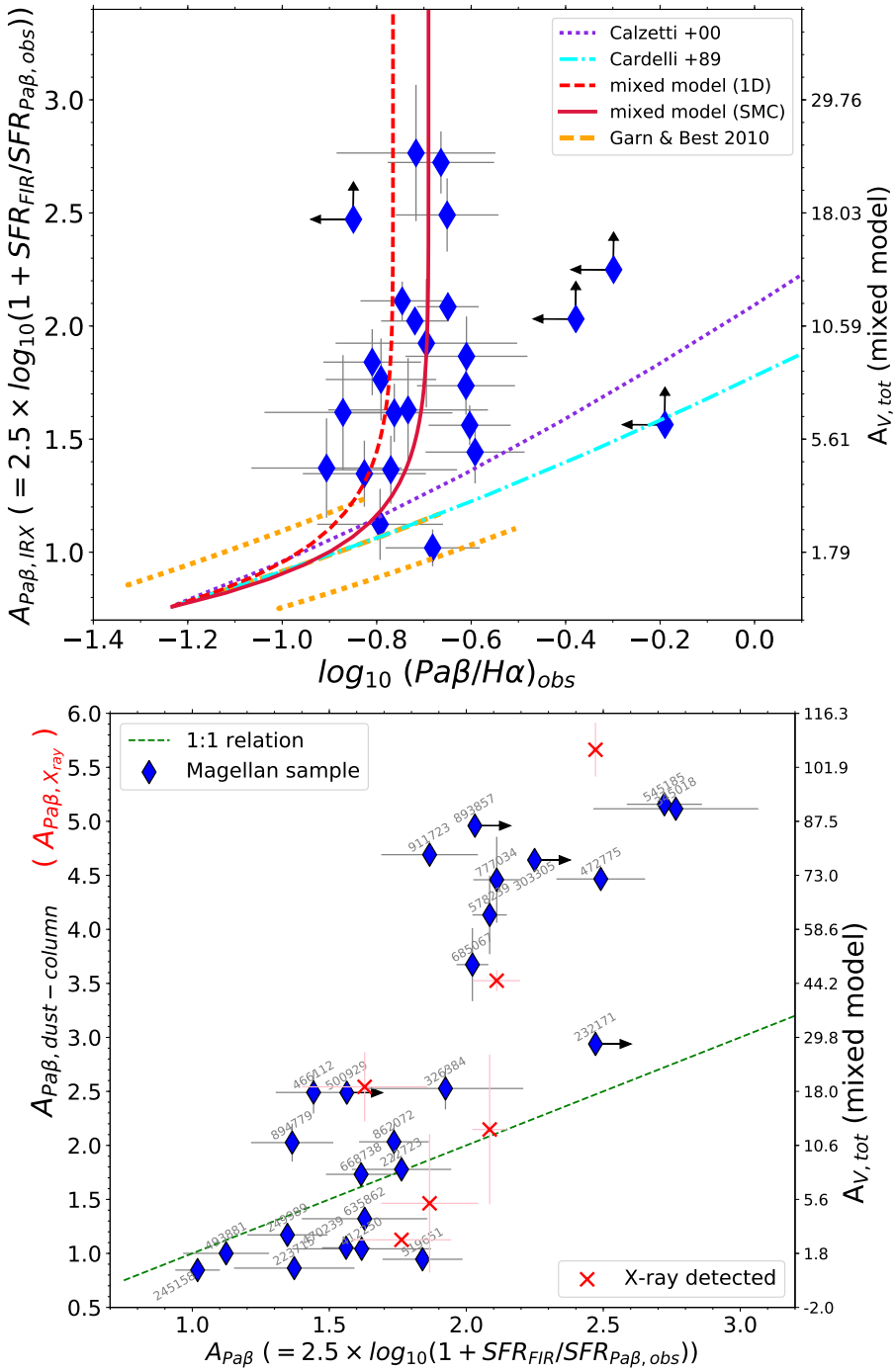

Figure 3.1: *Top:* Diagram comparing the observed Paβ/Hα ratio and $A_{Pa\beta,IRX}$. Upper and lower limits are shown with arrows for four galaxies in the sample. *Bottom:* Comparison between $A_{Pa\beta,IRX}$, which directly translates into the total A_V towards the center of a mixed model (right axis) with: (*blue circles*) $A_{Pa\beta}$ derived from the dust column-density and (*red crosses*) $A_{Pa\beta}$ calculated from X-ray hydrogen column-density N_H (Lanzuisi et al., 2017) for X-ray detected galaxies, as explained in the text.

dust may still be trapped in the ongoing SF site (Caplan and Deharveng, 1986; Bell and Kennicutt, 2001) particularly in these very dust rich galaxies.

This would *simulate* the existence of an optically thick SB core, just reducing the fraction of photons seen by HI. This could still represent a mixed model scenario, with mixing occurring at smaller scales. Whether this is a viable option depends on geometry and is difficult to model in detail.

Alternatively, the discrepant SFRs (coming from the lines and IR bolometric luminosity) may be due to time-variation effects, as L_{IR} probes longer SFR timescales than emission lines, due to the energy contribution of longer-lived B-type stars to ionizing O stars. In my case, this would require that most SBs have recently experienced a severe SFR truncation, which seems unlikely. Instantaneous and dust-free SFR tracers, like e.g., through CO[5-4] lines (Daddi et al., 2015), would shed light and help addressing definitely this possibility.

Due to the optically thick cores, the mixed model also implies that it might not be possible to detect AGNs from optical and near-IR observations, if located in the coalescing center. Interestingly, Fig. 3.2 shows that my SB galaxies often display high N2 ($\equiv$ log[NII]/Hα) indexes, which might suggest highly ionizing, AGN-dominated emission. We also see a correlation, significant at $> 95\%$ confidence level between N2 and $A_{V,\text{tot, mixed model}}$. This incidentally suggests that the four galaxies with Paβ upper limits are also very highly obscured, having relatively high N2. I argue that instead, in the majority of my targets with enhanced [NII]/Hα (and relatively higher obscurations), the line emission may be driven by shocks, which were already shown to contribute up to 50% in local ULIRGs in latest merger stages (Rich, Kewley, and Dopita, 2015). In case of shock contribution, the attenuations that I have inferred through $A_{Pa\beta,IRX}$ would represent lower limits, but the line ratios will not be affected as Case B recombination regime still holds. The correlation between [NII]/Hα and the attenuation, along with the physical interpretation, will be further investigated in Chapter 4.

Nevertheless, it would be crucial to obtain independent estimates of actual attenuations towards the cores. One possibility is provided by AGNs. I searched for evidence of AGNs among my SB sample using multiple dust-free multi-wavelength tracers in the radio and X-rays. While none of the SBs show significant radio excess, either following the criteria of Del Moro et al. (2013) and the less stringent requirements of Liu et al. (2018) (all assuming an IR-radio correlation), six galaxies (ID 578239, 635862, 777034, 232171, 222723, and 911723) are detected by XMM-Newton, Chandra or NuStar (Cappelluti et al., 2009; Marchesi et al., 2016; Civano et al., 2015) with luminosities much higher than what expected from their SFRs (Ranalli, 2004). The same objects are also the only ones in which I detect a mid-IR dusty torus component through SED fitting (only tentative for SB 578239). Their X-ray hardness ratios were converted in obscuring column densities (N_H) by Lanzuisi et al. (2017; see Fig.19 in LaMassa et al. (2016) for the method), which are N_H upper limits for gas/dust obscurations to the cores (part of the obscuration would happen within the torus itself). The relation of Güver and Özel (2009), that is, $N_H(\text{cm}^{-2}) = 2.21 \times 10^{21}\ A_V$ (mag), allows to convert N_H into a total

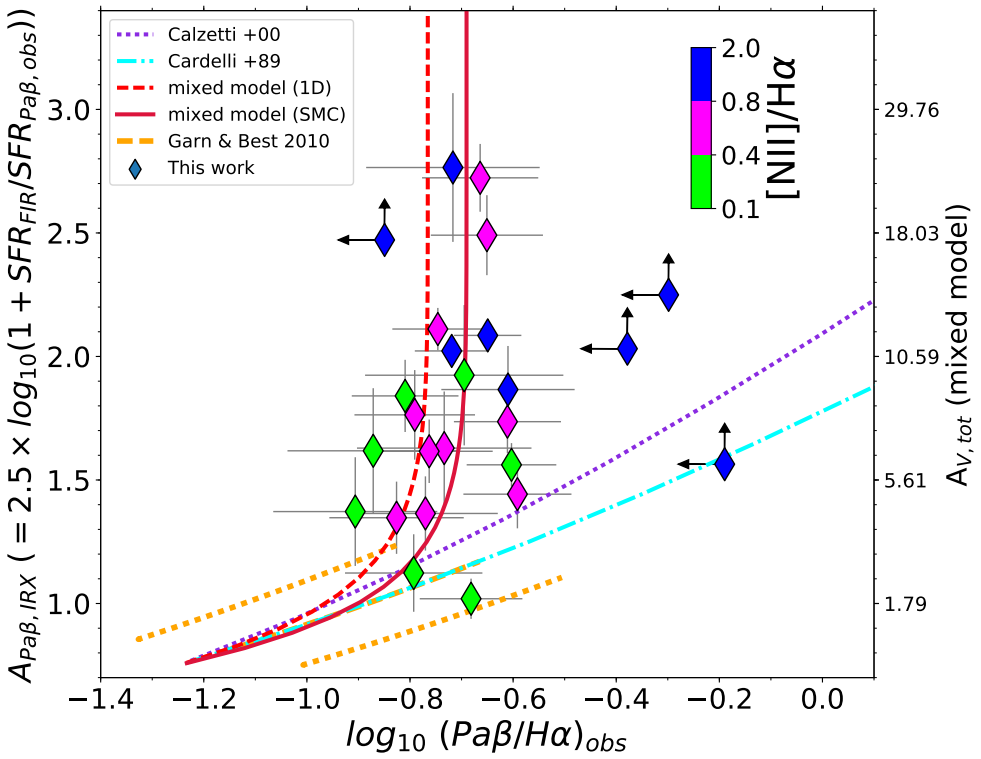

Figure 3.2: *Top:* Same diagram as in Figure 3.1, but here the galaxies are color coded according to their [NII]/Hα values. This shows that less obscured systems have lower [NII] to Hα ratios, while more attenuated starbursts preferentially show enhanced values.

A_V or viceversa. This returns generally very high X-ray obscurations for the AGNs (Fig. 3.1-*bottom*), supporting the presence of high obscuration in their center, as required by the mixed model.

As a further check, I computed the column density of gas in the starbursts cores using the total molecular mass M_{mol}, inferred as $M_{mol} = 8.05 + 0.81 \times$ log(SFR) (Sargent et al., 2014, assuming conservatively the starburst case) and the radio size, measured with GALFIT by fitting a gaussian profile (convolved with the PSF) to their VLA (3 GHz) images (see Section 2.6). From Fig. 3.1-*bottom* we can see that for half of my sample, at relatively low-moderate obscurations within the probed range, the attenuation inferred from this method is consistent with the mixed model. On the other hand, towards the highest obscurations, this approach suggests even larger attenuations. Some fraction of the emission line fluxes might come from foreground regions unrelated to the starbursting cores, presumably residual material from the merging galaxies. Accounting for this extra, modestly attenuated component would result in substantial increase of the $A_{V,tot}$ of the starburst core, providing better agreement with these column densities estimates. A proper correction for this effect would require IFU observations, that could also clarify whether my objects are similar to local ULIRGs, for which higher

values of nuclear attenuations ($A_V \sim$ 10-1000 mag) are reported in several studies (e.g., Scoville et al., 1998; Genzel et al., 1998). All in all, it appears that very heavily embedded cores are indeed present in these galaxies.

What is the origin of these extremely obscured cores? Unsurprisingly, the morphological classification derived in Section 2.8 (see Figures 2.5 and 2.6), indicates that over 83% of them are identified as mergers: 61% as major mergers, showing distorted or double nuclei, tidal tales, bridges or overlapping disks, and 21% as minor mergers, characterized by at least slightly disturbed morphology (e.g., warped disks, asymmetric spiral arms, small companion at same z, etc). A merger origin is thus plausible for the vast majority of my sample. Mergers are more commonly identified among less obscured systems (Table 2.7), which is understandable given that in the later coalescence phases any remaining merger signature becomes subtle (see, e.g., two of the three morphologically non-merger objects in my sample classified as Ellipticals/S0 by Kartaltepe et al. (2010), and the three of them have $A_{V,tot} > 9$). It is thus tempting to attribute the large range of observed properties apparently defining a sequence of obscurations as reflecting different merger phases, to varying progenitor properties (including, e.g., the gas fraction of merging galaxies and the impact geometry), or a combination of them. Nevertheless, we cannot definitely exclude with current data that the sequence may be also reflecting the amount of foreground contamination, thus unrelated to the real obscuration of the core.

My work suggests that deeply embedded merger events still largely dominate among samples of SBs galaxies at least to $z \sim 0.7$, which corresponds to 6.3 Gyr lookback time, an epoch with galaxy specific SFRs $> 5\times$ larger than local on average. At even higher redshifts, it becomes much harder to identify mergers from their morphological signatures due to surface brightness dimming and widespread presence of clumpy/irregular galaxies. I argue instead that higher-z mergers might be even more efficiently identified searching for evidence of extreme levels of obscurations, given my results and also consistently with simulations (e.g. Di Matteo, Springel, and Hernquist, 2005), representing a clear footprint of their origin. In fact, we are not aware of any viable alternative mechanism that could produce galaxy-wide obscurations of 10+ mag in the V-band: normal disk-like galaxies display much lower obscurations (orange lines in Fig. 3.1-top). Near-IR rest-frame spectra of galaxies will be easily accessible soon with JWST up to $z \simeq 7$ and down to much fainter levels, and will allow testing and applying this idea.

3.A Appendix Chapter 3

In this appendix of Chapter 3, I show some mathematical calculations related to the mixed dust and stars geometrical model. In the first part I will derive again the basic equation of this configuration, which allows to relate the intrinsic and observed flux of a source as a function of wavelength. Then I will demonstrate that in a mixed model, toward large attenuations, the

observed ratio between two emission lines tends to a constant value. Finally, I will derive for the mixed model an equivalent attenuation curve k(λ), which allows to describe it with the same formalism adopted for the dust screen geometry, even though in this case k also depends on the total attenuation of the system.

3.A.1 Derivation of the mixed model equation

To derive the characteristic equation of a mixed model, we can consider the simplest, one-dimensional configuration, as shown schematically in Fig. 3.3. I assumed a slab of length L, star-formation rate SFR_{tot} and total integrated attenuation $A_{V,tot}$, with a homogeneous mixture of dust and young stars. Even though this is an ideal situation, it can still be a good representation of the galaxy if L is >> than the sizes of single star-forming regions inside the system. Each element of the slab $\delta(L)$ will thus have an $A_V = A_{V,tot}/L$ and $SFR=SFR_{tot}/L$.

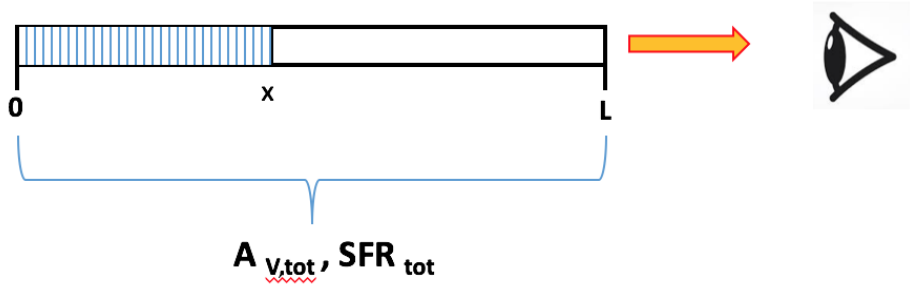

Figure 3.3: Schematic representation for the mixed model calculation in the one-dimensional case.

With this configuration, the total flux received by the observer will then be the sum of the fluxes coming from its elements, each of which is attenuated by the foreground part of the slab (decreasing from 0 to L). Since this part acts as a dust screen, the (local) attenuation seen by every element follows the typical behaviour expected for this configuration, such as a Calzetti, Cardelli, LMC or SMC law.

In formulae, the total observed flux is obtained as:

$$
\begin{aligned}
F_{obs} &= \int_0^L \frac{F_{intr}}{L} 10^{-0.4 \int_x^L \frac{A_{\lambda,tot}}{L} dx'} dx = \int_0^L \frac{F_{intr}}{L} 10^{-0.4(A_{\lambda,tot} - A_{\lambda,tot}\frac{x}{L})} dx \\
&= \frac{F_{intr}}{L} 10^{-0.4A_{\lambda,tot}} \int_0^L 10^{0.4A_{\lambda,tot}\frac{x}{L}} dx = F_{intr} \frac{10^{-0.4A_{\lambda,tot}}}{0.4A_{\lambda,tot}} \left[\frac{10^{0.4A_{\lambda,tot}\frac{x}{L}}}{ln(10)} \right]_0^L \\
&= F_{intr} \times log_{10}e \times 2.5 \times \frac{1 - 10^{-0.4A_{\lambda,tot}}}{A_{\lambda,tot}}, \text{with } A_{\lambda,tot} = A_{V,tot}\frac{k(\lambda)}{R_V}
\end{aligned}
\tag{3.3}
$$

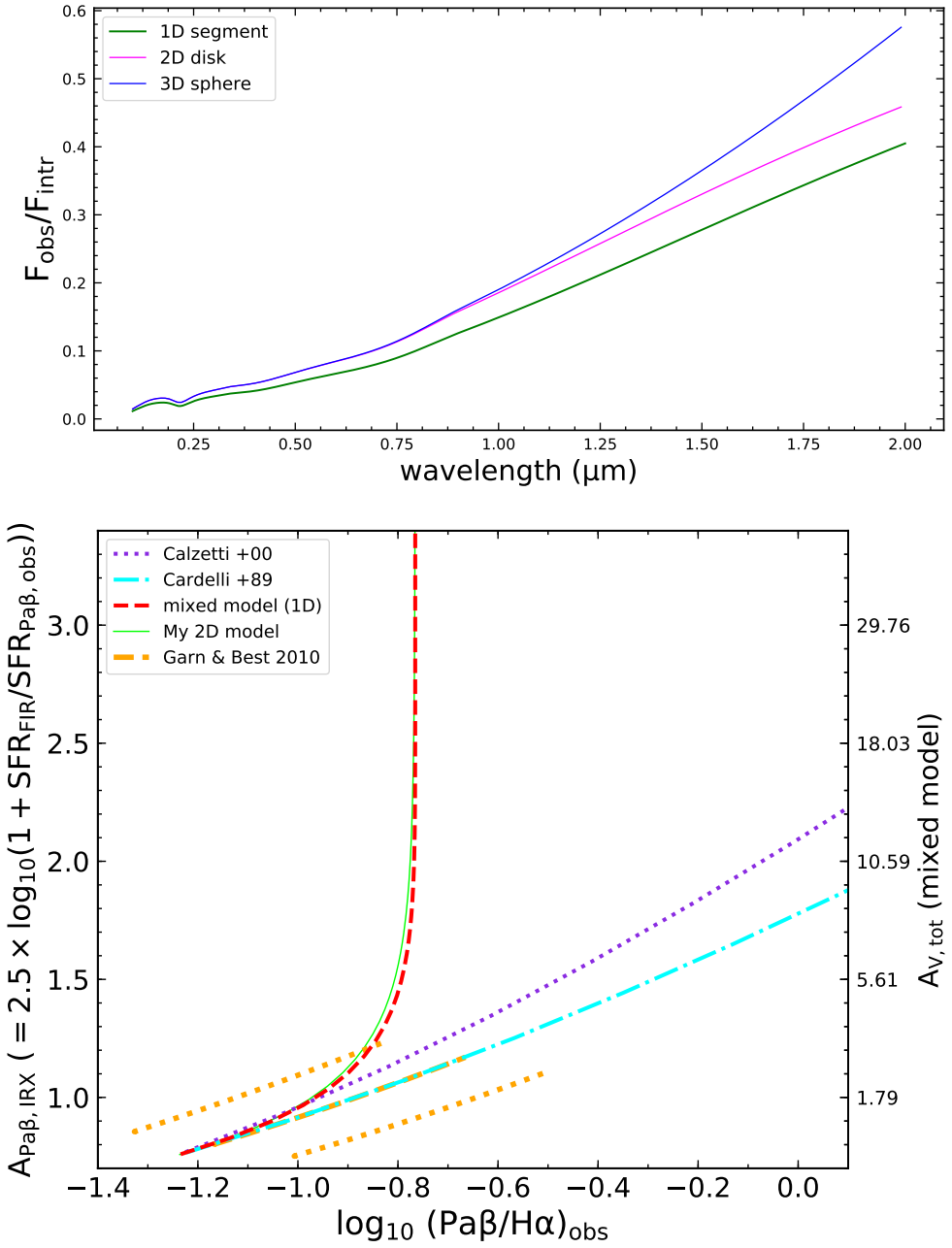

Figure 3.4: *Top:* Attenuation factor as a function of wavelength for a mixed model in 1 dimension (segment), 2D (disk) and 3D (sphere). In all the cases the total attenuation along the main diameter has been fixed to 18, which is the median of Magellan starbursts. *Bottom:* Same as Figure 3.1, but I highlight here the prediction of a 2D mixed model (i.e., a disk) with a green curve. It is clear that its behaviour is similar to that of a 1D mixed model.

In the last equation, $A_{V,tot}$ is integrated over the 1D segment, while k and R_V are given by the local attenuation (e.g., for a Cardelli, Clayton, and Mathis (1989) law $R_V = 3.1$).

I extended this calculation to a bidimensional and tridimensional geometrical configurations (i.e., a circle and a sphere), however the formula

derived is similar to Eq. 3.2 and Eq. 1.4. The 3D case yields slightly lower absolute attenuation factors (at the longest wavelengths) compared to the other configurations (Fig. 3.4-*top*). However, the multidimensional cases would give very similar predictions in the $A_{Pa\beta,IRX}$-Paβ/Hα diagram in Fig. 3.1, where they are almost not distinguishable from the 1D analysis (Fig. 3.4-*bottom*). The above qualitative result is thus broadly invariant to the number of dimensions, if we consider always a radially symmetric system. For reducing the computational time and for simplicity I have considered only the 1D case throughout this work.

An immediate consequence of the mixed model equation is that the ratio of any couple of emission lines tends to a fixed ratio (dependent on the line wavelengths) for sufficiently high attenuation.

Analytically, this ratio can be derived following the calculation below, in which we use the results of Eq. 3.2 and define x= $A_{V,tot}/R_V$:

$$\left.\frac{F_{\lambda_1}}{F_{\lambda_2}}\right|_{obs} = \left.\frac{F_{\lambda_1}}{F_{\lambda_2}}\right|_{intr} \times \frac{(1-10^{-0.4k(\lambda_1)x})}{(1-10^{-0.4k(\lambda_2)x})} \times \frac{k(\lambda_2)x}{k(\lambda_1)x} \tag{3.4}$$

If x $>>$ $k(\lambda_1)$ and x $>>$ $k(\lambda_1)$:

$$\left.\frac{F_{\lambda_1}}{F_{\lambda_2}}\right|_{obs} = \left.\frac{F_{\lambda_1}}{F_{\lambda_2}}\right|_{intr} \times \frac{k(\lambda_2)}{k(\lambda_1)} \tag{3.5}$$

In the case of $\lambda_1 =$ Hα and $\lambda_2 =$ Paβ, $\left.\frac{F_{\lambda_1}}{F_{\lambda_2}}\right|_{intr} = 0.05684$, k(Pa$\beta$)= 0.8397 and k(H$\alpha$)= 2.5350 (using the Cardelli, Clayton, and Mathis (1989) extinction law), which yields a constant ratio between Paβ and Hα of ~ 0.1716 in the limit of strong attenuation.

Finally, we can also ask whether we can express the attenuation of a mixed model configuration in terms of an equivalent k(λ), which has been defined for a dust screen model. If we consider the ratio between the observed and intrinsic flux in a mixed dust-stars geometry as:

$$coeff_{mixed}(A_{V,tot},\lambda) = 2.5 \times log_{10}(e) \times \frac{1-10^{-0.4\frac{A_{V,tot}}{R_V}k(\lambda)}}{\frac{A_{V,tot}}{R_V}k(\lambda)} \tag{3.6}$$

we can search for the new $k'(\lambda)$ such that:

$$coeff_{mixed}(A_{V,tot},\lambda) = 10^{-0.4\frac{A'_V}{R'_V}k'(\lambda)}, \tag{3.7}$$

where A'_V, R'_V and $k'(\lambda)$ are different from those of the local attenuation law assumed by the mixed model.

To find the new $k'(\lambda)$, we have to set two conditions for the attenuation law:

$$(1)\ k'(V) = R'(V) \Rightarrow coeff_{mixed}(A_{V,tot},V) = 10^{-0.4A'_V}, \tag{3.8}$$

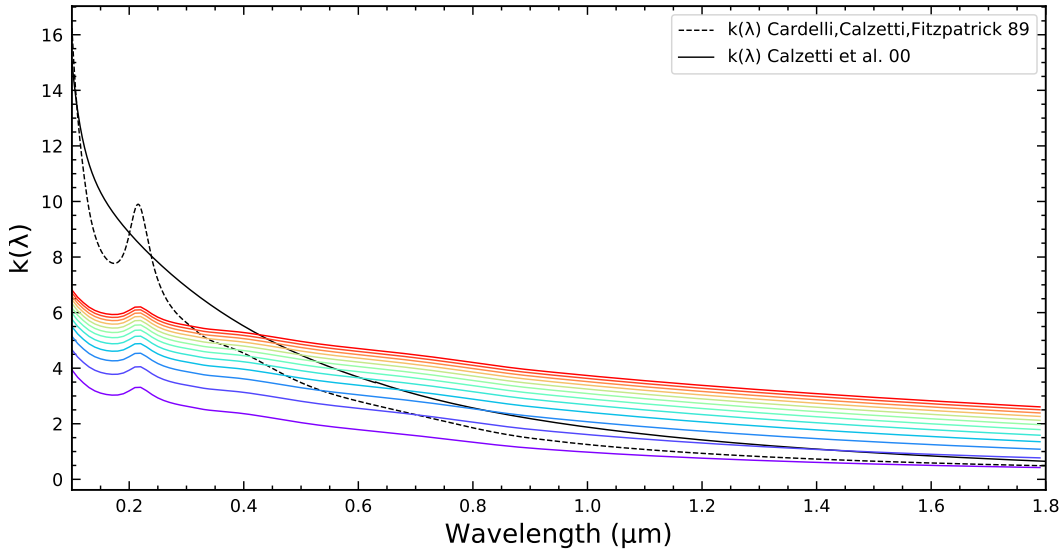

Figure 3.5: Equivalent k(λ) for mixed models with different values of the total attenuation $A_{V,tot}$ from 5 (violet curve) to 60 (red curve), in steps of 5. The Calzetti et al. (2000) and Cardelli, Clayton, and Mathis (1989) k(λ) are shown with black lines for comparison.

which yields a relation between $A_{V,tot}$ and A'_V, and

$$(2)\; k'(B) - k'(V) = 1 \Rightarrow coeff_{mixed}(A_{V,tot}, B) = 10^{-0.4\frac{A'_V}{R'_V}k'(B)} = 10^{-0.4\frac{A'_V}{R'_V}(1+R'_V)} \tag{3.9}$$

from which R'_V can be derived as a function of $A_{V,tot}$, using the result obtained in the previous step.

The analytic expressions of A'_V and R'_V are the following :

$$A'_V = -2.5 \times log_{10}(coeff_{mixed}(A_{V,tot}, V)) \tag{3.10}$$

$$R'_V = \left(\frac{log_{10}(coeff_{mixed}(A_{V,tot}, B))}{log_{10}(coeff_{mixed}(A_{V,tot}, V))} - 1\right)^{-1} \tag{3.11}$$

Then, using $A'_V(A_{V,tot})$ and $R'_V(A_{V,tot})$ just calculated in equations 3.10 and 3.11, also k$'(\lambda)$ can be finally calculated for each $A_{V,tot}$ as :

$$k'(\lambda) = \frac{-2.5 \times log_{10}(coeff_{mixed}(A_{V,tot}, \lambda))}{log_{10}(coeff_{mixed}(A_{V,tot}, B)) - log_{10}(coeff_{mixed}(A_{V,tot}, V))} \tag{3.12}$$

Figure 3.5 shows the profile of k$'(\lambda)$ with different values of the total attenuation (increasing from violet to red).

Chapter 4

Deciphering an evolutionary sequence of mergers

In the previous chapter I compared Hα, Paβ fluxes and bolometric IR luminosities, showing that the attenuation properties of intermediate redshift SBs are not consistent with the predictions of dust-foreground extinction models, but rather with those of a geometrical model in which dust and stars are homogeneously mixed. I also found that they are highly obscured on average, with median $A_{V,tot}$= 9 mag in a mixed model, while independently derived dust-column densities suggest $A_{V,tot}$ even higher for a large fraction of them, up to 75 magnitudes. This means that they have extremely obscured cores and that optical and near-IR lines only probe an external skin containing a fraction ($\sim$ 10-30%) of the total SFR. Even more, the presence of optically thick cores suggests itself a merger origin for them (like in local ULIRGs), as no other mechanisms are known to produce such large obscuring column densities of gas and dust. This can be used to identify other mergers in the high-redshift Universe, where other methods based on morphology become unfeasible.

Despite their higher average obscurations compared to MS galaxies, the same SB sample, while showing nearly constant Paβ/Hα ratios, spans a broad range of $A_{V,tot}$ between 2 and 30 (see Fig. 3.1), forming a sequence of increasing attenuations. This indicates that a substantial intrinsic diversity should exist among them, possibly related to different phases of the merger, to the gas properties (i.e., total gas mass, gas fraction) or to the morphology of preexisting colliding galaxies. In alternative, the sequence may be driven also by the orbital geometry of the merger.

Previous works have shown that starbursts and merger systems are not a homogeneous population, but their physical properties can change according to the merger phase. For example, Gao and Solomon (1999) and Leech et al. (2010) studied a sample of local (U)LIRGs with double merging nuclei. They found lower molecular gas masses and higher star-formation efficiency and gas excitation (probed by the CO(3-2)/CO(1-0) line ratio) with decreasing separation between merger components, that is, toward more advanced merger stages. However, since their sample only includes interacting pairs more distant than $\sim$ 1 kpc, this result is limited to relatively early stage mergers and does not necessarily apply also to coalesced systems. Furthermore, some

spatially resolved studies on local (U)LIRGs have found that there is a higher contribution of shocks accompanied by an increase of the nitrogen over hydrogen abundance and of gaseous component velocity dispersion toward later merger stages (Monreal-Ibero, Arribas, and Colina, 2006; Monreal-Ibero et al., 2010; Rich, Kewley, and Dopita, 2014; Rich, Kewley, and Dopita, 2015). A dependence of the attenuation on the [NII]/Hα ratio was also suggested by Fig. 3.2 in Chapter 3. On the other hand, Laine et al. (2003) and Haan et al. (2013) found no dependence on the evolutionary stage either of the morphology, luminosity density, or colors of the stellar component, and of the morphology or intensity of the ionized gas emission, apart from noticing that latest interaction times, during or after the coalescence, have among the highest infrared luminosities (L_{IR}). The absence of clear correlations in these works can be interpreted either with the difficulty of identifying correctly the merger phase from the optical morphology (which becomes even more problematic beyond the local Universe) or that other parameters are driving and tracing this transformation.

Other studies, based on simulations, have focused instead on the merger dynamics as an important factor shaping the galaxy properties during the whole interaction. For example, Di Matteo et al. (2008) have demonstrated that the inclination of the two encounters affects both the duration and intensity of the star formation, regulating the amount of gas that is funneled toward the coalescing center. Furthermore, Fensch et al. (2017) and Calabrò et al. (2019b) showed that the rotation coupling of the two colliding galaxies crucially affects the time spent by the merger system in the starburst phase, the number of starburst episodes and the spatial distribution or concentration of star-formation, as I will further discuss in the last part of this thesis (Chapter 6).

In this Chapter I investigate the origin of the obscuration sequence presented in Chapter 3 for the same sample of 25 starbursts observed at Magellan ($0.5 < z < 0.9$), and analyze whether it is possible to connect their attenuations $A_{V,tot}$ to other physical properties derived from imaging data or from their FIRE spectra, including the radio size, the [NII]/Hα ratio, the emission line velocity width and the equivalent width of Balmer and Paschen lines. In Section 4.1 I will show the main results of this analysis. Afterwards, in Section 4.2 I will describe the identification of a smaller subset of early-stage, precoalescence mergers. This is followed by a broad discussion about the physical interpretation of the connection between the attenuation and the other quantities (Section 4.3 to 4.6). Finally, I will show the location of the 25 starbursts in the stellar mass - size diagram (Section 4.7) and the properties of mid-IR and X-ray detected AGNs (Section 4.8). This last analysis will give the basis for a speculation on possible future evolutionary paths of starburst galaxies. A summary with conclusions and an appendix containing additional plots will be presented in Sections 4.9 and 4.10, respectively. I adopt the Chabrier (2003) initial mass function, AB magnitudes, and standard cosmology ($H_0 = 70$ kms^{-1}Mpc^{-1}, $\Omega_m = 0.3$, $\Omega_\Lambda = 0.7$). I also assume

by convention a positive equivalent width (EW) for emission lines and a negative EW for lines in absorption.

The results and discussions shown in this Chapter are publicly available in an *Astronomy & Astrophysics* journal article (Calabrò et al., 2019a), to which several research collaborators contributed.

I remind that the selection, observation and main physical properties of the sample used for this analysis has been described in Chapter 2, in Sections 2.3 and 2.5.2. Additionally, I refer to Sections 2.5.3, 2.5.4 and 2.5.5 for the spectral reduction and emission line measurements. Finally, the morphological properties, radio size measurements and AGN identification were presented, respectively, in Sections 2.6, 2.7 and 2.8.

4.1 A single parameter correlation sequence

The spectra that I have obtained at the Magellan telescope, along with longer wavelength radio images, provide us key information to understand both the attenuation sequence and the variety of morphological classes of my starbursts. First of all, since dissipative mergers are able to funnel the gas from the large scales of Milky-way-like disks ($\sim$ 10 kpc) to sizes that are more than one order of magnitude smaller (Di Matteo, Springel, and Hernquist, 2005), it is useful to analyze the characteristic star-forming sizes of these starbursts. Besides this, from the galaxy integrated Magellan spectra we can study together the excitation and kinematic state of the gas, and the aging of the stellar population in the outer starburst cores, traced respectively by the [NII]/Hα ratios, the intrinsic (resolution corrected) line velocity widths of single 1-D Gaussian components (=$\mathrm{FWHM_{line}}$, which is a proxy for the velocity dispersion in the system) and the Balmer/Paschen line equivalent widths (=$\mathrm{EW}_{H\alpha,Pa\beta}$).

In Fig. 4.1 and 4.2 I present the main result of this analysis, showing that the $\mathrm{FWHM_{radio}}$, the N2 parameter, the $\mathrm{FWHM_{line}}$ and the $\mathrm{EW}_{Pa\beta}$ are all correlated to the total dust attenuation $\mathrm{A_{V,tot}}$, which is used here as the reference quantity for comparison. This suggests that my starbursts can be described as, at first order, a one-parameter sequence: similar correlations at different significance levels are indeed found also when comparing on a single basis each pair of the above parameters.

I tested these correlations using three different approaches with all the available data, excluding from calculations only the upper limits and missing EW(Paβ) measurements. Firstly, I calculated the Spearman rank correlation coefficient R (the higher R, the stronger the correlation) and the corresponding p-value, which represents the probability of obtaining an equal (or stronger) R if no correlation exists. I defined a threshold probability of 5% to accept the correlation. Overall, I found that the p-values are nearly always lower than 0.05, meaning that the correlations are significant according to my criteria. In only one case ($\mathrm{EW}_{Pa\beta}$ vs $\mathrm{FWHM_{radio}}$) I determined a slightly higher p-value of 0.1 (thus a higher probability of no correlation), which

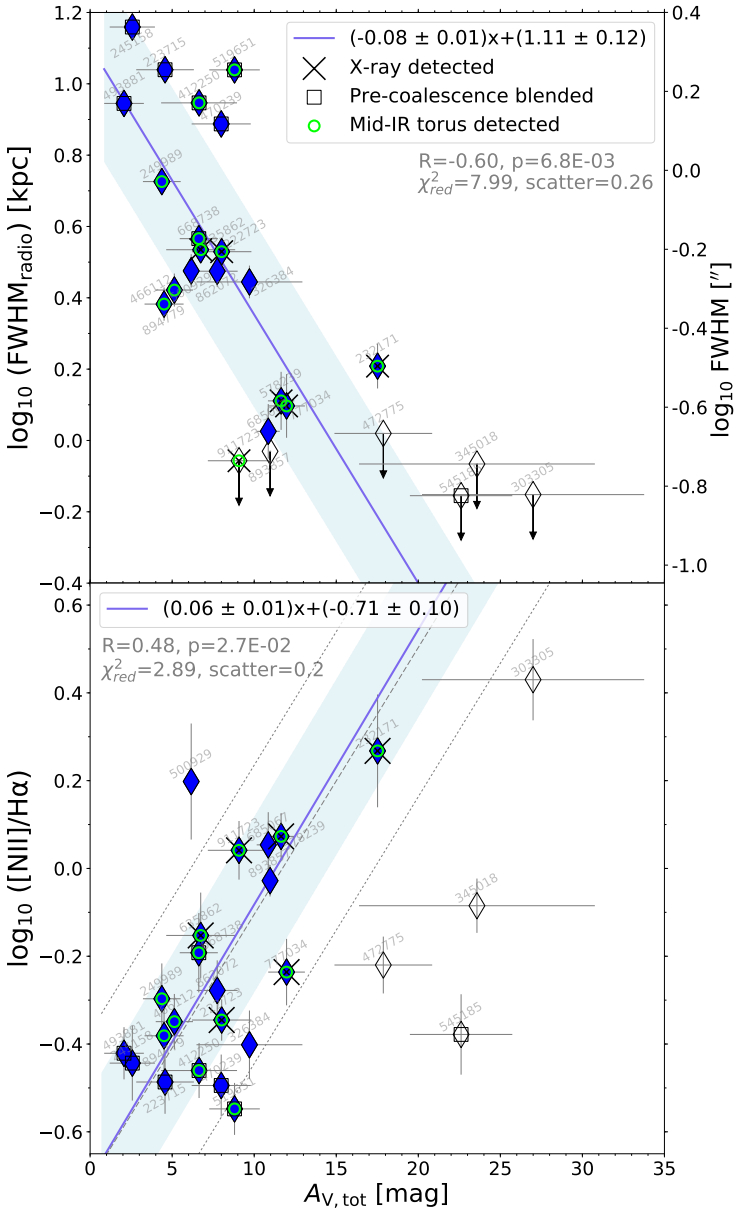

Figure 4.1: Correlations of $A_{V,tot}$ with the radio size (top), and with the N2 index (bottom). I show with filled blue diamonds all the Magellan SBs that were used to derive the best-fit linear relation (blue continuous line) and the $\pm 1\sigma$ dispersion (blue shaded area), while empty diamonds represent galaxies excluded from those calculations. The latter comprise the 4 outliers discussed in the text (ID 303305, 345018, 472775, 545185) and all the upper limits in the $A_{V,tot}$ vs $FWHM_{radio}$ plot. In the corners, I show in black the equation of the linear fit (which includes 1σ error of the two best-fit parameters), and in gray the Spearman correlation coefficient (R) with the corresponding p-value (p), the reduced chi-square of the fit (χ^2_{red}), and the 1σ scatter around the best-fit line, all of which do not take into account upper limits and the 4 outliers mentioned above. For comparison, the linear fit and 1σ dispersion including the 4 outlier galaxies are highlighted with a gray continuous dashed line and two dotted lines of the same color.

could be partly affected by the lowest number of data (i.e. lowest statistics) available here compared to the other diagrams. However, the other methods

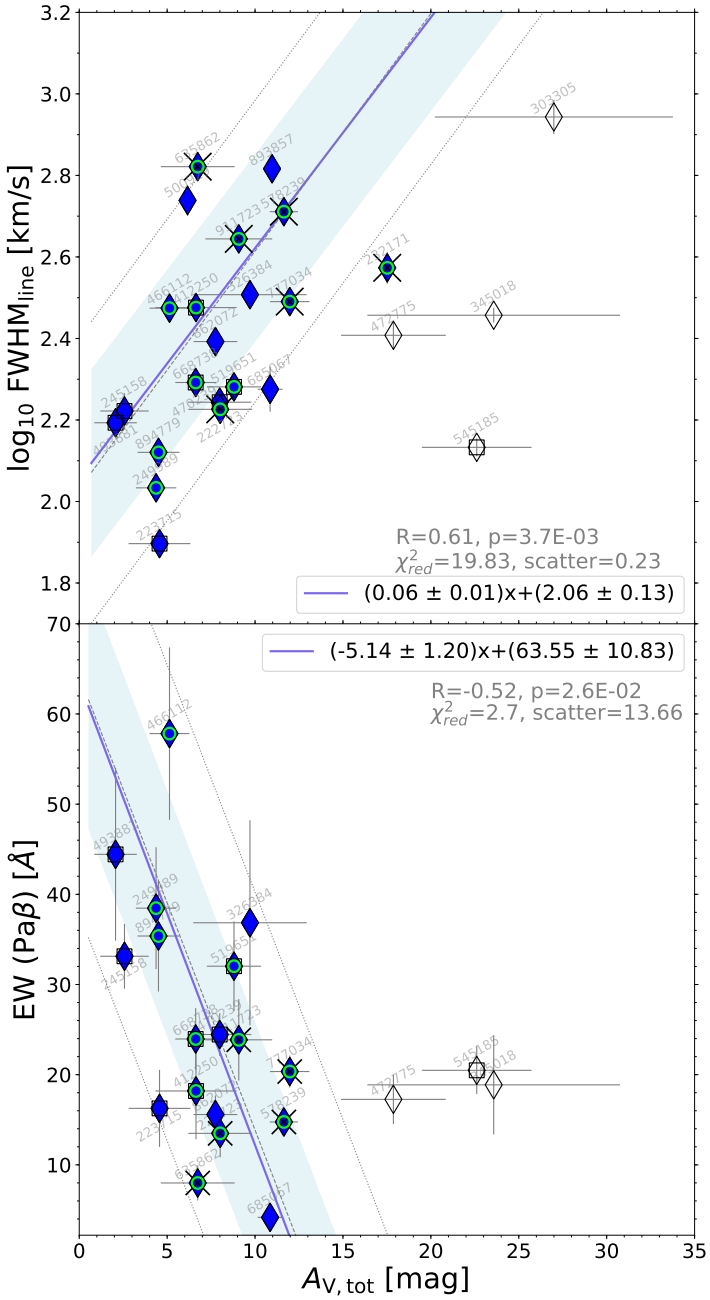

Figure 4.2: Correlations of $A_{V,tot}$ with the line velocity width (top), and with the EW(Paβ) (bottom). In the last diagram, 4 galaxies without EW(Paβ) measurements are not considered. The details are the same as Fig. 4.1.

indicate instead a stronger physical connection between the two quantities.

In the second approach, I fitted the galaxies in each diagram with a linear relation (in log-log space, except for the last diagram where the y-axis is in linear scale), by using an Orthogonal Distance Regression procedure (ODR), which allows to take into account measurement uncertainties in both axis (I discuss later possible outliers or different fitting functions). I determined

the SNR of the angular coefficient (i.e., how much it differs from 0), finding significant correlations at more than 3σ in 8 cases, while they are less strong ($2 < \mathrm{SNR} < 3$) for the remaining two diagrams. In the four correlations shown in Fig.4.1-4.2, I obtained a significance of 5.8, 5, 4.3 and 3.65σ for $A_{V,tot}$ vs N2, $FWHM_{line}$ and $EW_{Pa\beta}$, respectively. With this method, I also determined the 1σ dispersion of the data with respect to the best-fit linear relation.

	$\mathbf{FWHM_{radio}}$	**N2**	$\mathbf{FWHM_{line}}$	$\mathbf{EW_{Pa\beta}}$
$\mathbf{A_{V,tot}}$	-0.6 (0.007)	0.48 (0.027)	0.61 (0.0037)	-0.52 (0.026)
	5.8σ	6σ	4.3σ	4.3σ
	0.028%	< 0.001%	2.9%	0.12%
$\mathbf{FWHM_{radio}}$		-0.71 (0.0006)	-0.46 (0.049)	0.45 (0.1)
		5.74σ	2.93σ	4.9σ
		< 0.001%	0.033%	3%
N2			0.67 (0.0003)	-0.43 (0.05)
			5.45σ	3.85σ
			< 0.001%	0.15%
$\mathbf{FWHM_{line}}$				-0.46 (0.05)
				2.5σ
				12.9%

Figure 4.3: Correlation coefficients among the total attenuation toward the center in a mixed model ($A_{V,tot}$), the 3GHz radio FWHM size ($FWHM_{radio}$), N2, the line velocity width ($FWHM_{line}$) and the equivalent width of Paβ (which tightly correlates also with the EW of Hα, Hβ and Hδ). In each case I show in three colored lines: **(white)** the Spearman correlation coefficient and corresponding p-value; **(green)** the significance of the correlation derived from the ratio of the linear best-fit angular coefficient and its uncertainty; **(orange)** the probability of having a significance lower than 2σ if a random 20% of the sample is removed. For the calculations I excluded the upper limits, missing EW(Paβ) measurements, and the four outlier starbursts (ID 303305, 345018, 472775, 545185) in the three diagrams relating $A_{V,tot}$ to N2, $FWHM_{line}$ and EW(Paβ).

Finally, I also performed Monte Carlo simulations: for each relation, I run 100k simulations, removing each time at random 20% of the points, recalculating the significance of the correlation using my second approach. I then estimated the rate ($\sim$ probability) at which such correlations completely disappear with a significance falling below 2σ. This analysis allows to test the systematics and scatter of the correlations, ensuring they are robust and not driven by a few outliers. Overall, I find low probabilities (less than 5%) to obtain a less than 2σ significance when removing a random 20% of the galaxies, indicating that the correlations do not cancel out and are not found by chance. In the four diagrams of Fig.4.1-Fig.4.2, I obtained probabilities of 0.028%, 0.001%, 4.7% and 0.7%, in the same order as above.

I remind that $A_{V,tot}$ were determined from the Paβ observed fluxes and the bolometric L_{IR}, assuming a mixed model geometry. As explained in Calabrò et al. (2018), for one galaxy in the sample where Paβ resides in an opaque atmospheric region (ID 245158), I estimated the attenuation through the Paγ

line, adopting a flux ratio Paβ/Paγ = 2.2. This is the average expected observed ratio for all the attenuation values in my range, assuming either a mixed model or a foreground dust-screen geometry, and it was verified by nine starbursts with simultaneous detection of Paγ and Paβ.

However, for four galaxies in the sample (ID 303305, 500929, 893857 and 232171) I did not detect either Paβ or Paγ, thus in these cases I derived $A_{V,tot}$ in a similar way from their Hα fluxes (so to avoid upper limits), adding a representative error of 0.1 dex determined from the remaining sample as the scatter of the correlation between Paβ and Hα based $A_{V,tot}$. I also verified that including the upper limits in the calculations does not significantly alter the fitted trends. Hereafter, I discuss in detail on a single basis the most important findings.

In the first panel of Fig. 4.1, the FWHM radio sizes, while spanning a wide range from less than 600 pc to $\sim$12 kpc, are tightly anti-correlated to the dust obscuration level $A_{V,tot}$ (R=-0.6, p-value=0.007, and a scatter of 0.26 dex). Towards the smaller sizes and higher obscurations ($A_{V,tot} > 20$ mag), three galaxies are unresolved with VLA, thus they may be actually closer to the best-fit linear relation derived from the remaining sample. In this diagram, X-ray detected AGNs are found both at small and large radii, and have a similar distribution compared to the other galaxies, suggesting that radio size measurements and hence the result in Fig. 4.1 are not contaminated by AGNs.

In the second panel of Fig. 4.1 and in Fig. 4.2, the [NII]/Hα ratio, the line velocity width ($FWHM_{line}$) and the EW of Paβ[1] are also correlated to the total attenuation at more than 3σ significance level (R coefficients and p-values are 0.51(0.009), 0.48(0.015) and $-$0.46(0.034), respectively). However, I notice that 4 galaxies (ID= 303305, 472775, 345018 and 545185) are outside the 1σ dispersion of the best-fit relations in all the three diagrams (gray dashed and dotted thin lines). They show lower N2, $FWHM_{line}$, and higher EW than expected from their dust obscuration level. Alternatively, they have a larger $A_{V,tot}$ for their N2, $FWHM_{line}$ and EW values.

In order to understand the nature of these galaxies, I simulated 100k different realizations of the last three diagrams of Fig.4.1-4.2, with N2, $FWHM_{line}$, EW(Paβ) and $A_{V,tot}$ of 25 galaxies distributed according to the best-fit relations and the corresponding 1σ dispersions. Then I computed the probability of having at least 4 galaxies (3 for the last plot) with an orthogonal distance from the best-fit relation (gray dashed line) equal or greater than the 4 (or 3) outliers described above. I found, in the same order presented above, a probability of 0.2%, 0.025% and 0.005%, indicating that those 4 galaxies are

[1] I use this line for comparison since, being at longer wavelength, it is more representative of the whole system, allowing to probe a larger fraction of starburst cores if a mixed geometry holds. However, in the Appendix 4.10 I show that EW(Paβ) is tightly correlated to the EW of Hα, Hβ and Hδ, all of them being strongly sensitive to the age of the stellar population (at fixed SFH), thus similar results are obtained also if choosing a different line for the EW.

real outliers and cannot be simply explained by the 1σ scatter of the best-fit lines.

Given their deviant behavior, I excluded these outliers and derived again the best-fit relations, which are shown in Fig.4.1-4.2 with a blue continuous line. I found on average a reduction of the 1σ dispersion (shown with a light blue shaded area) by ~ 0.1 dex and a slight improvement of the correlation significance compared to the previous calculations. However, the best-fit linear equations are not significantly different, thus I give only the analytic expressions of this second fit where the outliers are not considered. The new results for the three diagrams, and all the diagnostics for the remaining 7 correlations are presented in Table 4.3. We notice that the 4 divergent starbursts have an upper limit on their radio size, and are not outliers in other diagrams that do not involve $A_{V,tot}$, thus the latter are not affected by this analysis. A possible physical explanation of the diverging behavior of these 4 galaxies will be discussed in Section 4.5.

Finally, if we look at all the correlations in Table 4.3, we can notice the presence of a subset of quantities that correlate better than others. Apart from the previously discussed $A_{V,tot}$ vs. $FWHM_{size}$, the line width, N2 and radio size are tightly and robustly correlated with each other. Indeed, from bootstrapping analysis, the probability that there is no correlation is less than 0.033%. As we will see in Section 4.3, this result hides a deeper physical link among them.

The results presented here show that the wide range of attenuations measured in Chapter 3 translate into a wide range of other physical properties, such as radio sizes, N2, velocity width, Balmer and Paschen EW, and even more, all these quantities appear to be connected to each other, defining a one-parameter sequence. In the following Sections I propose a physical interpretation of this sequence, and show that the correlating properties considered before are consistent with being primarily reflecting different evolutionary merger stages. Then I discuss the role played by each parameter into this sequence.

4.2 Identification of early-phase, precoalescence mergers

A first guess for a physical understanding of what is guiding the large spread of properties comes from the morphology. Indeed I have already verified that my sample comprises mergers at different stages of evolution (MI to MV), though this classification is very uncertain and sometimes misleading, as shown in Section 2.8: the faintness of tidal tails and residual interacting features make systems at the coalescence difficult to recognize, while multiple optical components and double nuclei in HST images may just reflect the dust attenuation pattern rather than the true distribution of SFR and M_*. As shown in Section 2.6, a double gaussian component fit on radio images

allowed to resolve three sources, suggesting that they may be composed of two interacting nuclei. However, the limited resolution of VLA (0.75″ of FWHM) does not allow us to derive solid conclusions on the remaining sample, which might contain more close pairs. New maps and ALMA follow-ups would increase the resolution and hopefully resolve these blended precoalescence systems.

A complementary way to find close interacting pairs in early merger stages comes from the analysis of their 2D spectra. With that aim, I performed a crude sky-subtraction procedure: I subtracted the 2D spectra taken for the same object but at different positions along the slit (A and B, separated by 2.2″), in order to remove the sky lines and allow a visual inspection of the emission line profiles. By construction, the lines appear twice in each sky-subtracted frame and exactly with the same shape: one time with a positive flux (when the object is in position A), and the other with a negative flux (when the galaxy is in position B).

By looking at these line profiles, I identified interacting pairs by requiring one of the following conditions. Firstly, I looked for detached Hα line components along the spatial direction, coming from separated merger components located at different slit positions (e.g., ID 223715, 519651, 545185, 668738 in Fig. 4.4). Alternatively, I required tilted Hα line with two different inclination angles (based on visual inspection), indicating the presence of two emitting regions with independent kinematic properties, inconsistent with a single rotating disk (e.g., ID 245158, 493881, 470239 in Fig. 4.4). In my sample, I identified from the two above conditions seven close-pair precoalescence starbursts, which are shown in Fig.4.4. For an additional source with a double radio emission component (ID 412250), one of the two nuclei was not falling inside the slit, thus it was not observable with FIRE. However, this SB should be considered a merging pair at the same level of the others.

As we can see in Fig. 4.1, the selected precoalescence starbursts are preferentially found at larger half-light radii, and all the systems with $\mathrm{FWHM_{radio}} >$ 6 kpc belong to this category. This result has two main implications. Firstly, the sizes measured in radio are not necessarily those of single merger components, but they should be interpreted primarily as separation between the two precoalescence starburst units (e.g., for all the three systems resolved in radio (ID 245158, 412250, 519651), their separation is larger than the size of single nuclei). Secondly, the early evolutionary phases are also characterized by lower dust obscurations, suggesting that the merger induced gas compaction (i.e., the increase of hydrogen column density in the center) has not yet completed.

This precoalescence subset identification provides an immediate physical interpretation for six galaxies of those that were simultaneously fitted with a double gaussian in the 1D spectrum (Section 2.5.5), explaining this profile as coming from different merger components. However, I warn that these diagnostics are not identical and the connection between the line profiles in the 1D and in the 2D spectrum is not straightforward. Starbursts with

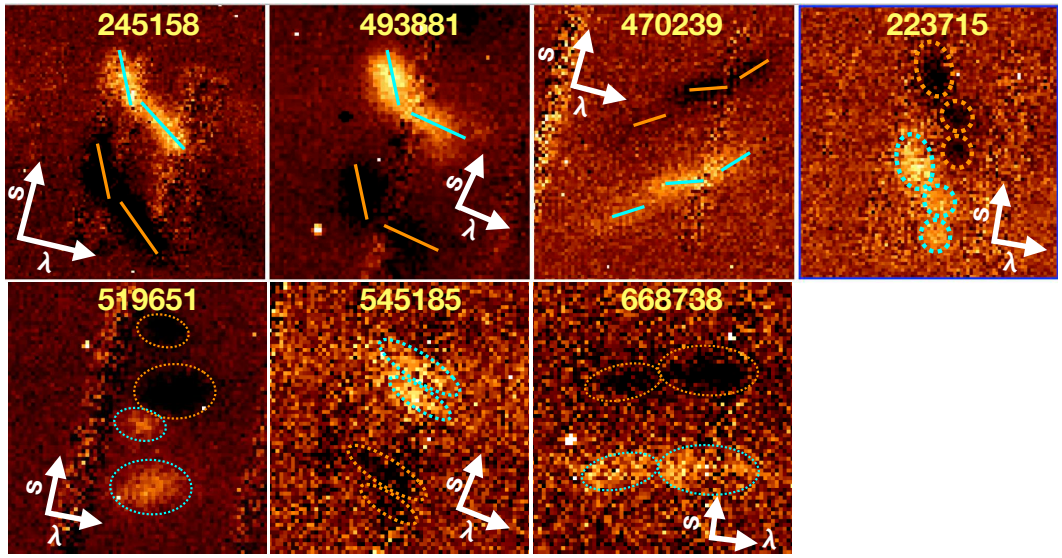

Figure 4.4: Close-up view of the Hα emission line profiles for the galaxies satisfying one of the two pre-coalescence criteria defined in Section 4.2. In each panel, as a consequence of the sky-subtraction procedure applied to the 2D spectra, the lines appear twice in different slit positions, in the first with a positive flux (in yellow) and in the second with a negative flux (in black). For each cutout, I show with two white arrows the slit position (s) and the dispersion direction (λ), which are slightly rotated due to the curved Magellan spectra. In order to clarify the classification criteria adopted in this work for finding pre-coalescence SBs, I highlight: (1) with continuous lines the different tilting angles of Hα line profiles (first 3 SBs); (2) with dotted ellipses the spatially separated Hα lines coming from different merger components (last 4 SBs).

multiple spatial emission lines do not necessarily display double gaussians in the 1D spectrum, because this is subject to projection effects and depends on the distribution in wavelength of each spatial component. Indeed, the lines of one of the galaxies shown in Fig. 4.4 (ID 519651) were still fitted with a single gaussian in the 1D.

Furthermore, my subset of six precoalescence starbursts identified from the 2D spectra is not necessarily complete, as many galaxies (e.g., ID 635862, 777034, 472775, 685067) have sky-subtracted 2D spectra with low S/N, not allowing to apply the visual criteria presented above in this Section. We would have required longer integration times or spatially resolved observations to build a complete sample of starbursts before the coalescence. Similarly, if the two merger nuclei are too close, it would be impossible to detect them even in the 2D spectra, and would need a significant improvement of spatial resolution to identify the pair.

4.3 Kinetic energy and shock enhancement toward the coalescence

BPT diagram and shocks

The second panel of Fig.4.1 shows that more obscured starbursts tend to have higher N2 relative to Hα, reaching [NII]/Hα ratios higher than 1, which are more typical of AGN and LINERs. Indeed, the classical BPT diagnostic diagram in Figure 4.5, performed on nine galaxies with [OIII] and Hβ available measurements, confirms that SBs with higher obscuration and line velocity width are found in the composite, AGN or LINER classification regions, according to empirical separation lines derived in the local Universe (Kauffmann et al., 2003; Kewley et al., 2001; Cid Fernandes et al., 2010; Veilleux and Osterbrock, 1987).

Two variants of the BPT using the [SII]6717+6731/Hα or the [OIII] λ5007 / [OII]λ3727+3729 ratios (S2BPT or O2BPT, respectively) are shown in Fig. 4.14 in the Appendix. We remind that, due to an enhanced ionization parameter and lower metallicity (at fixed mass) in the ISM at higher redshifts, the average star-forming galaxies population at z$=$ 0.7 occupies a region in the BPT diagram which is shifted rightwards by $\lesssim +0.1$ dex compared to z$=$ 0.1 (Faisst et al., 2018; Masters, Faisst, and Capak, 2016). However, there are currently no studies addressing how this will affect the separation lines among SB, AGN and LINERs. If we suppose that at z$\sim$ 0.7 the same shift applies also to these lines, galaxies at intermediate obscurations and line widths would still fall in the composite region with dominant LINER or AGN-like properties. Also, this would not affect the subsequent conclusions based on the comparison with shock models.

I noticed that the location of those galaxies shifted to the right compared to the purely SF region is consistent with the predictions of shock models, with varying shock contribution and velocity (compare with Fig. 10 and Fig. 2 of Rich, Kewley, and Dopita (2011) and Rich, Kewley, and Dopita (2014), respectively). Additionally, Lutz, Veilleux, and Genzel (1999) argue that LINER-like spectra in infrared selected galaxies are due to shocks, possibly related to galactic superwinds. The presence of increasing widespread shocks provides the most immediate interpretation for the spectra in my sample with enhanced [NII]/Hα, given that AGN emission would be highly suppressed (paper I).

However, I cannot exclude some residual influence by an AGN. Hydrodynamical simulations performed by Roos et al. (2015) show that even in the case of high obscuration an AGN can ionize the gas very far from the nucleus, reaching kpc scales and the circum-galactic medium. Furthermore, the accreting black hole might not be in the center, but that sounds unplausible: the attenuations toward the center derived independently from the X-ray detected AGNs are consistent with those derived from the mixed model (see

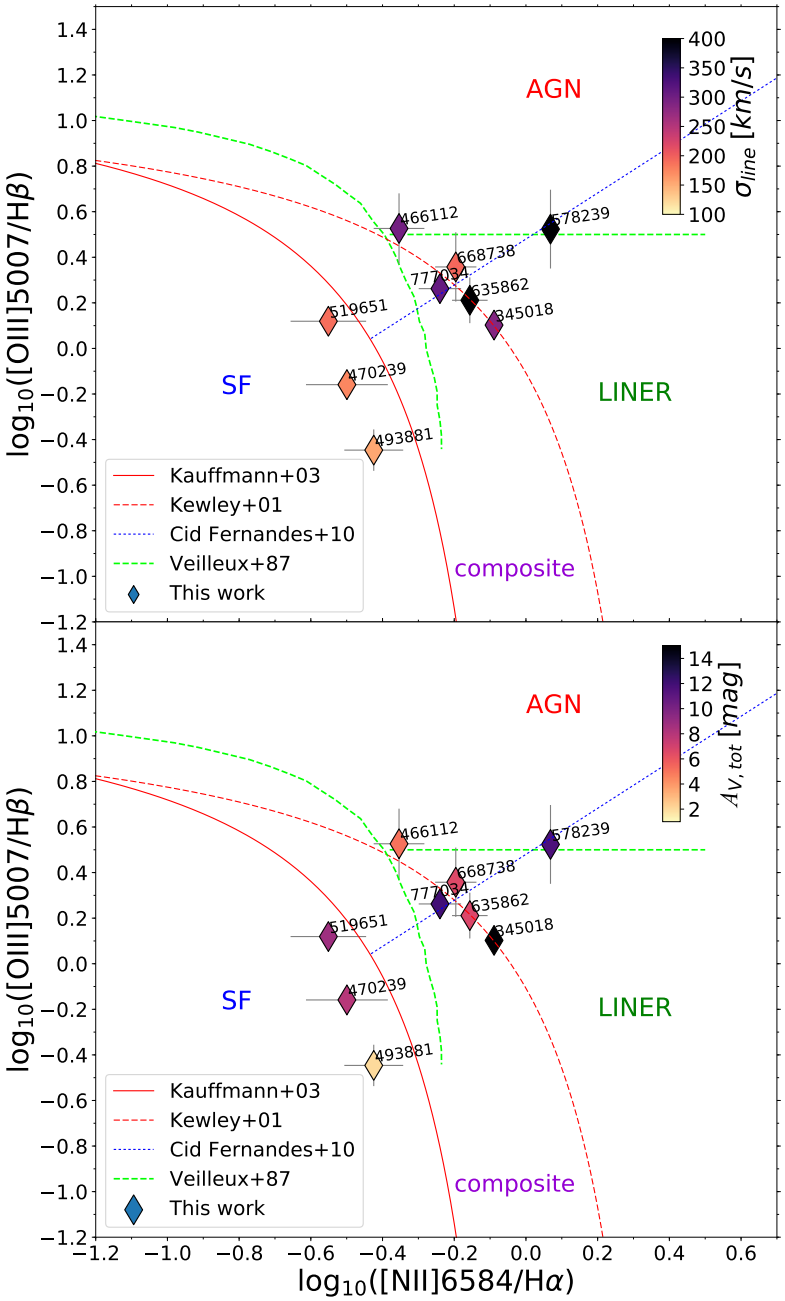

Figure 4.5: *Top:* BPT diagram of nine starbursts in my sample with optical spectra available (for one galaxy included in zCOSMOS, we did not detect both [OIII]5007 and Hβ). While three sources lie in the SF excitation region, the remaining galaxies are not consistent with SF, and their spectra show a mixture of composite, AGN and LINER properties. The color coding indicates that galaxies with higher N2 which are closer to the AGN and LINER regions also have increasingly higher line velocity widths ($\sigma_{\rm line}$). *Bottom:* Same diagram as above, but here the galaxies are color coded according to their total dust attenuation $A_{V,tot}$. More obscured starbursts preferentially display AGN or LINER properties.

paper I) and, even further, Rujopakarn et al. (2018) show that the AGN position correlates with that of active star forming regions. Finally, I also notice

that two galaxies (which simultaneously have X-rays and mid-IR dusty torus detection) were fit with broad Hα components (line width of $\sim$ 1000 km/s). Such large velocity widths have been observed in both shock-dominated regions (possibly supernova driven, Ghavamian et al. (2017)) and AGNs (Peterson, 1997; Gaskell, 2009; Netzer, 2015). IFU data would be needed to disentangle shock or AGN emission, as we expect the latter to be much more concentrated in the central part of the system.

The dynamical masses of Magellan starbursts

In order to better understand the dynamical status of the 25 Magellan starbursts and how far they are from relaxation, I compared their total masses M_{tot} to the dynamical masses M_{dyn} estimated from the line velocity widths and radio sizes. For the latter, I used the formulation of Daddi et al. (2010) as :

$$M_{\rm dyn} = 1.3 \times \frac{\rm FWHM_{radio} \times (FWHM_{line,total}/2)^2}{\rm G\ sin^2(\mathit{i})} \tag{4.1}$$

where $FWHM_{line,total}$ is the one-dimensional total line velocity width (accounting for both rotation and dispersion), while sin^2(i) is the correction for inclination that I take as the average value for randomly oriented galaxies (57°). In order to determine the total uncertainty on M_{dyn}, I considered an additional error on the inclination factor of 0.3 dex, as in Coogan et al. (2018). This represents the main contribution to the error ($\sim$ 90% in median), since the line width and radio sizes are always well measured with high S/N.

Then I compared this quantity to the total mass content (baryonic + dark matter) of the systems, estimated as :

$$\rm M_{tot} = M_* + M_{gas} + M_{dark\ matter} \tag{4.2}$$

in which M_{gas} was determined, as described in Calabrò et al. (2018), as $M_{gas} = 8.05 + 0.81 \times \log(SFR_{IR})$ (Sargent et al., 2014), valid for a starburst regime, and I assumed $M_{dark\ matter} = 10\% \pm 10\%$ of M_*. Since this contribution is highly uncertain, it was set nearly uncontrained. However, this range is consistent with studies of high-z (> 0.5) massive star-forming galaxies, which found a modest to negligible dark matter fraction inside the half-light radius (e.g., Daddi et al., 2010; Genzel et al., 2017). In any case, given the small contribution, its exact value does not affect the results of this paper. For the error determination, I considered the above uncertainty on $M_{dark\ matter}$, a 0.1 dex error on M_* (Laigle et al., 2016), and 20% incertitude on the gas mass (even though its contribution is negligible given that $M_{gas} \simeq 0.1\ M_*$ on average for my sample).

The comparison between M_{dyn} and M_{tot} in Fig. 4.6 shows that, on average, our galaxies are not completely virialized: while nearly half of the sample is consistent within 2σ with the 1:1 relation, the remaining part is located above at higher M_{dyn}. The largest departures from virialization are observed for

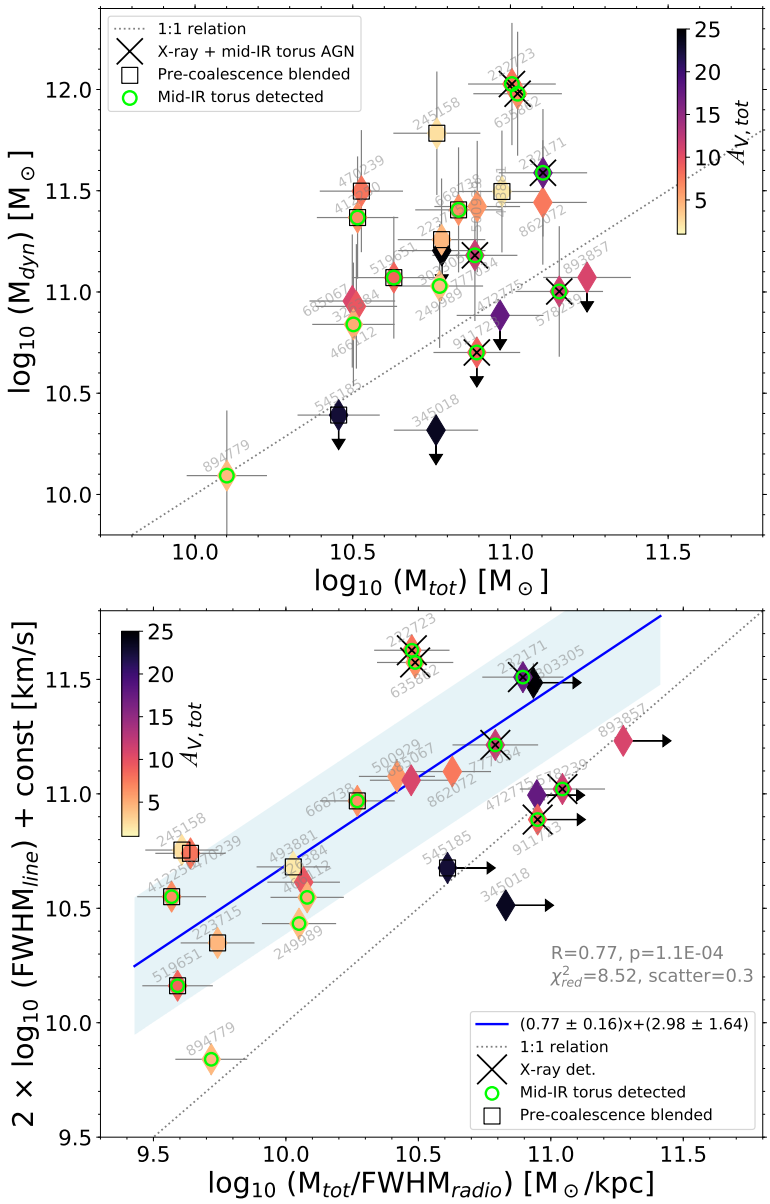

Figure 4.6: *Top:* Comparison between the dynamical mass M_{dyn} and the total mass content M_{tot} (= M_{gas}+M_*+$M_{dark\ matter}$) for my SBs sample, color coded by their total attenuation $A_{V,tot}$. *Bottom:* Diagram showing the square of the total FWHM velocity width as a function of $M_{tot}/FWHM_{radio}$, using the same color coding based on $A_{V,tot}$. On the y-axis, const= 1.3 × $G/(4<\sin^2(i)>)$ groups the coefficients in Equation 3 so as to facilitate comparison with the virialized case (1:1 relation, shown as a gray dotted line). The blue continuous line represents a linear fit to my sample, excluding galaxies with an upper limit on their radio size, while the blue shaded area shows the $\pm1\sigma$ limits of this best-fit relation. Both panels of the figure suggest that those galaxies may be approaching virialization, and more obscured starbursts are closer to the equilibrium.

the precoalescence and less obscured systems, which are supposedly earlier stage mergers. On the contrary, the systems with better agreement may be

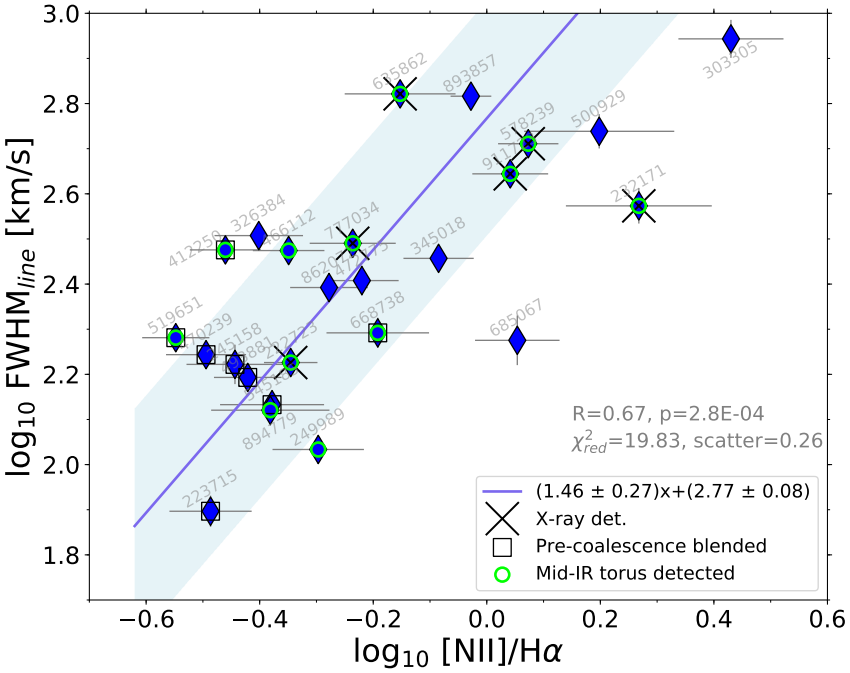

Figure 4.7: Correlation between the line velocity width of single gaussian components ($FWHM_{line}$) and the N2 index (both measured from the Magellan-FIRE spectra), indicating that the two quantities are tightly (scatter = 0.26 dex) physically related.

fully coalesced starburst cores with higher $A_{V,tot}$.

The tight connection between velocity and gravitational potential is clarified in the bottom panel of Fig. 4.6, as the $FWHM^2_{line}$ and $M_{tot}/FWHM_{radio}$ correlate at 5σ significance (with R=0.74 and p-value=0.0002). Also here, while precoalescence mergers have larger displacements from the 1:1 relation, they are confined in a region at lower velocity widths and shallower potential wells. This suggests that also other starbursts (ID 249989, 466112, 326384) in this region may be precoalescence mergers that I was not able to securely identify, due to their lower S/N 2D spectra, and indeed their optical morphology strengthens this suspicion. In the upper-right part of Fig. 4.6-*bottom*, separated from the previous sample, are clustered the more obscured starbursts, that is, supposedly coalesced mergers. I notice also that all X-ray detected AGNs are localized in this region of the diagram, indicating a possible link between evolutionary phase and AGN properties, that will be further investigated in the following Section.

Overall, the above results suggest a time-evolutionary scenario, in which more advanced, already coalesced mergers are close to virialization, and the increased central potential wells (due to the contribution of both merger components) are responsible for the enhancement of both the kinetic energy content and shocks toward later stages of the interaction. The tight relation between the line velocity width of single gaussian components (a proxy for the velocity dispersion in the system) and shock production (traced by the

N2 index) is further indicated by the color coding of the BPT diagram in Fig. 4.5-*top*, and by the correlation between $FWHM_{line}$ and NII/Hα in Fig. 4.7, which has a significance higher than 5σ (R=0.67, p-value=3×10^{-4}) and a dispersion of 0.26 dex.

4.4 Lower line equivalent widths toward late merger stages

The equivalent widths (EW) of hydrogen recombination lines give a relatively dust-unbiased picture (assuming that stars and emission lines are equally extincted) of the contribution of the SFR to the stellar mass content , and they are sensitive to the luminosity weighted age of the stellar populations, so that they could provide useful information about the evolutionary stage of the merger. However, these EWs would only probe what is happening in the outer parts of the system, since the core is completely obscured in optical/near-IR.

I show in the last diagram in Fig. 4.2 and the left part of Fig. 4.8 that, when the starbursts become more obscured, the EWs of Paβ, Hδ and Hβ decrease, indicating a gradual SFR decline in the outer skin of more obscured and compact starbursts. Additional correlations are found also independently between those EWs and the other quantities, such as the N2 index (Fig. 4.8-*right*). I additionally remark that the different Paschen and Balmer lines correlate with each other (see Fig. 4.15 in Section 5.A), for which reason my results, derived adopting the Paβ line as a reference (because it is the least attenuated), are also valid when considering the Hδ, Hβ and Hα lines.

In my sample, I also found that the Balmer EWs, while having a large dynamical range, can reach very low values: in five galaxies (ID 303305, 685067, 777034, 862072 and 345018) I measure an EW(Hδ) < -4 Å (i.e. in absorption), which are typically found in E+A dusty galaxies (Poggianti and Wu, 2000). Low EW hydrogen recombination lines (in strong absorption) are clear signatures of the prevalence of A-type stars, indicating that a recent (< 1 Gyr ago) massive star-formation episode has taken place during the past 10^8-10^9 yr, while the youngest stellar populations (mainly OB stars) are nearly all obscured by dust in the inner starburst core. These dusty starburst systems should also not be confused with post starburst (PSB) galaxies, which have similar absorption EWs (e.g., EW(Hδ) lower than ~ -5 Å as in Goto (2007) and Maltby et al. (2016)), but are thought to be nearly (or already) quenched systems, with much lower SFR levels and lower dust content compared to my sample (see Pawlik et al. (2018) for a full discussion of the different types of PSB galaxies). I caution that the quenched PSB selection from only the Balmer EW can actually return real starbursts and not post starburst systems.

Putting all together, the time-evolutionary scenario that I have suggested has the advantage of explaining in a simple way these new results. If we follow the merger evolution towards the coalescence, the outer starburst

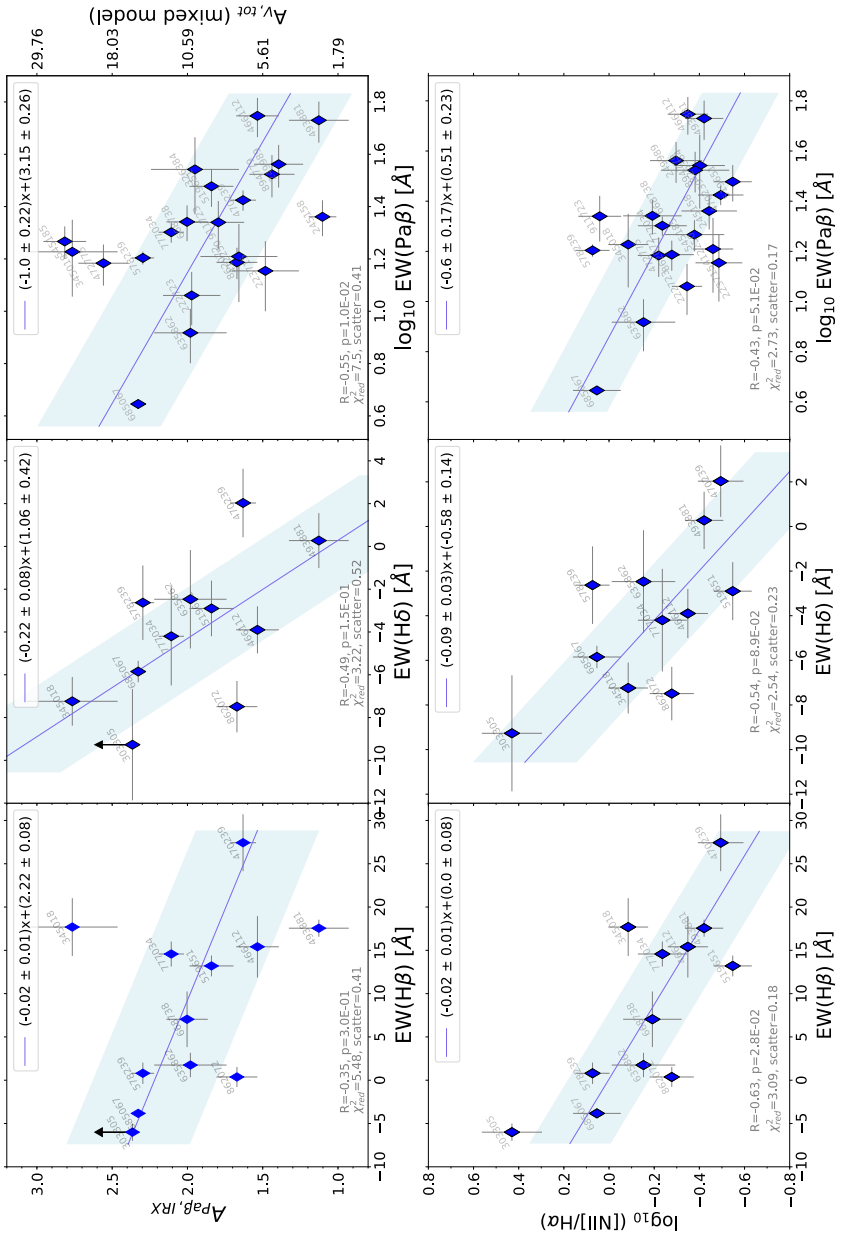

Figure 4.8: *Top:* Comparison between the EW of Hδ, Hβ and Paβ lines to the dust attenuation parameter $A_{Pa\beta,\mathrm{IRX}}$, defined as $2.5 \times log_{10}(1 + \mathrm{SFR_{IR}}/\mathrm{SFR}_{Pa\beta,\mathrm{obs}}$ (Section 3.1). I remark that the last panel is equivalent to the last plot in Fig. 4.2, even though a different scale has been used: the relation between $A_{Pa\beta,\mathrm{IRX}}$ and $A_{V,\mathrm{tot}}$ is explained in Section 3.1. *Bottom:* Correlations between the EW of Hδ, Hβ, Paβ lines and the N2 index ($= log_{10}([NII]/H\alpha)$). The blue continuous lines are the best-fit linear relations, determined as explained in Section 4.1, while the blue shaded area show the $\pm 1\sigma$ scatter of my data around the best-fit relations.

skin becomes increasingly dominated by A-type stars, recognizable through the deep absorption lines in the optical/near-IR and which were formed at earlier times when the separation between the merging nuclei was larger. At

the same time, the star-formation in the skin is being suppressed, possibly driven by supernova feedback.

4.5 Outliers

I found in Section 4.1 (Fig. 4.1-4.2) that 4 galaxies are outside the 1σ dispersion of the best-fit relations between the dust attenuation $A_{V,tot}$ and, simultaneously, the [NII]/Hα ratio (N2), the line velocity width ($FWHM_{line}$) and the EW(Paβ). In particular, they have lower N2, $FWHM_{line}$ and EW(Paβ) than expected from their $A_{V,tot}$, suggesting that, compared to other highly obscured galaxies, there is a minor impact from shocks or a dominant contribution of star-formation to the emission lines.

Within this SB sample, I recognize that these 4 outliers have the largest dust obscurations $A_{V,tot} \geq 18$ mag, and are among the most compact, with radio FWHM sizes below 1 kpc. These extreme and peculiar features suggest they may represent the very end stages of the merger evolution, and that the correlations with $A_{V,tot}$ may saturate toward these late phases. I also notice that the same objects are not systematically outliers when we consider their N2, $FWHM_{line}$ and EW(Paβ) values, confirming the close physical connection among these quantities, as shown in the two previous Sections 4.3 and 4.4.

4.6 The complete merger sequence at intermediate redshifts

Observations and results presented in previous sections, suggest we are starting to see an evolutionary sequence in high-redshift mergers. This can be traced through a variety of physical measurable quantities of my galaxies, including the total attenuation toward the center, the characteristic size of the starburst, the EW of hydrogen absorption lines, and finally the [NII]/Hα ratios and line velocity widths, which behave similarly. In Fig. 4.9 I schematize with a cartoon all the results found so far, showing with a red continuous line the qualitative trend of the different physical quantities as a function of time. I divided the time axis into five merger evolutionary stages, which are arranged in relation to the two most crucial transformation events during the merger: the coalescence and the blow-out (or QSO) appearance.

I notice that the first phase may not necessarily represent the beginning of the interaction, that is, when the two galaxies approach for the first time. Even though the whole merger episode may last 1-1.5 Gyr in total, from the first encounter to the formation of a passive spheroidal system, the starburst activity is typically shorter, ranging 200-300 Myr (Di Matteo et al., 2008) and may be triggered intermittently at various stages of the evolution. Furthermore, whether or not a strong burst is already activated at the first approach depends on many factors, including the impact geometry, the morphology,

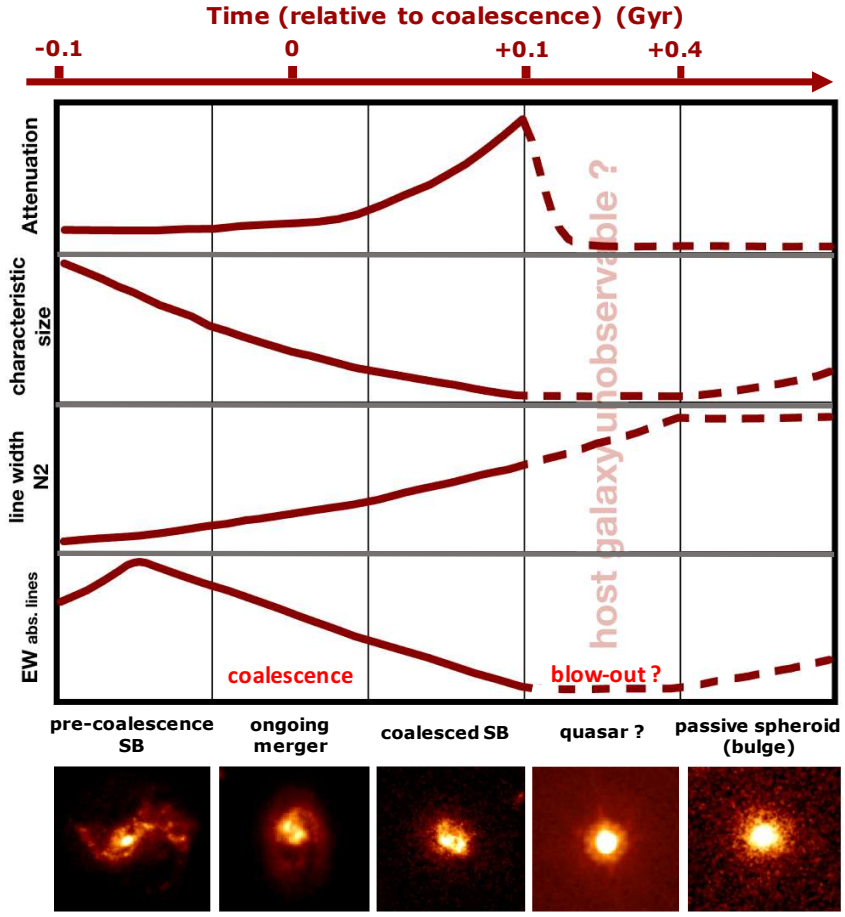

Figure 4.9: Schematic illustration of the time-evolutionary behavior of the physical parameters studied in the text: dust attenuation, characteristic size of the system, line velocity width (or, equivalently, the N2 index) and the EW of Balmer and Paschen lines. The time sequence is divided into five fundamental merger stages, with the QSO and passive spheroidal system representing the final stages according to the classical merger paradigm (Sanders and Mirabel, 1996; Hopkins et al., 2008b; Hopkins et al., 2008a). Solid lines are qualitative trends during the SB phase inferred from my results, while dashed lines are predictions for the future evolution of the four parameters shown on the y-axis (line width and N2 index behave similarly). In the upper part of the figure, I show a qualitative merger timescale following Fig. 1 of Hopkins et al. (2008a), assuming for the merger a total starburst duration of 200 Myr. For each phase, we show in the bottom part the ACS-F814W cutout of a representative case. The first three images are SB galaxies from my sample: ID 223715, ID 777034 and ID 472775. They were chosen as having increasing dust attenuations and radio compactness, suggestive of more advanced merger phases: the first was identified as a precoalescence merger in Section 4.2, while the latter is unresolved in radio and is highly obscured ($A_{V,tot} = 18$ mag). The last two cutouts show a quasar at $z = 0.73$ and an ETG at $z = 0.66$, selected in COSMOS field from the catalogs of Prescott et al. (2016) and Tasca et al. (2009), respectively.

the stellar mass ratio and the gas content of the colliding galaxies (Di Matteo et al., 2008).

Besides the observable starburst phases studied in this work, can we also make some predictions on the future evolution of these systems ? In general, it is very hard to demonstrate visually a connection between mergers and their descendants. Indeed, not all merger-induced starbursts exhibit morphological disturbances (Lotz et al., 2008), and when merger residual signatures are present, they fade rapidly, becoming almost invisible beyond the local Universe even in the deepest optical images (e.g., Hibbard and Vacca, 1997). We can in principle rely on hydrodynamical simulations, which allow to trace the full time-sequence of mergers, even though they also present limitations due to the many assumptions, initial conditions and physical complexity involved in such events.

In the classical theoretical merger paradigm, the infalling gas triggers obscured AGN accretion (Bennert et al., 2008a), whose peak of activity typically occurs $\sim$ 250 Myr after the onset of the starburst (Wild, Heckman, and Charlot, 2010), and $\sim$ 100 Myr after the peak of SFR (Davies et al., 2007; Hopkins, 2012). It is during these later starburst phases that the AGN feedback can blow out with strong feedback winds the surrounding dust and gas cocoon, eventually revealing itself as a bright QSO (Hopkins et al., 2008b). This phase is generally very short, lasting for $\lesssim$ 100 Myr (Hopkins and Elvis, 2010), and has been claimed since a long time: Lípari et al. (2003) suggested that QSOs could be indeed young IR active galaxies at the end phase of a strong starburst.

Since the QSO dominates the luminosity of the system at all wavelengths, it would be extremely hard to analyze the physical properties of the host galaxies during this phase. Indeed, Zakamska et al. (2016) show that even in radio-quiet QSOs both the infrared and the radio emission are dominated by the quasar activity, not by the host galaxy. An alternative possibility is to look far from the central bright source. Recent works are revealing Ly-α nebulae surrounding high-redshift quasars, with extension that can reach tens of kpc ($\lesssim$ 50 kpc) from the center (Arrigoni Battaia et al., 2019). On the other hand, one may focus on local samples, increasing simultaneously the images resolution. For example, Lípari et al. (2003) and Bennert et al. (2008b) discovered with HST the presence of outflows, arcs, bubbles and tidal tails in optical band in a sample of local QSOs, possibly formed through strong galactic winds or merger processes. Again in nearby ($z < 0.3$) QSOs, near-IR H band adaptive optics observations (Guyon, Sanders, and Stockton, 2006) revealed that $\sim$ 30% of their hosts show signs of disturbances, and the most luminous QSOs are harbored exclusively in ellipticals or in mergers (which may become ellipticals soon). Furthermore, while the SFRs of the hosts are similar to those of normal star-forming galaxies, their mid- and far-IR colors resemble those of warm ULIRGs, strengthening a connection between these two objects.

In the following two Sections 4.7 and 4.8, I discuss separately the two ending stages of the merger sequence, and investigate how my work can provide some clues to understand what are the physical properties of the

systems into which the starbursts will evolve. In the cartoon of Fig. 4.9, the predicted evolution for all the quantities studied in this paper (see Section 4.1) is shown with a dashed line. These qualitative trends are motivated mainly from simulations, and are not confirmed observationally.

4.7 Mass-size relation and comparison with higher and lower-z starbursts

The merger-induced starbursts are supposed to end up in a passive system, but we do not know the exact physical properties (e.g., size, stellar mass, morphology) of these merger remnants. Sub-millimeter galaxies (SMGs) at high redshift (> 2), which are commonly viewed as higher luminous counterparts of lower redshift ULIRGs, have been suggested to be direct progenitors of massive ETGs (Tacconi et al., 2008; Toft et al., 2014). We can investigate this connection by comparing in Fig. 4.10 the stellar masses and the characteristic sizes of starbursts with those of disk galaxies and spheroids at z $\sim$ 0.7 (van der Wel et al., 2014). To be conservative, I am adopting here the M_*-size relations for circularized radii. If we consider instead the non-circularized cases, the same relations would slightly shift upwards by $\sim$ 0.1 dex. In addition, I remark that I am comparing the radio (starburst) extensions to optical rest-frame sizes tracing the stellar mass distribution of disks and elliptical galaxies. Indeed, I implicitly assume that, after the gas in starburst cores is converted into stars, the extensions of these cores will represent also the stellar component sizes of their passive remnants. On the other hand, they may still represent the dense star-forming gas components of post-starburst systems if some residual is left after the merger, as they may remain compact for at least 1 Gyr (Davis et al., 2019).

In the diagram of Fig. 4.10, six SBs are consistent with the late-type galaxy (LTG) relation at z $\sim$ 0.7. However all of them are precoalescence SBs and, as we have seen before, they should not be considered disk galaxies as their size is primarily reflecting the separation between the merging components. For two of the three galaxies resolved in radio, the single values move to the bottom toward the early-type galaxy (ETG) relation. The characteristic sizes of this subset ($FWHM_{size}$ ranging 3-15 kpc in diameter, with median $FWHM_{size}$ of 8 kpc) are similar to those typical observed in SMGs (Casey et al., 2011; Tacconi et al., 2008; Biggs and Ivison, 2008), which suggests that SMGs at high-redshift (or at least a fraction of them) could be indeed intermediate-phase mergers composed of unresolved double nuclei, as argued by Iono et al. (2009) and Arribas et al. (2012).

In the bottom part instead, we can immediately notice that a major fraction of the sample (13 galaxies, i.e., 52% of the total sample) is not consistent with the ETG relation (taking 1-σ dispersion), and is located well below it by $\sim$ 0.5 dex, with an average size of $\leq$ 1.2 kpc, indicating that they are much more compact than their stellar envelopes and than typical ellipticals at z

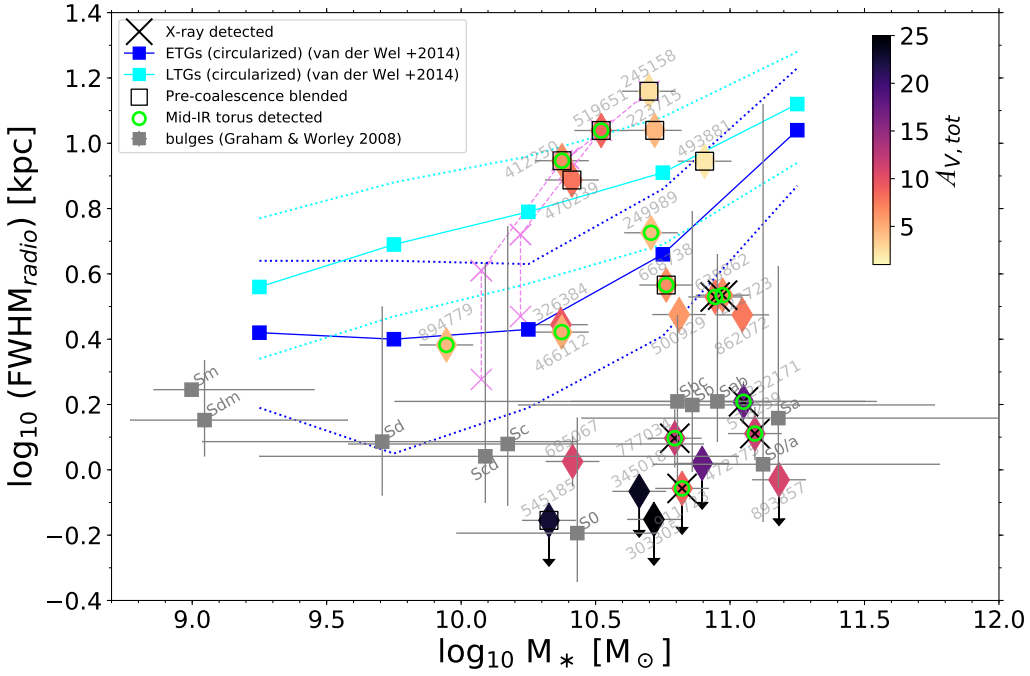

Figure 4.10: Diagram showing the radio size vs stellar mass for my sample. I compare my results to the stellar mass - stellar size relation of LTGs (cyan line with 1σ dispersion) and ETGs (blue line) at z=0.7 (van der Wel et al., 2014), and with the bulge properties of low redshift (z$\sim$0.1) spiral galaxies from Graham and Worley (2008) (gray squares). The eleven points shown here for the bulges represent the median ($\pm1\sigma$) of their distributions of stellar masses and stellar sizes (in K band) as a function of galaxy type, from S0 to Sm spirals. For three galaxies in my sample fit with a double gaussian, I also represent the 'deblended' radio sizes of each single component with violet crosses, connecting them with a dashed violet line. In these cases, I assigned to each component half of the total stellar mass of the system, even though a precise estimation requires a separate fit on deblended photometric data.

$\sim$ 0.7. I underline that such difference would be even higher if we compare this subset to the M$_*$-size relation at redshifts lower than 0.7, as the ETG sizes at z = 0.25 are a factor of 1.5 higher than those at z = 0.75, at the median stellar mass (van der Wel et al., 2014). This sample of very compact starbursts has typical extensions that are similar to those of dense star-forming regions in local ULIRGs (Genzel et al., 1998; Piqueras López et al., 2016), including Arp 220 and M82 (Sakamoto et al., 2017; Barker, de Grijs, and Cervino, 2008), suggesting they are driven by the same merger mechanisms (as also argued in paper I).

If we take for each galaxy its distance from the LTG relation:

$$dist_{\rm LTG} = \log_{10}(FWHM_{\rm size}/FWHM_{\rm LTG}) \tag{4.3}$$

, we can also use this quantity in place of the radius to trace the same sequence found in Section 4.1, taking into account the mild dependence on stellar mass.

As the merger proceeds, the system moves from the LTG to the ETG relation and then even below at significantly smaller sizes (by $\sim$ 0.5 dex at least), meaning that the compact starburst cores that form at the coalescence cannot produce directly the ellipticals seen at redshift 0.7 and below.

The sizes of those starbursts instead resemble those of typical bulges in lower redshift spirals and lenticular galaxies (Graham and Worley, 2008; Laurikainen et al., 2010), indicating a possible evolutionary link between mergers and bulges, as suggested by other works (e.g., Sanders and Mirabel, 1996; Lilly et al., 1999; Eliche-Moral et al., 2006; Querejeta et al., 2015b; Querejeta et al., 2015a). This idea is consistent with the typical observed gas fractions of the starbursts (derived as $M_{gas}/(M_*+M_{gas})$, with M_{gas} calculated in Section 4.3), which range between 0.02 and 0.25 ($\sim$ 0.1 in median). Assuming that all the remaining gas is consumed before the passivization and that the same amount of gas has been already converted into stars (which depends on the merger phase and dynamics), it means that the current starburst cores can produce approximately 20%, and up to 50%, of the final stellar mass of the galaxies. Higher resolution radio images targeting specific emission lines can further constrain the kinematic properties of the starbursting cores, by looking for rotation, or their luminosity profile, for example measuring their Sersic index. How this old stellar component is affected by the merger can depend on many conditions difficult to model in detail, including the geometry of the interaction, the gas content and the mass ratio of the colliding galaxies.

4.8 QSOs in formation at redshift $\sim$ 0.7 ?

In the starburst selection phase, I discarded several quasars because of the impossibility to study the properties of their host galaxies (dust attenuation, SFR, stellar mass), as discussed in Section 4.6. In order to overcome these limitations, several authors have extensively studied also the transitional moments (just preceding the final blow-out) in the dress of type-I and warm ULIRGs (Kawakatu et al., 2006; Sanders et al., 1988). Similarly, we can have some clues of the inner black-hole activity just before the hypothetical QSO by looking at the AGN diagnostics in the same starburst sample.

As mentioned in Section 2.7, I detected the mid-IR dusty torus AGN emission in 12 galaxies, and simultaneous X-ray emission in six of them. Notably, the latter are the only ones (among mid-IR AGNs) whose host galaxies lie below the ETG relation in the mass-size diagram (see Fig. 4.10), at systematically smaller sizes than ellipticals at $z \leq 0.7$. This suggests that during early merger stages the AGNs are predominantly obscured, while they start to appear in X-rays toward intermediate stages (i.e., when the host starbursts are more compact and obscured), possibly driven by rapid AGN feedback clearing the gas and dust around the black hole.

This can be seen better in Fig. 4.11, where all the host galaxies of X-ray detected AGNs are located at larger distances from the mass-size relation

of LTGs compared to X-ray undetected AGNs. Moreover, they have X-ray luminosities at least 1 order of magnitude higher ($\sim +1.5$ on average) than what is inferred from their SFR. For the X-undetected galaxies instead, the upper limit on $L_X = 10^{41.7}$ erg/s, determined by average-stacking their fluxes in the 2-10 keV band at the median z of the sample, is consistent with emission produced by star-formation only, suggesting that in this band the AGN is completely obscured.

In order to assess the level of obscuration, I computed the ratio between the observed and the intrinsic X-ray luminosity $L_{X,obs}/L_{X,intr}$, comparing this quantity to the total dust attenuation $A_{V,tot}$ inferred in a mixed model from Paβ and the bolometric IR luminosity (paper I). $L_{X,intr}$ comprises the contribution from both star-formation (as explained in Section 2.7) and from the AGN, assuming $L_{X,intr,AGN} = 0.04\times L_{BOL,AGN}$ (Vasudevan and Fabian, 2007) and a bolometric AGN luminosity $L_{BOL,AGN} = 1.5\times L_{AGN,IR}$ (Elvis et al., 1994) (Fig. 4.12-*left*). Alternatively, I considered the bolometric correction of Lusso et al. (2012) for type-2 AGNs, which depends on $L_{BOL,AGN}$ itself through the following, nonlinear equation:

$$\log_{10}\left(\frac{L_{BOL,AGN}}{L_{2\text{-}10keV}}\right) = 0.217x - 0.022x^2 - 0.027x^3 + 1.289 \qquad (4.4)$$

, where $x = \log_{10}(L_{BOL,AGN}) - 12$ and the scatter of the relation is 0.26 dex. However, the results derived with this second assumption (Fig. 4.12-*right*) do not change significantly compared to the first case.

The figures presented above confirm that the total attenuation inferred from the L_X may be the discriminating parameter between X-ray detected and undetected mid-IR AGNs: while the former are relatively unobscured, the X-ray emission from the second is suppressed at least by a factor of 30. Interestingly, this transition does not seem to be related to an increased bolometric luminosity, since no correlations are observed with this quantity. I also remind that for this analysis I am following the standard procedure, which does not take into account shock contribution to the X-ray luminosity. A possible non negligible shock emission at these high energies (which in any case is difficult to model) would result in an underestimation of the true effective X-ray attenuation toward the AGN.

The previous results suggest that the X-ray attenuation decreases as the starburst becomes more dust-obscured (probed by $A_{V,tot}$) during the last merger phases. In a standard framework (i.e., if we exclude dominant contribution from shocks to the X-ray luminosity), this apparent contradiction can be reconciled by considering the different timescales of our diagnostics. On the one hand, Paβ (used to calculate $A_{V,tot}$), yields a luminosity (or, equivalently, a SFR, by applying the Kennicutt, Tamblyn, and Congdon (1994) conversion) that is averaged over a timescale of 20-30 Myr. Conversely, the AGN luminosity that we measure in X-rays gives an instantaneous information of the AGN activity. As a consequence, with the X-ray analysis we are able to probe the current dust attenuation level, while $A_{V,tot}$ traces the

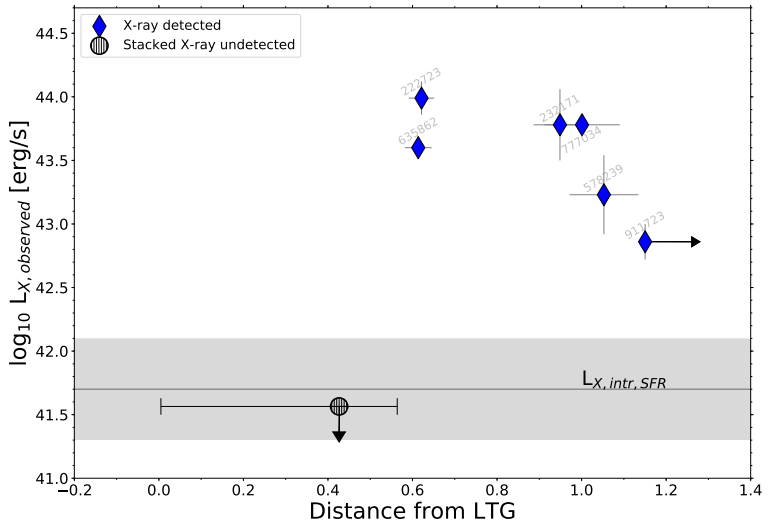

Figure 4.11: Comparison between the observed X-ray luminosity ($L_{X,obs}$) and the distance from the mass-size relation of LTGs at $z \sim 0.7$, for the six Magellan starbursts detected in X-rays. Upper limit on $L_{X,obs}$ for six mid-IR AGNs undetected in X is shown with a black circle, where the horizontal segment represents the range of $dist_{LTG}$ spanned by this subset. The intrinsic X-ray luminosity due to star-formation is highlighted with a gray line for the median SFR of the sample ($\pm$0.4 dex scatter from Mineo et al. (2014)), and may dominate the total X-ray observed emission for the X-undetected starbursts.

obscuration in the recent past ($\lesssim 30 Myr$). According to this speculation, the X-ray luminosities measured for a subset of six late stage mergers indicate that the AGN-induced blow-out may have already started since a few Myr ago, clearing the surrounding gas and dust content, and that we might be very close to the final QSO phase.

Furthermore, in Fig.4.13 I display the AGN accretion efficiencies of the galaxies as a function of their distance from the LTGs mass-size relation. The efficiencies were estimated by comparing the observed $L_{BOL,AGN}/M_*$ ratios to the maximum value allowed by Eddington ($L_{BOL,AGN}/M_* \mid_{EDD} \simeq 1.5$), from which I derived the so-called Eddington ratio $(L/L_{EDD}) \mid_{AGN}$. I assumed the typical correlation for AGNs between the stellar mass M_* and black hole mass M_{BH} of Reines and Volonteri (2015) and a spherically symmetric accreting BH, yielding $\log(L_{EDD}/M_*) \simeq 0.9685 + 0.05 \log_{10}(M_*)$. The M_* in the second term can be approximated with the median value of the sample $M_{*,median}$, leaving a small secondary dependence on stellar mass which, for our mass ranges (10^{10}-10^{11} $M_\odot$) produces variations of $< 5\%$. This variation, added to the uncertainty on the relation between M_* and M_{BH} reported by Reines and Volonteri (2015) (cfr. their equations 4 and 5), is highlighted in Fig.4.13 with a blue shaded area around the Eddington limit (blue line) calculated above.

From this analysis, I found that two AGNs have an Eddington ratio higher than 1 ($1.2 < (L/L_{EDD}) \mid_{AGN} < 1.85$), while additional three AGNs are

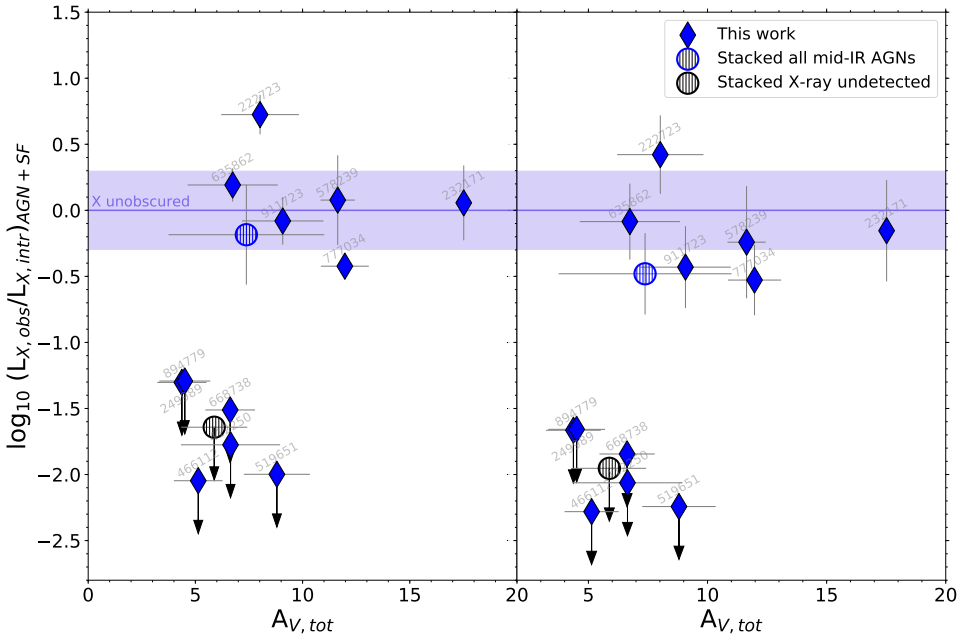

Figure 4.12: *Left:* X-ray attenuation $L_{X,obs}/L_{X,int}$ as a function of the infrared-based attenuation $A_{V,tot}$ (in a mixed model geometry and toward the center) for my sample of mid-IR detected AGNs. I assumed here a bolometric correction factor $L_{X,intr,AGN} = 0.04\times L_{BOL,AGN}$ (Vasudevan and Fabian, 2007). Stacks on the whole sample and on the X-undetected subset are displayed with hatched circles, while the violet shaded regions indicate the area of no obscuration, which incorporates a factor of two uncertainty in the conversion between intrinsic X-ray and bolometric AGN luminosity; *Right:* Same diagram as before, but assuming an $L_{BOL,AGN}$- dependent bolometric correction (Lusso et al., 2012), as explained in the text.

radiating between 57% and 79% of their maximum luminosity. However, all these five AGNs are still consistent within 2σ errors with $(L/L_{EDD})\,|_{AGN} = 1$ if we also consider the uncertainty on the conversion factor from the ratio $L_{BOL,AGN}/M_*$, as discussed before. I remark that additional uncertainties on the M_*- M_{BH} relation can come from the assumptions on the BH accretion geometry, which is not taken into account here. The remaining seven IR-detected AGNs have instead lower Eddington ratios between 0.35 and 0.08.

The galaxies which are undetected in X, radio and mid-IR may contain low-activity AGNs, even though current upper limits on the Eddington ratio are not so stringent and do not allow to discriminate them from the detected subset. The intrinsic variability of AGN accretion may thus explain why we are currently missing many of these sources in my sample, and that only deeper X-ray observations can potentially reveal. The duty cycles above 30% and 1% L_{EDD} seem to be at least $\sim$ 25% and $\sim$ 50%, respectively.

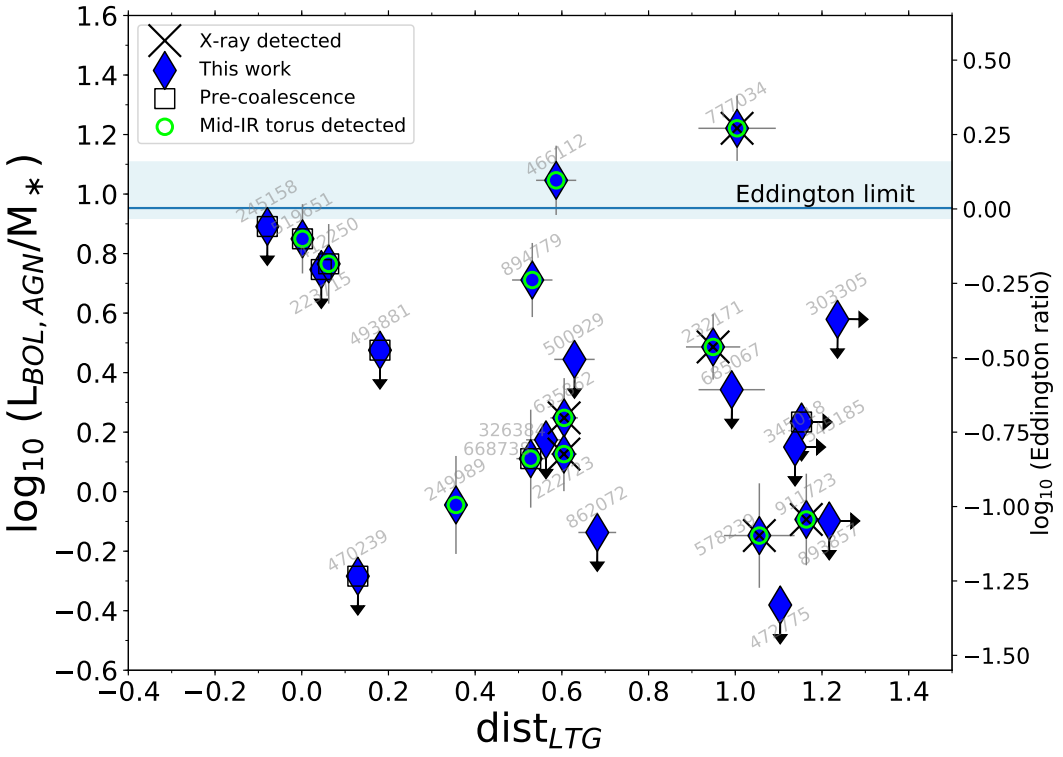

Figure 4.13: $L_{BOL,AGN}/M_*$ vs. distance from the mass-size relation of LTGs ($dist_{LTG}$) for my SBs sample. The Eddington limit is shown with a blue horizontal line, while the shaded area takes into account the spread of M_* among the same sample and the uncertainty of the relation between stellar mass and BH mass by Reines and Volonteri (2015). The Eddington ratio is shown on the right y-axis.

4.9 Summary and conclusions

Using a unique sample of 25 starburst galaxies (typically seven times above the star-forming main sequence) at $z = 0.5$-0.9 with near-IR rest frame spectroscopy of Paschen lines, Calabrò et al. (2018) found that they span a large range of attenuations toward the core centers from $A_V = 2$ to $A_V = 30$, forming a sequence which is consistent with a mixed model geometry of dust and stars. In this paper I have investigated with my collaborators the nature of this attenuation sequence, comparing A_V with other physical properties, such as the radio size (which traces the extension of the starburst), the emission lines velocity widths and [NII]/Hα ratios (which reflect the increasing potential well depth and likely the shock contribution toward final merger stages), and finally the EW of hydrogen absorption lines, which is sensitive to the luminosity-weighted age of the stellar populations surrounding the optically obscured core.

I summarize the main results of this paper as follows:

1. We found that the physical quantities introduced above, namely the radio sizes ($FWHM_{radio}$), the line velocity widths ($FWHM_{line}$), the

[NII]/Hα ratios (N2) and the equivalent widths (EW) of Paschen and Balmer lines, all correlate with each other (Fig.4.1-4.2), defining a single parameter sequence of z$\sim$0.7 starburst galaxies.

2. These correlations can be interpreted as a time evolutionary sequence of merger stages. As the merger evolves, the starburst becomes more compact and dust obscured, while the deep potential wells created by merging nuclei produce, according to the virial theorem, an increase of the kinetic energy and shocks in the system. At the same time, intermediate aged A-type stars in the outer starburst core regions are primarily responsible for the stronger optical+near-IR absorption lines in later phases.

3. Four galaxies are outliers simultaneously in three of the ten main correlations, which involve $A_{V,tot}$ and, respectively, N2, $FWHM_{line}$ and EW(Paβ). Having the largest dust attenuations and among the smallest radio sizes in our sample, these outliers may represent the very end phases of the merger evolution, where the above three relations may reach a saturation level.

4. Using sky-subtracted 2D spectra, we identified a subset of seven precoalescence mergers by the presence of spatially separated or kinematically detached (i.e., rotation-driven tilted lines with different inclination angles) Hα components, representing earlier, less obscured phases of the interaction. The radio sizes measured for these systems are likely tracing the separation between the merging nuclei rather than the dimensions of single cores. However, our sample may contain additional double nuclei which we are not currently able to resolve.

5. Half of our sample comprises extremely compact starbursts, with average half-light radii of 600 pc (six galaxies have only upper limits), similar to the sizes of starbursting cores observed in local ULIRGs. These sizes are also $\sim$ 0.5 dex smaller than ETGs at redshift $\sim$0.7 and below, indicating that our merger-driven starbursts cannot be direct progenitors of the population of massive ellipticals formed in the last $\sim$ 7 Gyr. On the contrary, they are more consistent with typical sizes and masses of bulge structures (Graham and Worley, 2008), suggesting a possible evolutionary connection between our starburst cores and bulges.

6. In our sample, we detected at $> 3\sigma$ the mid-IR dusty torus AGN emission in 12 starbursts, with Eddington ratios ranging from 1.9 to less than 0.08. Among them, only six galaxies are simultaneously detected (at 3σ) in X-rays. Intriguingly, the latter have the largest departures from the mass-size relation of LTGs (at $z \leq 0.7$), suggesting that AGNs start to appear in X-rays during the latest (compact) merger phases, as

the blow-out of surrounding dust and gas may precede a possible final QSO.

Overall, the relations among the above physical parameters converge toward a time-evolutionary sequence of merger stages, which represents an observational evidence (translated at higher redshift) of the theoretical merger-induced starbursts framework of Hopkins et al. (2008b), Hopkins et al. (2008a), and Di Matteo, Springel, and Hernquist (2005), and the evolutionary sequence postulated by Toomre and Toomre (1972). The future advent of JWST will allow to test this scenario up to very high redshift, where the conditions of the Universe and gas content of galaxies were even different compared to the epochs studied here.

4.10 Appendix. Additional plots

I display in Fig. 4.14 two different versions of the BPT diagram, involving the [SII]6717+6731/Hα line ratio (top panel), and the [OIII]5007/[OII]3727+3729 ratio (bottom panel), color coded according to the total velocity width of the lines (σ_{line}).

Finally, I display in Fig.4.15 the correlations among Hδ, Hβ, Hα and Paβ equivalent widths.

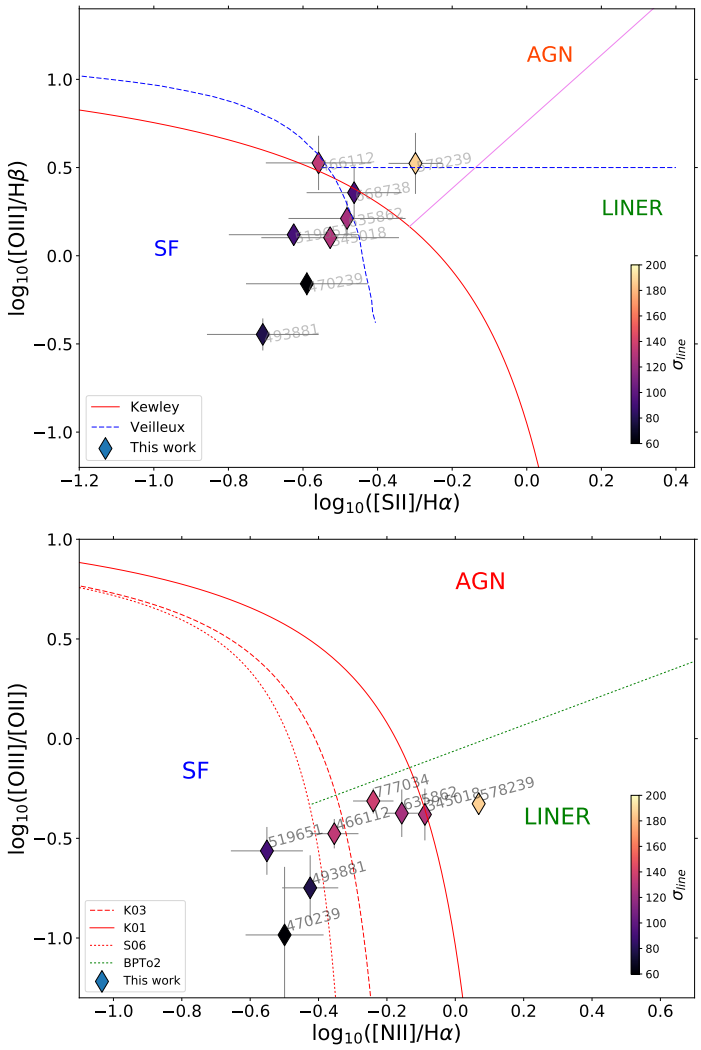

Figure 4.14: Diagram of [OIII]/Hβ compared to [SII]6717+6731/Hα (*Top*) and [OIII]5007/[OII]3727+3729 vs. [NII]6583/Hα (*bottom*) for 8 galaxies of the Magellan sample with optical spectra available and contemporary detection of [OIII] and one between [SII]+Hβ or [OII]. The two diagrams are also called the S2 and the O2 BPT diagrams, respectively. As in the classical BPT diagram in Fig. 4.5, they show that starbursts have different line excitation properties, and those with higher line velocity widths are generally shifted towards the AGN/LINER regions, according to empirical separation lines derived in the local ($z \lesssim 0.3$) Universe.

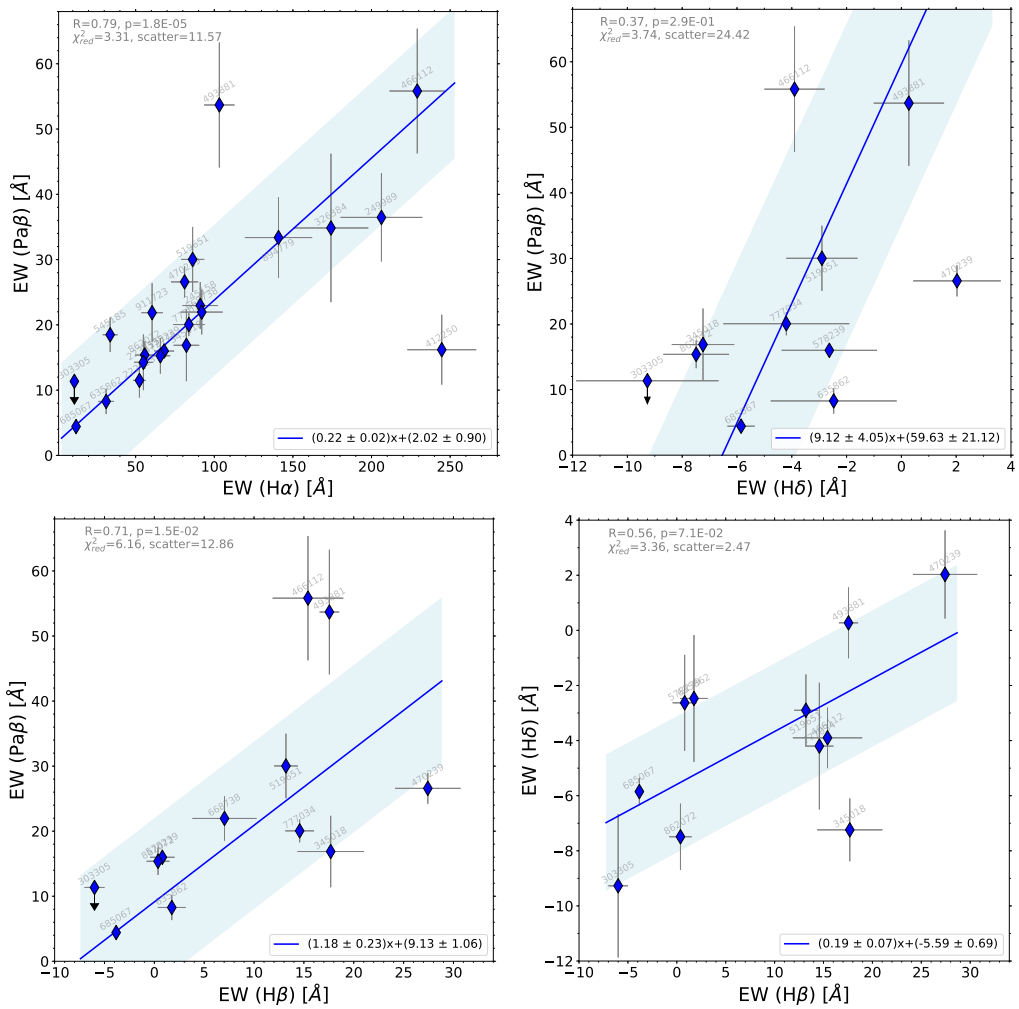

Figure 4.15: Comparison between the EWs of Hδ, Hβ, Hα and Paβ lines. The blue lines represent the best-fit linear relation, while the blue shaded areas indicate the $\pm1\sigma$ dispersion of the galaxies around the best-fit line. I display in the top-left corner of each panel the Spearman correlation coefficient 'R' and corresponding 'p'-value, the residual χ^2 of the correlation ('$\chi^2_{\rm red}$') and the 1σ scatter around the best-fit line, whose equation (comprising 1σ errors on the best-fit coefficients) is shown in the bottom-right corner. In the four diagrams, all the points with available measurements (excluding upper limits) were used in the fit.

Chapter 5

Morphology and clumpiness of starburst and MS galaxies

During the selection of starburst galaxies in Section 2.3 and the study of merger signatures in Section 2.8, I realized that the majority of highly star-forming systems are not only mergers (as discussed in Chapter 3), but they are also clumpy in high-resolution optical rest-frame images. This means that their optical morphology is usually dominated by bright stellar clumps, representing aggregations of relatively young stars arising from a smoother and fainter luminosity profile.

Clumpy, irregular, and morphologically disturbed galaxies are typically observed in star-forming galaxies when we go to higher redshifts, and they may have a very important role in galaxy evolution. Clumpy galaxies at redshift > 0.5 with stellar masses of 10^{10}-10^{11} $M_{\odot}$ are thought to be the progenitors of present-day spirals (Elmegreen et al., 2005; Bournaud, Elmegreen, and Elmegreen, 2007; Ceverino, Dekel, and Bournaud, 2010; Elmegreen et al., 2013). Moreover, if the clumps are sufficiently long lived, they can migrate toward the center and contribute to the formation of a central bar (Immeli et al., 2004a; Sheth et al., 2012; Kraljic, Bournaud, and Martig, 2012) or to the stellar bulge growth (Noguchi, 1999; Elmegreen, Bournaud, and Elmegreen, 2008; Bournaud, 2016), contributing to stabilize the disks (e.g., Ceverino, Dekel, and Bournaud, 2010) and to give the final imprint to the morphological shapes encoded in the Hubble sequence. According to Kraljic, Bournaud, and Martig (2012), today Milky-way like spirals acquired their disk morphology at $z \sim 0.8$-1, and they completely stabilized at redshift 0.5 or lower (Cacciato, Dekel, and Genel, 2012). Alternatively, clumps in distant galaxies may lead to the formation of super-star-clusters and globular clusters (Shapiro, Genzel, and Förster Schreiber, 2010).

Despite their importance, the formation and origin of clumps at all redshifts has always been unclear, as it can be ascribed to different triggering mechanisms. Usually, in clumpy galaxies at $z > 1$, they are thought to be triggered by violent disk instabilities in highly gas-rich, dense and turbulent disks, and they are continuously fed by cold gas streams from the circumgalactic medium (CGM) and the cosmic web (Genzel et al., 2008; Dekel, Sari, and Ceverino, 2009). These can sustain the high gas fractions of the order of

$\sim$ 0.4-0.5 that are typically found in high redshift galaxies (Daddi et al., 2010; Tacconi et al., 2010; Rodrigues et al., 2012).

Below $z \sim 1$, cosmological simulations predict a strong cut-off of cold-flow accretion into galaxies (Kereš et al., 2005; Dekel and Birnboim, 2006), which might indirectly result in the decrease of the average SFR density in the Universe (Madau and Dickinson, 2014) and of the gas content in galaxies down to $f_{gas} \sim$ 0.2-0.4. This strong suppression of gas fraction may then affect the physical properties and abundance of clumps, and could require alternative mechanisms of formation and evolution. For example, smooth accretion of gas from tidally disrupted companions or stripped satellites in cluster environments have been suggested to feed some low-mass, local analogs of high-z clumpy galaxies (Garland et al., 2015). Instead, a more common additional channel for producing clumps at any host stellar mass and epoch is represented by major mergers, as proposed in Somerville (2001), Lotz, Primack, and Madau (2004), and Di Matteo et al. (2008). However, at intermediate redshifts, there is no general consensus yet about the role of mergers and their relative importance.

From the observational point of view, Puech (2010) analyzed UV rest-frame clumps in 11 clumpy galaxies at $z \sim 0.6$. He claimed that interactions may be the dominant driver for clumps formation at that epoch, because of the complex kinematic structure observed for half of them. In contrast, Guo et al. (2015) and Murata et al. (2014) argue that major mergers have a negligible role for explaining the fraction of clumpy galaxies at all masses at $z \lesssim 1.5$, suggesting instead a prevalent role of violent disk instabilities or minor mergers. In the same direction, Bournaud et al. (2012) found that clumpy low-mass star-forming galaxies at $z \sim 0.7$ are similar to gas-rich turbulent disks observed at higher redshifts, suggesting that gravitational instabilities are the most important cause of gas fragmentation and clumps formation.

However, even with different sample selections, clumps identification methods and observed photometric band, these studies are interested on the main driver of clumpy galaxies among the whole star-forming galaxies population. Since they do not perform a merger identification, they neither analyze the implications that mergers have on the formation of clumps, nor they measure quantitatively the clumpiness parameter (i.e., fraction of light in clumps) in comparison to normal disks. Puech (2010) show a possible connection between mergers and UV clumps, but many of their substructures are not detected anymore in the optical, thus cannot be directly compared with my sample. Moreover, their subset is not representative of the whole merger population at intermediate redshifts, given the strict requirements of their selection criteria.

The connection between mergers and clumps is not clear also in hydrodynamical simulations: while some studies suggest that merger events can trigger turbulent modes in the ISM that lead to rapid gas fragmentation and clump formation (Teyssier, Chapon, and Bournaud, 2010; Bournaud

et al., 2011a; Renaud et al., 2014) , other morphological studies on simulated galaxies do not see any enhancement at all of clumpy emission during the merger (e.g., Nevin et al., 2019). The reason of these discrepancies resides in the different resolutions adopted, in feedback and turbulence modeling and in the specific initial conditions considered, such as the merger geometry, the stellar mass ratio and the initial gas fraction f_{gas} of colliding galaxies (e.g., Di Matteo et al., 2008; Governato et al., 2010; Fensch et al., 2017). Most of the simulations focus on local or high redshift galaxies, thus they have lower or higher gas fractions than the typical values at intermediate redshifts. The few simulations with similar f_{gas} values (Cox et al., 2006; Di Matteo et al., 2008) did not allow the gas to cool down below 10^4 K, which is necessary to study the evolution of the gas structure during the interactions (Teyssier, Chapon, and Bournaud, 2010; Bournaud et al., 2011b). In other cases, the resolutions are too low for the sub-kpc spatial scales we want to investigate for detecting clumpy structures (Sparre and Springel, 2016; Rodriguez-Gomez et al., 2016).

Additionally, while mergers produce very dense and compact starbursting cores, it is yet unclear what fraction of star-formation occurs in off-nuclear regions, possibly in the form of clumps, and what is the resulting mass and size distribution of these structures, which have been studied only in isolated galaxies. Given these uncertainties, more observations and constraints are needed to clarify the role of mergers on clump formation at intermediate redshift, and put constraints on feedback models in simulations of galaxy collisions.

Given that the majority of starbursts at redshift $0.5 < z < 0.9$ are mostly mergers, as suggested in Chapter 3, they represent the perfect sample to test the role of mergers for clumps formation. This observational evidence arised the following questions to us: Does this indicate that mergers can enhance even more the formation of clumps compared to violent gravitational instabilities, as suggested by previous studies on different samples (e.g., Puech, 2010) ? In case of strong causal influence, are the properties of merger triggered clumps similar to those of high redshift disks ? In order to properly answer these questions, we need to better quantify the galaxy morphology (compared to the analysis presented at the end of Chapter 2), the probability of being a merger, and especially the contribution of clumps to the total galaxy emission.

In a second step, a statistical comparison of those morphological quantities between SB and MS galaxies would be needed to establish any physical and causal influence of mergers on clumps formation. In addition to the starburst subset identified in Section 2.3, I thus needed a control sample of MS galaxies, at the same cosmic epoch, which are usually taken as representative of isolated, relatively undisturbed disks. I selected 150 normal star-forming systems from the parent star-forming sample (with available HST F814W images), randomly taken within $\Delta dist_{MS}$ of ± 0.47 dex (a factor of three) from the MS, in the same redshift and stellar mass range defined for SBs. I also required that they are star-forming according to the NUV-R/R-J

diagram to avoid quiescent galaxies (Laigle et al., 2016). This number was chosen to have a larger statistics and always have more MS than SB systems throughout the analysis. Even though this latter subset is representative of secularly evolving star forming disks, I remember that it may contain also a fraction of ongoing mergers. Indeed, at my redshifts, the merger fraction is expected to be higher than the relative number of starbursts (Schreiber et al., 2015), both because of SFR fluctuations during the merger process itself (Di Matteo et al., 2008) and because it might be more difficult for mergers to trigger starbursts as in the local Universe (Fensch et al., 2017).

In the following sections, I will then discuss several methods to identify these objects from the morphology. I will first describe a quantitative, non parametric approach for the morphological galaxy classification (which also identifies probable merger systems) (Section 5.1.3), and then the methodology adopted to estimate the contribution of clumps to the integrated light emission of the galaxies (Section 5.2). At the end I will define the final sample of galaxies that will be used for the analysis in Chapter 6. This and the following chapters are based on the article submitted to *Astronomy & Astrophysics* on 26 April 2019 (Calabrò et al., 2019b), in collaboration with other co-authors who helped me with the simulations and the interpretation of the results.

5.1 Morphological merger classification

5.1.1 HST images and morphology

In order to study the morphology and the presence of clumpy structures in galaxies, we need high resolution images that can probe spatial scales significantly below 1 kpc. For the sample analyzed in this paper, as for the 25 Magellan starburts analyzed in previous chapters, I adopted F814W ACS images (Koekemoer et al., 2007) retrieved from the COSMOS web service[1]. They represent so far the deepest and highest resolution publicly available data in this field, with $\sim$ 2000 s time integration, a magnitude limit of 25.61 mag for extended sources (assuming a circular aperture radius of 0.3″) and a median FWHM resolution of $\sim$ 0.095″ (with a pixel scale of 0.03″/pixel). At our redshift, this means that we are able to distinguish substructures with separations of at least $\simeq$ 600 pc at $z = 0.5$ to $\simeq$ 800 pc at $z = 0.9$, and thus detect clumps on this size scale (FWHM), which is enough for those typically found in high-redshift clumpy galaxies.

I remark that at the redshifts analyzed in this thesis, the optical HST images are more sensitive to the light of intermediate age (A to G type) stars, hence to the stellar mass of the clumps, rather than their current, unobscured SFR indicated by the UV emission of young massive O-B stars. Given the longer rest-frame wavelengths covered, I can study the clumpy morphology

[1] http://irsa.ipac.caltech.edu/data/COSMOS/

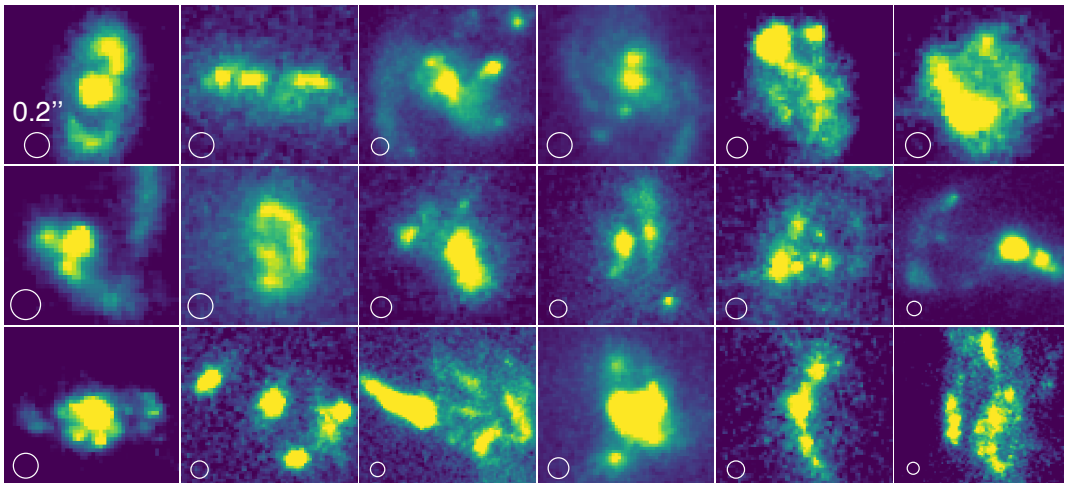

Figure 5.1: Representative sample of clumpy starbursts at $0.5 < z < 0.9$ in COSMOS field, observed by HST-ACS in the F814W band. The white circles in the bottom left corner have a diameter of $0.2''$.

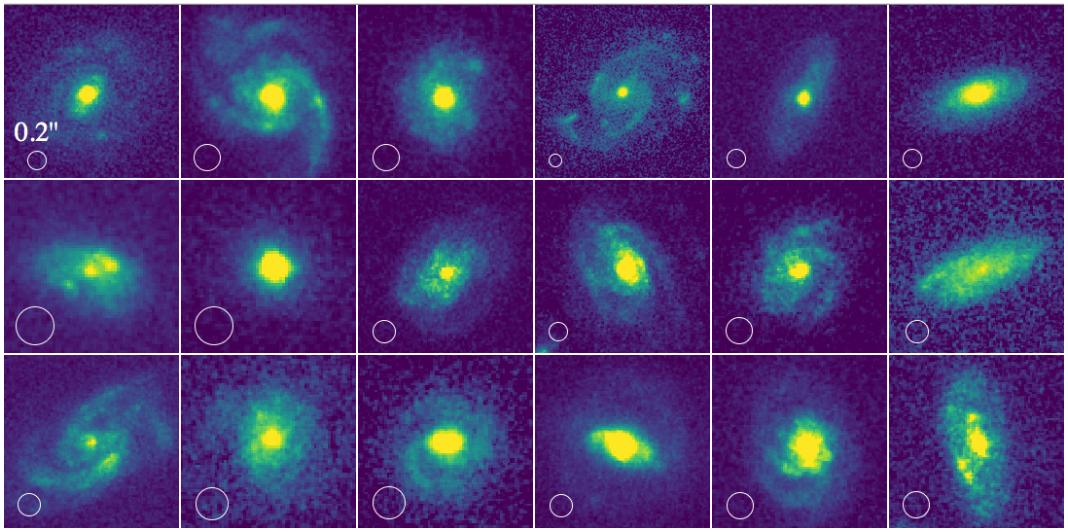

Figure 5.2: Representative sample of typical (randomly selected) main sequence disks at $0.5 < z < 0.9$ in COSMOS field. The image details are the same of Fig. 5.1.

in a way that is less affected by dust attenuation. This is particularly important in infrared luminous mergers, typically highly obscured, where their UV emission may not reflect the true stellar distribution. As an example, figures 5.1 and 5.2 show the HST i-band images for a representative sample of 18 starburst and main sequence galaxies, respectively.

5.1.2 Galaxy segmentation map

In the first step of my analysis, I created a segmentation map of the HST F814W ($15'' \times 15''$) cutouts using the python package PHOTUTILS[2]. In brief, it identifies the sources as groups of connected pixels with a flux higher than a constant threshold. The latter value is calculated at a given S/N per pixel above the background, which is estimated from the entire cutout using a sigma-clipped statistics. I found that a S/N threshold of 1.3 works well in all the cases to detect the galaxies contours, including the low surface-brightness external regions and wings, and separating different galaxies in the same cutout region. The few cases where two close-in-sky but spatially unrelated galaxies (i.e., located at completely different redshifts) are selected as the same source in the segmentation map, I applied the *deblending* function inside PHOTUTILS, keeping only the central object. The location of the final source was saved into a mask M_0: I assigned a value of 1 to all the pixels inside the galaxy contours identified by segmentation map, and 0 otherwise.

Afterwards, I run the galaxy morphology tool STATMORPH (Rodriguez-Gomez et al., 2019) to derive the elongation of the galaxy contained in the previously selected region, which crucially affects the detectability of clumpy structures. E is defined as $\frac{A}{B}$, where A and B are, as in SExtractor, the maximum and minimum *rms* dispersion of the object profile along all directions. Equivalently, they can be considered as the semi-major and semi-minor axis lengths of the ellipse that best describes the galaxy shape.

5.1.3 Non-parametric morphological parameters

In addition to the elongation, better characterizing the morphological properties is essential to identify which galaxies in the main sequence could be possibly mergers. To this aim, I pursued a twofold approach, one relying on non-parametric quantitative estimators, and the second based on a visual analysis, similarly to what has been done in Section 2.8 for the Magellan starbursts only.

In the first approach, the Gini and M20 coefficients, defined by Lotz, Primack, and Madau (2004), are usually adopted for selecting possible mergers and interacting systems. Gini (G) measures the degree of inequality of the flux distribution among the pixels in the image, and is higher for galaxies with bright clumps and nuclei. For my HST cutouts, I computed G with the following formula:

$$G = \frac{1}{\bar{X} n(n-1)} \sum_{i}^{n} (2i - n - 1) X_i, \tag{5.1}$$

[2]https://doi.org/10.5281/zenodo.2533376

where n is the number of pixels of the galaxy (defined by the mask M_0), X_i are the counts in each pixel i sorted in increasing order and $\bar{X}$ is the mean pixel value[3].

On the other hand, M20 is defined as the normalized second order moment of the brightest 20% pixels of the galaxy:

$$\begin{aligned} M_{20} &= log_{10}\left(\frac{\sum_i M_i}{M_{tot}}\right), \text{with} \sum_i f_i < 0.2 f_{tot} \\ \text{with } M_{tot} &= \sum_i^n M_i = \sum_i^n f_i[(x_i - x_c)^2 + (y_i - y_c)^2] \end{aligned} \tag{5.2}$$

In the above formula, x_i and y_i are the pixel coordinates, and x_c and y_c represent the galaxy's center, such that M_{tot} is minimized. f_i are the counts in each pixel, while f_{tot} symbolizes the total counts in the galaxy pixels identified by segmentation map derived before. In other words, this quantity measures the relative concentration of light around the position that minimizes M_{20} itself. It is higher in the presence of bright bars, spiral arms, tidal tails, off-center clumps, and it is very sensitive, for example, to multiple nuclei. Both parameters were calculated with python code routines by applying the equations 5.1 and 5.2.

The typical uncertainties of Gini and M_{20} estimations are of 0.02 and 0.1, respectively. They were estimated by Lotz et al. (2008) from ACS F814W galaxy images at our same redshifts in the EGS field, at a depth comparable with my analysis ($\sim$ 2000s of integration). In addition, the ULIRGs in their sample, to which they apply the classification, have $I_{F814W} < 23$ mag, thus largely applicable to my case.

Since Gini and M_{20} are very sensitive to typical merger features, increasing when these signatures become stronger, we can use both to identify a subset of galaxies with merger morphologies. Following the classification criteria of Lotz et al. (2008), I defined a 'mergerness' parameter m as:

$$mergerness = Gini + 0.14 \times M_{20} - 0.33, \tag{5.3}$$

where the coefficients were calibrated by Lotz et al. (2008) and do not vary with redshift (up to $z \simeq 1.2$). This quantity represents the difference between the estimated Gini and that required to classify the system as a merger. Therefore, according to this criterion, galaxies with $m > 0$ will be identified as morphological mergers throughout the paper. Among the MS population, 15 objects satisfy this condition. The exact *mergerness* values of all the galaxies are listed in Table 5.1 at the end of this Chapter.

I remark that for my sample I cannot apply the morphological analysis performed by Cibinel et al. (2019) on resolved stellar mass maps, since it requires multi-wavelength images. However, single band optical rest-frame

[3]Glasser, G. J. 1962, J. Am. Stat. Assoc., 57, 648

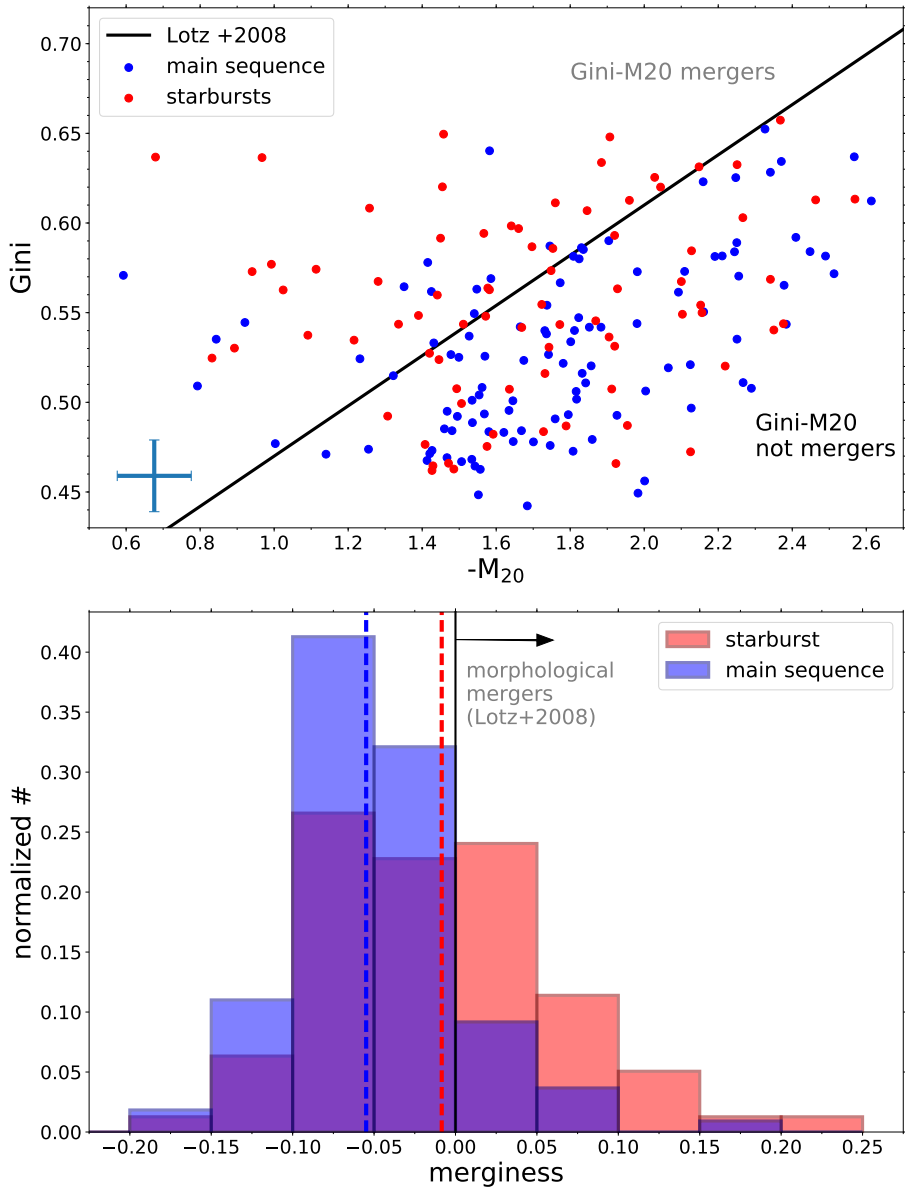

Figure 5.3: *Top:* Gini-M_{20} diagram for the final sample of starburst and main sequence galaxies analyzed in this work (in red and blue, respectively). Galaxies above the black continuous lines are morphological mergers, according to Lotz et al. (2008). The typical uncertainties of Gini and M_{20} are shown by the representative error bars in the lower left corner. *Bottom:* Histogram distribution (for SBs and MS) of the mergerness parameter, defined as the difference between the measured Gini coefficient and that required to classify the galaxy as a morphological merger. It shows that the majority of galaxies classified as mergers according to this criterion are also starbursts.

images are sensitive to the stellar mass of the system more than UV rest-frame observations, and this dataset represents so far the best compromise if I need high spatial resolution information.

I show in Fig. 5.3-*top* the distribution of the Gini and M_{20} coefficients for my galaxies, and highlight with the black continuous line the merger threshold of Lotz et al. (2008). In the bottom panel of Fig. 5.3 I display instead the histogram of the mergerness parameters, separately for main sequence and starburst galaxies. These two populations have overall a different distribution of m and different medians, where starbursts tend to have a higher mergerness compared to normal star-forming galaxies.

I notice that the threshold criterion of Lotz et al. (2008) defines a mergerness parameter space where SBs start to dominate in number over the MS population. In my case, 76% of the morphological merger systems ($m > 0$) turn out to be starbursts. However, this subset is not complete, representing a minor fraction (43%) of all the starburst population in my sample. This result should not be surprising. Indeed, the observability timescale of a merger in the upper part of the Gini-M_{20} diagram may not coincide with the starburst phase duration and depends on many factors, including the mass-ratio and the gas fraction of colliding galaxies, the viewing angle, the impact geometry, the dynamics of the disks (e.g., rotation direction) and the extinction. For example, the Gini parameter is more sensitive to face-on systems (Lotz et al., 2008). In addition, the surface brightness at redshift $z > 0.5$ decreases by more than one order of magnitude compared to the local Universe, making more difficult for interacting signatures to emerge from the noise. All these mechanisms are thus likely responsible for the fraction of low-*mergerness* SBs identified in my sample.

5.1.4 Visual classification

In order to mitigate these effects and select a more complete subset of merging systems in the main sequence, I also performed a visual classification. Based on a one-by-one inspection of MS galaxies, I flagged as 'visual mergers' all the pairs within a projected separation of 20 kpc and photometric redshift difference < 0.08, or systems that present a very disturbed morphology because of tidal tails, bridges or collisional rings. Compared to the previous criterion, this likely identifies mergers on a longer timescale. On the one hand, the pairs select a sample of very-early stage mergers that are going to coalesce in ~ 0.5 Gyr or more. On the other hand, I can evaluate more carefully by eye the presence and strength of faint merger features, whose importance may not have been properly weighted by the automatic procedure.

This yielded a sample of 24 visual mergers in the main sequence, representing $\sim 20\%$ of the MS population. These are 9 more objects compared to morphological mergers, which is understandable given that here I am considering also the pairs. Nevertheless, I remind that also this merger subset may not be complete, due to a combination of all the effects previously discussed.

5.2 Clumpiness measurement

In order to quantify the contribution of young stellar clumps to the total galaxy emission, I adopted the clumpiness parameter c, which measures the fraction of light residing in high spatial frequencies structures. For its estimation, I followed the simplest approach described in Conselice et al. (2003) and Lotz, Primack, and Madau (2004).

Firstly, I smoothed the original ACS F814W images (I_0) using a gaussian filter with a radius of 5 pixels. This corresponds to an angular scale of $0.15''$ and a physical radius of $\simeq 1$ kpc at $z \simeq 0.7$ (0.9 to 1.16 kpc in my full redshift range), which is the approximate size of the clumps I want to detect. Then I subtracted the smoothed image $I_{smoothed}$ from the original image, imposing 0 for all the pixels with a negative value in the residual image $I_{res} = I_0$ - $I_{smoothed}$, as done by Conselice et al. (2003).

In a second step, following the procedure adopted in Salmi et al. (2012), I selected all the pixels in I_{res} which are at least 5σ above the background of the galaxy, in order to reduce the noise contamination. The background level was estimated with a σ-clipping statistics procedure applied on all the regions of I_0 which have not been assigned to any sources in the segmentation map. The threshold limit was chosen empirically, and I found it was the minimum and best value allowing to recover clumpy structures that would have been identified also on a visual inspection. For all the pixels above the 5σ threshold, I assigned them a value of 1 (0 otherwise), in this way defining a mask for the clumps (M_{clumps}). I did not put any constraints on the number of connected pixels to be part of the clumps. However, even when requiring a small amount (e.g., 2-10) of connected pixels, the results are not significantly affected.

In the third step, I removed the galaxy nuclei from the clumpiness calculation, which, by definition, contains only off-nuclear clumpy structures. For example, the nuclei of spiral galaxies are usually made of old stellar population bulges that I do not want to consider in the above parameter. For this scope, I derived the segmentation map of the clump mask, deblending the regions containing more than 2 local luminosity peaks, by using the same *python* codes applied to the original image in the first step. Afterwards, I created the nucleus mask $M_{nucleus}$, setting $M_{nucleus} = 1$ for the clumps identified as nuclei by a visual inspection of the original i-band HST images, and 0 otherwise. In most of the cases, the centrally located nuclei correspond to the brightest clumps identified through my routine. However, this is not a necessary condition, since the nuclei (especially the merger cores) can be very obscured and even undetected in optical. Additionally, simulations have shown that the luminosity of newly formed clumps in merger systems can easily overcome that of the nuclei in the two colliding disks. Despite these uncertainties, I conservatively selected and removed at least two nuclei in all the starbursts and in clear MS mergers identified in Section 5.1.1. This represents a limiting case, since I expect that a large fraction of starbursts

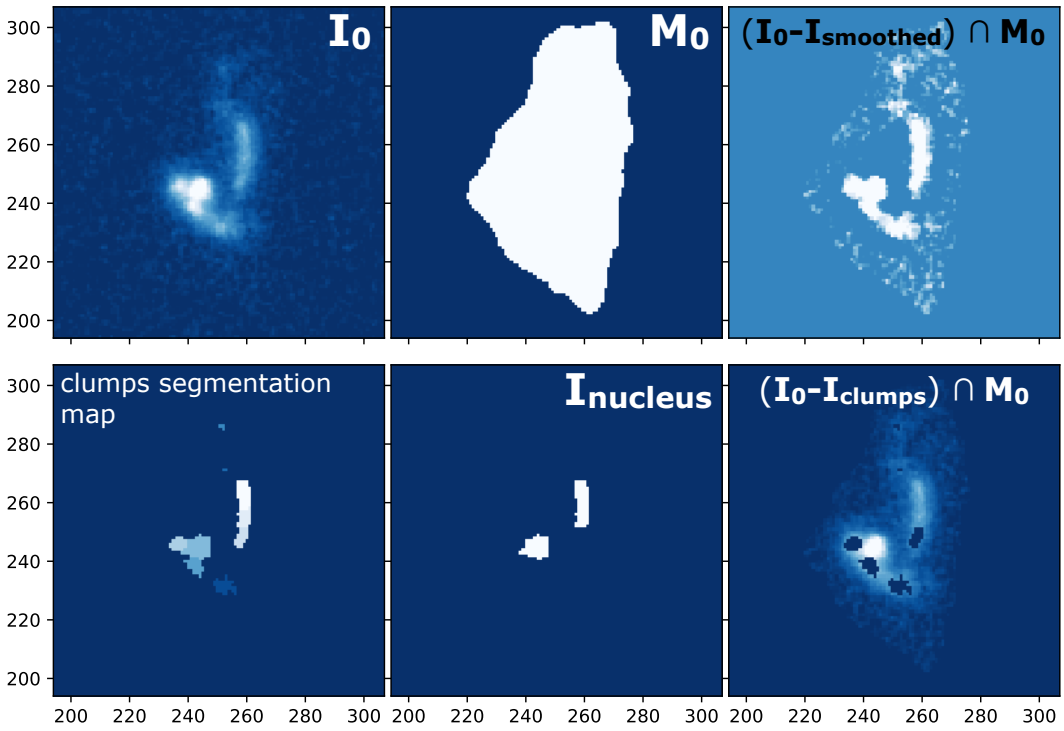

Figure 5.4: Flowchart of the clumpiness estimation procedure for one galaxy in my sample (ID 412250): (1) original HST F814W cutout image; (2) segmentation image identifying the galaxy contours; (3) original minus smoothed image, enhancing the visibility of high spatial frequency components; (4) clump detection after applying a 5σ threshold; (5) nuclei visual identification; (6) residual image after clumps light subtraction, which appear as black regions superimposed to the original galaxy image. This figure highlights the power of my approach. I am able to detect clumps very close to the nucleus that would instead have been removed by masking systematically a circular region around the center. It shows also the important role of the deblending function to separate multiple clumps based on the presence of multiple peaks in a single segmentation region, as explained in the text. This case additionally illustrates my conservative approach: I selected two nuclei in the clumps segmentation map even though I am not sure about the second on the right (which in alternative could be part of a tidal tail).

may actually be fully coalesced systems, even though it is hard to securely isolate them with my data.

Other works systematically mask an inner circle region with a fixed angular aperture for all the galaxies when computing the clumpiness (e.g., Lotz, Primack, and Madau, 2004). However, this method may remove clumps that are very close to the nucleus. In addition, it is difficult for any automatic procedure to identify the nucleus, especially in case of disturbed morphologies like in mergers, where a careful visual inspection can be more reliable. For these reasons, my method is more precise and can be easily kept under control, assuming that the size of my sample is not excessively large. I show in Fig. 5.4 a representative example (galaxy ID 412250) of the full clumps

identification procedure.

Finally, the clumpiness parameter c was derived in a standard way by dividing the total flux residing in previously detected clumps and the total flux of the galaxy, after masking the nucleus. This calculation can be written explicitely as:

$$c = \sum_{M_0 \oplus M_{\rm nucleus}} \frac{M_{\rm clumps}(i,j) \times I_0(i,j)}{I_0(i,j)} \tag{5.4}$$

where I_0 is the original image and M_0, $M_{\rm nucleus}$ and $M_{\rm clumps}$ are masks, already introduced before. The sum is done over all the galaxy pixels defined by the segmentation map (M_0), excluding the nucleus. I consider this quantity appropriate for my work, since it compares the flux of the clumps (outside the nucleus by definition) to the total flux in the same off-nuclear regions.

Another viable option is to compare the emission residing in high spatial frequencies to the total object emission (including the nucleus) as: $c' = \sum [\ |M_{\rm nucleus}(i,j) - 1| \times M_{\rm clumps}(i,j) \times I_0(i,j)] \ / \ \sum I_0(i,j)$, where the sum is over M_0. For clarity, since this would not change the results of my analysis, I adopt uniquely the definition in Eq.5.4 throughout the paper, and include both quantities c and c' in Table 5.1 at the end of the Chapter.

5.3 Magnitude and elongation cuts

At $z \sim 0.5$, the brightness of all the objects is approximately one order of magnitude lower (at fixed luminosity) compared to the local Universe, so it becomes increasingly difficult at higher redshifts to identify internal structures of galaxies, such as clumps. Moreover, when the galaxies become too faint, the visibility and detection of clumps is automatically affected, so that my method returns systematically lower c values close to 0. For this reason, to avoid the faintest objects, I used the i-band magnitudes of Laigle et al. (2016) and applied a threshold as $i_{\rm mag} < 22.5$, beyond which the average clumpiness of galaxies (computed in bins of 0.5 in $i_{\rm mag}$) drops by $> 50\%$ compared to the median value and becomes closer to zero (see Fig. 5.6 in Appendix). In addition, for all the galaxies with $i_{\rm mag} > 22.5$, it was harder to distinguish their internal morphology on a visual inspection.

Another important aspect that hampers clumps identification is the inclination of the galaxy. The primary consequence is that, for an edge-on system, the standard detection method can erroneously consider the whole disk as a single elongated (and eventually multiply deblended) clump, producing an artificial enhancement of the clumpiness up to a value close to 1. In some cases, the edge-on disk is very faint, probably attenuated by the increased dust column density along the line of sight, so that no substructures are detected and the clumpiness is 0. However, the majority of these objects would be removed by the first $i_{\rm mag}$ threshold.

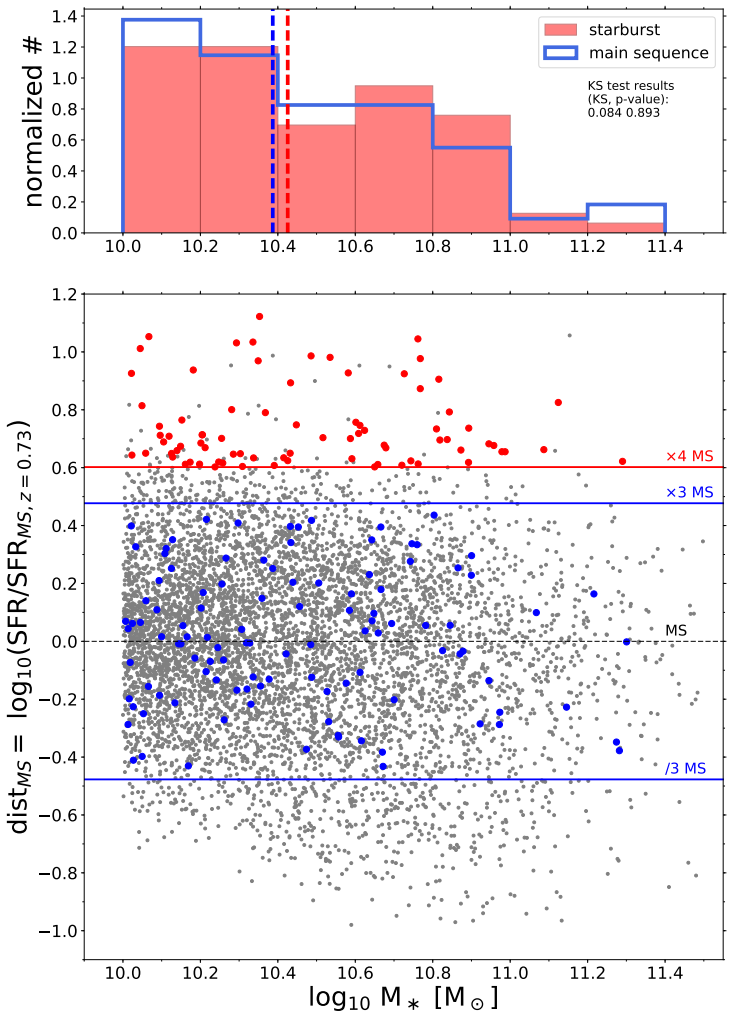

Figure 5.5: *Bottom:* Diagram showing for my parent sample of star-forming galaxies in COSMOS ($0.5 < z < 0.9$) their distance from the main sequence as a function of stellar mass. I highlight with a black horizontal line the 0 level. The blue and red lines indicate the limits taken for the main sequence and starburst selection, respectively. The final selected sample is highlighted with blue and red points, correspondingly. The SFR used in the y-axis is normalized to the median redshift of my sample (0.73), following the SFR-redshift evolution of Sargent et al. (2014). *Top:* Histogram distribution (normalized to unit area) of the stellar masses of my selected sample of starbursts (red) and main sequence galaxies (blue), showing that the two subsets have similar distributions. The two vertical lines indicate, according to their corresponding colors, the median values of M_* of SB and MS galaxies.

In order to avoid all these cases, I performed a visual inspection and removed all the edge-on galaxies that suffered from these problems. Since inclination effects can be different for each galaxy and both reduce or enhance their clumpiness, it was not possible to apply the same threshold procedure used for $i_{\rm mag}$. However, I found that almost all (96%) of the objects

discarded by eye have an elongation > 3.5, so I can consider this value as a representative threshold for my selection. For the full original sample, a comparison between the clumpiness and both the i-band magnitude and the elongation will be shown in the Appendix 5.A.

I remark that the i_{mag} and elongation cuts remove similar fractions of starburst and main sequence systems ($\sim$ 10% in each case), and also the same percentages of morphologically classified mergers and not mergers (according to Gini-M_{20} diagram), thus no systematic biases are introduced against one of the two populations. I also notice that almost all the objects removed by this procedure have very low clumpiness, below 0.05. After applying these cuts, I also verified that starburst and main sequence galaxies have similar histogram distributions in i-band magnitude and elongation in the allowed ranges, and very close medians of the two quantities. In particular, for SBs and MS galaxies, the median $i_{mag} = 21.25$ and 21.35, respectively, while the median elongations are 1.55 and 1.59. In any case, I verified that applying lower, more conservative thresholds in i_{mag} and elongation would not change the results of this paper.

After cleaning the sample from the contamination of faint or very elongated objects, I derived a final subset of 79 starbursts and 109 main sequence galaxies, that I will analyze in following sections. The final starbursts and main sequence sample selection can be visualized in Fig. 5.5. The stellar mass histogram, visible on the top of the figure, shows that the two selected populations have a similar distributions of M_*, with medians of $\log_{10}(M_*)= 10.42$ and 10.39, respectively, thus the previous cuts do not introduce systematic biases in M_* against one of the two populations.

In the following sections I will present the results of this analysis, discuss their physical implications for high redshift galaxies, and what we can learn about the merger phenomenon in connection to clumpy structures.

5.A Comparison between the clumpiness and other quantities

In this Appendix I show how the clumpiness parameter compares with other quantities considered in this Chapter. In Fig. 5.6 I display the clumpiness as a function of the i-band magnitude and the elongation of our targets. This explains the final sample selection made for our analysis (described in Sections 5.3), highlighted by the gray vertical lines. In Fig. 5.7 is presented the comparison of the clumpiness with different morphological indicators, that are, the Gini coefficient, the M_{20} parameter and the *mergerness*. The first two diagrams show the lack of correlation between the two quantities in the x and y-axis, even though a slightly increasing trend of c is found at higher Gini. In the last diagram can be noticed a much steeper increase of the clumpiness with the *mergerness*, which is used to define morphological mergers in Section 5.1.3. Finally, Fig. 5.8-top shows the redshift distribution

of our sample, ranging $0.5 < z < 0.9$ and with a median z of 0.73. Fig. 5.8-bottom and Fig. 5.9 demonstrate, respectively, that the clumpiness does not depend on the stellar mass, and does not significantly evolve with redshift (within our uncertainties). At the end of this Appendix of Chapter 5, I display the table with the main morphological properties of the sample analyzed here, including the clumpiness and the *mergerness* parameters.

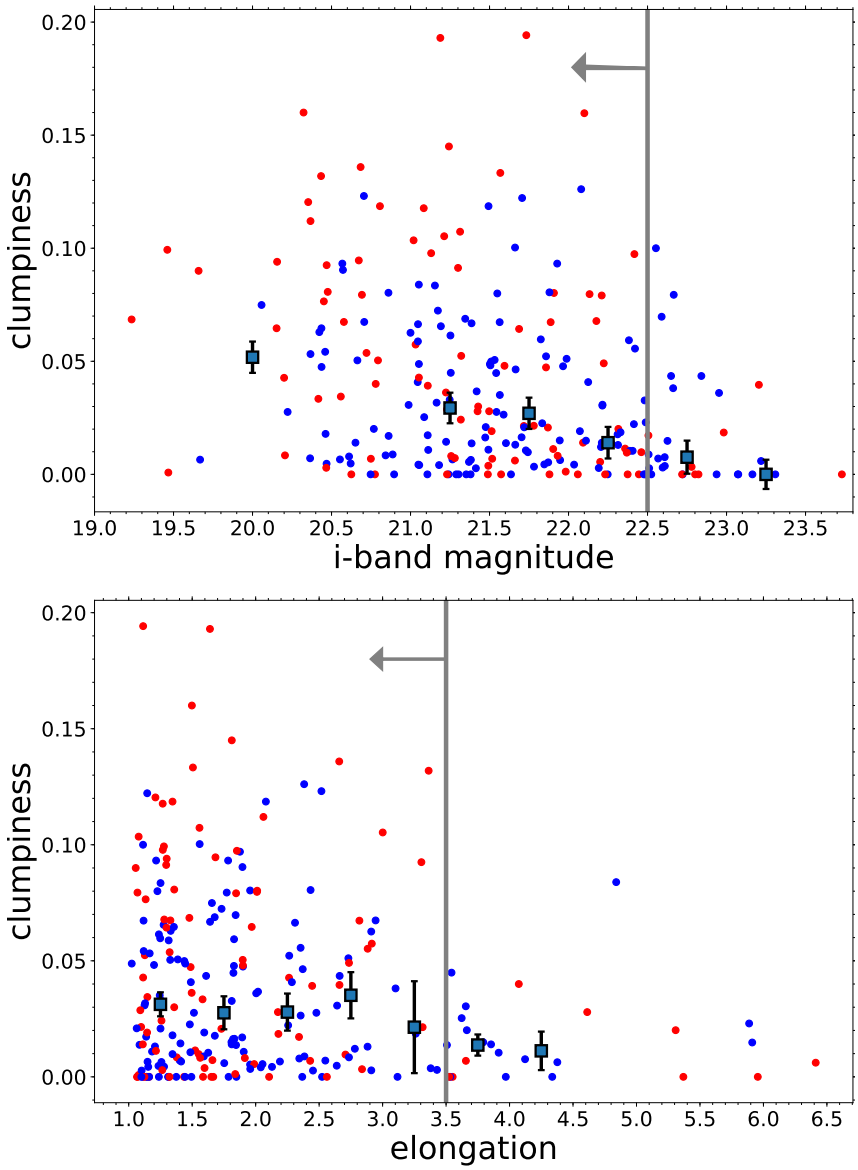

Figure 5.6: *Top:* Clumpiness vs i-band total magnitude (i_{mag}) for our initial sample of 150 main sequence and 96 starburst galaxies (in blue and red, respectively). Median clumpiness values and errors (gray squares with black error bars) are derived for 6 bins of i_{mag}. Our selection cut ($i_{mag} < 22.5$) is highlighted with a vertical gray line. *Bottom:* Clumpiness vs elongation for the same sample as above, with median clumpiness and errors estimated in 7 bins of elongation. The vertical gray line indicates our cut for the final selection (elongation < 3.5), even though we remember that one additional nearly edge-on MS galaxy was also removed by visual inspection.

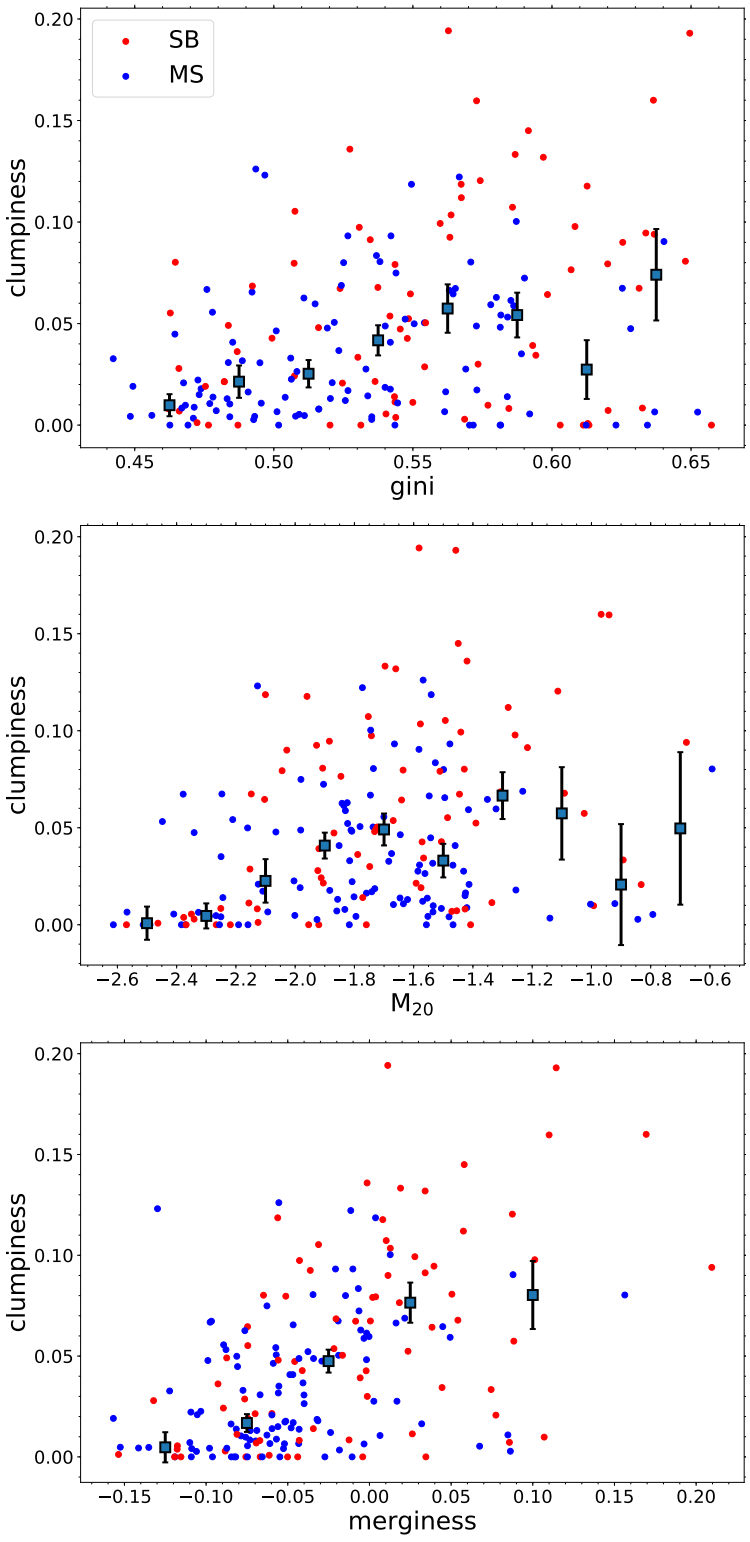

Figure 5.7: The three diagrams compare the clumpiness of our final galaxy sample to the Gini and M_{20} coefficients (first and second panels, respectively), and to the *mergerness* parameter, defined in Eq. 5.3. Starbursts are shown in red, while main sequence galaxies are color coded in blue. The median clumpiness (and errors) computed in bins of Gini, M_{20} and *mergerness* are represented with gray squares and black error bars.

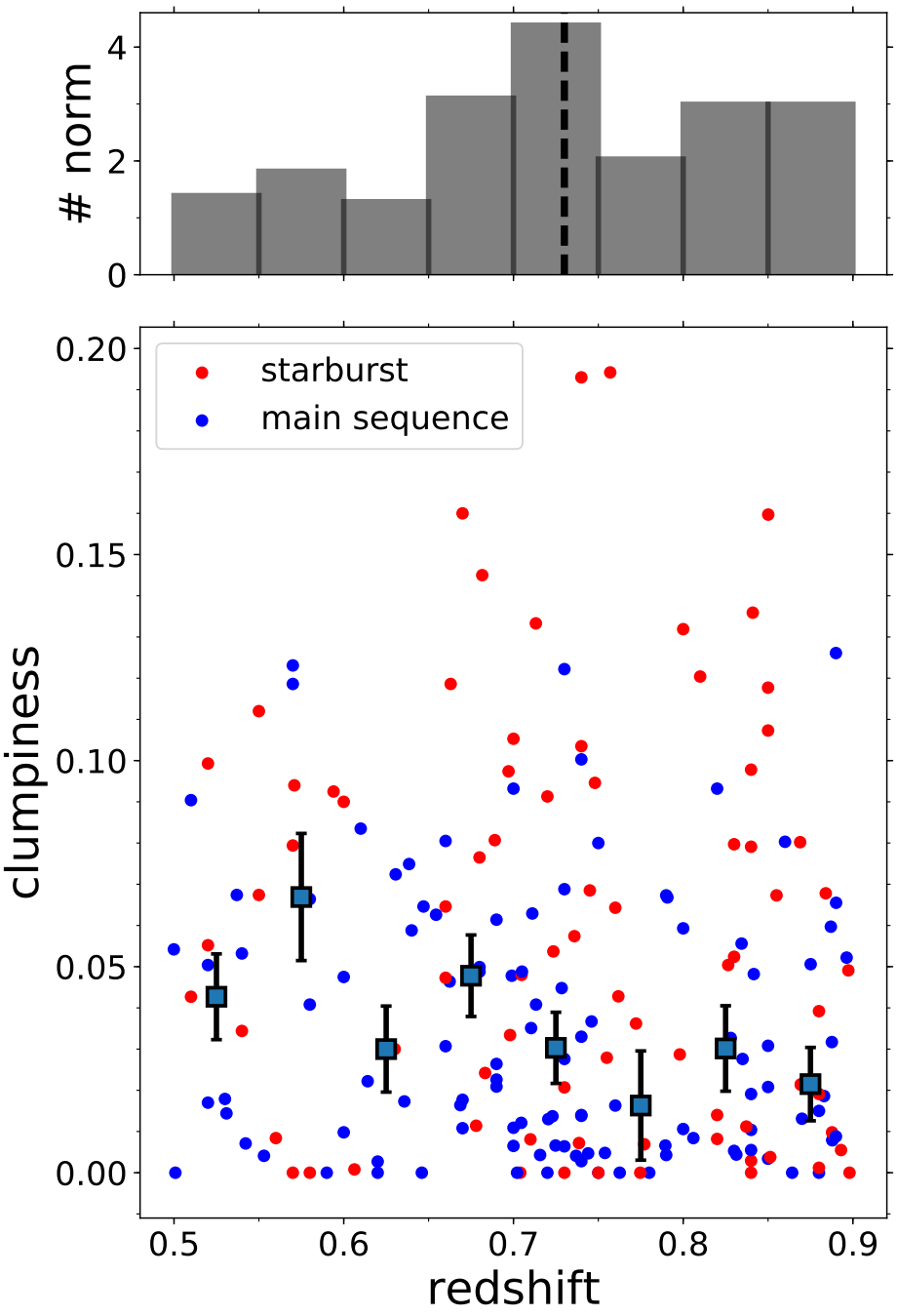

Figure 5.8: Redshift vs clumpiness for our final selected galaxies, with gray squares and black error bars representing the median clumpiness and error calculated inside 8 redshift bins. On the top of the panel is shown the histogram distribution of the redshifts of our galaxies, with the median redshift ($z_{med} = 0.73$) highlighted with a black dashed line.

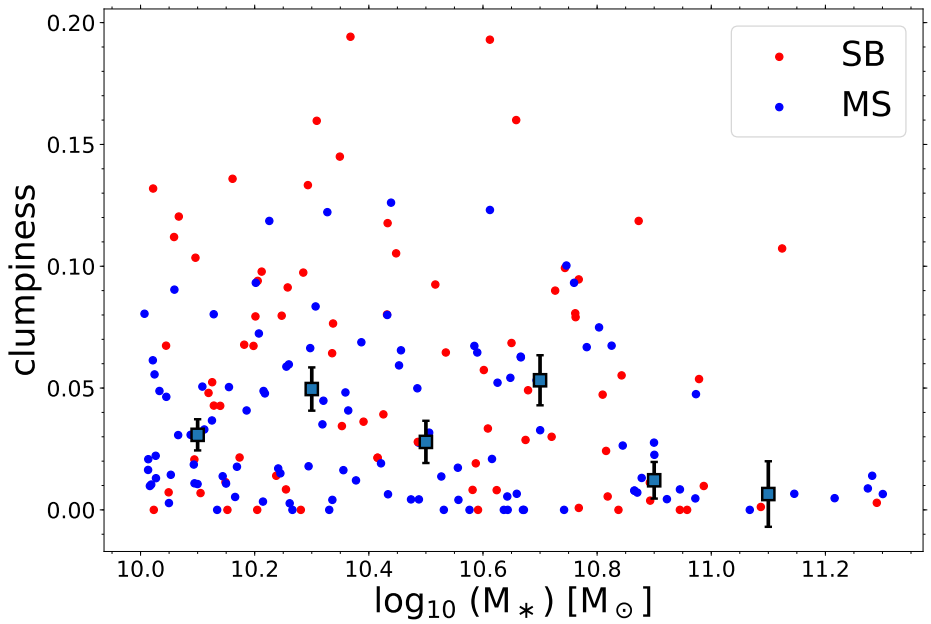

Figure 5.9: Stellar mass vs clumpiness for our final sample of MS and SB galaxies (in blue and red, respectively), with median clumpiness (and error) in 6 M_* bins superimposed with gray squares.

ID	**RA**	**DEC**	**redshift**	**c′**	**clumpiness**	**merginess**	M_* [$M_\odot$]	SFR_{IR} [$M_\odot$/yr]
217536	149.524108	1.606315	0.87 ± 0.03	0.02	0.02	0.07	10.4	74.25 ± 6.633
220514	149.58302	1.61253	0.89 ± 0.03	0.01	0.01	0.07	10.9	49.96 ± 4.284
222723	150.173213	1.616315	0.61 ± 0.01	0.0	0.0	0.06	10.8	151.2 ± 6.357
222977	150.414727	1.618189	0.75 ± 0.0	0.03	0.04	0.04	10.1	15.29 ± 2.6
223715	149.765371	1.617017	0.52 ± 0.0	0.09	0.1	-0.03	10.7	52.4 ± 0.805
228149	149.816844	1.627891	0.63 ± 0.12	0.06	0.07	0.01	10.2	14.57 ± 6.078
239406	150.338269	1.644141	0.73 ± 0.02	0.04	0.04	0.08	10.3	12.82 ± 1.733
244932	149.460788	1.651282	0.72 ± 0.02	0.01	0.01	0.06	10.7	19.61 ± 2.242
245158	150.188543	1.654977	0.52 ± 0.0	0.05	0.06	0.07	10.8	83.05 ± 1.227
247210	150.487543	1.656873	0.83 ± 0.0	0.05	0.05	-0.02	10.1	41.72 ± 1.106
249989	150.685402	1.661076	0.74 ± 0.04	0.06	0.06	-0.09	10.6	102.4 ± 14.72
259328	149.916036	1.676354	0.74 ± 0.0	0.03	0.03	0.08	10.1	26.09 ± 0.57
271645	149.607229	1.694341	0.74 ± 0.08	0.0	0.0	0.14	11.0	15.24 ± 3.196
275629	150.182349	1.700807	0.74 ± 0.0	0.14	0.19	-0.11	10.6	101.3 ± 0.924
280708	149.969049	1.710048	0.86 ± 0.0	0.09	0.1	0.02	10.1	36.63 ± 4.083
286337	149.808093	1.717684	0.75 ± 0.0	0.0	0.0	0.08	10.6	17.23 ± 1.73
287281	149.662106	1.719228	0.71 ± 0.02	0.06	0.06	0.01	10.7	44.15 ± 5.46
289993	149.951404	1.725684	0.68 ± 0.0	0.01	0.01	-0.03	10.1	42.29 ± 0.49
293450	149.496283	1.729198	0.86 ± 0.06	0.06	0.07	0.01	10.2	45.48 ± 7.794
294096	149.51561	1.731195	0.67 ± 0.06	0.01	0.02	-0.03	10.0	4.835 ± 1.635
295213	150.421274	1.731761	0.64 ± 0.04	0.07	0.07	0.06	10.8	47.17 ± 6.101
297678	149.582631	1.738114	0.87 ± 0.03	0.07	0.08	0.06	10.4	78.84 ± 5.764
300643	149.779375	1.741341	0.53 ± 0.0	0.02	0.02	0.03	10.3	5.695 ± 1.548
308894	150.259527	1.756639	0.88 ± 0.0	0.04	0.05	0.06	10.1	25.86 ± 3.1
314674	149.922125	1.764706	0.89 ± 0.01	0.06	0.07	0.05	10.5	22.89 ± 3.078
319784	150.073982	1.772639	0.73 ± 0.0	0.02	0.02	-0.08	10.1	47.72 ± 0.947
326384	149.517858	1.783572	0.71 ± 0.04	0.1	0.13	-0.02	10.3	125.0 ± 14.8
327954	149.493504	1.786618	0.61 ± 0.11	0.02	0.02	0.11	10.0	9.337 ± 4.839
331390	150.640087	1.78974	0.67 ± 0.0	0.01	0.01	0.06	10.1	10.15 ± 2.1
331485	149.494555	1.791539	0.71 ± 0.02	0.02	0.04	0.06	10.3	15.02 ± 2.365
332156	150.23588	1.791352	0.83 ± 0.16	0.0	0.0	0.14	10.9	29.63 ± 11.85
340778	150.458433	1.803992	0.75 ± 0.0	0.0	0.0	0.15	11.2	39.87 ± 1.179
350404	150.20613	1.822038	0.74 ± 0.0	0.0	0.0	0.05	10.3	14.75 ± 4.196
358661	149.710063	1.832255	0.5 ± 0.13	0.0	0.0	0.12	10.3	6.222 ± 3.722
366376	150.138331	1.844028	0.57 ± 0.0	0.08	0.09	-0.21	10.2	38.12 ± 0.414
368717	149.718723	1.849718	0.67 ± 0.0	0.14	0.16	-0.17	10.7	67.19 ± 0.758
371578	150.674055	1.85337	0.51 ± 0.0	0.04	0.04	0.0	10.1	26.9 ± 0.222
371675	149.901208	1.85448	0.74 ± 0.0	0.01	0.01	0.08	10.1	8.38 ± 2.119
371886	149.900477	1.854753	0.64 ± 0.0	0.01	0.02	0.05	10.6	7.781 ± 1.071
372591	150.503808	1.854601	0.75 ± 0.0	0.07	0.08	0.01	10.4	36.58 ± 1.03
387242	150.222431	1.878024	0.84 ± 0.0	0.08	0.1	-0.1	10.2	51.69 ± 1.204
387454	150.652196	1.877237	0.59 ± 0.0	0.08	0.09	0.04	10.5	64.74 ± 1.105
387747	149.916015	1.879961	0.84 ± 0.0	0.07	0.08	-0.0	10.8	102.4 ± 0.974
400118	150.051501	1.898621	0.57 ± 0.0	0.1	0.12	-0.0	10.2	11.69 ± 1.625
402258	150.648684	1.902372	0.74 ± 0.0	0.09	0.1	-0.01	10.1	42.46 ± 0.332
409602	149.578964	1.913372	0.83 ± 0.0	0.07	0.08	0.05	10.2	52.3 ± 0.685
409814	150.198597	1.914859	0.87 ± 0.0	0.02	0.02	0.06	10.2	46.7 ± 0.862
412250	150.741711	1.91764	0.68 ± 0.03	0.1	0.14	-0.06	10.3	109.4 ± 10.24
416314	150.663036	1.924054	0.83 ± 0.0	0.0	0.01	-0.07	10.2	12.06 ± 0.433
418804	149.935142	1.927629	0.68 ± 0.0	0.07	0.08	-0.02	10.3	47.2 ± 0.721
431551	149.568139	1.94866	0.54 ± 0.02	0.01	0.01	0.11	10.9	13.7 ± 1.814
431596	149.948236	1.950357	0.85 ± 0.0	0.03	0.03	0.07	10.1	15.5 ± 0.389
436769	150.617708	1.958166	0.65 ± 0.08	0.0	0.0	0.01	10.5	14.6 ± 5.141
439419	150.301785	1.962747	0.7 ± 0.02	0.01	0.01	0.02	10.4	15.06 ± 1.283
444878	150.687694	1.970867	0.76 ± 0.12	0.16	0.19	-0.01	10.4	85.03 ± 27.02
447374	150.543608	1.974443	0.79 ± 0.03	0.06	0.07	0.1	10.8	26.29 ± 3.279
451272	150.250512	1.980928	0.72 ± 0.0	0.08	0.09	-0.03	10.3	45.3 ± 0.57
451426	149.651824	1.981124	0.79 ± 0.0	0.0	0.0	0.1	10.5	14.85 ± 3.362
466112	149.999276	2.005995	0.76 ± 0.0	0.05	0.06	-0.04	10.3	144.0 ± 1.052
472775	150.481476	2.013621	0.68 ± 0.02	0.02	0.02	0.09	10.8	159.7 ± 11.82
473147	150.399682	2.014254	0.72 ± 0.0	0.05	0.05	0.02	11.0	107.1 ± 1.269
474838	149.543724	2.01889	0.77 ± 0.02	0.03	0.04	0.09	10.4	58.87 ± 3.831
475972	149.526013	2.020502	0.62 ± 0.0	0.0	0.0	0.05	10.7	8.241 ± 2.693
478933	150.666347	2.025354	0.8 ± 0.0	0.13	0.13	-0.03	10.0	53.94 ± 0.785
480125	149.749497	2.027741	0.7 ± 0.0	0.0	0.01	0.05	11.3	31.46 ± 1.037
486542	150.761399	2.040174	0.88 ± 0.0	0.06	0.07	-0.05	10.2	103.9 ± 2.043

ID	RA	DEC	redshift	c′	clumpiness	merginess	M_* [$M_\odot$]	SFR_{IR} [$M_\odot$/yr]
488940	149.831475	2.040881	0.53 ± 0.13	0.01	0.01	0.05	10.1	4.905 ± 2.899
493881	150.749674	2.047066	0.6 ± 0.0	0.08	0.09	-0.01	10.7	129.2 ± 1.006
500548	149.62879	2.05949	0.63 ± 0.0	0.02	0.03	0.0	10.7	67.56 ± 1.033
503971	150.65256	2.063559	0.6 ± 0.0	0.04	0.05	0.03	11.0	9.35 ± 1.21
505311	150.089164	2.065345	0.73 ± 0.0	0.03	0.03	-0.02	10.9	34.49 ± 3.37
506131	149.528615	2.0665	0.57 ± 0.0	0.06	0.08	-0.0	10.2	39.06 ± 0.442
508753	149.928339	2.07214	0.68 ± 0.0	0.04	0.05	0.03	10.2	23.69 ± 0.944
508907	149.856873	2.072084	0.69 ± 0.0	0.05	0.06	0.0	10.0	15.84 ± 1.112
515278	150.523885	2.082297	0.89 ± 0.0	0.11	0.13	0.06	10.4	28.73 ± 3.716
516551	150.205761	2.083436	0.78 ± 0.01	0.01	0.01	0.07	10.1	44.4 ± 2.191
518855	150.12551	2.08703	0.89 ± 0.0	0.0	0.01	0.12	10.8	142.3 ± 1.436
519651	150.430196	2.086883	0.66 ± 0.0	0.05	0.06	0.07	10.5	137.1 ± 1.312
529521	150.103938	2.104858	0.83 ± 0.0	0.03	0.03	0.12	10.7	15.19 ± 3.556
532321	149.893588	2.107745	0.74 ± 0.07	0.01	0.01	-0.09	10.0	52.17 ± 10.76
536590	149.918602	2.113077	0.72 ± 0.06	0.01	0.01	0.04	10.5	10.65 ± 3.274
539760	149.880566	2.120673	0.68 ± 0.0	0.04	0.05	0.08	10.5	15.08 ± 1.726
544522	150.052099	2.126677	0.66 ± 0.0	0.1	0.12	0.06	10.9	90.06 ± 0.794
545104	150.451931	2.127888	0.84 ± 0.0	0.0	0.0	0.12	10.3	85.6 ± 1.039
545185	149.528016	2.12725	0.54 ± 0.0	0.03	0.03	-0.04	10.4	127.3 ± 1.155
546483	150.674581	2.131899	0.9 ± 0.0	0.0	0.0	0.07	10.0	39.28 ± 1.527
562400	150.512919	2.152049	0.56 ± 0.0	0.01	0.01	0.01	10.3	40.5 ± 0.553
571040	149.509664	2.167659	0.84 ± 0.0	0.02	0.02	0.16	10.4	18.17 ± 1.262
574334	150.346743	2.170359	0.85 ± 0.0	0.1	0.12	-0.01	10.4	132.5 ± 1.197
577143	149.887635	2.175504	0.78 ± 0.0	0.0	0.0	0.11	10.7	15.76 ± 1.443
580153	150.259862	2.181773	0.67 ± 0.0	0.01	0.02	0.05	10.2	5.035 ± 1.073
581920	150.23722	2.183978	0.7 ± 0.0	0.08	0.09	0.01	10.2	17.91 ± 1.338
584271	149.729701	2.186421	0.59 ± 0.0	0.0	0.0	0.1	10.6	16.49 ± 0.88
586243	150.626379	2.187925	0.6 ± 0.0	0.01	0.01	0.08	10.0	5.475 ± 1.482
586666	149.68814	2.191839	0.89 ± 0.04	0.01	0.01	-0.11	11.0	146.4 ± 13.37
586799	150.024476	2.190772	0.76 ± 0.0	0.01	0.02	0.08	10.4	9.945 ± 1.957
587164	149.605886	2.190462	0.54 ± 0.0	0.06	0.07	0.02	10.8	13.38 ± 0.944
587556	150.211575	2.191062	0.87 ± 0.0	0.01	0.01	0.07	10.9	25.36 ± 0.477
588922	149.682152	2.193682	0.73 ± 0.0	0.07	0.07	-0.02	10.4	23.22 ± 0.597
601470	150.719972	2.211767	0.89 ± 0.03	0.03	0.03	0.06	10.5	34.8 ± 5.655
606235	150.508123	2.219968	0.82 ± 0.0	0.01	0.01	0.03	10.2	48.24 ± 0.716
607625	150.033442	2.221992	0.89 ± 0.03	0.05	0.06	0.0	10.3	14.44 ± 1.223
608991	150.478377	2.22183	0.83 ± 0.0	0.03	0.03	-0.0	10.5	45.74 ± 2.175
609835	150.678868	2.225219	0.77 ± 0.01	0.0	0.0	0.04	10.2	59.46 ± 2.104
619015	150.10376	2.237664	0.8 ± 0.0	0.02	0.03	0.08	10.7	100.7 ± 1.634
620032	150.626231	2.240874	0.66 ± 0.0	0.04	0.05	0.06	10.0	9.124 ± 0.871
622611	149.664939	2.241806	0.89 ± 0.0	0.01	0.01	0.06	11.3	12.98 ± 3.813
624991	149.9687	2.247664	0.85 ± 0.0	0.02	0.02	0.06	10.0	17.43 ± 1.755
625435	149.538265	2.248029	0.84 ± 0.0	0.01	0.01	0.08	10.0	26.65 ± 1.369
629919	150.477167	2.252186	0.84 ± 0.0	0.0	0.0	0.09	11.3	137.9 ± 9.384
638793	149.529624	2.266751	0.58 ± 0.0	0.06	0.07	-0.02	10.3	23.98 ± 1.356
650054	150.400428	2.286241	0.83 ± 0.16	0.05	0.06	0.09	10.0	20.26 ± 6.12
654259	149.872198	2.289675	0.7 ± 0.0	0.0	0.0	0.08	10.8	103.4 ± 1.199
666872	150.537907	2.310505	0.84 ± 0.0	0.0	0.01	0.07	10.6	21.74 ± 3.212
668065	149.937063	2.312279	0.52 ± 0.0	0.05	0.05	0.02	10.2	7.974 ± 1.205
668738	150.210203	2.31168	0.75 ± 0.0	0.07	0.09	-0.04	10.8	158.9 ± 1.188
668769	149.67653	2.313653	0.69 ± 0.0	0.02	0.02	0.1	10.9	41.91 ± 0.512
695086	150.05225	2.351018	0.72 ± 0.13	0.01	0.01	0.07	10.0	2.633 ± 1.312
706850	149.931017	2.370359	0.85 ± 0.03	0.15	0.16	-0.11	10.3	38.69 ± 1.226
708427	149.578884	2.370704	0.75 ± 0.0	0.06	0.07	0.02	10.6	70.09 ± 0.971
711307	150.53029	2.373861	0.66 ± 0.0	0.03	0.05	0.05	10.8	102.0 ± 1.356
720848	150.261788	2.391079	0.8 ± 0.0	0.01	0.01	-0.01	10.1	12.21 ± 1.839
721398	150.670506	2.391459	0.61 ± 0.0	0.08	0.08	0.01	10.3	14.31 ± 1.796
724796	150.597688	2.396014	0.58 ± 0.0	0.04	0.04	0.05	10.4	19.33 ± 0.723
739926	150.470841	2.419552	0.55 ± 0.0	0.0	0.0	0.11	10.6	4.908 ± 1.447
742281	150.641614	2.423434	0.73 ± 0.0	0.0	0.0	0.12	11.0	112.7 ± 0.43
743322	149.657291	2.425131	0.57 ± 0.0	0.1	0.12	0.13	10.6	9.331 ± 0.836
749126	150.427092	2.431647	0.88 ± 0.0	0.03	0.04	0.01	10.4	71.11 ± 0.756
753450	150.327658	2.44088	0.52 ± 0.0	0.02	0.02	0.05	10.2	5.353 ± 0.727

ID	**RA**	**DEC**	**redshift**	**c′**	**clumpiness**	**merginess**	M_* [$M_\odot$]	SFR_{IR} [$M_\odot$/yr]
764862	150.189794	2.45758	0.51 ± 0.0	0.08	0.09	-0.09	10.1	6.139 ± 0.292
773897	149.833747	2.481315	0.84 ± 0.0	0.12	0.14	0.0	10.2	40.46 ± 1.969
777034	150.150252	2.475166	0.69 ± 0.0	0.06	0.08	-0.05	10.8	211.7 ± 0.764
778756	150.548939	2.480459	0.8 ± 0.0	0.05	0.06	-0.05	10.5	41.11 ± 1.792
780365	150.398266	2.480753	0.85 ± 0.0	0.0	0.0	0.02	10.2	8.178 ± 3.15
783499	150.506268	2.486894	0.62 ± 0.0	0.0	0.0	0.11	10.3	10.15 ± 0.465
783743	149.93968	2.488034	0.72 ± 0.15	0.0	0.0	0.09	10.5	10.73 ± 3.42
789914	149.979212	2.498304	0.88 ± 0.0	0.0	0.0	0.08	10.1	9.062 ± 1.257
790685	150.370657	2.498115	0.82 ± 0.0	0.09	0.09	0.02	10.8	44.95 ± 0.6
794024	150.055643	2.504436	0.7 ± 0.0	0.07	0.1	0.04	10.3	50.4 ± 0.998
811857	149.913557	2.530162	0.69 ± 0.0	0.02	0.02	0.11	10.6	7.52 ± 1.842
819000	149.457523	2.539333	0.83 ± 0.02	0.05	0.05	0.02	10.3	58.92 ± 2.595
824508	149.862472	2.548484	0.74 ± 0.0	0.01	0.01	0.06	11.3	14.81 ± 0.813
830418	149.562546	2.557087	0.76 ± 0.03	0.0	0.0	0.03	10.7	39.12 ± 4.827
834449	150.1201	2.561479	0.5 ± 0.0	0.04	0.05	0.06	10.6	14.31 ± 0.228
837890	150.054801	2.569459	0.75 ± 0.0	0.03	0.03	0.13	10.5	156.8 ± 1.615
838188	149.77795	2.567252	0.72 ± 0.0	0.0	0.0	0.07	10.3	10.45 ± 0.524
840232	149.716601	2.572475	0.9 ± 0.01	0.04	0.05	0.09	10.7	117.4 ± 4.215
842149	150.342316	2.575943	0.75 ± 0.0	0.0	0.0	-0.03	10.2	54.86 ± 0.529
842173	149.733742	2.574995	0.71 ± 0.0	0.01	0.01	0.07	10.6	93.81 ± 1.129
844990	149.926835	2.580581	0.7 ± 0.0	0.04	0.05	0.1	10.2	14.41 ± 1.532
848785	150.42295	2.583241	0.81 ± 0.0	0.12	0.12	-0.09	10.1	83.81 ± 1.125
849397	149.976994	2.586831	0.73 ± 0.0	0.09	0.12	0.01	10.3	13.25 ± 1.373
853769	150.33873	2.593234	0.85 ± 0.0	0.0	0.0	0.12	10.9	154.6 ± 2.136
860071	150.27635	2.603899	0.7 ± 0.0	0.01	0.01	-0.08	10.1	7.279 ± 2.386
864706	150.531072	2.610881	0.79 ± 0.0	0.05	0.07	0.1	10.6	23.57 ± 1.955
865896	150.054261	2.612264	0.74 ± 0.0	0.0	0.0	-0.09	10.0	8.219 ± 0.209
866054	149.811584	2.610245	0.54 ± 0.0	0.04	0.05	0.09	10.7	14.02 ± 0.637
876155	150.564918	2.625331	0.65 ± 0.02	0.06	0.06	0.08	10.7	24.88 ± 1.983
878476	150.752013	2.62904	0.84 ± 0.11	0.03	0.05	0.0	10.4	18.84 ± 6.223
878551	150.046263	2.630447	0.76 ± 0.03	0.04	0.04	0.04	10.1	38.72 ± 4.129
880787	149.550391	2.632955	0.81 ± 0.06	0.01	0.01	0.07	10.9	23.8 ± 3.235
880925	149.937367	2.634136	0.71 ± 0.03	0.03	0.04	0.05	10.2	11.79 ± 1.779
886498	149.513205	2.643508	0.64 ± 0.0	0.05	0.06	+0.0	10.3	11.81 ± 0.759
887351	150.04403	2.643885	0.7 ± 0.0	0.03	0.03	-0.07	10.6	86.33 ± 0.814
893857	150.159952	2.654341	0.85 ± 0.0	0.09	0.11	-0.01	11.1	217.3 ± 2.864
894779	150.427097	2.656439	0.55 ± 0.0	0.05	0.07	-0.0	10.0	61.12 ± 0.869
901597	150.709924	2.667676	0.7 ± 0.08	0.04	0.05	0.06	10.1	44.59 ± 9.812
902885	150.136763	2.669235	0.7 ± 0.0	0.04	0.05	0.04	10.0	12.35 ± 0.37
909617	149.970409	2.677765	0.69 ± 0.0	0.02	0.03	0.04	10.8	22.88 ± 1.869
911723	149.681335	2.681084	0.58 ± 0.0	0.0	0.0	0.0	10.9	82.03 ± 0.502
912969	150.589787	2.684536	0.74 ± 0.0	0.1	0.1	-0.01	10.7	44.6 ± 2.707
915913	150.557165	2.688555	0.88 ± 0.0	0.02	0.02	0.03	10.1	20.01 ± 0.293
917600	150.029291	2.690141	0.79 ± 0.09	0.01	0.01	0.04	11.1	23.59 ± 6.409
921254	149.910328	2.695579	0.86 ± 0.14	0.0	0.0	0.08	11.1	39.36 ± 14.69
922401	150.035101	2.698678	0.65 ± 0.0	0.06	0.06	-0.04	10.6	18.22 ± 0.675
925981	150.433978	2.705011	0.88 ± 0.0	0.01	0.01	0.06	10.2	15.2 ± 1.928
927031	149.716671	2.705636	0.88 ± 0.0	0.0	0.0	0.15	11.1	155.3 ± 1.796
931390	150.586062	2.712214	0.66 ± 0.0	0.07	0.08	0.03	10.0	9.482 ± 2.196
937909	149.79431	2.722162	0.9 ± 0.02	0.05	0.05	0.04	10.6	28.88 ± 2.201
940851	150.539461	2.728218	0.66 ± 0.0	0.03	0.03	0.04	10.1	6.119 ± 0.435
946233	150.227312	2.737645	0.7 ± 0.09	0.0	0.0	0.07	10.6	29.97 ± 8.641
948557	149.627616	2.739277	0.55 ± 0.0	0.11	0.11	-0.06	10.1	25.99 ± 0.689
952356	149.886951	2.747311	0.88 ± 0.0	0.02	0.02	0.07	10.6	109.3 ± 1.016
960767	149.848315	2.760829	0.7 ± 0.0	0.1	0.11	0.03	10.4	78.83 ± 1.575
964786	150.126928	2.7654	0.57 ± 0.0	0.0	0.0	0.05	10.6	56.32 ± 0.274
970636	150.408721	2.777253	0.84 ± 0.09	0.01	0.01	0.08	10.9	114.8 ± 26.57
978011	150.155692	2.787663	0.73 ± 0.0	0.0	0.01	0.0	10.4	18.89 ± 0.559
981123	150.399371	2.794152	0.82 ± 0.0	0.01	0.01	0.04	10.6	170.4 ± 3.618

Table 5.1: Table columns: (1,2,3) Identification number, RA and DEC (in degree) from Laigle et al. (2016); (4) photometric redshift (or spectroscopic if available) from Jin et al. (2018); (5,6) clumpiness parameters (clumpiness is estimated as in equation 5.4), while in c' the flux of the clumps is divided by the total flux of the galaxy (including the nuclei) inside the segmentation map; (7) *mergerness* parameter, estimated as in Eq. 5.3; (8) stellar mass from Laigle et al. (2016), with typical uncertainty of 0.1 dex; (9) SFR_{IR} from Jin et al. (2018).

Chapter 6

Merger induced clump formation in distant IR-luminous starbursts

In this Chapter I analyze the morphological measurements described in previous sections, and make a comparison between the clumpiness in starburst galaxies and normal star-forming (isolated) disks. I also present a set of numerical simulations of merger interactions between typical z$\sim$ 0.7 galaxies, which will help to interpret the observational results. I remind again that these results have been described and discussed also in an *Astronomy & Astrophysics* article, submitted on 26 April 2019 (Calabrò et al., 2019b).

6.1 The clumpiness distribution of MS and SB galaxies

In this Section I present the results of the clumpiness measurements described in Section 5.2, and compare the properties of the starburst and main sequence populations, that I have taken as representatives of two star-formation modes: a higher efficiency stellar production induced by merger events in the first case, and a normal star-formation activity associated with secularly evolving disks in the latter.

In Fig.6.1 I show the histogram distribution of the clumpiness for starburst galaxies (in red) and main sequence galaxies (in blue). The clumpiness parameter spans a range between 0 and 0.20, meaning that clumps can contribute at maximum to one fifth of the total off-nuclear galaxy emission at this redshift.

We can see that the distributions of both subsamples are peaked at low clumpiness ($c < 0.02$) and, after this excess, they follow an approximately constant and then declining trend. However, the two histograms differ for many aspects. Main sequence systems are dominant in the first clumpiness bin, while, after a region where the relative abundances are consistent ($0.02 < c < 0.08$), starbursts are systematically more numerous above $c \simeq 0.08$. This translates into more than a factor of two higher median clumpiness for SBs compared to the MS population (0.05 and 0.022, respectively).

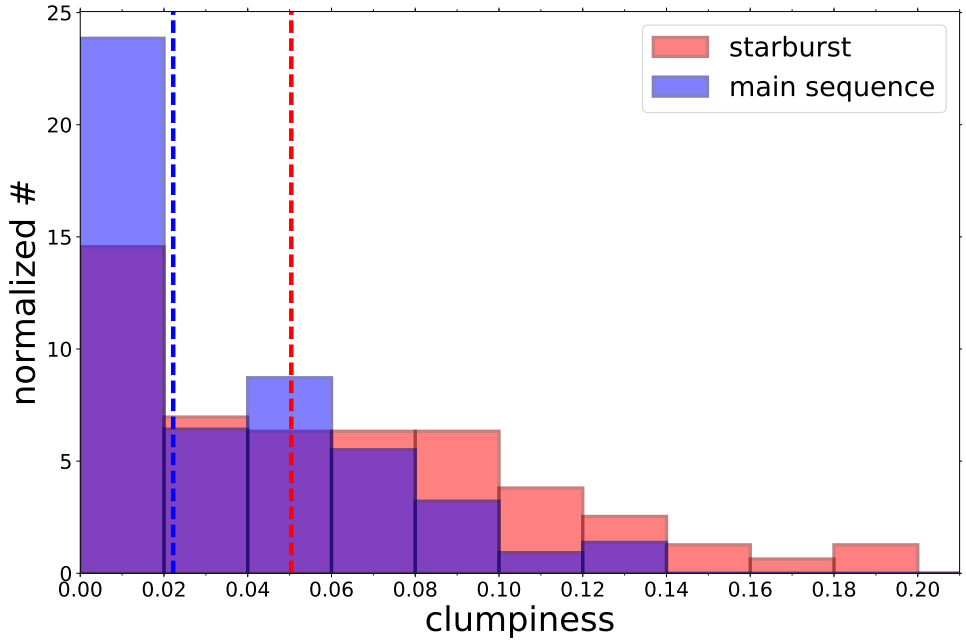

Figure 6.1: Distribution of the clumpiness parameter (normalized to unit area) for starburst galaxies (in red) and main sequence systems (in blue), showing that starbursts dominate in the high clumpiness tail. The results of the Kolmogorov-Smirnov test (KS statistics and p-value) between the two subsample distributions are 0.26 and 0.0029, respectively. The median clumpiness for SBs and MS (0.05 and 0.022) are drawn with dashed lines with their corresponding colors.

In order to test whether the two distributions (χ_1 and χ_2) are significantly different, I run a Kolmogorov-Smirnov (KS) test, which yields both the maximum difference D_{χ_1,χ_2} between the two cumulative distribution functions and the probability (p-value) to obtain the same D_{χ_1,χ_2} under the assumption that the two underlying one-dimensional probability distributions are equal. I found a $D_{\chi_1,\chi_2} = 0.26$ and p-value of 0.029%, thus the identity hypothesis can be rejected at $> 99.5\%$ confidence level, suggesting that the two subsets are intrinsically different.

I also characterized the two tails in the high clumpiness regime (excluding the objects falling in the first bin) for SB and MS galaxies separately. The first follow a smooth decreasing trend, reaching a maximum clumpiness of 0.194, while $c = 0.14$ comprises 90% of the starbursts in the tail. On the other hand, for main sequence systems, the highest clumpiness observed is 0.126, and in this case 90% of the population in the tail has $c < 0.1$.

The detailed properties of the clumpiness distribution among SB and MS systems in my sample can be better visualized in a scatter plot (Fig. 6.2) by comparing the clumpiness of single galaxies to their main sequence distance, $\mathrm{dist_{MS}}$. By definition, starbursts occupy the right part of the diagram at $\mathrm{dist_{MS}} > 0.6$, while main sequence objects span the range $-0.47 < \mathrm{dist_{MS}} < 0.47$. For the whole sample, I also computed the median clumpiness

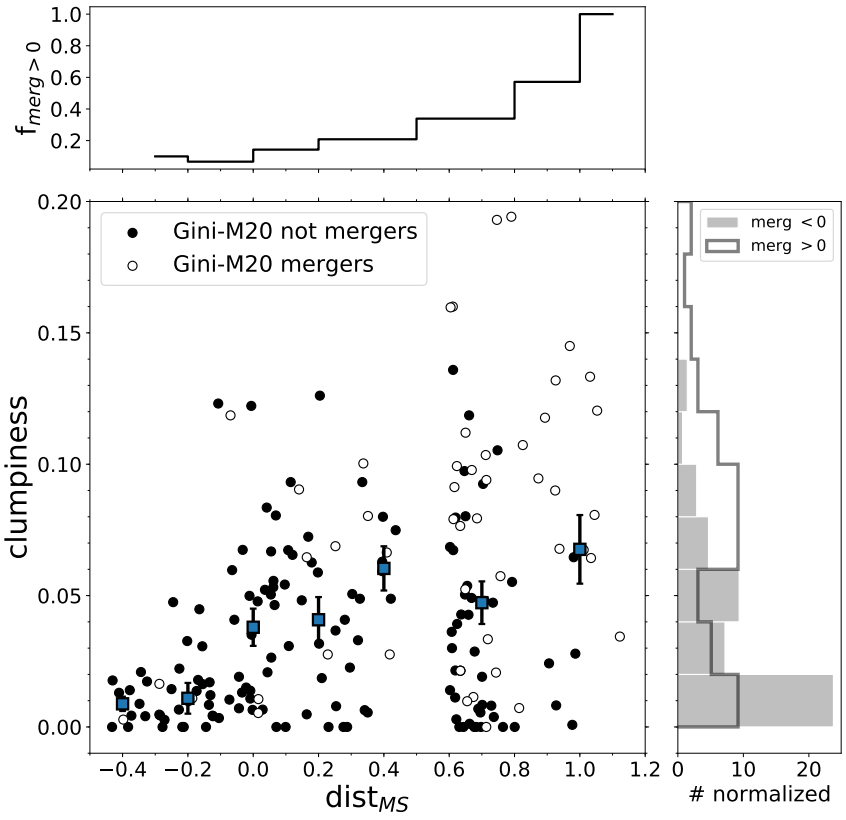

Figure 6.2: Scatter plot between the clumpiness and the distance from the main sequence (c vs. $dist_{MS}$) for my sample. Median clumpiness values are calculated in seven bins of $dist_{MS}$ of 0.2 dex approximately, and are shown as gray squares with their 1σ errors. We can see the strongest increase of the median clumpiness in the upper main sequence region. Each galaxy in the plot is color-coded according to its mergerness value. Morphological mergers identified in the Gini-M_{20} diagram (*mergerness* > 0) are shown with white filled circles, and their fraction f_{merg} (compared to the whole population) constantly increases toward higher $dist_{MS}$ (upper histogram). The histogram on the left compares instead the clumpiness distribution for morphologically selected mergers (*mergerness* > 0, in white) and not mergers (gray region, derived from the black circles in the scatter plot). In this case, a larger discrepancy is observed between the two distributions compared to Fig. 6.1, confirmed by the higher significance of the KS test (KS$= 0.432$, p-value$= 2 \times 10^{-8}$).

(shown with gray squares) in seven bins of $dist_{MS}$ with binsize of $\simeq 0.2$ dex, and the error on the median (shown with black symmetric error bars).

Overall, we can see that there is a large diversity among the main sequence population. Galaxies with $dist_{MS} < -0.1$ have a low median clumpiness of $\simeq 0.01$, with a maximum value of 0.05. Above that threshold instead, the clumpiness of 'upper main sequence' galaxies increases monotonically up to a factor of six, which then remains approximately constant (within the uncertainties) throughout the starburst regime. However, we can still

notice that the highest clumpiness values in Fig. 6.1 and 6.2 are found only within the starburst galaxies. A similar upward trend was also found when comparing the clumpiness to the specific SFR for my sample.

As I have mentioned in the previous Section, SBs and MS are complex populations and, in particular, the latter include also a fraction of merging systems. To test their effects, I considered the Gini-M_{20} classification in Fig. 6.2, flagging all galaxies with mergerness > 0 as empty circles (black filled circles otherwise). In this case, in contrast with the clumpiness trend, the fraction of Gini-M_{20} selected mergers is constantly rising across the whole $\mathrm{dist_{MS}}$ range, even in the starburst regime, where it goes from 35% to 100% at the rightmost extreme. This indicates that the fraction of starbursts not identified as morphological mergers ($m < 0$) contributes to keep the median clumpiness of SBs relatively low. A constantly rising trend would be indeed observed by considering only galaxies with mergerness > 0.

If we select galaxies according to their mergerness parameter and compare their clumpiness distributions (right histogram in Fig. 6.2), we find a more clear separation compared to previous histograms (KS$= 0.432$, p-value$= 2 \times 10^{-8}$). Interestingly, now the clumpiness distribution of morphological mergers is approximately constant over the whole range up to $c \simeq 0.12$, since the counts in all the bins are consistent with Poissonian statistic fluctuations with 95% confidence level.

If we consider together MS visual mergers and starburst galaxies (which are mostly merger triggered at $z < 0.9$), as argued in Calabrò et al. (2018)), and compare them with isolated, not visually interacting main sequence systems, a similar result of Fig. 6.2 is obtained (KS$= 0.307$, p-value $\simeq 0.1\%$), with the latter prevailing at $c < 0.06$ and starbursts being dominant at higher clumpiness.

The impact of the morphological merger classification on the clumpiness distributions suggests that I can decompose the entire population in 4 classes according to their mergerness and $\mathrm{dist_{MS}}$, to look for any trend in the SB and MS subsets. This exercise is made in Fig. 6.3, showing that, in this case, there is a more striking difference between morphological merger starbursts and not morphological merger systems, regardless of their distance from the MS, with the first having a median clumpiness more than a factor of three higher ($c_{\mathrm{median}} = 0.09$). On the other hand, the clumpiness distribution of MS morphological mergers is also slightly different (at $> 90\%$ confidence level) from the rest of the MS population (KS$= 0.34$, p-value$= 0.075$), with a clumpiness distribution skewed toward a larger median ($c_{\mathrm{median}} = 0.06$), and a big contribution in the higher clumpiness tail (cyan line at $0.06 < c < 0.12$) compared to other not-merging systems, suggesting that mergers might increase the clumpiness even with a moderate enhancement of the SFR.

I remind that the mergerness (i.e., the morphological classification) can be affected by the presence of clumps by construction, hence I remark the importance of using an alternative merger classification based on visual inspection, where I carefully identify mergers based on the presence of tidal

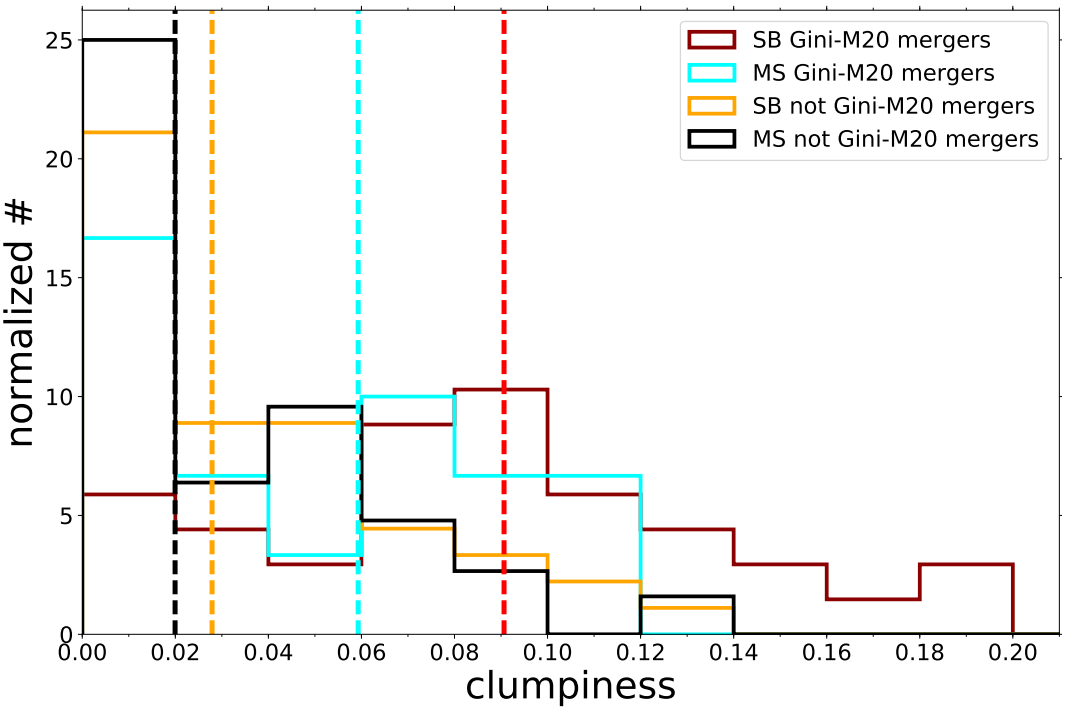

Figure 6.3: Normalized distribution (continuous line) and medians (vertical dashed lines) of the clumpiness for four types of galaxies: main sequence galaxies with mergerness < 0 and > 0 (in black and cyan, respectively), and starbursts (in orange those with mergerness < 0 and in red the morphological merger subset). I notice that the merger-selected starbursts dominate the high clumpiness tail, while the remaining SBs are basically indistinguishable from the population of main sequence galaxies with *mergerness* < 0. A substantial contribution to the high clumpiness population also comes from mergers inside the MS, as shown by the cyan excess at $0.06 < c < 0.12$. A Kolmogorov-Smirnov (KS) test between merger and not-merger MS systems (cyan and black subsets) yields 0.302 (p-value $= 0.094$).

tails, strongly disturbed and asymmetric features, and not on the presence of clumpy structures in the system. However, I do not see a correlation of the clumpiness with either the Gini parameter or M_{20} separately (first and second panel of Fig. 5.7, in the Appendix of Chapter 5). Even though a slightly increasing trend of the clumpiness is observed on average with higher Gini, many galaxies (both MS and SBs) have a low clumpiness value despite their high M_{20} or Gini coefficients.

These results do not depend significantly on the mergerness threshold used in Section 5.1.3 to identify morphological mergers. Actually, if I consider, to be conservative, a lower *mergerness* parameter threshold between -0.1 and 0, this would strengthen the result of Fig. 6.3, since the median clumpiness of main sequence mergers (cyan vertical line) would move rightwards. For example, if I choose a threshold of -0.05, I would obtain for the above subset a median $c_{\rm med} = 0.048$, and the difference with respect to not merging MS sources would be more significant (KS$= 0.364$, p-value < 0.001).

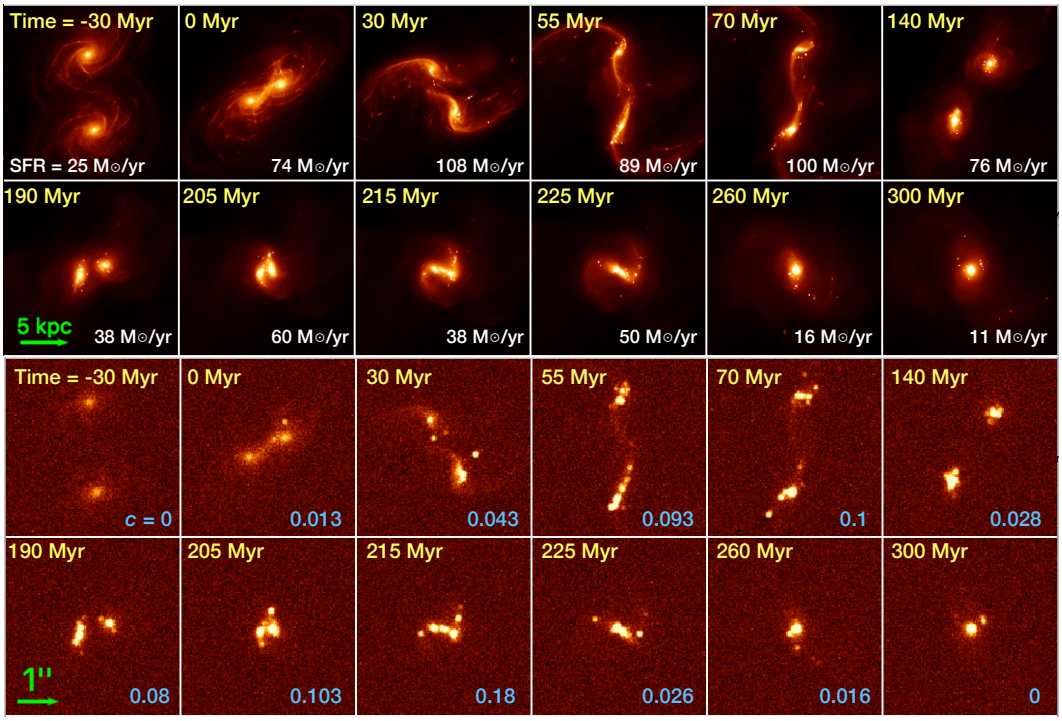

Figure 6.4: *Top:* Snapshots of the stellar mass density from the simulation of two colliding galaxies with prograde-prograde orbit coupling, at different times. The images have a physical scale of 200 pc/pixel, comparable to my observations (assuming the median redshift of my galaxies $\simeq 0.7$). *Bottom:* Mock HST F814W observations obtained from the above simulated cutouts after conversion to the $\sim 0.095''$ PSF resolution of my images (through a gaussian filter) and addition of the noise. The instantaneous SFR and the estimated clumpiness for each time step is indicated in the corner. 24 $M_\odot$/yr is the SFR of two isolated disks, according to the fiducial run.

A comparison diagram between the clumpiness and the mergerness can be seen in Fig. 5.7.

I also remark that these results are not affected by the choice of the bin size and by the sample cuts. Indeed, similar histogram distributions, trends and significances (Fig. 6.1 to 6.3) are obtained when varying the first parameter by small amounts within a factor of 2 of the chosen bin size. The same conclusion holds for different thresholds of the i-band magnitude for the final sample selection, as in case of more conservative choices, to keep only the brightest sources (e.g., i-mag cut < 22.5).

Furthermore, I have so far analyzed a limiting, very conservative situation, according to which I systematically search for two nuclei to remove in all ongoing merging starbursts, while only one nucleus is removed in main sequence disk galaxies. Even for MS morphological mergers I keep this approach, unless there is clearly a merging pair or two distinguished merger components, in which case I also remove two nuclei. This implies that I am likely underestimating the clumpiness of starburst systems, while simultaneously overestimating that of normal star-forming galaxies.

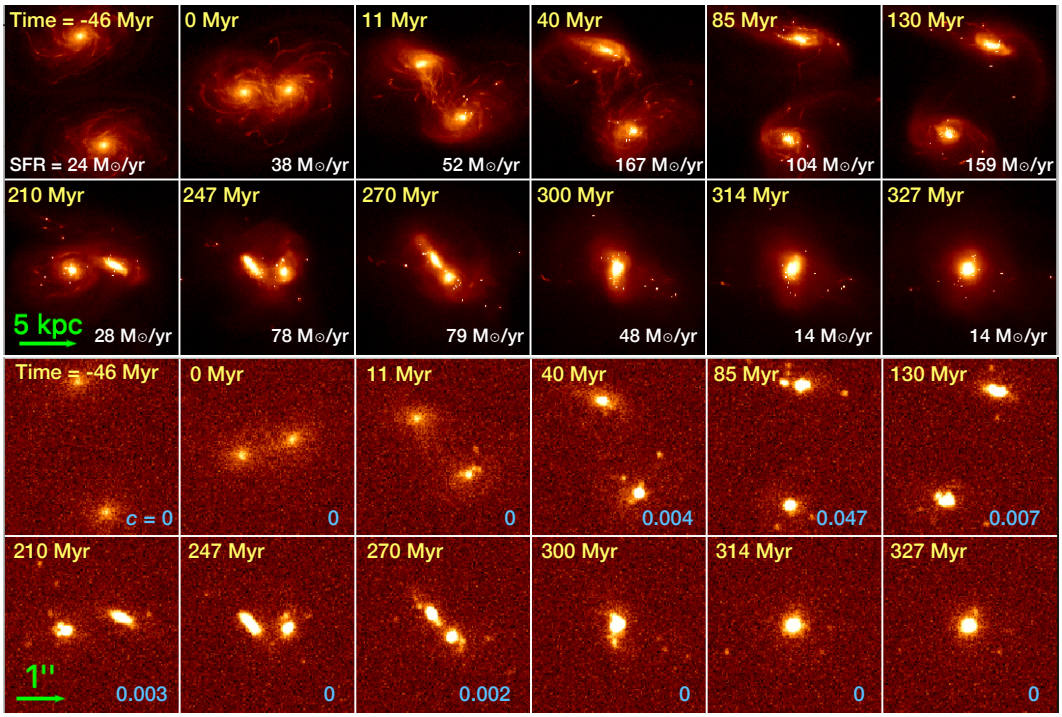

Figure 6.5: Same as Figure 6.4, but for a retrograde-retrograde collision.

Finally, I found no correlation between the stellar mass and the clumpiness (Fig. 5.8-top), indicating that the stellar content is not the main driving parameter for the increasing patchy morphology among my sample. Similarly, there is no significant evolution of the clumpiness with redshift, as shown in Fig. 5.8-bottom at the end of the Appendix of Chapter 5.

In the following part, I compare my observational results to novel hydrodynamical simulations of merger systems, performed by my collaborator Dr. J.Fensch, at the same redshift of my study. Later, I will discuss the young nature of the clumps in three galaxies for which multi-wavelength HST images are available. I will conclude by discussing a possible merger evolutionary trend of the clumpiness and suggesting a possible extension of my results to interpret clumpy galaxies observed at higher redshifts.

6.2 Confirming merger-induced clumps formation with simulations

It is interesting to compare my results with numerical predictions. However, to this aim, proper initial conditions characteristic of my redshift range should be adopted. For this reason, I used a series of hydrodynamical simulations of mergers with a gas fraction of 30% (typical of z $\sim$ 0.7) (Combes et al., 2013; Freundlich et al., 2019). As mentioned in the beginning of Chapter 5, previous simulations of galaxy collisions with such high gas fraction did

not reach the low gas temperatures needed for properly reproducing the gas distribution during merger events.

The setup is based on the simulations described in Fensch et al. (2017) using the adaptive mesh refinement code RAMSES (Teyssier, 2002). The galaxies have the same characteristics as the ones in Fensch et al. (2017). The refinement strategy is based on the density and the highest resolution elements are 6 pc. Gas in cells that are denser than 10 cm^{-3} and cooler than 2×10^4 K is converted into stars following a Schmidt (1959) law, with an efficiency per free-fall time set to 10%. Three types of stellar feedback are included, as described in Fensch et al. (2017). The energy output from SNII explosions is released by a kinetic kick and a thermal energy injection, each accounting for half of the total energy ouptut (Dubois and Teyssier, 2008). The HII regions are modelled by Strömgren spheres, whose sizes are done considering that the gas surrounding the source has a minimal density above 300 cm^{-3}. Gas inside the sphere is heated to 5×10^4 K and receives a radial velocity kick modeling the radiation pressure.

One isolated and two merger simulations were performed. To account for numerical diffusion effect, in the isolated simulation the galaxy moves along the same orbit as one of the galaxies in the interaction orbits. The spin-orbit coupling plays a significant role in the interaction. For instance, only galaxies with spins aligned with that of the interaction, what is called a *prograde coupling*, can create tidal tails (see review by Duc et al., 2013). I asked to run one prograde-prograde (or, equivalently, direct-direct) and one retrograde-retrograde encounter. The two orbits correspond to Orbit #1 from Fensch et al. (2017). After an intermediate apocenter, they coalesce within $\sim$ 230 and $\sim$ 300 Myr, respectively. Stellar density maps are shown in the upper pannel of Fig. 6.4 and Fig. 6.5. On it we see the formation of stellar condensations during the interaction, similar to what is observed in collisions at low-redshift (Di Matteo et al., 2008; Renaud et al., 2014; Matsui, Tanikawa, and Saitoh, 2019).

The simulation results were used to mock HST observations in the F814W filter by assuming $z = 0.7$, the median redshift of my sample. The Bruzual and Charlot (2003) stellar evolution model, with solar metallicity and Chabrier (2003) initial mass function was used. The stars from the initial conditions are given a random age between 500 Myr and 7 Gyr following a uniform law. After that, I started to work on the images, convolving them to the HST resolution, and adding the noise corresponding to COSMOS field data acquisition. The resulting images are shown in the bottom panels of Fig. 6.4 and Fig. 6.5.

In the mock observations, the tidal tails created by the merger are not detected anymore. In contrast, bright clumps, corresponding to the blending of star clusters, are clearly visible at the new resolution in several steps of the evolution. Remarkably, some configurations are very similar to the morphology of my observed galaxies. In particular, the eigth cutout closely resembles the galaxy ID 705860 shown in Fig. 5.1.1 (the second of the third

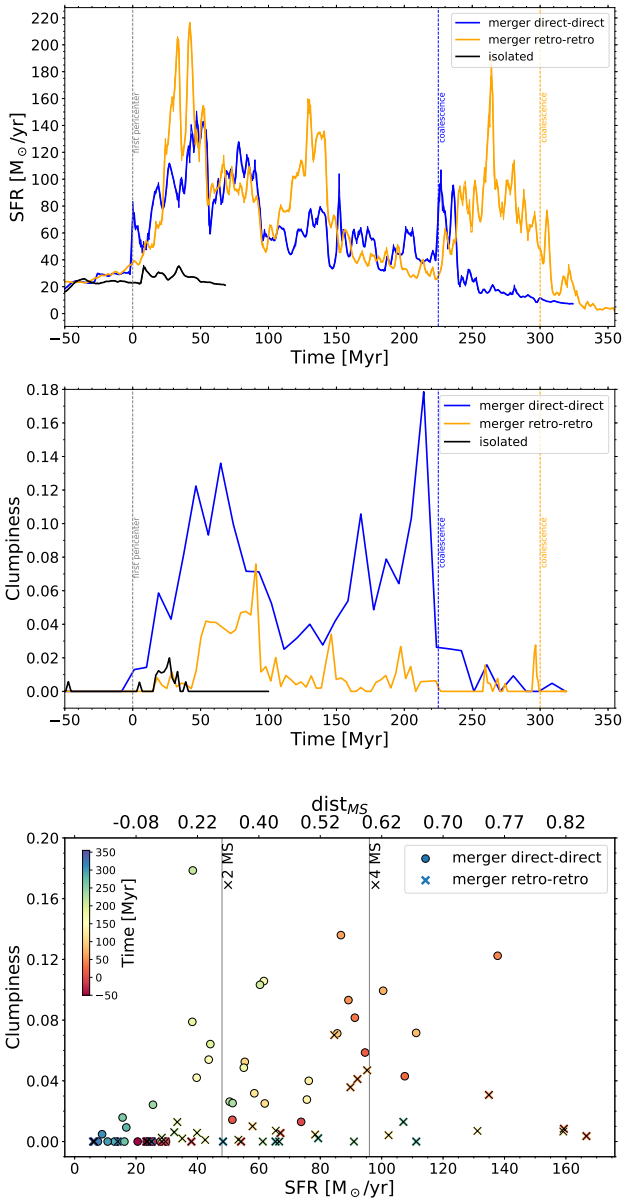

Figure 6.6: *Top and center:* The SFR and the clumpiness (respectively) are shown as a function of time for the direct-direct (i.e., prograde-prograde) merger (in blue), retrograde-retrograde merger (in orange) and for the fiducial run of an isolated galaxy multiplied by two (in black). In the latter, only the evolution during 200 Myr is shown as a representative case, while in the other two runs the time range considered ($\sim$ 450 to $\sim$ 820 Myr from the onset of the simulation) encompasses the effective merging period, from the first pericenter passage to the final coalescence (vertical dashed lines colored accordingly). *Bottom:* Comparison between the clumpiness and the SFR at different timesteps (colorbar on the left), for direct-direct and retrograde-retrograde mergers (with circles and crosses, respectively). In the first case, we can notice also a correlation between the two quantities.

row), reinforcing the interpretation that the clumps (including the nuclei)

are probably all part of the same 'two-body' merger system, even though their physical association is not obvious by eye. Finally, I calculated the clumpiness from the mock images with the same procedure adopted for the observations.

The evolution of the SFR and the clumpiness for the three simulations is shown in Fig. 6.6. In the upper pannel of this Figure, we can see the evolution of the SFR. We notice a rapid increase of the SFR after the first pericenter passage and at the coalescence, similarly to previous simulations of galaxy collisions. we can also see that the SFR increases by a factor four to five, which is an intermediate value between the high enhancement (10-100) that can occur with 10% gas fraction, and the low enhancement obtained for the same orbits and a 60% gas fraction (below 4) (Fensch et al., 2017). This effect will be discussed in more details in a companion paper (Fensch et al., *in prep.*). I additionally remark that a time averaging of the SFR (and of the clumpiness) in the past 50 Myr could be applied if we want to match the average SFR timescale of my observations, even though the diagrams would not change qualitatively.

The evolution of the clumpiness is displayed instead in the middle pannel of Fig. 6.6. While we see that for both collision orbits the clumpiness increases compared to the fiducial run, the relative values are quite different. The prograde-prograde orbit reaches high values of the clumpiness 50 Myrs after the first pericenter and right before the coalescence, and peaks at 0.17, which is in the range of observed clumpiness in the COSMOS field. On the contrary, the clumpiness does not increase much during the retrograde-retrograde orbit, reaching only 0.05, 75 Myrs after the first pericenter.

On Fig. 6.4, we can see that the high values of the clumpiness in the prograde-prograde case are obtained by the blending of star clusters, which tend to happen at the base of the tidal features. This blending result in the accumulation of star clusters in this region, as we can see in the fourth cut out. The formation of the tidal tail resulting from the prograde spin-orbit coupling, the accumulation of star clusters and the enhanced clumpiness do not happen in the retrograde-retrograde collision. Thus, the scatter in the clumpiness observed in my sample, and especially the low clumpiness values for highly star-forming starbursts, could be in part explained by a variety of spin-orbit couplings.

Overall, numerical simulations are able to explain qualitatively many of my observational findings. First of all, mergers are powerful triggering mechanisms for the formation of clumps in intermediate redshift galaxies ($0.5 < z < 0.9$), and they can increase the clumpiness parameter (i.e., the fraction of light coming from clumpy structures) up to values that are similar to those observed. On average, they also reproduce the increasing trend of the clumpiness with specific SFR (Fig. 6.6-bottom).

Secondly, during a merger event, a significant increase of the clumpiness can be obtained even in correspondence of a modest SFR enhancement,

below the threshold for starburst classification. This can explain the fraction of morphological mergers in the main sequence with a relatively large clumpiness parameter.

Finally, the dynamics of the interaction likely plays an important role. Indeed, in the case of a retrograde-retrograde merger, only a very small enhancement of the clumpiness is found during the starburst, or no increase at all. Thus a high clumpiness parameter is not obtained neither in all mergers, nor in all starbursting systems. I remark that very low clumpiness parameters (< 0.04) in correspondence of elevated SFRs ($\times 4$ above the MS), are not inconsistent with my data, which comprise a significant number of starbursts with a similar low fraction of clumpy emission (cf. Fig. 6.1). A forthcoming paper will study the physical properties and evolution of simulated clumps with more detail, with a more diverse set of galactic disks (Fensch et al. in prep.).

6.3 Clumpiness evolution during the merger

In Section 6.1 I have divided the sample in SBs and MS galaxies, finding that the two subsets have different clumpiness distributions, with the former prevailing in the high clumpiness end, while the latter are dominant at very low $c < 0.02$. However, this classification is too simplistic, and the complexity of the MS and SB populations can be resolved in part by considering their apparent morphology. We have indeed seen in Fig. 6.3 that morphological merger starbursts, selected by their large Gini and M20 coefficients, are the major responsible for the high-end tail of the clumpiness distribution, with a median $c = 0.09$ and a maximum fraction of light in the clumps of 20%. On the other hand, the subset of starbursts that are not merger selected from their morphology is essentially indistinguishable from that of isolated (not merger) main sequence systems (Fig. 6.3).

As highlighted in previous works, my morphological classification criterion, firstly defined by Lotz, Primack, and Madau (2004), is able to identify mergers over a relatively short temporal window compared to the whole merger duration. The observability timescale of a merger in the Gini-M_{20} diagram is approximately $0.2 - 0.3$ Gyr according to Nevin et al. (2019), corresponding to the period when the interaction signatures are more evident in the form of bright tidal tails or very disturbed, elongated or asymmetric global structures. In contrast, at the coalescence, residual merging features rapidly fade below the surface brightness detection threshold, hampering its true nature recognition visually, especially at the redshifts of this work. Their increasingly difficult identification at the coalescence is also seen in simulations. This suggests that different time evolutionary merger phases can in part explain the large spread of merginess and clumpiness in the SB distribution.

In order to test this interpretation, I analyzed the subset of 19 starbursts, with available HST images and in our redshift range, that were presented

in Calabrò et al. (2018) as representatives of off-MS systems at $0.5 < z < 0.9$ above a M_* of 10^{10} $M_\odot$. I showed that this sample comprises a sequence of different evolutionary merger stages, which can be traced by the equivalent width (EW) of Balmer or Paschen lines, and by the total attenuation ($A_{V,tot}$) toward the center of the starburst core in a mixed dust and stars configuration (Calabrò et al., 2019a).

In Fig. 6.7 I compare the clumpiness of this SB subset to $A_{V,tot}$ and the EW of Hα and Paβ lines, measured in (Calabrò et al., 2019a). In the first upper panel, I find no significant correlation between c and $A_{V,tot}$, with a Spearman correlation coefficient R$= -0.34$ (p-value$= 0.13$) and angular coefficient of the best-fit line consistent with 0. However, if I assume no correlation, the four starbursts with the highest obscurations $A_{V,tot}$ above 15 mag all have a low clumpiness below 0.04. This confirms that an important fraction of galaxies (50% in our Magellan dataset) contributing to the first two low clumpiness bins in Fig. 6.1 may be actually late stage mergers observed after the coalescence. On the other hand, early and intermediate merger systems with $0 < A_{V,tot} < 15$ mag can show the full variety of clumpiness values, and these are the only phases where we observe a substantial clumpiness enhancement above the average population level and above 0.1.

In analogy to the former result, when comparing the clumpiness to the equivalent width of Paβ and Hα, I also measure an angular coefficient slightly below 2σ. However, in the latter case the Spearman coefficient R is equal to 0.53 (p-value$= 0.014$), indicating that the correlation is significant according to this statistical test. The existence of the latter (even though mild) correlation, and the position of the Magellan SBs in the first panel of Fig. 6.7, can shed light on the possible triggering mechanisms and fate of the observed clumps. Following the results of previous simulation works, clumps can form with the increasing compressive turbulence modes and subsequent fragmentation induced by the merger during early-intermediate stages (Renaud et al., 2014). The absence of late stage mergers with high clumpiness suggests that, after the main triggering events, clumps could be rapidly destroyed by strong stellar radiation or AGN feedback, or they could be incorporated in the central galactic bulge.

Intriguingly, I noticed that 4 out of 5 X-ray detected AGNs in this small subset have a very low clumpiness below 0.02. As suggested in Calabrò et al. (2019a), these systems may be in an advanced phase of the AGN activity and central black hole growth, and possibly approaching the blow-out phase, thus an impact on clumps survival cannot be excluded. If we do not consider these objects, we would obtain a higher statistical significance of the $A_{V,tot}$-c correlation.

Another possibility is that clumps become too faint in i-band compared to the host galaxy, following the aging of the stellar populations or the higher dust obscurations expected in advanced phases, and they are not detected anymore in this band. However, I remind that testing the impact of feedback processes and studying the final fate of the clumps is beyond the scope of

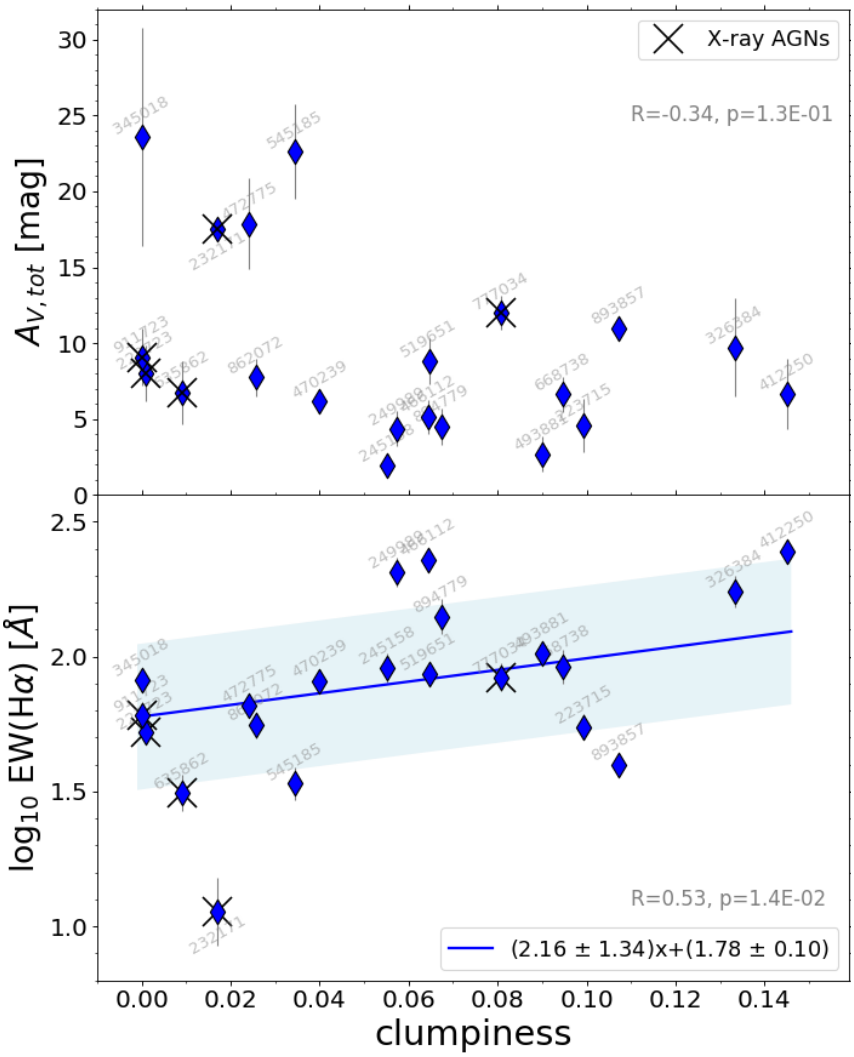

Figure 6.7: Comparison between the clumpiness and the mixed-model attenuation $A_{V,tot}$ toward the center (upper plot), and the equivalent width (EW) of Hα (lower panel) for 21 starbursts in our same redshift range $0.5 < z < 0.9$, and analyzed in Calabrò et al. (2019a). The corresponding IDs are added to each galaxy, while black crosses indicate X-ray detected sources. The Spearman correlation coefficient R and the corresponding p-value are highlighted in each panel. I derive no correlation for the first diagram, and a mild correlation $> 3\sigma$ for the second, thus only in the latter case I derive the best linear fit (blue line, with equation included the legend) and 1σ dispersion (blue shaded region). However, even in the first plot, the highest clumpiness values are found only for the less attenuated starbursts, while the most obscured objects ($A_{V,tot} > 15$) have systematically low c. Given that $A_{V,tot}$ and EW(Hα) have been used as merger stage indicators in Calabrò et al. (2019a), our findings provide an indication for a possible clumpiness evolution, decreasing from early-intermediate phases to late stage mergers. This is corroborated by the subset of X-ray AGNs (likely close to the blow-out phase) showing preferentially a lower clumpiness.

this work, and it will be investigated in future papers.

Even though the time evolutionary sequence is a tantalizing interpretation, the absence of very strong correlations may indicate that other effects also play a role on clumps formation, such as the impact geometry, the dynamics and mass ratio of the two components, and the viewing angle toward the system, all of which would be in any case very difficult to quantify from current observational data. In particular, the strong dependences on the orbital configuration (Section 6.2) suggest that we may have large object by object variations in the clumpiness while having still a strong SFR enhancement (Fig. 6.6).

6.4 Multi-wavelength morphology from CANDELS

I have identified clumps in single broad-band (F814W) images, which are available for the majority of galaxies in the 2 degree^2 COSMOS field. A possible limitation of our approach relies on the fact that we can probe the emission of clumpy structures only in a limited wavelength range, which, considering the filter transmission curve and our redshift interval, covers approximately the 3700 Å to 6400 Å rest-frame range. The morphology of clumpy features can potentially change if we go to the UV rest-frame or at longer wavelengths (near-IR).

We can check the multi-wavelength behavior for three starburst galaxies in the COSMOS-CANDELS field, observed at high-resolution by HST (Koekemoer et al., 2011) in four broad-band filters (F160W, F814W, F125W and F160W) at resolutions of 0.08″, 0.09″, 0.12″ and 0.18″, respectively (Fig. 6.8). In order to have a larger statistics, I have considered in this analysis one galaxy in the subset analyzed so far (ID 619015), and other two galaxies (ID 586698 and 719406) belonging to the parent sample but excluded from the final selection adopted in this paper: while the first has a slighly higher redshift (0.92) than our selection criteria, the second has a distance from the MS of 0.51 dex (above a factor of 3). However, it has clearly a merger-like morphology given the presence of a long tidal feature in the upper part. Having similar clumpy morphologies (from i-band) to the population of galaxies considered in this work, they can yield important informations on clump properties also for the remaining sample.

Analyzing each starburst in more detail, we can clearly see in the first galaxy two clumps in i-band and four clumps in the UV, while all of them become fainter and undetected at longer wavelengths. They also occupy part of a ring structure surrounding the central nucleus. Simulations predict that this configuration could represent the late phase of a collision between disk galaxies (Bekki, 1998), or created by tidal accretion of material from a gas rich donor galaxy (Bournaud and Combes, 2003).

Also in the second galaxy the clumps become brighter in the UV rest-frame and they are displaced along half a ring. Longer wavelength images reveal that this elongated structure is connected to a single bigger system

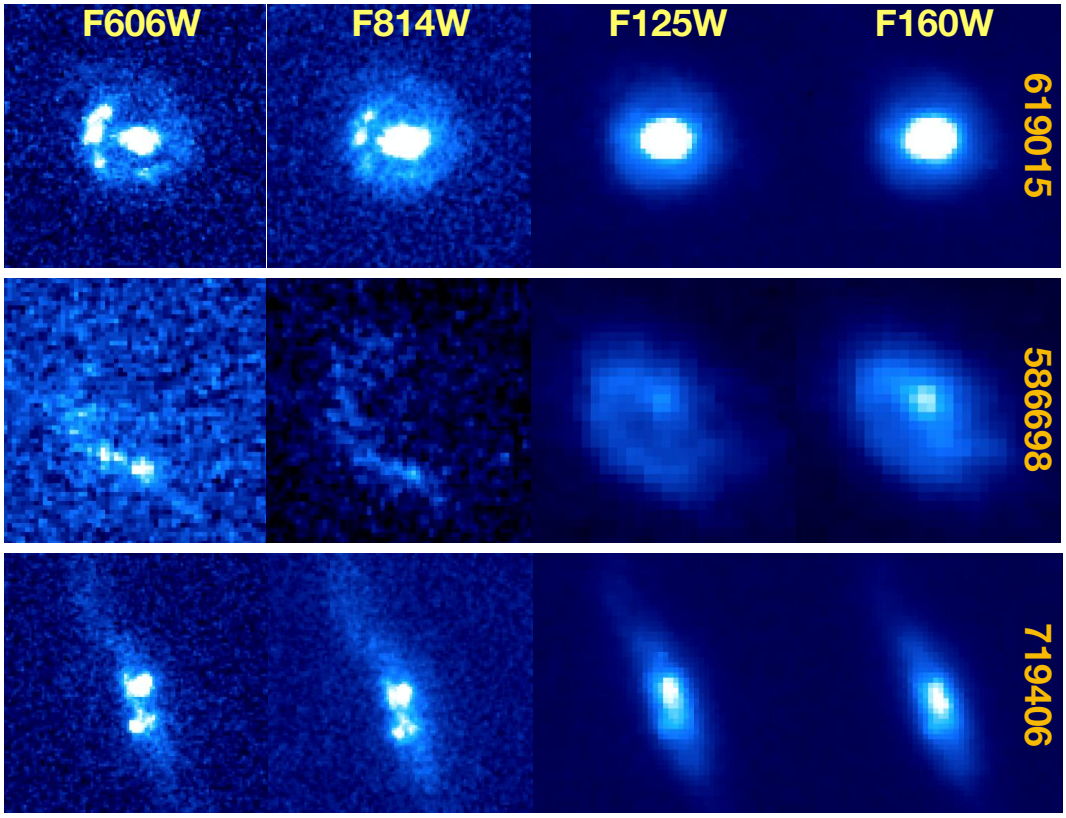

Figure 6.8: HST cutout images in the F606W, F814W, F125W and F160W broad band filters for three starbursts in the COSMOS-CANDELS field. As explained in the text, the second galaxy has a photometric redshift of 0.92, while the third has a SFR a factor of 3 above the main sequence at the same redshift $z = 0.74$, but clearly shows a merger morphology (in spite of its edge-on profile). The multi-wavelength comparison shows that clumps become brighter at shorter wavelengths, thus they likely represent merger-induced young stellar associations rather than old pre-existing structures. The IDs shown in the right part of the figure come from Laigle et al. (2016).

with just one main nucleus, highly attenuated or very old, invisible in F606W and F814W filters.

Finally, the last system shows multiple clumps in i and U band images, below the main central nucleus visible in all the bands. In particular, the brightest clump falls at the border of the main edge-on stellar disk.

Overall, the clumps shown in the above three galaxies become more prominent from redder to bluer bands (where sometimes they can outshine the nucleus itself), which would yield an increased clumpiness in the UV compared to i-band. On the opposite side, they become undetected in near-IR bands (even though the resolution is slightly lower). This result indicates that they are likely young structures induced by the merger rather than pre-existing aggregations of older stars. Furthermore, they seem to have a low mass fraction and possibly a low SFR fraction, despite their UV prominence.

A systematic investigation of the physical properties of the clumps formed

by merger events at these redshifts, including their dust attenuation, stellar ages and masses, gravitational stability and kinematics, could be possible in the future with the availability of high spatial resolution multi-wavelength bands for a larger subset of objects. This will additionally allow to compare their size and stellar mass distributions to those observed in main sequence systems and at higher redshifts.

6.5 Comparison with other studies

As mentioned in the Introduction, several studies have investigated the origin of clumpy galaxies at redshifts overlapping with our range. Puech (2010) claimed that mergers may be the dominant triggering mechanisms of clumpy galaxies at $z < 1$. However, his limited sample of 11 objects is representative of a very specific redshift ($\simeq 0.6$), galaxy stellar mass ($\log_{10}$ $M_* \sim 10.2$ [$M_\odot$]) and type (e.g., absence of a central bulge), which cannot be representative of all the star-forming population and of the same dynamic range spanned in our work. In addition, he found that the majority of UV clumps tend to vanish when looking at longer wavelengths, so they could be biased towards lower attenuations or higher ongoing SFRs. Also Ribeiro et al. (2017), while focusing on much higher redshift than our work ($2 < z < 6$), interprets double clumps as possible merging systems. However, if it is true, the clumps likely represent the nuclei of the two colliding galaxies, thus they should not be considered anymore as clumpy galaxies by our definition.

On the other hand, Murata et al. (2014) noticed that the redshift evolution of the fraction of clumpy galaxies is inconsistent with that expected from the merger rate, thus concluding that mergers do not contribute to the clumpy population at all epochs. However, they detected clumps directly on the images without an intermediate smoothing step, which is important to facilitate the identification of high spatial frequency components and separate them from equally bright regions with smoother profiles. In addition, they identified clumpy galaxies preferentially on the main sequence. Indeed, their SFRs are derived from SED fitting (from UV to mid-IR), not allowing to select systems with obscured star-formation, which is a dominant component in infrared-luminous mergers (Goldader et al., 2002; Calabrò et al., 2018). A similar conclusion based on the same argument is reached by Guo et al. (2015) for clumpy galaxies at $0.5 < z < 3$. They suggest instead that violent disk instabilities are the main triggering mechanism at high stellar masses ($M_* > 10^{10.6}$ $M_\odot$), while minor mergers may contribute the most for intermediate mass systems with $10^{9.8} < M_* < 10^{10.6}$ $M_\odot$. However, they consider UV clumps, which may disappear in the optical rest-frame, as shown by Puech (2010).

My result should be considered as complementary to all these studies. I am showing the importance of mergers as responsible for triggering clump formation in intermediate redshift galaxies, enhancing the clumpiness at higher levels compared to other mechanisms at this cosmic epoch. However,

I do not claim that all clumps are induced by mergers. Indeed, a fraction of main sequence galaxies (which are the majority 96-98% of the star-forming population) with higher clumpiness are not identified as mergers and may be consistent with other formation channels, such as minor mergers or disk instabilities. Therefore, I am not in contradiction with the two previous works.

Finally, Lotz, Primack, and Madau (2004) showed that local ULIRGs (which are all mergers) have an enhanced clumpiness compared to the main sequence star-forming population. My work thus suggests that this result can be extended up to redshift ~ 1 to starburst galaxies and to morphologically selected mergers.

6.6 Interpreting high redshift clumpy galaxies

I have demonstrated in previous sections that mergers can trigger the formation of stellar clumps in galaxies at $0.5 < z < 0.9$. Given this explanation at intermediate redshifts, we can wonder whether a similar connection also holds at earlier cosmic times.

At high redshifts ($z >> 1$), young massive clumps observed in the UV and optical rest-frame, having $M_* \sim 10^8$ $M_\odot$ and ages of 100-500 Myr, are generally thought to be driven by violent gravitational instabilities in gas-rich highly turbulent primordial disks, typically lying in the star-forming MS (e.g., Noguchi, 1999; Immeli et al., 2004a; Immeli et al., 2004b; Elmegreen et al., 2005; Elmegreen, 2007; Bournaud, Elmegreen, and Elmegreen, 2007; Förster Schreiber et al., 2006; Förster Schreiber et al., 2009). The fuel needed for star-formation and clumps triggering may be provided by relatively smooth accretion of cold gas from the cosmic web and from the CGM (Kereš et al., 2005; Dekel, Sari, and Ceverino, 2009; Aumer et al., 2010). Furthermore, many studies have revealed that clumpy galaxies have kinematics consistent with rotating disks, even though highly disturbed (Bournaud et al., 2008; Daddi et al., 2008; Shapiro et al., 2008; Epinat et al., 2009).

Even though this scenario is physically motivated, we cannot rule out a-priori a possible role of mergers in favouring and triggering clumps, in analogy to what has been shown at $z < 1$. The fraction of mergers increases monotonically at earlier times, as shown by Conselice et al. (2003), thus we may expect that they have a constantly higher influence on galaxy morphology. Despite mergers can be less efficient to enhance the SFR at starburst levels at higher redshifts (Fensch et al., 2017), our results at intermediate z show that a large clumpiness parameter can be obtained even without a strong enhancement of SFR.

In addition, it is possible to preserve some degree of global rotation even during a merger event, and also a disk could rapidly reform in the latest stages (Rothberg and Joseph, 2006; Springel and Hernquist, 2002; Fensch et al., 2017). Thus, many of the high-z systems showing global rotation in the stellar or gaseous component can still be mergers. As complementary

probes to recognize merger systems, we could instead look for the presence of compact, highly obscured cores in the host galaxy, indicative of a late or post-merger phase (Calabrò et al., 2019a; Puglisi et al., 2019).

In this context, Hodge et al. (2019) and Tadaki et al. (2018) observed sub-kpc clumpy structures with ALMA in the dust continuum or CO emission for a small subset of luminous submillimeter galaxies (SMGs) in the redshift range 1.5-5. Among the sample of 11 SMGs presented by Hodge et al. (2019), the low Sersic index profile measured in one galaxy suggests it might be a late stage merger, while interacting signatures in the optical are revealed for some of their remaining systems. They showed that these structures are displaced in the inner 5-10 kpc regions, analogous to the spatial distribution of our brightest clumps (in both observations and simulations), which form close to the nuclei and in the beginning of tidal tails. Additionally, the ALMA clumps produce 2 to 10% of the total galaxy emission, in agreement with the range of clumpiness that I found in the optical. This suggests that, being highly star-forming and dusty, their structures may represent still early phases of clump formation.

On the contrary, normal star-forming isolated disks are smoother at the same sub-mm wavelengths. Cibinel et al. (2017) found that UV clumps in a main sequence galaxy at redshift $= 1.5$ are not visible anymore with ALMA in the CO(5-4) transition, which could be due to lower gas content (or equivalently, higher SFE), or to lower SFRs of the clumps. Rujopakarn et al. (2016) studied 11 normal star-forming galaxies at redshifts 1.3-3 with $\sim 0.4''$ resolution ALMA images. They also found no evidence of clumpy structures, which instead appear at UV wavelengths as unobscured regions, owing small SFR fractions from 0.1 to 5% of the whole systems. Future observations with ALMA could further constrain these different scenarios and better characterize the clumps detected in our COSMOS sample for both the MS and SB population.

Overall, my study suggests that a dicotomy of clumps properties and total clumpiness exists even at earlier cosmic epochs, depending on the level of SFR of the host galaxy. If my results still apply here, and given the possible merger nature of a fraction of SMGs (Tacconi et al., 2008), it seems reasonable to think that many of the ALMA clumps observed in high-z infrared luminous galaxies may be actually produced by merger interactions.

6.7 Summary and conclusions

Inspired by the merger nature of infrared luminous starbursts at $0.5 < z < 0.9$ shown in previous works, I have studied in the same redshift range the effects of mergers on clumps formation by comparing the high-resolution HST optical rest-frame morphologies of 79 starbursts to a control sample of 109 normal star-forming main sequence galaxies. I performed an additional visual merger identification among the main sequence population and applied

the classical Gini-M_{20} classification to select galaxies with merger-like shapes. The main results of this work are summarized as follows:

- The merger classification criterion of Lotz et al. (2008) (based on the Gini-M_{20} morphological parameters) also separates the two regions where starbursts and main sequence galaxies dominate, respectively, with a fraction of 76%. However, only 43% of the starbursts lie in merger region, suggestive of different merger phases probed by the two diagnostics and of the large incompleteness of Gini-M_{20} for the merger selection, likely due to multiple effects, including the galaxy inclinations, impact parameters and dust attenuation.

- Starburst and main sequence galaxies have different clumpiness histogram distributions: the former dominate in the high clumpiness regime, while the latter are more numerous at lower values. Given the merger nature of intermediate-z starbursts, this suggests that mergers are likely responsible for clumps formation and their increased luminosity with respect to normal star-forming isolated disks.

- A larger difference of the clumpiness histogram distributions is obtained when including visually selected mergers in the SB subset and when comparing morphological mergers to not mergers. In particular, Gini-M_{20} mergers, regardless of their level of SFR, have a median clumpiness a factor of three higher compared to the rest of the population, and are almost entirely responsible for the high clumpiness tail observed among our sample. I also found that the fraction of morphological mergers and their median clumpiness increase monotonically with the distance from the main sequence.

- From hydrodynamical simulations of merger galaxies with initial conditions typical for our redshift range, I found that mergers can significantly enhance the clumpiness of the system compared to isolated main sequence galaxies, by a similar amount to that observed in real images. Different spin-orbit coupling of merging galaxies can fully explain the scatter of the observed clumpiness values from 0 to 20%.

- For a sample of 19 SBs with Magellan-FIRE spectra, there is a mild correlation between the clumpiness and the equivalent width of Balmer and Paschen lines, suggesting a possible clumpiness evolution during the merger, decreasing from early-intermediate to later stages after the coalescence. X-ray detected AGNs are preferentially found in low-clumpiness systems, suggesting a possible clump suppression induced by AGN feedback. However, other effects (including galaxy inclination, rotation, attenuation and impact parameter) are likely responsible for the low correlation strength ($\simeq 2\sigma$).

- Using four band high-resolution images for three clumpy galaxies in the COSMOS-CANDELS field, I have showed that merger induced clumps

are generally young and UV-bright, likely formed during the merger rather than being older pre-existing stellar structures. However, a larger sample is needed to study the statistical properties of the clumps (e.g., sizes, stellar masses and ages) and investigate their evolution.

Merger triggered gas compression and fragmentation can provide the physical explanation for the formation of stellar bright clumps. I expect that this mechanism is more frequent at high redshift, given the increasing fraction of mergers at earlier epochs. This work arises questions on the real nature of clumps observed in high redshift galaxies, suggesting that mergers could be an alternative, powerful channel for enhancing the clumpiness. If this is true, the clumpiness could be used as a complementary merger diagnostic (though still incomplete) to identify mergers from the morphology when the typical low-surface brightness interacting features (e.g. tidal tails) become too faint.

Deeper images in the optical and near-IR rest-frame with Euclid and JWST will allow in the near future clumps detection and their physical characterization (through a multi-λ approach) for larger statistical samples of clumpy galaxies at higher redshifts and similar spatial resolutions to those considered here. In addition, they will facilitate the study of the environment and the morphological properties (including merger signatures) of their host galaxies.

Chapter 7

Future perspectives

In previous chapters I presented the results obtained during the last three years of my PhD. These findings are related to the physical properties and nature of starburst galaxies beyond the local Universe. The increasing specific SFR and gas content in high-redshift systems does not guarantee that starbursts are triggered and form stars in the same way of main sequence outliers at $z = 0$. Unfortunately, the high obscuring column density of these galaxies, and the lower resolution and surface brightness at higher redshifts have not allowed so far to confirm their association with mergers. While the two latter limitations would require bigger telescopes or unrealistically long integration times for dozens of objects, the first can be partly overcome by performing observations in the near-IR rest-frame spectral range, which is significantly less affected by dust attenuation compared to the optical regime, and is currently accessible from ground-based instruments up to K band ($\simeq 2.5\mu m$).

To this aim, I presented in Chapter 2 novel near-IR spectroscopic observations for a statistical sample of 25 Herschel-selected starbursts at $0.5 < z < 0.9$ in the COSMOS field, representative of the infrared luminous starburst population at intermediate redshifts. For this subset, I have compared their Paβ, Hα and IR bolometric luminosities, finding that their dust attenuation pattern does not follow a dust screen model. This is instead consistent with an optically thick mixed model with average total diameter optical depth of 18 magnitudes in V band (Chapter 3). I have interpreted the presence of such highly embedded cores as a strong suggestion of merger triggering, since mergers are the only mechanism known to efficiently shrink the gas and dust, reaching order of magnitudes higher densities compared to normal galaxies.

In Chapter 4 I searched for possible relations among the attenuation (the key parameter differentiating our sample from normal galaxies), and other physical properties available for the same objects. In particular, I found relatively tight correlations between total obscuration, emission line ionisation, starburst core size and effective age, as traced by line EWs. The existence of a single parameter sequence has been extensively discussed in the same chapter, and attributed to the presence of a time-evolutionary sequence of merger stages, whereas later phases of the collision are systematically more obscured and compact.

Intriguingly, X-ray emission was detected for six mergers only in the late phases, suggesting emergent AGNs possibly leading to a final bright QSO for these systems. The qualitative agreement between the X-ray attenuation and that inferred from the infrared also suggests that most of the obscuration affecting the AGN emission is produced in the host galaxy ISM, on scales of 10^2-10^3 pc, rather than in the AGN torus.

Furthermore, current ongoing starbursts are so small in size that they cannot directly form ellipticals. They could instead explain the rapid growth in the system of a substantial bulge component of sub-kpc size. It is thus plausible that an important fraction of bulges that we observe in local SO and spiral galaxies may have built up through major merger episodes in the past, even though this possibility remains to be fully demonstrated.

Finally, the last part of the thesis is dedicated to a morphological analysis of starburst and normal star-forming galaxies in the same redshift range. I noticed that, while main sequence galaxies appear mainly as smooth disks, the morphologies of starburst systems (in the whole COSMOS field) are significantly more clumpy, that is, the majority of them have multiple off-nuclear stellar clumps in their HST i-band images (Chapter 5). This indicates that part of the star-formation in starbursts (and in a minor fraction of MS galaxies with merger morphology) occurs outside of the central core. This activity is likely enhanced by gas collapse and fragmentation induced by the recent merger episode, as also seen in simulations of colliding galaxies with properties matching those typical at redshift 0.7.

Overall, this thesis shows that, like the ULIRG-merger connection in the local Universe, a relation between IR-luminous starbursts and mergers seems to hold also at higher redshifts, at least up to $z \simeq 0.9$. This redshift regime is very important as it marks the beginning of the declining star-formation rate density in the Universe, which has not been yet understood. The AGN feedback in late phase mergers and the rapid build-up of a bulge suggested by this study may provide additional mechanisms (along with natural gas consumption) to prevent further star-formation in the system, and could be in part responsible for such decrease.

This work can shed light also on galaxy evolution at earlier cosmic times. For example, we know from simulations that mergers should constantly increase toward earlier epochs (Conselice, Yang, and Bluck, 2009), but the starburst fraction is observed to remain constant with time (Schreiber et al., 2015). This leads to think that the majority of mergers at high-z ($z > 1$) may not enhance dramatically the SFR, so that the galaxy still remains in the main sequence (Fensch et al., 2017). Testing this scenario and constraining the merger rate evolution from the observed morphology is very difficult, given the problems of surface brightness dimming. Nevertheless, my results (and other recent publications) suggest that we can identify mergers in an indirect way through physical quantities that are relatively easier to measure or less ambiguous, that is, the radio (or sub-mm) size, the attenuation and the clumpiness.

In particular, the results of Jiménez-Andrade et al. (2019) and Calabrò et al. (2019a) suggest that we can use the compactness of the whole star-forming galaxy to identify mergers. This idea lies on the fact that starbursts are 1.5-2 times more compact in radio (3 GHz) than normal star-forming systems, even more compact than early type galaxies at the same redshift. Similar compact sizes have been recently measured also for main sequence objects with ALMA in CO and dust-continuum emission (Puglisi et al., 2019), which is interpreted as an evidence of early post-starburst (i.e., post-merger) systems.

Alternatively, future surveys (e.g., with JWST, Euclid, MOONS, ERIS) will be able to trace Hα and Paβ up to very high redshift at deeper levels, allowing to infer dust attenuations (eventually spatially resolved) for hundreds of star-forming galaxies, and identify the most dust obscured, likely due to mergers.

Finally, Calabrò et al. (2019b) arise questions on the real nature of clumps observed in the high redshift Universe, suggesting that mergers could be an alternative, powerful channel for enhancing the clumpiness even at earlier times. If this is true, the clumpiness could be used as a complementary merger diagnostic (though still incomplete) to identify mergers from the morphology when the typical low-surface brightness interacting features (including distortions, bridges and tidal tails) become invisible. Deeper images in the optical and near-IR rest-frame will also allow in the near future the detection of clumps and their physical characterization (with a multi-λ approach) for larger statistical samples at similar spatial resolutions to those currently achievable at $z \sim 0.7$.

In the next sections, I will discuss possible ways of improving the interpretation and understanding of the results presented in this thesis. I will then describe in more detail some further developments of this study and new directions that can be undertaken in the same field during the following years, starting from already available data.

7.1 Confirming the attenuation sequence of distant starbursts

In Chapter 3 I showed that starbursts at intermediate redshifts follow tightly the predictions of an optically thick mixed model, with A_V (inferred from Hα, Paβ and bolometric IR luminosity) spanning from 1 to 30 magnitudes towards the center. Moreover, in Chapter 4, I presented intriguing correlations between the total dust attenuation of the mixed model and other physical quantities, in particular the radio FWHM size, meaning that more obscured starburst cores (likely representing later merger stages) are also more compact.

Despite these clear results and relations, their interpretation should be further strengthened. Using ancillary optical spectra, I surprisingly discovered

that in some galaxies, while being starbursts forming stars at ~ 100 $M_\odot$/yr (inferred from IR), Hδ, Hγ and Hβ are globally in absorption. The EW of Hδ reaches -10Å, resembling that of post-starburst galaxies (Poggianti et al., 2009), as if star-formation has been completely shut down (possibly because of AGN or supernova feedback, at least in the skin). This new evidence suggests then the possibility that the starbursts dust attenuation pattern (Fig.3.1 in Chapter 3) is mainly driven by the infrared luminosity tracing the SFR on longer timescales compared to the lines, thus discarding dust geometry effects. In order to investigate this possibility and address several connected questions, observations of the cold molecular gas, and in particular of total instantaneous SFR, are crucial. To this aim, I got a B rated NOEMA proposal targeting the CO[3-2] line (in band 3) in 8 representative starbursts (among 25) along the attenuation sequence. During the last cycle (ended in May 2019), only one galaxy has been observed. For this reason, in order to observe a larger statistical sample, I will resubmit a new NOEMA proposal next September. Moreover, I recently submitted an ALMA proposal (Call 7) to detect CO[4-3] line and dust continuum in 22 out of the 25 Magellan starbursts.

The first objective of these proposals is thus to test SFR time variations. The aim is to measure the CO luminosity (L'CO) for 22 targets in total, checking whether they all obey the tight correlation known to exist with LIR (Liu et al., 2015). For the galaxies deviating below from such correlation, which may be candidates where the final blow-out phase has already started and their SFR has been experiencing a strong suppression, I can use their L'CO to derive a crude estimate of their instantaneous SFR. Given the 0.2 dex correlation dispersion, I can select deviants at 2σ, corresponding to a suppression of a factor of ~ 3 (models predict that abruptly decreasing SFRs by orders of magnitudes could apply), and statistically detect (by averaging) even finer departures. I will then use this instantaneous indicator in place of SFR_{IR} (which probes longer SF timescales of ~ 100 Myr) to compute more realistic attenuations as $A_{CO,Pa\beta}=2.5 \times log_{10}(1+SFR_{CO}/SFR_{Pa\beta,obs})$, redrawing the dust attenuation diagram of Fig. 3.1 with this new quantity and the observed Paβ/Hα ratio. This will clarify whether the large attenuations A_{IRX} are entirely caused by comparing SFRs (from LIR and from the lines) with different timescales, and whether the mixed model prediction is still valid.

A second question that these proposals will try to answer is whether the range of different attenuations measured in the whole sample could be interpreted as a time merger sequence. If this idea is correct, we would observe a decreasing L'CO/LIR in correspondence of an also decreasing EW. On the contrary, if CO properties are independent and uncorrelated to other measurements (i.e., sizes, attenuations and EWs), different explanations of the correlations shown in Calabrò et al. (2019a) should be found, some of which could be tested through the following arguments.

With $0.1-0.2''$ resolution ALMA CO-maps, I will be able to resolve the starburst cores down to a physical scale of 0.8-1 kpc, looking for multiple

nuclei, as well as additional clumps on smaller scales. While radio sizes are tracing somewhat indirectly the distribution of SFR (Condon, Anderson, and Helou, 1991) on long timescales ($\sim$ 100-200 Myr, representing synchrotron radiation powered by different physical mechanisms that are not yet fully understood), CO sizes can probe directly the cold molecular content of galaxies, which is directly connected to the current level of star-formation. As another advantage, they do not suffer from possible contaminations from an AGN. Therefore, these data will clarify if the A_V-size relation is real and thus the starburst cores are more obscured as they become more compact. As a second test, by reconstructing the dynamical state from CO maps, I will estimate the dynamical masses and put constraints on the total gas masses, as successfully done in Silverman et al. (2018b). This could possibly reveal a primary driving role of the gas fraction of merger galaxies into the observed correlations.

Furthermore, these extremely rich observations would provide independent ways to probe the star-formation mechanism in these galaxies and the validity of the dust attenuation model suggested by my previous results.

First, by comparing the gas-mass surface density (derived from dust continuum assuming a typical dust to gas conversion) with CO-based SFR maps, I can test the Kennicutt-Schmidt relation for high-z starbursts and measure their star formation efficiencies (SFE). This will further check the merger-driven scenario, of which the increased SFE with respect to normal SF systems would be an objective signature. I will also verify that SFE and velocity width correlate with compactness and size, as expected from this scenario.

Secondly, I will compare the dust and gas resolved column densities (N_H) with existing measurements of the total column density (that I will re-derive with the new size estimates) and with the same quantity derived from the X-rays and from the attenuation A_V. This will further test the validity of the mixed model, and clarify why indirect measurements of the dust-column density presented in Fig. 3.1-*below* are systematically diverging from those predicted by a mixed model at the highest obscurations, for which no explanations are currently known. In addition, for the X-ray AGNs (which are found only in the latest merger phases, according to Calabrò et al. (2019a)), I can check the surprising general consistency between the N_H inferred from the X-rays and from the infrared SFR. If confirmed, this would query the classical AGN paradigm, suggesting a peculiar dust distribution as a possible by-product of the AGN blow-out starting to clean the very central regions around the black hole, or that the AGN is not centrally located.

Finally, related to the clumpiness investigation presented in Chapter 5 and 6, ALMA observations would allow to compare sub-mm clumps with those observed in HST (optical rest-frame), checking whether there is a correlation between these two substructures, which trace respectively the current SFR and the stellar mass. If HST clumps contain a significant fraction of SFR (10-20%) (which could implying also high SFEs) I will be able to detect their

CO emission with ALMA. This could suggest a connection between SMGs and merger-triggered starbursts at lower redshifts, whereas SMGs may be scaled-up analogues with a common merger origin.

Overall, in addition to solidly confirming the attenuation sequence and the time evolution interpretation proposed in my two previous works (Calabrò et al., 2018; Calabrò et al., 2019a), these projects (in particular the ALMA proposal) will shed light more generally on the dynamical process related to starburst-triggering in mergers.

7.2 Toward a systematic investigation of near-IR lines

In the literature, only small samples of galaxies, mostly in the local Universe, have been observed and studied so far in the near-infrared rest-frame spectral range (Martins et al., 2013; Mason et al., 2015). Similarly, the 25 starbursts observed at Magellan and analyzed in Chapters 2 to 4, even though representing a first sizeable sample with near-IR coverage at intermediate redshifts ($z < 1$), cannot be exhaustive of the whole galaxy population. If we want to address a systematic study of near-IR galaxy properties in statistical terms (which is still missing), much larger datasets are necessarily required.

To this aim, we observed 7 starbursts and $\sim$ 120 main sequence galaxies at redshifts 0.5-0.9 with KMOS, as part of the program ID 0100.A-0506(A) (P.I. E. Daddi). In addition, we performed 2 half nights of observations (9-10/05/2017) in visitor mode at the Subaru Telescope with the MOIRCS instrument, to observe HK band spectra in other 6 starbursts and $\sim$ 50 main sequence galaxies in the same redshift range (Program ID: S17A-133, PI: M. Onodera).

In both cases, I have almost completed the spectral reduction. Figures 7.1 to 7.2 show some examples of the reduction for VLT/KMOS and Subaru/MOIRCS, respectively. KMOS observations, covering the $1\mu m$-$2.4\mu m$ range (with λ-dependent spectral resolution between R$=$ 1500 in HK and 4000 in YJ), benefitted from good seeing conditions ($\sim$ 0.7-0.8$''$ on average), despite our request of 1.2$''$. They will thus allow in some cases to perform a kinematic analysis, mainly from Hα space and velocity maps, because of the higher S/N.

On the other hand, Subaru observations, done in collaboration with Dr. M.Onodera, were also successful, with good atmospheric conditions (seeing $\sim$ 0.6$''$). Despite the lower resolving power, we were able to detect multiple emission lines in HK band, including Paβ and [FeII]. However, in this case, we did not use YJ grism, because originally we wanted to maximize the number of targets with a detection of Paβ, the least attenuated line reachable within K band at our redshifts. After later realizing the importance of Hα for inferring the dust properties, we have been applying for extra observing time in order to recover the smaller wavelength ranges for our targets.

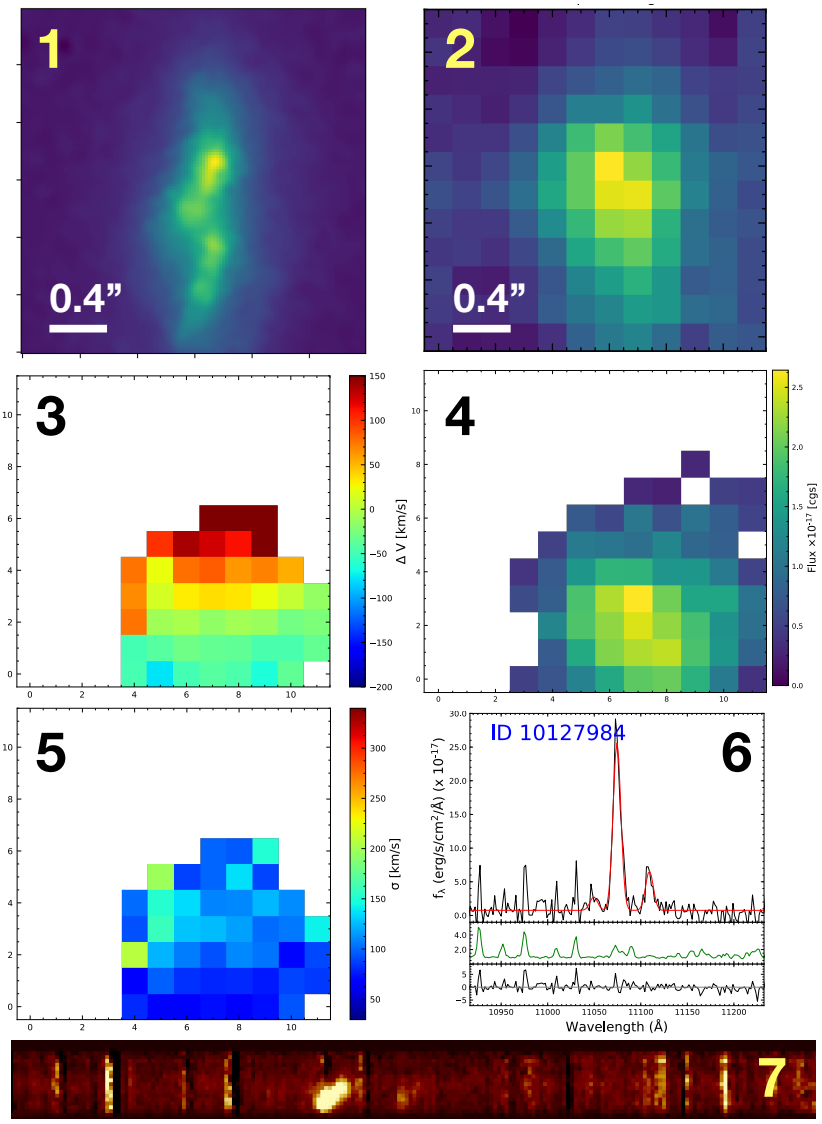

Figure 7.1: (1) HST-WFPC3 F125W image of a starburst galaxy in COSMOS field (ID 10127984) at redshift 0.688, reprojected into the KMOS IFU field of view. The size of the image is 2.4″. (2) Collapsed spectral cube along the wavelength axis. For each spaxel, the median flux has been considered. (3) Velocity map of Hα, with respect to the median value. The velocity ha been calculated as the peak of Hα gaussian profile in each spaxel. Spaxels with a S/N lower than 3 have been masked in white. (4) Flux map of Hα emission, with the same mask as before. (5) Velocity dispersion map for Hα. σ has been calculated from the best fit Hα profile in each spaxel and converted to velocity units. (6) 1D spectrum including the two [NII] emission lines bracketing Hα, obtained with a boxcar extraction procedure including all the spaxels where Hα is detected with a S/N$>$ 3. (7) 2D spectrum including Hα and [NII] lines, obtained simulating a slit centered in the peak of the Hα emission and oriented along the major axis of the system.

Once the KMOS reduction is fully complete, and waiting for additional Subaru YJ band spectral observations, I will start to measure Hα and Paβ fluxes to probe the level of obscuration and test the different attenuation laws in normal star-forming galaxies, which are expected to be dustier compared

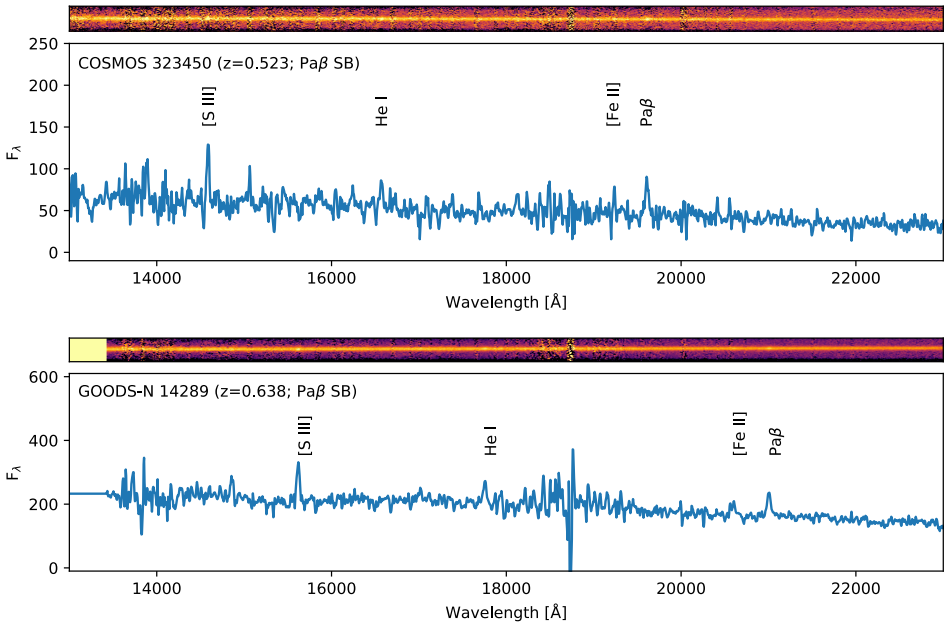

Figure 7.2: Subaru/MOIRCS fully reduced and calibrated HK spectra for two SB galaxies at $z = 0.523$ and $z = 0.638$, respectively, observed in May 2017). The 2D spectrum is in the upper part, while the 1D version is presented in the bottom of each panel. Prominent near-IR emission lines, labeled in the 1D spectra, have been successfully detected in all cases.

to local samples at similar distances from the main sequence. If significant departures are found from the Cardelli/Calzetti relations, this would revise a big part of literature of the past ∼30 years. Moreover, this analysis can provide estimations (or at least lower limits) of near-IR emission line fluxes that we should expect (thus the integration times required) for the most embedded galaxies at high-z, targeted systematically in future surveys (e.g., JWST).

From Hα velocity maps (especially for the brightest and most extended sources), I can also put constraints on the nature of the starburst phenomenon: if they are anomalously gas-rich disk galaxies they must show a coherent rotation pattern of the gaseous and stellar component, whereas if they are merger triggered their gas velocity maps should appear more disturbed and chaotic, at least in early and ongoing coalescing phases.

Afterwards, it will be very interesting to exploit the full potential of my entire near-infrared coverage. As already mentioned before, in addition to hydrogen, the emission lines of heavier species were detected in the 25 Magellan-FIRE spectra, including [SIII] λ 9530, [CI] λ 9850, HeI λ 10830 and [FeII] λ 1.32μm. We may thus expect to be able to detect (with good signal to noise) at least the same lines for a significant fraction of the whole galaxy dataset.

Similarly to optical ones, these lines encode information on key physical parameters including excitation mechanism (e.g., shock/starburst/AGN),

ionization parameter and metallicity, while having the advantage to probe larger optical depths, as discussed before.

The first goal would be to build empirical line ratio diagrams (e.g., combining optical and IR lines, or only IR tracers), to investigate the powering excitation mechanism of all that emission. For example, using CLOUDY models on normal star-forming MS galaxies, I have verified that star formation/AGN can be expected to be distinguished using IR lines. Similarly, shock-driven line ratios can be estimated with MAPPINGS models (Allen et al., 2008). From Fig. 7.3, we can see that AGN/shocks produce enhanced [FeII] emission at fixed [SIII]/Paβ ratios. For moderately obscured galaxies I can calibrate this result against the BPT diagram, and then apply the diagnostic to all galaxies. This will allow to identify with near-IR lines which galaxies contain significant contamination from AGN or shocks, and potentially discover a new population of highly attenuated near-IR selected AGNs.

Another fundamental diagnostic that can be studied is the metallicity, which will be discussed more in detail in the following section. Overall, I expect that the new evidences provided for the first time by near-IR rest-frame observations should trigger much interest from other groups, including observers and modelers from the community, providing unique preparatory work for JWST, MOONS and ERIS. This will be useful not only to study the nature of starburst galaxies, but also the properties of main sequence systems, which become dustier as we approach the peak of the SFR density toward $z \sim 2.5$ (Daddi et al., 2008).

7.3 The role of metallicity in understanding the real nature of distant starbursts

As remarked throughout the whole thesis, the key goal of my work is to understand which is exactly the triggering mechanism of a starburst galaxy. The crucial question is why this population has a SFR much higher than typical star-forming galaxies at the same redshift and stellar mass. There are two currents of thoughts: it is possible that they have an enhanced activity simply because they have more gas (which is the fuel of star-formation), or, on the other hand, they may have the same quantity of gas of main sequence galaxies but a higher star formation efficiency. Thus, in any case, it appears that studying their total gas content is fundamental to constrain the different hypothesys.

In Section 7.1 I showed that, if the ALMA proposal is accepted, I will derive the gas mass through the dynamical mass inferred from CO-based high-resolution maps, assuming a constant ratio of dark matter mass. In the absence of such data, and also as independent probes, the same quantity could be estimated from the molecular hydrogen mass M_{H_2}, which is the dominant gaseous component (fixed ratios with the neutral and ionized

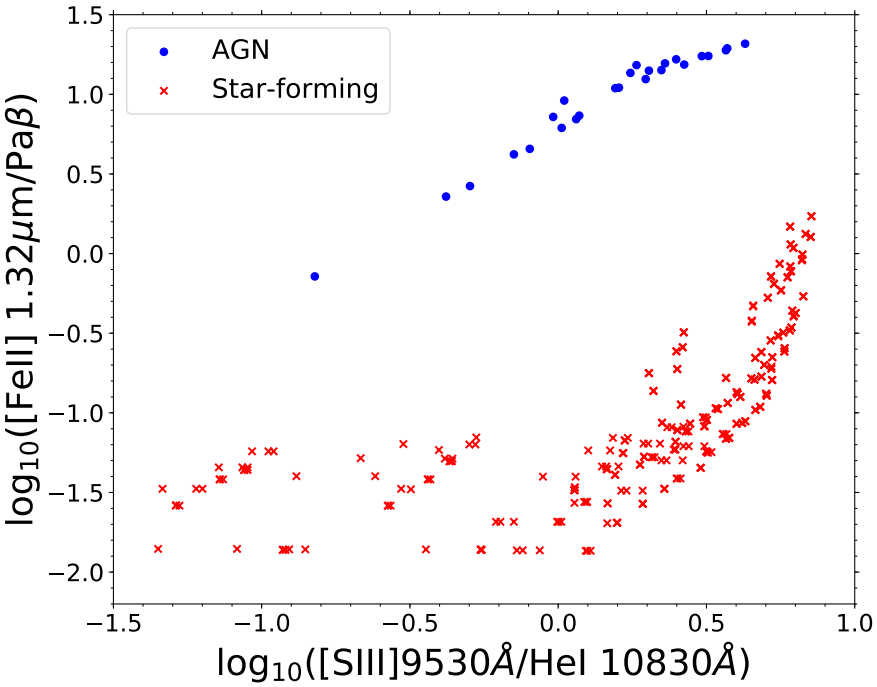

Figure 7.3: Segregation between galaxies with star-formation or AGN excitation (red crosses and blue circles, respectively), found with CLOUDY for varying gas properties (i.e., metallicity, density, temperature).

hydrogen or helium can be assumed). The M_{H_2} is then inferred through the luminosity L'(CO) of the CO(1-0) molecular transition or from the total dust mass indicated by the best-fit infrared SED. In the first case, M_{H_2} is written as $\alpha_{CO} \times L'(CO_{1-0})$, where the coefficient α_{CO} depends on the metallicity and likely the star-formation mode (i.e., normal or starburst). In the second case, we can adopt a relation like Magdis et al. (2012) as:

$$log_{10}(M_{dust}/M_{gas}) = (10.54 \pm 1.0) - (0.99 \pm 0.12) \times (12 + log_{10}(O/H))) \quad (7.1)$$

From the two above equations it is clear that the metallicity plays a fundamental role in the estimation of the gas mass in both approaches. Unfortunately, it is also the most controversial and difficult quantity to measure, because of the strong attenuation affecting optical emission lines from which it is typically derived. From this quantity depends most of the understanding of the starburst phenomenon: with solar metallicity we would obtain higher gas fractions and thus lower efficiencies, while with super-solar chemical abundances we get the opposite situation.

During a collision of spiral galaxies in the local Universe we typically observe a flattening of the metallicity gradients of pre-existing disks, and sometimes a negative gradient, that is, decreasing toward the center. This is due to redistribution of the gas during the merger and central accretion of

material that was originally located in the outskirts of colliding galaxies. The intense starburst episode inevitably enhances the metallicity in the core, but it is not clear whether there is enough time for the new metals to pervade the whole system, and thus justify a variation of the α_{CO} conversion factor between L'(CO) and M_{gas}.

Important clues on the metallicity of dusty star-forming systems could be derived through the analysis of KMOS and Subaru spectroscopic data, which have been presented in Section 7.2. Firstly, taking only purely star-forming systems (identified on the basis of Fig. 7.3), I will build the R23 metallicity estimators from the optical lines (available from ancillary spectra present in the literature) and compare them to IR line ratios. Using the objects in my sample with moderate dust obscuration, I will then establish empirical metallicity calibrations for those near-IR lines. For example, [SIII]0.953 μm/Paβ could be the most promising ratio, following the successful work by Díaz and Pérez-Montero (2000) and Kehrig et al. (2006). I remark that the availability of a large statistical sample of normal star-forming galaxies will be crucial here to calibrate all the relations. The resulting calibration of IR line ratios would then be applicable to the whole sample, in particular to heavily obscured starbursts.

I remind that the mixed model implies the presence of a completely obscured, optically thick core in the center of the system, surrounded by an external, less attenuated, optically thin shell from which near-IR and optical lines can escape (the optical depth increases with wavelength). Essentially, this external shell behaves as a dust screen, thus the results obtained with CLOUDY and tested on main sequence galaxies would still be applicable to starburst galaxies, even though the properties derived would be representative of the starburst skin region only. However, these new tracers would represent a significant advantage compared to optical ones: I showed indeed that near-IR lines can probe up to 50% per cent of the total system SFR, at least $\sim$ 30%-40% more than optical lines.

Finally, thanks to the new near-IR diagnostics, I will look for empirical variations of line ratios and physical properties between the 25 (+7) SBs and normal MS galaxies. Finding any observational difference would be already a very promising result, and would give the basis for systematic investigations of dusty starbursts at higher redshifts with future infrared surveys.

Furthermore, the [Fe II] emission line could be used in principle as a metallicity indicator, as inferred from CLOUDY models. However, in contrast with sulfur, the iron element can be highly depleted onto dust grains. Nevertheless, it is possible to estimate this effect following a similar procedure to that adopted successfully in De Cia et al. (2016). In particular, from a sample of normal star-forming galaxies having a similar metallicity, as traced by non-refractory elements (e.g., Sulfur), I can compare their abundances to those of highly depleted species (e.g., Iron). Drawing a [SIII]/Paβ vs [FeII]/Paβ diagram, any correlation emerging between these two quantities

could be interpreted as produced by different depletion factors, possibly related also to the amount of dust attenuation, which we control with Paβ to IR ratios. From the slope and normalization of this depletion sequence I would be able to finally derive a correction factor, calculating the total intrinsic iron abundance, hence the metallicity.

The scatter of the correlation or a deviation from a linear behaviour would be instead an indication of the different SFR timescales probed by the two tracers. Different [SIII]/[FeII] are indeed expected at different phases of a starburst (increasing and then decreasing) because, while sulfur is produced by type II supernovae, iron is mainly the product of type Ia supernovae explosions, which last for longer timescales. I then expect that the sulfur over iron overabundance can be used as additional test for the evolutionary sequence interpretation, whereas later phases would have lower ratios.

Overall, this analysis could shed light on the star-formation history and metallicity of starburst galaxies, which are notoriously difficult quantities to measure. On a longer perspective, the SPICA space mission, whose launch is predicted in 2032, will be able to push the observations to longer infrared wavelengths (34 to 230μm), eliminating the problem of the atmospheric absorption, and reaching higher sensitivity compared to Herschel. Here we can really start to approach the optically thin regime (at least for a fraction of less obscured starbursts). Indeed, if the mixed model is valid, with the average $A_{V,tot} \simeq 9$ mag found for the Magellan SBs, already at 8μm we should be able to recover 90% of the intrinsic line fluxes. Additionally, this will allow to better identify and investigate the properties of obscured AGNs, whose torus emission has its maximum at those mid-infrared wavelengths probed by SPICA.

In the meantime, on shorter timescales, we could use JWST for targeting Paβ and Paα lines in intermediate and high redshift starbursts. Thanks to the larger optical depths of such lines (compared to optical tracers), we can test the attenuation laws with bigger samples and at earlier cosmic epochs, or test a possible increasing trend of metallicity towards the core, expected in the merger driven starburst scenario.

7.4 Dust temperature and opacity in infrared luminous starbursts

After discussing emission line diagnostics in the near and mid infrared, we should also focus on the properties of the dust. In Chapter 2 Section 2.3, for the sample of 25 starbursts observed at Magellan, I derived the total dust mass and the intensity of the radiation field (<U>) that is heating the dust. The latter quantity, which is strongly related to the dust temperature T_{dust} and to the metallicity-weighted star-formation efficiency (i.e., SFE/Z, Magdis et al. 2012), has already been studied for different populations of galaxies in the local and in the high redshift Universe. For example, main sequence

galaxies have increasing <U> and T_{dust} going from <U>$\simeq$ 5 at $z = 0$ to $\simeq$ 20 at $z = 2$ (or T_{dust} from 25 to 30K), following the trend $(1 + z)^{1.8}$ reported by Béthermin et al. (2015). On the other side, starburst galaxies have typically warmer ISM and higher SFEs compared to main sequence systems. They follow a different trend with time, displaying almost constant <U> $\simeq$ 30 from $z = 0$ to 2 (Béthermin et al., 2015; Schreiber et al., 2018), corresponding to dust temperatures ranging 30-70K. Beyond redshift 2 instead, this trend is almost unconstrained.

In the local Universe, ULIRGs are the best representatives of this outlier population, with warmer dust and higher star-formation efficiency than spiral galaxies, as a result of the merger process (Renaud et al., 2018; Renaud et al., 2019). The ULIRG called GN20, located at $z = 4.05$ (Daddi et al., 2009; Tan et al., 2014), is the prototypical system of high redshift starbursts, and its infrared SED ($T_{dust} = 33$K) is actually used as a reference to fit the SBs SEDs at any redshift, with good results (Jin et al., 2018). However, this remains an approximation. Since SBs can show a variety of dust temperature distributions, we set <U> as a free parameter in the SED fitting procedure (Chapter 2.3), choosing as final the one that minimizes the χ^2 probability distribution of the fit.

In a preliminary work, I started analyzing the relation of the radiation strength and dust mass with the attenuation and the merger sequence, for the same sample of 25 starbursts. The results, presented in Fig. 7.4, show an absence of correlations between $A_{Pa\beta,IRX}$, M_{dust} and <U>, indicating that the dust temperature and mass (including the gas mass, if we assume a common conversion factor) do not seem to play a role and are not driving parameters of the attenuation sequence. If the time evolutionary sequence interpretation holds, these diagrams suggest that different configurations or initial conditions within the sample are probably canceling out any appreciable signature of evolution of the gas content during the merger.

The bottom panel of Fig. 7.4 also shows that a fraction of starbursts ($\sim$ 25%) have <U> significantly below the values expected for off-MS star-forming galaxies, and are more similar to those found in normal systems, which typically have <U> below 10. Another way to test the dust temperatures is shown in Figure 7.5, where T_{dust} is compared to the infrared luminosity surface brightness $\Sigma_{IR} = L_{IR}/(2\pi R_e^2)$ of the galaxies. T_{dust} is derived here inverting the relation <U>=$(T_{dust}/18.9)^{6.04}$. It is evident that the 25 Magellan starbursts have a large variety of Σ_{IR} within their range of temperatures. However, when we compare our data with the Stefan-Boltzmann blackbody law for a single emitting, homogeneous starburst core, we notice that only a subset of starbursts are qualitatively consistent with that relation. While reinforcing the idea presented in Sections 4.2-4.7 that less attenuated SBs (likely earlier merger phases) are still constituted of multiple nuclei (thus their radio sizes are not representative of single cores), this figure suggests instead that T_{dust} of the most obscured, already coalesced systems might be underestimated. A higher temperature could indeed reconcile these objects

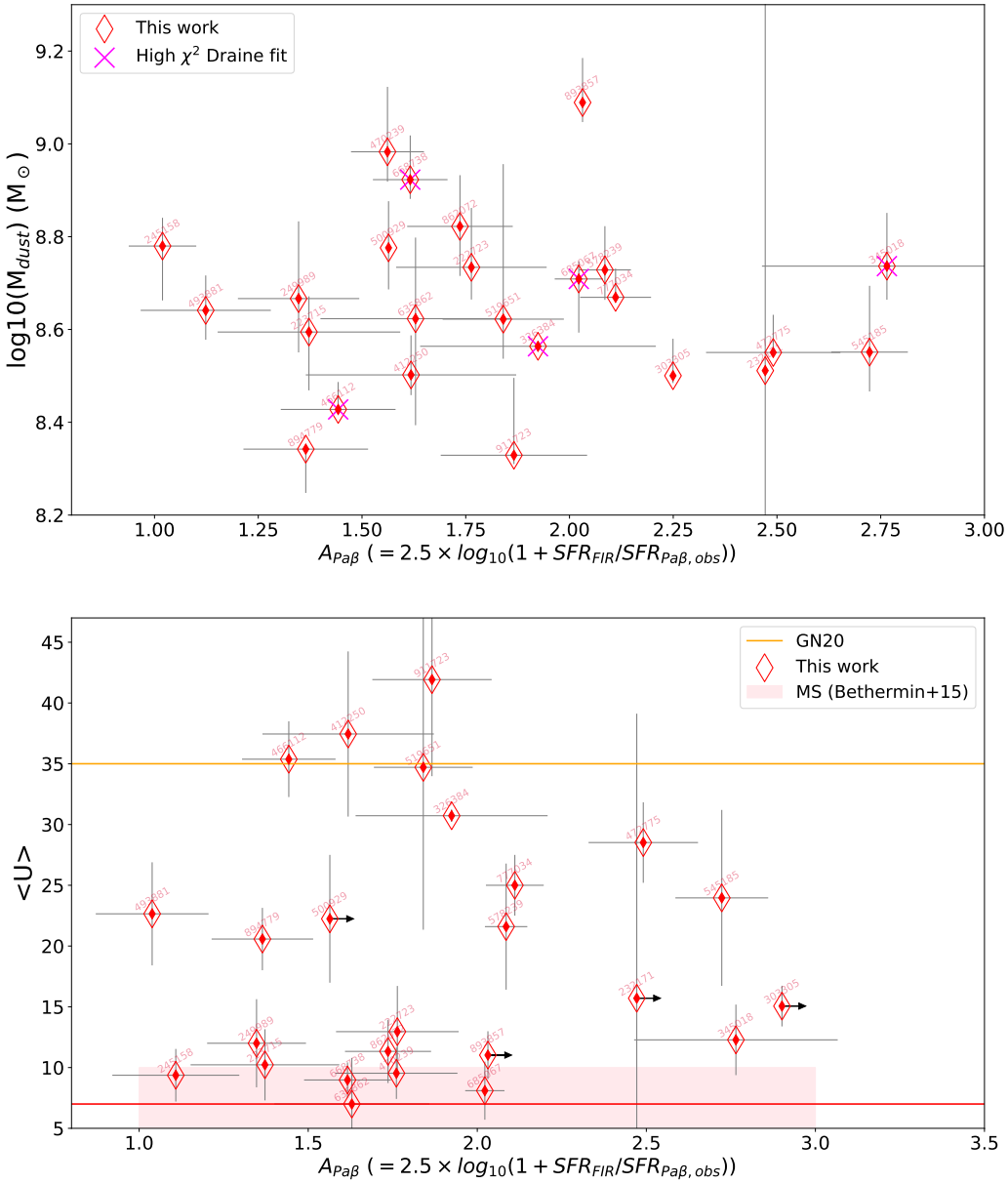

Figure 7.4: *Top:* Diagram comparing the dust mass to the attenuation at Paβ ($A_{Pa\beta,IRX}$) for the 25 starbursts observed with Magellan FIRE; *Bottom:* Comparison between the attenuation and the average radiation field <U> for the same sample.

with the blackbody S-B limit.

A possible explanation of this surprising result can come from CO and dust-continuum ALMA observations that were presented in a recent work by Jin et al. (2019) (of which I am co-author). This study found a class of exceptionally cold dusty SBs at $3.62 < z < 5.85$, colder than typical starburst galaxies and even MS systems at the same redshift, as if they have low star-formation efficiency or extremely high metallicity. The dust to stellar mass ratios of the coldest galaxies also seem very large, reaching

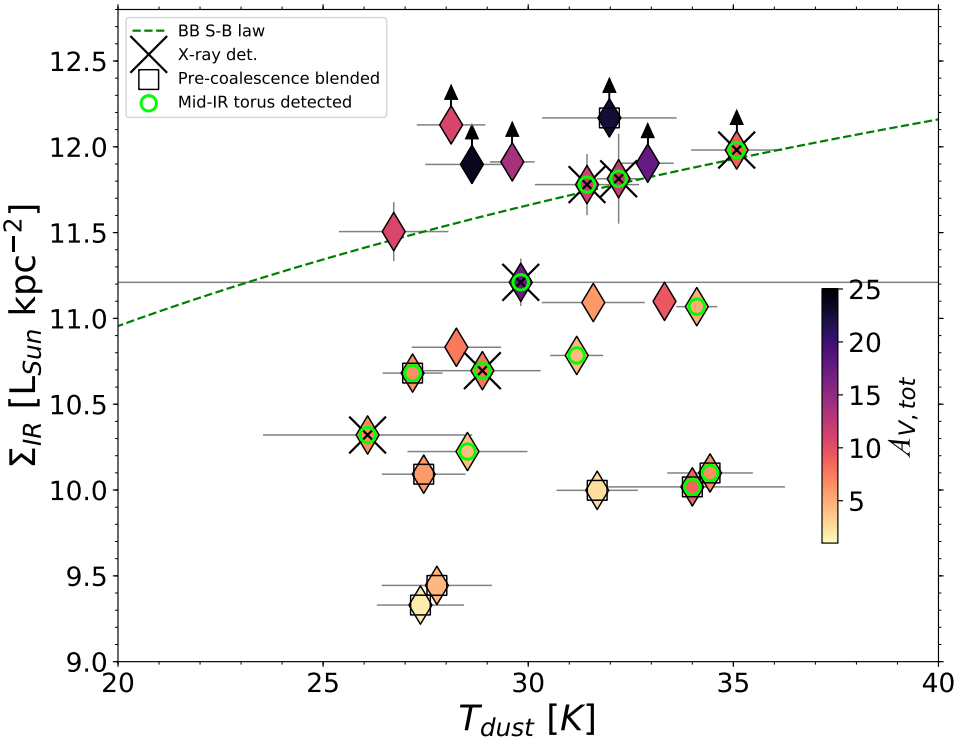

Figure 7.5: IR surface luminosity density versus dust temperature for the sample of 25 Magellan starbursts, color coded by their total attenuation $A_{V,tot}$. The Stefen-Boltzmann law is shown in green dashed line, which is only valid for blackbody dust clouds that are optically thick at all IR wavelengths.

10%, again suggesting extreme Z. Similarly, gas masses to stellar masses are unrealistically high ($\sim$ 10), as if they were primordial galaxies.

To reconcile these apparent inconsistencies, we have proposed that dust emission is optically thick even in the infrared rest-frame, up to same wavelength ($\sim 100\mu m$). If this is true, we are only seeing dust emission from the external regions, while that present in the most enshrouded core remains invisible. Additionally, this implies that dust temperatures and <U> are underestimated, while dust and gas masses are overestimated.

If the nature and structure of these SMGs is the same of lower redshift starbursts, optically thick dust may explain also part of my Magellan galaxies with unusually low T_{dust}. At this point, two important directions should be followed in future work for my Magellan sample :

- Why is this unusually low dust temperature found only for a subset of $z \sim 0.7$ starbursts and not in all the population ? Does <U> correlate with other properties ? Is this discrepancy equally important at $z \sim 3$ and at $z \sim 0.7$?

- afterwards, it will be crucial to test the validity of the above explanation: using the excitation temperature of [CI] (an optically thin dust tracer, Cortzen et al. 2019 in prep.) and comparing it with the value derived from the observed <U>, should already clarify our hypothesis.

If that idea is confirmed, we have to reconsider our previous knowledge on the dust and gas distribution and properties in galaxies, with significant impact on the understanding of the starburst phenomenon.

7.5 The environment of starburst galaxies

So far, throughout the thesis, I have considered starbursts and mergers as isolated identities, separated from the rest of the Universe. However, the cosmic environment on Mpc distances can also have a large impact on the star-formation rate of a galaxy and on its internal feedback processes. For example, all galaxies are known to move from low-density to high-density regions, hence during their life they are expected to experience, with different intensities, tidal forces, harassment and ram pressure stripping typical of dense environments. While these mechanisms are typically associated to quenching of star-formation activity in the local Universe, some observations at earlier cosmic epochs ($\sim$ 1 and above) suggest that in those high density regions the star-formation increases (Elbaz et al., 2007). However, we don't know why and when this reversal happens, and this is likely due to our poor comprehension of the environmental impacts on galaxy evolution.

Nowadays, the quality of photometric redshift determinations has reached a so high level that it allows to map the geometry of the Universe up to redshift $\sim \mathbf{1}$ (Laigle et al., 2018), enabling to study accurately the neighborhood of galaxies at intermediate redshift, not only their location in clusters but also with respect to the cosmic web filaments. The times are yet mature to address in a more systematic way the study of galaxies large scale structures. In a preliminary analysis with my collaborator G. Gozaliasl, I found that the Magellan SBs populate very different environments, from rich X-ray clusters to small groups (Fig. 7.6), indicating there is a lot of physical information to interpret from the distribution of these objects on the largest scales, and that it is worth to continue this investigation.

In the next years, as a possible development of my thesis, it would be extremely interesting to start a systematic study of the environment of all starburst galaxies in COSMOS field, taking this unique timing opportunity. For all of them I already have complete photometric data, SFRs, AGN-torus luminosities, dust masses, radio sizes, and, for a large subset of them, also dust obscurations and metallicities, derived from KMOS and Magellan spectra. This wealth of information will allow to answer the following fundamental, still unexplored questions: When exactly does the reversal of the SFR-galaxy density relation occur and what is the cause ? do higher redshift starbursts preferentially reside in small groups or in rich mature clusters ? At which

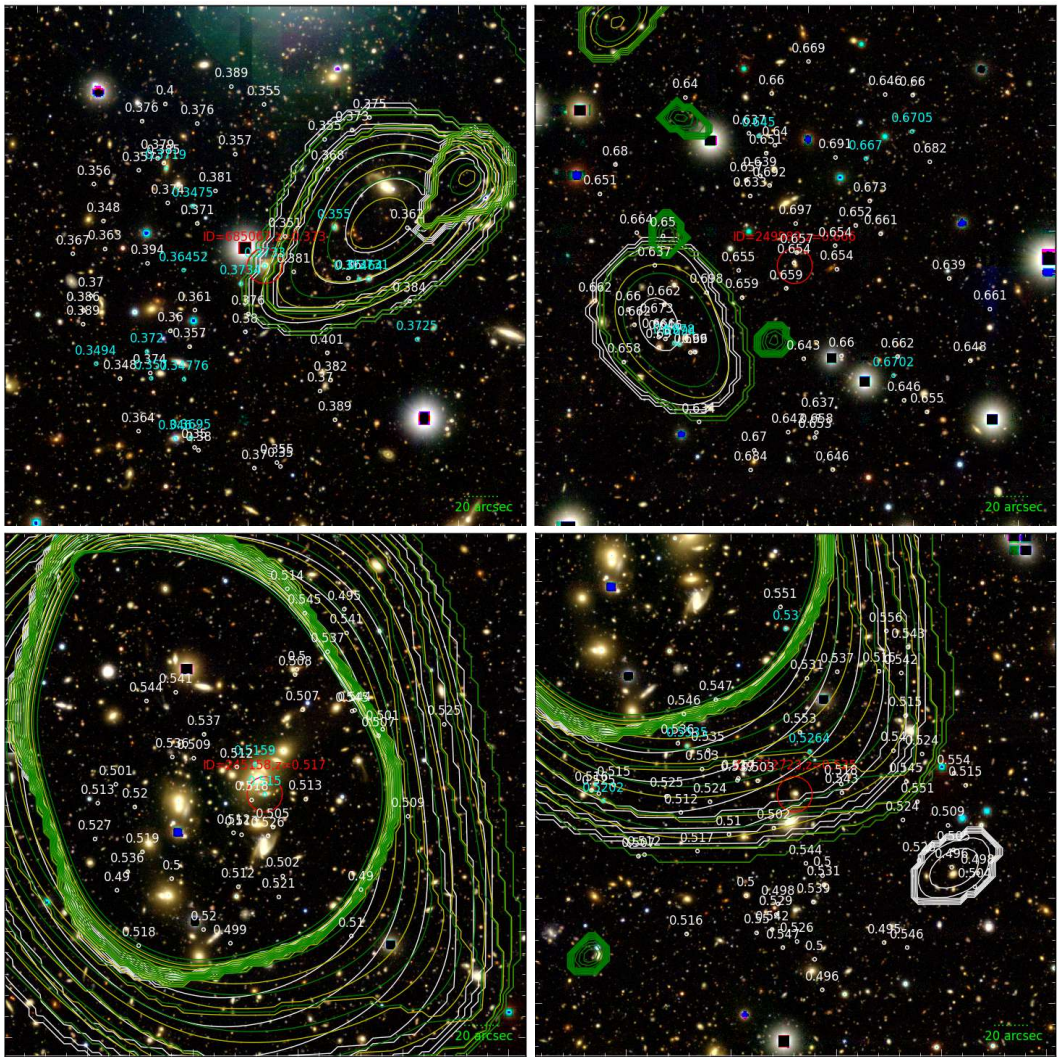

Figure 7.6: Large scale optical RGB images of four starbursts (each per panel) from my Magellan sample. The starburst target is written in red, along with its ID and spectroscopic redshift. The contours trace the X-ray emission from the intra-cluster hot gas. Spectroscopically confirmed cluster members are highlighted in cyan, while cluster member candidates according to their photometric redshifts are drawn in white. The figure highlights the great variety of environments: the majority of starburst appear located in the outskirts of mature X-ray galaxy clusters, some are inside, and others are part of smaller and younger associations (e.g., protoclusters), not detected in X-rays. Credits: Ghassem Gozaliasl

clustercentric distance are they located, and how far from the filaments ? Relating such distances to the physical properties of single galaxies (e.g., SFR, size, gas fractions) can shed light on the possible influence of large scale structures on the evolution and processes at galactic scales, including merger activity. In this topic, I will have the opportunity to collaborate with experts in this field, including C.Laigle, G.Gozaliasl and A.Finoguenov.

7.6 The properties and final fate of merger triggered clumps

In Chapter 6, I showed that merger triggered starbursts at $z \sim 0.7$, and at some degree morphological mergers in the main sequence, are more clumpy than normal star-forming disks at the same redshift. In other words, they have brighter concentrations of young stars in high-resolution HST i-band images. This result corroborates the idea that mergers have a key influence on the formation of clumps. It can be physically motivated by the enhancement of compressive turbulent motions in the ISM, hence gas concentration and fragmentation in smaller substructures, as seen in numerical simulations (e.g. Renaud et al., 2014).

These findings open the avenue for further investigations that could be addressed after the PhD. We still do not understand whether the physical properties and star-forming efficiency of these clumps are similar to those of clumpy main sequence galaxies observed at redshift > 1 (typically associated to violent instabilities), and whether there is an evolution of these properties with redshift. Additionally, we do not know whether these structures can be sustained for a long time against dissipation or stellar/AGN feedback. To address the above questions, a full exploitation of HST-CANDELS high resolution ($0.095''$-$0.2''$) image data are required, as well as additional follow-ups with SINFONI in the near-IR, or ALMA in the sub-mm.

From CANDELS multi-wavelength photometry (comprising four optical to near-IR broadbands), already available for a small subset (< 10) of starbursts at $0.5 < z < 1$, I will derive the stellar masses of the clumps, and then compare their mass function to those of normal star-forming clumpy systems. With near-IR integral field spectrographs, I will have information on the age of the clumps since the start of the last SF episode (combining Balmer/Paschen line equivalent widths and stellar SED analysis). If I find old ages (comparable to the dynamical timescale), it means that feedback effects are likely not sufficient to destroy them, and would actually have time to migrate to the center and contribute to the bulge growth, which possibility is suggested by some recent numerical simulations (Bournaud, 2016). Alternatively, they can form globular clusters and tidal dwarf galaxies, as suggested by Renaud et al. (2014). On the contrary, finding only very young stellar clumps would suggest a crucial influence of feedback or turbulence dissipation.

On the other hand, as mentioned in Section 7.1, ALMA will enable measurements of the gas masses, temperatures, gas depletion timescales $\tau_{\rm depl}$, gas velocity dispersion and dynamical stability (thanks to the Toomre parameter). In particular, with $\tau_{\rm depl}$ I will compare the efficiency of star-formation with that occurring in the central core of starbursts, to see whether they are driven by the same underlying mechanism.

Overall, this study can provide a useful reference for the next decades

in this research field, which will be focused, among all, on better understanding feedback processes in galaxies and on their role on the morphology of the whole system. For this part of the project, I will work in synergy with researchers doing simulations, as J.Fensch and F.Bournaud in France. Numerical simulations alone are indeed very difficult to perform, due to the large number of parameters and complexity in modeling these physical phenomena. Therefore, inputs and constraints from direct observations, and a real collaboration among different groups, are undoubtedly needed.

Bibliography

Ahn, Christopher P. et al. (2012). "The Ninth Data Release of the Sloan Digital Sky Survey: First Spectroscopic Data from the SDSS-III Baryon Oscillation Spectroscopic Survey". In: *ApJS* 203.2, 21, p. 21. DOI: 10.1088/0067-0049/203/2/21. arXiv: 1207.7137 [astro-ph.IM].

Allen, Mark G. et al. (2008). "The MAPPINGS III Library of Fast Radiative Shock Models". In: *ApJS* 178.1, pp. 20–55. DOI: 10.1086/589652. arXiv: 0805.0204 [astro-ph].

Aretxaga, I. et al. (2011). "AzTEC millimetre survey of the COSMOS field - III. Source catalogue over 0.72 deg^2 and plausible boosting by large-scale structure". In: *MNRAS* 415.4, pp. 3831–3850. DOI: 10.1111/j.1365-2966.2011.18989.x. arXiv: 1105.0890 [astro-ph.CO].

Arnouts, S. et al. (1999). "Measuring and modelling the redshift evolution of clustering: the Hubble Deep Field North". In: *MNRAS* 310.2, pp. 540–556. DOI: 10.1046/j.1365-8711.1999.02978.x. arXiv: astro-ph/9902290 [astro-ph].

Arnouts, S. et al. (2007). "The SWIRE-VVDS-CFHTLS surveys: stellar mass assembly over the last 10 Gyr. Evidence for a major build up of the red sequence between $z = 2$ and $z = 1$". In: *A&A* 476.1, pp. 137–150. DOI: 10.1051/0004-6361:20077632. arXiv: 0705.2438 [astro-ph].

Arnouts, S. et al. (2013). "Encoding of the infrared excess in the NUVrK color diagram for star-forming galaxies". In: *A&A* 558, A67, A67. DOI: 10.1051/0004-6361/201321768. arXiv: 1309.0008 [astro-ph.CO].

Arribas, S. et al. (2012). "Integral field spectroscopy based Hα sizes of local luminous and ultraluminous infrared galaxies. A direct comparison with high-z massive star-forming galaxies". In: *A&A* 541, A20, A20. DOI: 10.1051/0004-6361/201118007. arXiv: 1203.0036 [astro-ph.CO].

Arrigoni Battaia, Fabrizio et al. (2019). "QSO MUSEUM I: a sample of 61 extended Lyα-emission nebulae surrounding $z \sim 3$ quasars." In: *MNRAS* 482.3, pp. 3162–3205. DOI: 10.1093/mnras/sty2827. arXiv: 1808.10857 [astro-ph.GA].

Aumer, Michael et al. (2010). "The Structure of Gravitationally Unstable Gas-rich Disk Galaxies". In: *ApJ* 719.2, pp. 1230–1243. DOI: 10.1088/0004-637X/719/2/1230. arXiv: 1007.0169 [astro-ph.GA].

Avni, Y. and N.A. Bahcall (1976). "Statistical simulations of clusters of galaxies." In: *ApJ* 209, pp. 16–21. DOI: 10.1086/154688.

Baillard, A. et al. (2011). "The EFIGI catalogue of 4458 nearby galaxies with detailed morphology". In: *A&A* 532, A74, A74. DOI: 10.1051/0004-6361/201016423. arXiv: 1103.5734 [astro-ph.CO].

Baldry, I.K. et al. (2006). "Galaxy bimodality versus stellar mass and environment". In: *MNRAS* 373.2, pp. 469–483. DOI: 10.1111/j.1365-2966.2006.11081.x. arXiv: astro-ph/0607648 [astro-ph].

Baldry, Ivan K. et al. (2004). "Quantifying the Bimodal Color-Magnitude Distribution of Galaxies". In: *ApJ* 600.2, pp. 681–694. DOI: 10.1086/380092. arXiv: astro-ph/0309710 [astro-ph].

Barker, S., R. de Grijs, and M. Cervino (2008). "Star cluster versus field star formation in the nucleus of the prototype starburst galaxy M 82". In: *A&A* 484.3, pp. 711–720. DOI: 10.1051/0004-6361:200809653. arXiv: 0804.1913 [astro-ph].

Barnes, Joshua E. and Lars E. Hernquist (1991). "Fueling Starburst Galaxies with Gas-rich Mergers". In: *ApJL* 370, p. L65. DOI: 10.1086/185978.

Battisti, A. J., D. Calzetti, and R. R. Chary (2017). "Characterizing Dust Attenuation in Local Star-forming Galaxies: Near-infrared Reddening and Normalization". In: *ApJ* 840.2, 109, p. 109. DOI: 10.3847/1538-4357/aa6fb2. arXiv: 1704.07426 [astro-ph.GA].

Bekki, Kenji (1998). "Formation of a Polar Ring Galaxy in a Galaxy Merger". In: *ApJ* 499.2, pp. 635–649. DOI: 10.1086/305680. arXiv: astro-ph/9804220 [astro-ph].

Bell, Eric F. and Jr. Kennicutt Robert C. (2001). "A Comparison of Ultraviolet Imaging Telescope Far-Ultraviolet and Hα Star Formation Rates". In: *ApJ* 548.2, pp. 681–693. DOI: 10.1086/319025. arXiv: astro-ph/0010340 [astro-ph].

Bell, Eric F. et al. (2007). "Star Formation and the Growth of Stellar Mass". In: *ApJ* 663.2, pp. 834–843. DOI: 10.1086/518594. arXiv: 0704.3077 [astro-ph].

Bender, R., S. Doebereiner, and C. Moellenhoff (1988). "Isophote shapes of elliptical galaxies. I. The data." In: *A&AS* 74, pp. 385–426.

Bennert, N. et al. (2008a). "Fueling QSOs: the relevance of mergers". In: *Mem. Società Astronomica Italiana* 79, p. 1247. arXiv: 0807.3371 [astro-ph].

Bennert, Nicola et al. (2008b). "Evidence for Merger Remnants in Early-Type Host Galaxies of Low-Redshift QSOs". In: *ApJ* 677.2, pp. 846–857. DOI: 10.1086/529068. arXiv: 0801.0832 [astro-ph].

Bertoldi, F. et al. (2007). "COSBO: The MAMBO 1.2 Millimeter Imaging Survey of the COSMOS Field". In: *ApJS* 172.1, pp. 132–149. DOI: 10.1086/520511.

Béthermin, Matthieu et al. (2015). "Evolution of the dust emission of massive galaxies up to $z = 4$ and constraints on their dominant mode of star formation". In: *A&A* 573, A113, A113. DOI: 10.1051/0004-6361/201425031. arXiv: 1409.5796 [astro-ph.GA].

Biggs, A.D. and R.J. Ivison (2008). "High-resolution radio observations of submillimetre galaxies". In: *MNRAS* 385.2, pp. 893–904. DOI: 10.1111/j.1365-2966.2008.12869.x. arXiv: 0712.3047 [astro-ph].

Bolzonella, M., J. M. Miralles, and R. Pelló (2000). "Photometric redshifts based on standard SED fitting procedures". In: *A&A* 363, pp. 476–492. arXiv: astro-ph/0003380 [astro-ph].

Boquien, M. et al. (2009). "Star-Forming or Starbursting? The Ultraviolet Conundrum". In: *ApJ* 706.1, pp. 553–570. DOI: 10.1088/0004-637X/706/1/553. arXiv: 0910.0774 [astro-ph.CO].

Boquien, M. et al. (2012). "The IRX-β relation on subgalactic scales in star-forming galaxies of the Herschel Reference Survey". In: *A&A* 539, A145, A145. DOI: 10.1051/0004-6361/201118624. arXiv: 1201.2405 [astro-ph.CO].

Bouchet, P. et al. (1985). "The visible and infrared extinction law and the gas-to-dust ratio in the Small Magellanic Cloud." In: *A&A* 149, pp. 330–336.

Boulade, Olivier et al. (2003). "MegaCam: the new Canada-France-Hawaii Telescope wide-field imaging camera". In: *Proceedings of the SPIE*. Ed. by Masanori Iye and Alan F.M. Moorwood. Vol. 4841. Society of Photo-Optical Instrumentation Engineers (SPIE) Conference Series, pp. 72–81. DOI: 10.1117/12.459890.

Bournaud, F. and F. Combes (2003). "Formation of polar ring galaxies". In: *A&A* 401, pp. 817–833. DOI: 10.1051/0004-6361:20030150. arXiv: astro-ph/0301391 [astro-ph].

Bournaud, F. et al. (2008). "Observations and modeling of a clumpy galaxy at $z = 1.6$. Spectroscopic clues to the origin and evolution of chain galaxies". In: *A&A* 486.3, pp. 741–753. DOI: 10.1051/0004-6361:20079250. arXiv: 0803.3831 [astro-ph].

Bournaud, Frédéric (2016). "Bulge Growth Through Disc Instabilities in High-Redshift Galaxies". In: *Galactic Bulges*. Ed. by Eija Laurikainen, Reynier Peletier, and Dimitri Gadotti. Vol. 418. Astrophysics and Space Science Library, p. 355. DOI: 10.1007/978-3-319-19378-6_13. arXiv: 1503.07660 [astro-ph.GA].

Bournaud, Frédéric, Bruce G. Elmegreen, and Debra Meloy Elmegreen (2007). "Rapid Formation of Exponential Disks and Bulges at High Redshift from the Dynamical Evolution of Clump-Cluster and Chain Galaxies". In: *ApJ* 670.1, pp. 237–248. DOI: 10.1086/522077. arXiv: 0708.0306 [astro-ph].

Bournaud, Frédéric et al. (2011a). "Black Hole Growth and Active Galactic Nuclei Obscuration by Instability-driven Inflows in High-redshift Disk Galaxies Fed by Cold Streams". In: *ApJL* 741.2, L33, p. L33. DOI: 10.1088/2041-8205/741/2/L33. arXiv: 1107.1483 [astro-ph.CO].

Bournaud, Frédéric et al. (2011b). "Star formation in galaxy mergers: ISM turbulence, dense gas excess, and scaling relations for disks and starbusts". In: *Astrophysical Dynamics: From Stars to Galaxies*. Ed. by Nicholas H. Brummell et al. Vol. 271. IAU Symposium, pp. 160–169. DOI: 10.1017/S1743921311017571. arXiv: 1012.5227 [astro-ph.CO].

Bournaud, Frédéric et al. (2012). "An Observed Link between Active Galactic Nuclei and Violent Disk Instabilities in High-redshift Galaxies". In: *ApJ*

757.1, 81, p. 81. DOI: 10.1088/0004-637X/757/1/81. arXiv: 1111.0987 [astro-ph.CO].

Brammer, G.B. et al. (2009). "The Dead Sequence: A Clear Bimodality in Galaxy Colors from $z = 0$ to $z = 2.5$". In: *ApJL* 706.1, pp. L173–L177. DOI: 10.1088/0004-637X/706/1/L173. arXiv: 0910.2227 [astro-ph.CO].

Bruzual, G. and S. Charlot (2003). "Stellar population synthesis at the resolution of 2003". In: *MNRAS* 344.4, pp. 1000–1028. DOI: 10.1046/j.1365-8711.2003.06897.x. arXiv: astro-ph/0309134 [astro-ph].

Buat, V. et al. (2002). "Star formation and dust extinction in nearby star-forming and starburst galaxies". In: *A&A* 383, pp. 801–812. DOI: 10.1051/0004-6361:20011832.

Buat, V. et al. (2005). "Dust Attenuation in the Nearby Universe: A Comparison between Galaxies Selected in the Ultraviolet and in the Far-Infrared". In: *ApJL* 619.1, pp. L51–L54. DOI: 10.1086/423241. arXiv: astro-ph/0411343 [astro-ph].

Buat, V. et al. (2012). "GOODS-Herschel: dust attenuation properties of UV selected high redshift galaxies". In: *A&A* 545, A141, A141. DOI: 10.1051/0004-6361/201219405. arXiv: 1207.3528 [astro-ph.CO].

Burkert, Andreas et al. (2008). "SAURON's Challenge for the Major Merger Scenario of Elliptical Galaxy Formation". In: *ApJ* 685.2, pp. 897–903. DOI: 10.1086/591632. arXiv: 0710.0663 [astro-ph].

Cacciato, Marcello, Avishai Dekel, and Shy Genel (2012). "Evolution of violent gravitational disc instability in galaxies: late stabilization by transition from gas to stellar dominance". In: *MNRAS* 421.1, pp. 818–831. DOI: 10.1111/j.1365-2966.2011.20359.x. arXiv: 1110.2412 [astro-ph.CO].

Calabrò, A. et al. (2018). "Near-infrared Emission Lines in Starburst Galaxies at $0.5 < z < 0.9$: Discovery of a Merger Sequence of Extreme Obscurations". In: *ApJL* 862.2, L22, p. L22. DOI: 10.3847/2041-8213/aad33e. arXiv: 1807.04350 [astro-ph.GA].

Calabrò, A. et al. (2019a). "Deciphering an evolutionary sequence of merger stages in infrared-luminous starburst galaxies at z $\sim$ 0.7". In: *A&A* 623, A64, A64. DOI: 10.1051/0004-6361/201834522. arXiv: 1901.05013 [astro-ph.GA].

Calabrò, A. et al. (2019b). "Merger induced clump formation in distant infrared luminous starburst galaxies". In: *submitted to A&A*.

Calzetti, D. et al. (2005). "Star Formation in NGC 5194 (M51a): The Panchromatic View from GALEX to Spitzer". In: *ApJ* 633.2, pp. 871–893. DOI: 10.1086/466518. arXiv: astro-ph/0507427 [astro-ph].

Calzetti, Daniela (1997). "Reddening and Star Formation in Starburst Galaxies". In: *AJ* 113, pp. 162–184. DOI: 10.1086/118242. arXiv: astro-ph/9610184 [astro-ph].

— (2001). "The Dust Opacity of Star-forming Galaxies". In: *PASP* 113.790, pp. 1449–1485. DOI: 10.1086/324269. arXiv: astro-ph/0109035 [astro-ph].

Calzetti, Daniela, Anne L. Kinney, and Thaisa Storchi-Bergmann (1994). "Dust Extinction of the Stellar Continua in Starburst Galaxies: The Ultraviolet and Optical Extinction Law". In: *ApJ* 429, p. 582. DOI: 10.1086/174346.

— (1996). "Dust Obscuration in Starburst Galaxies from Near-Infrared Spectroscopy". In: *ApJ* 458, p. 132. DOI: 10.1086/176797.

Calzetti, Daniela et al. (2000). "The Dust Content and Opacity of Actively Star-forming Galaxies". In: *ApJ* 533.2, pp. 682–695. DOI: 10.1086/308692. arXiv: astro-ph/9911459 [astro-ph].

Caplan, J. and L. Deharveng (1986). "Extinction and reddening of H II regions in the Large Magellanic Cloud." In: *A&A* 155, pp. 297–313.

Cappelluti, N. et al. (2009). "The XMM-Newton wide-field survey in the COSMOS field. The point-like X-ray source catalogue". In: *A&A* 497.2, pp. 635–648. DOI: 10.1051/0004-6361/200810794. arXiv: 0901.2347 [astro-ph.HE].

Cardelli, Jason A., Geoffrey C. Clayton, and John S. Mathis (1989). "The Relationship between Infrared, Optical, and Ultraviolet Extinction". In: *ApJ* 345, p. 245. DOI: 10.1086/167900.

Casey, Caitlin M., Desika Narayanan, and Asantha Cooray (2014). "Dusty star-forming galaxies at high redshift". In: *Physics Reports* 541.2, pp. 45–161. DOI: 10.1016/j.physrep.2014.02.009. arXiv: 1402.1456 [astro-ph.CO].

Casey, C.M. et al. (2011). "Molecular gas in submillimetre-faint, star-forming ultraluminous galaxies at $z > 1$." In: *MNRAS* 415.3, pp. 2723–2743. DOI: 10.1111/j.1365-2966.2011.18885.x. arXiv: 0910.5756 [astro-ph.CO].

Ceverino, Daniel, Avishai Dekel, and Frederic Bournaud (2010). "High-redshift clumpy discs and bulges in cosmological simulations". In: *MNRAS* 404.4, pp. 2151–2169. DOI: 10.1111/j.1365-2966.2010.16433.x. arXiv: 0907.3271 [astro-ph.CO].

Chabrier, Gilles (2003). "Galactic Stellar and Substellar Initial Mass Function". In: *PASP* 115.809, pp. 763–795. DOI: 10.1086/376392. arXiv: astro-ph/0304382 [astro-ph].

Charlot, Stéphane and S. Michael Fall (2000). "A Simple Model for the Absorption of Starlight by Dust in Galaxies". In: *ApJ* 539.2, pp. 718–731. DOI: 10.1086/309250. arXiv: astro-ph/0003128 [astro-ph].

Cibinel, A. et al. (2017). "ALMA constraints on star-forming gas in a prototypical $z = 1.5$ clumpy galaxy: the dearth of CO(5-4) emission from UV-bright clumps". In: *MNRAS* 469.4, pp. 4683–4704. DOI: 10.1093/mnras/stx1112. arXiv: 1703.02550 [astro-ph.GA].

Cibinel, A. et al. (2019). "Early-and late-stage mergers among main sequence and starburst galaxies at $0.2 \leq z \leq 2$". In: *MNRAS* 485.4, pp. 5631–5651. DOI: 10.1093/mnras/stz690. arXiv: 1809.00715 [astro-ph.GA].

Cid Fernandes, R. et al. (2010). "Alternative diagnostic diagrams and the 'forgotten' population of weak line galaxies in the SDSS". In: *MNRAS* 403.2, pp. 1036–1053. DOI: 10.1111/j.1365-2966.2009.16185.x. arXiv: 0912.1643 [astro-ph.CO].

Cisternas, Mauricio et al. (2011). "The Bulk of the Black Hole Growth Since z ∼1 Occurs in a Secular Universe: No Major Merger-AGN Connection". In: *ApJ* 726.2, 57, p. 57. DOI: 10.1088/0004-637X/726/2/57. arXiv: 1009.3265 [astro-ph.CO].

Civano, F. et al. (2015). "The Nustar Extragalactic Surveys: Overview and Catalog from the COSMOS Field". In: *ApJ* 808.2, 185, p. 185. DOI: 10.1088/0004-637X/808/2/185. arXiv: 1511.04185 [astro-ph.HE].

Civano, F. et al. (2016). "The Chandra Cosmos Legacy Survey: Overview and Point Source Catalog". In: *ApJ* 819.1, 62, p. 62. DOI: 10.3847/0004-637X/819/1/62. arXiv: 1601.00941 [astro-ph.GA].

Combes, F. (2003). "AGN Fueling: The observational point of view". In: *Active Galactic Nuclei: From Central Engine to Host Galaxy*. Ed. by Suzy Collin, Francoise Combes, and Isaac Shlosman. Vol. 290. Astronomical Society of the Pacific Conference Series, p. 411. arXiv: astro-ph/0210232 [astro-ph].

Combes, F. et al. (1990). "Box and peanut shapes generated by stellar bars." In: *A&A* 233, p. 82.

Combes, F. et al. (2013). "ALMA observations of feeding and feedback in nearby Seyfert galaxies: an AGN-driven outflow in NGC 1433". In: *A&A* 558, A124, A124. DOI: 10.1051/0004-6361/201322288. arXiv: 1309.7486 [astro-ph.CO].

Condon, J. J., M. L. Anderson, and G. Helou (1991). "Correlations between Far-Infrared, Radio, and Blue Luminosities of Spiral Galaxies". In: *ApJ* 376, p. 95. DOI: 10.1086/170258.

Condon, J.J. (1992). "Radio emission from normal galaxies." In: *ARA&A* 30, pp. 575–611. DOI: 10.1146/annurev.aa.30.090192.003043.

Conselice, Christopher J., Cui Yang, and Asa F.L. Bluck (2009). "The structures of distant galaxies - III. The merger history of over 20000 massive galaxies at $z < 1.2$." In: *MNRAS* 394.4, pp. 1956–1972. DOI: 10.1111/j.1365-2966.2009.14396.x. arXiv: 0812.3237 [astro-ph].

Conselice, Christopher J. et al. (2003). "A Direct Measurement of Major Galaxy Mergers at z<∼3". In: *AJ* 126.3, pp. 1183–1207. DOI: 10.1086/377318. arXiv: astro-ph/0306106 [astro-ph].

Coogan, R.T. et al. (2018). "Merger-driven star formation activity in Cl J1449+0856 at $z = 1.99$ as seen by ALMA and JVLA". In: *MNRAS* 479.1, pp. 703–729. DOI: 10.1093/mnras/sty1446. arXiv: 1805.09789 [astro-ph.GA].

Cowie, L. L. et al. (2017). "A Submillimeter Perspective on the GOODS Fields (SUPER GOODS). I. An Ultradeep SCUBA-2 Survey of the GOODS-N". In: *ApJ* 837.2, 139, p. 139. DOI: 10.3847/1538-4357/aa60bb. arXiv: 1702.03002 [astro-ph.GA].

Cox, T. J. et al. (2006). "The Kinematic Structure of Merger Remnants". In: *ApJ* 650.2, pp. 791–811. DOI: 10.1086/507474. arXiv: astro-ph/0607446 [astro-ph].

da Cunha, Elisabete, Stéphane Charlot, and David Elbaz (2008). "A simple model to interpret the ultraviolet, optical and infrared emission from galaxies". In: *MNRAS* 388.4, pp. 1595–1617. DOI: 10.1111/j.1365-2966.2008.13535.x. arXiv: 0806.1020 [astro-ph].

Daddi, E. et al. (2007). "Multiwavelength Study of Massive Galaxies at $z \sim 2$. I. Star Formation and Galaxy Growth". In: *ApJ* 670.1, pp. 156–172. DOI: 10.1086/521818. arXiv: 0705.2831 [astro-ph].

Daddi, E. et al. (2008). "Vigorous Star Formation with Low Efficiency in Massive Disk Galaxies at $z = 1.5$." In: *ApJL* 673.1, p. L21. DOI: 10.1086/527377. arXiv: 0711.4995 [astro-ph].

Daddi, E. et al. (2009). "Two Bright Submillimeter Galaxies in a z = 4.05 Protocluster in Goods-North, and Accurate Radio-Infrared Photometric Redshifts". In: *ApJ* 694.2, pp. 1517–1538. DOI: 10.1088/0004-637X/694/2/1517. arXiv: 0810.3108 [astro-ph].

Daddi, E. et al. (2010). "Very High Gas Fractions and Extended Gas Reservoirs in $z = 1.5$ Disk Galaxies". In: *ApJ* 713.1, pp. 686–707. DOI: 10.1088/0004-637X/713/1/686. arXiv: 0911.2776 [astro-ph.CO].

Daddi, E. et al. (2015). "CO excitation of normal star-forming galaxies out to $z = 1.5$ as regulated by the properties of their interstellar medium". In: *A&A* 577, A46, A46. DOI: 10.1051/0004-6361/201425043. arXiv: 1409.8158 [astro-ph.GA].

Dasyra, K.M. et al. (2006). "Dynamical Properties of Ultraluminous Infrared Galaxies. I. Mass Ratio Conditions for ULIRG Activity in Interacting Pairs". In: *ApJ* 638.2, pp. 745–758. DOI: 10.1086/499068. arXiv: astro-ph/0510670 [astro-ph].

Davies, R.I. et al. (2007). "A Close Look at Star Formation around Active Galactic Nuclei". In: *ApJ* 671.2, pp. 1388–1412. DOI: 10.1086/523032. arXiv: 0704.1374 [astro-ph].

Davis, Timothy A. et al. (2019). "Evolution of the cold gas properties of simulated post-starburst galaxies". In: *MNRAS* 484.2, pp. 2447–2461. DOI: 10.1093/mnras/stz180. arXiv: 1810.00882 [astro-ph.GA].

De Cia, A. et al. (2016). "Dust-depletion sequences in damped Lyman-α absorbers. A unified picture from low-metallicity systems to the Galaxy". In: *A&A* 596, A97, A97. DOI: 10.1051/0004-6361/201527895. arXiv: 1608.08621 [astro-ph.GA].

de Vaucouleurs, Gerard (1948). "Recherches sur les Nebuleuses Extragalactiques". In: *Annales d'Astrophysique* 11, p. 247.

Dekel, Avishai and Yuval Birnboim (2006). "Galaxy bimodality due to cold flows and shock heating". In: *MNRAS* 368.1, pp. 2–20. DOI: 10.1111/j.1365-2966.2006.10145.x. arXiv: astro-ph/0412300 [astro-ph].

Dekel, Avishai, Re'em Sari, and Daniel Ceverino (2009). "Formation of Massive Galaxies at High Redshift: Cold Streams, Clumpy Disks, and Compact Spheroids". In: *ApJ* 703.1, pp. 785–801. DOI: 10.1088/0004-637X/703/1/785. arXiv: 0901.2458 [astro-ph.GA].

Del Moro, A. et al. (2013). "GOODS-Herschel: radio-excess signature of hidden AGN activity in distant star-forming galaxies". In: *A&A* 549, A59, A59. DOI: 10.1051/0004-6361/201219880. arXiv: 1210.2521 [astro-ph.CO].

Di Matteo, P. et al. (2008). "On the frequency, intensity, and duration of starburst episodes triggered by galaxy interactions and mergers". In: *A&A* 492.1, pp. 31–49. DOI: 10.1051/0004-6361:200809480. arXiv: 0809.2592 [astro-ph].

Di Matteo, Tiziana, Volker Springel, and Lars Hernquist (2005). "Energy input from quasars regulates the growth and activity of black holes and their host galaxies". In: *Nature* 433.7026, pp. 604–607. DOI: 10.1038/nature03335. arXiv: astro-ph/0502199 [astro-ph].

Díaz, Angeles I. and Enrique Pérez-Montero (2000). "An empirical calibration of nebular abundances based on the sulphur emission lines". In: *MNRAS* 312.1, pp. 130–138. DOI: 10.1046/j.1365-8711.2000.03117.x. arXiv: astro-ph/9909492 [astro-ph].

Draine, B. T. (2003). "Scattering by Interstellar Dust Grains. I. Optical and Ultraviolet". In: *ApJ* 598.2, pp. 1017–1025. DOI: 10.1086/379118. arXiv: astro-ph/0304060 [astro-ph].

Draine, B.T. and Aigen Li (2007). "Infrared Emission from Interstellar Dust. IV. The Silicate-Graphite-PAH Model in the Post-Spitzer Era". In: *ApJ* 657.2, pp. 810–837. DOI: 10.1086/511055. arXiv: astro-ph/0608003 [astro-ph].

Draper, A.R. and D.R. Ballantyne (2012). "A Tale of Two Populations: The Contribution of Merger and Secular Processes to the Evolution of Active Galactic Nuclei". In: *ApJ* 751.1, 72, p. 72. DOI: 10.1088/0004-637X/751/1/72. arXiv: 1203.5117 [astro-ph.CO].

Dubois, Y. and R. Teyssier (2008). "Supernova Feedback in Galaxy Formation". In: *Pathways Through an Eclectic Universe*. Ed. by J.H. Knapen, T.J. Mahoney, and A. Vazdekis. Vol. 390. Astronomical Society of the Pacific Conference Series, p. 388.

Duc, P. A. et al. (2013). "Probing the mass assembly of massive nearby galaxies with deep imaging". In: *The Intriguing Life of Massive Galaxies*. Ed. by Daniel Thomas, Anna Pasquali, and Ignacio Ferreras. Vol. 295. IAU Symposium, pp. 358–361. DOI: 10.1017/S174392131300536X. arXiv: 1302.6628 [astro-ph.CO].

Dunne, Loretta and Stephen A. Eales (2001). "The SCUBA Local Universe Galaxy Survey - II. 450-μm data: evidence for cold dust in bright IRAS galaxies". In: *MNRAS* 327.3, pp. 697–714. DOI: 10.1046/j.1365-8711.2001.04789.x. arXiv: astro-ph/0106362 [astro-ph].

Elbaz, D. et al. (2007). "The reversal of the star formation-density relation in the distant universe". In: *A&A* 468.1, pp. 33–48. DOI: 10.1051/0004-6361:20077525. arXiv: astro-ph/0703653 [astro-ph].

Elbaz, David and Catherine J. Cesarsky (2003). "A Fossil Record of Galaxy Encounters". In: *Science* 300.5617, pp. 270–274. DOI: 10.1126/science.1081525. arXiv: astro-ph/0304492 [astro-ph].

Eliche-Moral, M.C. et al. (2006). "Growth of galactic bulges by mergers. II. Low-density satellites". In: *A&A* 457.1, pp. 91–108. DOI: 10.1051/0004-6361:20065394. arXiv: astro-ph/0606751 [astro-ph].

Ellison, S.L., D.R. Patton, and R.C. Hickox (2015). "Galaxy pairs in the Sloan Digital Sky Survey - XII. The fuelling mechanism of low-excitation radio-loud AGN." In: *MNRAS* 451, pp. L35–L39. DOI: 10.1093/mnrasl/slv061. arXiv: 1504.06255 [astro-ph.GA].

Elmegreen, Bruce G., Frédéric Bournaud, and Debra Meloy Elmegreen (2008). "Bulge Formation by the Coalescence of Giant Clumps in Primordial Disk Galaxies". In: *ApJ* 688.1, pp. 67–77. DOI: 10.1086/592190. arXiv: 0808.0716 [astro-ph].

Elmegreen, Bruce G. et al. (2005). "On the Origin of Exponential Disks at High Redshift". In: *ApJ* 634.1, pp. 101–108. DOI: 10.1086/496952. arXiv: astro-ph/0510244 [astro-ph].

Elmegreen, Bruce G. et al. (2013). "Massive Clumps in Local Galaxies: Comparisons with High-redshift Clumps". In: *ApJ* 774.1, 86, p. 86. DOI: 10.1088/0004-637X/774/1/86. arXiv: 1308.0306 [astro-ph.CO].

Elmegreen, Debra Meloy (2007). "Clumpy Galaxies in the Early Universe". In: *Galaxy Evolution across the Hubble Time*. Ed. by Françoise Combes and Jan Palouš. Vol. 235. IAU Symposium, pp. 376–380. DOI: 10.1017/S1743921306010210.

Elvis, Martin et al. (1994). "Atlas of Quasar Energy Distributions". In: *ApJS* 95, p. 1. DOI: 10.1086/192093.

Epinat, B. et al. (2009). "Integral field spectroscopy with SINFONI of VVDS galaxies. I. Galaxy dynamics and mass assembly at $1.2 < z < 1.6$." In: *A&A* 504.3, pp. 789–805. DOI: 10.1051/0004-6361/200911995. arXiv: 0903.1216 [astro-ph.CO].

Faisst, Andreas L. et al. (2018). "Empirical Modeling of the Redshift Evolution of the [NII]/H_α Ratio for Galaxy Redshift Surveys". In: *ApJ* 855.2, 132, p. 132. DOI: 10.3847/1538-4357/aab1fc. arXiv: 1710.00834 [astro-ph.GA].

Fensch, J. et al. (2017). "High-redshift major mergers weakly enhance star formation". In: *MNRAS* 465.2, pp. 1934–1949. DOI: 10.1093/mnras/stw2920. arXiv: 1610.03877 [astro-ph.GA].

Fitzpatrick, Edward L. (1986). "An average interstellar extinction curve for the Large Magellanic Cloud." In: *AJ* 92, pp. 1068–1073. DOI: 10.1086/114237.

— (1999). "Correcting for the Effects of Interstellar Extinction". In: *PASP* 111.755, pp. 63–75. DOI: 10.1086/316293. arXiv: astro-ph/9809387 [astro-ph].

Förster Schreiber, N.M. et al. (2006). "SINFONI Integral Field Spectroscopy of $z \sim 2$ UV-selected Galaxies: Rotation Curves and Dynamical Evolution". In: *ApJ* 645.2, pp. 1062–1075. DOI: 10.1086/504403. arXiv: astro-ph/0603559 [astro-ph].

Förster Schreiber, N.M. et al. (2009). "The SINS Survey: SINFONI Integral Field Spectroscopy of $z \sim 2$ Star-forming Galaxies". In: *ApJ* 706.2,

pp. 1364–1428. DOI: 10.1088/0004-637X/706/2/1364. arXiv: 0903.1872 [astro-ph.CO].

Franzetti, P. et al. (2007). "The VIMOS-VLT deep survey. Color bimodality and the mix of galaxy populations up to $z \sim 2$." In: *A&A* 465.3, pp. 711–723. DOI: 10.1051/0004-6361:20065942. arXiv: astro-ph/0607075 [astro-ph].

Freundlich, J. et al. (2019). "PHIBSS2: survey design and $z = 0.5$-0.8 results. Molecular gas reservoirs during the winding-down of star formation". In: *A&A* 622, A105, A105. DOI: 10.1051/0004-6361/201732223. arXiv: 1812.08180 [astro-ph.GA].

Gao, Yu and Philip M. Solomon (1999). "Molecular Gas Depletion and Starbursts in Luminous Infrared Galaxy Mergers". In: *ApJL* 512.2, pp. L99–L103. DOI: 10.1086/311878. arXiv: astro-ph/9812320 [astro-ph].

Garland, C.A. et al. (2015). "Nearby Clumpy, Gas Rich, Star-forming Galaxies: Local Analogs of High-redshift Clumpy Galaxies". In: *ApJ* 807.2, 134, p. 134. DOI: 10.1088/0004-637X/807/2/134. arXiv: 1506.04649 [astro-ph.GA].

Gaskell, C. Martin (2009). "What broad emission lines tell us about how active galactic nuclei work". In: *newAR* 53.7-10, pp. 140–148. DOI: 10.1016/j.newar.2009.09.006. arXiv: 0908.0386 [astro-ph.CO].

Geach, J. E. et al. (2017). "The SCUBA-2 Cosmology Legacy Survey: 850 μm maps, catalogues and number counts". In: *MNRAS* 465.2, pp. 1789–1806. DOI: 10.1093/mnras/stw2721. arXiv: 1607.03904 [astro-ph.GA].

Genzel, R. et al. (1998). "What Powers Ultraluminous IRAS Galaxies?" In: *ApJ* 498.2, pp. 579–605. DOI: 10.1086/305576. arXiv: astro-ph/9711255 [astro-ph].

Genzel, R. et al. (2008). "From Rings to Bulges: Evidence for Rapid Secular Galaxy Evolution at $z \sim 2$ from Integral Field Spectroscopy in the SINS Survey". In: *ApJ* 687.1, pp. 59–77. DOI: 10.1086/591840. arXiv: 0807.1184 [astro-ph].

Genzel, R. et al. (2017). "Strongly baryon-dominated disk galaxies at the peak of galaxy formation ten billion years ago". In: *Nature* 543.7645, pp. 397–401. DOI: 10.1038/nature21685. arXiv: 1703.04310 [astro-ph.GA].

Ghavamian, Parviz et al. (2017). "Integral Field Spectroscopy of Balmer-dominated Shocks in the Magellanic Cloud Supernova Remnant N103B". In: *ApJ* 847.2, 122, p. 122. DOI: 10.3847/1538-4357/aa83b8. arXiv: 1705.03086 [astro-ph.HE].

Gil de Paz, Armando et al. (2007). "The GALEX Ultraviolet Atlas of Nearby Galaxies". In: *ApJS* 173.2, pp. 185–255. DOI: 10.1086/516636. arXiv: astro-ph/0606440 [astro-ph].

Goldader, Jeffrey D. et al. (2002). "Far-Infrared Galaxies in the Far-Ultraviolet". In: *ApJ* 568.2, pp. 651–678. DOI: 10.1086/339165. arXiv: astro-ph/0112352 [astro-ph].

Gordon, Karl D. and Geoffrey C. Clayton (1998). "Starburst-like Dust Extinction in the Small Magellanic Cloud". In: *ApJ* 500.2, pp. 816–824. DOI: 10.1086/305774. arXiv: astro-ph/9802003 [astro-ph].

Goto, Tomotsugu (2007). "A catalogue of local E+A (post-starburst) galaxies selected from the Sloan Digital Sky Survey Data Release 5". In: *MNRAS* 381.1, pp. 187–193. DOI: 10.1111/j.1365-2966.2007.12227.x. arXiv: 0801.1106 [astro-ph].

Governato, F. et al. (2010). "Bulgeless dwarf galaxies and dark matter cores from supernova-driven outflows". In: *Nature* 463.7278, pp. 203–206. DOI: 10.1038/nature08640. arXiv: 0911.2237 [astro-ph.CO].

Graham, Alister W. and C. Clare Worley (2008). "Inclination- and dust-corrected galaxy parameters: bulge-to-disc ratios and size-luminosity relations". In: *MNRAS* 388.4, pp. 1708–1728. DOI: 10.1111/j.1365-2966.2008.13506.x. arXiv: 0805.3565 [astro-ph].

Granato, G. L. et al. (2000). "The Infrared Side of Galaxy Formation. I. The Local Universe in the Semianalytical Framework". In: *ApJ* 542.2, pp. 710–730. DOI: 10.1086/317032. arXiv: astro-ph/0001308 [astro-ph].

Guo, Yicheng et al. (2015). "Clumpy Galaxies in CANDELS. I. The Definition of UV Clumps and the Fraction of Clumpy Galaxies at $0.5 < z < 3$." In: *ApJ* 800.1, 39, p. 39. DOI: 10.1088/0004-637X/800/1/39. arXiv: 1410.7398 [astro-ph.GA].

Güver, Tolga and Feryal Özel (2009). "The relation between optical extinction and hydrogen column density in the Galaxy". In: *MNRAS* 400.4, pp. 2050–2053. DOI: 10.1111/j.1365-2966.2009.15598.x. arXiv: 0903.2057 [astro-ph.GA].

Guyon, O., D.B. Sanders, and Alan Stockton (2006). "Near-Infrared Adaptive Optics Imaging of QSO Host Galaxies". In: *ApJS* 166.1, pp. 89–127. DOI: 10.1086/505030. arXiv: astro-ph/0605079 [astro-ph].

Haan, S. et al. (2013). "The build-up of nuclear stellar cusps in extreme starburst galaxies and major mergers". In: *MNRAS* 434.2, pp. 1264–1286. DOI: 10.1093/mnras/stt1087. arXiv: 1306.4337 [astro-ph.CO].

Heinis, S. et al. (2014). "HerMES: dust attenuation and star formation activity in ultraviolet-selected samples from $z \sim 4$ to ~ 1.5." In: *MNRAS* 437.2, pp. 1268–1283. DOI: 10.1093/mnras/stt1960. arXiv: 1310.3227 [astro-ph.CO].

Hernquist, Lars (1989). "Tidal triggering of starbursts and nuclear activity in galaxies". In: *Nature* 340.6236, pp. 687–691. DOI: 10.1038/340687a0.

Hibbard, J.E. and W.D. Vacca (1997). "The Apparent Morphology of Peculiar Galaxies at Intermediate to High Redshifts". In: *AJ* 114, p. 1741. DOI: 10.1086/118603. arXiv: astro-ph/9707275 [astro-ph].

Hodge, J.A. et al. (2019). "ALMA Reveals Potential Evidence for Spiral Arms, Bars, and Rings in High-redshift Submillimeter Galaxies". In: *ApJ* 876.2, 130, p. 130. DOI: 10.3847/1538-4357/ab1846. arXiv: 1810.12307 [astro-ph.GA].

Hopkins, Philip F. (2012). "Dynamical delays between starburst and AGN activity in galaxy nuclei". In: *MNRAS* 420.1, pp. L8–L12. DOI: 10.1111/j.1745-3933.2011.01179.x. arXiv: 1101.4230 [astro-ph.CO].

Hopkins, Philip F. and Martin Elvis (2010). "Quasar feedback: more bang for your buck". In: *MNRAS* 401.1, pp. 7–14. DOI: 10.1111/j.1365-2966.2009.15643.x. arXiv: 0904.0649 [astro-ph.CO].

Hopkins, Philip F. et al. (2008a). "A Cosmological Framework for the Co-Evolution of Quasars, Supermassive Black Holes, and Elliptical Galaxies. I. Galaxy Mergers and Quasar Activity". In: *ApJS* 175.2, pp. 356–389. DOI: 10.1086/524362. arXiv: 0706.1243 [astro-ph].

Hopkins, Philip F. et al. (2008b). "A Cosmological Framework for the Co-Evolution of Quasars, Supermassive Black Holes, and Elliptical Galaxies. II. Formation of Red Ellipticals". In: *ApJS* 175.2, pp. 390–422. DOI: 10.1086/524363. arXiv: 0706.1246 [astro-ph].

Hopkins, Philip F. et al. (2010). "Mergers in ΛCDM: Uncertainties in Theoretical Predictions and Interpretations of the Merger Rate". In: *ApJ* 724.2, pp. 915–945. DOI: 10.1088/0004-637X/724/2/915. arXiv: 1004.2708 [astro-ph.CO].

Horne, K. (1986). "An optimal extraction algorithm for CCD spectroscopy." In: *PASP* 98, pp. 609–617. DOI: 10.1086/131801.

Howell, Justin H. et al. (2010). "The Great Observatories All-sky LIRG Survey: Comparison of Ultraviolet and Far-infrared Properties". In: *ApJ* 715.1, pp. 572–588. DOI: 10.1088/0004-637X/715/1/572. arXiv: 1004.0985 [astro-ph.GA].

Ibar, Edo et al. (2008). "Exploring the infrared/radio correlation at high redshift". In: *MNRAS* 386.2, pp. 953–962. DOI: 10.1111/j.1365-2966.2008.13077.x. arXiv: 0802.2694 [astro-ph].

Ilbert, O. et al. (2006). "Accurate photometric redshifts for the CFHT legacy survey calibrated using the VIMOS VLT deep survey". In: *A&A* 457.3, pp. 841–856. DOI: 10.1051/0004-6361:20065138. arXiv: astro-ph/0603217 [astro-ph].

Ilbert, O. et al. (2009). "Cosmos Photometric Redshifts with 30-Bands for 2-deg^2". In: *ApJ* 690.2, pp. 1236–1249. DOI: 10.1088/0004-637X/690/2/1236. arXiv: 0809.2101 [astro-ph].

Ilbert, O. et al. (2013). "Mass assembly in quiescent and star-forming galaxies since $z \simeq 4$ from UltraVISTA". In: *A&A* 556, A55, A55. DOI: 10.1051/0004-6361/201321100. arXiv: 1301.3157 [astro-ph.CO].

Ilbert, O. et al. (2015). "Evolution of the specific star formation rate function at z< 1.4 Dissecting the mass-SFR plane in COSMOS and GOODS". In: *A&A* 579, A2, A2. DOI: 10.1051/0004-6361/201425176. arXiv: 1410.4875 [astro-ph.GA].

Immeli, A. et al. (2004a). "Gas physics, disk fragmentation, and bulge formation in young galaxies". In: *A&A* 413, pp. 547–561. DOI: 10.1051/0004-6361:20034282. arXiv: astro-ph/0312139 [astro-ph].

Immeli, Andreas et al. (2004b). "Subgalactic Clumps at High Redshift: A Fragmentation Origin?" In: *ApJ* 611.1, pp. 20–25. DOI: 10.1086/422179. arXiv: astro-ph/0406135 [astro-ph].

Iono, Daisuke et al. (2009). "Luminous Infrared Galaxies with the Submillimeter Array. II. Comparing the CO (3-2) Sizes and Luminosities of Local and High-Redshift Luminous Infrared Galaxies". In: *ApJ* 695.2, pp. 1537–1549. DOI: 10.1088/0004-637X/695/2/1537. arXiv: 0902.0121 [astro-ph.CO].

Ivison, R.J. et al. (2010). "The far-infrared/radio correlation as probed by Herschel". In: *A&A* 518, L31, p. L31. DOI: 10.1051/0004-6361/201014552. arXiv: 1005.1072 [astro-ph.CO].

Jiménez-Andrade, E. F. et al. (2019). "Radio continuum size evolution of star-forming galaxies over 0.35 < z < 2.25". In: *A&A* 625, A114, A114. DOI: 10.1051/0004-6361/201935178. arXiv: 1903.12217 [astro-ph.GA].

Jin, S. et al. (2019). "Discovery of four cold dusty galaxies at $z = 3.62$-5.85 in the COSMOS field: direct evidence of CMB impact on high-redshift galaxy observables". In: *arXiv e-prints*, arXiv:1906.00040, arXiv:1906.00040. arXiv: 1906.00040 [astro-ph.GA].

Jin, Shuo-Wen et al. (2014). "Color-Magnitude Distribution of Face-on nearby Galaxies in Sloan Digital Sky Survey DR7". In: *ApJ* 787.1, 63, p. 63. DOI: 10.1088/0004-637X/787/1/63. arXiv: 1404.2398 [astro-ph.GA].

Jin, Shuowen et al. (2018). "Super-deblended Dust Emission in Galaxies. II. Far-IR to (Sub)millimeter Photometry and High-redshift Galaxy Candidates in the Full COSMOS Field". In: *ApJ* 864.1, 56, p. 56. DOI: 10.3847/1538-4357/aad4af. arXiv: 1807.04697 [astro-ph.GA].

Johnson, Benjamin D. et al. (2007). "Ultraviolet through Infrared Spectral Energy Distributions from 1000 SDSS Galaxies: Dust Attenuation". In: *ApJS* 173.2, pp. 392–403. DOI: 10.1086/522960. arXiv: 0712.3573 [astro-ph].

Joseph, R.D. and G.S. Wright (1985). "Recent star formation in interacting galaxies - II. Super starbursts in merging galaxies." In: *MNRAS* 214, pp. 87–95. DOI: 10.1093/mnras/214.2.87.

Juneau, S. et al. (2009). "Enhanced Dense Gas Fraction in Ultraluminous Infrared Galaxies". In: *ApJ* 707.2, pp. 1217–1232. DOI: 10.1088/0004-637X/707/2/1217. arXiv: 0911.0413 [astro-ph.CO].

Kartaltepe, Jeyhan S. et al. (2010). "A Multiwavelength Study of a Sample of 70 μm Selected Galaxies in the COSMOS Field. II. The Role of Mergers in Galaxy Evolution". In: *ApJ* 721.1, pp. 98–123. DOI: 10.1088/0004-637X/721/1/98. arXiv: 1006.4956 [astro-ph.CO].

Kauffmann, Guinevere et al. (2003). "The host galaxies of active galactic nuclei". In: *MNRAS* 346.4, pp. 1055–1077. DOI: 10.1111/j.1365-2966.2003.07154.x. arXiv: astro-ph/0304239 [astro-ph].

Kawakatu, Nozomu et al. (2006). "Type I Ultraluminous Infrared Galaxies: Transition Stage from ULIRGs to QSOs". In: *ApJ* 637.1, pp. 104–113. DOI: 10.1086/498255. arXiv: astro-ph/0509459 [astro-ph].

Kehrig, C. et al. (2006). "A spectroscopic study of the near-IR [SIII] lines in a sample of HII galaxies: chemical abundances". In: *A&A* 457.2, pp. 477–

484. DOI: 10.1051/0004-6361:20054488. arXiv: astro-ph/0606453 [astro-ph].

Kelson, Daniel D. (2003). "Optimal Techniques in Two-dimensional Spectroscopy: Background Subtraction for the 21st Century". In: *PASP* 115.808, pp. 688–699. DOI: 10.1086/375502. arXiv: astro-ph/0303507 [astro-ph].

Kennicutt Robert C., Jr., Peter Tamblyn, and Charles E. Congdon (1994). "Past and Future Star Formation in Disk Galaxies". In: *ApJ* 435, p. 22. DOI: 10.1086/174790.

Kereš, Dušan et al. (2005). "How do galaxies get their gas?" In: *MNRAS* 363.1, pp. 2–28. DOI: 10.1111/j.1365-2966.2005.09451.x. arXiv: astro-ph/0407095 [astro-ph].

Kewley, L.J. et al. (2001). "Theoretical Modeling of Starburst Galaxies". In: *ApJ* 556.1, pp. 121–140. DOI: 10.1086/321545. arXiv: astro-ph/0106324 [astro-ph].

Kim, Sungeun et al. (1999). "H I Shells in the Large Magellanic Cloud". In: *AJ* 118.6, pp. 2797–2823. DOI: 10.1086/301116.

Kocevski, Dale D. et al. (2012). "CANDELS: Constraining the AGN-Merger Connection with Host Morphologies at z ~2". In: *ApJ* 744.2, 148, p. 148. DOI: 10.1088/0004-637X/744/2/148. arXiv: 1109.2588 [astro-ph.CO].

Koekemoer, A.M. et al. (2007). "The COSMOS Survey: Hubble Space Telescope Advanced Camera for Surveys Observations and Data Processing". In: *ApJS* 172.1, pp. 196–202. DOI: 10.1086/520086. arXiv: astro-ph/0703095 [astro-ph].

Koekemoer, Anton M. et al. (2011). "CANDELS: The Cosmic Assembly Near-infrared Deep Extragalactic Legacy Survey—The Hubble Space Telescope Observations, Imaging Data Products, and Mosaics". In: *ApJS* 197.2, 36, p. 36. DOI: 10.1088/0067-0049/197/2/36. arXiv: 1105.3754 [astro-ph.CO].

Kormendy, John et al. (2009). "Structure and Formation of Elliptical and Spheroidal Galaxies". In: *ApJS* 182.1, pp. 216–309. DOI: 10.1088/0067-0049/182/1/216. arXiv: 0810.1681 [astro-ph].

Kraljic, Katarina, Frédéric Bournaud, and Marie Martig (2012). "The Two-phase Formation History of Spiral Galaxies Traced by the Cosmic Evolution of the Bar Fraction". In: *ApJ* 757.1, 60, p. 60. DOI: 10.1088/0004-637X/757/1/60. arXiv: 1207.0351 [astro-ph.GA].

Laigle, C. et al. (2016). "The COSMOS2015 Catalog: Exploring the $1 < z < 6$ Universe with Half a Million Galaxies". In: *ApJS* 224.2, 24, p. 24. DOI: 10.3847/0067-0049/224/2/24. arXiv: 1604.02350 [astro-ph.GA].

Laigle, C. et al. (2018). "COSMOS2015 photometric redshifts probe the impact of filaments on galaxy properties". In: *MNRAS* 474.4, pp. 5437–5458. DOI: 10.1093/mnras/stx3055. arXiv: 1702.08810 [astro-ph.GA].

Laine, Seppo et al. (2003). "A Hubble Space Telescope WFPC2 Investigation of the Nuclear Morphology in the Toomre Sequence of Merging Galaxies". In: *AJ* 126.6, pp. 2717–2739. DOI: 10.1086/379676. arXiv: astro-ph/0309377 [astro-ph].

LaMassa, Stephanie M. et al. (2016). "On R-W1 as A Diagnostic to Discover Obscured Active Galactic Nuclei in Wide-area X-Ray Surveys". In: *ApJ* 818.1, 88, p. 88. DOI: 10.3847/0004-637X/818/1/88. arXiv: 1511.02883 [astro-ph.GA].

Lanzuisi, G. et al. (2017). "Active galactic nuclei vs. host galaxy properties in the COSMOS field". In: *A&A* 602, A123, A123. DOI: 10.1051/0004-6361/201629955. arXiv: 1702.07357 [astro-ph.GA].

Laurikainen, E. et al. (2010). "Photometric scaling relations of lenticular and spiral galaxies". In: *MNRAS* 405.2, pp. 1089–1118. DOI: 10.1111/j.1365-2966.2010.16521.x. arXiv: 1002.4370 [astro-ph.CO].

Le Fèvre, Oliver et al. (2003). "Commissioning and performances of the VLT-VIMOS instrument". In: *Proceedings of the SPIE*. Ed. by Masanori Iye and Alan F.M. Moorwood. Vol. 4841. Society of Photo-Optical Instrumentation Engineers (SPIE) Conference Series, pp. 1670–1681. DOI: 10.1117/12.460959.

Le Floc'h, Emeric et al. (2009). "Deep Spitzer 24μm COSMOS Imaging. I. The Evolution of Luminous Dusty Galaxies—Confronting the Models". In: *ApJ* 703.1, pp. 222–239. DOI: 10.1088/0004-637X/703/1/222. arXiv: 0909.4303 [astro-ph.CO].

Leech, J. et al. (2010). "A CO(3-2) survey of a merging sequence of luminous infrared galaxies". In: *MNRAS* 406.2, pp. 1364–1378. DOI: 10.1111/j.1365-2966.2010.16775.x. arXiv: 1004.2650 [astro-ph.CO].

Leisawitz, D. and M. G. Hauser (1988). "On the Redistribution of OB Star Luminosity and the Warming of Nearby Molecular Clouds". In: *ApJ* 332, p. 954. DOI: 10.1086/166704.

Lilly, S. et al. (1999). "Deep sub-mm Surveys: High-z ULIRGs and the Formation of Spheroids". In: *The Formation of Galactic Bulges*. Ed. by C.M. Carollo, H.C. Ferguson, and R.F.G. Wyse, p. 26.

Lilly, S.J. et al. (2007). "zCOSMOS: A Large VLT/VIMOS Redshift Survey Covering $0 < z < 3$ in the COSMOS Field". In: *ApJS* 172.1, pp. 70–85. DOI: 10.1086/516589. arXiv: astro-ph/0612291 [astro-ph].

Lípari, S. et al. (2003). "Extreme galactic wind and Wolf-Rayet features in infrared mergers and infrared quasi-stellar objects". In: *MNRAS* 340.1, pp. 289–303. DOI: 10.1046/j.1365-8711.2003.06309.x. arXiv: astro-ph/0007316 [astro-ph].

Liu, Daizhong et al. (2015). "High-J CO versus Far-infrared Relations in Normal and Starburst Galaxies". In: *ApJL* 810.2, L14, p. L14. DOI: 10.1088/2041-8205/810/2/L14. arXiv: 1504.05897 [astro-ph.GA].

Liu, Daizhong et al. (2018). "Super-deblended Dust Emission in Galaxies. I. The GOODS-North Catalog and the Cosmic Star Formation Rate Density out to Redshift 6." In: *ApJ* 853.2, 172, p. 172. DOI: 10.3847/1538-4357/aaa600. arXiv: 1703.05281 [astro-ph.GA].

Lotz, Jennifer M., Joel Primack, and Piero Madau (2004). "A New Non-parametric Approach to Galaxy Morphological Classification". In: *AJ*

128.1, pp. 163–182. DOI: 10.1086/421849. arXiv: astro-ph/0311352 [astro-ph].

Lotz, Jennifer M. et al. (2008). "Galaxy merger morphologies and time-scales from simulations of equal-mass gas-rich disc mergers". In: *MNRAS* 391.3, pp. 1137–1162. DOI: 10.1111/j.1365-2966.2008.14004.x. arXiv: 0805.1246 [astro-ph].

Luo, Wentao, Xiaohu Yang, and Youcai Zhang (2014). "Connections between Galaxy Mergers and Starburst: Evidence from the Local Universe". In: *ApJL* 789.1, L16, p. L16. DOI: 10.1088/2041-8205/789/1/L16. arXiv: 1406.5315 [astro-ph.GA].

Lusso, E. et al. (2012). "Bolometric luminosities and Eddington ratios of X-ray selected active galactic nuclei in the XMM-COSMOS survey". In: *MNRAS* 425.1, pp. 623–640. DOI: 10.1111/j.1365-2966.2012.21513.x. arXiv: 1206.2642 [astro-ph.CO].

Lutz, D., S. Veilleux, and R. Genzel (1999). "Mid-Infrared and Optical Spectroscopy of Ultraluminous Infrared Galaxies: A Comparison". In: *ApJL* 517.1, pp. L13–L17. DOI: 10.1086/312014. arXiv: astro-ph/9903152 [astro-ph].

Lutz, D. et al. (2011). "PACS Evolutionary Probe (PEP) - A Herschel key program". In: *A&A* 532, A90, A90. DOI: 10.1051/0004-6361/201117107. arXiv: 1106.3285 [astro-ph.CO].

Madau, Piero and Mark Dickinson (2014). "Cosmic Star-Formation History". In: *ARA&A* 52, pp. 415–486. DOI: 10.1146/annurev-astro-081811-125615. arXiv: 1403.0007 [astro-ph.CO].

Magdis, Georgios E. et al. (2012). "The Evolving Interstellar Medium of Star-forming Galaxies since $z = 2$ as Probed by Their Infrared Spectral Energy Distributions". In: *ApJ* 760.1, 6, p. 6. DOI: 10.1088/0004-637X/760/1/6. arXiv: 1210.1035 [astro-ph.CO].

Maltby, David T. et al. (2016). "The identification of post-starburst galaxies at $z \sim 1$ using multiwavelength photometry: a spectroscopic verification". In: *MNRAS* 459.1, pp. L114–L118. DOI: 10.1093/mnrasl/slw057. arXiv: 1603.08941 [astro-ph.GA].

Mannucci, F. et al. (2001). "Near-infrared template spectra of normal galaxies: k-corrections, galaxy models and stellar populations". In: *MNRAS* 326.2, pp. 745–758. DOI: 10.1046/j.1365-8711.2001.04628.x. arXiv: astro-ph/0104427 [astro-ph].

Marchesi, S. et al. (2016). "The Chandra COSMOS-Legacy Survey: Source X-Ray Spectral Properties". In: *ApJ* 830.2, 100, p. 100. DOI: 10.3847/0004-637X/830/2/100. arXiv: 1608.05149 [astro-ph.GA].

Markwardt, C.B. (2009). "Non-linear Least-squares Fitting in IDL with MPFIT". In: *Astronomical Data Analysis Software and Systems XVIII*. Ed. by D.A. Bohlender, D. Durand, and P. Dowler. Vol. 411. Astronomical Society of the Pacific Conference Series, p. 251. arXiv: 0902.2850 [astro-ph.IM].

Martins, Lucimara P. et al. (2013). "Spectral synthesis of star-forming galaxies in the near-infrared". In: *MNRAS* 435.4, pp. 2861–2877. DOI: 10.1093/mnras/stt1482. arXiv: 1308.1380 [astro-ph.CO].

Mason, R.E. et al. (2015). "The Nuclear Near-Infrared Spectral Properties of Nearby Galaxies". In: *ApJS* 217.1, 13, p. 13. DOI: 10.1088/0067-0049/217/1/13. arXiv: 1503.01836 [astro-ph.GA].

Masters, Daniel, Andreas Faisst, and Peter Capak (2016). "A Tight Relation between N/O Ratio and Galaxy Stellar Mass Can Explain the Evolution of Strong Emission Line Ratios with Redshift". In: *ApJ* 828.1, 18, p. 18. DOI: 10.3847/0004-637X/828/1/18. arXiv: 1605.04314 [astro-ph.GA].

Matsui, Hidenori, Ataru Tanikawa, and Takayuki R. Saitoh (2019). "Property of young massive clusters in a galaxy-galaxy merger remnant". In: *PASJ* 71.1, 19, p. 19. DOI: 10.1093/pasj/psy139. arXiv: 1811.04547 [astro-ph.GA].

McCracken, H.J. et al. (2012). "UltraVISTA: a new ultra-deep near-infrared survey in COSMOS". In: *A&A* 544, A156, A156. DOI: 10.1051/0004-6361/201219507. arXiv: 1204.6586 [astro-ph.CO].

Meurer, Gerhardt R., Timothy M. Heckman, and Daniela Calzetti (1999). "Dust Absorption and the Ultraviolet Luminosity Density at z $\sim$3 as Calibrated by Local Starburst Galaxies". In: *ApJ* 521.1, pp. 64–80. DOI: 10.1086/307523. arXiv: astro-ph/9903054 [astro-ph].

Mihos, J. Christopher and Lars Hernquist (1994). "Ultraluminous Starbursts in Major Mergers". In: *ApJL* 431, p. L9. DOI: 10.1086/187460.

— (1996). "Gasdynamics and Starbursts in Major Mergers". In: *ApJ* 464, p. 641. DOI: 10.1086/177353. arXiv: astro-ph/9512099 [astro-ph].

Milvang-Jensen, Bo et al. (2013). "On-sky characterisation of the VISTA NB118 narrow-band filters at 1.19μm". In: *A&A* 560, A94, A94. DOI: 10.1051/0004-6361/201321814. arXiv: 1305.0262 [astro-ph.IM].

Mineo, S. et al. (2014). "X-ray emission from star-forming galaxies - III. Calibration of the L_X-SFR relation up to redshift $z \sim 1.3$." In: *MNRAS* 437.2, pp. 1698–1707. DOI: 10.1093/mnras/stt1999. arXiv: 1207.2157 [astro-ph.HE].

Misselt, K. A., Geoffrey C. Clayton, and Karl D. Gordon (1999). "A Reanalysis of the Ultraviolet Extinction from Interstellar Dust in the Large Magellanic Cloud". In: *ApJ* 515.1, pp. 128–139. DOI: 10.1086/307010. arXiv: astro-ph/9811036 [astro-ph].

Momcheva, Ivelina G. et al. (2016). "The 3D-HST Survey: Hubble Space Telescope WFC3/G141 Grism Spectra, Redshifts, and Emission Line Measurements for $\sim$ 100000 Galaxies". In: *ApJS* 225.2, 27, p. 27. DOI: 10.3847/0067-0049/225/2/27. arXiv: 1510.02106 [astro-ph.GA].

Monreal-Ibero, A., S. Arribas, and L. Colina (2006). "LINER-like Extended Nebulae in ULIRGs: Shocks Generated by Merger-Induced Flows". In: *ApJ* 637.1, pp. 138–146. DOI: 10.1086/498257. arXiv: astro-ph/0509681 [astro-ph].

Monreal-Ibero, A. et al. (2010). "VLT-VIMOS integral field spectroscopy of luminous and ultraluminous infrared galaxies. II. Evidence for shock ionization caused by tidal forces in the extra-nuclear regions of interacting and merging LIRGs". In: *A&A* 517, A28, A28. DOI: 10.1051/0004-6361/200913239. arXiv: 1004.3933 [astro-ph.CO].

Moreno, Jorge et al. (2015). "Mapping galaxy encounters in numerical simulations: the spatial extent of induced star formation". In: *MNRAS* 448.2, p. 1117. DOI: 10.1093/mnras/stv094. arXiv: 1501.03573 [astro-ph.GA].

Mullaney, J.R. et al. (2011). "Defining the intrinsic AGN infrared spectral energy distribution and measuring its contribution to the infrared output of composite galaxies". In: *MNRAS* 414.2, pp. 1082–1110. DOI: 10.1111/j.1365-2966.2011.18448.x. arXiv: 1102.1425 [astro-ph.CO].

Murata, K.L. et al. (2014). "Evolution of the Fraction of Clumpy Galaxies at $0.2 < z < 1.0$ in the COSMOS Field". In: *ApJ* 786.1, 15, p. 15. DOI: 10.1088/0004-637X/786/1/15. arXiv: 1403.1496 [astro-ph.GA].

Murphy T.W., Jr. et al. (1996). "Visual and Near-Infrared Imaging of Ultraluminous Infrared Galaxies: The IRAS 2 Jy Sample". In: *AJ* 111, p. 1025. DOI: 10.1086/117849.

Muzzin, Adam et al. (2013). "A Public K_s -selected Catalog in the COSMOS/ULTRAVISTA Field: Photometry, Photometric Redshifts, and Stellar Population Parameters". In: *ApJS* 206.1, 8, p. 8. DOI: 10.1088/0067-0049/206/1/8. arXiv: 1303.4410 [astro-ph.CO].

Naab, Thorsten, Sadegh Khochfar, and Andreas Burkert (2006). "Properties of Early-Type, Dry Galaxy Mergers and the Origin of Massive Elliptical Galaxies". In: *ApJL* 636.2, pp. L81–L84. DOI: 10.1086/500205. arXiv: astro-ph/0509667 [astro-ph].

Netzer, Hagai (2015). "Revisiting the Unified Model of Active Galactic Nuclei". In: *ARA&A* 53, p. 408. DOI: 10.1146/annurev-astro-082214-122302. arXiv: 1505.00811 [astro-ph.GA].

Nevin, R. et al. (2019). "Accurate Identification of Galaxy Mergers with Imaging". In: *ApJ* 872.1, 76, p. 76. DOI: 10.3847/1538-4357/aafd34.

Noeske, K.G. et al. (2007). "Star Formation in AEGIS Field Galaxies since $z = 1.1$: The Dominance of Gradually Declining Star Formation, and the Main Sequence of Star-forming Galaxies". In: *ApJL* 660.1, pp. L43–L46. DOI: 10.1086/517926. arXiv: astro-ph/0701924 [astro-ph].

Noguchi, Masafumi (1999). "Early Evolution of Disk Galaxies: Formation of Bulges in Clumpy Young Galactic Disks". In: *ApJ* 514.1, pp. 77–95. DOI: 10.1086/306932. arXiv: astro-ph/9806355 [astro-ph].

Noll, S. et al. (2009). "Analysis of galaxy spectral energy distributions from far-UV to far-IR with CIGALE: studying a SINGS test sample". In: *A&A* 507.3, pp. 1793–1813. DOI: 10.1051/0004-6361/200912497. arXiv: 0909.5439 [astro-ph.CO].

Overzier, Roderik A. et al. (2011). "Dust Attenuation in UV-selected Starbursts at High Redshift and Their Local Counterparts: Implications for

the Cosmic Star Formation Rate Density". In: *ApJL* 726.1, L7, p. L7. DOI: 10.1088/2041-8205/726/1/L7. arXiv: 1011.6098 [astro-ph.CO].

Pak, Soojong et al. (1998). "Molecular Cloud Structure in the Magellanic Clouds: Effect of Metallicity". In: *ApJ* 498.2, pp. 735–756. DOI: 10.1086/305584. arXiv: astro-ph/9712158 [astro-ph].

Pawlik, M.M. et al. (2018). "The origins of post-starburst galaxies at $z < 0.05$". In: *MNRAS* 477.2, pp. 1708–1743. DOI: 10.1093/mnras/sty589. arXiv: 1803.02201 [astro-ph.GA].

Peng, Chien Y. et al. (2010). "Detailed Decomposition of Galaxy Images. II. Beyond Axisymmetric Models". In: *AJ* 139.6, pp. 2097–2129. DOI: 10.1088/0004-6256/139/6/2097. arXiv: 0912.0731 [astro-ph.CO].

Peterson, Bradley M. (1997). *An Introduction to Active Galactic Nuclei*.

Piqueras López, J. et al. (2016). "VLT-SINFONI sub-kpc study of the star formation in local LIRGs and ULIRGs. Analysis of the global Σ_{SFR} structure and characterisation of individual star-forming clumps". In: *A&A* 590, A67, A67. DOI: 10.1051/0004-6361/201527671. arXiv: 1603.03707 [astro-ph.GA].

Poggianti, Bianca M. and Hong Wu (2000). "Optical Spectral Signatures of Dusty Starburst Galaxies". In: *ApJ* 529.1, pp. 157–169. DOI: 10.1086/308243. arXiv: astro-ph/9908180 [astro-ph].

Poggianti, Bianca M. et al. (2009). "The Environments of Starburst and Post-Starburst Galaxies at z = 0.4-0.8". In: *ApJ* 693.1, pp. 112–131. DOI: 10.1088/0004-637X/693/1/112. arXiv: 0811.0252 [astro-ph].

Polletta, M. et al. (2007). "Spectral Energy Distributions of Hard X-Ray Selected Active Galactic Nuclei in the XMM-Newton Medium Deep Survey". In: *ApJ* 663.1, pp. 81–102. DOI: 10.1086/518113. arXiv: astro-ph/0703255 [astro-ph].

Powell, Leila C. et al. (2013). "Beyond the nuclear starburst? Clustered star formation in major mergers". In: *MNRAS* 434.2, pp. 1028–1042. DOI: 10.1093/mnras/stt1036. arXiv: 1306.2641 [astro-ph.CO].

Prescott, Matthew et al. (2016). "Galaxy And Mass Assembly (GAMA): the 325 MHz radio luminosity function of AGN and star-forming galaxies". In: *MNRAS* 457.1, pp. 730–744. DOI: 10.1093/mnras/stv3020. arXiv: 1601.00003 [astro-ph.GA].

Prevot, M. L. et al. (1984). "The typical interstellar extinction in the Small Magellanic Cloud." In: *A&A* 132, pp. 389–392.

Puech, M. (2010). "Clumpy galaxies at z $\sim$0.6: kinematics, stability and comparison with analogues at other redshifts". In: *MNRAS* 406.1, pp. 535–547. DOI: 10.1111/j.1365-2966.2010.16689.x. arXiv: 1003.3116 [astro-ph.CO].

Puglisi, A. et al. (2017). "The Bright and Dark Sides of High-redshift Starburst Galaxies from Herschel and Subaru Observations". In: *ApJL* 838.2, L18, p. L18. DOI: 10.3847/2041-8213/aa66c9. arXiv: 1703.04801 [astro-ph.GA].

Puglisi, A. et al. (2019). "The Main Sequence at z $\sim$ 1.3 Contains a Sizable Fraction of Galaxies with Compact Star Formation Sizes: A New Population of Early Post-starbursts?" In: *ApJL* 877.2, L23, p. L23. DOI: 10.3847/2041-8213/ab1f92. arXiv: 1905.02958 [astro-ph.GA].

Querejeta, M. et al. (2015a). "Formation of S0 galaxies through mergers. Bulge-disc structural coupling resulting from major mergers". In: *A&A* 573, A78, A78. DOI: 10.1051/0004-6361/201424303. arXiv: 1409.5126 [astro-ph.GA].

Querejeta, M. et al. (2015b). "Formation of S0 galaxies through mergers. Explaining angular momentum and concentration change from spirals to S0s". In: *A&A* 579. DOI: 10.1051/0004-6361/201526354. arXiv: 1506.00640 [astro-ph.GA].

Ranalli, Piero (2004). "High energy emission from starburst galaxies". PhD thesis. -.

Reddy, Naveen A. et al. (2010). "Dust Obscuration and Metallicity at High Redshift: New Inferences from UV, Hα, and 8 μm Observations of z $\sim$2 Star-forming Galaxies". In: *ApJ* 712.2, pp. 1070–1091. DOI: 10.1088/0004-637X/712/2/1070. arXiv: 1002.0837 [astro-ph.CO].

Reddy, Naveen A. et al. (2015). "The MOSDEF Survey: Measurements of Balmer Decrements and the Dust Attenuation Curve at Redshifts z $\sim$1.4-2.6". In: *ApJ* 806.2, 259, p. 259. DOI: 10.1088/0004-637X/806/2/259. arXiv: 1504.02782 [astro-ph.GA].

Reines, Amy E. and Marta Volonteri (2015). "Relations between Central Black Hole Mass and Total Galaxy Stellar Mass in the Local Universe". In: *ApJ* 813.2, 82, p. 82. DOI: 10.1088/0004-637X/813/2/82. arXiv: 1508.06274 [astro-ph.GA].

Renaud, F. et al. (2014). "Starbursts triggered by intergalactic tides andinterstellar compressive turbulence." In: *MNRAS* 442, pp. L33–L37. DOI: 10.1093/mnrasl/slu050. arXiv: 1403.7316 [astro-ph.GA].

Renaud, F. et al. (2018). "Morphology and enhanced star formation in a Cartwheel-like ring galaxy". In: *MNRAS* 473.1, pp. 585–602. DOI: 10.1093/mnras/stx2360. arXiv: 1709.02826 [astro-ph.GA].

Renaud, F. et al. (2019). "A diversity of starburst-triggering mechanisms in interacting galaxies and their signatures in CO emission". In: *A&A* 625, A65, A65. DOI: 10.1051/0004-6361/201935222. arXiv: 1902.02353 [astro-ph.GA].

Ribeiro, B. et al. (2017). "The VIMOS Ultra-Deep Survey: A major merger origin for the high fraction of galaxies at $2 < z < 6$ with two bright clumps". In: *A&A* 608, A16, A16. DOI: 10.1051/0004-6361/201630057. arXiv: 1611.05869 [astro-ph.GA].

Rich, J.A., L.J. Kewley, and M.A. Dopita (2011). "Galaxy-wide Shocks in Late-merger Stage Luminous Infrared Galaxies". In: *ApJ* 734.2, 87, p. 87. DOI: 10.1088/0004-637X/734/2/87. arXiv: 1104.1177 [astro-ph.CO].

— (2014). "Composite Spectra in Merging U/LIRGs Caused by Shocks". In: *ApJL* 781.1, L12, p. L12. DOI: 10.1088/2041-8205/781/1/L12. arXiv: 1310.3441 [astro-ph.CO].

— (2015). "Galaxy Mergers Drive Shocks: An Integral Field Study of GOALS Galaxies". In: *ApJS* 221.2, 28, p. 28. DOI: 10.1088/0067-0049/221/2/28. arXiv: 1509.08468 [astro-ph.GA].

Rodighiero, G. et al. (2011). "The Lesser Role of Starbursts in Star Formation at $z = 2$." In: *ApJL* 739.2, L40, p. L40. DOI: 10.1088/2041-8205/739/2/L40. arXiv: 1108.0933 [astro-ph.CO].

Rodrigues, M. et al. (2012). "A decrease of the gas exchanges between galaxies and the intergalactic medium, from 12 to 6 billion years ago". In: *MNRAS* 421.4, pp. 2888–2903. DOI: 10.1111/j.1365-2966.2012.20518.x. arXiv: 1203.6248 [astro-ph.CO].

Rodriguez-Gomez, Vicente et al. (2016). "The stellar mass assembly of galaxies in the Illustris simulation: growth by mergers and the spatial distribution of accreted stars". In: *MNRAS* 458.3, pp. 2371–2390. DOI: 10.1093/mnras/stw456. arXiv: 1511.08804 [astro-ph.GA].

Rodriguez-Gomez, Vicente et al. (2019). "The optical morphologies of galaxies in the IllustrisTNG simulation: a comparison to Pan-STARRS observations". In: *MNRAS* 483.3, pp. 4140–4159. DOI: 10.1093/mnras/sty3345. arXiv: 1809.08239 [astro-ph.GA].

Roos, Orianne et al. (2015). "Thermal and Radiative Active Galactic Nucleus Feedback have a Limited Impact on Star Formation in High-redshift Galaxies". In: *ApJ* 800.1, 19, p. 19. DOI: 10.1088/0004-637X/800/1/19. arXiv: 1405.7971 [astro-ph.GA].

Rothberg, B. and R.D. Joseph (2006). "A Survey of Merger Remnants. III. Are Merger Remnants Supported by Rotation or Anisotropy?" In: *AJ* 132.3, pp. 976–988. DOI: 10.1086/505491. arXiv: astro-ph/0604493 [astro-ph].

Rujopakarn, W. et al. (2016). "VLA and ALMA Imaging of Intense Galaxy-wide Star Formation in $z \sim 2$ Galaxies". In: *ApJ* 833.1, 12, p. 12. DOI: 10.3847/0004-637X/833/1/12. arXiv: 1607.07710 [astro-ph.GA].

Rujopakarn, W. et al. (2018). "Cospatial Star Formation and Supermassive Black Hole Growth in $z \sim 3$ Galaxies: Evidence for In Situ Co-evolution". In: *ApJL* 854.1, L4, p. L4. DOI: 10.3847/2041-8213/aaa9b3. arXiv: 1801.07072 [astro-ph.GA].

Sakamoto, Kazushi et al. (2017). "Resolved Structure of the Arp 220 Nuclei at $\lambda \sim 3$ mm". In: *ApJ* 849.1, 14, p. 14. DOI: 10.3847/1538-4357/aa8f4b. arXiv: 1709.08537 [astro-ph.GA].

Salmi, F. et al. (2012). "Dissecting the Stellar-mass-SFR Correlation in $z = 1$ Star-forming Disk Galaxies". In: *ApJL* 754.1, L14, p. L14. DOI: 10.1088/2041-8205/754/1/L14. arXiv: 1206.1704 [astro-ph.CO].

Sanders, D.B. and I.F. Mirabel (1996). "Luminous Infrared Galaxies". In: *ARA&A* 34, p. 749. DOI: 10.1146/annurev.astro.34.1.749.

Sanders, D.B. et al. (1988). "Ultraluminous Infrared Galaxies and the Origin of Quasars". In: *ApJ* 325, p. 74. DOI: 10.1086/165983.

Sanders, D.B. et al. (2007). "S-COSMOS: The Spitzer Legacy Survey of the Hubble Space Telescope ACS 2 deg^2 COSMOS Field I: Survey Strategy and First Analysis". In: *ApJS* 172.1, pp. 86–98. DOI: 10.1086/517885. arXiv: astro-ph/0701318 [astro-ph].

Sargent, M.T. et al. (2012). "The Contribution of Starbursts and Normal Galaxies to Infrared Luminosity Functions at $z < 2$." In: *ApJL* 747.2, L31, p. L31. DOI: 10.1088/2041-8205/747/2/L31. arXiv: 1202.0290 [astro-ph.CO].

Sargent, M.T. et al. (2014). "Regularity Underlying Complexity: A Redshift-independent Description of the Continuous Variation of Galaxy-scale Molecular Gas Properties in the Mass-star Formation Rate Plane". In: *ApJ* 793.1, 19, p. 19. DOI: 10.1088/0004-637X/793/1/19. arXiv: 1303.4392 [astro-ph.CO].

Schawinski, Kevin et al. (2014). "The green valley is a red herring: Galaxy Zoo reveals two evolutionary pathways towards quenching of star formation in early- and late-type galaxies". In: *MNRAS* 440.1, pp. 889–907. DOI: 10.1093/mnras/stu327. arXiv: 1402.4814 [astro-ph.GA].

Schinnerer, E. et al. (2007). "The VLA-COSMOS Survey. II. Source Catalog of the Large Project". In: *ApJS* 172.1, pp. 46–69. DOI: 10.1086/516587. arXiv: astro-ph/0612314 [astro-ph].

Schinnerer, E. et al. (2010). "The VLA-COSMOS Survey. IV. Deep Data and Joint Catalog". In: *ApJS* 188.2, pp. 384–404. DOI: 10.1088/0067-0049/188/2/384. arXiv: 1005.1641 [astro-ph.CO].

Schmidt, Maarten (1959). "The Rate of Star Formation." In: *ApJ* 129, p. 243. DOI: 10.1086/146614.

Schreiber, C. et al. (2015). "The Herschel view of the dominant mode of galaxy growth from $z = 4$ to the present day". In: *A&A* 575, A74, A74. DOI: 10.1051/0004-6361/201425017. arXiv: 1409.5433 [astro-ph.GA].

Schreiber, C. et al. (2018). "Dust temperature and mid-to-total infrared color distributions for star-forming galaxies at 0 < z < 4". In: *A&A* 609, A30, A30. DOI: 10.1051/0004-6361/201731506. arXiv: 1710.10276 [astro-ph.GA].

Scoville, N. et al. (2016). "ISM Masses and the Star formation Law at $z = 1$ to 6: ALMA Observations of Dust Continuum in 145 Galaxies in the COSMOS Survey Field". In: *ApJ* 820.2, 83, p. 83. DOI: 10.3847/0004-637X/820/2/83. arXiv: 1511.05149 [astro-ph.GA].

Scoville, N.Z. et al. (1998). "NICMOS Imaging of the Nuclei of Arp 220". In: *ApJL* 492.2, pp. L107–L110. DOI: 10.1086/311099. arXiv: astro-ph/9801006 [astro-ph].

Sérsic, J.L. (1963). "Influence of the atmospheric and instrumental dispersion on the brightness distribution in a galaxy". In: *Boletin de la Asociacion Argentina de Astronomia La Plata Argentina* 6, p. 41.

Shapiro, Kristen L., Reinhard Genzel, and Natascha M. Förster Schreiber (2010). "Star-forming galaxies at $z \sim 2$ and the formation of the metal-rich globular cluster population". In: *MNRAS* 403.1, pp. L36–L40. DOI: 10.1111/j.1745-3933.2010.00810.x. arXiv: 1001.1740 [astro-ph.CO].

Shapiro, Kristen L. et al. (2008). "Kinemetry of SINS High-Redshift Star-Forming Galaxies: Distinguishing Rotating Disks from Major Mergers". In: *ApJ* 682.1, pp. 231–251. DOI: 10.1086/587133. arXiv: 0802.0879 [astro-ph].

Sheth, Kartik et al. (2012). "Hot Disks and Delayed Bar Formation". In: *ApJ* 758.2, 136, p. 136. DOI: 10.1088/0004-637X/758/2/136. arXiv: 1208.6304 [astro-ph.CO].

Silva, Laura et al. (1998). "Modeling the Effects of Dust on Galactic Spectral Energy Distributions from the Ultraviolet to the Millimeter Band". In: *ApJ* 509.1, pp. 103–117. DOI: 10.1086/306476.

Silverman, J.D. et al. (2018a). "Concurrent Starbursts in Molecular Gas Disks within a Pair of Colliding Galaxies at $z = 1.52$." In: *ApJ* 868.1, 75, p. 75. DOI: 10.3847/1538-4357/aae64b. arXiv: 1810.01595 [astro-ph.GA].

Silverman, J.D. et al. (2018b). "The Molecular Gas Content and Fuel Efficiency of Starbursts at $z \sim 1.6$ with ALMA". In: *ApJ* 867.2, 92, p. 92. DOI: 10.3847/1538-4357/aae25e. arXiv: 1810.01596 [astro-ph.GA].

Simcoe, Robert A. et al. (2013). "FIRE: A Facility Class Near-Infrared Echelle Spectrometer for the Magellan Telescopes". In: *PASP* 125.925, p. 270. DOI: 10.1086/670241.

Smolčić, V. et al. (2017). "The VLA-COSMOS 3 GHz Large Project: Continuum data and source catalog release". In: *A&A* 602, A1, A1. DOI: 10.1051/0004-6361/201628704. arXiv: 1703.09713 [astro-ph.GA].

Soifer, B.T. et al. (1984). "Infrared galaxies in the IRAS minisurvey." In: *ApJL* 278, pp. L71–L74. DOI: 10.1086/184226.

Soifer, B.T. et al. (2000). "High Resolution Mid-Infrared Imaging of Ultraluminous Infrared Galaxies". In: *AJ* 119.2, pp. 509–523. DOI: 10.1086/301233. arXiv: astro-ph/9911045 [astro-ph].

Somerville, R.S. (2001). "Disks at High Redshift: Interactions, Mergers, and Starbursts". In: *Galaxy Disks and Disk Galaxies*. Ed. by José G. Funes and Enrico Maria Corsini. Vol. 230. Astronomical Society of the Pacific Conference Series, pp. 477–486. arXiv: astro-ph/0010350 [astro-ph].

Sparre, Martin and Volker Springel (2016). "Zooming in on major mergers: dense, starbursting gas in cosmological simulations". In: *MNRAS* 462.3, pp. 2418–2430. DOI: 10.1093/mnras/stw1793. arXiv: 1604.08205 [astro-ph.GA].

Springel, Volker, Tiziana Di Matteo, and Lars Hernquist (2005). "Modelling feedback from stars and black holes in galaxy mergers". In: *MNRAS* 361.3, pp. 776–794. DOI: 10.1111/j.1365-2966.2005.09238.x. arXiv: astro-ph/0411108 [astro-ph].

Springel, Volker and Lars Hernquist (2002). "Cosmological smoothed particle hydrodynamics simulations: the entropy equation". In: *MNRAS* 333.3,

pp. 649–664. DOI: 10.1046/j.1365-8711.2002.05445.x. arXiv: astro-ph/0111016 [astro-ph].

Storey, P.J. and D.G. Hummer (1988). "Recombination line intensities for hydrogenic ions. II. Case B calculations for C VI, N VII and O VIII." In: *MNRAS* 231, pp. 1139–1144. DOI: 10.1093/mnras/231.4.1139.

Strateva, Iskra et al. (2001). "Color Separation of Galaxy Types in the Sloan Digital Sky Survey Imaging Data". In: *AJ* 122.4, pp. 1861–1874. DOI: 10.1086/323301. arXiv: astro-ph/0107201 [astro-ph].

Tacconi, L.J. et al. (2008). "Submillimeter Galaxies at $z \sim 2$: Evidence for Major Mergers and Constraints on Lifetimes, IMF, and CO-H_2 Conversion Factor". In: *ApJ* 680.1, pp. 246–262. DOI: 10.1086/587168. arXiv: 0801.3650 [astro-ph].

Tacconi, L.J. et al. (2010). "High molecular gas fractions in normal massive star-forming galaxies in the young Universe". In: *Nature* 463.7282, pp. 781–784. DOI: 10.1038/nature08773. arXiv: 1002.2149 [astro-ph.CO].

Tadaki, K. et al. (2018). "The gravitationally unstable gas disk of a starburst galaxy 12 billion years ago". In: *Nature* 560.7720, pp. 613–616. DOI: 10.1038/s41586-018-0443-1. arXiv: 1808.09592 [astro-ph.GA].

Takeuchi, Tsutomu T. et al. (2012). "Reexamination of the Infrared Excess-Ultraviolet Slope Relation of Local Galaxies". In: *ApJ* 755.2, 144, p. 144. DOI: 10.1088/0004-637X/755/2/144. arXiv: 1206.3905 [astro-ph.CO].

Tan, Q. et al. (2014). "Dust and gas in luminous proto-cluster galaxies at $z = 4.05$: the case for different cosmic dust evolution in normal and starburst galaxies". In: *A&A* 569, A98, A98. DOI: 10.1051/0004-6361/201423905. arXiv: 1403.7992 [astro-ph.GA].

Taniguchi, Y. et al. (2007). "The Cosmic Evolution Survey (COSMOS): Subaru Observations of the HST Cosmos Field". In: *ApJS* 172.1, pp. 9–28. DOI: 10.1086/516596. arXiv: astro-ph/0612295 [astro-ph].

Tasca, L.A.M. et al. (2009). "The zCOSMOS redshift survey: the role of environment and stellar mass in shaping the rise of the morphology-density relation from $z \sim 1$." In: *A&A* 503.2, pp. 379–398. DOI: 10.1051/0004-6361/200912213. arXiv: 0906.4556 [astro-ph.CO].

Teyssier, R. (2002). "Cosmological hydrodynamics with adaptive mesh refinement. A new high resolution code called RAMSES". In: *A&A* 385, pp. 337–364. DOI: 10.1051/0004-6361:20011817. arXiv: astro-ph/0111367 [astro-ph].

Teyssier, Romain, Damien Chapon, and Frédéric Bournaud (2010). "The Driving Mechanism of Starbursts in Galaxy Mergers". In: *ApJL* 720.2, pp. L149–L154. DOI: 10.1088/2041-8205/720/2/L149. arXiv: 1006.4757 [astro-ph.CO].

Toft, S. et al. (2014). "Submillimeter Galaxies as Progenitors of Compact Quiescent Galaxies". In: *ApJ* 782.2, 68, p. 68. DOI: 10.1088/0004-637X/782/2/68. arXiv: 1401.1510 [astro-ph.GA].

Toomre, Alar and Juri Toomre (1972). "Galactic Bridges and Tails". In: *ApJ* 178, pp. 623–666. DOI: 10.1086/151823.

Trager, S.C. et al. (2000). "The Stellar Population Histories of Local Early-Type Galaxies. I. Population Parameters". In: *AJ* 119.4, pp. 1645–1676. DOI: 10.1086/301299. arXiv: astro-ph/0001072 [astro-ph].

Tremonti, Christy A. et al. (2001). "Star Formation in the Field and Clusters of NGC 5253". In: *ApJ* 555.1, pp. 322–337. DOI: 10.1086/321436. arXiv: astro-ph/0103432 [astro-ph].

Valentino, F. et al. (2015). "Metal Deficiency in Cluster Star-Forming Galaxies At $z = 2$." In: *ApJ* 801.2, 132, p. 132. DOI: 10.1088/0004-637X/801/2/132. arXiv: 1410.1437 [astro-ph.GA].

van der Wel, A. et al. (2014). "3D-HST+CANDELS: The Evolution of the Galaxy Size-Mass Distribution since $z = 3$". In: *ApJ* 788.1, 28, p. 28. DOI: 10.1088/0004-637X/788/1/28. arXiv: 1404.2844 [astro-ph.GA].

Vasudevan, R.V. and A.C. Fabian (2007). "Piecing together the X-ray background: bolometric corrections for active galactic nuclei". In: *MNRAS* 381.3, pp. 1235–1251. DOI: 10.1111/j.1365-2966.2007.12328.x. arXiv: 0708.4308 [astro-ph].

Veilleux, Sylvain and Donald E. Osterbrock (1987). "Spectral Classification of Emission-Line Galaxies". In: *ApJS* 63, p. 295. DOI: 10.1086/191166.

Walcher, C.J. et al. (2008). "The VVDS-SWIRE-GALEX-CFHTLS surveys: physical properties of galaxies at z below 1.2 from photometric data". In: *A&A* 491.3, pp. 713–730. DOI: 10.1051/0004-6361:200810704. arXiv: 0807.4636 [astro-ph].

Wild, Vivienne, Timothy Heckman, and Stéphane Charlot (2010). "Timing the starburst-AGN connection". In: *MNRAS* 405.2, pp. 933–947. DOI: 10.1111/j.1365-2966.2010.16536.x. arXiv: 1002.3156 [astro-ph.CO].

Zakamska, Nadia L. et al. (2016). "Star formation in quasar hosts and the origin of radio emission in radio-quiet quasars". In: *MNRAS* 455.4, pp. 4191–4211. DOI: 10.1093/mnras/stv2571. arXiv: 1511.00013 [astro-ph.GA].

Zamojski, M.A. et al. (2007). "Deep GALEX Imaging of the COSMOS HST Field: A First Look at the Morphology of $z \sim 0.7$ Star-forming Galaxies". In: *ApJS* 172.1, pp. 468–493. DOI: 10.1086/516593. arXiv: astro-ph/0701478 [astro-ph].

Zaritsky, Dennis (1999). "Dust and Stellar Populations in the Large Magellanic Cloud". In: *AJ* 118.6, pp. 2824–2838. DOI: 10.1086/301131. arXiv: astro-ph/9908363 [astro-ph].

Appendix A

Publications

- **Calabrò, A.**; Daddi, E.; Fensch, J.; Bournaud, F.; Cibinel A.; Puglisi, A.; Jin, S.; Delvecchio, I.; D'Eugenio, C. : *"**Merger induced clump formation in distant infrared luminous starburst galaxies**"* submitted to A&A on 26 April 2019; The first report has been received on 25 June 2019; Link: https://tinyurl.com/y5rzy4o2

- **Calabrò, A.**; Daddi, E.; Puglisi, A.; Oliva, E.; Gobat, R.; Cassata, P.; Amorín, R.; Arimoto, N.; Boquien, M.; Carraro R.; Delvecchio, I.; Ibar, E.; Jin, S.; Juneau, S.; Liu, D.; Onodera, M.; Mannucci, F.; Méndez Hernánez, H.; Rodi-ghiero, G.; Valentino, F.; Zanella, A.; 2019, A&A, 623, A64 : *"**Deciphering an evolutionary sequence of merger stages in infrared-luminous starburst galaxies at $z \sim 0.7$**"* doi:10.1051/0004-6361/201834522

- **Calabrò, A.**; Daddi, E.; Cassata, P.; Onodera, M.; Gobat, R.; Puglisi, A.; Jin, S.; Liu, D.; Amorín, R.; Arimoto, N.; Boquien, M.; Carraro, R.; Elbaz, D.; Ibar, E.; Juneau, S.; Mannucci, F.; Méndez Hernánez, H.; Oliva, E.; Rodighiero, G.; Valentino, F.; Zanella, A.; 2018, ApJ, 862, L22 : *"**Near-infrared Emission Lines in Starburst Galaxies at $0.5 < z < 0.9$: Discovery of a Merger Sequence of Extreme Obscurations**"*. doi:10.3847/2041-8213/aad33e

- **Calabrò, A.**; Amorín, R.; Fontana, A.; Pérez-Montero, E.; Lemaux, B. C.; Ribeiro, B.; Bardelli, S.; Castellano, M.; Contini, T.; De Barros, S.; Garilli, B.; Grazian, A.; Guaita, L.; Hathi, N. P.; Koekemoer, A. M.; Le Fèvre, O.; Maccagni, D.; Pentericci, L.; Schaerer, D.; Talia, M.; Tasca, L. A. M.; Zucca, E.; 2017, A&A, 601, A95 : *"**Characterization of star-forming dwarf galaxies at $0.1 \leq z \leq 0.9$ in VUDS: probing the low-mass end of the mass-metallicity relation**"*. doi:10.1051/0004-6361/201629762

- Jin, S.; Daddi, E.; Liu, D.; Smolcić, V.; Schinnerer, E.; **Calabrò, A.**; Bertoldi, F.; Sargent, M.; Magdis, G.; Capak, P.; 2019 : *"**Cold dusty galaxies at $z = 4$-6: direct evidence of CMB impact on high-redshift galaxy observables**"*. Submitted to ApJ.

- Puglisi, A.; Daddi, E.; Liu, D.; Bournaud, F.; Silverman, J. D.; Circosta, C.; **Calabrò, A.**; Aravena, M.; Dannerbauer, H.; Delvecchio, I.; Elbaz,

D.; Gao, Y.; Gobat, R.; Le Floc'h, E.; Magdis, G.; Mancini, C.; Riechers, D.A.; Rodighiero, G.; Sargent, M.; Valentino, F.; Zanisi, L.; 2019, ApJ Letters : *"**The main sequence at $z \sim 1.3$ contains a sizeable fraction of galaxies with compact star formation sizes: a new population of early post-starbursts ?**"* arXiv:1905.02958.

- Cibinel, A.; Daddi, E.; Sargent, M. T.; Le Floc'h, E.; Liu, D.; Bournaud, F.; Oesch, P. A.; Amram, P.; **Calabrò, A.**; Duc, P.A.; Pannella, M.; Puglisi, A.; Perret, V.; Elbaz, D.; Kokorev, V.; 2019, MNRAS, 485, 5631 : *"**Early- and late-stage mergers among main sequence and starburst galaxies at $0.2 \leq z \leq 2$**"*. doi:10.1093/mnras/stz690

- Jin, S.; Daddi, E.; Liu, D.; Smolcić, V.; Schinnerer, E.; **Calabrò, A.**; Gu, Q.; Delhaize, J.; Delvecchio, I.; Gao, Y.; Salvato, M.; Puglisi, A.; Dickinson, M.; Bertoldi, F.; Sargent, M.; Novak, M.; Magdis, G.; Aretxaga, I.; Wilson, G. W.; Capak, P.; 2018, ApJ, 864, 56 : *"**Super-deblended Dust Emission in Galaxies. II. Far-IR to (Sub)millimeter Photometry and High-redshift Galaxy Candidates in the Full COSMOS Field**"*. doi:10.3847/1538-4357/aad4af

- Daddi, E.; Jin, S.; Strazzullo, V.; Sargent, M. T.; Wang, T.; Ferrari, C.; Schinnerer, E.; Smolcić, V.; **Calabrò, A.**; Coogan, R.; Delhaize, J.; Delvecchio, I.; Elbaz, D.; Gobat, R.; Gu, Q.; Liu, D.; Novak, M.; Valentino, F.; 2017, ApJ, 846, L31 : *"**Radio Selection of the Most Distant Galaxy Clusters**"*. doi:10.3847/2041-8213/aa8808

- Puglisi, A.; Daddi, E.; Renzini, A.; Rodighiero, G.; Silverman, J. D.; Kashino, D.; Rodríguez-Munoz, L.; Mancini, C.; Mainieri, V.; Man, A.; Franceschini, A.; Valentino, F.; **Calabrò, A.**; Jin, S.; Darvish, B.; Maier, C.; Kartaltepe, J. S.; Sanders, D. B.; 2017, ApJ, 838, L18 : *"**The Bright and Dark Sides of High-redshift Starburst Galaxies from Herschel and Subaru Observations**"*. doi:10.3847/2041-8213/aa66c9

The Astrophysical Journal Letters, 862:L22 (7pp), 2018 August 1 https://doi.org/10.3847/2041-8213/aad33e
© 2018. The American Astronomical Society. All rights reserved.

Near-infrared Emission Lines in Starburst Galaxies at $0.5 < z < 0.9$: Discovery of a Merger Sequence of Extreme Obscurations

A. Calabrò[1], E. Daddi[1], P. Cassata[2], M. Onodera[3,4], R. Gobat[5], A. Puglisi[1], S. Jin[1,6], D. Liu[7], R. Amorín[8,9], N. Arimoto[10], M. Boquien[11], R. Carraro[12], D. Elbaz[1], E. Ibar[12], S. Juneau[13], F. Mannucci[14], H. Méndez Hernánez[12], E. Oliva[14], G. Rodighiero[2], F. Valentino[15,16], and A. Zanella[17]

[1] CEA, IRFU, DAp, AIM, Université Paris-Saclay, Université Paris Diderot, Sorbonne Paris Cité, CNRS, F-91191 Gif-sur-Yvette, France
[2] Dipartimento di Fisica e Astronomia G. Galilei, Università di Padova, Vicolo dell'Osservatorio 3, I-35122, Italy
[3] Subaru Telescope, National Astronomical Observatory of Japan, National Institutes of Natural Sciences (NINS), 650 North A'ohoku Place, Hilo, HI 96720, USA
[4] Department of Astronomical Science, SOKENDAI (The Graduate University for Advanced Studies), 650 North A'ohoku Place, Hilo, HI 96720, USA
[5] Instituto de Física, Pontificia Universidad Católica de Valparaíso, Casilla 4059, Valparaíso, Chile
[6] School of Astronomy and Space Science, Nanjing University, Nanjing 210093, People's Republic of China
[7] Max Planck Institute for Astronomy, Konigstuhl 17, D-69117 Heidelberg, Germany
[8] Cavendish Laboratory, University of Cambridge, 19 JJ Thomson Avenue, Cambridge, CB3 0HE, UK
[9] Kavli Institute for Cosmology, University of Cambridge, Madingley Road, Cambridge CB3 0HA, UK
[10] Astronomy Program, Department of Physics and Astronomy, Seoul National University, 599 Gwanak-ro, Gwanak-gu, Seoul, 151-742, Republic of Korea
[11] Centro de Astronomía (CITEVA), Universidad de Antofagasta, Avenida Angamos 601, Antofagasta, Chile
[12] Instituto de Fisica y Astronomía, Facultad de Ciencias, Universidad de Valparaíso, Gran Bretaña 1111, Playa Ancha, Valparaíso, Chile
[13] National Optical Astronomy Observatory, 950 N. Cherry Avenue, Tucson, AZ 85719, USA
[14] INAF-Osservatorio Astrofisico di Arcetri, Largo Enrico Fermi 5, I-50125 Firenze, Italy
[15] Dawn Cosmic Center, Niels Bohr Institute, University of Copenhagen Juliane Maries Vej 30, DK-2100 Copenhagen, Denmark
[16] Dark Cosmology Centre, Niels Bohr Institute, University of Copenhagen, Juliane Maries Vej 30, DK-2100 Copenhagen, Denmark
[17] European Southern Observatory, Karl Schwarzschild Straße 2, D-85748 Garching, Germany
Received 2018 May 31; revised 2018 July 2; accepted 2018 July 10; published 2018 August 1

Abstract

We obtained optical/near-IR rest-frame Magellan FIRE spectra (including Paβ and Paγ) of 25 starburst galaxies at $0.5 < z < 0.9$, with average star formation rates (SFRs) seven times above the main sequence (MS). We find that Paschen-to-Balmer line ratios saturate around a constant value corresponding to $A_V \sim 2$–3 mag, while line-to-IR-luminosity ratios suggest a large range of more extreme obscurations and appear to be uncorrelated with the former. This behavior is not consistent with standard attenuation laws derived for local and distant galaxies, yet is remarkably consistent with observations of starburst cores in which young stars and dust are homogeneously mixed. This model implies $A_V = 2$–30 mag attenuation to the center of starburst cores, with a median of $\sim$9 mag (a factor of 4000). X-ray hardness ratios for six AGNs in our sample and column densities derived from observed dust masses and radio sizes independently confirm this level of attenuation. In these conditions observed optical/near-IR emission comes from surface regions, while inner starburst cores are invisible. We thus attribute the high [N II]/Hα ratios to widespread shocks from accretion, turbulence, and dynamic disturbances rather than to AGNs. The large range of optical depths demonstrates that substantial diversity is present within the starburst population, possibly connected to different merger phases or progenitor properties. The majority of our targets are, in fact, morphologically classified as mergers. We argue that the extreme obscuration provides in itself smoking gun evidence of their merger origin, and a powerful tool for identifying mergers at even higher redshifts.

Key words: dust, extinction – galaxies: evolution – galaxies: high-redshift – galaxies: ISM – galaxies: starburst – infrared: galaxies

1. Introduction

Starburst galaxies (SBs), outliers from the main sequence (MS; e.g., Daddi et al. 2007; Noeske et al. 2007), might be key to solving a long-standing mystery in galaxy formation and evolution: the transition from star-forming galaxies to massive, passively evolving ellipticals. According to a popular scenario (e.g., Di Matteo et al. 2005; Hopkins et al. 2010), this transition is attributed to major mergers producing strong bursts of star formation in very dense cores and triggering obscured black hole accretion, which can both remove the gas and dust content in the galaxy.

Local ultra-luminous infrared galaxies (ULIRGs) are textbook examples of merger-induced starbursts, showing compact and heavily obscured cores (e.g., Soifer et al. 2000; Juneau et al. 2009) in agreement with the above scenario. Using standard attenuation recipes in ULIRGs (Cardelli et al. 1989; Calzetti et al. 2000) leads to UV-based, optical-based, and near-IR-based star formation rates (SFRs) being systematically underestimated compared to the total infrared luminosities, implying optically thick conditions for these tracers (Goldader et al. 2002; García-Marín et al. 2009; Rieke et al. 2009).

The nature and evolution of SBs in the distant universe is debated. While they might still be major merger events, there are also claims that they might be instead very gas-rich galaxies (e.g., Scoville et al. 2016), possibly due to exceptionally strong gas accretion events. This is supported by ideas that at higher redshifts, with higher gas fractions, major mergers might only rarely result in strong SFR enhancements (Fensch et al. 2017). Comparisons of both dust-free and dust-affected SFRs are required to study their degree of obscuration, providing clues to the ULIRGs/distant-SB connection. Puglisi et al. (2017) showed that on average, Balmer emission lines of Herschel-selected $z \sim 1.6$ SBs are mainly coming from regions producing <10% of the total SFR, suggesting that rest-optical

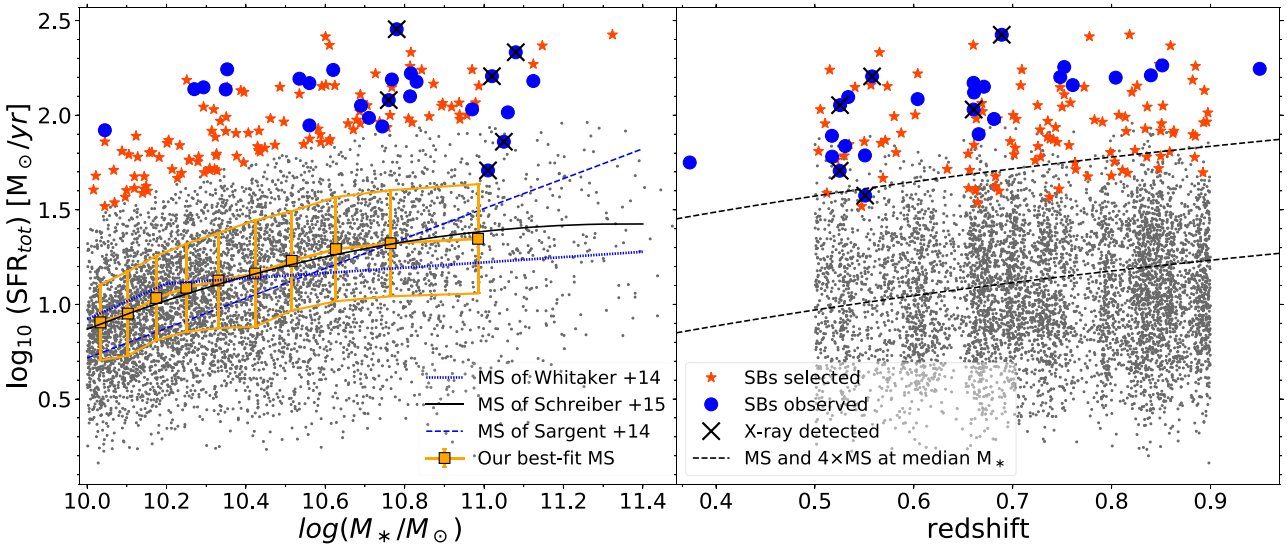

Figure 1. Left: SFR–$M\star$ diagram for galaxies in our parent sample ($0.5 < z < 0.9$) , where $\mathrm{SFR_{tot}}$ is defined as $\mathrm{SFR_{UV,obs}}$+$\mathrm{SFR_{IR}}$, and is normalized to their median redshift (0.73) using the evolving trend from Sargent et al. (2014). For sources detected only at 24 μm, we estimated the SFR from their 24 μm flux using Magdis et al. (2012) templates. Right: $\mathrm{SFR_{tot}}$ vs. redshift for the same sample.

lines cannot be used to infer the physical properties of the whole starburst system. These results prompted us to use Magellan FIRE to obtain spectroscopy of starbursts in the near-IR rest-frame with the aim of providing enhanced sensitivity and constraining power to study their attenuation properties (hence their nature). In this Letter we present the first results of this effort. We adopt Chabrier (2003) IMF, AB magnitudes, and standard cosmology ($H_0 = 70$ km s^{-1} Mpc^{-1}, $\Omega_\mathrm{m} = 0.3$, $\Omega_\Lambda = 0.7$).

2. Sample Selection

We select starbursts galaxies for observations with Magellan FIRE in the COSMOS field, with the following criteria:

1. Spectroscopic redshift $0.5 < z < 0.9$[18] (from optical surveys, Salvato et al. 2018, in preparation), placing Paβ within the K band, and Hα above 0.82 μm, thus observable with FIRE.[19]
2. SFR $> 4 \times \mathrm{SFR_{MS}}$ (Rodighiero et al. 2011).[20] SFRs are derived using the IR catalog from Jin et al. (2018).[21] As shown in Figure 1, the MS for our sample, derived through a running median over 10 bins in $M_\star$, agrees with the literature (Sargent et al. 2014; Schreiber et al. 2015). Our SFRs are decontaminated from AGN torus emission (3% median contribution to L_IR; see Liu et al. (2018) and Jin et al. (2018) for the procedure).
3. $M_* > 10^{10}\,M_\odot$, for sample completeness: above this mass limit and up to $z = 0.9$, all SBs would be *Herschel*-detected at $\mathrm{S/N_{FIR}} > 5$ (see Figure 13 in Jin et al. 2018). Stellar masses are from Laigle et al. (2016).

These criteria yield a total of 152 starburst candidates for our Magellan observations (Figure 1). They represent 2%–3% of the whole star-forming population in the same mass range and redshift (see, e.g., Sargent et al. 2012, 2014; Schreiber et al. 2015).

3. Magellan FIRE Observations

FIRE is a single-slit near-infrared spectrometer mounted at the Magellan 6.5 m Baade Telescope, covering the wavelength range 0.82–2.4 μm. We observed in the cross-dispersed echelle mode, choosing a slit width of 1″ to maximize the incoming light from our targets. This configuration provides a spectral resolution $R \simeq 3000$, which helps reducing the effect of OH sky-emission. We refer to Simcoe et al. (2013) for a complete description of the instrument and its performances.

Our observations were performed in two runs during the nights of 2017 March 17–18 and 2018 March 22–23. We prioritized targets for observations based on two criteria: (1) the presence of a nearby ($\lesssim$30″ from the target) bright ($J < 19$–20 mag) star to facilitate acquisition, and (2) maximization of the ratio $\mathrm{SFR_{IR}}/D_L^2(z)$, where D_L is the luminosity distance. The latter condition selects galaxies with the intrinsically brightest emission lines, and tends to bias our observed sample toward the most massive objects (Figure 1). We observed 11 targets during the first run and 14 in the second, for a total of 25 starbursts. Integration times ranged between 30 and 80 minutes, longer for galaxies with lower Hα S/N (from real-time reductions), to improve the detection of fainter lines.

The spectra were reduced using the FIRE pipeline (Gagné et al. 2015). Full details will be given in a forthcoming paper (Calabrò et al. 2018, in preparation) that also presents science results for the complete range of observed emission lines. In Figure 2, we show examples of Hα and Paβ (or Paγ) for some

[18] We also added four galaxies with photometric redshifts (Laigle et al. 2016) lying in the same range.
[19] Existing spectroscopic redshifts were incorrect for two galaxies with new redshifts placing them outside of our selection range (Figure 1, right panel). We keep them in the sample because they satisfy the other selection criteria.
[20] Because of the unavoidable variations of the IR photometry among different catalog versions, while they were being built, two objects now appear slightly below this ×4 threshold (Figure 1, left panel).
[21] Accurate SFR measurements were derived by fitting IRAC to radio 20 cm photometry from Jin et al. (2018) with four components as follows: a Bruzual & Charlot (2003) SED for the stellar component (with an age of 200 Myr, constant SFH, $Z_\odot$, Chabrier IMF, and Calzetti attenuation law), a mid-infrared AGN template from Mullaney et al. (2011), and a warm+cold dust SED from the full Draine & Li (2007) library.

Table 1
Main Properties of the Magellan Starbursts

ID	R.A. (deg)	Decl. (deg)	z_{spec}	$\log(M_*)$ ($M_\odot$)	$\log(\mathrm{LIR_{SFR}})$ ($L_\odot$)	$H\alpha$ (10^{-17} $\frac{erg}{s\ cm^2}$)	Paβ (10^{-17} $\frac{erg}{s\ cm^2}$)	$A_{V,tot}$ (mag)	$N_{H,X}$ (cm^{-2})	M_{type}
245158	150.18854	1.65498	0.5172	10.7	11.89 ± 0.07	249.6 ± 30.1	52.0 ± 5.6[a]	1.9 ± 0.1	⋯	S, m
493881	150.74967	2.04707	0.6039	10.8	12.09 ± 0.06	330.9 ± 30.2	53.3 ± 11.5	2.7 ± 0.2	⋯	⋯
223715	149.76537	1.61702	0.5174	10.7	11.78 ± 0.03	204.0 ± 20.8	28.5 ± 6.6	3.6 ± 0.2	⋯	m, S
249989	150.68540	1.66108	0.6656	10.6	11.90 ± 0.08	127.6 ± 15.9	19.0 ± 3.3	4.4 ± 0.2	⋯	MIII
894779	150.42710	2.65644	0.5506	10.0	11.79 ± 0.03	129.7 ± 19.3	22.0 ± 3.8	4.5 ± 0.2	⋯	MIV
466112	149.99928	2.00599	0.7607	10.3	12.16 ± 0.04	81.7 ± 6.2	20.9 ± 3.5	5.2 ± 0.3	⋯	MIII
470239	150.48155	2.01096	0.6609	10.6	12.12 ± 0.17	92.3 ± 9.5	23.0 ± 2.2	6.2 ± 0.2	⋯	⋯
500929	149.76844	2.05935	0.9498	10.8	12.25 ± 0.14	21.9 ± 5.3	<14.3[a]	>6.2	⋯	MIII
412250	150.74171	1.91764	0.8397	10.3	12.21 ± 0.04	118.6 ± 10.5	16.0 ± 4.7	6.7 ± 0.6	⋯	MIII
668738	150.21020	2.31168	0.7481	10.8	12.20 ± 0.04	81.4 ± 7.5	14.1 ± 1.4	6.7 ± 0.2	⋯	MIII
635862	149.69589	2.26450	0.5508	11.0	11.58 ± 0.10	59.7 ± 8.8	11.0 ± 2.7	6.8 ± 0.6	22.54 ± 0.14	⋯
862072	150.12329	2.60376	0.6811	11.1	11.98 ± 0.07	58.3 ± 6.0	14.3 ± 1.9	7.8 ± 0.4	⋯	m, S
222723	150.17321	1.61632	0.5254	11.0	12.05 ± 0.05	150.7 ± 11.1	24.4 ± 4.8	8.1 ± 0.5	<21.66	MV
519651	150.43020	2.08688	0.6709	10.5	12.15 ± 0.05	126.0 ± 10.5	19.5 ± 3.0	8.8 ± 0.5	⋯	MIV
911723	149.68134	2.68108	0.6606	10.8	12.03 ± 0.02	65.9 ± 7.2	16.2 ± 3.1	9.1 ± 0.6	21.98 ± 0.36	E
326384	149.51786	1.78357	0.8042	10.3	12.20 ± 0.07	68.8 ± 8.8	12.4 ± 3.8	9.8 ± 1.1	⋯	S
685067	149.74730	2.34574	0.3735	11.0	11.75 ± 0.01	136.9 ± 16.5	26.1 ± 1.2	10.9 ± 0.3	⋯	⋯
893857	150.15995	2.65434	0.8512	11.1	12.26 ± 0.09	27.4 ± 1.6	<11.5[a]	>11	⋯	E
578239	150.76543	2.18099	0.5578	11.1	12.21 ± 0.23	116.5 ± 10.4	26.1 ± 1.6	11.7 ± 0.3	22.36 ± 0.31	⋯
777034	150.15025	2.47517	0.6889	10.8	12.43 ± 0.08	114.0 ± 13.3	20.5 ± 1.8	12.0 ± 0.4	22.96 ± 0.04	MIV
303305	150.48305	1.74796	0.5306	10.7	11.84 ± 0.10	19.9 ± 3.6	<10.0[a]	>13.9	⋯	⋯
232171	150.06033	1.63269	0.5251	11.1	11.71 ± 0.02	60.1 ± 14.2	<8.5	>17.6	23.83 ± 0.1	MII
472775	150.48148	2.01362	0.6604	10.8	12.17 ± 0.06	44.3 ± 4.1	9.9 ± 1.6	18.0 ± 1.3	⋯	⋯
545185	149.52802	2.12725	0.5337	10.4	12.10 ± 0.06	49.8 ± 4.2	10.9 ± 0.9	22.5 ± 1.0	⋯	MIII
345018	149.72556	1.81069	0.7521	10.6	12.25 ± 0.06	37.0 ± 3.6	7.1 ± 2.1	23.7 ± 3.4	⋯	m, S

Note. ID, R.A., decl. (J2000), and M_* are from Laigle et al. (2016). The 1-σ error on M_* is 0.1 dex. Line fluxes are measured from aperture-corrected spectra. Aperture correction errors (∼0.04 dex) are included in the uncertainties. The infrared luminosities (integrated between 8 and 1000 μm), are AGN-torus-decontaminated. Hα and Paβ are corrected for stellar absorption, assuming $EW_{abs} = 2.6$ and 2 Å, respectively. The morphological type (M_{type}) of Kartaltepe et al. (2010): E = elliptical/S0; S = spiral/disc; m = minor merger; M = major merger (I: first approach, II: first contact, III: pre-merger, IV: merger, V: old merger/merger remnant). The galaxies are ordered with increasing $A_{V,tot}$.
[a] Derived as Paβ = 2.2 × Paγ.

of the galaxies with good detection (S/N > 5) of both lines. Double-Gaussian components were fitted to line profiles whenever single-Gaussian fits could be rejected based on χ^2 statistics, always resulting in good fits ($\chi^2_{red} < 1.5$). We attribute these double-Gaussians to either rotation or the presence of physically separated components.

The target list with the main physical properties is presented in Table 1, while i-band, H-band, and radio (3 GHz) cutout images of representative targets are shown in Figure 3.

4. Results

The wide spectral coverage of FIRE and the wealth of photometric data available for our targets makes this a unique sample to investigate attenuation through the use of different indicators as emission lines and the total infrared luminosity. In the left panel[22] of Figure 4 we compare the ratio of Hα and Paβ (Paschen-Balmer decrement) to the ratio of SFRs derived from the observed Paβ and bolometric IR ($A_{Pa\beta,IRX} = 2.5 \times \log_{10}(1 + SFR_{IR}/SFR_{Pa\beta,obs})$,[23] where $SFR_{Pa\beta,obs}$ has been derived from the observed Paβ luminosity, adopting an intrinsic ratio Paβ/Hα = 0.057 and a standard Kennicutt et al. (1994) calibration, valid for case B recombination and $T_e = 10^4$ K. We show that for our 25 starbursts, these two ratios, both independent measures of attenuation, do not generally scale as predicted by the Calzetti et al. (2000) and Cardelli et al. (1989) attenuation curves.[24] The value of Paβ/Hα rather saturates at ∼0.18 (with a dispersion of ∼0.08 dex), qualitatively consistent with an optically thick "mixed model," in which different lines probe different optical depths.

As opposed to the foreground dust-screen, a mixed model is made of a uniform extended distribution of young stars and dust inside a volume. In the one-dimensional case, a simple analytic relation can be derived between the observed and intrinsic SFR by integrating along a segment of the luminosity contribution from each differential volume element, subject to the extinction of the full optical depth in front of it. This yields

$$\frac{SFR_{obs}(\lambda)}{SFR_{intr}(\lambda)} = \frac{L(\lambda)_{obs}}{L(\lambda)_{intr}} = \frac{\log_{10}(e)}{0.4} \times \left(\frac{1 - 10^{-0.8A_{tot}(\lambda)}}{2A_{tot}(\lambda)}\right), \quad (1)$$

where $L(\lambda)$ is the luminosity of a line at a wavelength λ and $A_{tot}(\lambda)$ is the total absolute attenuation at λ toward the center defined as $k(\lambda)A_{V,tot}/R_V$. In the last expression, $k(\lambda)$ and R_V correspond to the local extinction, for which we assumed two

[22] This plot is equivalent to an IRX-β plot (Meurer et al. 1999).
[23] For three galaxies in our sample where Paβ falls in nearly opaque atmospheric spectral regions or out of FIRE coverage, we use the Paγ line to infer the attenuation, estimating Paβ flux as 2.2 × Paγ (Table 1). Indeed, both in a mixed model and foreground dust-screen geometry, the expected observed ratio Paβ/Paγ ranges between 2.1 and 2.3, for all the attenuation values in our range.
[24] The Cardelli relation is actually an extinction law.

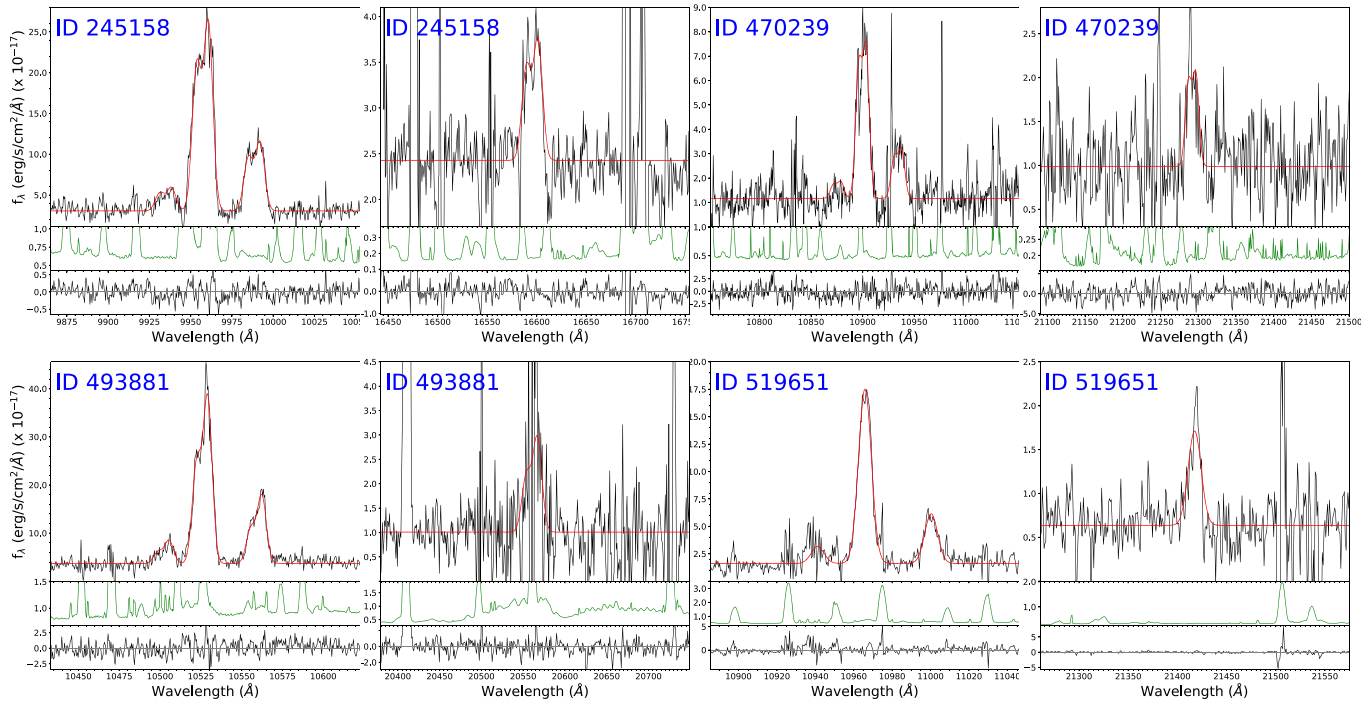

Figure 2. Hα and Paβ (Paγ for ID 245158) emission lines for four representative galaxies. In each panel, the spectra around the lines are shown, together with their best-fit Gaussians in red, derived with MPFIT (Markwardt 2009). In the bottom panels we display the noise and the residual of the fit (data-model) normalized by the noise.

extreme cases of a Cardelli et al. (1989) and an SMC (Bouchet et al. 1985) law, yielding an asymptotic Paβ/Hα ratio of 0.17 and 0.2, respectively. Using Equation (1),[25] we can predict the observed fluxes at all wavelengths as a function of a single parameter, $A_{\rm V,tot}$. For small values of $A_{\rm V,tot}$ this model coincides with the standard attenuation curves adopted. For large $A_{\rm V,tot}$, the local extinction inside the starburst core increases toward the center until the photons are not able to escape anymore from the galaxy, and are fully absorbed by the outer layers of dust. This leads us to depict heavily obscured starbursts as made of a central optically thick core, invisible to us, and a surrounding *skin*, producing the observed optical and near-IR nebular lines.

This picture naturally explains both the larger attenuation and SFR fraction that can be recovered by near-IR observations with respect to optical studies (Puglisi et al. 2017), as near-IR wavelengths allow us to penetrate deeper in the system. Because only the less attenuated light from the skin comes out, from Paβ we can recover, on average, 30% of the total IR SFR (center panel of Figure 4). However, inside the skin the optical depth quickly becomes large, with median $A_{\rm V,tot,mixedmodel} = 9$, corresponding to a suppression of $\times$4000 of V-band light from the starburst core centers and up to extreme cases with $A_{\rm V,tot,mixedmodel} \sim 30$ (10^{12} in linear scale). Hence, we cannot directly see the starburst cores in the optical/near-IR.

5. Discussion

Can we conclude that $z \sim 0.7$ SBs contain extremely obscured cores that are well described by mixed stars/dust models? It is worthwhile to consider alternative explanations. It might be possible that the UV radiation from newly born massive stars is absorbed by dust within H II regions, before reaching to ionize H I outside. While strong stellar winds push the dust away to form a screen (Calzetti et al. 2000), a substantial amount of absorbing dust may still be trapped in the ongoing SF site (Caplan & Deharveng 1986; Bell & Kennicutt 2001), particularly in these very dust-rich galaxies. This would *simulate* the existence of an optically thick SB core, just reducing the fraction of photons seen by H I, and could still represent a mixed model scenario, with mixing occurring at smaller scales. Whether this is a viable option depends on geometry and is difficult to model in detail.

Alternatively, the discrepant SFRs (coming from the lines and IR bolometric luminosity) may be due to time-variation effects, as $L_{\rm IR}$ probes longer SFR timescales than emission lines, due to the energy contribution of longer-lived B-type stars to ionizing O stars. In our case, this would require that most SBs have recently experienced a severe SFR truncation, which seems unlikely. Instantaneous and dust-free SFR tracers, like e.g., through CO[5-4] lines (Daddi et al. 2015), would shed light and help with definitively addressing this possibility.

Due to the optically thick cores, the mixed model also implies that it might not be possible to detect AGNs from optical and near-IR observations, if they are located in the coalescing center. Interestingly, Figure 4 shows that our SB galaxies often display high N2 ($\equiv \log$[N II]/Hα) indexes, which might suggest highly ionizing, AGN-dominated emission. We also see a correlation, significant at >95% confidence level (Spearman correlation coefficient $r = 0.5$), between N2 and $A_{\rm V,tot,mixedmodel}$.[26] We argue that instead, in the majority of our targets with enhanced

[25] Calzetti et al. (1994) derived a similar equation (n.19) for a mixing geometry.

[26] This incidentally suggests that the four galaxies with Paβ upper limits are also very highly obscured, having relatively high N2.

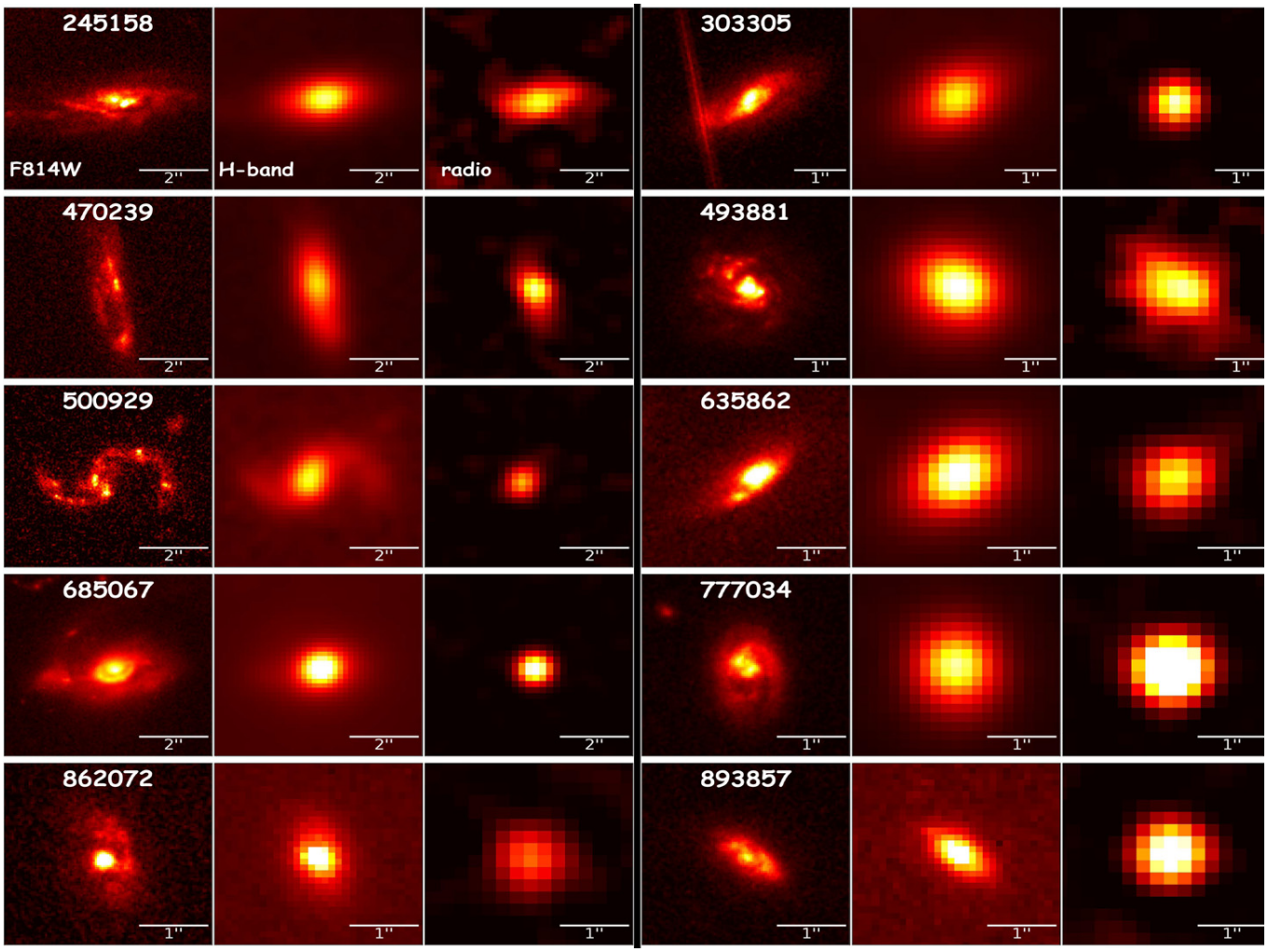

Figure 3. Left: *HST*-ACS F814W cutout images for the galaxies observed in the first Magellan run. Their FWHM resolution is 0.″095. Center: H-band UltraVISTA images with the same field of view and with $\mathrm{FWHM_{res}} \sim 0.''75$. Right: 3 GHz radio images from the VLA-COSMOS 3 GHz Large Project (Smolčić et al. 2017), FWHM $\sim 0.''75$. For the galaxies 862072 and 893857, higher-resolution (0.″2) H-band cutouts from the COSMOS-DASH program are shown (Momcheva et al. 2016).

[N II]/Hα (and relatively higher obscurations), the line emission may be driven by shocks, which were already shown to contribute up to 50% in local ULIRGs in latest merger stages (Rich et al. 2015). In case of shock contribution, the attenuations that we have inferred through $A_{\mathrm{Pa}\beta,\mathrm{IRX}}$ would represent lower limits, but the line ratios will not be affected as Case B recombination regime still holds.

Nevertheless, it would be crucial to obtain independent estimates of actual attenuations toward the cores. One possibility is provided by AGNs. We searched for evidence of AGNs among our SBs using multiple dust-free multi-wavelength tracers in the radio and X-rays. While none of our SBs show significant radio excess, either following the criteria of Del Moro et al. (2013) and the less stringent requirements of Liu et al. (2018; all assuming an IR-radio correlation), six galaxies (ID 578239, 635862, 777034, 232171, 222723, and 911723) are detected by *XMM-Newton*, *Chandra,* or *NuStar* (Cappelluti et al. 2009; Civano et al. 2015; Marchesi et al. 2016) with luminosities much higher than what was expected from their SFRs (Ranalli et al. 2004). These objects also have a mid-IR dusty torus component detected through SED fitting. Their X-ray hardness ratios were converted in obscuring column densities (N_{H}) by Lanzuisi et al. (2017; see Figure 19 in LaMassa et al. 2016 for the method), which are N_{H} upper limits for gas/dust obscurations to the cores (part of the obscuration would happen within the torus itself). The relation of Güver & Özel (2009) allows us to convert N_{H} into total A_{V} and $(N_{\mathrm{H}}(\mathrm{cm}^2) = 2.21 \times 10^{21}\, A_{\mathrm{V}}(\mathrm{mag}))$. This generally returns very high X-ray obscurations for the AGNs (Figure 4-right), supporting the presence of high obscuration in their center, as required by the mixed model.

As a further check, we computed the column density of gas in the SB cores using the total molecular mass M_{mol}, inferred as $M_{\mathrm{mol}} = 8.05 + 0.81 \times \log(\mathrm{SFR})$ (Sargent et al. 2014, assuming conservatively the starburst case) and the radio size, measured with GALFIT by fitting a Gaussian profile (convolved with the PSF) to their VLA (3 GHz) images (Figure 3). From the right panel Figure 4 we can see that for half of our sample, at relatively low-moderate obscurations within the probed range, the attenuation inferred from this method is consistent with the mixed model. On the other hand, toward the highest obscurations, this approach suggests even larger attenuations. Some fraction of the emission line fluxes might come from foreground regions unrelated to the

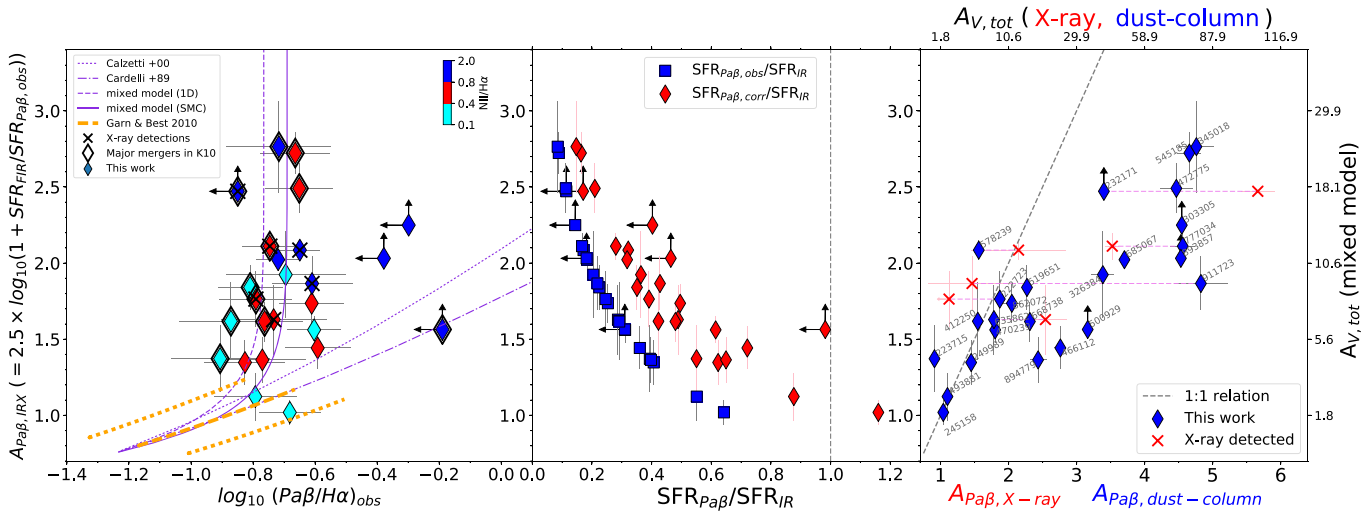

Figure 4. Left: diagram comparing the observed Paβ/Hα ratio and $A_{\mathrm{Pa}\beta,\mathrm{IRX}}$. Upper and lower limits are shown with arrows for four galaxies in the sample, while a color-coding highlights their [N II]/Hα values. Center: ratio of the SFR (relative to IR) derived from the observed Paβ line (blue) and after correcting the Paβ fluxes using the Balmer(Hα)–Paschen(β) decrement and a Calzetti et al. (2000) attenuation law (red). We remark that the unobscured UV SFR represents $\sim$1% of that derived from the IR, thus its contribution to the total SFR is negligible for our sample. Right: comparison between $A_{\mathrm{Pa}\beta,\mathrm{IRX}}$, which directly translates into the total A_{V} toward the center of a mixed model (right axis) with: (blue circles) $A_{\mathrm{Pa}\beta}$ derived from the dust column-density and (red crosses) $A_{\mathrm{Pa}\beta}$ calculated from X-ray hydrogen column-density N_{H} (Lanzuisi et al. 2017) for X-ray-detected galaxies, as explained in the text.

starbursting cores, presumably residual material from the merging galaxies. Accounting for this extra, modestly attenuated component, would result in a substantial increase of the $A_{\mathrm{V,tot}}$ of the starburst core, providing better agreement with these column densities estimates. A proper correction for this effect would require IFU observations, which could also clarify whether our objects are similar to local ULIRGs, for which higher values of nuclear attenuations ($A_{\mathrm{V}} \sim$ 10–1000 mag) are reported in several studies (e.g., Genzel et al. 1998; Scoville et al. 1998). All in all, it appears that very heavily embedded cores are indeed present in these galaxies.

What is the origin of these extremely obscured cores? Unsurprisingly (Figure 3), morphological classification was independently derived for 18 starbursts in our sample (Kartaltepe et al. 2010, see Table 1), and over 83% of them were identified as mergers: 11 as major mergers (61%), showing distorted or double nuclei, tidal tales, bridges, or overlapping disks; and 4 (22%) as minor mergers, characterized by at least slightly disturbed morphology (e.g., warped disks, asymmetric spiral arms, small companion at same z, etc.). Visual inspection for the remaining sources suggests that merger origin is at least plausible for the vast majority of our sample. Mergers are, in fact, more commonly identified among less obscured systems (Table 1), which is understandable given that in the later coalescence phases any remaining merger signature becomes subtle (see, e.g., two of the three morphologically non-merger objects in our sample classified as Ellipticals/S0 by Kartaltepe et al. (2010), and the three of them have $A_{\mathrm{V,tot}} > 9$). It is thus tempting to attribute the large range of observed properties apparently defining a sequence of obscurations as reflecting different merger phases, to varying progenitor properties (including, e.g., the gas fraction of merging galaxies and the impact geometry), or a combination of them. Nevertheless, we cannot definitely exclude with our data that the sequence may also be reflecting the amount of foreground contamination, which would make our data unrelated to the real obscuration of the core.

Our work suggests that deeply embedded merger events still largely dominate among sample of SBs galaxies at least to $z \sim 0.7$, which corresponds to a 6.3 Gyr lookback time, an epoch with galaxy specific SFRs that are on average $> 5\times$ larger than local rates. At even higher redshifts, it becomes much harder to identify mergers from their morphological signatures ,due to surface brightness dimming and widespread presence of clumpy/irregular galaxies. We argue instead that higher-z mergers might be even more efficiently identified when searching for evidence of extreme levels of obscuration, given our results; also, consistent with simulations (e.g., Di Matteo et al. 2005), these mergers might represent a clear footprint of the origin of these obscurations. In fact, we are not aware of any viable alternative mechanism that could produce galaxy-wide obscurations of 10+ mag in the V-band: normal disk-like galaxies display much lower obscurations (see the orange lines in the left panel of Figure 4). Near-IR rest-frame spectra of galaxies will soon be easily accessible with *JWST* up to $z \simeq 7$ and down to much fainter levels, and will allow for tests and applications of this idea.

We thank the referee for useful suggestions; thank G.Rudie for assistence with Magellan observations, thank Nicolás Ignacio Godoy for data reduction, and thank Daniela Calzetti for discussions. We acknowledge support from FONDECYT regular programs 1150216, 1171710, and 1170618, ERC Advanced Grant 695671 "QUENCH", JSPS KAKENHI grant No. JP17K14257, CONICYT D.N.21161487, the Brain Pool Program, funded by the Ministry of Science and ICT through the Korean National Research Foundation (2018H1D3A2000902), and RadioNet conference funding.

ORCID iDs

A. Calabrò https://orcid.org/0000-0003-2536-1614
E. Daddi https://orcid.org/0000-0002-3331-9590
P. Cassata https://orcid.org/0000-0002-6716-4400
M. Onodera https://orcid.org/0000-0003-3228-7264

R. Gobat https://orcid.org/0000-0003-0121-6113
A. Puglisi https://orcid.org/0000-0001-9369-1805
S. Jin https://orcid.org/0000-0002-8412-7951
R. Amorín https://orcid.org/0000-0001-5758-1000
M. Boquien https://orcid.org/0000-0003-0946-6176
R. Carraro https://orcid.org/0000-0002-6089-1947
D. Elbaz https://orcid.org/0000-0002-7631-647X
S. Juneau https://orcid.org/0000-0002-0000-2394
G. Rodighiero https://orcid.org/0000-0002-9415-2296
F. Valentino https://orcid.org/0000-0001-6477-4011
A. Zanella https://orcid.org/0000-0001-8600-7008

References

Bell, E. F., & Kennicutt, R. C., Jr. 2001, ApJ, 548, 681
Bouchet, P., Lequeux, J., Maurice, E., Prevot, L., & Prevot-Burnichon, M. L. 1985, A&A, 149, 330
Bruzual, G., & Charlot, S. 2003, MNRAS, 344, 1000
Calzetti, D., Armus, L., Bohlin, R. C., et al. 2000, ApJ, 533, 682
Calzetti, D., Kinney, A. L., & Storchi-Bergmann, T. 1994, ApJ, 429, 582
Caplan, J., & Deharveng, L. 1986, A&A, 155, 297
Cappelluti, N., Brusa, M., Hasinger, G., et al. 2009, A&A, 497, 635
Cardelli, J. A., Clayton, G. C., & Mathis, J. S. 1989, ApJ, 345, 245
Chabrier, G. 2003, PASP, 115, 763
Civano, F., Hickox, R. C., Puccetti, S., et al. 2015, ApJ, 808, 185
Daddi, E., Dannerbauer, H., Liu, D., et al. 2015, A&A, 577, A46
Daddi, E., Dickinson, M., Morrison, G., et al. 2007, ApJ, 670, 156
Del Moro, A., Alexander, D. M., Mullaney, J. R., et al. 2013, A&A, 549, A59
Di Matteo, T., Springel, V., & Hernquist, L. 2005, Natur, 433, 604
Draine, B. T., & Li, A. 2007, ApJ, 657, 810
Fensch, J., Renaud, F., Bournaud, F., et al. 2017, MNRAS, 465, 1934
Gagné, J., Lambrides, E., Faherty, J. K., & Simcoe, R. 2015, FireHose_v2: Firehose v2.0. Zenodo, doi:10.5281/zenodo.18775
García-Marín, M., Colina, L., & Arribas, S. 2009, A&A, 505, 1017
Genzel, R., Lutz, D., Sturm, E., et al. 1998, ApJ, 498, 579
Goldader, J. D., Meurer, G., Heckman, T. M., et al. 2002, ApJ, 568, 651
Güver, T., & Özel, F. 2009, MNRAS, 400, 2050
Hopkins, P. F., Bundy, K., Croton, D., et al. 2010, ApJ, 715, 202
Jin, S., Daddi, E., et al. 2018, ApJ, submitted (arXiv:1807.04697)
Juneau, S., Narayanan, D. T., Moustakas, J., et al. 2009, ApJ, 707, 1217
Kartaltepe, J. S., Sanders, D. B., Le Floc'h, E., et al. 2010, ApJ, 721, 98
Kennicutt, R. C., Jr., Tamblyn, P., & Congdon, C. E. 1994, ApJ, 435, 22
Laigle, C., McCracken, H. J., Ilbert, O., et al. 2016, ApJS, 224, 24
LaMassa, S. M., Civano, F., Brusa, M., et al. 2016, ApJ, 818, 88
Lanzuisi, G., Delvecchio, I., Berta, S., et al. 2017, A&A, 602, A123
Liu, D., Daddi, E., Dickinson, M., et al. 2018, ApJ, 853, 172
Magdis, G. E., Daddi, E., Béthermin, M., et al. 2012, ApJ, 760, 6
Marchesi, S., Lanzuisi, G., Civano, F., et al. 2016, ApJ, 830, 100
Markwardt, C. B. 2009, adass XVIII, 411, 251
Meurer, G. R., Heckman, T. M., & Calzetti, D. 1999, ApJ, 521, 64
Momcheva, I. G., Brammer, G. B., van Dokkum, P. G., et al. 2016, ApJS, 225, 27
Mullaney, J. R., Alexander, D. M., Goulding, A. D., & Hickox, R. C. 2011, MNRAS, 414, 1082
Noeske, K. G., Weiner, B. J., Faber, S. M., et al. 2007, ApJL, 660, L43
Puglisi, A., Daddi, E., Renzini, A., et al. 2017, ApJL, 838, L18
Ranalli, P., Comastri, A., & Setti, G. 2004, in Proc. Guillermo Haro Conference 2003, Multiwavelength AGN Surveys, ed. R. Mújica & R. Maiolino (Singapore: World Scientific Publishing), 43
Rich, J. A., Kewley, L. J., & Dopita, M. A. 2015, ApJS, 221, 28
Rieke, G. H., Alonso-Herrero, A., Weiner, B. J., et al. 2009, ApJ, 692, 556
Rodighiero, G., Daddi, E., Baronchelli, I., et al. 2011, ApJL, 739, L40
Sargent, M. T., Béthermin, M., Daddi, E., & Elbaz, D. 2012, ApJL, 747, L31
Sargent, M. T., Daddi, E., Béthermin, M., et al. 2014, ApJ, 793, 19
Schreiber, C., Pannella, M., Elbaz, D., et al. 2015, A&A, 575, A74
Scoville, N., Sheth, K., Aussel, H., et al. 2016, ApJ, 820, 83
Scoville, N. Z., Evans, A. S., Dinshaw, N., et al. 1998, ApJL, 492, L107
Simcoe, R. A., Burgasser, A. J., Schechter, P. L., et al. 2013, PASP, 125, 270
Smolčić, V., Novak, M., Bondi, M., et al. 2017, A&A, 602, A1
Soifer, B. T., Neugebauer, G., Matthews, K., et al. 2000, AJ, 119, 509

A&A 623, A64 (2019)
https://doi.org/10.1051/0004-6361/201834522
© A. Calabrò et al. 2019

Astronomy & Astrophysics

Deciphering an evolutionary sequence of merger stages in infrared-luminous starburst galaxies at $z \sim 0.7$

A. Calabrò[1], E. Daddi[1], A. Puglisi[1], E. Oliva[2], R. Gobat[3], P. Cassata[4], R. Amorín[5,6], N. Arimoto[7], M. Boquien[8], R. Carraro[9], I. Delvecchio[1], E. Ibar[9], S. Jin[1,10], S. Juneau[11], D. Liu[12], M. Onodera[13,14], F. Mannucci[2], H. Méndez-Hernández[9], G. Rodighiero[4], F. Valentino[15], and A. Zanella[16]

[1] CEA, IRFU, DAp, AIM, Université Paris-Saclay, Université Paris Diderot, Sorbonne Paris Cité, CNRS, 91191 Gif-sur-Yvette, France
e-mail: antonello.calabro@cea.fr
[2] INAF–Osservatorio Astrofisico di Arcetri, Largo Enrico Fermi 5, 50125 Firenze, Italy
[3] Instituto de Física, Pontificia Universidad Católica de Valparaíso, Casilla 4059, Valparaíso, Chile
[4] Dipartimento di Fisica e Astronomia "G. Galilei", Università di Padova, Vicolo dell'Osservatorio 3, 35122, Italy
[5] Departamento de Física y Astronomía, Universidad de La Serena, Av. Juan Cisternas 1200 Norte, La Serena, Chile
[6] Instituto de Investigación Multidisciplinar en Ciencia y Tecnología, Universidad de La Serena, Raúl Bitrán 1305, La Serena, Chile
[7] Astronomy Program, Department of Physics and Astronomy, Seoul National University, 599 Gwanak-ro, Gwanak-gu, Seoul 151-742, Korea
[8] Centro de Astronomía (CITEVA), Universidad de Antofagasta, Avenida Angamos 601, Antofagasta, Chile
[9] Instituto de Física y Astronomía, Facultad de Ciencias, Universidad de Valparaíso, Gran Bretaña 1111, Playa Ancha, Valparaíso, Chile
[10] Key Laboratory of Modern Astronomy and Astrophysics in Ministry of Education, School of Astronomy and Space Science, Nanjing University, Nanjing 210093, PR China
[11] National Optical Astronomy Observatory, 950 N. Cherry Avenue, Tucson, AZ 85719, USA
[12] Max Planck Institute for Astronomy, Konigstuhl 17, 69117 Heidelberg, Germany
[13] Subaru Telescope, National Astronomical Observatory of Japan, National Institutes of Natural Sciences (NINS), 650 North A'ohoku Place, Hilo, HI 96720, USA
[14] Department of Astronomical Science, SOKENDAI (The Graduate University for Advanced Studies), 650 North A'ohoku Place, Hilo, HI 96720, USA
[15] Cosmic Dawn Center (DAWN), Niels Bohr Institute, University of Copenhagen, Juliane Maries Vej 30, 2100 Copenhagen Ø; DTU-Space, Technical University of Denmark, Elektrovej 327, 2800 Kgs. Lyngby, Denmark
[16] European Southern Observatory, Karl Schwarzschild Straße 2, 85748 Garching, Germany

Received 27 October 2018 / Accepted 15 January 2019

ABSTRACT

Based on optical and near-IR *Magellan* FIRE spectra of 25 starburst galaxies at $0.5 < z < 0.9$, a recent publication showed that their attenuation properties can be explained by a single-parameter sequence of total obscurations ranging from $A_V = 2$ to $A_V = 30$ toward the starburst core centers in a mixed stars and dust configuration. We investigate here the origin of this sequence for the same sample. We show that total attenuations anticorrelate with the starburst sizes in radio (3 GHz) with a significance larger than 5σ and a scatter of 0.26 dex. More obscured and compact starbursts also show enhanced N2 (=[NII]/Hα) ratios and larger line velocity widths that we attribute to an increasing shock contribution toward later merger phases, driven by deeper gravitational potential wells at the coalescence. Additionally, the attenuation is also linked to the equivalent width (EW) of hydrogen recombination lines, which is sensitive to the luminosity weighted age of the relatively unobscured stellar populations. Overall, the correlations among $A_{V,\mathrm{tot}}$, radio size, line width, N2 and EW of Balmer and Paschen lines converge toward suggesting an evolutionary sequence of merger stages: all of these quantities are likely to be good time-tracers of the merger phenomenon, and their large spanned range appears to be characteristic of the different merger phases. Half of our sample at higher obscurations have radio sizes approximately 3 times smaller than early type galaxies at the same redshift, suggesting that, in analogy with local ultraluminous infrared galaxies (ULIRGs), these cores cannot be directly forming elliptical galaxies. Finally, we detect mid-IR AGN torus for half of our sample and additional X-ray emission for 6 starbursts; intriguingly, the latter have systematically more compact sizes, suggestive of emerging AGNs toward later merger stages, possibly precursors of a later QSO phase.

Key words. galaxies: evolution – galaxies: formation – galaxies: high-redshift – galaxies: interactions – galaxies: starburst – galaxies: star formation

1. Introduction

Starburst galaxies (SBs) host the most powerful star-formation events in the Universe, with star-formation rates (SFR) that, following to the definition of Rodighiero et al. (2011), are at least four times higher compared to the average galaxy population at a given redshift, identified by the star-forming main sequence (MS; Brinchmann et al. 2004; Noeske et al. 2007; Elbaz et al. 2007; Daddi et al. 2007a). In the local Universe these systems are called ultra-luminous infrared galaxies (ULIRGs) and have a global infrared luminosity higher than $10^{12}\,L_{\odot}$, due to their high stellar production. ULIRGs are characterized by peculiar

Open Access article, published by EDP Sciences, under the terms of the Creative Commons Attribution License (http://creativecommons.org/licenses/by/4.0), which permits unrestricted use, distribution, and reproduction in any medium, provided the original work is properly cited.

and rather homogeneous properties: they show very compact starbursting cores of dense gas, with typical diameter sizes of 0.5−2 kpc, and may contain double nuclei (Genzel et al. 1998; Díaz-Santos et al. 2010). As a consequence of the enhanced SFR density, these cores are also highly dust-rich and completely obscured in the optical/UV, with A_V ranging 5−50 mag in a foreground dust screen model (Genzel et al. 1998; Goldader et al. 2002).

SBs represent a small fraction of the whole star-forming (SF) galaxy population (2−3%), almost constant with redshift, according to Sargent et al. (2012, 2014) and Schreiber et al. (2015), but they constitute a key event in the life of a galaxy. Indeed, at $z \sim 0$ the only viable option to explain these concentrations of gas, dust and SFR is through highly dissipative major merger events (Sanders & Mirabel 1996), in which the gas of colliding galaxies loses angular momentum and energy during the interaction, falling into the coalescing center of the system. Here it serves as fuel for the starburst and for the growth of a supermassive black hole in the center. This scenario is sustained by studies of both local ULIRGs and higher redshift merging and starburst galaxies, showing the presence of an AGN with optical (Ellison et al. 2011), mid-IR (Daddi et al. 2007b; Weston et al. 2017; Satyapal et al. 2017; Goulding et al. 2018), X-ray (Brusa et al. 2010; Aird et al. 2019) and radio (Best & Heckman 2012; Chiaberge et al. 2015) diagnostics. The starburst activity and subsequent AGN feedback can cause gas consumption and removal through powerful winds (Sanders et al. 1988; Silk & Rees 1998), leading to a passively evolving elliptical galaxy (Kormendy & Sanders 1992; Springel et al. 2005a; Hopkins et al. 2008a).

Hydrodynamical simulations indicate that the morphology of merger remnants is consistent with early type galaxies (ETGs), suggesting the scenario that gas-rich major mergers are primarily responsible for the formation of the massive ellipticals (Barnes & Hernquist 1991; Mihos & Hernquist 1994, 1996). This evolutionary sequence is strengthened by observations of low surface brightness tidal tales and residual interacting features in local ETGs (Duc et al. 2013), which may come from major mergers. Other studies have shown that ULIRGs lie on or close to the fundamental plane (effective radius-velocity dispersion-surface brightness) of intermediate-mass ellipticals, S0 galaxies and bulges of local spirals, suggesting that these systems are the final step of gas-rich merger episodes (Genzel et al. 2001).

The morphological transformation during the merger happens in different phases that are well represented by the so-called Toomre sequence (Toomre & Toomre 1972). Following the result of their simulations, several studies have tried to characterize this sequence by looking at different physical properties of the nuclear regions of merger galaxies, but found no correlations with evolutionary stages (e.g., Laine et al. 2003), apart from noticing that latest interaction times, during or after the coalescence, have among the highest infrared luminosities ($L_{\rm IR}$) (Laine et al. 2003; Haan et al. 2013). The absence of clear correlations in these works can be interpreted either with the difficulty of identifying correctly the merger phase from the optical morphology (which becomes even more problematic beyond the local Universe) or that other parameters are driving and tracing this transformation. For example, Gao & Solomon (1999) and Leech et al. (2010) studied a sample of local (U)LIRGs with double merging nuclei. They found lower molecular gas masses and higher star-formation efficiency and gas excitation (probed by the CO(3–2)/CO(1–0) line ratio) with decreasing separation between merger components, that is, toward more advanced merger stages. However, since their sample only includes interacting pairs more distant than ∼1 kpc, this result is limited to relatively early stage mergers and does not necessarily apply also to coalesced systems. Furthermore, some spatially resolved studies on local (U)LIRGs have found that there is a higher contribution of shocks accompanied by an increased velocity dispersion of the gas toward later merger stages (Monreal-Ibero et al. 2006, 2010; Rich et al. 2014, 2015).

While in the local Universe the relation between starbursts and mergers is well settled observationally (e.g., Murphy et al. 1996; Luo et al. 2014), at higher redshift the interpretation becomes less clear. Due to the enhanced gas fractions and disk instabilities of high redshift star-forming galaxies, mergers as a result might increase SFRs less dramatically (Fensch et al. 2017), and starburst galaxies may be triggered by anomalous gas accretion events (Scoville et al. 2016). However, other studies have shown that the most extreme starbursts are still merger-driven, displaying disturbed morphologies (Elbaz & Cesarsky 2003) and increased star-formation efficiencies compared to MS galaxies (Sargent et al. 2014; Silverman et al. 2018a,b, 2015). Similarly, the connection between mergers and AGNs is still debated. Even though it may still hold for the most luminous cases (Combes 2003), some studies (focused especially on optical wavelengths) do not find systematic differences in merger fraction and galaxy distortions between active and non-active systems (Cisternas et al. 2011; Kocevski et al. 2012), and not all AGNs are triggered by mergers, according to, for example, Draper & Ballantyne (2012) and Ellison et al. (2015).

The solution to these long-standing problems is further complicated due to the intrinsic faintness of interacting features (e.g., tidal tales, bridges) and their elevated obscurations, which hamper their identification and physical characterization. Puglisi et al. (2017) have selected a sample of starbursts (SFR × 4 above the MS) at $z \sim 1.6$, showing that optical lines, including Hα and Hβ, only probe a small nearly-unattenuated component of the galaxies, accounting for ∼10% of the total $\rm SFR_{IR}$. Therefore, a possible solution to study the properties of the dusty starburst population at high redshift is to observe at longer wavelengths, targeting near-infrared rest-frame lines, such as the Paschen line series of hydrogen. Current ground-based spectrographs can observe Paβ (the second brightest Paschen recombination line) in K band up to a redshift of ∼0.9. Motivated by this idea, we followed-up of a sample of 25 SBs at $0.5 < z < 0.9$ with FIRE (folded port infrared echellette), a near-IR spectrograph mounted at the *Magellan* telescope, in order to detect optical and near-IR lines ranging $0.6 < \lambda < 1.3$ Å rest-frame. This sample was presented in Calabrò et al. (2018), which hereafter is referred as Paper I.

By comparing Hα, Paβ fluxes and bolometric IR luminosities, we found that the attenuation properties of intermediate redshift SBs are not consistent with the predictions of dust-foreground extinction models, but rather with those of a geometrical model in which dust and stars are homogeneously mixed (Paper I). We also found that they are highly obscured on average, with median $A_{V,\rm tot} = 9$ mag in a mixed model, while independently derived dust-column densities suggest $A_{V,\rm tot}$ even higher for a large fraction of them, up to 75 mag. This means that they have extremely obscured cores and that optical and near-IR lines only probe an external skin containing a fraction (∼10−30%) of the total SFR. Even more, we argued that the presence of optically thick cores are themselves striking evidence of the merger origin of intermediate-z SBs (like in local ULIRGs), as no other mechanisms are known to produce such large obscuring column densities of gas and dust. This can

be used to identify other mergers in the high-redshift Universe (Calabrò et al. 2018), where other methods based on morphology become unfeasible.

Despite their higher average obscurations compared to MS galaxies, we found that our sample, while showing a nearly constant Paβ/Hα ratios, spans a large range of $A_{V,\rm tot}$ between 2 and 30 (see Fig. 4 in Paper I), thus forming a sequence of increasing attenuations. This indicates that a substantial intrinsic diversity should exist among them, possibly related to different phases of the merger, to the gas properties (i.e., total gas mass, gas fraction) or to the morphology of preexisting colliding galaxies. In alternative, the sequence may be driven also by the orbital geometry of the merger. For example, Di Matteo et al. (2008) have shown that the inclination of the two encounters affects both the duration and intensity of the star formation, regulating the amount of gas that is funneled toward the coalescing center.

In this paper we investigate the origin of the obscuration sequence that was found in Paper I, analyzing the attenuations $A_{V,\rm tot}$ of our starbursts in relation with other physical properties derived from our *Magellan* spectra and from available multi-wavelength images. In Sect. 2 we describe how the starbursts are selected from the parent photometric catalog along with our *Magellan*-FIRE observations, spectra reduction (which includes also the analysis of public optical spectra available for a fraction galaxies) and subsequent emission line fluxes (and equivalent width) measurements. This will be followed by a description of the morphological properties, radio size measurements and AGN identification within our sample. In Sect. 3 we will show the main results of this work, which are discussed extensively in Sect. 4. A summary with conclusions will be presented in the last Sect. 5. We adopt the Chabrier (2003) initial mass function, AB magnitudes, and standard cosmology ($H_0 = 70\,\rm km\,s^{-1}\,Mpc^{-1}$, $\Omega_{\rm m} = 0.3$, $\Omega_\Lambda = 0.7$). We also assume by convention a positive equivalent width (EW) for emission lines and a negative EW for lines in absorption.

2. Methodology

In this section we outline the general starburst selection procedure, and then describe the observations, the spectral reduction and the emission line measurements that were performed for a representative subset of 25 of them. We will then present their morphological classification, radio size measurements and AGN identification procedure.

As described in Paper I, we already calculated for this subset the absolute dust attenuation in V band toward the center (=$A_{V,\rm tot}$) in two steps. First, we considered the ratio ($\rm SFR_{IR}/SFR_{Pa\beta,obs}$), where $\rm SFR_{IR}$ is the intrinsic SFR from the infrared and $\rm SFR_{Pa\beta,obs}$ is derived from the observed Paβ luminosity, adopting an intrinsic ratio Paβ/Hα = 0.057 and a standard Kennicutt et al. (1994) calibration, valid for case B recombination and $T_{\rm e} = 10^4$ K. $A_{\rm Pa\beta,IRX}$ can be eventually inferred from that quantity as $= 2.5 \times \log_{10}(1 + \rm SFR_{IR}/SFR_{Pa\beta,obs})$. In the final step, the attenuation in V band is obtained by solving for $A_{V,\rm tot}$ the following equation valid for a mixed geometry model of dust and ionizing stars:

$$\frac{\rm SFR_{Pa\beta,obs}}{\rm SFR_{IR}} = \frac{\log_{10}(e)}{0.4} \times \left(\frac{1-10^{-0.8A_{\rm tot}(\rm Pa\beta)}}{2A_{\rm tot}(\rm Pa\beta)}\right) \quad (1)$$

where $A_{\rm tot}$(Paβ) is the total absolute attenuation at Paβ toward the center defined as k(Paβ) $\times$ $A_{V,\rm tot}/R_V$. In the last expression, k(Paβ) corresponds to the local extinction at Paβ, assuming a Cardelli et al. (1989) law ($R_V = 3.1$). More details on the derivation and the implications of Eq. (1) can be found in Paper I.

2.1. Sample selection and Magellan FIRE observations

The starburst candidates were selected from the IR+(sub)mm catalog of Jin et al. (2018) by first requiring the spectroscopic redshift (coming from optical surveys, Salvato et al., in prep.) to be in the range between 0.5 and 0.9. This guarantees that Paβ and Hα fall, respectively, in the K and YJ bands, thus within the wavelength coverage of FIRE (0.82 μm–2.4 μm). For two galaxies, we found that their previous spectroscopic redshift measurements were not correct. Even though they are outside of our selection range, we did not remove them since they satisfy the other selection criteria.

Secondly, we required $\rm SFR_{norm}$ to be more than a factor of four higher than $\rm SFR_{MS,\it z}$ = 0.73, as in Rodighiero et al. (2011)[1], where $\rm SFR_{norm}$ is the total SFR ($\rm SFR_{tot} = SFR_{IR} + SFR_{UV,unobscured}$), normalized to the median redshift of the sample (0.73) using the evolution of Sargent et al. (2014):

$$\rm SFR_{norm} = (SFR_{IR} + SFR_{UV,unobs}) \times \left(\frac{1+0.73}{1+z}\right)^{2.8}, \quad (2)$$

while $\rm SFR_{MS,\it z=0.73}$ is the SFR of the main sequence at redshift 0.73 from Schreiber et al. (2015). This latter was found in Paper I to agree well with the MS derived independently for our parent sample through a running median on ten stellar mass bins from 10^{10} to $10^{12}\,M_\odot$. We chose this selection procedure in order to compare all the galaxies with a single MS (cf. Fig. 1 of Calabrò et al. 2018), instead of considering different relations for each galaxy redshift. However, the two procedures yielded the same number of starbursts among the whole sample. For the targets studied in this paper, the mean distance from the MS ($\rm dist_{MS} = \log_{10}(SFR_{tot}/SFR_{MS})$) would change by 1.8%, thus it would not affect in any case the results.

The $\rm SFR_{IR}$ was derived following the methodology of Jin et al. (2018) and Liu et al. (2018), which is based on fitting the photometry from IRAC to radio 1.4 GHz with four components: a stellar Bruzual & Charlot (2003) SED (with age 200 Myr, constant star-formation history, solar metallicity $Z_\odot$, Chabrier IMF and Calzetti attenuation law), a warm+cold dust emission template from Draine & Li (2007) and Magdis et al. (2012), and a mid-infrared AGN SED from Mullaney et al. (2011) to separate the IR contributions of the AGN and SF. The unobscured UV-based SFRs ($\rm SFR_{UV,unobscured}$) were calculated instead from the u-band magnitudes (Laigle et al. 2016), which probes the UV rest-frame at our redshift, following Heinis et al. (2014). Overall, the contributions of the AGN and of the UV-unobscured SFR to the total SFR are on average small (3% and 1%, respectively).

Finally, as a last requirement, we asked for M_* to be greater than $10^{10}\,M_\odot$, where M_* comes from Laigle et al. (2016) and is computed at the photometric redshift. This condition ensures that, within the mass and redshift constraints adopted here, all SBs would be IR-detected with a $S/N_{\rm IR} > 5$ (cf. Fig. 13 in Jin et al. 2018), thus we have a SFR complete sample of SBs. Then, for the whole sample, we considered the spectroscopic redshifts (when available) instead of the photometric values, however this does not significantly affect the stellar masses: the two estimates for the parent sample are in agreement within a 1σ scatter of 0.11 dex, compatible with the uncertainties reported by Laigle et al. (2016). Only for one SB analyzed in this work (ID 685067, $z_{\rm spec} = 0.37$), the new stellar mass was remarkably lower (−0.56 dex), due to the large difference with previous

[1] Two starbursts that we have previously selected and observed turned out to have slightly lower SFRs than the ×4 limit, because of subsequent updates of the photometric catalog.

photometric redshift ($z_{\rm phot}$ = 0.71). Therefore, $\rm dist_{MS}$ was even higher, strengthening its starburst selection.

This criteria yielded 152 SBs, 25 of which were observed during four nights at the *Magellan* 6.5 m Baade telescope (17−18/03/2017 and 22−23/03/2018). The observed 25 galaxies were chosen from the preselected SB sample according to a priority list. We preferentially observed sources close to bright stars (J < 19−20 mag), so as to facilitate target acquisition, although we eventually avoided blind offsets, since our galaxies are already sufficiently bright (peak magnitudes <19 mag) to be detected in ∼20−60 s in the good seeing conditions of those observations. In addition, we targeted intrinsically brighter sources first, maximizing $\rm SFR/D_L^2(z)$ ratio ($D_{\rm L}$ is the luminosity distance), and assuming no prior knowledge about the dust attenuation of the system, which was set to 0 in all cases. This introduces a small bias in our selection toward the more massive objects. However, our galaxies span the full range of stellar masses above $10^{10}\,M_{\odot}$. We refer to Fig. 1 in Paper I, where we presented the redshift, the SFR and the stellar mass distribution of our observed starbursts and our parent galaxy sample.

Our targets were observed with the single-slit echelle spectrograph FIRE (Simcoe et al. 2013), which has a wavelength range of 0.82−2.4 μm. We refer to Simcoe et al. (2013) for the full technical description of the instrument. We chose a slit width of 1″, (yielding a spectral resolution of R = 3000) to minimize slit losses (the average intrinsic FWHM angular size in K_s-band for our sample is ∼0.6″) and reduce the impact of OH sky emission. In all the cases, the slits were oriented along the semi-major axis of each galaxy, as determined from HST i-band images. Additionally, we benefited from good seeing conditions over all the four nights, with an average of 0.7″ and a minimum of 0.45″. The majority of our starbursts were observed in AB sequence, with single exposure times of 15−20 min. We chose single frame integrations of 20 min during the first run and 15 min in the second run, which significantly reduces saturation of OH lines in K band, thus helping spectral reduction in that band. We decided to double the integration times (completing the ABBA sequence) for galaxies with a lower S/N of the Hα+[N II] complex (based on real-time reduction), to improve the detection of fainter lines. In practice, doing an AB sequence is irrelevant for the spectral reduction, as the pipeline reduces each frame separately (see Sect. 2.2), though it allowed us to easily derive 2D emission line maps with the standard IRAF tasks IMARITH and IMCOMBINE.

2.2. Spectroscopic reduction

The spectra were fully reduced using the publicly available IDL-based FIREHOSE pipeline (Gagné et al. 2015). For each exposure, we used internal quartz lamps (one for each observing session) to trace the 21 orders of the echelle spectra and to apply the flat field correction. Then, the wavelength calibration was performed by fitting a low (one to five) order polynomial (depending on the spectral order) to ThAr lines of lamp exposures (taken close in time to the corresponding science frames). We checked that the residuals of the lines to the best-fit wavelength solution are less than 1 pixel in all the cases, and are <0.1 pixel for the majority of the orders. This translates into an average wavelength accuracy of $\Delta\lambda/\lambda \simeq 5 \times 10^{-5}$, nearly constant across the entire spectral range. Finally, the sky subtraction was applied independently for each single frame following the method of Kelson (2003). In this step, the OH lines in the spectra were used to refine the wavelength calibration.

The 1D spectra were extracted from the 2D frames using an optimal extraction method (Horne 1986). However, this procedure cannot be applied when there is a rapidly varying spatial profile of the object flux (Horne 1986), as in the presence of spatially extended and tilted emission lines. We used in these cases a boxcar extraction procedure, with a sufficiently large extraction aperture (always >1.3″) in order to include all the line emission from the 2D exposure. We adopted the boxcar extraction for three galaxies in our sample, which are the IDs 245158, 493881 and 470239. Given the agreement within the uncertainties between the fluxes measured with the two approaches for the remaining galaxies, the use of the boxcar procedure did not appear to introduce a systematic flux bias.

After the spectral extraction, we applied the flux calibration to each 1D extracted spectrum, using telluric spectra derived from the observations of A0V stars. Before dividing the object and telluric spectra in the pipeline, we could interactively refine the wavelength matching between the two by minimizing the rms of the product. However, slightly different times or airmasses between science and standard star observations at infrared wavelengths can produce non-negligible telluric line residuals, affecting the subsequent analysis. We found that this problem was more relevant in K-band, where strong telluric features are present in the observed wavelength ranges 19 950−20 250 Å and 20 450−20 800 Å. The residuals in these regions could produce artificial variations of the real flux up to a factor of 2, while it was less significant at shorter wavelengths (Y to H). In order to remove these artifacts, we followed the procedure described in Mannucci et al. (2001): we first considered a standard star at an airmass of ∼1.5 and calibrated it with two different stars observed at significantly lower and higher airmasses (e.g., 1.2 and 1.9). Then the two obtained spectra were divided, yielding a global correction function (which is different from 1 only in the regions of strong telluric features defined above) that applies to all the single-exposure spectra, each of them with a different multiplicative factor until the telluric line residuals disappear We fit a linear function in nearby regions free of telluric regions and emission lines, and then determined the correction function through minimizing the rms of the difference between the corrected spectrum and the aforementioned continuum fit. Finally, we combined (with a weighted-average) all the 1D calibrated spectra of the same object.

The error on the flux density f_λ obtained from the FIRE pipeline was checked over all the spectral range, analyzing the continuum of each galaxy in spectral windows of 200 Å and steps of 100 Å, masking emission lines. In each window, we rescaled the rms noise so as to have the $\chi^2_{\rm reduced}$ = 1 when fitting the continuum with a low-order ($\lesssim$1) polynomial. A spline of order 1 spanning the whole wavelength range was used as a correction function. This criterion, equivalently, ensured that the noise level matched the 1σ dispersion of the object spectrum in each window. Typical corrections were within a factor of 2, variable across the spectral bands.

Due to slit losses, variable seeing conditions and the spatial extension of our objects, which are typically larger than the slit width (1″), part of the total flux of the galaxies is lost. In order to recover the total absolute flux, we matched the whole spectrum to the photometric SED. This was done by applying a 5σ clipping and error-weighted average to the *Magellan* spectrum inside z++, Y, J, H and K_s photometric bands, and comparing the obtained mean f_λ in each filter to the corresponding broad-band photometry (Laigle et al. 2016). Since the SED shapes derived from the spectra are generally in agreement with the photometric

SED shapes, we rescaled our spectra with a constant factor, determined through a least squares minimization procedure. The aperture correction factors for our sample range between 0.8 and 3, with a median of 1.4. They are subject to multiple contributions, such as slit position with respect to the object, seeing conditions during the target and the standard stars observations. The few cases in which the aperture correction was lower than 1 could be due indeed to a much better seeing of the standard star compared to the target observation. We remind that this procedure assumes that lines and continuum are equally extended, which is clearly an approximation. Spatially resolved near-IR line maps (e.g., with SINFONI) would be required to test possible different gradients of the two emission components, and to derive better total flux corrections.

2.3. Complementary optical spectra

A subset of our *Magellan* sample also has publicly available optical spectra: ten starbursts in our sample have been observed with the VIMOS spectrograph (Le Fèvre et al. 2003) by the zCOSMOS survey (Lilly et al. 2007), and their optical spectra are publicly available through the LAM website (`cesam.lam.fr/zCOSMOS`). They span the range $5550 < \lambda < 9650$ Å, which includes [O II]λ3727 Å, Hγ, Hβ and [O III]λ5007 Å lines for our galaxies. The spectral resolution is on average $R = 600$, constant across the whole range, while the noise level increases from the blue to the red part of the spectrum, due to the increased OH sky emission at longer wavelengths. Due to the absence of the noise spectrum in the public zCOSMOS release, we used instead a sky spectrum at the same resolution of VIMOS, rescaled with a spline to match the flux standard deviation in spectral regions free of emission lines, similarly to what has been done before on the *Magellan* spectra. Even though it is a first approximation, this procedure allows to reproduce the increasing noise in correspondence of OH lines, where strong sky-subtraction residuals are expected, and take into account the higher average noise level of the red part of the spectrum. For one galaxy in our sample (ID 493881), we took its optical spectrum from SDSS-III DR9 (Ahn et al. 2012), which spans a wider wavelength range $3600 < \lambda < 10400$ Å at higher resolution ($R \sim 2000$), thus allowing a better sky subtraction and a higher S/N. In both cases, the spectra were already fully reduced, wavelength and flux calibrated, as described in the respective papers. We apply only an aperture correction by matching the observed spectrum to the photometric SED (Laigle et al. 2016) with the same methodology adopted for the *Magellan* spectra. However, we warn that there could be some mis-matches compared to our *Magellan* observations in the slit centering and orientation, as also in the seeing conditions, thus the spectra may not be exactly representative of the same regions.

2.4. Line measurements

We measured emission line fluxes, line widths and uncertainties on fully calibrated and aperture corrected spectra using the python anaconda distribution (Mark Rivers, 2002[2]) of the IDL routine MPFIT (Markwardt 2009). Given the FWHM resolution of FIRE for 1″ slit width (=100 km s^{-1}), all our emission lines are resolved, owing to intrinsically higher velocity widths.

We fit the lines with a single Gaussian on top of an underlying order-1 polynomial continuum. In each case, we required a statistical significance of the fit of 95%, as determined from the residual χ^2. When a single Gaussian did not satisfy the above condition, we used a double Gaussian (with varying flux ratio and same FWHM, in km/s, for the two components), which instead provided a better fit, placing its χ^2 within the asked confidence level. The flux uncertainties were derived by MPFIT itself, and they were always well behaved, with best-fit $\chi^2_{\rm reduced} \simeq 1$. For non detected lines (i.e., $S/N < 2$ in our case), we adopted a 2σ upper limit. We remark that we were guided by the wavelength position, line width and flux ratio (for double line components) of Hα, which was always detected at $>4\sigma$. The Gaussian amplitude remained thus the only variable to constrain the fit for the other lines. However, we highlight that our detected emission lines have always high S/N ratios: Hα, [N II]λ6584 Å and Paβ were identified on average at 9.3, 8.4 and 7.4σ, respectively (lowest S/N were 4, 5.3 and 3.3 for the same lines).

We fit a double Gaussian for 12 galaxies in our sample. As we will see later in Sect. 4.1 by combining the informations of their 1D and 2D spectra, in six of them we interpret the two Gaussians as coming from different merger components. For the remaining galaxies, in two cases the lines are consistent with global rotation, while for the last four we were not able to derive firm conclusions, even though we favor the contribution of multiple system parts to their emission. In Appendix C, we show the 1D emission line fits for all our 25 starbursts, and we discuss in more detail the origin of double Gaussians line components.

We applied the stellar absorption correction on Balmer and Paschen emission lines, rescaling upwards their fluxes. In order to determine the level of absorption for these lines, we adopted Bruzual & Charlot (2003) synthetic spectra with solar metallicity and constant star-formation history for 200−300 Myr, which are the typical merger-triggered starburst timescales (Di Matteo et al. 2008). The current starburst activity imposed by our selection suggests that the final coalescence of the major merger occurred relatively recently, certainly within the last 200 Myr. Numerical simulations of major mergers with different masses and dynamical times indicate indeed that star formation stops within 100–200 Myr after the coalescence, even without AGN quenching (Springel et al. 2005b; Bournaud et al. 2011; Powell et al. 2013; Moreno et al. 2015). Averaging the results over this interval, we applied an EW$_{\rm abs}$ of 5, 2.5, 2.5 and 2 Å for Hβ, Hα, Paγ and Paβ, respectively. The EW$_{\rm abs}$ of Hβ and Hα are consistent with those adopted in previous works (e.g., Valentino et al. 2015), while it was not possible to make comparisons for Paγ and Paβ. In the same order, we estimated for those lines an average absorption correction of 35%, 7%, 26%, 13% of the total flux. If we allow an uncertainty of ±1 Å on the EW$_{\rm abs}$ correction of either Paγ and Paβ, this will produce variations on the final fluxes that are 6% on median average, and thus it will not significantly affect our results.

All the lines in the *Magellan* spectra, either in emission or in absorption, were analyzed based on the following steps. Firstly, Hα and [N II]$\lambda\lambda$6548, 6583, which are the lines with the highest S/N, were fit together assuming a common linear continuum and a fixed ratio of the [N II] doublet of 3.05 (Storey & Hummer 1988). From this fit we derived the redshift of the galaxy, the intrinsic FWHM of Hα (in terms of velocity), and the flux ratio of the two Hα components for double Gaussian fits. The instrinsic total line widths were obtained by subtracting in quadrature the FIRE resolution width (100 km s^{-1}) from the best-fit observed FWHM. For double Gaussians, the total FWHM was

[2] GitHub Repository: `https://github.com/spacetelescope/stsci.tools/blob/master/lib/stsci/tools/nmpfit.py`

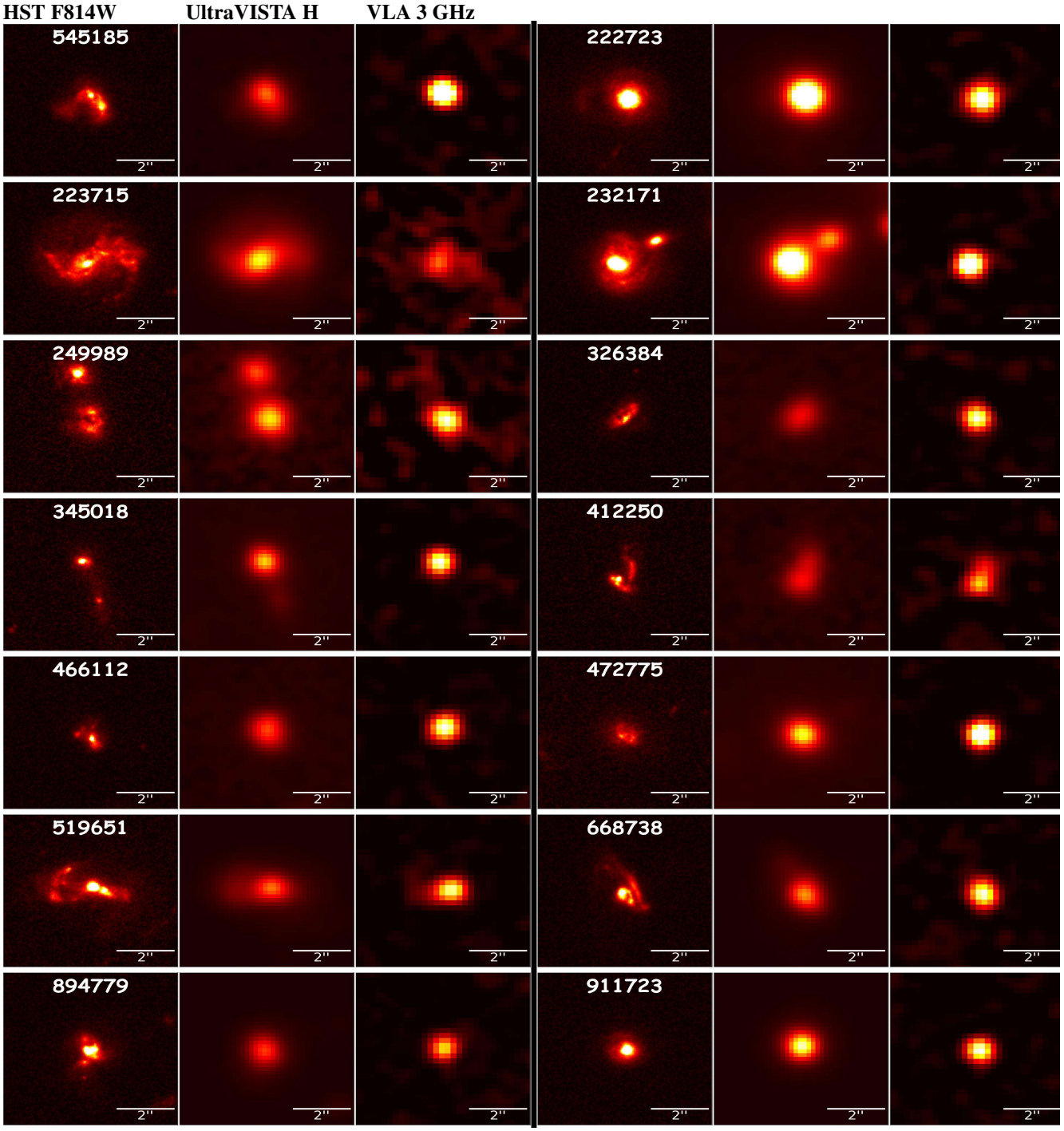

Fig. 1. For each of the galaxies observed in our second observing run at *Magellan* from *left* to *right*: HST-ACS F814W images (FWHM$_{res}$ = 0.095″), *H*-band UltraVISTA cutouts (same f.o.v. and $FWHM_{res} \sim 0.75''$) and 3 GHz radio images from VLA-COSMOS 3 GHz large project (Smolčić et al. 2017; $FWHM \sim 0.75''$). Cutout images for the sample of the first observing run were presented in Paper I.

calculated adding the single FWHM and the separation between the two component peaks, as this quantity is more representative of the whole system.

Then, the three parameters defined above were fixed and used to fit all other emission lines, including those in the optical zCOSMOS and SDSS spectra, after rescaling the FWHM to account for the different spectral resolutions. For the galaxies with the highest S/N of Paβ (>8σ), we verified that even without fixing its FWHM a priori, the fit yields a line velocity width consistent within the errors with the value found from Hα, indicating that our assumption is generally valid. Given the rms wavelength calibration accuracy (see Sect. 2.2), we allowed the line central wavelength to vary in the fit by 3σ, corresponding to 1.5 Å at 10 000 Å, and 3 Å at 20 000 Å. For each measured flux, we also added in quadrature an error due to the uncertainty of the absolute flux calibration. This additional uncertainty ranges between 5% and 10%, and is determined as the maximum residual difference between the average fluxes estimated from the photometry and from the aperture corrected spectra, among all the bands ranging from z++ to K_s. Finally,

the equivalent widths of the lines were derived following its definition ($= \int (F(\lambda) - F_{\rm cont}(\lambda))/F_{\rm cont}(\lambda)$), where $F(\lambda)$ is the best-fit Gaussian flux distribution and $F_{\rm cont}$ is the fit underlying continuum. Since the fluxes of Hα and Paβ were presented in Paper I, here we show in Table A.1 the FWHM of the lines, the EWs of Hα, Hδ and Paβ, the fluxes of [O III]5007 and Hβ that have been used in the BPT diagram.

2.5. Ancillary data

Almost all of our starbursts (24) were observed by HST-ACS in the F814W filter (Koekemoer et al. 2007) at an angular resolution of 0.095″ (∼0.7 kpc at $z = 0.7$). The UltraVISTA survey (McCracken et al. 2012) observed our galaxies in $YJHK$ bands at a spatial FWHM resolution of ∼0.75″, comparable to the average seeing during our *Magellan* observations. Two galaxies in the subset have higher resolution (0.19″) F160W HST images from the DASH program (Momcheva et al. 2016). Finally, all our galaxies are well detected in radio 3 GHz VLA images (Smolčić et al. 2017) (owing a similar a spatial resolution of ≃0.75″), with an average S/N of 18. In Calabrò et al. (2018) we showed the HST F814W, H-band UltraVISTA and radio 3 GHz VLA cutout images for only ten galaxies in our whole sample, for reason of space. Therefore, we include here in Fig. 1 the same types of images for the remaining sample of 14 starbursts, all of which have been observed during the second *Magellan* run (we remind that galaxy ID 578239 was not observed by HST, so we do not show it).

2.6. Morphological classification

Even though the light emission of dusty starbursts at optical and NIR wavelengths might be still severely affected by dust, the high resolutions offered by HST F814W images allows us to investigate the global structure of these systems. In Paper I we showed that the morphology of 18 galaxies has been already classified by (Kartaltepe et al. 2010; K10), revealing a merger origin for the majority of them. Adopting the same criteria of K10, we classified visually the remaining six galaxies (one has no HST coverage), but the results do not change significantly: 61% of our total sample are major mergers, as revealed by their highly disturbed morphology, tidal tales and bridges, 23% are classified as minor mergers from the presence of only slightly perturbed structures (e.g., warped disks, asymmetric spiral arms, etc.) without large companions, 11% are classified as spheroidal or S0 galaxies and the remaining 5% as spirals. The major merger subset is additionally divided in five smaller classes according to their merger state (I: first approach, II: first contact, III: pre-merger, IV: merger, V: old-merger or merger remnant), following K10.

However, we remind that the merger recognition and, even more, the merger stage classification from the optical morphology is very uncertain and more difficult at higher redshifts, due to lower resolution and to surface brightness dimming, which hampers the detection of faint tidal tales or interacting features, especially after the coalescence. The galaxy ID 245158 represents a show-case example of this uncertainty: it has been classified as spiral or minor merger from its global morphology, but it clearly shows a double nucleus in the central region, further confirmed by a double component Hα in the 2D and 1D spectrum, indicating rather an ongoing merger system.

2.7. Radio size measurements

The radio continuum emission has been used as a dust-free tracer of the SFR in galaxies in the absence of contamination from an AGN (e.g., Condon 1992). Since all our galaxies do not show either radio jets or radio flux excess compared to that expected from the SFR only (as we will show in Sect. 2.8), we used 3 GHz VLA images for measuring the FWHM size of their starburst cores, where the bulk of star-formation is taking place. For each SB, we used GALFIT (Peng et al. 2010) to fit a 2D function, convolved with the VLA synthesized beam, to their radio emission. We tested several 2D profiles, which include a Gaussian, a Sérsic function and the VLA beam itself, requiring a significance of the fit (probed by the χ^2) of at least 95% confidence level, as for the emission line measurements. In addition to the χ^2 analysis, all the GALFIT residuals of the fit (original-model) were checked by eye inspection, and the excluded fittings have always worst residuals. The best-fit profiles obtained for our sample are summarized as follows.

Firstly, a single 2D Gaussian with varying FWHM, axis ratio and position angle provided the best fit for 13 starbursts. In one case (ID 470239), the required conditions were obtained only by fitting a single Sérsic profile with varying parameters, but its half light diameter (calculated as $2 \times r_{\rm e}$, with $r_{\rm e}$ the effective radius) was only 3% different from the total FWHM of a single Gaussian fit, thus we assumed the latter as the final value. We also tried to fit a single and double Sérsic profile for all the other sources. However, given the larger number of parameters of this profile and the limited VLA resolution, we did not obtain convergence for the majority of them, or the resulting $\chi^2_{\rm reduced}$ were too high.

A double 2D Gaussian was required by three galaxies (ID 245158, 412250 and 519651), allowing to resolve them and measure single components FWHM and their relative separation.

As a third option, fitting the VLA synthesized beam yielded the best solution for six galaxies, which are then unresolved with current resolution (0.75″).

Finally, a single 2D Gaussian with fixed axis ratio and position angle (to 1 and 0, respectively) were used for two sources (ID 578239 and 685067). We remark that, in case the 95% significance level of the fit was satisfied with either this or the previous approach (as in the case of some very compact sources), we adopted the Gaussian solution only if the associated χ^2 probability level was at least double compared to the fit with the VLA beam.

As shown later, for a few galaxies we measured angular sizes that are much smaller than the synthesized beam FWHM (∼0.75″), down to ∼0.2″ and to a physical scale of 1 kpc. To demonstrate that it is possible to reliably determine the sizes even for these extreme, compact sources, we show in Fig. 2a comparison between the GALFIT residuals obtained when fitting the image with a Gaussian (convolved to the VLA beam) (upper row) and with the radio synthesized beam itself (bottom row). It is evident that a Gaussian provides a better fit of the original source profile and a cleaner residual compared to the VLA beam alone.

The uncertainties on the sizes were recalculated for all the starbursts from their radio S/N, using the fact that better detected radio sources also have the smallest radio size uncertainties, as shown for example in Coogan et al. (2018). We used then the same formulation as:

$$FWHM_{\rm err} \simeq 1 \times \frac{FWHM_{\rm beam}}{S/N}, \quad (3)$$

where $\rm FWHM_{beam}$ is the circularized FWHM of the VLA synthetized beam, and the multiplying coefficient was determined from simulations, following Coogan et al. (2018). All the size measurements with relative uncertainties and the method used for their determination are included in Table A.1.

Since our galaxies are well detected in radio band (average S/N of 18) and the VLA synthetized beam is well known,

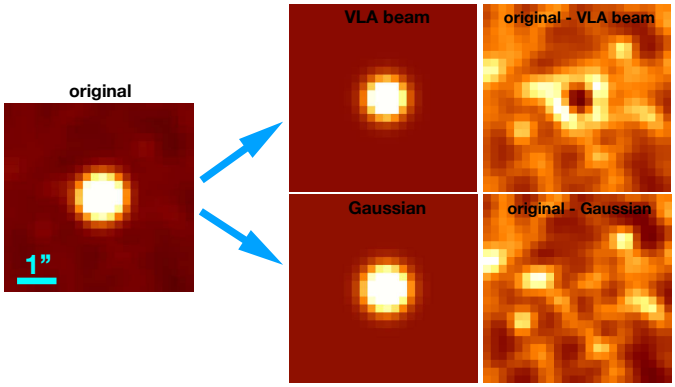

Fig. 2. GALFIT fitting of the radio VLA image (3 GHz) of the galaxy ID 685067 ($z = 0.37$) with the VLA synthesized beam in the *upper row* and with a Gaussian profile (convolved with the beam) in the *bottom row*. In horizontal sequence are shown, from *left* to *right*, the original image, the fitted model and the residual (original-model). For this galaxy, we derive an angular size of $0.20 \pm 0.04''$ (the pixel scale is $0.2''$ pixel^{-1}), which corresponds to a physical size of 1.06 ± 0.19 kpc. We notice that here GALFIT converges when fixing the position angle (PA) and axis ratio (q) parameters, to 0 and 1, respectively (Table A.1). This example illustrates the possibility to reliably measure the radio sizes of our objects even when they are smaller than the FWHM resolution of VLA ($0.75''$). In this case, the difference between the two models is recognized by looking at the residual images (i.e., original-model).

we always obtained a good fit for the resolved sources. Among them, we were able to fit a double Gaussian for three objects. In these cases, their total FWHM (adopted throughout the paper) were determined as the sum of the average single FWHM sizes and the separation between the two components. However, we will also consider the single sizes in some cases, such as in Fig. 10. This finding suggests that also some other galaxies may represent double nuclei that are blended in $0.75''$ resolution VLA images. For the unresolved galaxies instead (i.e., those fitted with the VLA beam, as explained above), we adopted a 3σ upper limit on their FWHM. Within the most compact starbursts, some of them may be affected by pointlike emission from an AGN, which decreases artificially the observed size. However, we tend to discard this possibility since, as we will see later, none of our AGN candidates show a radio-excess compared to the radio emission due to their SFR.

2.8. AGN identification

We started searching for AGN components in the mid-IR. Through the multicomponent SED fitting of IR+(sub)mm photometry (described in Sect. 2.1) we detected at $>3\sigma$ the dusty torus emission component for a subset of 12 SBs. The significance of the detection was derived from the ratio between the total best-fit dusty torus luminosity ($=L_{\rm AGN,IR}$) and its 1σ uncertainty, inferred as the luminosity range (symmetrized) yielding a variation of the $\chi^2_{\rm red} \leq 1$ with respect to the minimum value of best-fit (Avni & Bahcall 1976). More details about the torus estimation method are described in Liu et al. (2018) and Jin et al. (2018). Among the 12 mid-IR AGNs, we detected the dusty torus emission at high significance level ($>5\sigma$) for six starbursts (ID 777034, 519651, 222723, 232171, 466112, 894779), while for the remaining objects we obtained a lower significance ranging $3\sigma < L_{\rm AGN,IR} < 5\sigma$ (see Table A.1). The SED fitting of all the galaxies can be found in the Appendix B.

Within the sample of IR-detected AGNs, six galaxies (ID 777034, 222723, 232171, 635862, 578239, 911723) were also detected in X-rays at more than 3σ by *XMM-Newton*, *Chandra* or NuStar (Cappelluti et al. 2009; Marchesi et al. 2016; Civano et al. 2015). Throughout the paper, we will consider the X-ray luminosities L_X measured by Lanzuisi et al. (2017), integrated over the energy range 2−10 keV. To estimate the contribution of star-formation to the total intrinsic L_X, we used the relation between SFR and $L_{\rm X,SFR}$ of Mineo et al. (2014), rescaled to a Chabrier IMF and applying a correction factor of 0.6761 to convert the X-ray luminosity from the 0.5−8 keV to the 2−10 keV band.

We remind that the column densities $N_{\rm H}$ inferred from their hardness ratios (Lanzuisi et al. 2017) are consistent with those derived from the dust attenuations (toward the centers) assuming a mixed model (Paper I), suggesting that also the X-ray emission is coming from the nucleus, where the AGN is expected to be located. Furthermore, all our starbursts do not show radio jets in VLA images, and do not have significant radio excess than expected from their SFR, assuming a typical IR-radio correlation with $q_{\rm IR} = 2.4$, as in Ibar et al. (2008), Ivison et al. (2010) and Liu et al. (2018).

3. Results

The spectra that we obtained at the *Magellan* telescope, along with longer wavelength radio images, provide us key information to understand both the attenuation sequence and the variety of morphological classes of our starbursts. First of all, since dissipative mergers are able to funnel the gas from the large scales of Milky-way-like disks (∼10 kpc) to sizes that are more than one order of magnitude smaller (Di Matteo et al. 2005), it is useful to analyze the characteristic star-forming sizes of our starbursts. Besides this, from the galaxy integrated *Magellan* spectra we can study together the excitation and kinematic state of the gas, and the aging of the stellar population in the outer starburst cores, traced respectively by the [N II]/Hα ratios, the intrinsic (resolution corrected) line velocity widths of single 1D Gaussian components ($=$FWHM$_{\rm line}$, which is a proxy for the velocity dispersion in the system) and the Balmer (or Paschen) line equivalent widths ($=$EW$_{\rm H\alpha,Pa\beta}$).

In Fig. 3 we present the main result of this analysis, showing that the FWHM$_{\rm radio}$, the N2 parameter, the FWHM$_{\rm line}$ and the EW$_{\rm Pa\beta}$ are all correlated to the total dust attenuation $A_{V,\rm tot}$, which is used here as the reference quantity for comparison. This suggests that our starbursts can be described as, at first order, a one-parameter sequence: similar correlations at different significance levels are indeed found also when comparing on a single basis each pair of the above parameters.

We tested these correlations using three different approaches with all the available data, excluding from the calculations only the upper limits and missing EW(Paβ) measurements. Firstly, we calculated the Spearman rank correlation coefficient R (the higher R, the stronger the correlation) and the corresponding p-value, which represents the probability of obtaining an equal (or stronger) R if no correlation exists. We defined a threshold probability of 5% to accept the correlation. Overall, we found that the p-values are nearly always lower than 0.05, meaning that the correlations are significant according to our criteria. In only one case (EW$_{\rm Pa\beta}$ vs. FWHM$_{\rm radio}$) we determined a slightly higher p-value of 0.1 (thus a higher probability of no correlation), which could be partly affected by the lowest number of data (i.e., lowest statistics) available here compared to the other diagrams. However, the other methods indicate instead a stronger physical connection between the two quantities.

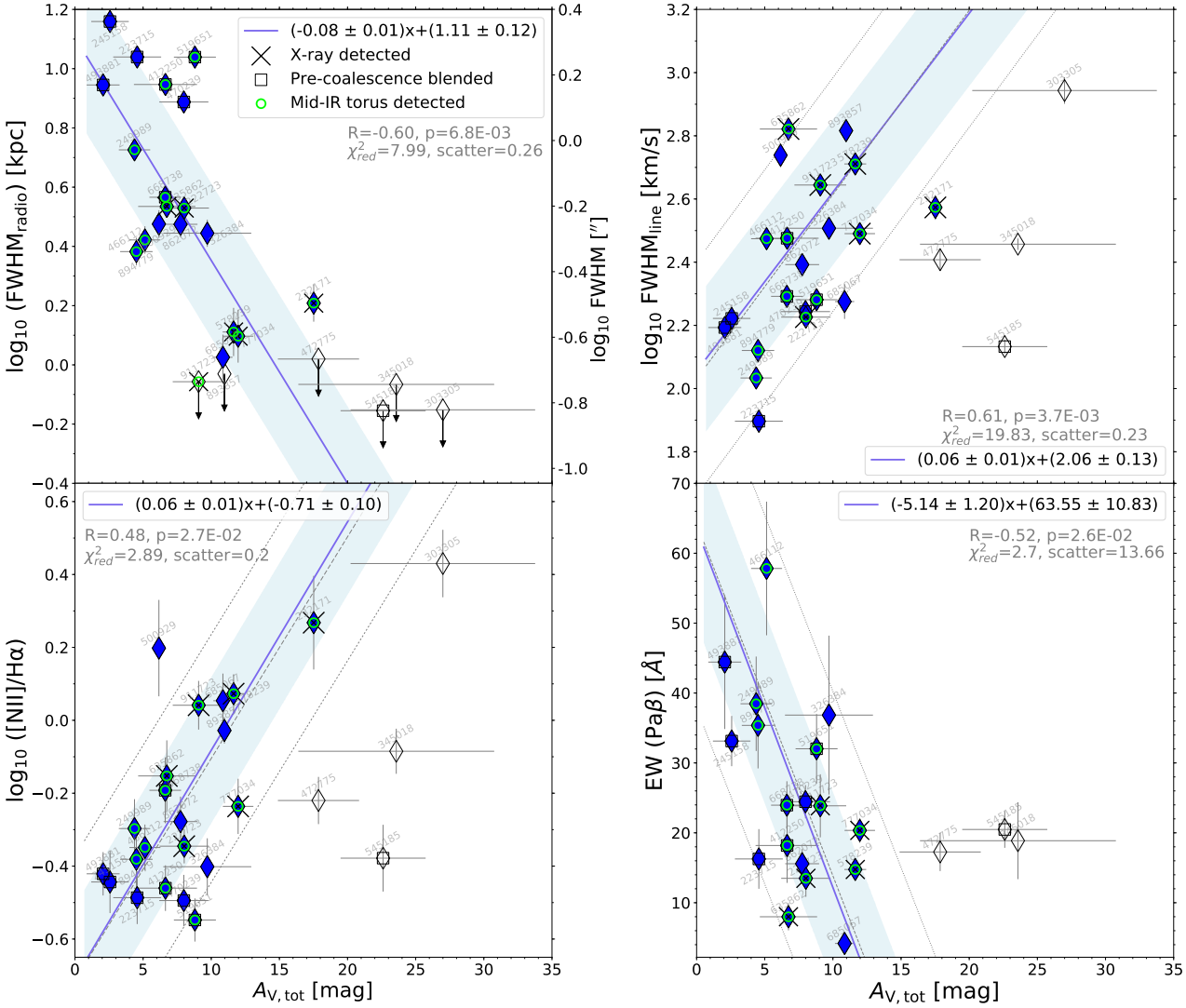

Fig. 3. *Left column*: correlations of $A_{V,\mathrm{tot}}$ with the radio size (*top*), and with the N2 index (*bottom*). We show with filled blue diamonds all the *Magellan* SBs that were used to derive the best-fit linear relation (blue continuous line) and the $\pm1\sigma$ dispersion (blue shaded area), while empty diamonds represent galaxies excluded from those calculations. The latter comprise the four outliers discussed in the text (ID 303305, 345018, 472775, 545185) and all the upper limits in the $A_{V,\mathrm{tot}}$ vs. $\mathrm{FWHM_{radio}}$ plot. In the corners, we show in black the equation of the linear fit (which includes 1σ error of the two best-fit parameters), and in gray the Spearman correlation coefficient (R) with the corresponding p-value (p), the reduced chi-square of the fit (χ^2_{red}), and the 1σ scatter of our SBs around the best-fit line, all of which do not take into account upper limits and the four outliers mentioned above. For comparison, the linear fit and 1σ dispersion including the four outlier galaxies are highlighted with a gray continuous dashed line and two dotted lines of the same color. *Right column*: correlations of $A_{V,\mathrm{tot}}$ with the line velocity width (*top*), and with the EW(Paβ) (*bottom*). In the last diagram, four galaxies without EW(Paβ) measurements are not considered.

In the second approach, we fit the galaxies in each diagram with a linear relation (in log–log space, except for the last diagram where the y-axis is in linear scale), by using an orthogonal distance regression procedure (ODR), which allows to take into account measurement uncertainties in both axis (we discuss later possible outliers or different fitting functions). We determined the S/N of the angular coefficient (i.e., how much it differs from 0), finding significant correlations at more than 3σ in eight cases, while they are less strong ($2 < S/N < 3$) for the remaining two diagrams. In the four correlations shown in Fig. 3, we obtained a significance of 5.8, 5, 4.3 and 3.65σ for $A_{V,\mathrm{tot}}$ vs. N2, $\mathrm{FWHM_{line}}$ and $\mathrm{EW_{Pa\beta}}$, respectively. With this method, we also determined the 1σ dispersion of our data with respect to the best-fit linear relation.

Finally, we also performed Monte Carlo simulations: for each relation, we run 100 k simulations, removing each time at random 20% of the points, recalculating the significance of the correlation using our second approach. We then estimated the rate (~probability) at which such correlations completely disappear with a significance falling below 2σ. This analysis allows to test the systematics and scatter of the correlations, ensuring they are robust and not driven by a few outliers. Overall, we found low probabilities (less than 5%) to obtain a less than 2σ significance when removing a random 20% of the galaxies, indicating that our correlations do not cancel out and are not found by chance. In the four diagrams of Fig. 3, we obtained probabilities of 0.028%, 0.001%, 4.7% and 0.7%, in the same order as above.

We remind that $A_{V,\mathrm{tot}}$ were determined from the Paβ observed fluxes and the bolometric L_{IR}, assuming a mixed model geometry. As explained in Paper I, for one galaxy in our sample where Paβ resides in an opaque atmospheric region (ID 245158), we estimated the attenuation through the Paγ line, adopting a flux ratio Paβ/Paγ = 2.2. This is the average expected observed ratio

Table 1. Correlation coefficients among the total attenuation toward the center in a mixed model ($A_{V,\mathrm{tot}}$), the 3 GHz radio FWHM size ($\mathrm{FWHM_{radio}}$), the line velocity width ($\mathrm{FWHM_{line}}$) and the equivalent width of Paβ (which tightly correlates also with the EW of Hα, Hβ and Hδ).

	$FWHM_{\mathrm{radio}}$	N2	$FWHM_{\mathrm{line}}$	$\mathrm{EW_{Pa\beta}}$
$A_{V,\mathrm{tot}}$	−0.6 (0.007) 5.8σ 0.028%	0.48 (0.027) 6σ <0.001%	0.61 (0.0037) 4.3σ 2.9%	−0.52 (0.026) 4.3σ 0.12%
$FWHM_{\mathrm{radio}}$		−0.71 (0.0006) 5.74σ <0.001%	−0.46 (0.049) 2.93σ 0.033%	0.45 (0.1) 4.9σ 3%
N2			0.67 (0.0003) 5.45σ <0.001%	−0.43 (0.05) 3.85σ 0.15%
$FWHM_{\mathrm{line}}$				−0.46 (0.05) 2.5σ 12.9%

Notes. In each case we show: the Spearman correlation coefficient and corresponding p-value (*first row*); the significance of the correlation derived from the ratio of the linear best-fit angular coefficient and its uncertainty (*second row*); the probability of having a significance lower than 2σ if a random 20% of the sample is removed (*third row*). For the calculations we excluded the upper limits, missing EW(Paβ) measurements, and the four outlier starbursts (ID 303305, 345018, 472775, 545185) in the three diagrams relating $A_{V,\mathrm{tot}}$ to N2, $\mathrm{FWHM_{line}}$ and EW(Paβ).

for all the attenuation values in our range, assuming either a mixed model or a foreground dust-screen geometry, and it was verified by nine starbursts with simultaneous detection of Paγ and Paβ.

However, for four galaxies in the sample (ID 303305, 500929, 893857 and 232171) we did not detect either Paβ or Paγ, thus in these cases we derived $A_{V,\mathrm{tot}}$ in a similar way from their Hα fluxes (so to avoid upper limits), adding a representative error of 0.1 dex determined from the remaining sample as the scatter of the correlation between Paβ and Hα based $A_{V,\mathrm{tot}}$. We also verified that including the upper limits in the calculations does not significantly alter the fitted trends. Hereafter, we discuss in detail on a single basis the most important findings.

In the first (top-left) panel of Fig. 3, the FWHM radio sizes, while spanning a wide range from less than 600 pc to ∼12 kpc, are tightly anticorrelated to the dust obscuration level $A_{V,\mathrm{tot}}$ (R = −0.6, p-value = 0.007, and a scatter of 0.26 dex). Toward the smaller sizes and higher obscurations ($A_{V,\mathrm{tot}} > 20$ mag), three galaxies are unresolved with VLA, thus they may be actually closer to the best-fit linear relation derived from the remaining sample. In this diagram, X-ray detected AGNs are found both at small and large radii, and have a similar distribution compared to the other galaxies, suggesting that radio size measurements and hence the result in Fig. 3 are not contaminated by AGNs.

In the last three panels of Fig. 3, the [N II]/Hα ratio, the line velocity width ($\mathrm{FWHM_{line}}$) and the EW of Paβ are also correlated to the total attenuation at more than 3σ significance level (R coefficients and p-values are 0.51(0.009), 0.48(0.015) and −0.46(0.034), respectively).

We used the EW of Paβ for comparison since, being at longer wavelength, it is more representative of the whole system, allowing to probe a larger fraction of starburst cores if a mixed geometry holds. However, in the Appendix B we show that EW(Paβ) is tightly correlated to the EW of Hα, Hβ and Hδ, all of them being strongly sensitive to the age of the stellar population (at fixed SFH), thus similar results are obtained also if choosing a different line for the EW.

We also notice that four galaxies (ID = 303305, 472775, 345018 and 545185) are outside the 1σ dispersion of the best-fit relations in all the three diagrams (gray dashed and dotted thin lines). They show lower N2, $\mathrm{FWHM_{line}}$, and higher EW than expected from their dust obscuration level. Alternatively, they have a larger $A_{V,\mathrm{tot}}$ for their N2, $\mathrm{FWHM_{line}}$ and EW values.

In order to understand the nature of these galaxies, we simulated 100 k different realizations of the last three diagrams of Fig. 3, with N2, $\mathrm{FWHM_{line}}$, EW(Paβ) and $A_{V,\mathrm{tot}}$ of 25 galaxies distributed according to the best-fit relations and the corresponding 1σ dispersions. Then we computed the probability of having at least four galaxies (three for the last plot) with an orthogonal distance from the best-fit relation (gray dashed line) equal or greater than the four (or three) outliers described above. We found, in the same order presented above, a probability of 0.2%, 0.025% and 0.005%, indicating that those four galaxies are real outliers and cannot be simply explained by the 1σ scatter of the best-fit lines.

Given their deviant behavior, we excluded these outliers and derived again the best-fit relations, which are shown in Fig. 3 with a blue continuous line. We found on average a reduction of the 1σ dispersion (shown with a light blue shaded area) by ∼0.1 dex and a slight improvement of the correlation significance compared to the previous calculations. However, the best-fit linear equations are not significantly different, thus we give only the analytic expressions of this second fit where the outliers are not considered. The new results for the three diagrams, and all the diagnostics for the remaining seven correlations are presented in Table 1. We notice that the four divergent starbursts have an upper limit on their radio size, and are not outliers in other diagrams that do not involve $A_{V,\mathrm{tot}}$, thus the latter are not affected by this analysis. A possible physical explanation of the diverging behavior of these four galaxies will be discussed in Sect. 4.4.

Finally, if we look at all the correlations in Table 1, we can notice the presence of a subset of quantities that correlate better than others. Apart from the previously discussed $A_{V,\mathrm{tot}}$ vs. $\mathrm{FWHM_{size}}$, the line width, N2 and radio size are tightly and robustly correlated with each other. Indeed, from bootstrapping analysis, the probability that there is no correlation is less than 0.033%. As we will see in Sect. 4.2, this result hides a deeper physical link among them.

4. Discussion

The results presented in the previous section show that the wide range of attenuations measured in Paper I translate into

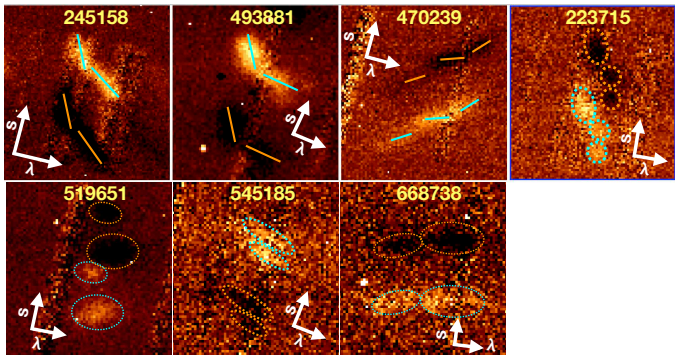

Fig. 4. Close-up view of the Hα emission line profiles for the galaxies satisfying one of the two precoalescence criteria defined in Sect. 4.1. In each panel, as a consequence of the sky-subtraction procedure applied to the 2D spectra, the lines appear twice in different slit positions, in the first with a positive flux (in yellow) and in the second with a negative flux (in black). For each cutout, we show with two white arrows the slit position (s) and the dispersion direction (λ), which are slightly rotated due to the curved *Magellan* spectra. In order to clarify the classification criteria adopted in this work for finding precoalescence SBs, we highlight: (1) with continuous lines the different tilting angles of Hα line profiles (first three SBs); (2) with dotted ellipses the spatially separated Hα lines coming from different merger components (last four SBs).

a wide range of other physical properties, such as radio sizes, N2, velocity width, Balmer and Paschen EW, and even more, all these quantities appear to be connected to each other, defining a one-parameter sequence. In this section we propose a physical interpretation of this sequence, and show that the correlating properties considered before are consistent with being primarily reflecting different evolutionary merger stages. Then we discuss the role played by each parameter into this sequence.

4.1. Identification of early-phase, precoalescence mergers

A first guess for a physical understanding of what is guiding the large spread of properties comes from the morphology. Indeed we have already seen that our sample comprises mergers at different stages of evolution (MI to MV), though this classification is very uncertain and sometimes misleading, as shown in Sect. 2.6: the faintness of tidal tails and residual interacting features make systems at the coalescence difficult to recognize, while multiple optical components and double nuclei in HST images may just reflect the dust attenuation pattern rather than the true distribution of SFR and M_*. As shown in Sect. 2.7, a double Gaussian component fit on radio images allowed to resolve three sources, suggesting that they may be composed of two interacting nuclei. However, the limited resolution of VLA (0.75″ of FWHM) does not allow us to derive solid conclusions on the remaining sample, which might contain more close pairs. New maps and ALMA follow-ups would increase the resolution and hopefully resolve these blended precoalescence systems.

A complementary way to find close interacting pairs in early merger stages comes from the analysis of their 2D spectra. With that aim, we performed a crude sky-subtraction procedure: we subtracted the 2D spectra taken for the same object but at different positions along the slit (A and B, separated by 2.2″), in order to remove the sky lines and allow a visual inspection of the emission line profiles. For construction, the lines appear twice in each sky-subtracted frame and exactly with the same shape: one time with a positive flux (when the object is in position A), and the other with a negative flux (when the galaxy is in position B).

By looking at these line profiles, we identified interacting pairs by requiring one of the following conditions. Firstly, we looked for detached Hα line components along the spatial direction, coming from separated merger components located at different slit positions (e.g., ID 223715, 519651, 545185, 668738 in Fig. 4). Alternatively, we required tilted Hα line with two different inclination angles (based on visual inspection), indicating the presence of two emitting regions with independent kinematic properties, inconsistent with a single rotating disk (e.g., ID 245158, 493881, 470239 in Fig. 4). In our sample, we identified from the two above conditions seven close-pair precoalescence starbursts, which are shown in Fig. 4. For an additional source with a double radio emission component (ID 412250), one of the two nuclei was not falling inside the slit, thus it was not observable with FIRE. However, this SB should be considered a merging pair at the same level of the others.

As we can see in Fig. 3, the selected precoalescence starbursts are preferentially found at larger half-light radii, and all the systems with $\mathrm{FWHM_{radio}} > 6$ kpc belong to this category. This result has two main implications. Firstly, the sizes measured in radio are not necessarily those of single merger components, but they should be interpreted primarily as separation between the two precoalescence starburst units (e.g., for all the three systems resolved in radio (ID 245158, 412250, 519651), their separation is larger than the size of single nuclei). Secondly, the early evolutionary phases are also characterized by lower dust obscurations, suggesting that the merger induced gas compaction (i.e., the increase of hydrogen column density in the center) has not yet completed.

This precoalescence subset identification provides an immediate physical interpretation for six galaxies of those that were simultaneously fitted with a double Gaussian in the 1D spectrum (Sect. 2.4), explaining this profile as coming from different merger components. However, we warn that these diagnostics are not identical and the connection between the line profiles in the 1D and in the 2D spectrum is not straightforward. Starbursts with multiple spatial emission lines do not necessarily display double Gaussians in the 1D spectrum, because this is subject to projection effects and depends on the distribution in wavelength of each spatial component. Indeed, the lines of one of the galaxies shown in Fig. 4 (ID 519651) were still fitted with a single Gaussian in the 1D.

Furthermore, our subset of six precoalescence starbursts identified from the 2D spectra is not necessarily complete, as many galaxies (e.g., ID 635862, 777034, 472775, 685067) have sky-subtracted 2D spectra with low S/N, not allowing to apply the visual criteria presented above in this Section. We would have required longer integration times or spatially resolved observations to build a complete sample of starbursts before the coalescence. Similarly, if the two merger nuclei are too close, it would be impossible to detect them even in the 2D spectra, and would need a significant improvement of spatial resolution to identify the pair.

4.2. Velocity enhancement and shocks toward the coalescence

4.2.1. BPT diagram and shocks

The second (bottom-left) panel of Fig. 3 shows that more obscured starbursts tend to have higher N2 relative to Hα, reaching [N II]/Hα ratios higher than 1, which are more typical of AGN and LINERs. Indeed, the classical BPT diagnostic diagram in Fig. 5, performed on nine galaxies with

[O III] and Hβ available measurements, confirms that SBs with higher obscuration and line velocity width are found in the composite, AGN or LINER classification regions, according to empirical separation lines derived in the local Universe (Kauffmann et al. 2003; Kewley et al. 2001; Cid Fernandes et al. 2010; Veilleux & Osterbrock 1987).

Two variants of the BPT using the [SII]6717+6731/Hα or the [OIII]λ5007/[OII]λ3727+3729 ratios (S2BPT or O2BPT, respectively) are shown in Fig. B.1. We remind that, due to an enhanced ionization parameter and lower metallicity (at fixed mass) in the ISM at higher redshifts, the average star-forming galaxies population at $z = 0.7$ occupies a region in the BPT diagram which is shifted rightwards by $\lesssim +0.1$ dex compared to $z = 0.1$ (Faisst et al. 2018; Masters et al. 2016). However, there are currently no studies addressing how this will affect the separation lines among SB, AGN and LINERs. If we suppose that at $z \sim 0.7$ the same shift applies also to these lines, galaxies at intermediate obscurations and line widths would still fall in the composite region with dominant LINER or AGN-like properties. Also, this would not affect our subsequent conclusions based on the comparison with shock models.

We noticed that the location of those galaxies shifted to the right compared to the purely SF region is consistent with the predictions of shock models, with varying shock contribution and velocity (compare with Figs. 10 and 2 of Rich et al. 2011, 2014, respectively). Additionally, Lutz et al. (1999) argue that LINER-like spectra in infrared selected galaxies are due to shocks, possibly related to galactic superwinds. The presence of increasing widespread shocks provides the most immediate interpretation for the spectra in our sample with enhanced [N II]/Hα, given that AGN emission would be highly suppressed (Paper I).

However, we cannot exclude some residual influence by an AGN. Hydrodynamical simulations performed by Roos et al. (2015) show that even in the case of high obscuration an AGN can ionize the gas very far from the nucleus, reaching kpc scales and the circum-galactic medium. Furthermore, the accreting black hole might not be in the center, but that sounds unplausible: the attenuations toward the center derived independently from the X-ray detected AGNs are consistent with those derived from the mixed model (see Paper I) and, even further, Rujopakarn et al. (2018) show that the AGN position correlates with that of active star forming regions. Finally, we also notice that two galaxies (which simultaneously have X-rays and mid-IR dusty torus detection) were fit with broad Hα components (line width of $\sim$1000 km s^{-1}). Such large velocity widths have been observed in both shock-dominated regions (possibly supernova driven, Ghavamian et al. 2017) and AGNs (Peterson 1997; Gaskell 2009; Netzer 2015). IFU data would be needed to disentangle shock or AGN emission, as we expect the latter to be much more concentrated in the central part of the system.

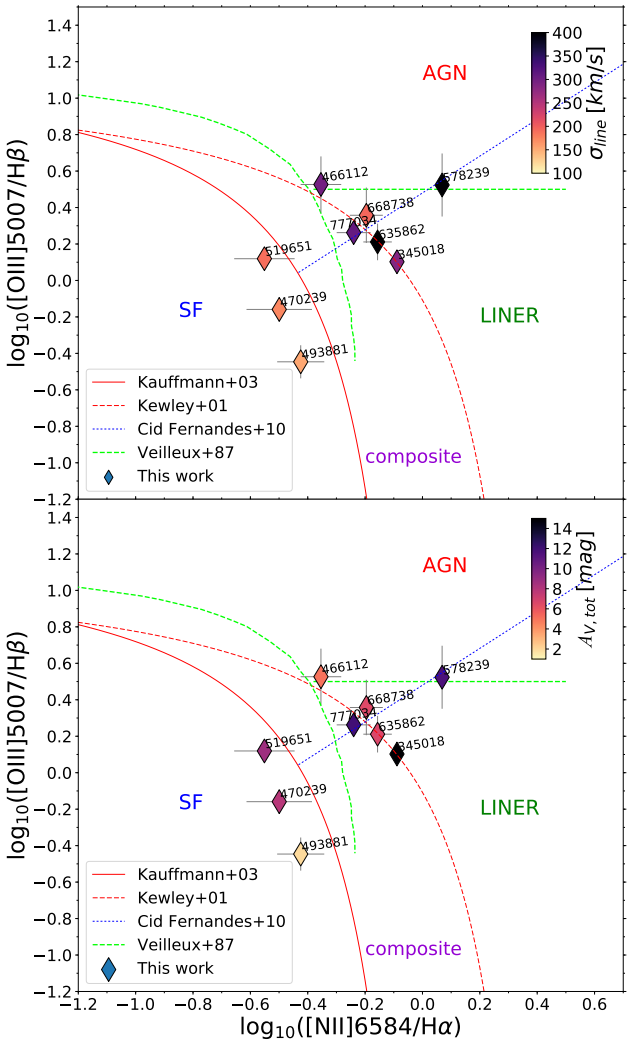

Fig. 5. *Top panel*: BPT diagram of nine starbursts in our sample with optical spectra available (for one galaxy included in zCOSMOS, we did not detect both [O III]5007 and Hβ). While three sources lie in the SF excitation region, the remaining galaxies are not consistent with SF, and their spectra show a mixture of composite, AGN and LINER properties. The color coding indicates that galaxies with higher N2 which are closer to the AGN and LINER regions also have increasingly higher line velocity widths ($\sigma_{\rm line}$). *Bottom panel*: same diagram as above, but here the galaxies are color coded according to their total dust attenuation $A_{V,\rm tot}$. More obscured starbursts preferentially display AGN or LINER properties.

4.2.2. The dynamical masses of our sample

In order to better understand the dynamical status of our starbursts and how far they are from relaxation, we compared their total masses $M_{\rm tot}$ to the dynamical masses $M_{\rm dyn}$ estimated from the line velocity widths and radio sizes. For the latter, we used the formulation of Daddi et al. (2010) as :

$$M_{\rm dyn} = 1.3 \times \frac{FWHM_{\rm radio}}{\times} (FWHM_{\rm line,total}/2)^2 {\rm G} \sin^2(i) \qquad (4)$$

where FWHM$_{\rm line,total}$ is the one-dimensional total line velocity width (accounting for both rotation and dispersion), while $\sin^2(i)$ is the correction for inclination that we take as the average value for randomly oriented galaxies (57°). In order to determine the total uncertainty on $M_{\rm dyn}$, we considered an additional error on the inclination factor of 0.3 dex, as in Coogan et al. (2018). This represents the main contribution to the error (~90% in median), since the line width and radio sizes are always well measured with high S/N.

Then we compared this quantity to the total mass content (baryonic + dark matter) of the systems, estimated as:

$$M_{\rm tot} = M_* + M_{\rm gas} + M_{\rm darkmatter} \qquad (5)$$

in which $M_{\rm gas}$ was determined, as described in Paper I, as $M_{\rm gas} = 8.05 + 0.81\times \log({\rm SFR_{IR}})$ (Sargent et al. 2014), valid for a starburst regime, and we assumed $M_{\rm darkmatter} = 10\% \pm 10\%$ of M_*. Since this contribution is highly uncertain, it was set nearly uncontrained. However, this range is consistent with studies

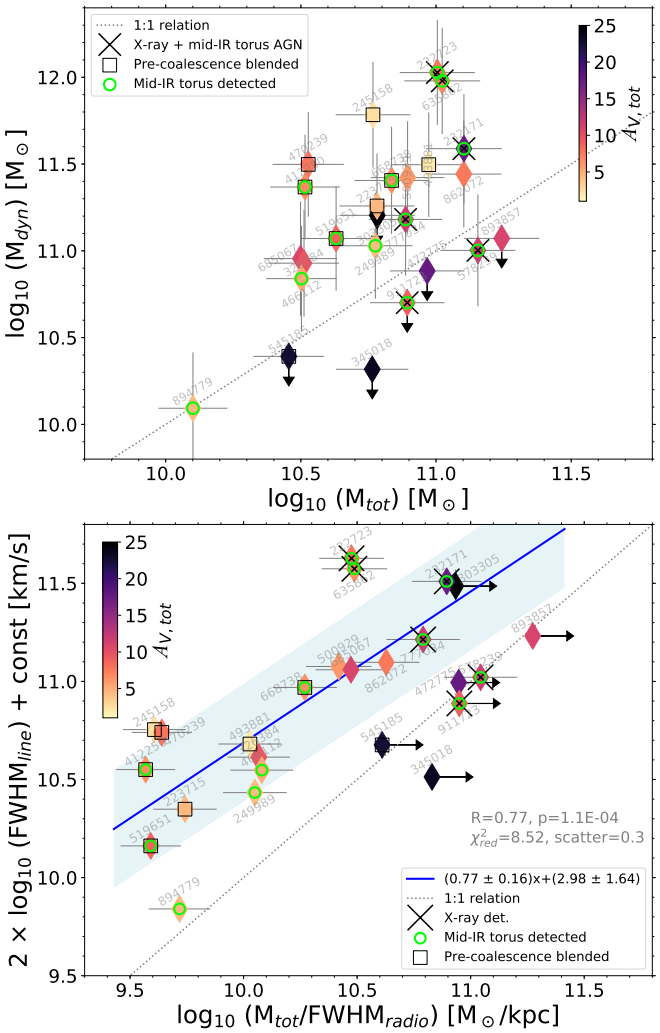

Fig. 6. *Top panel*: comparison between the dynamical mass $M_{\rm dyn}$ and the total mass content $M_{\rm tot}$ (=$M_{\rm gas}$ + M_* + $M_{\rm darkmatter}$) for our SBs sample, color coded by their total attenuation $A_{V,\rm tot}$. *Bottom panel*: diagram showing the square of the total FWHM velocity width as a function of $M_{\rm tot}/{\rm FWHM}_{\rm radio}$, using the same color coding based on $A_{V,\rm tot}$. On the y-axis, const = $1.3 \times G/(4\langle \sin^2(i)\rangle)$ groups the coefficients in Eq. (3) so as to facilitate comparison with the virialized case (1:1 relation, shown as a gray dotted line). The blue continuous line represents a linear fit to our sample, excluding galaxies with an upper limit on their radio size, while the blue shaded area shows the $\pm 1\sigma$ limits of this best-fit relation. Both panels of the figure suggest that our galaxies may be approaching virialization, and more obscured starbursts are closer to the equilibrium.

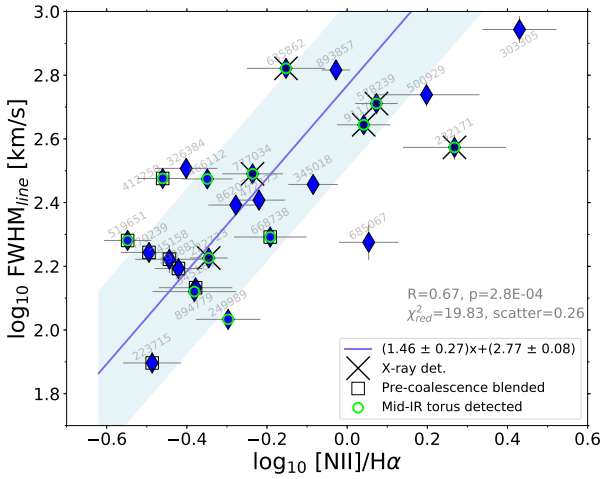

Fig. 7. Correlation between the line velocity width of single Gaussian components ($\rm FWHM_{line}$) and the N2 index (both measured from our *Magellan*-FIRE spectra), indicating that the two quantities are tightly (scatter = 0.26 dex) physically related.

of high-z (>0.5) massive star-forming galaxies, which found a modest to negligible dark matter fraction inside the half-light radius (e.g., Daddi et al. 2010; Genzel et al. 2017). In any case, given the small contribution, its exact value does not affect the results of this paper. For the error determination, we considered the above uncertainty on $M_{\rm darkmatter}$, a 0.1 dex error on M_* (Laigle et al. 2016), and 20% incertitude on the gas mass (even though its contribution is negligible given that $M_{\rm gas} \simeq 0.1\ M_*$ on average for our sample).

The comparison between $M_{\rm dyn}$ and $M_{\rm tot}$ in Fig. 6 shows that, on average, our galaxies are not completely virialized: while nearly half of the sample is consistent within 2σ with the 1:1 relation, the remaining part is located above at higher $M_{\rm dyn}$. The largest departures from virialization are observed for the precoalescence and less obscured systems, which are supposedly earlier stage mergers. On the contrary, the systems with better agreement may be fully coalesced starburst cores with higher $A_{V,\rm tot}$.

The tight connection between velocity and gravitational potential is clarified in the bottom panel of Fig. 6, as the $\rm FWHM^2_{line}$ and $M_{\rm tot}/{\rm FWHM}_{\rm radio}$ correlate at 5σ significance (with R = 0.74 and p-value = 0.0002). Also here, while precoalescence mergers have larger displacements from the 1:1 relation, they are confined in a region at lower velocity widths and shallower potential wells. This suggests that also other starbursts (ID 249989, 466112, 326384) in this region may be precoalescence mergers that we were not able to securely identify, due to their lower S/N 2D spectra, and indeed their optical morphology strengthens this suspicion. In the upper-right part of Fig. 6-*bottom*, separated from the previous sample, are clustered the more obscured starbursts, that is, supposedly coalesced mergers. We notice also that all X-ray detected AGNs are localized in this region of the diagram, indicating a possible link between evolutionary phase and AGN properties, that we will further investigate in the following Section.

Overall, the above results suggest a time-evolutionary scenario, in which more advanced, already coalesced mergers are close to virialization, and the increased central potential wells (due to the contribution of both merger components) are responsible for the enhancement of both the kinetic energy content and shocks toward later stages of the interaction. The tight relation between the line velocity width of single Gaussian components (a proxy for the velocity dispersion in the system) and shock production (traced by the N2 index) is further indicated by the color coding of the BPT diagram in Fig. 5-top, and by the correlation between $\rm FWHM_{line}$ and N II/Hα in Fig. 7, which has a significance higher than 5σ (R = 0.67, p-value = 3×10^{-4}) and a dispersion of 0.26 dex.

4.3. Lower line equivalent widths toward late merger stages

The equivalent widths (EW) of hydrogen recombination lines give a relatively dust-unbiased picture (assuming that stars and emission lines are equally extincted) of the contribution of the SFR to the stellar mass content, and they are sensitive to the luminosity weighted age of the stellar populations, so that they could provide useful information about the evolutionary stage

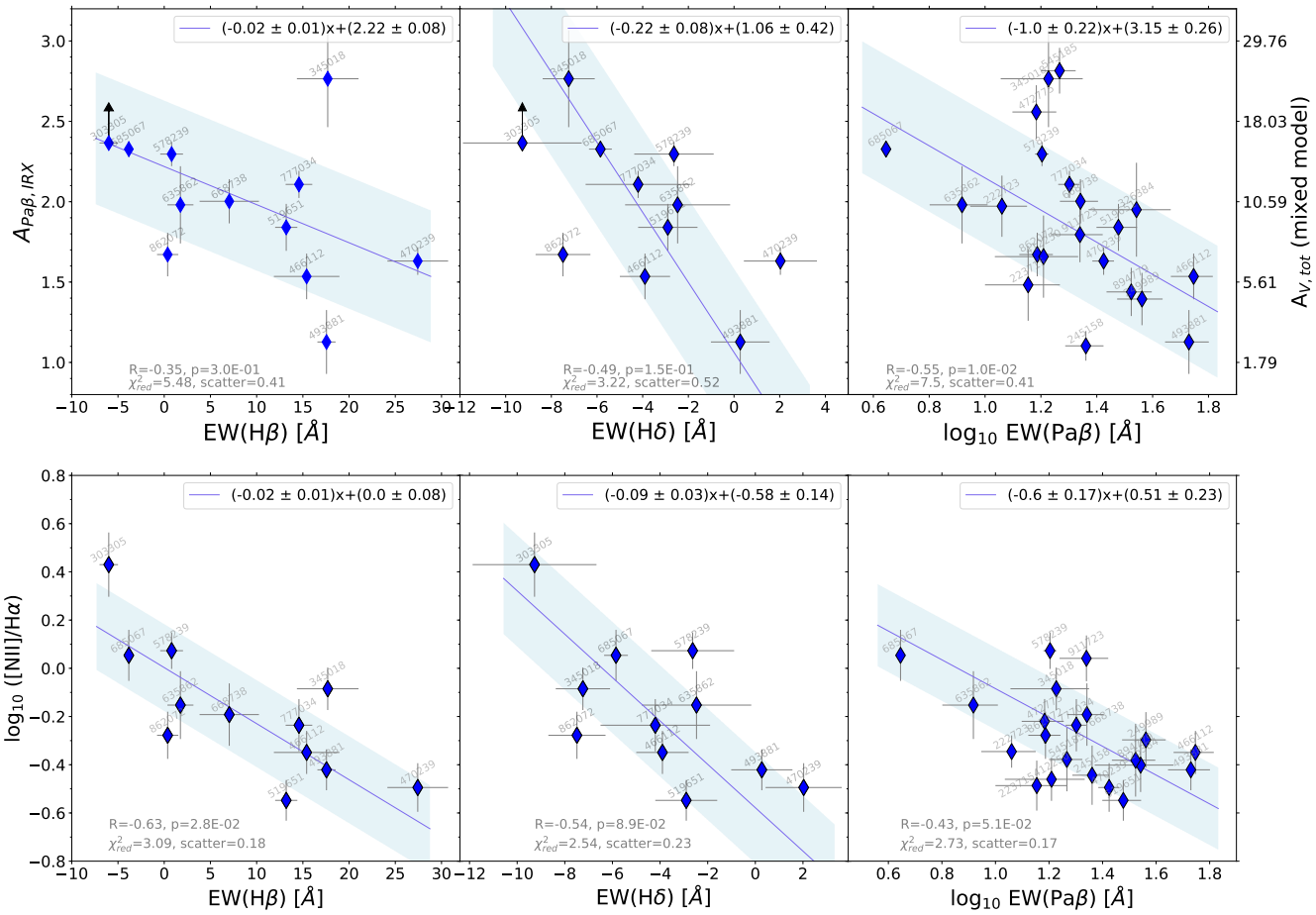

Fig. 8. *Top panels*: comparison between the EW of Hδ, Hβ and Paβ lines to the dust attenuation parameter $A_{\mathrm{Pa}\beta,\mathrm{IRX}}$, defined as $2.5 \times \log_{10}(1 + \mathrm{SFR_{IR}}/\mathrm{SFR_{Pa}}\beta,\mathrm{obs})$ (Paper I). We remark that the last panel is equivalent to the bottom-right plot in Fig. 3, even though a different scale has been used (the relation between $A_{\mathrm{Pa}\beta,\mathrm{IRX}}$ and $A_{V,\mathrm{tot}}$ is given in Eq. (1)). *Bottom panels*: correlations between the EW of Hδ, Hβ, Paβ lines and the N2 index (= $\log_{10}$([NII]/Hα)). The blue continuous lines are the best-fit linear relations, determined as explained in Sect. 3, while the blue shaded area show the $\pm 1\sigma$ scatter of our data around the best-fit relations.

of the merger. However, these EWs would only probe what is happening in the outer parts of the system, since the core is completely obscured in optical and near-IR.

We show in the last diagram in Fig. 3 and the upper part of Fig. 8 that, when the starbursts become more obscured, the EWs of Paβ, Hδ and Hβ decrease, indicating a gradual SFR decline in the outer skin of more obscured and compact starbursts. Additional correlations were found also independently between those EWs and the other quantities, such as the N2 index (Fig. 8-*bottom*). We additionally remark that the different Paschen and Balmer lines correlate each other (see Fig. B.3), for which reason our results, derived adopting the Paβ line as a reference (because it is the least attenuated), are also valid when considering the Hδ, Hβ and Hα lines.

In our sample, we also found that the Balmer EWs, while having a large dynamical range, can reach very low values: in five galaxies (ID 303305, 685067, 777034, 862072 and 345018) we measured an EW(Hδ) < -4 Å (i.e., in absorption), which are typically found in E+A dusty galaxies (Poggianti & Wu 2000). Low EW hydrogen recombination lines (in strong absorption) are clear signatures of the prevalence of A-type stars, indicating that a recent (<1 Gyr ago) massive star-formation episode has taken place during the past 10^8–10^9 yr, while the youngest stellar populations (mainly OB stars) are nearly all obscured by dust in the inner starburst core. Our dusty starburst systems should also not be confused with post-starburst (PSB) galaxies, which have similar absorption EWs (e.g., EW(Hδ) lower than ~ -5 Å as in the selection of Goto 2007 and Maltby et al. 2016), but are nearly or already quenched systems, owing much lower SFR levels and lower dust content compared to our sample (see Pawlik et al. 2018 for a full discussion of the different types of PSB galaxies). We caution that the quenched PSB selection from only the Balmer EW may be contaminated by real starburst systems.

Putting all together, the time-evolutionary scenario that we have suggested has the advantage of explaining in a simple way these new results. If we follow the merger evolution toward the coalescence, the outer starburst skin becomes increasingly dominated by A-type stars, recognizable through the deep absorption lines in the optical and near-IR, and which were formed at earlier times when the separation between the merging nuclei was larger. At the same time, the star-formation in the skin is being suppressed, possibly driven by supernova feedback.

4.4. Outliers

We found in Sect. 3 (Fig. 3) that four galaxies are outside the 1σ dispersion of the best-fit relations between the dust attenuation $A_{V,\mathrm{tot}}$ and, simultaneously, the [NII]/Hα ratio (N2), the line velocity width ($\mathrm{FWHM_{line}}$) and the EW(Paβ). In particular, they have lower N2, $\mathrm{FWHM_{line}}$ and EW(Paβ) than expected from

their $A_{V,\rm tot}$, suggesting that, compared to other highly obscured galaxies, there is a minor impact from shocks or a dominant contribution of star-formation to the emission lines.

Within our SB sample, we recognize that these four outliers have the largest dust obscurations $A_{V,\rm tot} \geq 18$ mag, and are among the most compact, with radio FWHM sizes below 1 kpc. These extreme and peculiar features suggest they may represent the very end stages of the merger evolution, and that the correlations with $A_{V,\rm tot}$ may saturate toward these late phases. We also notice that the same objects are not systematically outliers when we consider their N2, $\rm FWHM_{line}$ and EW(Paβ) values, confirming the close physical connection among these quantities, as shown in Sects. 4.2 and 4.3.

4.5. The complete sequence of merger stages at intermediate redshift

Our observations and results, presented in previous sections, suggest we are starting to see an evolutionary sequence in high-redshift mergers. This can be traced through a variety of physical measurable quantities of our galaxies, including the total attenuation toward the center, the characteristic size of the starburst, the EW of hydrogen absorption lines, and finally the [N II]/Hα ratios and line velocity widths, which behave similarly. In Fig. 9 we schematize with a cartoon all the results that we have found so far, showing with a red continuous line the qualitative trend of the different physical quantities as a function of time. We divided the time axis into five merger evolutionary stages, which are arranged in relation to the two most crucial transformation events during the merger: the coalescence and the blow-out (or QSO) appearance.

We notice that the first phase may not necessarily represent the beginning of the interaction, that is, when the two galaxies approach for the first time. Even though the whole merger episode may last 1–1.5 Gyr in total, from the first encounter to the formation of a passive spheroidal system, the starburst activity is typically shorter, ranging 200–300 Myr (Di Matteo et al. 2008) and may be triggered intermittently at various stages of the evolution. Furthermore, whether or not a strong burst is already activated at the first approach depends on many factors, including the impact geometry, the morphology, the stellar mass ratio and the gas content of the colliding galaxies (Di Matteo et al. 2008).

Besides the observable starburst phases studied in this work, can we also make some predictions on the future evolution of these systems? In general, it is very hard to demonstrate visually a connection between mergers and their descendants. Indeed, not all merger-induced starbursts exhibit morphological disturbances (Lotz et al. 2008), and when merger residual signatures are present, they fade rapidly, becoming almost invisible beyond the local Universe even in the deepest optical images (e.g., Hibbard & Vacca 1997). We can in principle rely on hydrodynamical simulations, which allow to trace the full time-sequence of mergers, even though they also present limitations due to the many assumptions, initial conditions and physical complexity involved in such events.

In the classical theoretical merger paradigm, the infalling gas triggers obscured AGN accretion (Bennert et al. 2008a), whose peak of activity typically occurs ∼250 Myr after the onset of the starburst (Wild et al. 2010), and ∼100 Myr after the peak of SFR (Davies et al. 2007; Hopkins 2012). It is during these later starburst phases that the AGN feedback can blow out with strong feedback winds the surrounding dust and gas cocoon, eventually revealing itself as a bright QSO (Hopkins et al. 2008b). This phase is generally very short, lasting for $\lesssim$100 Myr (Hopkins & Elvis 2010), and has been claimed since a long time: Lípari et al. (2003) suggested that QSOs could be indeed young IR active galaxies at the end phase of a strong starburst.

Since the QSO dominates the luminosity of the system at all wavelengths, it would be extremely hard to analyze the physical properties of the host galaxies during this phase. Indeed, Zakamska et al. (2016) show that even in radio-quiet QSOs both the infrared and the radio emission are dominated by the quasar activity, not by the host galaxy. An alternative possibility is to look far from the central bright source. Recent works are revealing Ly-α nebulae surrounding high-redshift quasars, with extension that can reach tens of kpc ($\lesssim$50 kpc) from the center (Arrigoni Battaia et al. 2019). On the other hand, one may focus on local samples, increasing simultaneously the images resolution. For example, Lípari et al. (2003) and Bennert et al. (2008b) discovered with HST the presence of outflows, arcs, bubbles and tidal tales in optical band in a sample of local QSOs, possibly formed through strong galactic winds or merger processes. Again in nearby ($z < 0.3$) QSOs, near-IR H band adaptive optics observations (Guyon et al. 2006) revealed that ∼30% of their hosts show signs of disturbances, and the most luminous QSOs are harbored exclusively in ellipticals or in mergers (which may become ellipticals soon). Furthermore, while the SFRs of the hosts are similar to those of normal star-forming galaxies, their mid- and far-IR colors resemble those of warm ULIRGs, strengthening a connection between these two objects.

In the following two Sects. 4.6 and 4.7, we discuss separately the two ending stages of the merger sequence, and investigate how our work can provide some clues to understand what are the physical properties of the systems into which our starbursts will evolve. In the cartoon of Fig. 9, the predicted evolution for all the quantities studied in this paper (see Sect. 3) is shown with a dashed line. These qualitative trends are motivated mainly from simulations, and are not confirmed observationally.

4.6. Mass-size relation and comparison with higher and lower-z starbursts

The merger-induced starbursts are supposed to end up in a passive system, but we do not know the exact physical properties (e.g., size, stellar mass, morphology) of these merger remnants. Sub-millimeter galaxies (SMGs) at high redshift (>2), which are commonly viewed as higher luminous counterparts of lower redshift ULIRGs, have been suggested to be direct progenitors of massive ETGs (Tacconi et al. 2008; Toft et al. 2014). We can investigate this connection by comparing in Fig. 10 the stellar masses and the characteristic sizes of our starbursts with those of disk galaxies and spheroids at $z \sim 0.7$ (van der Wel et al. 2014). To be conservative, we are adopting here the $\rm M_*$-size relations for circularized radii. If we consider instead the non-circularized cases, the same relations would slightly shift upwards by ∼0.1 dex. In addition, we remark that we are comparing our radio (starburst) extensions to optical rest-frame sizes tracing the stellar mass distribution of disks and elliptical galaxies. Indeed, we implicitly assume that, after the gas in our starburst cores is converted into stars, the extensions of these cores will represent also the stellar component sizes of their passive remnants. On the other hand, they may still represent the dense star-forming gas components of post-starburst systems if some residual is left after the merger, as they may remain compact for at least 1 Gyr (Davies et al. 2019).

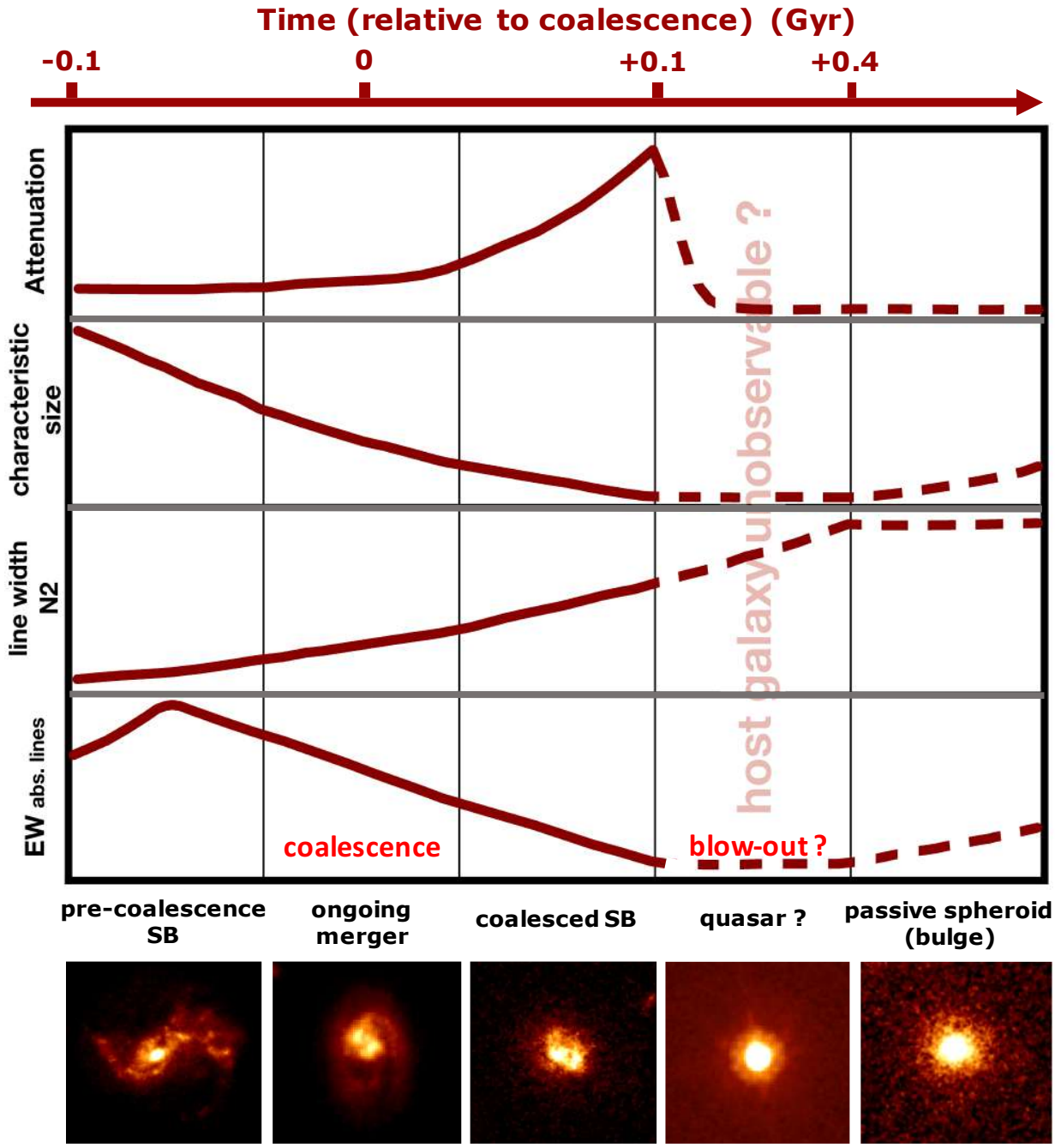

Fig. 9. Schematic illustration of the time-evolutionary behavior of the physical parameters studied in the text: dust attenuation, characteristic size of the system, line velocity width (or, equivalently, the N2 index) and the EW of Balmer and Paschen lines. The time sequence is divided into five fundamental merger stages, with the QSO and passive spheroidal system representing the final stages according to the classical merger paradigm (Sanders & Mirabel 1996; Hopkins et al. 2008a,b). Solid lines are qualitative trends during the SB phase inferred from our results, while dashed lines are predictions for the future evolution of the four parameters shown on the *y*-axis (line width and N2 index behave similarly). In the upper part of the figure, we show a qualitative merger timescale following Fig. 1 of Hopkins et al. (2008b), assuming for the merger a total starburst duration of 200 Myr. For each phase, we show in the bottom part the ACS-F814W cutout of a representative case. The first three images are SB galaxies from our sample: ID 223715, ID 777034 and ID 472775. They were chosen as having increasing dust attenuations and radio compactness, suggestive of more advanced merger phases: the first was identified as a precoalescence merger in Sect. 4.1, while the latter is unresolved in radio and is highly obscured ($A_{V,\mathrm{tot}}$ = 18 mag). The last two cutouts show a quasar at z = 0.73 and an ETG at z = 0.66, selected in COSMOS field from the catalogs of Prescott et al. (2006) and Tasca et al. (2009), respectively.

In the diagram of Fig. 10, six SBs are consistent with the late-type galaxy (LTG) relation at $z \sim 0.7$. However all of them are precoalescence SBs and, as we have seen before, they should not be considered disk galaxies as their size is primarily reflecting the separation between the merging components. For two of the three galaxies resolved in radio, the single values return below on the early-type galaxy (ETG) relation. The characteristic sizes of this subset ($\mathrm{FWHM_{size}}$ ranging 3–15 kpc in diameter, with median $\mathrm{FWHM_{size}}$ of 8 kpc) are similar to those typical observed in SMGs (Casey et al. 2011; Tacconi et al. 2008; Biggs & Ivison 2008), which suggests that SMGs at high-redshift (or at least a fraction of them) could be indeed intermediate-phase mergers

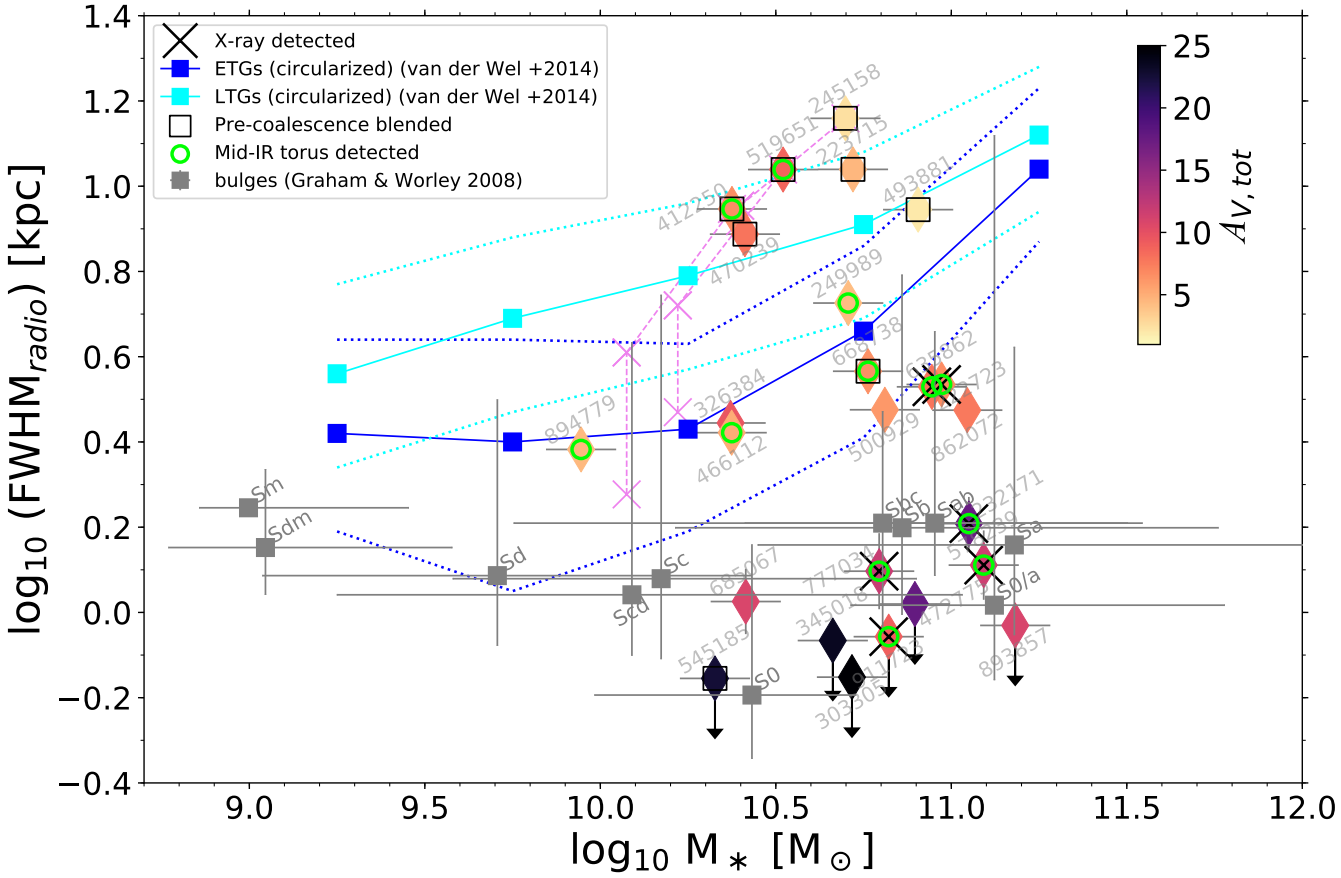

Fig. 10. Diagram showing the radio size vs. stellar mass for our sample. We compare our results to the stellar mass–stellar size relation of LTGs (cyan line with 1σ dispersion) and ETGs (blue line) at $z = 0.7$ (van der Wel et al. 2014), and with the bulge properties of low redshift ($z \sim 0.1$) spiral galaxies from Graham & Worley (2008; gray squares). The eleven points shown here for the bulges represent the median ($\pm 1\sigma$) of their distributions of stellar masses and stellar sizes (in K band) as a function of galaxy type, from S0 to Sm spirals. For three galaxies in our sample fit with a double Gaussian, we also represent the "deblended" radio sizes of each single component with violet crosses, connecting them with a dashed violet line. In these cases, we assigned to each component half of the total stellar mass of the system, even though a precise estimation requires a separate fit on deblended photometric data.

composed of unresolved double nuclei, as argued by Iono et al. (2009) and Arribas et al. (2012).

In the bottom part instead, we can immediately notice that a major fraction of our sample (13 galaxies, i.e., 52% of the total sample) is not consistent with the ETG relation (taking 1σ dispersion), and is located well below it by ~0.5 dex, with an average size of ≤1.2 kpc, indicating that they are much more compact than their stellar envelopes and than typical ellipticals at $z \sim 0.7$. We underline that such difference would be even higher if we compare this subset to the M_*-size relation at redshifts lower than 0.7, as the ETG sizes at $z = 0.25$ are a factor of 1.5 higher than those at $z = 0.75$, at our median stellar mass (van der Wel et al. 2014). This sample of very compact starbursts has typical extensions that are similar to those of dense star-forming regions in local ULIRGs (Genzel et al. 1998; Piqueras López et al. 2016), including Arp 220 (Sakamoto et al. 2017) and M82 (Barker et al. 2008), suggesting they are driven by the same merger mechanisms (as also argued in Paper I).

If we take for each galaxy its distance from the LTG relation ($\mathrm{dist_{LTG}} = \log_{10}(\mathrm{FWHM_{size}}/\mathrm{FWHM_{LTG}})$), we can also use this quantity in place of the radius to trace the same sequence found in Sect. 3, taking into account the mild dependence on stellar mass. As the merger proceeds, the system moves from the LTG to the ETG relation and then even below at significantly smaller sizes (by ~0.5 dex at least), meaning that the compact starburst cores that form at the coalescence cannot produce directly the ellipticals seen at redshift 0.7 and below.

The sizes of our starbursts instead resemble those of typical bulges in lower redshift spirals and lenticular galaxies (Graham & Worley 2008; Laurikainen et al. 2010), indicating a possible evolutionary link between mergers and bulges, as suggested by other works (e.g., Sanders & Mirabel 1996; Lilly et al. 1999; Eliche-Moral et al. 2006; Querejeta et al. 2015). This idea is consistent with the typical observed gas fractions of our starbursts (derived as $M_{\rm gas}/(M_* + M_{\rm gas})$, with $M_{\rm gas}$ calculated in Sect. 4.2.2), which range between 0.02 and 0.25 (~0.1 in median). Assuming that all the remaining gas is consumed before the passivization and that the same amount of gas has been already converted into stars (which depends on the merger phase and dynamics), it means that the current starburst cores can produce approximately 20%, and up to 50%, of the final stellar mass of the galaxies. Higher resolution radio images targeting specific emission lines can further constrain the kinematic properties of the starbursting cores, by looking for rotation, or their luminosity profile, for example measuring their Sersic index. How this old stellar component is affected by the merger can depend on many conditions difficult to model in detail, including the geometry of the interaction, the gas content and the mass ratio of the colliding galaxies.

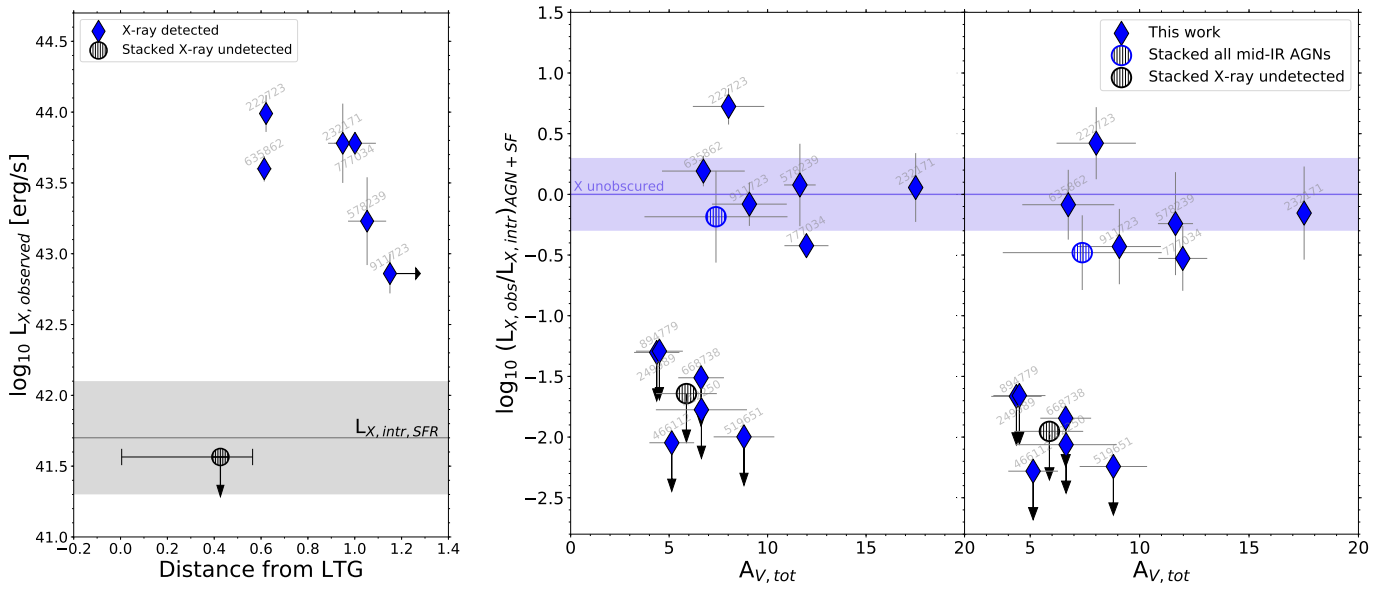

Fig. 11. *Left panel*: comparison between the observed X-ray luminosity ($L_{\rm X,obs}$) and the distance from the mass-size relation of LTGs at $z \sim 0.7$, for our six starbursts detected in X-rays. Upper limit on $L_{\rm X,obs}$ for six mid-IR AGNs undetected in X is shown with a black circle, where the horizontal segment represents the range of $\rm dist_{LTG}$ spanned by this subset. The intrinsic X-ray luminosity due to star-formation is highlighted with a gray line for the median SFR of the sample (±0.4 dex scatter from Mineo et al. 2014), and may dominate the total X-ray observed emission for the X-undetected starbursts. *Center panel*: X-ray attenuation $L_{\rm X,obs}/L_{\rm X,int}$ as a function of the infrared-based attenuation $A_{V,\rm tot}$ (in a mixed model geometry and toward the center) for our sample of mid-IR detected AGNs. We assumed here a bolometric correction factor $L_{\rm X,intr,AGN} = 0.04 \times L_{\rm BOL,AGN}$ (Vasudevan & Fabian 2007). Stacks on the whole sample and on the X-undetected subset are displayed with hatching circles, while the violet shaded regions indicate the area of no obscuration, which incorporates a factor of two uncertainty in the conversion between intrinsic X-ray and bolometric AGN luminosity. *Right panel*: same diagram as before, but assuming an $L_{\rm BOL,AGN}$- dependent bolometric correction (Lusso et al. 2012), as explained in the text.

4.7. QSOs in formation at $z \sim 0.7$?

In the starburst selection phase, we discarded several quasars because of the impossibility to study the properties of their host galaxies (dust attenuation, SFR, stellar mass), as discussed in Sect. 4.5. In order to overcome these limitations, several authors have extensively studied also the transitional moments (just preceding the final blow-out) in the dress of type-I and warm ULIRGs (Kawakatu et al. 2006; Sanders et al. 1988). Similarly, we can have some clues of the inner black-hole activity just before the hypothetical QSO by looking at the AGN diagnostics in our starburst sample.

As mentioned in Sect. 2.8, we detected the mid-IR dusty torus AGN emission in 12 galaxies, and simultaneous X-ray emission in six of them. Notably, the latter are the only ones (among mid-IR AGNs) whose host galaxies lie below the ETG relation in the mass-size diagram (see Fig. 10), at systematically smaller sizes than ellipticals at $z \leq 0.7$. This suggests that during early merger stages the AGNs are predominantly obscured, while they start to appear in X-rays toward intermediate stages (i.e., when the host starbursts are more compact and obscured), possibly driven by rapid AGN feedback clearing the gas and dust around the black hole.

This can be seen better in Fig. 11-left, where all the host galaxies of X-ray detected AGNs are located at larger distances from the mass-size relation of LTGs compared to X-ray undetected AGNs. Moreover, they have X-ray luminosities at least 1 order of magnitude higher (∼+1.5 on average) than what inferred from their SFR. For the X-undetected galaxies instead, the upper limit on $L_{\rm X} = 10^{41.7}\,\rm erg\,s^{-1}$, determined by average-stacking their fluxes in the 2−10 keV band at the median z of the sample, is consistent with emission produced by star-formation only, suggesting that in this band the AGN is completely obscured.

In order to assess the level of obscuration, we computed the ratio between the observed and the intrinsic X-ray luminosity $L_{\rm X,obs}/L_{\rm X,intr}$, comparing this quantity to the total dust attenuation $A_{V,\rm tot}$ inferred in a mixed model from Paβ and the bolometric IR luminosity (Paper I). $L_{\rm X,intr}$ comprises the contribution from both star-formation (as explained in Sect. 2.8) and from the AGN, assuming $L_{\rm X,intr,AGN} = 0.04 \times L_{\rm BOL,AGN}$ (Vasudevan & Fabian 2007) and a bolometric AGN luminosity $L_{\rm BOL,AGN} = 1.5 \times L_{\rm AGN,IR}$ (Elvis et al. 1994; Fig. 11-center). Alternatively, we considered the bolometric correction of Lusso et al. (2012) for type-2 AGNs, which depends on $L_{\rm BOL,AGN}$ itself through the following, nonlinear equation:

$$\log_{10}\left(\frac{L_{\rm BOL}}{L_{2-10\,\rm keV}}\right) = 0.217x - 0.022x^2 - 0.027x^3 + 1.289, \qquad (6)$$

where $x = \log_{10}(L_{\rm BOL}) - 12$ and the scatter of the relation is 0.26 dex. However, the results derived with this second assumption (Fig. 11-*left*) do not change significantly compared to the first case.

The figures presented above confirm that the total attenuation inferred from $L_{\rm X}$ may be the discriminating parameter between X-ray detected and undetected mid-IR AGNs: while the former are relatively unobscured, the X-ray emission from the second is suppressed at least by a factor of 30. Interestingly, this transition does not seem to be related to an increased bolometric luminosity, since no correlations are observed with this quantity. We also remind that for this analysis we are following the standard procedure, which does not take into account shock contribution to the X-ray luminosity. A possible non negligible shock emission at these high energies (which in any case is difficult to model) would result in an underestimation of the true effective X-ray attenuation toward the AGN.

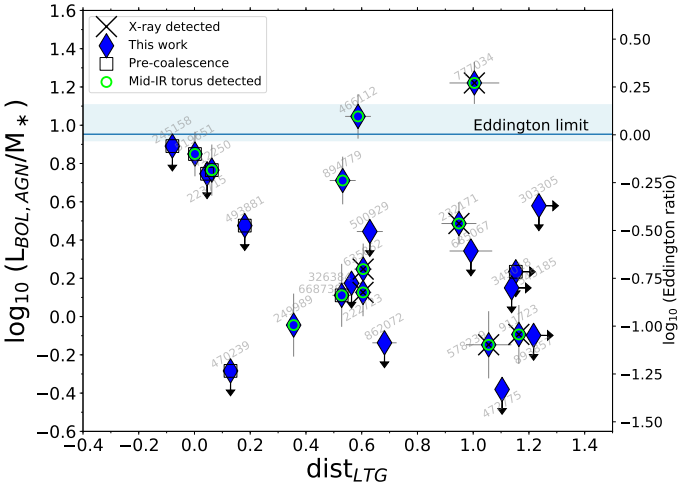

Fig. 12. $L_{\rm BOL,AGN}/M_*$ vs. distance from the mass-size relation of LTGs ($\rm dist_{LTG}$) for our SBs sample. The Eddington limit is shown with a blue horizontal line, while the shaded area takes into account the spread of M_* among our sample and the uncertainty of the relation between stellar mass and BH mass by Reines & Volonteri (2015). The Eddington ratio is shown on the right y-axis.

The previous results suggest that the X-ray attenuation decreases as the starburst becomes more dust-obscured (probed by $A_{V,\rm tot}$) during the last merger phases. In a standard framework (i.e., if we exclude dominant contribution from shocks to the X-ray luminosity), this apparent contradiction can be reconciled by considering the different timescales of our diagnostics. On the one hand, Paβ (used to calculate $A_{V,\rm tot}$), yields a luminosity (or, equivalently, a SFR, by applying the Kennicutt et al. (1994) conversion) that is averaged over a timescale of 20−30 Myr. Conversely, the AGN luminosity that we measure in X-rays gives an istantaneous information of the AGN activity. As a consequence, with the X-ray analysis we are able to probe the current dust attenuation level, while $A_{V,\rm tot}$ traces the obscuration in the recent past ($\lesssim$30 Myr). According to this speculation, the X-ray luminosities measured for a subset of six late stage mergers indicate that the AGN-induced blow-out may have already started since a few Myr ago, clearing the surrounding gas and dust content, and that we might be very close to the final QSO phase.

Furthermore, in Fig. 12 we display the AGN accretion efficiencies of our galaxies as a function of their distance from the LTGs mass-size relation. The efficiencies were estimated by comparing the observed $L_{\rm BOL,AGN}/M_*$ ratios to the maximum value allowed by Eddington ($L_{\rm BOL,AGN}/M_*|_{\rm EDD} \simeq 1.5$), from which we derived the so-called Eddington ratio $(L/L_{\rm EDD})|_{\rm AGN}$. We assumed the typical correlation for AGNs between the stellar mass M_* and black hole mass $M_{\rm BH}$ of Reines & Volonteri (2015) and a spherically symmetric accreting BH, yielding $\log(L_{\rm EDD}/M_*) \simeq 0.9685 + 0.05\log_{10}(M_*)$. The M_* in the second term can be approximated with the median value of the sample $M_{*,\rm median}$, leaving a small secondary dependence on stellar mass which, for our mass ranges (10^{10}−10^{11} $M_\odot$) produces variations of <5%. This variation, added to the uncertainty on the relation between M_* and $M_{\rm BH}$ reported by Reines & Volonteri (2015) (cf. their Eqs. (4) and (5)), is highlighted in Fig. 12 with a blue shaded area around the Eddington limit (blue line) calculated above.

From this analysis, we found that two AGNs have an Eddington ratio higher than 1 ($1.2 < (L/L_{\rm EDD})|_{\rm AGN} < 1.85$), while additional three AGNs are radiating between 57% and 79% of their maximum luminosity. However, all these five AGNs are still consistent within 2σ errors with $(L/L_{\rm EDD})|_{\rm AGN} = 1$ if we also consider the uncertainty on the conversion factor from the ratio $L_{\rm BOL,AGN}/M_*$, as discussed before. We remark that additional uncertainties on the M_*−$M_{\rm BH}$ relation, which depends on the assumptions about the BH accretion geometry, are not taken into account here. The remaining seven IR-detected AGNs have instead lower Eddington ratios between 0.35 and 0.08.

The galaxies which are undetected in X, radio and mid-IR may contain low-active AGNs, even though current upper limits on the Eddington ratio are not so stringent and do not allow to discriminate them from the detected subset. The intrinsic variability of AGN accretion may thus explain why we are currently missing many of these sources in our sample, and that only deeper X-ray observations can potentially reveal. The duty cycles above 30% and 1% $L_{\rm EDD}$ seem to be at least ∼25% and ∼50%, respectively.

5. Summary and conclusions

Using our unique sample of 25 starburst galaxies (typically seven times above the star-forming main sequence) at $z = 0.5$−0.9 with near-IR rest frame spectroscopy of Paschen lines, we found in Paper I that they span a large range of attenuations toward the core centers from $A_V = 2$ to $A_V = 30$, forming a sequence which is consistent with a mixed model geometry of dust and stars. In this paper we have investigated the nature of this attenuation sequence, comparing A_V with other physical properties, such as the radio size (which traces the extension of the starburst), the emission lines velocity widths and [N II]/Hα ratios (which depend on the internal motions of the gas and the contribution from shocks), and finally the EW of hydrogen absorption lines, which is sensitive to the luminosity-weighted age of the stellar populations surrounding the optically obscured core.

We summarize the main results of this paper as follows:

1. We found that the physical quantities introduced above, namely the radio sizes ($\rm FWHM_{radio}$), the line velocity widths ($\rm FWHM_{line}$), the [N2]/Hα ratios (N2) and the equivalent widths of Paschen and Balmer lines ($\rm EW_{Balmer,Paschen}$), all correlate each other (Fig. 3), defining a one-parameter sequence of $z \sim 0.7$ starburst galaxies.
2. These correlations can be interpreted as a time-evolutionary sequence of merger stages. As the merger evolves, the starburst becomes more compact and dust obscured, while the deep potential wells created by merging nuclei produce, according to the virial theorem, an increase of the kinetic energy and shocks in the system. At the same time, intermediate aged A-type stars in the outer starburst core regions are primarily responsible for the stronger optical+near-IR absorption lines in later phases.
3. Four galaxies are outliers simultaneously in three of the ten main correlations, which involve $A_{V,\rm tot}$ and, respectively, N2, $\rm FWHM_{line}$ and EW(Paβ). Having the largest dust attenuations and among the smallest radio sizes in our sample, these outliers may represent the very end phases of the merger evolution, where the above three relations may reach a saturation level.
4. Using sky-subtracted 2D spectra, we identified a subset of seven precoalescence mergers by the presence of spatially separated or kinematically detached (i.e., rotation-driven tilted lines with different inclination angles) Hα components, representing earlier, less obscured phases of the interaction. The radio sizes measured for these systems are likely tracing the separation between the merging nuclei rather than the dimensions of single cores. However, our sample may

contain additional double nuclei which we are not currently able to resolve.

5. Half of our sample comprises extremely compact starbursts, with average half-light radii of 600 pc (six galaxies have only upper limits), similar to the sizes of starbursting cores observed in local ULIRGs. These sizes are also ∼0.5 dex smaller than ETGs at redshift ∼0.7 and below, indicating that our merger-driven starbursts cannot be direct progenitors of the population of massive ellipticals formed in the last ∼7 Gyr. On the contrary, they are more consistent with typical sizes and masses of bulge structures in spiral galaxies (Graham & Worley 2008), suggesting a possible evolutionary connection between our starburst cores and bulges.
6. In our sample, we detected at $>3\sigma$ the mid-IR dusty torus AGN emission in 12 starbursts, with Eddington ratios ranging from 1.9 to <0.08. Among them, only six galaxies are simultaneously detected (at 3σ) in X-rays. Intriguingly, the latter have the largest departures from the mass-size relation of LTGs (at $z \leq 0.7$), suggesting that AGNs start to appear in X-rays during the latest (compact) merger phases, as the blow-out of surrounding dust and gas may precede a possible final QSO.

Overall, the relations among the above physical parameters converge toward a time-evolutionary sequence of merger stages, which represents an observational evidence (translated at higher redshift) of the theoretical merger-induced starbursts framework of Hopkins et al. (2008a,b), Di Matteo et al. (2005), and the evolutionary sequence postulated by Toomre & Toomre (1972). The future advent of JWST will allow to test this scenario up to very high redshift in different galactic physical conditions compared to the epochs studied here.

Acknowledgements. We thank the anonymous referee for useful suggestions that improved the quality of this manuscript, G.Rudie for assistence with *Magellan* observations, Nicolás Ignacio Godoy for data reduction, and Daniela Calzetti for discussions. M.O. acknowledges support from JSPS KAKENHI Grant Number JP17K14257. N.A. acknowledges support from the Brain Pool Program, funded by the Ministry of Science and ICT through the Korean National Research Foundation (2018H1D3A2000902). M.B. acknowledges FONDECYT regular grant 1170618. R.C. acknowledges financial support from CONICYT Doctorado Nacional No. 21161487 and CONICYT PIA. ACT172033. A.C. acknowledges RadioNet conference funding. This research has made use of the zCosmos database, operated at CeSAM/LAM, Marseille, France.

References

Ahn, C. P., Alexandroff, R., Allende Prieto, C., et al. 2012, ApJS, 203, 21
Aird, J., Coil, A. L., & Georgakakis, A. 2019, MNRAS, 484, 4360
Arribas, S., Colina, L., Alonso-Herrero, A., et al. 2012, A&A, 541, A20
Arrigoni Battaia, F., Hennawi, J. F., Prochaska, J. X., et al. 2019, MNRAS, 482, 3162
Avni, Y., & Bahcall, N. A. 1976, ApJ, 209, 16
Barker, S., de Grijs, R., & Cerviño, M. 2008, A&A, 484, 711
Barnes, J. E., & Hernquist, L. E. 1991, ApJ, 370, L65
Bennert, N., Canalizo, G., Jungwiert, B., et al. 2008a, Mem. Soc. Astron. It., 79, 1247
Bennert, N., Canalizo, G., Jungwiert, B., et al. 2008b, ApJ, 677, 846
Best, P. N., & Heckman, T. M. 2012, MNRAS, 421, 1569
Biggs, A. D., & Ivison, R. J. 2008, MNRAS, 385, 893
Bournaud, F., Chapon, D., Teyssier, R., et al. 2011, ApJ, 730, 4
Brinchmann, J., Charlot, S., White, S. D. M., et al. 2004, MNRAS, 351, 1151
Brusa, M., Civano, F., Comastri, A., et al. 2010, ApJ, 716, 348
Bruzual, G., & Charlot, S. 2003, MNRAS, 344, 1000
Calabrò, A., Daddi, E., Cassata, P., et al. 2018, ApJ, 862, L22
Cappelluti, N., Brusa, M., Hasinger, G., et al. 2009, A&A, 497, 635
Cardelli, J. A., Clayton, G. C., & Mathis, J. S. 1989, ApJ, 345, 245
Casey, C. M., Chapman, S. C., Neri, R., et al. 2011, MNRAS, 415, 2723
Chabrier, G. 2003, PASP, 115, 763
Chiaberge, M., Gilli, R., Lotz, J. M., & Norman, C. 2015, ApJ, 806, 147
Cid Fernandes, R., Stasińska, G., Schlickmann, M. S., et al. 2010, MNRAS, 403, 1036
Cisternas, M., Jahnke, K., Inskip, K. J., et al. 2011, ApJ, 726, 57
Civano, F., Hickox, R. C., Puccetti, S., et al. 2015, ApJ, 808, 185
Combes, F. 2003, Active Galactic Nuclei: From Central Engine to Host Galaxy, 290, 411
Condon, J. J. 1992, ARA&A, 30, 575
Coogan, R. T., Daddi, E., Sargent, M. T., et al. 2018, MNRAS, 479, 703
Díaz-Santos, T., Charmandaris, V., Armus, L., et al. 2010, ApJ, 723, 993
Daddi, E., Dickinson, M., Morrison, G., et al. 2007a, ApJ, 670, 156
Daddi, E., Alexander, D. M., Dickinson, M., et al. 2007b, ApJ, 670, 173
Daddi, E., Bournaud, F., Walter, F., et al. 2010, ApJ, 713, 686
Davies, R. I., Müller Sánchez, F., Genzel, R., et al. 2007, ApJ, 671, 1388
Davies, T. A., Van de Voort, F., Rowlands, K., et al. 2019, MNRAS, 484, 2447
Di Matteo, T., Springel, V., & Hernquist, L. 2005, Nature, 433, 604
Di Matteo, P., Bournaud, F., Martig, M., et al. 2008, A&A, 492, 31
Draine, B. T., & Li, A. 2007, ApJ, 657, 810
Duc, P.-A., Cuillandre, J.-C., Alatalo, K., et al. 2013, The Intriguing Life of Massive Galaxies, 295, 358
Draper, A. R., & Ballantyne, D. R. 2012, ApJ, 751, 72
Elbaz, D., & Cesarsky, C. J. 2003, Science, 300, 270
Elbaz, D., Daddi, E., Le Borgne, D., et al. 2007, A&A, 468, 33
Eliche-Moral, M. C., Balcells, M., Aguerri, J. A. L., & González-García, A. C. 2006, A&A, 457, 91
Ellison, S. L., Patton, D. R., Mendel, J. T., & Scudder, J. M. 2011, MNRAS, 418, 2043
Ellison, S. L., Patton, D. R., & Hickox, R. C. 2015, MNRAS, 451, L35
Elvis, M., Wilkes, B. J., McDowell, J. C., et al. 1994, ApJS, 95, 1
Faisst, A. L., Masters, D., Wang, Y., et al. 2018, ApJ, 855, 132
Fensch, J., Renaud, F., Bournaud, F., et al. 2017, MNRAS, 465, 1934
Gagné, J., Lambrides, E., Faherty, J. K., & Simcoe, R. 2015, FireHose_v2: Firehose v2.0. Zenodo, 10
Gao, Y., & Solomon, P. M. 1999, ApJ, 512, L99
Gaskell, C. M. 2009, New A Rev., 53, 140
Genzel, R., Lutz, D., Sturm, E., et al. 1998, ApJ, 498, 579
Genzel, R., Tacconi, L. J., Rigopoulou, D., Lutz, D., & Tecza, M. 2001, ApJ, 563, 527
Genzel, R., Schreiber, N. M. F., Übler, H., et al. 2017, Nature, 543, 397
Ghavamian, P., Seitenzahl, I. R., Vogt, F. P. A., et al. 2017, ApJ, 847, 122
Goldader, J. D., Meurer, G., Heckman, T. M., et al. 2002, ApJ, 568, 651
Goto, T. 2007, MNRAS, 381, 187
Goulding, A. D., Greene, J. E., Bezanson, R., et al. 2018, PASJ, 70, S37
Graham, A. W., & Worley, C. C. 2008, MNRAS, 388, 1708
Guyon, O., Sanders, D. B., & Stockton, A. 2006, ApJS, 166, 89
Haan, S., Armus, L., Surace, J. A., et al. 2013, MNRAS, 434, 1264
Heinis, S., Buat, V., Béthermin, M., et al. 2014, MNRAS, 437, 1268
Hibbard, J. E., & Vacca, W. D. 1997, AJ, 114, 1741
Hopkins, P. F. 2012, MNRAS, 420, L8
Hopkins, P. F., & Elvis, M. 2010, MNRAS, 401, 7
Hopkins, P. F., Cox, T. J., Kereš, D., & Hernquist, L. 2008a, ApJS, 175, 390
Hopkins, P. F., Hernquist, L., Cox, T. J., & Kereš, D. 2008b, ApJS, 175, 356
Horne, K. 1986, PASP, 98, 609
Ibar, E., Cirasuolo, M., Ivison, R., et al. 2008, MNRAS, 386, 953
Iono, D., Wilson, C. D., Yun, M. S., et al. 2009, ApJ, 695, 1537
Ivison, R. J., Magnelli, B., Ibar, E., et al. 2010, A&A, 518, L31
Jin, S., Daddi, E., Liu, D., et al. 2018, ApJ, 864, 56
Kartaltepe, J. S., Sanders, D. B., Le Floc'h, E., et al. 2010, ApJ, 721, 98
Kauffmann, G., Heckman, T. M., Tremonti, C., et al. 2003, MNRAS, 346, 1055
Kawakatu, N., Anabuki, N., Nagao, T., Umemura, M., & Nakagawa, T. 2006, ApJ, 637, 104
Kelson, D. D. 2003, PASP, 115, 688
Kennicutt, Jr., R. C., Tamblyn, P., & Congdon, C. E. 1994, ApJ, 435, 22
Kewley, L. J., Dopita, M. A., Sutherland, R. S., Heisler, C. A., & Trevena, J. 2001, ApJ, 556, 121
Kocevski, D. D., Faber, S. M., Mozena, M., et al. 2012, ApJ, 744, 148
Koekemoer, A. M., Aussel, H., Calzetti, D., et al. 2007, ApJS, 172, 196
Kormendy, J., & Sanders, D. B. 1992, ApJ, 390, L53
Laigle, C., McCracken, H. J., Ilbert, O., et al. 2016, ApJS, 224, 24
Laine, S., van der Marel, R. P., Rossa, J., et al. 2003, AJ, 126, 2717
Lanzuisi, G., Delvecchio, I., Berta, S., et al. 2017, A&A, 602, A123
Laurikainen, E., Salo, H., Buta, R., Knapen, J. H., & Comerón, S. 2010, MNRAS, 405, 1089
Le Fèvre, O., Saisse, M., Mancini, D., et al. 2003, Proc. SPIE, 4841, 1670
Leech, J., Isaak, K. G., Papadopoulos, P. P., Gao, Y., & Davis, G. R. 2010, MNRAS, 406, 1364
Lilly, S., Eales, S. A., Gear, W. K., et al. 1999, The Formation of Galactic Bulges, 26

Lilly, S. J., Le Fèvre, O., Renzini, A., et al. 2007, ApJS, 172, 70
Lípari, S., Terlevich, R., Díaz, R. J., et al. 2003, MNRAS, 340, 289
Liu, D., Daddi, E., Dickinson, M., et al. 2018, ApJ, 853, 172
Lotz, J. M., Jonsson, P., Cox, T. J., & Primack, J. R. 2008, MNRAS, 391, 1137
Luo, W., Yang, X., & Zhang, Y. 2014, ApJ, 789, L16
Lusso, E., Comastri, A., Simmons, B. D., et al. 2012, MNRAS, 425, 623
Lutz, D., Veilleux, S., & Genzel, R. 1999, ApJ, 517, L13
Magdis, G. E., Daddi, E., Béthermin, M., et al. 2012, ApJ, 760, 6
Maltby, D. T., Almaini, O., Wild, V., et al. 2016, MNRAS, 459, L114
Mannucci, F., Basile, F., Poggianti, B. M., et al. 2001, MNRAS, 326, 745
Marchesi, S., Lanzuisi, G., Civano, F., et al. 2016, ApJ, 830, 100
Markwardt, C. B. 2009, Astron. Data Anal. Softw. Syst. XVIII, 411, 251
Masters, D., Faisst, A., & Capak, P. 2016, ApJ, 828, 18
McCracken, H. J., Milvang-Jensen, B., Dunlop, J., et al. 2012, A&A, 544, A156
Mihos, J. C., & Hernquist, L. 1994, ApJ, 431, L9
Mihos, J. C., & Hernquist, L. 1996, ApJ, 464, 641
Mineo, S., Gilfanov, M., Lehmer, B. D., Morrison, G. E., & Sunyaev, R. 2014, MNRAS, 437, 1698
Momcheva, I. G., Brammer, G. B., van Dokkum, P. G., et al. 2016, ApJS, 225, 27
Monreal-Ibero, A., Arribas, S., & Colina, L. 2006, ApJ, 637, 138
Monreal-Ibero, A., Arribas, S., Colina, L., et al. 2010, A&A, 517, A28
Moreno, J., Torrey, P., Ellison, S. L., et al. 2015, MNRAS, 448, 1107
Mullaney, J. R., Alexander, D. M., Goulding, A. D., & Hickox, R. C. 2011, MNRAS, 414, 1082
Murphy, Jr., T. W., Armus, L., Matthews, K., et al. 1996, AJ, 111, 1025
Netzer, H. 2015, ARA&A, 53, 365
Noeske, K. G., Weiner, B. J., Faber, S. M., et al. 2007, ApJ, 660, L43
Pawlik, M. M., Taj Aldeen, L., Wild, V., et al. 2018, MNRAS, 477, 1708
Peng, C. Y., Ho, L. C., Impey, C. D., & Rix, H.-W. 2010, AJ, 139, 2097
Peterson, B. M. 1997, in An Introduction to Active Galactic Nuclei (Cambridge, New York: Cambridge University Press), Phys. Description XVI, 238
Piqueras López, J., Colina, L., Arribas, S., Pereira-Santaella, M., & Alonso-Herrero, A. 2016, A&A, 590, A67
Poggianti, B. M., & Wu, H. 2000, ApJ, 529, 157
Powell, L. C., Bournaud, F., Chapon, D., et al. 2013, The Intriguing Life of Massive Galaxies, 295, 13
Prescott, M. K. M., Impey, C. D., Cool, R. J., & Scoville, N. Z. 2006, ApJ, 644, 100
Puglisi, A., Daddi, E., Renzini, A., et al. 2017, ApJ, 838, L18
Querejeta, M., Eliche-Moral, M. C., Tapia, T., et al. 2015, A&A, 573, A78
Reines, A. E., & Volonteri, M. 2015, ApJ, 813, 82
Rich, J. A., Kewley, L. J., & Dopita, M. A. 2011, ApJ, 734, 87
Rich, J. A., Kewley, L. J., & Dopita, M. A. 2014, ApJ, 781, L12
Rich, J. A., Kewley, L. J., & Dopita, M. A. 2015, ApJS, 221, 28
Rodighiero, G., Daddi, E., Baronchelli, I., et al. 2011, ApJ, 739, L40
Roos, O., Juneau, S., Bournaud, F., & Gabor, J. M. 2015, ApJ, 800, 19
Rujopakarn, W., Nyland, K., Rieke, G. H., et al. 2018, ApJ, 854, L4
Sakamoto, K., Aalto, S., Barcos-Muñoz, L., et al. 2017, ApJ, 849, 14
Sanders, D. B., & Mirabel, I. F. 1996, ARA&A, 34, 749
Sanders, D. B., Soifer, B. T., Elias, J. H., et al. 1988, ApJ, 325, 74
Sargent, M. T., Béthermin, M., Daddi, E., & Elbaz, D. 2012, ApJ, 747, L31
Sargent, M. T., Daddi, E., Béthermin, M., et al. 2014, ApJ, 793, 19
Satyapal, S., Secrest, N. J., Ricci, C., et al. 2017, ApJ, 848, 126
Schreiber, C., Pannella, M., Elbaz, D., et al. 2015, A&A, 575, A74
Scoville, N., Sheth, K., Aussel, H., et al. 2016, ApJ, 820, 83
Silk, J., & Rees, M. J. 1998, A&A, 331, L1
Silverman, J. D., Daddi, E., Rodighiero, G., et al. 2015, ApJ, 812, L23
Silverman, J., Daddi, E., Rujopakarn, W., et al. 2018a, ApJ, 868, 75
Silverman, J., Rujopakarn, W., Daddi, E., et al. 2018b, ApJ, 867, 92
Simcoe, R. A., Burgasser, A. J., Schechter, P. L., et al. 2013, PASP, 125, 270
Smolčić, V., Novak, M., Bondi, M., et al. 2017, A&A, 602, A1
Springel, V., Di Matteo, T., & Hernquist, L. 2005a, ApJ, 620, L79
Springel, V., Di Matteo, T., & Hernquist, L. 2005b, MNRAS, 361, 776
Storey, P. J., & Hummer, D. G. 1988, MNRAS, 231, 1139
Tacconi, L. J., Genzel, R., Smail, I., et al. 2008, ApJ, 680, 246
Tasca, L. A. M., Kneib, J.-P., Iovino, A., et al. 2009, A&A, 503, 379
Toft, S., Smolčić, V., Magnelli, B., et al. 2014, ApJ, 782, 68
Toomre, A., & Toomre, J. 1972, ApJ, 178, 623
van der Wel, A., Franx, M., van Dokkum, P. G., et al. 2014, ApJ, 788, 28
Valentino, F., Daddi, E., Strazzullo, V., et al. 2015, ApJ, 801, 132
Vasudevan, R. V., & Fabian, A. C. 2007, MNRAS, 381, 1235
Veilleux, S., & Osterbrock, D. E. 1987, ApJS, 63, 295
Weston, M. E., McIntosh, D. H., Brodwin, M., et al. 2017, MNRAS, 464, 3882
Wild, V., Heckman, T., & Charlot, S. 2010, MNRAS, 405, 933
Zakamska, N. L., Lampayan, K., Petric, A., et al. 2016, MNRAS, 455, 4191

Appendix A: Additional table

Table A.1. Main physical quantities derived for our *Magellan* sample of starbursts.

ID	z_{spec}	$A_{V,tot}$	$FWHM_{radio}$	$FWHM_{line}$	EW(Hα)	EW(Paβ)	EW(Hδ)	[O III]5007	H$_\beta$	$\log_{10}(L_{bol,AGN})$	$\sigma_{AGN,IR}$	M_{type}
		mag	kpc	km s^{-1}	Å	Å	Å	erg cm^{-2} s^{-1}	erg cm^{-2} s^{-1}	$L_\odot$		
(1)	(2)	(3)	(4)	(5)	(6)	(7)	(8)	(9)	(10)	(11)	(12)	(13)
245158	0.5172	1.9 ± 0.1	14.43 ± 0.24‡	378.1 ± 20.4	91.1 ± 11.3	33.1 ± 3.6	–	–	–	<11.59	<3	S, m*
470239	0.6609	6.2 ± 0.2	7.72 ± 0.26	372.0 ± 6.7	81.1 ± 8.6	24.5 ± 2.4	2.0 ± 1.6	17.7 ± 5.7	22.7 ± 2.3	<10.13	<3	MIII
493881	0.6039	2.7 ± 0.2	8.81 ± 0.26	347.4 ± 3.5	103.2 ± 9.6	44.4 ± 9.6	0.3 ± 1.3	23.1 ± 3.7	59.6 ± 2.6	<11.38	<3	S, m
578239	0.5578	11.7 ± 0.3	1.29 ± 0.24†	514.0 ± 21.5	68.1 ± 6.3	14.8 ± 0.9	−2.6 ± 1.7	50.1 ± 5.9	13.5 ± 2.9	10.94 ± 0.14	3.0	no-HST
635862	0.5508	6.8 ± 0.6	3.43 ± 0.25	971.4 ± 32.6	31.2 ± 5.0	8.0 ± 1.9	−2.5 ± 2.3	15.0 ± 4.0	8.4 ± 1.8	11.22 ± 0.09	4.9	m
685067	0.3735	10.9 ± 0.3	1.06 ± 0.19†	537.2 ± 35.7	12.1 ± 1.8	4.2 ± 0.2	−5.9 ± 0.5	8.8 ± 4.1	–	<10.76	<3	MV
777034	0.6889	12 ± 0.4	1.25 ± 0.26	641.7 ± 25.2	83.8 ± 10.0	20.3 ± 1.8	−4.2 ± 2.3	43.6 ± 4.9	21.7 ± 1.6	12.02 ± 0.04	9.7	MIV*
862072	0.6811	7.8 ± 0.4	2.98 ± 0.30	561.2 ± 15.2	55.8 ± 6.0	15.6 ± 2.1	−7.5 ± 1.2	–	3.7 ± 0.8	<10.91	<3	m, S*
545185	0.5337	22.5 ± 1.0	<0.70	345.6 ± 11.7	33.8 ± 4.8	20.5 ± 2.6	–	–	–	<10.56	<3	MIII*
222723	0.5254	8.1 ± 0.5	3.38 ± 0.23	168.3 ± 3.9	52.4 ± 4.0	13.5 ± 2.6	–	–	–	11.07 ± 0.07	5.8	MV*
223715	0.5174	3.6 ± 0.2	10.95 ± 0.28	237.0 ± 6.3	54.9 ± 6.0	16.3 ± 4.3	–	–	–	<11.47	<3	m, S*
249989	0.6656	4.4 ± 0.2	5.32 ± 0.30	261.2 ± 10.1	206.3 ± 26.0	38.5 ± 6.8	–	–	–	10.66 ± 0.13	3.3	MIII*
326384	0.8042	9.8 ± 1.1	2.78 ± 0.29	321.7 ± 7.8	174.2 ± 23.7	36.8 ± 11.4	–	–	–	<10.55	<3	S*
345018	0.7521	23.7 ± 3.4	<0.86	286.4 ± 11.9	82.3 ± 8.2	18.9 ± 5.5	−7.2 ± 1.1	16.7 ± 4.4	12.0 ± 1.8	<10.81	<3	m, S*
412250	0.8397	6.7 ± 0.6	8.84 ± 0.31‡	299.1 ± 6.5	244.7 ± 21.9	18.2 ± 5.4	–	–	–	11.14 ± 0.09	4.9	MIII*
466112	0.7607	5.2 ± 0.3	2.64 ± 0.28	298.1 ± 3.7	229.1 ± 17.6	57.8 ± 9.6	−3.9 ± 1.1	34.0 ± 4.0	9.0 ± 1.6	11.42 ± 0.06	7.3	MIII*
472775	0.6604	18.0 ± 1.3	<1.05	498.3 ± 27.9	65.7 ± 6.3	17.3 ± 2.7	–	–	–	<10.52	<3	MIII
519651	0.6709	8.8 ± 0.5	10.94 ± 0.26‡	191.1 ± 3.6	86.2 ± 7.4	32.0 ± 5.0	−2.9 ± 1.3	38.9 ± 7.1	27.3 ± 1.8	11.37 ± 0.06	7.3	MIV
668738	0.7481	6.7 ± 0.2	3.68 ± 0.28	484.2 ± 22.3	92.0 ± 13.3	24.0 ± 3.4	–	28.0 ± 4.4	11.3 ± 3.0	10.87 ± 0.13	3.3	MIII*
894779	0.5506	4.5 ± 0.2	2.41 ± 0.26	132.0 ± 10.5	140.8 ± 21.4	35.4 ± 6.2	–	–	–	10.66 ± 0.07	5.8	MIV*
911723	0.6606	9.1 ± 0.6	<0.88	440.8 ± 10.3	60.5 ± 6.8	23.9 ± 4.5	–	–	–	10.73 ± 0.12	3.7	E*
303305	0.5306	>13.9	<0.71	877.7 ± 85.1	11.0 ± 2.4	–	−9.3 ± 2.6	11.6 ± 1.3	–	<11.30	<3	E
500929	0.9498	>6.2	2.99 ± 0.32	547.6 ± 48.0	42.3 ± 10.8	–	–	–	–	<11.26	<3	MIII*
893857	0.8512	>11	<0.93	655.1 ± 29.6	39.6 ± 2.5	–	–	–	-	<11.08	<3	E*
232171	0.5251	>17.6	1.62 ± 0.23	374.4 ± 33.8	11.3 ± 3.3	–	–	–	–	11.54 ± 0.04	9.7	MII*

Notes. Table columns: (1) identification number from Laigle et al. (2016), as in Calabrò et al. (2018); (2) spectroscopic redshift inferred from *Magellan* spectra; (3) total attenuation $A_{V,tot}$ toward the center in a mixed model geometry, calculated in Calabrò et al. (2018) and explained in Section 2 ; (4) FWHM size in radio 3 GHz band (from VLA-COSMOS); †: fit with a single 2D Gaussian but with fixed axis ratio and position angle (1 and 0); ‡: fit with a Double 2D Gaussian, we give here the total FWHM (average of single component sizes + separation between the two); we put a 3σ upper limit for unresolved sources, while the remaining starbursts are fit with a single 2D Gaussian and free parameters; (5) line velocity width of emission lines, derived from fitting the *Magellan* spectra with MPFIT (for double Gaussians, this quantity is the sum of the single Gaussian FWHM and the separation in velocity between the two peaks); (6,7,8) observed equivalent width of Hα,Paβ and Hδ, the latter coming from zCOSMOS or SDSS optical spectra; (9,10) fluxes of [O III]λ5007 Å and Hβ (in units of 10^{-17}) inferred from optical spectra. Hβ fluxes have been corrected for underlying absorption assuming EW_{abs} = 5 Å as determined from Bruzual & Charlot (2003) synthetic stellar spectra; (11) bolometric AGN luminosity derived as $1.4 \times L_{AGN,IR}$, the latter being the AGN luminosity in the infrared inferred from SED fitting (see Liu et al. 2018 and Jin et al. 2018 for the methodology); (12) significance of mid-IR dusty-torus detection from SED fitting (<3 means that it is not detected); (13) morphological type following the visual criteria of Kartaltepe et al. (2010) (objects with a $*$ have been already classified in the same paper). We remind that the coordinates of our targets, their stellar masses, SFRs and Hα (Paβ) flux measurements can be retrieved from Calabrò et al. (2018).

Appendix B: Additional plots

We display in Fig. B.1 two different versions of the BPT diagram, involving the [S II]6717+6731/Hα line ratio (top panel), and the [O III]5007/[O II]3727+3729 ratio (bottom panel), color coded according to the total velocity width of the lines ($\sigma_{\rm line}$).

In Fig. B.2 we show the SED fitting of all the 25 starbursts in our sample, performed as explained in Sect. 2.1. The majority of our galaxies were fit with a GN20 template from Magdis et al. (2012). However, for six objects (ID 245158, 223715, 470239, 493881, 635862 and 862072), a MS template gave a better χ^2 than the GN20 SED. This is due to the fact that this particular template is not universal for all starbursts, and the true SB SED can have multiple dust temperatures.

Finally, we display in Fig. B.3 the correlations among Hδ, Hβ, Hα and Paβ equivalent widths.

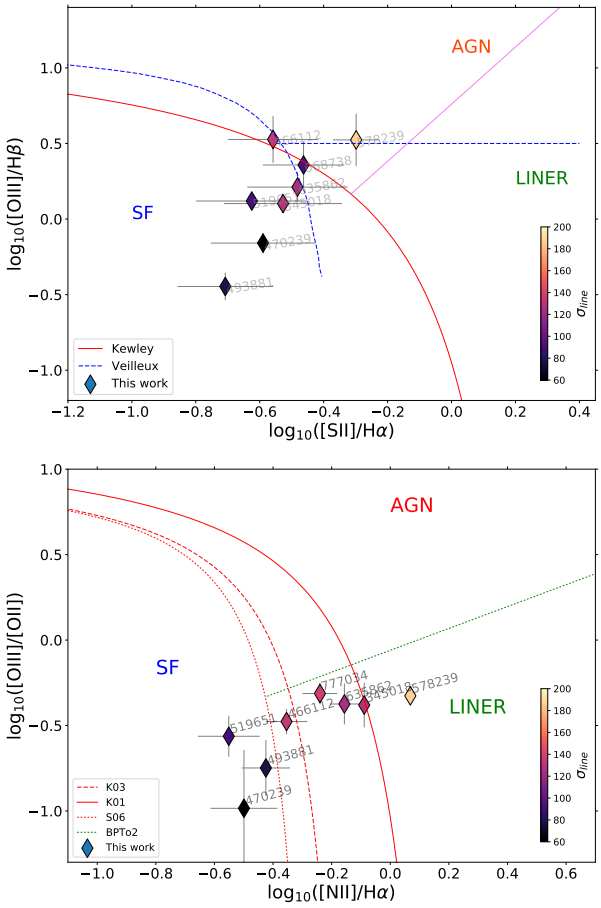

Fig. B.1. Diagram of [O III]/Hβ compared to [S II]6717+6731/Hα (*top*) and [O III]5007/[O II]3727+3729 vs. [N II]6583/Hα (*bottom*) for 8 galaxies of our sample with optical spectra available and contemporary detection of [O III] and one between [S II]+Hβ or [O II]. The two diagrams are also called the S2 and the O2 BPT diagrams, respectively. As in the classical BPT diagram in Fig. 5, they show that our starbursts have different line excitation properties, and those with higher line velocity widths are generally shifted toward the AGN and LINER regions, according to empirical separation lines derived in the local ($z \lesssim 0.3$) Universe.

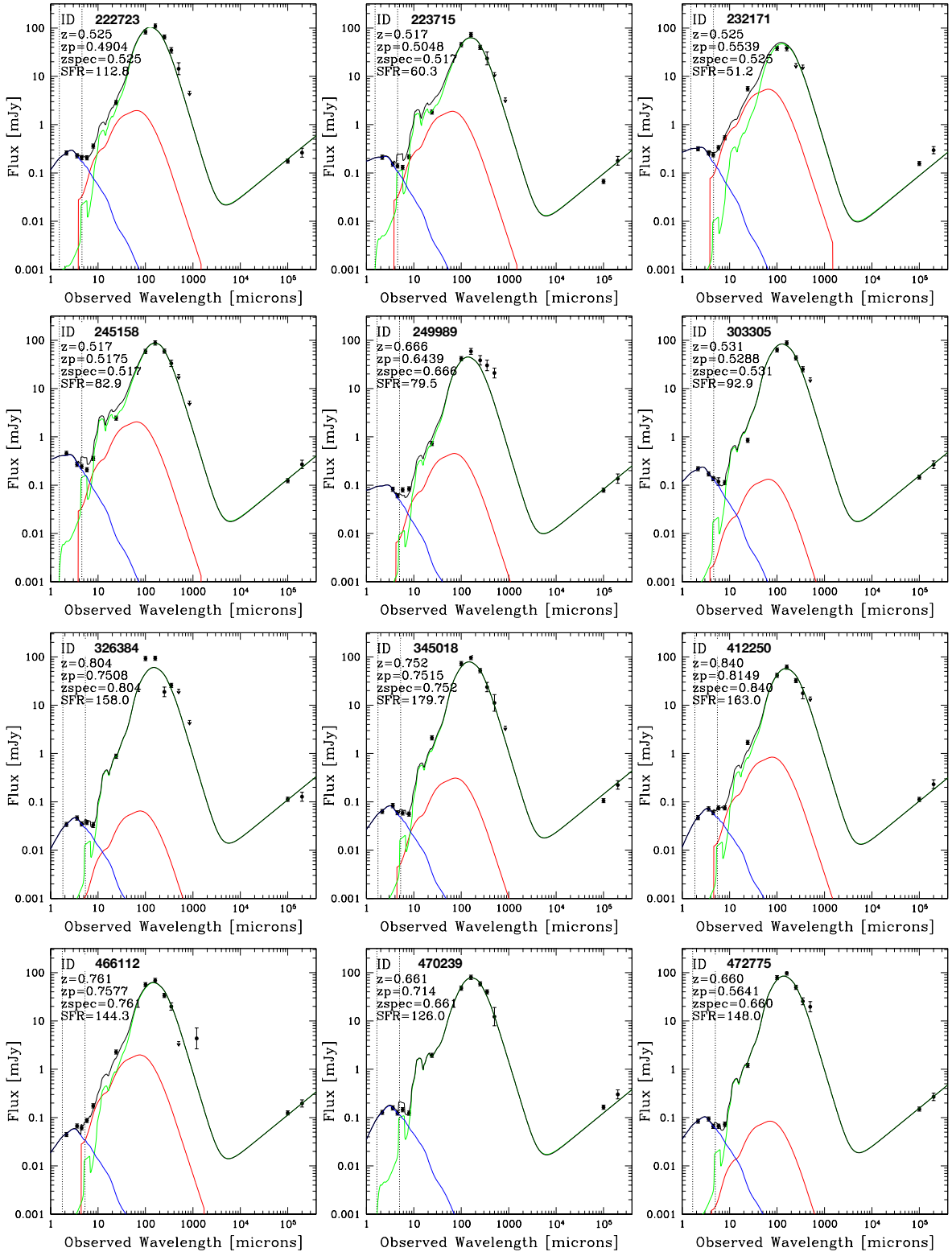

Fig. B.2. SED fitting of the 25 starburst galaxies studied in this paper, presented in numerical order. The SED fitting procedure is described in Sect. 2.1. Blue and red curves show the stellar component (Bruzual & Charlot 2003) and the AGN torus emission (Mullaney et al. 2011), while the dust continuum emission is shown in green (Magdis et al. 2012). Downward arrows show the 2σ upper limit photometry at given wavelength. In each panel, $z_{\rm spec}$ is the spectroscopic redshift from our *Magellan* spectra, $z_{\rm phot}$ is the photometric redshift from Laigle et al. (2016), z is the output redshift of the best-fit SED (which in our cases was fixed to the spectroscopic value), and SFR is the best-fit infrared star-formation rate. The vertical dotted lines indicates the optimized range for fitting the stellar SED only (in order to avoid contamination from AGN torus and dust emission). The rightmost line also indicates the starting wavelength for fitting the AGN + dust SED in our paper. We remind the reader that the radio photometry (at 1.4 and 3 GHz) was not used in the fit, as explained in Sect. 2.1.

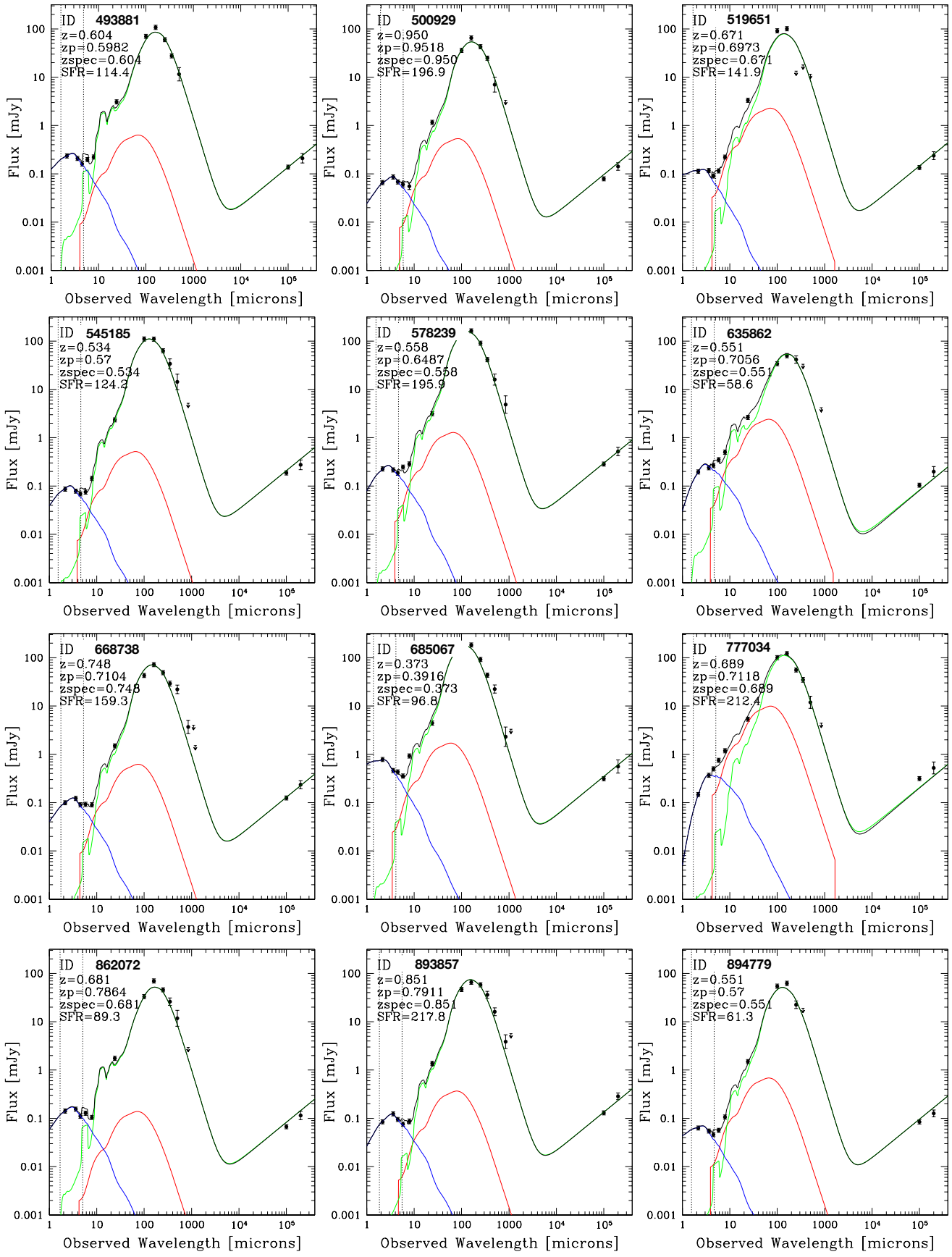

Fig. B.2. continued.

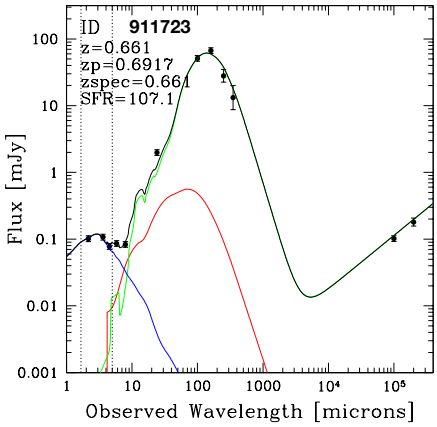

Fig. B.2. continued.

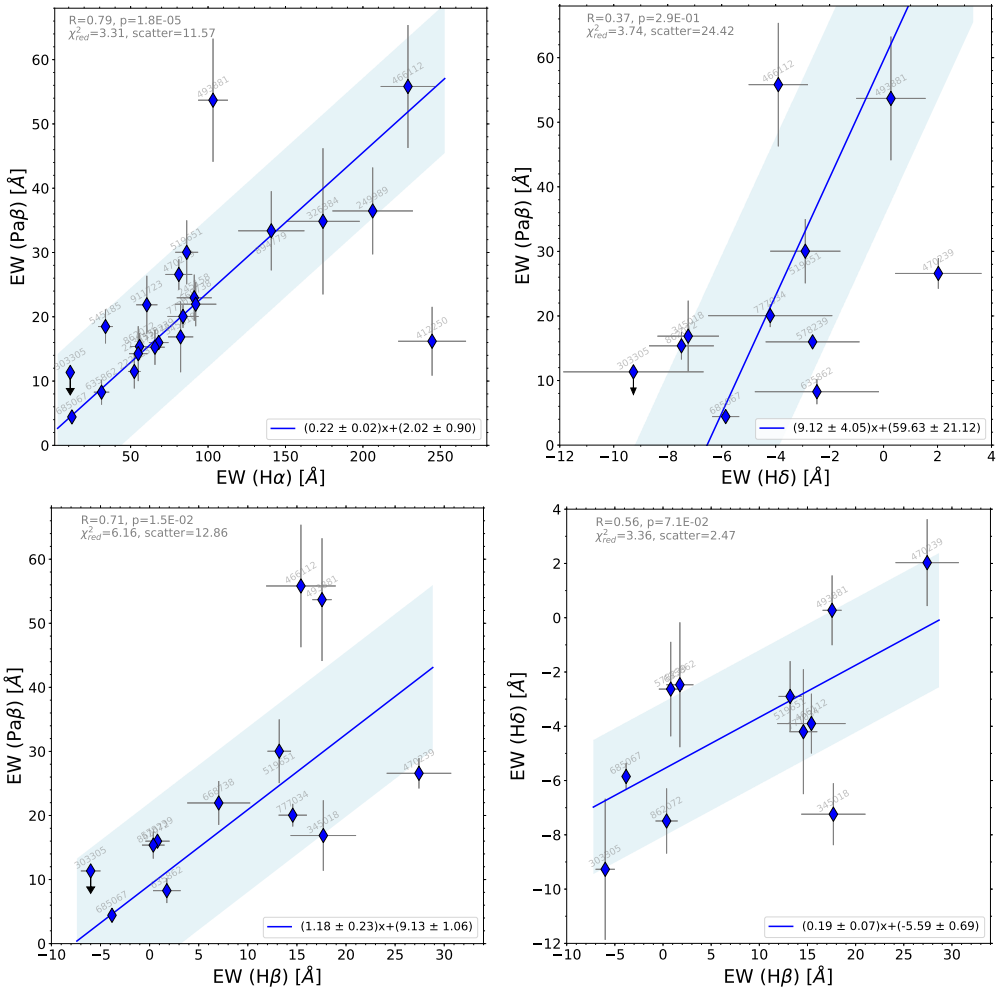

Fig. B.3. Comparison between the EWs of Hδ, Hβ, Hα and Paβ lines. The blue lines represent the best-fit linear relation, while the blue shaded areas indicate the $\pm 1\sigma$ dispersion of the galaxies around the best-fit line. We display in top-left corner of each panel the Spearman correlation coefficient "R" and corresponding "p"-value, the residual χ^2 of the correlation ("$\chi^2_{\rm red}$") and the 1σ scatter around the best-fit line, whose equation (comprising 1σ errors on the best-fit coefficients) is shown in the bottom-right corner. In the four diagrams, all the points with available measurements (excluding upper limits) were used in the fit.

Merger induced clump formation in distant infrared luminous starburst galaxies

Antonello Calabrò[1], Emanuele Daddi[1], Jérémy Fensch[2], Frédéric Bournaud[1], Anna Cibinel[3], Annagrazia Puglisi[1], Shuowen Jin[4,5], and Ivan Delvecchio[1]

[1] CEA, IRFU, DAp, AIM, Université Paris-Saclay, Université de Paris, CNRS, F-91191 Gif-sur-Yvette, France (antonello.calabro@cea.fr)
[2] European Southern Observatory, Karl Schwarzschild Straße 2, 85748 Garching, Germany
[3] Astronomy Centre, Department of Physics and Astronomy, University of Sussex, Brighton, BN1 9QH, UK
[4] Instituto de Astrofísica de Canarias (IAC), E-38205 La Laguna, Tenerife, Spain
[5] Universidad de La Laguna, Dpto. Astrofísica, E-38206 La Laguna, Tenerife, Spain

ABSTRACT

While the formation of stellar clumps in distant galaxies is usually attributed to gravitational violent disk instabilities, we show here that major mergers also represent a competitive mechanism to form bright clumps. Using $\sim 0.1''$ resolution ACS F814W images in the entire COSMOS field, we measure the fraction of clumpy emission in 109 main sequence (MS) and 79 Herschel-detected starbursts (off-MS) galaxies at $0.5 < z < 0.9$, representative of normal versus merger induced star-forming activity, respectively. We additionally identify merger samples from visual inspection and from Gini-M20 morphological parameters. Regardless of the merger criteria adopted, the clumpiness distribution of merging systems is different from that of normal isolated disks at > 99.5% confidence level, with the first reaching higher clumpiness values, up to 20% of the total galaxy emission. We confirm the merger induced clumpiness enhancement with novel hydrodynamical simulations of colliding galaxies with gas fractions typical of $z \sim 0.7$. Multi-wavelength images of 3 starbursts in the CANDELS field support the young nature of clumps, which are likely merger products rather than older pre-existing structures. Finally, for a subset of 19 starbursts with existing near-IR rest frame spectroscopy, we find that the clumpiness is mildly anti-correlated with the merger phase, decreasing towards final coalescence. Our result can explain recent ALMA detections of clumps in hyperluminous high-z starbursts, while normal objects are smooth. This work raises a question on the role of mergers on the origin of clumps in high redshift galaxies in general.

Key words. galaxies: evolution — galaxies: formation — galaxies: interaction — galaxies: starburst — galaxies: star formation — galaxies: structure — galaxies: high-redshift

1. Introduction

While local galaxies have well defined morphological types described by the so called Hubble sequence, higher redshift systems are more irregular and clumpy, which makes increasingly more difficult to associate to them one of the Hubble classes. At redshift ~ 0.6 for example, the fraction of irregular systems increases by 40% compared to the local Universe (Delgado-Serrano et al. 2010).

The clumpy substructures detected in the average star-forming galaxy population at intermediate and high redshift represent aggregations of relatively young stars (depending on the observed spectral window) arising from a smoother and fainter disk luminosity profile. They have stellar masses ranging 10^7-10^9 $M_\odot$ and sizes of approximately 100-1000 pc (Elmegreen et al. 2005), and are typically identified through highly resolved observations in the rest-frame UV (e.g. Chapman et al. 2003; Puech 2010), optical (e.g. Murata et al. 2014) and near-IR (Förster Schreiber et al. 2006, 2009).

Clumpy galaxies at redshift > 0.5 with stellar masses of 10^{10}-10^{11} $M_\odot$ are thought to be the progenitors of present-day spirals (Elmegreen et al. 2005; Bournaud et al. 2007; Ceverino et al. 2010; Elmegreen et al. 2013). Moreover, if the clumps are sufficiently long lived, they can migrate toward the center and contribute to the formation of a central bar (Immeli et al. 2004b; Sheth et al. 2012; Kraljic et al. 2012) or to the stellar bulge growth (Noguchi 1999; Elmegreen et al. 2008; Bournaud 2016), contributing to stabilize the disks (e.g., Ceverino et al. 2010) and to give the final imprint to the morphological shapes encoded in the Hubble sequence. According to Kraljic et al. (2012), today Milky-way like spirals acquired their disk morphology at $z \sim 0.8$-1, and they completely stabilized at redshift 0.5 or lower (Cacciato et al. 2012). Alternatively, clumps in distant galaxies may lead to the formation of super-star-clusters and globular clusters (Shapiro et al. 2010).

The formation and origin of clumps at all redshifts is not completely assessed, as it can be ascribed to different triggering mechanisms. Usually, in clumpy galaxies at $z > 1$, they are thought to be triggered by violent disk instabilities in highly gas-rich, dense and turbulent disks, and they are continuously fed by cold gas streams from the circumgalactic medium (CGM) and the cosmic web (Genzel et al. 2008; Dekel et al. 2009). These can sustain the high gas fractions of the order of ~ 0.4-0.5 that are typically found in high redshift galaxies (Daddi et al. 2010; Tacconi et al. 2010; Rodrigues et al. 2012).

Below $z \sim 1$, cosmological simulations predict a strong cut-off of cold-flow accretion into galaxies (Kereš et al. 2005; Dekel & Birnboim 2006), which might indirectly result in the decrease of the average SFR density in the Universe (Madau & Dickinson 2014) and of the gas content in galaxies down to $f_{gas} \sim 0.2$-0.4.

This strong suppression of gas fraction may then affect the physical properties and abundance of clumps, and could require alternative mechanisms of formation and evolution. For example, smooth accretion of gas from tidally disrupted companions or stripped satellites in cluster environments have been suggested to feed some low-mass, local analogs of high-z clumpy galaxies (Garland et al. 2015). Instead, a more common additional channel for producing clumps at any host stellar mass and epoch is represented by major mergers, as proposed in Somerville (2001); Lotz et al. (2004); Di Matteo et al. (2008). However, at intermediate redshifts, there is no general consensus yet about the role of mergers and their relative importance.

From the observational point of view, Puech (2010) analyzed UV rest-frame clumps in 11 clumpy galaxies at $z \sim 0.6$. He claimed that interactions may be the dominant driver for clumps formation at that epoch, because of the complex kinematic structure observed for half of them. In contrast, Guo et al. (2015) and Murata et al. (2014) argue that major mergers have a negligible role for explaining the fraction of clumpy galaxies at all masses at $z \lesssim 1.5$, suggesting instead a prevalent role of violent disk instabilities or minor mergers. In the same direction, Bournaud et al. (2012) found that clumpy low-mass star-forming galaxies at $z \sim 0.7$ are similar to gas-rich turbulent disks observed at higher redshifts, suggesting that gravitational instabilities are the most important cause of gas fragmentation and clumps formation.

However, even with different sample selections, clumps identification methods and observed photometric band, these studies are interested on the main driver of clumpy galaxies among the whole star-forming galaxies population. Since they do not perform a merger identification, they neither analyze the implications that mergers have on the formation of clumps, nor they measure quantitatively the clumpiness parameter (i.e., fraction of light in clumps) in comparison to normal disks. Puech (2010) show a possible connection between mergers and UV clumps, but many of their substructures are not detected anymore in the optical, thus cannot be directly compared with our sample. Morevoer, their subset is not representative of the whole merger population at intermediate redshifts, given the strict requirements of their selection criteria.

The connection between mergers and clumps is not clear also in hydrodynamical simulations : while some studies suggest that merger events can trigger turbulent modes in the ISM that lead to rapid gas fragmentation and clump formation (Teyssier et al. 2010; Bournaud et al. 2011; Renaud et al. 2014) , other morphological studies on simulated galaxies do not see any enhancement at all of clumpy emission during the merger (e.g., Nevin et al. 2019). The reason of these discrepancies resides in the different resolutions adopted, in feedback and turbulence modeling and in the specific initial conditions considered, such as the merger geometry, the stellar mass ratio and the initial gas fraction f_{gas} of colliding galaxies (e.g., Di Matteo et al. 2008; Governato et al. 2010; Fensch et al. 2017). Most of the simulations focus on local or high redshift galaxies, thus they have lower or higher gas fractions than the typical values at intermediate redshifts. The few simulations with similar f_{gas} values (Cox et al. 2006; Di Matteo et al. 2008) did not allow the gas to cool down below 10^4 K, which is necessary to study the evolution of the gas structure during the interactions (Teyssier et al. 2010; Bournaud et al. 2011). In other cases, the resolutions are too low for the sub-kpc spatial scales we want to investigate for detecting clumpy structures (Sparre & Springel 2016; Rodriguez-Gomez et al. 2016).

Additionally, while mergers produce very dense and compact starbursting cores, it is yet unclear what fraction of star-formation occurs in off-nuclear regions, possibly in the form of clumps, and what is the resulting mass and size distribution of these structures, which have been studied only in isolated galaxies.

Given these uncertainties, more observations and constraints are needed to clarify the role of mergers on clump formation at intermediate redshift, and put constraints on feedback models in simulations of galaxy collisions. In the local Universe, a deep connection has been established between ultra-luminous infrared galaxies (ULIRGs) and mergers (Sanders & Mirabel 1996; Clements et al. 1996). This connection has been extended at higher redshifts to starburst galaxies, defined by their SFR excess (typically a factor of 4) with respect to the star-forming main sequence (Noeske et al. 2007; Daddi et al. 2007; Elbaz et al. 2007). According to Calabrò et al. (2018), starbursts at $0.5 < z < 0.9$ are mostly merger triggered, as revealed by their morphology or by the presence of extremely obscured starbursting cores. In addition, Cibinel et al. (2019) show that the merger fraction above the main sequence is of $\sim 80\%$. These criteria offer thus a powerful tool to select merger systems beyond the local Universe, complementary to a visual inspection and to non parametric approaches (Conselice et al. 2003; Lotz et al. 2004), which could be highly incomplete. This tool is also better than looking at kinematics signatures: Law et al. (2009) show indeed that clear merger candidates at $z > 1$ can also have regular rotation patterns typical of disk galaxies.

The COSMOS field allows to select the largest (so far) statistical sample of starbursts with plenty of ancillary data, including an almost complete imaging coverage in at least one HST band, photometric data ranging from UV to far-IR and sub-mm (Laigle et al. 2016; Jin et al. 2018), and IR-based SFRs (Jin et al. 2018). In this paper, we exploit high resolution (0.095″) HST/ACS F814W public images over the whole $\simeq 2$ deg^2 COSMOS field to build a large sample of starburst galaxies and investigate with unprecedented statistics the role of mergers on the formation of clumps at intermediate redshifts. To this aim, we compare the starbursts to a control sample of randomly selected normal star-forming main sequence galaxies at the same cosmic epoch, which are usually taken as representative of isolated, relatively undisturbed disks.

At our redshifts, the HST images probe the optical rest-frame spectral range that, compared to UV emission (dominated by young massive O-B stars), is more sensitive to the light of intermediate age (A to G type) stars. Given the longer rest-frame wavelengths covered, we can study the clumpy morphology in a way which is less affected by dust attenuation. This is particularly important in infrared luminous mergers, typically highly obscured, where their UV emission may not reflect the true stellar distribution.

We also present a set of numerical simulations of merger interactions between typical z~0.7 galaxies, which could help to interpret our observational results. To this aim, these simulations consider the proper gas fractions for this cosmic epoch ($f_{gas} \simeq 0.3$), while simultaneously allowing the gas component to cool below 10^4 K and to be resolved on small spatial scales of 6 pc, necessary to study its evolution during the merger.

The paper is organized as follows. In Section 2 we describe our selection of starburst galaxies and of a control sample of main sequence systems in COSMOS field. We also present their HST F814W images, from which we derive basic morphological properties and an estimation of the clumpiness parameter. After showing our observational results in Section 3, we describe in Section 4 the hydrodynamical simulations used to verify the connection between mergers and clumps at intermedi-

ate redshift. Then we discuss possible physical interpretations of our findings, and we show the summary and conclusions in Section 5. We adopt the Chabrier (2003) initial mass function, AB magnitudes, and standard cosmology (H_0 = 70 kms^{-1}Mpc^{-1}, Ω_m = 0.3, Ω_Λ = 0.7).

2. Methodology

In this section we describe our sample selection and the derivation of the morphological properties from single-band HST images, also quantifying, through the clumpiness parameter, the contribution of off-nuclear clumps to the galaxy emission.

2.1. Starbursts and main sequence galaxies selection

Starbursts and main sequence galaxies at low to intermediate redshifts are associated, respectively, to a highly efficient star-formation mode and gas consumption induced by major merger events, and to a quasi-steady star-formation activity with much longer gas depletion timescales of ∼ 1-2 Gyr (Sargent et al. 2014). In Calabrò et al. (2018), we showed that luminous-infrared starbursts at $0.5 < z < 0.9$ are mostly major mergers, in analogy with local ULIRGs, hence they represent the perfect type of galaxies to test the effects of mergers on the formation and evolution of clumps. At the same time, main sequence isolated systems provide a control sample for this analysis.

All the galaxies in this work were selected from the IR+(sub)mm catalog of Jin et al. (2018), which includes ∼ 15k star-forming galaxies in COSMOS field in the same redshift interval, with deblended photometry ranging from Spitzer 24μm to VLA 1.4 GHz bands. The stellar masses M_* of the sources are computed by Laigle et al. (2016) at the photometric redshifts by fitting 16 bands from near-ultraviolet to mid-infrared. As explained in Calabrò et al. (2018), using the spectroscopic redshift (when available) does not affect significantly the stellar masses, as they are in general agreement within the uncertainties of 0.1 dex reported by the same authors.

We adopted the infrared SFRs (= SFR_{IR}) derived by Jin et al. (2018) by fitting multi-wavelength broad-band photometric data from IRAC to radio VLA bands. Four components were used to determine the best-fit SED: a Bruzual & Charlot (2003) stellar model (at different ages and metallicities, constant SFH, Chabrier IMF and Calzetti et al. (2000) attenuation law), a mid-infrared template for AGNs (Mullaney et al. 2011), and Draine & Li (2007) dust emission models. When available, the spectroscopic redshift was fixed in the fit. For main sequence galaxies that are undetected in the 100μm - 850μm bands (including Herschel and SCUBA2 photometry) at $S/N_{IR} < 5$, the SFRs were computed from their 24μm fluxes as explained in Jin et al. (2018). Finally, we calculated the total SFRs as $SFR_{TOT}=SFR_{IR}+SFR_{UV,unobscured}$, where the UV unobscured SFRs were inferred from their Laigle et al. (2016) u-band total magnitudes, as shown in Calabrò et al. (2018).

Following the procedure described in Calabrò et al. (2018, 2019), we compared the $M_\star$ and SFR of our galaxies to the star-forming main-sequence of Schreiber et al. (2015) (which was shown to agree well with our data) in order to derive the distance from the main sequence $dist_{MS} = \log_{10}(SFR/SFR_{MS})$. Finally, starbursts are taken above the typical threshold of $dist_{MS} > 0.6$ (i.e., above a factor of four), following Rodighiero et al. (2011).

We required also the redshift, either spectroscopic or photometric (from Jin et al. 2018), to be in the range between 0.5 and 0.9. As mentioned in the Introduction, we want to focus on the intermediate redshift regime to build-up on the growing understanding generated by our previous works (Calabrò et al. 2018, 2019). Indeed, it would allow to follow-up some of the clumps with near-infrared integral-field spectrographs to detect Hα and Paβ within Y and K bands. In addition, it is in this cosmic epoch that we may have the final imprint on the morphology of present-day galaxies.

As an additional constraint for our sample, we imposed the stellar mass M_* to be greater than 10^{10} $M_\odot$, since above this limit and up to z = 0.9, all SBs would be Herschel-detected at $S/N_{IR} > 5$ (see Figure 13 in Jin et al. (2018)), and we have a mass-complete sample of normal star-forming galaxies down to a factor of three below the main sequence.

These three criteria yielded a subset of 118 Herschel-detected (S/N_{IR}) starbursts, from which we discarded two residual quasar-like objects and additional 20 galaxies without HST-ACS coverage, leaving a sample of 96 starbursts in total.

Afterwards, we selected a control sample of 145 MS galaxies with HST F814W images, in order to have a larger statistics and avoid that additional sample cuts in our analysis would produce a lower number of MS systems than SBs. Our normal star-forming galaxies were randomly selected within $\Delta dist_{MS}$ of ±0.47 dex (a factor of three) from the MS, in the same redshift and stellar mass range defined for SBs, and requiring that they are star-forming according to the NUV-R/R-J diagram to avoid quiescent galaxies (Laigle et al. 2016).

Even though this latter subset is representative of secularly evolving star-forming disks, we remember that it may contain also a fraction of ongoing mergers. Indeed, at our redshifts, the merger fraction is expected to be higher than the relative number of starbursts (Schreiber et al. 2015), both because of SFR fluctuations during the merger process itself (Di Matteo et al. 2008) and because it might be more difficult for mergers to trigger starbursts as in the local Universe (Fensch et al. 2017). We will discuss about several methods to identify these objects in Section 2.3.

2.2. HST images and morphology

In order to study the morphology and the presence of clumpy structures in our galaxies, we need high resolution images that can probe spatial scales significantly below 1 kpc. For the sample analyzed in this paper, we adopted F814W ACS images (Koekemoer et al. 2007), which we retrieved from the COSMOS web service (http://irsa.ipac.caltech.edu/data/COSMOS/). They represent so far the deepest and highest resolution publicly available data, with ∼ 2000 s time integration, a magnitude limit of 25.61 mag for extended sources (assuming a circular aperture radius of 0.3″) and a median FWHM resolution of ∼ 0.095″ (with a pixel scale of 0.03″/pixel). At our redshift, this means that we are able to distinguish substructures with separations of at least ≃ 600 pc at z = 0.5 to ≃ 800 pc at z = 0.9, and thus detect clumps on this size scale (FWHM), which is enough for those typically found in high-redshift clumpy galaxies. We remark that, in all our redshift range, the clumps are observed in their optical rest-frame emission, which is more sensitive to their stellar mass than to their current, unobscured SFR. Compared to UV rest-frame observations, our images have also the advantage to be less affected by dust attenuation effects, which in mergers systems can be very high and not spatially homogeneous.

In the first step of our analysis, we created a segmentation map of the HST F814W (15″ × 15″) cutouts using the python

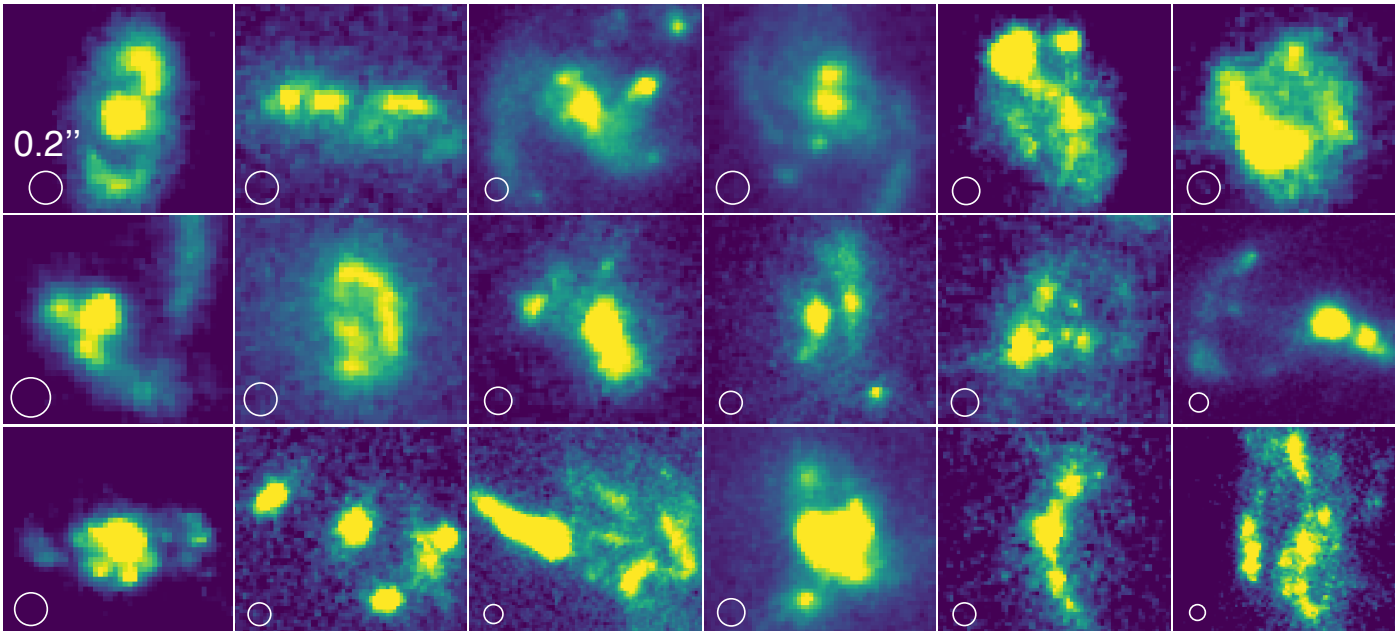

Fig. 1. Representative sample of clumpy starbursts at $0.5 < z < 0.9$ in COSMOS field, observed by HST-ACS in the F814W band. The white circles in the bottom left corner have a diameter of 0.2″.

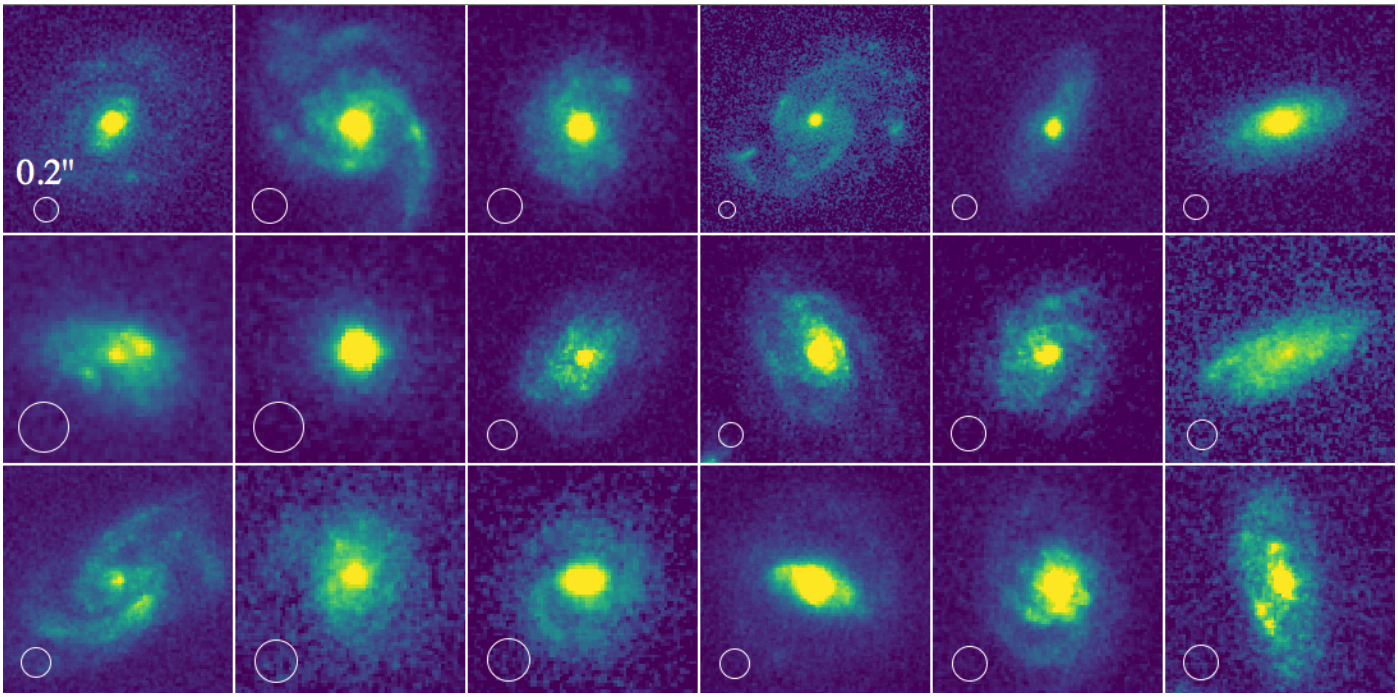

Fig. 2. Representative sample of typical (randomly selected) main sequence disks at $0.5 < z < 0.9$ in COSMOS field. The image details are the same of Fig. 1.

package PHOTUTILS[1]. In brief, it identifies the sources as groups of connected pixels with a flux higher than a constant threshold. The latter value is calculated at a given S/N per pixel above the background, which is estimated from the entire cutout using a sigma-clipped statistics. We found that a S/N threshold of 1.3 works well in all the cases to detect the galaxies contours, including the low surface-brightness external regions and wings, and separating different galaxies in the same cutout region. The few cases where two close-in-sky but spatially unrelated galaxies (i.e., located at completely different redshifts) are selected as the same source in the segmentation map, we applied the *deblending* function inside PHOTUTILS, keeping only the central object. The location of the final source was saved into a mask M_0: we assigned a value of 1 to all the pixels inside the galaxy contours defined in the segmentation map, and 0 otherwise.

Afterwards, we run the galaxy morphology tool STATMORPH (Rodriguez-Gomez et al. 2019) to derive the elongation of the galaxy contained in the previously selected region, which crucially affects the detectability of clumpy structures. E is defined as $\frac{A}{B}$, where A and B are, as in SExtractor, the maximum and

[1] https://doi.org/10.5281/zenodo.2533376

minimum *rms* dispersion of the object profile along all directions. Equivalently, they can be considered as the semi-major and semi-minor axis lengths of the ellipse that best describes the galaxy shape.

2.3. Morphological merger classification

In addition to the elongation, better characterizing the morphological properties is essential to identify which galaxies in the main sequence could be possibly mergers. To this aim, we pursued a twofold approach, one relying on non-parametric quantitative estimators, and the second based on a visual analysis.

In the first approach, the Gini and M20 coefficients, defined by Lotz et al. (2004), are usually adopted for selecting possible mergers and interacting systems. Gini (G) measures the degree of inequality of the flux distribution among the pixels in the image, and is higher for galaxies with bright clumps and nuclei. For our HST cutouts, we computed G with the following formula:

$$G = \frac{1}{\bar{X}n(n-1)} \sum_{i}^{n} (2i - n - 1)X_i, \quad (1)$$

where n is the number of pixels of the galaxy (defined by the mask M_0), X_i are the counts in each pixel i sorted in increasing order and $\bar{X}$ is the mean pixel value (Glasser 1962).

On the other hand, M20 is defined as the normalized second order moment of the brightest 20% pixels of the galaxy:

$$M_{20} = log_{10}\left(\frac{\sum_i M_i}{M_{tot}}\right), \text{ with } \sum_i f_i < 0.2 f_{tot}$$
$$\text{with } M_{tot} = \sum_{i}^{n} M_i = \sum_{i}^{n} f_i[(x_i - x_c)^2 + (y_i - y_c)^2] \quad (2)$$

In the above formula, x_i and y_i are the pixel coordinates, and x_c and y_c represent the galaxy's center, such that M_{tot} is minimized. f_i are the counts in each pixel, while f_{tot} symbolizes the total counts in the galaxy pixels identified by segmentation map derived before. In other words, this quantity measures the relative concentration of light around the position that minimizes M_{20} itself. It is higher in the presence of bright bars, spiral arms, tidal tails, off-center clumps, and it is very sensitive, for example, to multiple nuclei. Both parameters were calculated with python code routines by applying the equations 1 and 2.

The typical uncertainties of Gini and M_{20} estimations are of 0.02 and 0.1, respectively. They were estimated by Lotz et al. (2008) from ACS F814W galaxy images at our same redshifts in the EGS field, at a depth comparable with our analysis ($\sim$ 2000 s of integration). In addition, the ULIRGs in their sample, to which they apply the classification, have $I_{F814W} < 23$ mag, thus largely applicable to our case.

Since Gini and M_{20} are very sensitive to typical merger features, increasing when these signatures become stronger, we can use both to identify a subset of galaxies with merger morphologies. Following the classification criteria of Lotz et al. (2008), we defined a 'merginess' parameter m as:

$$merginess = Gini - 0.14 \times M_{20} + 0.33, \quad (3)$$

where the coefficients were calibrated by Lotz et al. (2008) and do not vary with redshift (up to $z \simeq 1.2$). This quantity represents the difference between the estimated Gini and that required to classify the system as a merger. Therefore, according to this criterion, galaxies with $m > 0$ will be identified as morphological mergers throughout the paper. Among the MS population, 15 objects satisfy this condition. The exact *merginess* values of all the galaxies are listed in Table A.1 in the Appendix.

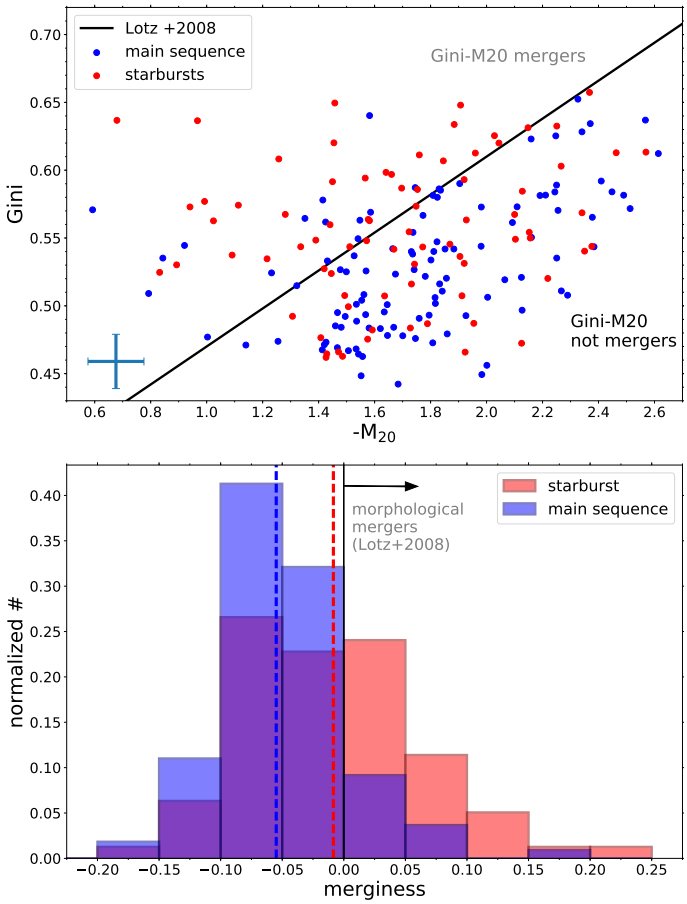

Fig. 3. *Top:* Gini-M_{20} diagram for the final sample of starburst and main seuqnece galaxies analyzed in this work (in red and blue, respectively). Galaxies above the black continuous lines are morphological mergers, according to Lotz et al. (2008). The typical uncertainties of Gini and M_{20} are shown by the representative error bars in the lower left corner. *Bottom:* Histogram distribution (for SBs and MS) of the merginess parameter, defined as the difference between the measured Gini coefficient and that required to classify the galaxy as a morphological merger. It shows that the majority of galaxies classified as mergers according to this criterion are also starbursts.

We remark that for our sample we cannot apply the morphological analysis performed by Cibinel et al. (2019) on resolved stellar mass maps, since it requires multi-wavelength images. However, our single band optical rest-frame images are sensitive to the stellar mass of the system more than UV rest-frame observations, and this dataset represents so far the best compromise if we need high spatial resolution information.

We show in Fig. 3-*top* the distribution of the Gini and M_{20} coefficients for our galaxies, and highlight with a black continuous line the merger threshold of Lotz et al. (2008). In the bottom panel of Fig. 3 we display instead the histogram of the merginess parameters, separately for main sequence and starburst galaxies. These two populations have overall a different distribution of m and different medians, where starbursts tend to have a higher merginess compared to normal star-forming galaxies.

We notice that the threshold criterion of Lotz et al. (2008) defines a merginess parameter space where SBs start to dominate in number over the MS population. In our case, 76% of the morphological merger systems ($m > 0$) turn out to be starbursts.

However, this subset is not complete, representing a minor fraction (43%) of all the starburst population in our sample. This result should not be surprising. Indeed, the observability timescale of a merger in the upper part of the Gini-M_{20} diagram may not coincide with the starburst phase duration and depends on many factors, including the mass-ratio and the gas fraction of colliding galaxies, the viewing angle, the impact geometry, the dynamics of the disks (e.g., rotation direction) and the extinction. For example, the Gini parameter is more sensitive to face-on systems (Lotz et al. 2008). In addition, the surface brightness at redshift $z > 0.5$ decreases by more than one order of magnitude compared to the local Universe, making more difficult for interacting signatures to emerge from the noise. All these mechanisms are thus likely responsible for the fraction of low-*merginess* SBs identified in our sample.

In order to mitigate these effects and select a more complete subset of merging systems in the main sequence, we also performed a visual classification. Based on a one-by-one inspection of MS galaxies, we flagged as 'visual mergers' all the pairs within a projected separation of 20 kpc and photometric redshift difference < 0.08, or systems that present a very disturbed morphology because of tidal tails, bridges or collisional rings. Compared to the previous criterion, this likely identifies mergers on a longer timescale. On the one hand, the pairs select a sample of very-early stage mergers that are going to coalesce in ~ 0.5 Gyr or more. On the other hand, we can evaluate more carefully by eye the presence and strength of faint merger features, whose importance may not have been properly weighted by the automatic procedure.

This yielded a sample of 24 visual mergers in the main sequence, representing $\sim$ 20% of the MS population. These are 9 more objects compared to morphological mergers, which is comprehensible given that here we are considering also the pairs. Nevertheless, we remind that also this merger subset may not be complete, due to a combination of all the effects previously discussed.

2.4. Clumpiness measurement

In order to quantify the contribution of young stellar clumps to the total galaxy emission, we adopted the clumpiness parameter c, which measures the fraction of light residing in high spatial frequencies structures. For its estimation, we follow the simplest approach described in Conselice et al. (2003) and Lotz et al. (2004).

Firstly, we smoothed the original ACS F814W images (I_0) using a gaussian filter with a radius of 5 pixels. This corresponds to an angular scale of 0.15″ and a physical radius of $\simeq$ 1 kpc at $z \simeq 0.7$ (0.9 to 1.16 kpc in our full redshift range), which is the approximate size of the clumps we want to detect (see Section 1). Then we subtracted the smoothed image $I_{smoothed}$ from the original image, imposing 0 for all the pixels with a negative value in the residual image $I_{res} = I_0 - I_{smoothed}$, as done by Conselice et al. (2003).

In a second step, following the procedure adopted in Salmi et al. (2012), we selected all the pixels in I_{res} which are at least 5σ above the background of the galaxy, in order to reduce the noise contamination. The background level was estimated with a σ-clipping statistics procedure applied on all the regions of I_0 which have not been assigned to any sources in the segmentation map. The threshold limit was chosen empirically, and we found it was the minimum and best value allowing to recover clumpy structures that would have been identified also on a visual inspection. For all the pixels above the 5σ threshold, we assigned them a value of 1 (0 otherwise), in this way defining a mask for the clumps (M_{clumps}). We did not put any constraints on the number of connected pixels to be part of the clumps. However, even when requiring a small amount (e.g., 2-10) of connected pixels, the results are not significantly affected.

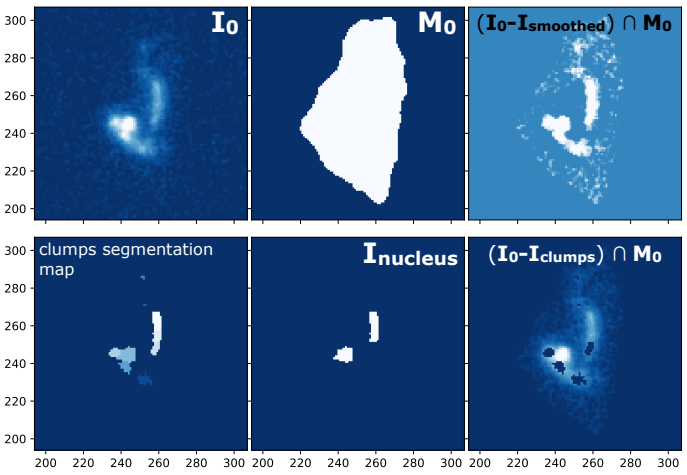

Fig. 4. Flowchart of the clumpiness estimation procedure for one galaxy in our sample (ID 412250): (1) original HST F814W cutout image; (2) segmentation image identifying the galaxy contours; (3) original minus smoothed image, enhancing the visibility of high spatial frequency components; (4) clump detection after applying a 5σ threshold; (5) nuclei visual identification; (6) residual image after clumps light subtraction, which appear as black regions superimposed to the original galaxy image. This figure highlights the power of our approach. We are able to detect clumps very close to the nucleus that would instead have been removed by masking systematically a circual region around the center. It shows also the important role of the deblending function to separate multiple clumps based on the presence of multiple peaks in a single segmentation region, as explained in the text. This case additionally elucidates our conservative approach: we select two nuclei in the clumps segmentation map even though we are not sure about the second on the right (which in alternative could be part of a tidal tail).

In the third step, we removed the galaxy nuclei from the clumpiness calculation, which, by definition, contains only off-nuclear clumpy structures. For example, the nuclei of spiral galaxies are usually made of old stellar population bulges that we do not want to consider in the above parameter. For this scope, we derived the segmentation map of the clump mask, deblending the regions containing more than 2 local luminosity peaks, by using the same *python* codes applied to the original image in the first step. Afterwards, we created the nucleus mask $M_{nucleus}$, setting $M_{nucleus} = 1$ for the clumps identified as nuclei by a visual inspection of the original i-band HST images, and 0 otherwise. In most of the cases, the centrally located nuclei correspond to the brightest clumps identified through our routine. However, this is not a necessary condition, since the nuclei (especially the merger cores) can be very obscured and even undetected in optical. Additionally, simulations have shown that the luminosity of newly formed clumps in merger systems can easily overcome that of the nuclei in the two colliding disks. Despite these uncertainties, we conservatively selected and removed at least two nuclei in all the starbursts and in clear MS mergers identified in Section 2.2. This represents a limiting case, since we expect that a large fraction of starbursts may actually be fully coalesced systems, even though is hard to securely isolate them with our data.

Other works systematically mask an inner circle region with a fixed angular aperture for all the galaxies when computing the

clumpiness (e.g., Lotz et al. 2004). However, this method may remove clumps that are very close to the nucleus. In addition, it is difficult for any automatic procedure to identify the nucleus, especially in case of disturbed morphologies like in mergers, where a careful visual inspection can be more reliable. For these reasons, our method is more precise and can be easily kept under control, assuming that the size of our sample is not excessively large. We show in Fig. 4 a representative example (galaxy ID 412250) of the full identification procedure of our clumps.

Finally, the clumpiness parameter c was derived in a standard way by dividing the total flux residing in previously detected clumps and the total flux of the galaxy, after masking the nucleus. This calculation can be written explicitely as:

$$c = \sum_{M_0 \bigoplus M_{\rm nucleus}} \frac{M_{\rm clumps}(i,j) \times I_0(i,j)}{I_0(i,j)} \quad (4)$$

where I_0 is the original image and M_0, $M_{\rm nucleus}$ and $M_{\rm clumps}$ are masks, already introduced before. The sum is done over all the galaxy pixels defined by the segmentation map (M_0), excluding the nucleus. We consider this quantity appropriate for our work, since it compares the flux of the clumps (outside the nucleus by definition) to the total flux in the same off-nuclear regions.

Another viable option is to compare the emission residing in high spatial frequencies to the total object emission (including the nucleus) as: $c' = \sum [\,|M_{\rm nucleus}(i,j)-1| \times M_{\rm clumps}(i,j) \times I_0(i,j)] \,/\, \sum I_0(i,j)$, where the sum is over M_0. For clarity, since this would not change the results of our analysis, we adopt uniquely the definition in Eq.4 throughout the paper, and include both quantities c and c' in Table A.1 in the Appendix.

2.5. Magnitude and elongation cuts: building the final sample

At $z \sim 0.5$, the brightness of all the objects is approximately one order of magnitude lower (at fixed luminosity) compared to the local Universe, so it becomes increasingly difficult at higher redshifts to identify internal structures of galaxies, such as clumps. Moreover, when the galaxies become too faint, the visibility and detection of clumps is automatically affected, so that our method returns systematically lower c values close to 0. For this reason, to avoid the faintest objects, we used the i-band magnitudes of Laigle et al. (2016) and applied a threshold as $i_{\rm mag} < 22.5$, beyond which the average clumpiness of galaxies (computed in bins of 0.5 in $i_{\rm mag}$) drops by $> 50\%$ compared to the median value and becomes closer to zero (see Fig. A.1 in Appendix). In addition, for all the galaxies with $i_{\rm mag} > 22.5$, it was harder to distinguish their internal morphology on a visual inspection.

Another important aspect that hampers clumps identification is the inclination of the galaxy. The primary consequence is that, for an edge-on system, the standard detection method can erroneously consider the whole disk as a single elongated (and eventually multiply deblended) clump, producing an artificial enhancement of the clumpiness up to a value close to 1. In some cases, the edge-on disk is very faint, probably attenuated by the increased dust column density along the line of sight, so that no substructures are detected and the clumpiness is 0. However, the majority of these objects would be removed by the first $i_{\rm mag}$ threshold.

In order to avoid all these cases, we performed a visual inspection and removed all the edge-on galaxies that suffered from these problems. Since inclination effects can be different for each galaxy and both reduce or enhance their clumpiness, it was not possible to apply the same threshold procedure used for $i_{\rm mag}$.

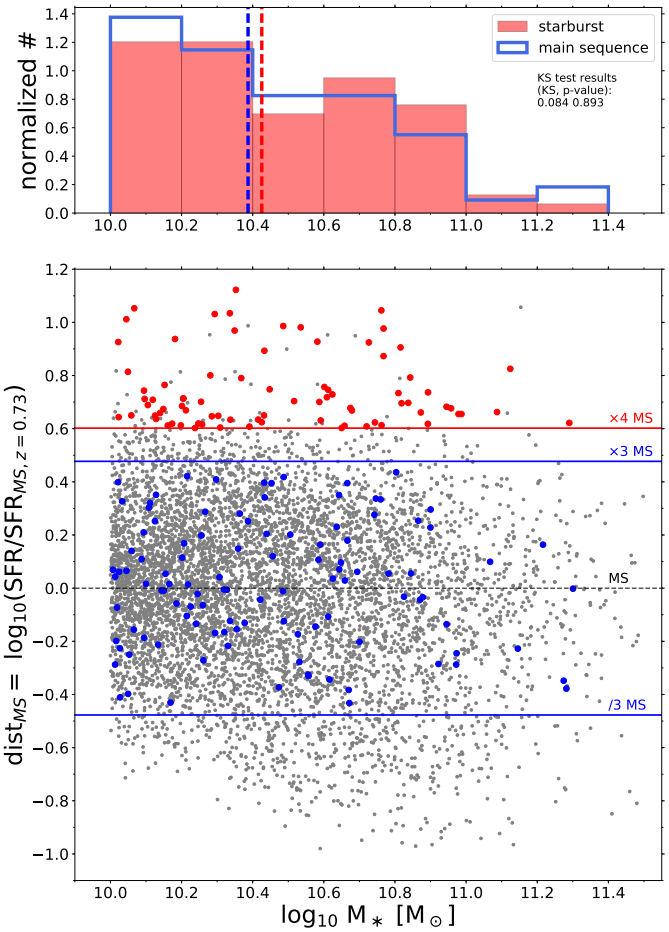

Fig. 5. *Bottom:* Diagram showing for our parent sample of star-forming galaxies in COSMOS ($0.5 < z < 0.9$) their distance from the main sequence as a function of stellar mass. We highlight with a black horizontal line the 0 level. The blue and red lines indicate the limits taken for our main sequence and starburst selection, respectively. The final selected sample is highlighted with blue and red points, correspondingly. The SFR used in the y-axis is normalized to the median redshift of our sample (0.73), following the SFR-redshift evolution of Sargent et al. (2014). *Top:* Histogram distribution (normalized to unit area) of the stellar masses of our selected sample of starbursts (red) and main sequence galaxies (blue), showing that the two subsets have similar distributions. The two vertical lines indicate, according to their corresponding colors, the median values of M_* of SB and MS galaxies.

However, we found that almost all (96%) of the objects discarded by eye have an elongation > 3.5, so we can consider this value as a representative threshold for our selection. For the full original sample, a comparison between the clumpiness and both the i-band magnitude and the elongation will be shown in the Appendix A.

We remark that the $i_{\rm mag}$ and elongation cuts remove similar fractions of starburst and main sequence systems ($\sim 10\%$ in each case), and also the same percentages of morphologically classified mergers and not mergers (according to Gini-M_{20} diagram), thus no systematic biases are introduced against one of the two populations. We also notice that almost all the objects removed by this procedure have very low clumpiness, below 0.05. After applying these cuts, we also verified that starburst and main sequence galaxies have similar histogram distributions in i-band magnitude and elongation in the allowed ranges, and very close

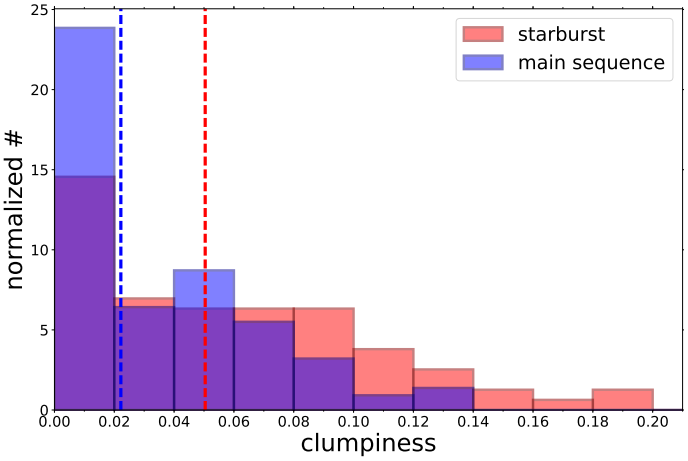

Fig. 6. Distribution of the clumpiness parameter (normalized to unit area) for starburst galaxies (in red) and main sequence systems (in blue), showing that starbursts dominate in the high clumpiness tail. The results of the Kolmogorov-Smirnov test (KS statistics and p-value) between the two subsample distributions are 0.26 and 0.0029, respectively. The median clumpiness for SBs and MS (0.05 and 0.022) are drawn with dashed lines with their corresponding colors.

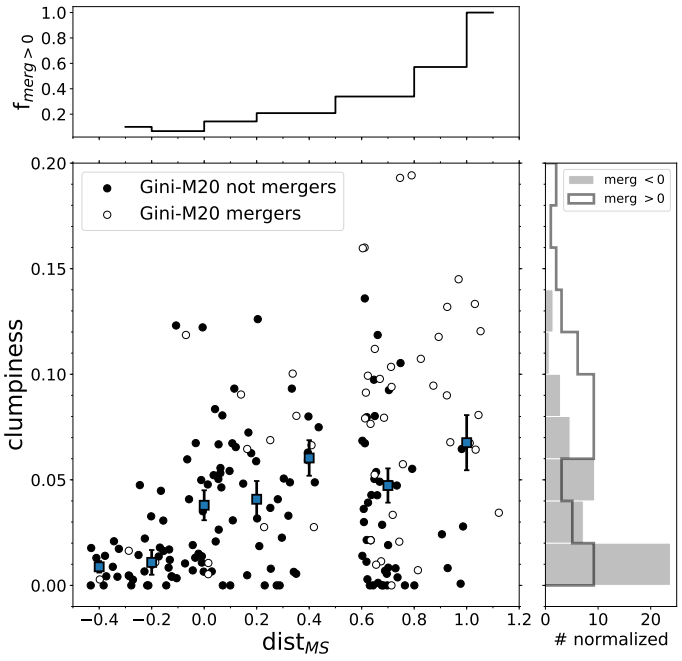

Fig. 7. Scatter plot between the clumpiness and the distance from the main sequence (c vs. $\mathrm{dist_{MS}}$) for our sample. Median clumpiness values are calculated in seven bins of $\mathrm{dist_{MS}}$ of 0.2 dex approximately, and are shown as gray squares with their 1σ errors. We can see the strongest increase of the median clumpiness in the upper main sequence region. Each galaxy in the plot is color-coded according to its merginess value. Morphological mergers identified in the Gini-$\mathrm{M_{20}}$ diagram (*merginess* > 0) are shown with white filled circles, and their fraction $\mathrm{f_{merg}}$ (compared to the whole population) constantly increases toward higher $\mathrm{dist_{MS}}$ (upper histogram). The histogram on the left compares instead the clumpiness distribution for morphologically selected mergers (*merginess* > 0, in white) and not mergers (gray region, derived from the black circles in the scatter plot). In this case, a larger discrepancy is observed between the two distributions compared to Fig. 6, confirmed by the higher significance of the KS test (KS= 0.432, p-value= 2×10^{-8}).

medians of the two quantities. In particular, for SBs and MS galaxies, the median $\mathrm{i_{mag}}$ = 21.25 and 21.35, respectively, while the median elongations are 1.55 and 1.59. In any case, we verified that applying lower, more conservative thresholds in i_{mag} and elongation would not change the results of this paper.

After cleaning the sample from the contamination of faint or very elongated objects, we derived a final subset of 79 starbursts and 109 main sequence galaxies, that we will analyze in following sections. The final starbursts and main sequence sample selection can be visualized in Fig. 5. The stellar mass histogram, visible on the top of the figure, shows that the two selected populations have a similar distributions of $\mathrm{M_*}$, with medians of $\log_{10}(\mathrm{M_*})$= 10.42 and 10.39, respectively, thus our cuts do not introduce systematic biases in $\mathrm{M_*}$ against one of the two populations.

3. Results

In this Section we present the results of our clumpiness measurements, and compare the properties of the starburst and main sequence populations, that we have taken as representatives of two star-formation modes: a higher efficiency stellar production induced by merger events in the first case, and a normal star-formation activity associated with secularly evolving disks in the latter.

In Fig.6 we show the histogram distribution of the clumpiness for starburst galaxies (in red) and main sequence galaxies (in blue). The clumpiness parameter spans a range between 0 and 0.20, meaning that clumps can contribute at maximum to one fifth of the total off-nuclear galaxy emission at this redshift.

We can see that the distributions of both subsamples are peaked at low clumpiness ($c < 0.02$) and, after this excess, they follow an approximately constant and then declining trend. However, the two histograms differ for many aspects. Main sequence systems are dominant in the first clumpiness bin, while, after a region where the relative abundances are consistent ($0.02 < c < 0.08$), starbursts are systematically more numerous above $c \simeq 0.08$. This translates into more than a factor of two higher median clumpiness for SBs compared to the MS population (0.05 and 0.022, respectively).

In order to test whether the two distributions (χ_1 and χ_2) are significantly different, we run a Kolmogorov-Smirnov (KS) test, which yields both the maximum difference D_{χ_1,χ_2} between the two cumulative distribution functions and the probability (p-value) to obtain the same D_{χ_1,χ_2} under the assumption that the two underlying one-dimensional probability distributions are equal. We found a D_{χ_1,χ_2} = 0.26 and p-value of 0.029%, thus the identity hypothesis can be rejected at > 99.5% confidence level, suggesting that the two subsets are intrinsically different.

We also characterized the two tails in the high clumpiness regime (excluding the objects falling in the first bin) for SB and MS galaxies separately. The first follow a smooth decreasing trend, reaching a maximum clumpiness of 0.194, while $c = 0.14$ comprises 90% of the starbursts in the tail. On the other hand, for main sequence systems, the highest clumpiness observed is 0.126, and in this case 90% of the population in the tail has $c < 0.1$.

The detailed properties of the clumpiness distribution among SB and MS systems in our sample can be better visualized in a scatter plot (Fig. 7) by comparing the clumpiness of single galaxies to their main sequence distance, $\mathrm{dist_{MS}}$. By definition, starbursts occupy the right part of the diagram at $\mathrm{dist_{MS}} > 0.6$, while

main sequence objects span the range $-0.47 < \mathrm{dist_{MS}} < 0.47$. For the whole sample, we also computed the median clumpiness (shown with gray squares) in seven bins of $\mathrm{dist_{MS}}$ with binsize of $\simeq$ 0.2 dex, and the error on the median (shown with black symmetric error bars).

Overall, we can see that there is a large diversity among the main sequence population. Galaxies with $\mathrm{dist_{MS}} < -0.1$ have a low median clumpiness of $\simeq$ 0.01, with a maximum value of 0.05. Above that threshold instead, the clumpiness of 'upper main sequence' galaxies increases monotonically up to a factor of six, which then remains approximately constant (within the uncertainties) throughout the starburst regime. However, we can still notice that the highest clumpiness values in Fig. 6 and 7 are found only within the starburst galaxies. A similar upward trend was also found when comparing the clumpiness to the specific SFR for our sample.

As we have mentioned in the previous Section, SBs and MS are complex populations and, in particular, the latter include also a fraction of merging systems. To test their effects, we considered the Gini-M_{20} classification in Fig. 7, flagging all galaxies with merginess > 0 as empty circles (black filled circles otherwise). In this case, in contrast with the clumpiness trend, the fraction of Gini-M_{20} selected mergers is constantly rising across the whole $\mathrm{dist_{MS}}$ range, even in the starburst regime, where it goes from 35% to 100% at the rightmost extreme. This indicates that the fraction of starbursts not identified as morphological mergers ($m < 0$) contributes to keep the median clumpiness of SBs relatively low. A constantly rising trend would be indeed observed by considering only galaxies with merginess > 0.

If we select galaxies according to their merginess parameter and compare their clumpiness distributions (right histogram in Fig. 7), we find a more clear separation compared to previous histograms (KS= 0.432, p-value= 2×10^{-8}). Interestingly, now the clumpiness distribution of morphological mergers is approximately constant over the whole range up to $c \simeq 0.12$, since the counts in all the bins are consistent with Poissonian statistic fluctuations with 95% confidence level.

If we consider together MS visual mergers and starburst galaxies (which are mostly merger triggered at our redshift, as argued in Calabrò et al. (2018)), and compare them with isolated, not visually interacting main sequence systems, we obtained a similar result of Fig. 7 (KS= 0.307, p-value $\simeq$ 0.1%), with the latter prevailing at $c < 0.06$ and starbursts being dominant at higher clumpiness.

The impact of the morphological merger classification on the clumpiness distributions suggests that we can decompose the entire population in 4 classes according to their merginess and $\mathrm{dist_{MS}}$, to look for any trend in the SB and MS subsets. This exercise is made in Fig. 8, showing that, in this case, there is a more striking difference between morphological merger starbursts and not morphological merger systems, regardless of their distance from the MS, with the first having a median clumpiness more than a factor of three higher ($c_{\mathrm{median}} = 0.09$). On the other hand, the clumpiness distribution of MS morphological mergers is also slightly different (at $> 90\%$ confidence level) from the rest of the MS population (KS= 0.34, p-value= 0.075), with a clumpiness distribution skewed toward a larger median ($c_{\mathrm{median}} = 0.06$), and a big contribution in the higher clumpiness tail (cyan line at $0.06 < c < 0.12$) compared to other not-merging systems, suggesting that mergers might increase the clumpiness even with a moderate enhancement of the SFR.

We remind that the merginess (i.e., the morphological classification) can be affected by the presence of clumps by construction, hence we remark the importance of using an alternative merger classification based on visual inspection, where we carefully identify mergers based on the presence of tidal tails, strongly disturbed and asymmetric features, and not on the presence of clumpy structures in the system. However, we do not see a correlation of the clumpiness with either the Gini parameter or M_{20} separately (first and second panel of Fig. A.2 in the Appendix). Even though a slightly increasing trend of the clumpiness is observed on average with higher Gini, many galaxies (both MS and SBs) have a low clumpiness value despite their high M_{20} or Gini coefficients.

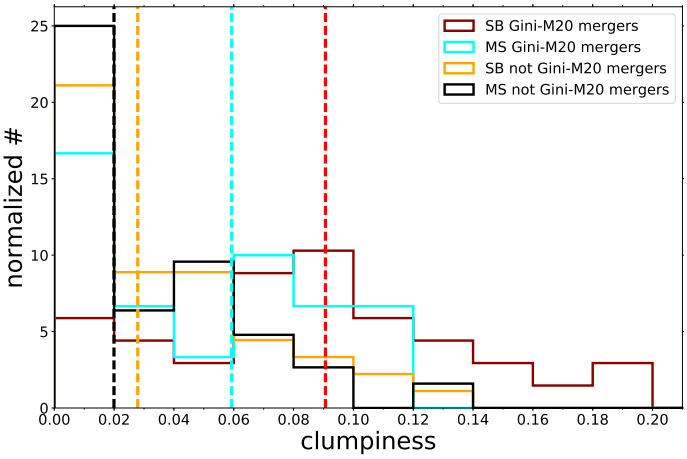

Fig. 8. Normalized distribution (continuous line) and medians (vertical dashed lines) of the clumpiness for four types of galaxies: main sequence galaxies with merginess < 0 and > 0 (in black and cyan, respectively), and starbursts (in orange those with merginess < 0 and in red the morphological merger subset). We notice that the merger-selected starbursts dominate the high clumpiness tail, while the remaining SBs are basically indistinguishable from the population of main sequence galaxies with *merginess* < 0. A substantial contribution to the high clumpiness population also comes from mergers inside the MS, as shown by the cyan excess at $0.06 < c < 0.12$. A Kolmogorov-Smirnov (KS) test between merger and not-merger MS systems (cyan and black subsets) yields 0.302 (p-value = 0.094).

These results do not depend significantly on the merginess threshold used in Section 2.3 to identify morphological mergers. Actually, if we consider, to be conservative, a lower *merginess* parameter threshold between -0.1 and 0, this would strengthen the result of Fig. 8, since the median clumpiness of main sequence mergers (cyan vertical line) would move rightwards. For example, if we choose a threshold of -0.05, we would obtain for the above subset a median $c_{\mathrm{med}} = 0.048$, and the difference with respect to not merging MS sources would be more significant (KS= 0.364, p-value < 0.001). A comparison diagram between the clumpiness and the merginess can be seen in Fig. A.2 in the Appendix.

We also remark that these results are not affected by the choice of the bin size and by the sample cuts. Indeed, similar histogram distributions, trends and significances (Fig. 6 to 8) are obtained when varying the first parameter by small amounts within a factor of 2 of the chosen bin size. The same conclusion holds for different thresholds of the i-band magnitude for the final sample selection, as in case of more conservative choices, to keep only the brightest sources (e.g., i-mag cut < 22.5).

Furthermore, we have so far analyzed a limiting, very conservative situation, according to which we systematically search for two nuclei to remove in all ongoing merging starbursts, while only one nucleus is removed in main sequence disk galaxies.

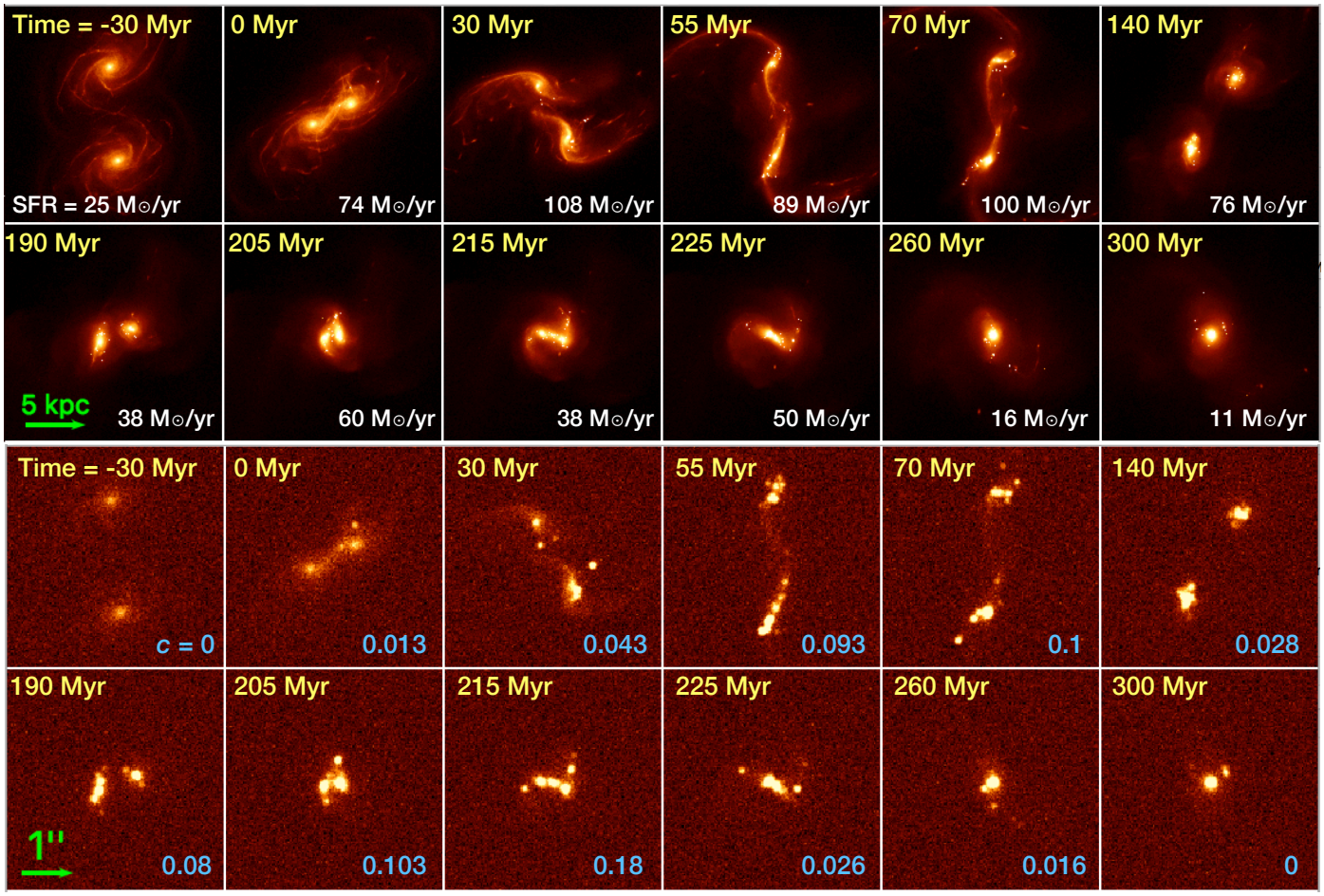

Fig. 9. *Top:* Snapshots of the stellar mass density from the simulation of two colliding galaxies with prograde-prograde orbit coupling, at different times. The images have a physical scale of 200 pc/pixel, comparable to our observations (assuming the median redshift of our galaxies $\simeq$ 0.7). *Bottom:* Mock HST F814W observations obtained from the above simulated cutouts after conversion to the $\sim$ 0.095″ PSF resolution of our images (through a gaussian filter) and addition of the noise. The instantaneous SFR and the estimated clumpiness for each time step is indicated in the corner. 24 $M_\odot$/yr is the SFR of two isolated disks, according to our fiducial run.

Even for MS morphological mergers we keep this approach, unless there is clearly a merging pair or two distinguished merger components, in which case we also remove two nuclei. This implies that we are likely underestimating the clumpiness of starburst systems, while simultaneously overestimating that of normal star-forming galaxies.

Finally, we found no correlation between the stellar mass and the clumpiness (Fig. A.3-top in the Appendix), indicating that the stellar content is not the main driving parameter for the increasing patchy morphology among our sample. Similarly, there is no significant evolution of the clumpiness with redshift, as shown in Fig. A.3-bottom in the Appendix.

4. Discussion

In the following part, we compare our observational results to novel hydrodynamical simulations of merger systems at the same redshift of our study. Later in this section, we support the young nature of the clumps in three galaxies for which multi-wavelength HST images are available. We conclude by discussing a possible merger evolutionary trend of the clumpiness and suggesting a possible extension of our results to interpret clumpy galaxies observed at higher redshifts.

4.1. Confirming merger-induced clumps formation with simulations

It is interesting to compare our results with numerical predictions. However, to this aim, proper initial conditions characteristic of our redshift range should be adopted. For this reason, we performed a series of hydrodynamical simulations of mergers with a gas fraction of 30% (typical of z $\sim$ 0.7) (Combes et al. 2013; Freundlich et al. 2019). As mentioned in the Introduction, previous simulations of galaxy collisions with such high gas fraction did not reach the low gas temperatures needed for properly reproduce the gas distribution during merger events.

The setup is based on the simulations described in Fensch et al. (2017) using the adaptive mesh refinement code RAMSES (Teyssier 2002). The galaxies have the same characteristics as the ones in Fensch et al. (2017). The refinement strategy is based on the density and the highest resolution elements are 6 pc. Gas in cells that are denser than 10 cm^{-3} and cooler than 2×10^4 K is converted into stars following a Schmidt (1959) law, with an efficiency per free-fall time set to 10%. We include three types of stellar feedback, described in Fensch et al. (2017). The energy output from SNII explosions is released by a kinetic kick and a thermal energy injection, each accounting for half of the total energy ouptut (Dubois & Teyssier 2008). The HII regions are modelled by Strömgren spheres, whose sizes are done consid-

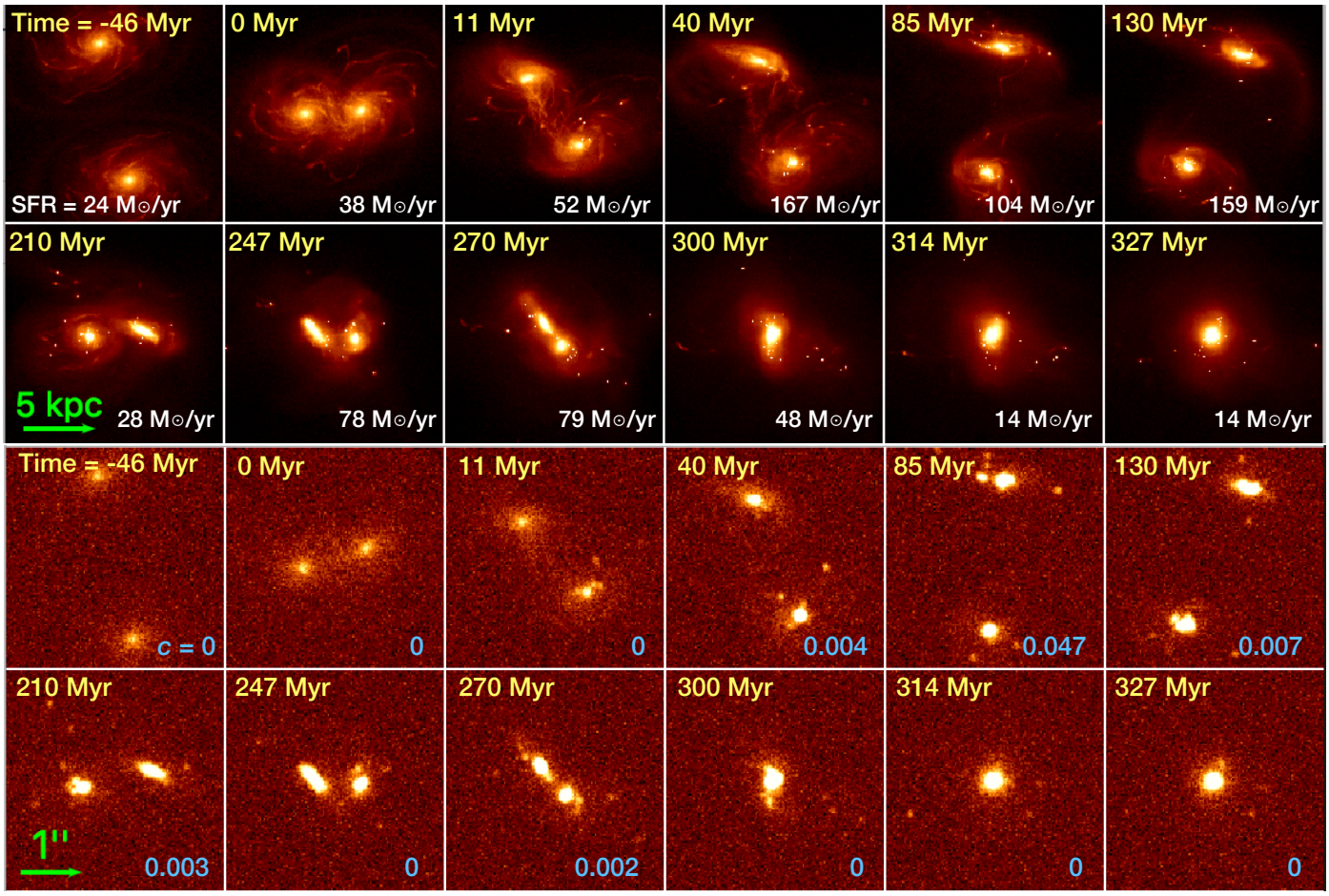

Fig. 10. Same as Figure 9, but for a retrograde-retrograde collision.

ering that the gas surrounding the source has a minimal density above 300 cm^{-3}. Gas inside the sphere is heated to 5×10^4 K and receives a radial velocity kick modeling the radiation pressure.

We performed one isolated and two merger simulations. To account for numerical diffusion effect, in the isolated simulation the galaxy moves along the same orbit as one of the galaxies in the interaction orbits. The spin-orbit coupling plays a significant role in the interaction. For instance, only galaxies with spins aligned with that of the interaction, what is called a *prograde coupling*, can create tidal tails (see review by Duc & Renaud 2013). We run one prograde-prograde (or, equivalently, direct-direct) and one retrograde-retrograde encounter. The two orbits correspond to Orbit #1 from Fensch et al. (2017). After an intermediate apocenter, they coalesce within $\sim$ 230 and $\sim$ 300 Myr, respectively. Stellar density maps are shown in the upper pannel of Fig. 9 and Fig. 10. On it we see the formation of stellar condensations during the interaction, similar to what is observed in collisions at low-redshift (Di Matteo et al. 2008; Renaud et al. 2014; Matsui et al. 2019).

We then mock HST observations in the F814W filter by assuming $z = 0.7$, the median redshift of our sample. We use the Bruzual & Charlot (2003) stellar evolution model, with solar metallicity and Chabrier (2003) initial mass function. The stars from the initial conditions are given a random age between 500 Myr and 7 Gyr following a uniform law. The image is convolved to the HST resolution, and the noise corresponding to COSMOS field data acquisition is added to the images. The resulting images are shown in the bottom pannels of Fig. 9 and Fig. 10.

In the mock observations, the tidal tails created by the merger are not detected anymore. In contrast, bright clumps, corresponding to the blending of star clusters, are clearly visible at the new resolution in several steps of the evolution. Remarkably, some configurations are very similar to the morphology of our observed galaxies. In particular, the eight cutout closely resembles the galaxy ID 705860 shown in Fig. 2.2 (the second of the third row), reinforcing the interpretation that the clumps (including the nuclei) are probably all part of the same 'two-body' merger system, even though their physical association is not obvious by eye. Finally, we calculated the clumpiness from the mock images with the same procedure adopted for the observations.

The evolution of the SFR and the clumpiness for the three simulations is shown in Fig. 11. In the upper pannel of this Figure, we can see the evolution of the SFR. We notice a rapid increase of the SFR after the first pericenter passage and at the coalescence, similarly to previous simulations of galaxy collisions. We can also see that the SFR increases by a factor four to five, which is an intermediate value between the high enhancement (10-100) that can occur with 10% gas fraction, and the low enhancement obtained for the same orbits and a 60% gas fraction (below 4) (Fensch et al. 2017). This effect will be discussed in more details in a companion paper (Fensch et al., *in prep.*). We additionally remark that a time averaging of the SFR (and of the clumpiness) in the past 50 Myr could be applied if we want to match the average SFR timescale of our observations, even though the diagrams would not change qualitatively.

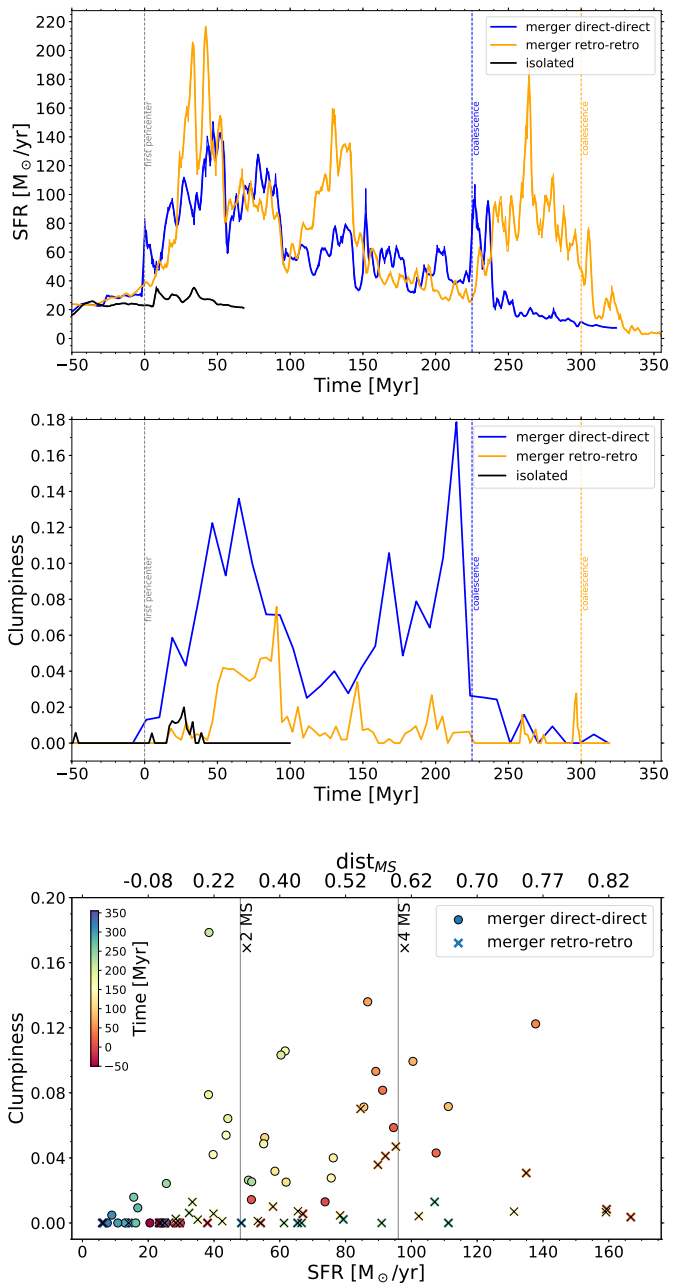

Fig. 11. *Top and center:* The SFR and the clumpiness (respectively) are shown as a function of time for the direct-direct (i.e., prograde-prograde) merger (in blue), retrograde-retrograde merger (in orange) and for the fiducial run of an isolated galaxy multiplied by two (in black). In the latter, only the evolution during 200 Myr is shown as a representative case, while in the other two runs the time range considered (∼ 450 to ∼ 820 Myr from the onset of the simulation) encompasses the effective merging period, from the first pericenter passage to the final coalescence (vertical dashed lines colored accordingly). *Bottom:* Comparison between the clumpiness and the SFR at different timesteps (colorbar on the left), for direct-direct and retrograde-retrograde mergers (with circles and crosses, respectively). In the first case, we can notice also a correlation between the two quantities.

The evolution of the clumpiness is displayed instead in the middle pannel of Fig. 11. While we see that for both collision orbits the clumpiness increases compared to the fiducial run, the relative values are quite different. The prograde-prograde orbit reaches high values of the clumpiness 50 Myrs after the first pericenter and right before the coalescence, and peaks at 0.17, which is in the range of observed clumpiness in the COSMOS field. On the contrary, the clumpiness does not increase much during the retrograde-retrograde orbit, reaching only 0.05, 75 Myrs after the first pericenter.

On Fig. 9, we can see that the high values of the clumpiness in the prograde-prograde case are obtained by the blending of star clusters, which tend to happen at the base of the tidal features. This blending result in the accumulation of star clusters in this region, as we can see in the fourth cut out. The formation of the tidal tail resulting from the prograde spin-orbit coupling, the accumulation of star clusters and the enhanced clumpiness do not happen in the retrograde-retrograde collision. Thus, the scatter in the clumpiness observed in our sample, and especially the low clumpiness values for highly star-forming starbursts, could be in part explained by a variety of spin-orbit couplings.

Overall, numerical simulations are able to explain qualitatively many of our observational findings. First of all, mergers are powerful triggering mechanisms for the formation of clumps in intermediate redshift galaxies ($0.5 < z < 0.9$), and they can increase the clumpiness parameter (i.e., the fraction of light coming from clumpy structures) up to values that are similar to those observed. On average, they also reproduce the increasing trend of the clumpiness with specific SFR (Fig. 11-bottom).

Secondly, during a merger event, a significant increase of the clumpiness can be obtained even in correspondence of a modest SFR enhancement, below the threshold for starburst classification. This can explain the fraction of morphological mergers in the main sequence with a relatively large clumpiness parameter.

Finally, the dynamics of the interaction likely plays an important role. Indeed, in the case of a retrograde-retrograde merger, only a very small enhancement of the clumpiness is found during the starburst, or no increase at all. Thus a high clumpiness parameter is not obtained neither in all mergers, nor in all starbursting systems. We remark that very low clumpiness parameters (< 0.04) in correspondence of elevated SFRs (×4 above the MS), are not inconsistent with our data, which comprise a significant number of starbursts with a similar low fraction of clumpy emission (cf. Fig. 6). A forthcoming paper will study the physical properties and evolution of simulated clumps with more detail, with a more diverse set of galactic disks (Fensch et al. in prep.).

4.2. Clumpiness evolution during the merger

In Section 3 we have divided the sample in SBs and MS galaxies, finding that the two subsets have different clumpiness distributions, with the former prevailing in the high clumpiness end, while the latter are dominant at very low $c < 0.02$. However, this classification is too semplicistic, and the complexity of the MS and SB populations can be resolved in part by considering their apparent morphology. We have indeed seen in Fig. 8 that morphological merger starbursts, selected by their large Gini and M20 coefficients, are the major responsible for the high-end tail of the clumpiness distribution, with a median $c = 0.09$ and a maximum fraction of light in the clumps of 20%. On the other hand, the subset of starbursts that are not merger selected from their morphology is essentially indistinguishable from that of isolated (not merger) main sequence systems (Fig. 8).

As highlighted in previous works, our morphological classification criterion, firstly defined by Lotz et al. (2004), is able to identify mergers over a relatively short temporal window compared to the whole merger duration. The observability timescale of a merger in the Gini-M_{20} diagram is approximately 0.2 – 0.3

Gyr according to Nevin et al. (2019), corresponding to the period when the interaction signatures are more evident in the form of bright tidal tails or very disturbed, elongated or asymmetric global structures. In contrast, at the coalescence, residual merging features rapidly fade below the surface brightness detection threshold, hampering its true nature recognition visually, especially at our redshifts. Their increasingly difficult identification at the coalescence is also seen in simulations. This suggests that different time evolutionary merger phases can in part explain the large spread of merginess and clumpiness in the SB distribution.

In order to test this interpretation, we analyzed the subset of 19 starbursts, with available HST images and in our redshift range, that were presented in Calabrò et al. (2018) as representatives of off-MS systems at $0.5 < z < 0.9$ above a M_* of 10^{10} $M_\odot$. We showed that this sample comprises a sequence of different evolutionary merger stages, which can be traced by the equivalent width (EW) of Balmer or Paschen lines, and by the total attenuation ($A_{V,tot}$) toward the center of the starburst core in a mixed dust and stars configuration (Calabrò et al. 2019).

In Fig. 12 we compare the clumpiness of this SB subset to $A_{V,tot}$ and the EW of Hα and Paβ lines, measured in (Calabrò et al. 2019). In the first upper panel, we find no significant correlation between c and $A_{V,tot}$, with a Spearman correlation coefficient R= −0.34 (p-value= 0.13) and angular coefficient of the best-fit line consistent with 0. However, if we assume no correlation, the four starbursts with the highest obscurations $A_{V,tot}$ above 15 mag all have a low clumpiness below 0.04. This confirms that an important fraction of galaxies (50% in our Magellan dataset) contributing to the first two low clumpiness bins in Fig. 6 may be actually late stage mergers observed after the coalescence. On the other hand, early and intermediate merger systems with $0 < A_{V,tot} < 15$ mag can show the full variety of clumpiness values, and these are the only phases where we observe a substantial clumpiness enhancement above the average population level and above 0.1.

In analogy to the former result, when comparing the clumpiness to the equivalent width of Paβ and Hα, we also measure an angular coefficient slightly below 2σ. However, in the latter case the Spearman coefficient R is equal to 0.53 (p-value= 0.014), indicating that the correlation is significant according to this statistical test. The existence of the latter (even though mild) correlation, and the position of the Magellan SBs in the first panel of Fig. 12, can shed light on the possible triggering mechanisms and fate of the observed clumps. Following the results of previous simulation works, clumps can form with the increasing compressive turbulence modes and subsequent fragmentation induced by the merger during early-intermediate stages (Renaud et al. 2014). The absence of late stage mergers with high clumpiness suggests that, after the main triggering events, clumps could be rapidly destroyed by strong stellar radiation or AGN feedback, or they could be incorporated in the central galactic bulge.

Intriguingly, we notice that 4 out of 5 X-ray detected AGNs in this small subset have a very low clumpiness below 0.02. As suggested in Calabrò et al. (2019), these systems may be in an advanced phase of the AGN activity and central black hole growth, and possibly approaching the blow-out phase, thus an impact on clumps survival cannot be excluded. If we do not consider these objects, we would obtain a higher statistical significance of the $A_{V,tot}$-c correlation.

Another possibility is that clumps become too faint in i-band compared to the host galaxy, following the aging of the stellar populations or the higher dust obscurations expected in advanced phases, and they are not detected anymore in this band. However, we remind that testing the impact of feedback processes and studying the final fate of the clumps is beyond the scope of this work, and it will be investigated in future papers.

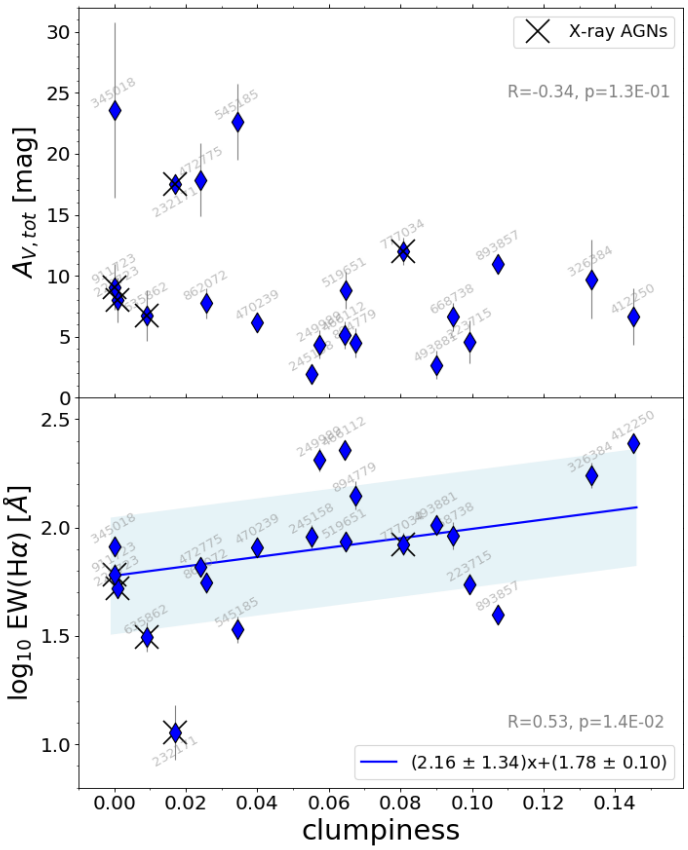

Fig. 12. Comparison between the clumpiness and the mixed-model attenuation $A_{V,tot}$ toward the center (upper plot), and the equivalent width (EW) of Hα (lower panel) for 21 starbursts in our same redshift range $0.5 < z < 0.9$, and analyzed in Calabrò et al. (2019). The corresponding IDs are added to each galaxy, while black crosses indicate X-ray detected sources. The Spearman correlation coefficient R and the corresponding p-value are highlighted in each panel. We derive no correlation for the first diagram, and a mild correlation $> 3\sigma$ for the second, thus only in the latter case we derive the best linear fit (blue line, with equation included the legend) and 1σ dispersion (blue shaded region). However, even in the first plot, the highest clumpiness values are found only for the less attenuated starbursts, while the most obscured objects ($A_{V,tot} > 15$) have systematically low c. Given that $A_{V,tot}$ and EW(Hα) have been used as merger stage indicators in Calabrò et al. (2019), our findings provide an indication for a possible clumpiness evolution, decreasing from early-intermediate phases to late stage mergers. This is corroborated by the subset of X-ray AGNs (likely close to the blow-out phase) showing preferentially a lower clumpiness.

Even though the time evolutionary sequence is a tantalizing interpretation, the absence of very strong correlations may indicate that other effects also play a role on clumps formation, such as the impact geometry, the dynamics and mass ratio of the two components, and the viewing angle toward the system, all of which would be in any case very difficult to quantify from current observational data. In particular, the strong dependences on the orbital configuration (Section 4.1) suggests that we may have large object by object variations in the clumpiness while having still a strong SFR enhancement (Fig. 11).

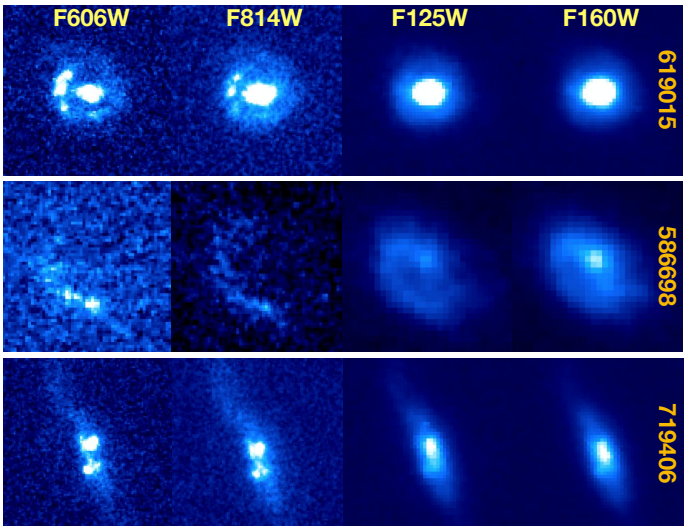

Fig. 13. HST cutout images in the F606W, F814W, F125W and F160W broad band filters for three starbursts in the COSMOS-CANDELS field. As explained in the text, the second galaxy has a photometric redshift of 0.92, while the third has a SFR a factor of 3 above the main sequence at the same redshift $z = 0.74$, but clearly shows a merger morphology (in spite of its edge-on profile). The multi-wavelength comparison shows that clumps become brighter at shorter wavelengths, thus they likely represent merger-induced young stellar associations rather than old pre-existing structures. The IDs shown in the right part of the figure come from Laigle et al. (2016).

4.3. Multi-wavelength morphology from CANDELS

We have identified clumps in single broad-band (F814W) images, which are available for the majority of galaxies in the 2 degree^2 COSMOS field. A possible limitation of our approach relies on the fact that we can probe the emission of clumpy structures only in a limited wavelength range, which, considering the filter transmission curve and our redshift interval, covers approximately the 3700 Å to 6400 Å rest-frame range. The morphology of clumpy features can potentially change if we go to the UV rest-frame or at longer wavelengths (near-IR).

We can check the multi-wavelength behavior for three starburst galaxies in the COSMOS-CANDELS field, observed at high-resolution by HST (Koekemoer et al. 2011) in four broad-band filters (F160W, F814W, F125W and F160W) at resolutions of 0.08″, 0.09″, 0.12″ and 0.18″, respectively (Fig. 13). In order to have a larger statistics, we have considered in this analysis two galaxies (ID 586698 and 719406) belonging to the parent sample but excluded from the final selection adopted in this paper: while the first has a slighly higher redshift (0.92) than our selection criteria, the second has a distance from the MS of 0.51 (above a factor of 3). However, it has clearly a merger-like morphology given the presence of a long tidal feature in un the upper part. Having similar clumpy morphologies (from i-band) to the population of galaxies considered in this work, they can yield important informations on clump properties also for the remaining sample.

Analyzing each starburst in more detail, we can clearly see in the first galaxy two clumps in i-band and four clumps in the UV, while all of them become fainter and undetected at longer wavelengths. They also occupy part of a ring structure surrounding the central nucleus. Simulations predict that this configuration could represent the late phase of a collision between disk galaxies (Bekki 1998), or created by tidal accretion of material from a gas rich donor galaxy (Bournaud & Combes 2003).

Also in the second galaxy the clumps become brighter in the UV rest-frame and they are displaced along half a ring. Longer wavelength images reveal that this elongated structure is connected to a single bigger system with just one main nucleus, highly attenuated or very old, invisible in F606W and F814W filters.

Finally, the last system shows multiple clumps in *i* and U band images, below the main central nucleus visible in all the bands. In particular, the brightest clump falls at the border of the main edge-on stellar disk.

Overall, the clumps shown in the above three galaxies become more prominent from redder to bluer bands (where sometimes they can outshine the nucleus itself), which would yield an increased clumpiness in the UV compared to i-band. On the opposite side, they become undetected in near-IR bands (even though the resolution is slightly lower). This result indicates that they are likely young structures induced by the merger rather than pre-existing aggregations of older stars. Furthermore, they seem to have a low mass fraction and possibly a low SFR fraction, despite their UV prominence.

A systematic investigation of the physical properties of the clumps formed by merger events at these redshifts, including their dust attenuation, stellar ages and masses, gravitational stability and kinematics, could be possible in the future with the availability of high spatial resolution multi-wavelength bands for a larger subset of objects. This will additionally allow to compare their size and stellar mass distributions to those observed in main sequence systems and at higher redshifts.

4.4. Comparison with other studies

As mentioned in the Introduction, several studies have investigated the origin of clumpy galaxies at redshifts overlapping with our range. Puech (2010) claimed that mergers may be the dominant triggering mechanisms of clumpy galaxies at $z < 1$. However, his limited sample of 11 objects is representative of a very specific redshift ($\simeq 0.6$), galaxy stellar mass ($\log_{10} M_* \sim 10.2$ [$M_\odot$]) and type (e.g., absence of a central bulge), which cannot be representative of all the star-forming population and of the same dynamic range spanned in our work. In addition, he found that the majority of UV clumps tend to vanish when looking at longer wavelengths, so they could be biased towards lower attenuations or higher ongoing SFRs. Also Ribeiro et al. (2017), while focusing on much higher redshift than our work ($2 < z < 6$), interprets double clumps as possible merging systems. However, if it is true, the clumps likely represent the nuclei of the two colliding galaxies, thus they should not be considered anymore as clumpy galaxies by our definition.

On the other hand, Murata et al. (2014) noticed that the redshift evolution of the fraction of clumpy galaxies is inconsistent with that expected from the merger rate, thus concluding that mergers do not contribute to the clumpy population at all epochs. However, they detected clumps directly on the images without an intermediate smoothing step, which is important to facilitate the identification of high spatial frequency components and separate them from equally bright regions with smoother profiles. In addition, they identified clumpy galaxies preferentially on the main sequence. Indeed, their SFRs are derived from SED fitting (from UV to mid-IR), not allowing to select systems with obscured star-formation, which is a dominant component in infrared-luminous mergers (Goldader et al. 2002; Calabrò et al. 2018). A similar conclusion based on the same argument is reached by Guo et al. (2015) for clumpy galaxies at $0.5 < z < 3$. They suggest instead that violent disk instabilities are the main

triggering mechanism at high stellar masses ($M_* > 10^{10.6}$ $M_\odot$), while minor mergers may contribute the most for intermediate mass systems with $10^{9.8} < M_* < 10^{10.6}$ $M_\odot$. However, they consider UV clumps, which may disappear in the optical rest-frame, as shown by Puech (2010).

Our result should be considered as complementary to all these studies. We are showing the importance of mergers as responsible for triggering clump formation in intermediate redshift galaxies, enhancing the clumpiness at higher levels compared to other mechanisms at this cosmic epoch. However, we do not claim that all clumps are induced by mergers. Indeed, a fraction of main sequence galaxies (which are the majority 96-98% of the star-forming population) with higher clumpiness are not identified as mergers and may be consistent with other formation channels, such as minor mergers or disk instabilities. Therefore, we are not in contradiction with the two previous works.

Finally, Lotz et al. (2004) showed that local ULIRGs (which are all mergers) have an enhanced clumpiness compared to the main sequence star-forming population. Our paper thus suggests that this result can be extended up to redshift $\sim$ 1 to starburst galaxies and to morphologically selected mergers.

4.5. Interpreting high redshift clumpy galaxies

We have demonstrated in previous sections that mergers can trigger the formation of stellar clumps in galaxies at $0.5 < z < 0.9$. Given this explanation at intermediate redshifts, we can wonder whether a similar connection also holds at earlier cosmic times.

At high redshifts ($z >> 1$), young massive clumps observed in the UV and optical rest-frame, having $M_* \sim 10^8$ $M_\odot$ and ages of 100-500 Myr, are generally thought to be driven by violent gravitational instabilities in gas-rich highly turbulent primordial disks, typically lying in the star-forming MS (e.g., Noguchi 1999; Immeli et al. 2004a,b; Elmegreen & Elmegreen 2005; Elmegreen et al. 2007; Elmegreen 2008; Bournaud et al. 2007; Förster Schreiber et al. 2006, 2009). The fuel needed for star-formation and clumps triggering may be provided by relatively smooth accretion of cold gas from the cosmic web and from the CGM (Kereš et al. 2005; Dekel et al. 2009; Aumer et al. 2010). Furthermore, many studies have revealed that clumpy galaxies have kinematics consistent with rotating disks, even though highly disturbed (Bournaud et al. 2008; Daddi et al. 2008; Shapiro et al. 2008; Epinat et al. 2009).

Even though this scenario is physically motivated, we cannot rule out a-priori a possible role of mergers in favouring and triggering clumps, in analogy to what has been shown at $z < 1$. The fraction of mergers increases monotonically at earlier times, as shown by Conselice et al. (2003), thus we may expect that they have a constantly higher influence on galaxy morphology. Despite mergers can be less efficient to enhance the SFR at starburst levels at higher redshifts (Fensch et al. 2017), our results at intermediate z show that a large clumpiness parameter can be obtained even without a strong enhancement of SFR.

In addition, it is possible to preserve some degree of global rotation even during a merger event, and also a disk could rapidly reform in the latest stages (Rothberg & Joseph 2006; Springel & Hernquist 2002; Fensch et al. 2017). Thus, many of the high-z systems showing global rotation in the stellar or gaseous component can still be mergers. As complementary probes to recognize merger systems, we could instead look for the presence of compact, highly obscured cores in the host galaxy, indicative of a late or post-merger phase (Calabrò et al. 2019; Puglisi et al. 2019).

In this context, Hodge et al. (2018) and Tadaki et al. (2018) observed sub-kpc clumpy structures with ALMA in the dust continuum or CO emission for a small subset of luminous submillimeter galaxies (SMGs) in the redshift range 1.5-5. Among the sample of 11 SMGs presented by Hodge et al. (2018), the low Sersic index profile measured in one galaxy suggests it might be a late stage merger, while interacting signatures in the optical are revealed for some of their remaining systems. They showed that these structures are displaced in the inner 5-10 kpc regions, analogous to the spatial distribution of our brightest clumps (in both observations and simulations), which form close to the nuclei and in the beginning of tidal tails. Additionally, the ALMA clumps produce 2 to 10% of the total galaxy emission, in agreement with the range of clumpiness that we found in the optical. This suggests that, being highly star-forming and dusty, their structures may represent still early phases of clump formation.

On the contrary, normal star-forming isolated disks are smoother at the same sub-mm wavelengths. Cibinel et al. (2017) found that UV clumps in a main sequence galaxy at redshift = 1.5 are not visible anymore with ALMA in the CO(5-4) transition, which could be due to lower gas content (or equivalently, higher SFE), or to lower SFRs of the clumps. Rujopakarn et al. (2016) studied 11 normal star-forming galaxies at redshifts 1.3-3 with $\sim 0.4''$ resolution ALMA images. They also found no evidence of clumpy structures, which instead appear at UV wavelengths as unobscured regions, owing small SFR fractions from 0.1 to 5% of the whole systems. Future observations with ALMA could further constrain these different scenarios and better characterize the clumps detected in our COSMOS sample for both the MS and SB population.

Overall, our paper suggests that a dicotomy of clumps properties and total clumpiness exists even at earlier cosmic epochs, depending on the level of SFR of the host galaxy. If our results still apply here, and given the possible merger nature of a fraction of SMGs (Tacconi et al. 2008), it seems reasonable to think that many of the ALMA clumps observed in high-z infrared luminous galaxies may be actually produced by merger interactions.

5. Summary and conclusions

Inspired by the merger nature of infrared luminous starbursts at $0.5 < z < 0.9$ shown in previous works, we have studied in the same redshift range the effects of mergers on clumps formation by comparing the high-resolution HST optical rest-frame morphologies of 79 starbursts to a control sample of 109 normal star-forming main sequence galaxies. We performed an additional visual merger identification among the main sequence population and applied the classical Gini-M_{20} classification to select galaxies with merger-like shapes. Our main results are summarized as follows:

- The merger classification criterion of Lotz et al. (2008) (based on the Gini-M_{20} morphological parameters) also separates the two regions where starbursts and main sequence galaxies dominate, respectively, with a fraction of 76%. However, only 43% of the starbursts lie in merger region, suggestive of different merger phases probed by the two diagnostics and of the large incompleteness of Gini-M_{20} for the merger selection, likely due to multiple effects, including the galaxy inclinations, impact parameters and dust attenuation.
- Starburst and main sequence galaxies have different clumpiness histogram distributions: the former dominate in the high clumpiness regime, while the latter are more numerous at

lower values. Given the merger nature of intermediate-z starbursts, this suggests that mergers are likely responsible for clumps formation and their increased luminosity with respect to normal star-forming isolated disks.

- A larger difference of the clumpiness histogram distributions is obtained when including visually selected mergers in the SB subset and when comparing morphological mergers to not mergers. In particular, Gini-M_{20} mergers, regardless of their level of SFR, have a median clumpiness a factor of three higher compared to the rest of the population, and are almost entirely responsible for the high clumpiness tail observed among our sample. We also found that the fraction of morphological mergers and their median clumpiness increase monotonically with the distance from the main sequence.
- From hydrodynamical simulations of merger galaxies with initial conditions typical for our redshift range, we found that mergers can significantly enhance the clumpiness of the system compared to isolated main sequence galaxies, by a similar amount to that observed in real images. Different spin-orbit coupling of merging galaxies can fully explain the scatter of the observed clumpiness values from 0 to 20%.
- For a sample of 19 SBs with Magellan-FIRE spectra, there is a mild correlation between the clumpiness and the equivalent width of Balmer and Paschen lines, suggesting a possible clumpiness evolution during the merger, decreasing from early-intermediate to later stages after the coalescence. X-ray detected AGNs are preferentially found in low-clumpiness systems, suggesting a possible clump suppression induced by AGN feedback. However, other effects (including galaxy inclination, rotation, attenuation and impact parameter) are likely responsible for the low correlation strength ($\simeq 2\sigma$).
- Using four band high-resolution images for three clumpy galaxies in the COSMOS-CANDELS field, we have showed that merger induced clumps are generally young and UV-bright, likely formed during the merger rather than being older pre-existing stellar structures. However, a larger sample is needed to study the statistical properties of the clumps (e.g., sizes, stellar masses and ages) and investigate their evolution.

Merger triggered gas compression and fragmentation can provide the physical explanation for the formation of stellar bright clumps. We expect that this mechanism is more frequent at high redshift, given the increasing fraction of mergers at earlier epochs. This work arises questions on the real nature of clumps observed in high redshift galaxies, suggesting that mergers could be an alternative, powerful channel for enhancing the clumpiness. If this is true, the clumpiness could be used as a complementary merger diagnostic (though still incomplete) to identify mergers from the morphology when the typical low-surface brightness interacting features (e.g. tidal tails) become too faint.

Deeper images in the optical and near-IR rest-frame with Euclid and JWST will allow in the near future clumps detection and their physical characterization (through a multi-λ approach) for larger statistical samples of clumpy galaxies at higher redshifts and similar spatial resolutions than those considered here. In addition, they will facilitate the study of the environment and the morphological properties (including merger signatures) of their host galaxies.

Acknowledgements. I would like to thank everybody who actively contributed to this article.

References

Aumer, M., Burkert, A., Johansson, P. H., & Genzel, R. 2010, ApJ, 719, 1230
Bekki, K. 1998, ApJ, 499, 635
Bournaud, F., & Combes, F. 2003, A&A, 401, 817
Bournaud, F., Elmegreen, B. G., & Elmegreen, D. M. 2007, ApJ, 670, 237
Bournaud, F., Daddi, E., Elmegreen, B. G., et al. 2008, A&A, 486, 741
Bournaud, F., Powell, L. C., Chapon, D., & Teyssier, R. 2011, Astrophysical Dynamics: From Stars to Galaxies, 271, 160
Bournaud, F., Dekel, A., Teyssier, R., et al. 2011, ApJ, 741, L33
Bournaud, F., Juneau, S., Le Floc'h, E., et al. 2012, ApJ, 757, 81
Bournaud, F. 2016, Galactic Bulges, 418, 355
Bruzual, G., & Charlot, S. 2003, MNRAS, 344, 1000
Cacciato, M., Dekel, A., & Genel, S. 2012, MNRAS, 421, 818
Calabrò, A., Daddi, E., Cassata, P., et al. 2018, ApJ, 862, L22
Calabrò, A., Daddi, E., Puglisi, A., et al. 2019, A&A, 623, A64
Calzetti, D., Armus, L., Bohlin, R. C., et al. 2000, ApJ, 533, 682
Ceverino, D., Dekel, A., & Bournaud, F. 2010, MNRAS, 404, 2151
Chabrier, G. 2003, PASP, 115, 763
Chapman, S. C., Windhorst, R., Odewahn, S., Yan, H., & Conselice, C. 2003, ApJ, 599, 92
Cibinel, A., Daddi, E., Bournaud, F., et al. 2017, MNRAS, 469, 4683
Cibinel, A., Daddi, E., Sargent, M. T., et al. 2019, MNRAS, 485, 5631
Clements, D. L., Sutherland, W. J., McMahon, R. G., & Saunders, W. 1996, MNRAS, 279, 477
Combes, F., García-Burillo, S., Braine, J., et al. 2013, A&A, 550, A41
Conselice, C. J., Bershady, M. A., Dickinson, M., & Papovich, C. 2003, AJ, 126, 1183
Cox, T. J., Jonsson, P., Primack, J. R., & Somerville, R. S. 2006, MNRAS, 373, 1013
Daddi, E., Dickinson, M., Morrison, G., et al. 2007, ApJ, 670, 156
Daddi, E., Dannerbauer, H., Elbaz, D., et al. 2008, ApJ, 673, L21
Daddi, E., Bournaud, F., Walter, F., et al. 2010, ApJ, 713, 686
Dekel, A., & Birnboim, Y. 2006, MNRAS, 368, 2
Dekel, A., Sari, R., & Ceverino, D. 2009, ApJ, 703, 785
Delgado-Serrano, R., Hammer, F., Yang, Y. B., et al. 2010, A&A, 509, A78
Di Matteo, P., Bournaud, F., Martig, M., et al. 2008, A&A, 492, 31
Draine, B. T., & Li, A. 2007, ApJ, 657, 810
Dubois, Y., & Teyssier, R. 2008, Pathways Through an Eclectic Universe, 390, 388
Duc, P.-A., & Renaud, F. 2013, Lecture Notes in Physics, Berlin Springer Verlag, 861, 327
Elbaz, D., Daddi, E., Le Borgne, D., et al. 2007, A&A, 468, 33
Elmegreen, D. M., Elmegreen, B. G., Rubin, D. S., & Schaffer, M. A. 2005, ApJ, 631, 85
Elmegreen, B. G., & Elmegreen, D. M. 2005, ApJ, 627, 632
Elmegreen, D. M. 2007, Galaxy Evolution across the Hubble Time, 235, 376
Elmegreen, D. M., Elmegreen, B. G., Ferguson, T., & Mullan, B. 2007, ApJ, 663, 734
Elmegreen, B. G., Bournaud, F., & Elmegreen, D. M. 2008, ApJ, 688, 67
Elmegreen, B. G. 2008, Mass Loss from Stars and the Evolution of Stellar Clusters, 388, 249
Elmegreen, B. G., Elmegreen, D. M., Sánchez Almeida, J., et al. 2013, ApJ, 774, 86
Epinat, B., Contini, T., Le Fèvre, O., et al. 2009, A&A, 504, 789
Fensch, J., Renaud, F., Bournaud, F., et al. 2017, MNRAS, 465, 1934
Förster Schreiber, N. M., Genzel, R., Lehnert, M. D., et al. 2006, ApJ, 645, 1062
Förster Schreiber, N. M., Genzel, R., Bouché, N., et al. 2009, ApJ, 706, 1364
Freundlich, J., Combes, F., Tacconi, L. J., et al. 2019, A&A, 622, A105
Garland, C. A., Pisano, D. J., Mac Low, M.-M., et al. 2015, ApJ, 807, 134
Genzel, R., Burkert, A., Bouché, N., et al. 2008, ApJ, 687, 59
Glasser, G. J. 1962, J. Am. Stat. Assoc., 57, 648
Goldader, J. D., Meurer, G., Heckman, T. M., et al. 2002, ApJ, 568, 651
Governato, F., Brook, C., Mayer, L., et al. 2010, Nature, 463, 203
Guo, Y., Ferguson, H. C., Bell, E. F., et al. 2015, ApJ, 800, 39
Hodge, J. A., Smail, I., Walter, F., et al. 2018, arXiv:1810.12307
Jin, S., Daddi, E., Liu, D., et al. 2018, ApJ, 864, 56
Immeli, A., Samland, M., Westera, P., & Gerhard, O. 2004, ApJ, 611, 20
Immeli, A., Samland, M., Gerhard, O., & Westera, P. 2004, A&A, 413, 547
Kereš, D., Katz, N., Weinberg, D. H., & Davé, R. 2005, MNRAS, 363, 2
Koekemoer, A. M., Aussel, H., Calzetti, D., et al. 2007, ApJS, 172, 196
Koekemoer, A. M., Faber, S. M., Ferguson, H. C., et al. 2011, ApJS, 197, 36
Kraljic, K., Bournaud, F., & Martig, M. 2012, ApJ, 757, 60
Laigle, C., McCracken, H. J., Ilbert, O., et al. 2016, ApJS, 224, 24
Law, D. R., Steidel, C. C., Erb, D. K., et al. 2009, ApJ, 697, 2057
Lotz, J. M., Primack, J., & Madau, P. 2004, AJ, 128, 163
Lotz, J. M., Jonsson, P., Cox, T. J., & Primack, J. R. 2008, MNRAS, 391, 1137
Madau, P., & Dickinson, M. 2014, ARA&A, 52, 415
Matsui, H., Tanikawa, A., & Saitoh, T. R. 2019, PASJ, 71, 19
Mullaney, J. R., Alexander, D. M., Goulding, A. D., & Hickox, R. C. 2011, MNRAS, 414, 1082

Murata, K. L., Kajisawa, M., Taniguchi, Y., et al. 2014, ApJ, 786, 15
Nevin, R., Blecha, L., Comerford, J., & Greene, J. 2019, ApJ, 872, 76
Noeske, K. G., Weiner, B. J., Faber, S. M., et al. 2007, ApJ, 660, L43
Noguchi, M. 1999, ApJ, 514, 77
Puech, M. 2010, MNRAS, 406, 535
Puglisi, A., Daddi, E. et al. (submitted to ApjL)
Renaud, F., Bournaud, F., Kraljic, K., & Duc, P.-A. 2014, MNRAS, 442, L33
Ribeiro, B., Le Fèvre, O., Cassata, P., et al. 2017, A&A, 608, A16
Rodrigues, M., Puech, M., Hammer, F., Rothberg, B., & Flores, H. 2012, MNRAS, 421, 2888
Rodriguez-Gomez, V., Snyder, G. F., Lotz, J. M., et al. 2019, MNRAS, 483, 4140
Rodriguez-Gomez, V., Pillepich, A., Sales, L. V., et al. 2016, MNRAS, 458, 2371
Rothberg, B., & Joseph, R. D. 2006, AJ, 132, 976
Rujopakarn, W., Dunlop, J. S., Rieke, G. H., et al. 2016, ApJ, 833, 12
Rujopakarn, W., Daddi, E., Rieke, G. H., et al. 2019, arXiv:1904.04507
Salmi, F., Daddi, E., Elbaz, D., et al. 2012, ApJ, 754, L14
Rodighiero, G., Daddi, E., Baronchelli, I., et al. 2011, ApJ, 739, L40
Rujopakarn, W., Nyland, K., Rieke, G. H., et al. 2018, ApJ, 854, L4
Sanders, D. B., & Mirabel, I. F. 1996, ARA&A, 34, 749
Sargent, M. T., Daddi, E., Béthermin, M., et al. 2014, ApJ, 793, 19
Schreiber, C., Pannella, M., Elbaz, D., et al. 2015, A&A, 575, A74
Shapiro, K. L., Genzel, R., Förster Schreiber, N. M., et al. 2008, ApJ, 682, 231
Shapiro, K. L., Genzel, R., & Förster Schreiber, N. M. 2010, MNRAS, 403, L36
Sheth, K., Melbourne, J., Elmegreen, D. M., et al. 2012, ApJ, 758, 136
Schmidt, M. 1959, ApJ, 129, 243
Silverman, J. D., Daddi, E., Rodighiero, G., et al. 2015, ApJ, 812, L23
Somerville, R. S. 2001, Galaxy Disks and Disk Galaxies, 230, 477
Sparre, M., & Springel, V. 2016, MNRAS, 462, 2418
Springel, V., & Hernquist, L. 2002, MNRAS, 333, 649
Tacconi, L. J., Genzel, R., Smail, I., et al. 2008, ApJ, 680, 246
Tacconi, L. J., Genzel, R., Neri, R., et al. 2010, Nature, 463, 781
Tadaki, K., Iono, D., Yun, M. S., et al. 2018, Nature, 560, 613
Teyssier, R. 2002, A&A, 385, 337
Teyssier, R., Chapon, D., & Bournaud, F. 2010, ApJ, 720, L149

Appendix A: Comparison between the clumpiness and other quantities

In this Appendix we show how the clumpiness compares with other parameters considered in the main part of the paper. The Fig. A.1 displays the clumpiness as a function of the i-band magnitude and the elongation of our targets. This explains the final sample selection made for our analysis (described in Sections 2.5 and 3), highlighted by the gray vertical lines. In Fig. A.2 is presented the comparison of the clumpiness with different morphological indicators, that are, the Gini coefficient, the M_{20} parameter and the *merginess*. The first two diagrams show the lack of correlation between the two quantities in the x and y-axis, even though a slightly increasing trend of c is found at higher Gini. In the last diagram can be noticed a much steeper increase of the clumpiness with the *merginess*, which is used to define morphological mergers in Section 2.3. Finally, Fig. A.3-top shows the redshift distribution of our sample, ranging $0.5 < z < 0.9$ and with a median z of 0.73. Fig. A.3-bottom and Fig. A.4 demonstrate, respectively, that the clumpiness does not depend on the stellar mass, and does not significantly evolve with redshift (within our uncertainties).

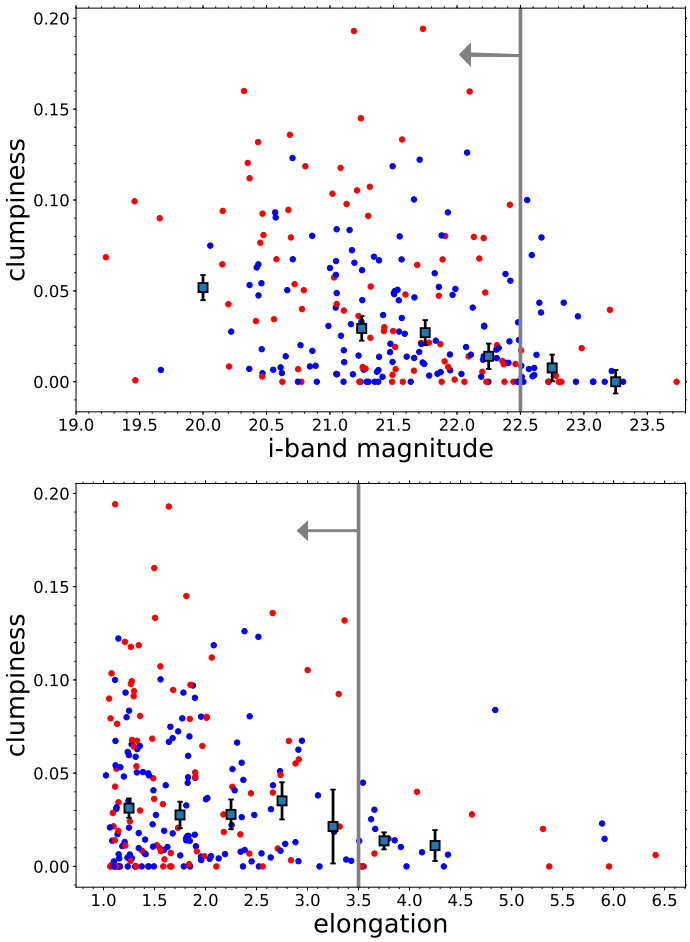

Fig. A.1. *Top:* Clumpiness vs i-band total magnitude (i_{mag}) for our initial sample of 145 main sequence and 96 starburst galaxies (in blue and red, respectively). Median clumpiness values and errors (gray squares with black error bars) are derived for 6 bins of i_{mag}. Our selection cut ($i_{mag} < 22.5$) is highlighted with a vertical gray line. *Bottom:* Clumpiness vs elongation for the same sample as above, with median clumpiness and errors estimated in 7 bins of elongation. The vertical gray line indicates our cut for the final selection (elongation < 3.5), even though we remember that one additional nearly edge-on MS galaxy was also removed by visual inspection.

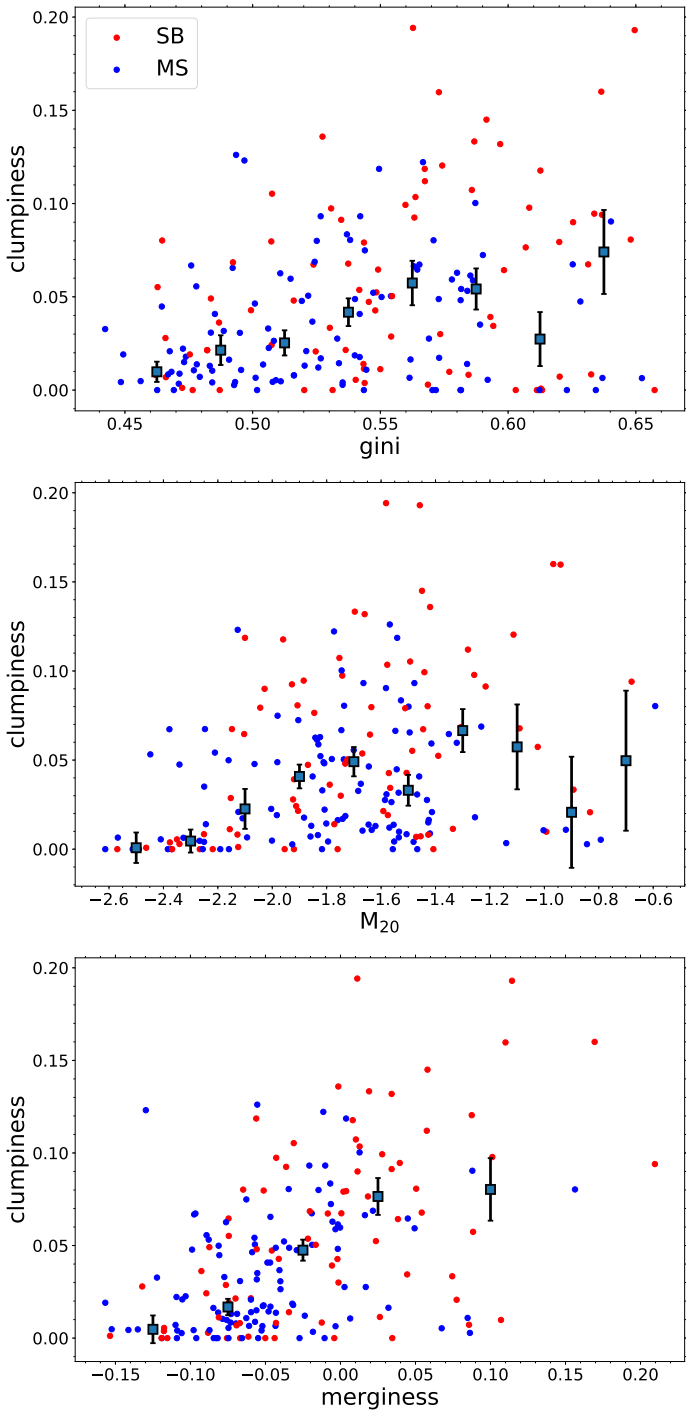

Fig. A.2. The three diagrams compare the clumpiness of our final galaxy sample to the Gini and M_{20} coefficients (first and second panels, respectively), and to the *merginess* parameter, defined in Eq. 3. Starbursts are shown in red, while main sequence galaxies are color coded in blue. The median clumpiness (and errors) computed in bins of Gini, M_{20} and *merginess* are represented with gray squares and black error bars.

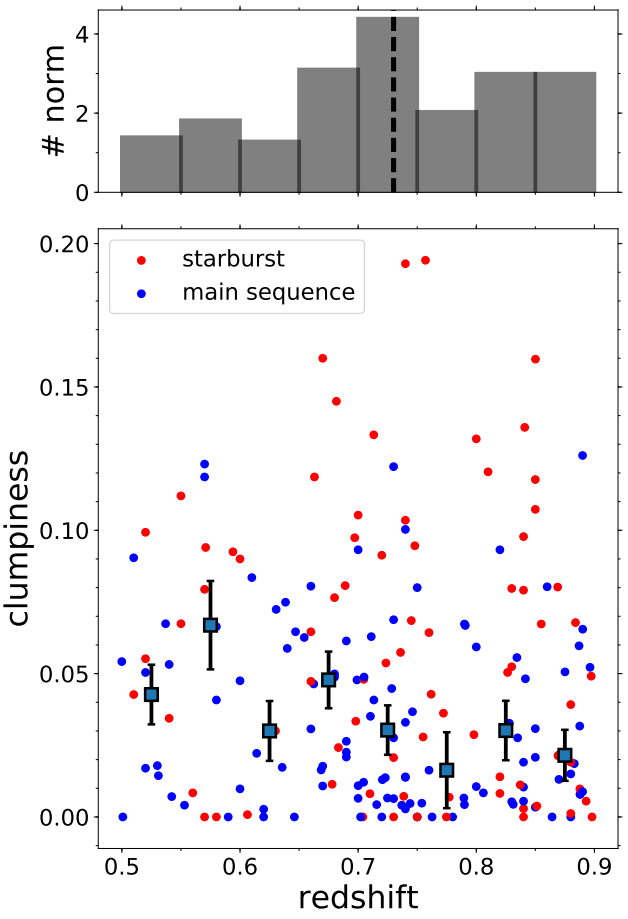

Fig. A.3. Redshift vs clumpiness for our final selected galaxies, with gray squares and black error bars representing the median clumpiness and error calculated inside 8 redshift bins. On the top of the panel is shown the histogram distribution of the redshifts of our galaxies, with the median redshift (z_{med} = 0.73) highlighted with a black dashed line.

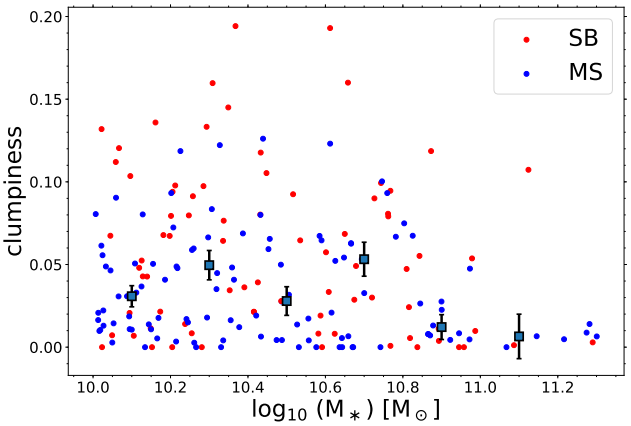

Fig. A.4. Stellar mass vs clumpiness for our final sample of MS and SB galaxies (in blue and red, respectively), with median clumpiness (and error) in 6 M_* bins superimposed with gray squares.

ID	RA	DEC	redshift	c′	clumpiness	merginess	M_* [$M_\odot$]	SFR_{IR} [$M_\odot$/yr]
217536	149.524108	1.606315	0.87 ± 0.03	0.02	0.02	0.07	10.4	74.25 ± 6.633
220514	149.58302	1.61253	0.89 ± 0.03	0.01	0.01	0.07	10.9	49.96 ± 4.284
222723	150.173213	1.616315	0.61 ± 0.01	0.0	0.0	0.06	10.8	151.2 ± 6.357
222977	150.414727	1.618189	0.75 ± 0.0	0.03	0.04	0.04	10.1	15.29 ± 2.6
223715	149.765371	1.617017	0.52 ± 0.0	0.09	0.1	-0.03	10.7	52.4 ± 0.805
228149	149.816844	1.627891	0.63 ± 0.12	0.06	0.07	0.01	10.2	14.57 ± 6.078
239406	150.338269	1.644141	0.73 ± 0.02	0.04	0.04	0.08	10.3	12.82 ± 1.733
244932	149.460788	1.651282	0.72 ± 0.02	0.01	0.01	0.06	10.7	19.61 ± 2.242
245158	150.188543	1.654977	0.52 ± 0.0	0.05	0.06	0.07	10.8	83.05 ± 1.227
247210	150.487543	1.656873	0.83 ± 0.0	0.05	0.05	-0.02	10.1	41.72 ± 1.106
249989	150.685402	1.661076	0.74 ± 0.04	0.06	0.06	-0.09	10.6	102.4 ± 14.72
259328	149.916036	1.676354	0.74 ± 0.0	0.03	0.03	0.08	10.1	26.09 ± 0.57
271645	149.607229	1.694341	0.74 ± 0.08	0.0	0.0	0.14	11.0	15.24 ± 3.196
275629	150.182349	1.700807	0.74 ± 0.0	0.14	0.19	-0.11	10.6	101.3 ± 0.924
280708	149.969049	1.710048	0.86 ± 0.0	0.09	0.1	0.02	10.1	36.63 ± 4.083
286337	149.808093	1.717684	0.75 ± 0.0	0.0	0.0	0.08	10.6	17.23 ± 1.73
287281	149.662106	1.719228	0.71 ± 0.02	0.06	0.06	0.01	10.7	44.15 ± 5.46
289993	149.951404	1.725684	0.68 ± 0.0	0.01	0.01	-0.03	10.1	42.29 ± 0.49
293450	149.496283	1.729198	0.86 ± 0.06	0.06	0.07	0.01	10.2	45.48 ± 7.794
294096	149.51561	1.731195	0.67 ± 0.06	0.01	0.02	-0.03	10.0	4.835 ± 1.635
295213	150.421274	1.731761	0.64 ± 0.04	0.07	0.07	0.06	10.8	47.17 ± 6.101
297678	149.582631	1.738114	0.87 ± 0.03	0.07	0.08	0.06	10.4	78.84 ± 5.764
300643	149.779375	1.741341	0.53 ± 0.0	0.02	0.02	0.03	10.3	5.695 ± 1.548
308894	150.259527	1.756639	0.88 ± 0.0	0.04	0.05	0.06	10.1	25.86 ± 3.1
314674	149.922125	1.764706	0.89 ± 0.01	0.06	0.07	0.05	10.5	22.89 ± 3.078
319784	150.073982	1.772639	0.73 ± 0.0	0.02	0.02	-0.08	10.1	47.72 ± 0.947
326384	149.517858	1.783572	0.71 ± 0.04	0.1	0.13	-0.02	10.3	125.0 ± 14.8
327954	149.493504	1.786618	0.61 ± 0.11	0.02	0.02	0.11	10.0	9.337 ± 4.839
331390	150.640087	1.78974	0.67 ± 0.0	0.01	0.01	0.06	10.1	10.15 ± 2.1
331485	149.494555	1.791539	0.71 ± 0.02	0.02	0.04	0.06	10.3	15.02 ± 2.365
332156	150.23588	1.791352	0.83 ± 0.16	0.0	0.0	0.14	10.9	29.63 ± 11.85
340778	150.458433	1.803992	0.75 ± 0.0	0.0	0.0	0.15	11.2	39.87 ± 1.179
350404	150.20613	1.822038	0.74 ± 0.0	0.0	0.0	0.05	10.3	14.75 ± 4.196
358661	149.710063	1.832255	0.5 ± 0.13	0.0	0.0	0.12	10.3	6.222 ± 3.722
366376	150.138331	1.844028	0.57 ± 0.0	0.08	0.09	-0.21	10.2	38.12 ± 0.414
368717	149.718723	1.849718	0.67 ± 0.0	0.14	0.16	-0.17	10.7	67.19 ± 0.758
371578	150.674055	1.85337	0.51 ± 0.0	0.04	0.04	0.0	10.1	26.9 ± 0.222
371675	149.901208	1.85448	0.74 ± 0.0	0.01	0.01	0.08	10.1	8.38 ± 2.119
371886	149.900477	1.854753	0.64 ± 0.0	0.01	0.02	0.05	10.6	7.781 ± 1.071
372591	150.503808	1.854601	0.75 ± 0.0	0.07	0.08	0.01	10.4	36.58 ± 1.03
387242	150.222431	1.878024	0.84 ± 0.0	0.08	0.1	-0.1	10.2	51.69 ± 1.204
387454	150.652196	1.877237	0.59 ± 0.0	0.08	0.09	0.04	10.5	64.74 ± 1.105
387747	149.916015	1.879961	0.84 ± 0.0	0.07	0.08	-0.0	10.8	102.4 ± 0.974
400118	150.051501	1.898621	0.57 ± 0.0	0.1	0.12	-0.0	10.2	11.69 ± 1.625
402258	150.648684	1.902372	0.74 ± 0.0	0.09	0.1	-0.01	10.1	42.46 ± 0.332
409602	149.578964	1.913372	0.83 ± 0.0	0.07	0.08	0.05	10.2	52.3 ± 0.685
409814	150.198597	1.914859	0.87 ± 0.0	0.02	0.02	0.06	10.2	46.7 ± 0.862
412250	150.741711	1.91764	0.68 ± 0.03	0.1	0.14	-0.06	10.3	109.4 ± 10.24
416314	150.663036	1.924054	0.83 ± 0.0	0.0	0.01	-0.07	10.2	12.06 ± 0.433
418804	149.935142	1.927629	0.68 ± 0.0	0.07	0.08	-0.02	10.3	47.2 ± 0.721
431551	149.568139	1.94866	0.54 ± 0.02	0.01	0.01	0.11	10.9	13.7 ± 1.814
431596	149.948236	1.950357	0.85 ± 0.0	0.03	0.03	0.07	10.1	15.5 ± 0.389
436769	150.617708	1.958166	0.65 ± 0.08	0.0	0.0	0.01	10.5	14.6 ± 5.141
439419	150.301785	1.962747	0.7 ± 0.02	0.01	0.01	0.02	10.4	15.06 ± 1.283
444878	150.687694	1.970867	0.76 ± 0.12	0.16	0.19	-0.01	10.4	85.03 ± 27.02
447374	150.543608	1.974443	0.79 ± 0.03	0.06	0.07	0.1	10.8	26.29 ± 3.279
451272	150.250512	1.980928	0.72 ± 0.0	0.08	0.09	-0.03	10.3	45.3 ± 0.57
451426	149.651824	1.981124	0.79 ± 0.0	0.0	0.0	0.1	10.5	14.85 ± 3.362
466112	149.999276	2.005995	0.76 ± 0.0	0.05	0.06	-0.04	10.3	144.0 ± 1.052
472775	150.481476	2.013621	0.68 ± 0.02	0.02	0.02	0.09	10.8	159.7 ± 11.82
473147	150.399682	2.014254	0.72 ± 0.0	0.05	0.05	0.02	11.0	107.1 ± 1.269
474838	149.543724	2.01889	0.77 ± 0.02	0.03	0.04	0.09	10.4	58.87 ± 3.831
475972	149.526013	2.020502	0.62 ± 0.0	0.0	0.0	0.05	10.7	8.241 ± 2.693
478933	150.666347	2.025354	0.8 ± 0.0	0.13	0.13	-0.03	10.0	53.94 ± 0.785
480125	149.749497	2.027741	0.7 ± 0.0	0.0	0.01	0.05	11.3	31.46 ± 1.037
486542	150.761399	2.040174	0.88 ± 0.0	0.06	0.07	-0.05	10.2	103.9 ± 2.043

ID	RA	DEC	redshift	c′	clumpiness	merginess	M_* [$M_\odot$]	SFR_{IR} [$M_\odot$/yr]
488940	149.831475	2.040881	0.53 ± 0.13	0.01	0.01	0.05	10.1	4.905 ± 2.899
493881	150.749674	2.047066	0.6 ± 0.0	0.08	0.09	-0.01	10.7	129.2 ± 1.006
500548	149.62879	2.05949	0.63 ± 0.0	0.02	0.03	0.0	10.7	67.56 ± 1.033
503971	150.65256	2.063559	0.6 ± 0.0	0.04	0.05	0.03	11.0	9.35 ± 1.21
505311	150.089164	2.065345	0.73 ± 0.0	0.03	0.03	-0.02	10.9	34.49 ± 3.37
506131	149.528615	2.0665	0.57 ± 0.0	0.06	0.08	-0.0	10.2	39.06 ± 0.442
508753	149.928339	2.07214	0.68 ± 0.0	0.04	0.05	0.03	10.2	23.69 ± 0.944
508907	149.856873	2.072084	0.69 ± 0.0	0.05	0.06	0.0	10.0	15.84 ± 1.112
515278	150.523885	2.082297	0.89 ± 0.0	0.11	0.13	0.06	10.4	28.73 ± 3.716
516551	150.205761	2.083436	0.78 ± 0.01	0.01	0.01	0.07	10.1	44.4 ± 2.191
518855	150.12551	2.08703	0.89 ± 0.0	0.0	0.01	0.12	10.8	142.3 ± 1.436
519651	150.430196	2.086883	0.66 ± 0.0	0.05	0.06	0.07	10.5	137.1 ± 1.312
529521	150.103938	2.104858	0.83 ± 0.0	0.03	0.03	0.12	10.7	15.19 ± 3.556
532321	149.893588	2.107745	0.74 ± 0.07	0.01	0.01	-0.09	10.0	52.17 ± 10.76
536590	149.918602	2.113077	0.72 ± 0.06	0.01	0.01	0.04	10.5	10.65 ± 3.274
539760	149.880566	2.120673	0.68 ± 0.0	0.04	0.05	0.08	10.5	15.08 ± 1.726
544522	150.052099	2.126677	0.66 ± 0.0	0.1	0.12	0.06	10.9	90.06 ± 0.794
545104	150.451931	2.127888	0.84 ± 0.0	0.0	0.0	0.12	10.3	85.6 ± 1.039
545185	149.528016	2.12725	0.54 ± 0.0	0.03	0.03	-0.04	10.4	127.3 ± 1.155
546483	150.674581	2.131899	0.9 ± 0.0	0.0	0.0	0.07	10.0	39.28 ± 1.527
562400	150.512919	2.152049	0.56 ± 0.0	0.01	0.01	0.01	10.3	40.5 ± 0.553
571040	149.509664	2.167659	0.84 ± 0.0	0.02	0.02	0.16	10.4	18.17 ± 1.262
574334	150.346743	2.170359	0.85 ± 0.0	0.1	0.12	-0.01	10.4	132.5 ± 1.197
577143	149.887635	2.175504	0.78 ± 0.0	0.0	0.0	0.11	10.7	15.76 ± 1.443
580153	150.259862	2.181773	0.67 ± 0.0	0.01	0.02	0.05	10.2	5.035 ± 1.073
581920	150.23722	2.183978	0.7 ± 0.0	0.08	0.09	0.01	10.2	17.91 ± 1.338
584271	149.729701	2.186421	0.59 ± 0.0	0.0	0.0	0.1	10.6	16.49 ± 0.88
586243	150.626379	2.187925	0.6 ± 0.0	0.01	0.01	0.08	10.0	5.475 ± 1.482
586666	149.68814	2.191839	0.89 ± 0.04	0.01	0.01	-0.11	11.0	146.4 ± 13.37
586799	150.024476	2.190772	0.76 ± 0.0	0.01	0.02	0.08	10.4	9.945 ± 1.957
587164	149.605886	2.190462	0.54 ± 0.0	0.06	0.07	0.02	10.8	13.38 ± 0.944
587556	150.211575	2.191062	0.87 ± 0.0	0.01	0.01	0.07	10.9	25.36 ± 0.477
588922	149.682152	2.193682	0.73 ± 0.0	0.07	0.07	-0.02	10.4	23.22 ± 0.597
601470	150.719972	2.211767	0.89 ± 0.03	0.03	0.03	0.06	10.5	34.8 ± 5.655
606235	150.508123	2.219968	0.82 ± 0.0	0.01	0.01	0.03	10.2	48.24 ± 0.716
607625	150.033442	2.221992	0.89 ± 0.03	0.05	0.06	0.0	10.3	14.44 ± 1.223
608991	150.478377	2.22183	0.83 ± 0.0	0.03	0.03	-0.0	10.5	45.74 ± 2.175
609835	150.678868	2.225219	0.77 ± 0.01	0.0	0.0	0.04	10.2	59.46 ± 2.104
619015	150.10376	2.237664	0.8 ± 0.0	0.02	0.03	0.08	10.7	100.7 ± 1.634
620032	150.626231	2.240874	0.66 ± 0.0	0.04	0.05	0.06	10.0	9.124 ± 0.871
622611	149.664939	2.241806	0.89 ± 0.0	0.01	0.01	0.06	11.3	12.98 ± 3.813
624991	149.9687	2.247664	0.85 ± 0.0	0.02	0.02	0.06	10.0	17.43 ± 1.755
625435	149.538265	2.248029	0.84 ± 0.0	0.01	0.01	0.08	10.0	26.65 ± 1.369
629919	150.477167	2.252186	0.84 ± 0.0	0.0	0.0	0.09	11.3	137.9 ± 9.384
638793	149.529624	2.266751	0.58 ± 0.0	0.06	0.07	-0.02	10.3	23.98 ± 1.356
650054	150.400428	2.286241	0.83 ± 0.16	0.05	0.06	0.09	10.0	20.26 ± 6.12
654259	149.872198	2.289675	0.7 ± 0.0	0.0	0.0	0.08	10.8	103.4 ± 1.199
666872	150.537907	2.310505	0.84 ± 0.0	0.0	0.01	0.07	10.6	21.74 ± 3.212
668065	149.937063	2.312279	0.52 ± 0.0	0.05	0.05	0.02	10.2	7.974 ± 1.205
668738	150.210203	2.31168	0.75 ± 0.0	0.07	0.09	-0.04	10.8	158.9 ± 1.188
668769	149.67653	2.313653	0.69 ± 0.0	0.02	0.02	0.1	10.9	41.91 ± 0.512
695086	150.05225	2.351018	0.72 ± 0.13	0.01	0.01	0.07	10.0	2.633 ± 1.312
706850	149.931017	2.370359	0.85 ± 0.03	0.15	0.16	-0.11	10.3	38.69 ± 1.226
708427	149.578884	2.370704	0.75 ± 0.0	0.06	0.07	0.02	10.6	70.09 ± 0.971
711307	150.53029	2.373861	0.66 ± 0.0	0.03	0.05	0.05	10.8	102.0 ± 1.356
720848	150.261788	2.391079	0.8 ± 0.0	0.01	0.01	-0.01	10.1	12.21 ± 1.839
721398	150.670506	2.391459	0.61 ± 0.0	0.08	0.08	0.01	10.3	14.31 ± 1.796
724796	150.597688	2.396014	0.58 ± 0.0	0.04	0.04	0.05	10.4	19.33 ± 0.723
739926	150.470841	2.419552	0.55 ± 0.0	0.0	0.0	0.11	10.6	4.908 ± 1.447
742281	150.641614	2.423434	0.73 ± 0.0	0.0	0.0	0.12	11.0	112.7 ± 0.43
743322	149.657291	2.425131	0.57 ± 0.0	0.1	0.12	0.13	10.6	9.331 ± 0.836
749126	150.427092	2.431647	0.88 ± 0.0	0.03	0.04	0.01	10.4	71.11 ± 0.756
753450	150.327658	2.44088	0.52 ± 0.0	0.02	0.02	0.05	10.2	5.353 ± 0.727

ID	RA	DEC	redshift	c′	clumpiness	merginess	M_* [$M_\odot$]	SFR_{IR} [$M_\odot$/yr]
764862	150.189794	2.45758	0.51 ± 0.0	0.08	0.09	-0.09	10.1	6.139 ± 0.292
773897	149.833747	2.481315	0.84 ± 0.0	0.12	0.14	0.0	10.2	40.46 ± 1.969
777034	150.150252	2.475166	0.69 ± 0.0	0.06	0.08	-0.05	10.8	211.7 ± 0.764
778756	150.548939	2.480459	0.8 ± 0.0	0.05	0.06	-0.05	10.5	41.11 ± 1.792
780365	150.398266	2.480753	0.85 ± 0.0	0.0	0.0	0.02	10.2	8.178 ± 3.15
783499	150.506268	2.486894	0.62 ± 0.0	0.0	0.0	0.11	10.3	10.15 ± 0.465
783743	149.93968	2.488034	0.72 ± 0.15	0.0	0.0	0.09	10.5	10.73 ± 3.42
789914	149.979212	2.498304	0.88 ± 0.0	0.0	0.0	0.08	10.1	9.062 ± 1.257
790685	150.370657	2.498115	0.82 ± 0.0	0.09	0.09	0.02	10.8	44.95 ± 0.6
794024	150.055643	2.504436	0.7 ± 0.0	0.07	0.1	0.04	10.3	50.4 ± 0.998
811857	149.913557	2.530162	0.69 ± 0.0	0.02	0.02	0.11	10.6	7.52 ± 1.842
819000	149.457523	2.539333	0.83 ± 0.02	0.05	0.05	0.02	10.3	58.92 ± 2.595
824508	149.862472	2.548484	0.74 ± 0.0	0.01	0.01	0.06	11.3	14.81 ± 0.813
830418	149.562546	2.557087	0.76 ± 0.03	0.0	0.0	0.03	10.7	39.12 ± 4.827
834449	150.1201	2.561479	0.5 ± 0.0	0.04	0.05	0.06	10.6	14.31 ± 0.228
837890	150.054801	2.569459	0.75 ± 0.0	0.03	0.03	0.13	10.5	156.8 ± 1.615
838188	149.77795	2.567252	0.72 ± 0.0	0.0	0.0	0.07	10.3	10.45 ± 0.524
840232	149.716601	2.572475	0.9 ± 0.01	0.04	0.05	0.09	10.7	117.4 ± 4.215
842149	150.342316	2.575943	0.75 ± 0.0	0.0	0.0	-0.03	10.2	54.86 ± 0.529
842173	149.733742	2.574995	0.71 ± 0.0	0.01	0.01	0.07	10.6	93.81 ± 1.129
844990	149.926835	2.580581	0.7 ± 0.0	0.04	0.05	0.1	10.2	14.41 ± 1.532
848785	150.42295	2.583241	0.81 ± 0.0	0.12	0.12	-0.09	10.1	83.81 ± 1.125
849397	149.976994	2.586831	0.73 ± 0.0	0.09	0.12	0.01	10.3	13.25 ± 1.373
853769	150.33873	2.593234	0.85 ± 0.0	0.0	0.0	0.12	10.9	154.6 ± 2.136
860071	150.27635	2.603899	0.7 ± 0.0	0.01	0.01	-0.08	10.1	7.279 ± 2.386
864706	150.531072	2.610881	0.79 ± 0.0	0.05	0.07	0.1	10.6	23.57 ± 1.955
865896	150.054261	2.612264	0.74 ± 0.0	0.0	0.0	-0.09	10.0	8.219 ± 0.209
866054	149.811584	2.610245	0.54 ± 0.0	0.04	0.05	0.09	10.7	14.02 ± 0.637
876155	150.564918	2.625331	0.65 ± 0.02	0.06	0.06	0.08	10.7	24.88 ± 1.983
878476	150.752013	2.62904	0.84 ± 0.11	0.03	0.05	0.0	10.4	18.84 ± 6.223
878551	150.046263	2.630447	0.76 ± 0.03	0.04	0.04	0.04	10.1	38.72 ± 4.129
880787	149.550391	2.632955	0.81 ± 0.06	0.01	0.01	0.07	10.9	23.8 ± 3.235
880925	149.937367	2.634136	0.71 ± 0.03	0.03	0.04	0.05	10.2	11.79 ± 1.779
886498	149.513205	2.643508	0.64 ± 0.0	0.05	0.06	+0.0	10.3	11.81 ± 0.759
887351	150.04403	2.643885	0.7 ± 0.0	0.03	0.03	-0.07	10.6	86.33 ± 0.814
893857	150.159952	2.654341	0.85 ± 0.0	0.09	0.11	-0.01	11.1	217.3 ± 2.864
894779	150.427097	2.656439	0.55 ± 0.0	0.05	0.07	-0.0	10.0	61.12 ± 0.869
901597	150.709924	2.667676	0.7 ± 0.08	0.04	0.05	0.06	10.1	44.59 ± 9.812
902885	150.136763	2.669235	0.7 ± 0.0	0.04	0.05	0.04	10.0	12.35 ± 0.37
909617	149.970409	2.677765	0.69 ± 0.0	0.02	0.03	0.04	10.8	22.88 ± 1.869
911723	149.681335	2.681084	0.58 ± 0.0	0.0	0.0	0.0	10.9	82.03 ± 0.502
912969	150.589787	2.684536	0.74 ± 0.0	0.1	0.1	-0.01	10.7	44.6 ± 2.707
915913	150.557165	2.688555	0.88 ± 0.0	0.02	0.02	0.03	10.1	20.01 ± 0.293
917600	150.029291	2.690141	0.79 ± 0.09	0.01	0.01	0.04	11.1	23.59 ± 6.409
921254	149.910328	2.695579	0.86 ± 0.14	0.0	0.0	0.08	11.1	39.36 ± 14.69
922401	150.035101	2.698678	0.65 ± 0.0	0.06	0.06	-0.04	10.6	18.22 ± 0.675
925981	150.433978	2.705011	0.88 ± 0.0	0.01	0.01	0.06	10.2	15.2 ± 1.928
927031	149.716671	2.705636	0.88 ± 0.0	0.0	0.0	0.15	11.1	155.3 ± 1.796
931390	150.586062	2.712214	0.66 ± 0.0	0.07	0.08	0.03	10.0	9.482 ± 2.196
937909	149.79431	2.722162	0.9 ± 0.02	0.05	0.05	0.04	10.6	28.88 ± 2.201
940851	150.539461	2.728218	0.66 ± 0.0	0.03	0.03	0.04	10.1	6.119 ± 0.435
946233	150.227312	2.737645	0.7 ± 0.09	0.0	0.0	0.07	10.6	29.97 ± 8.641
948557	149.627616	2.739277	0.55 ± 0.0	0.11	0.11	-0.06	10.1	25.99 ± 0.689
952356	149.886951	2.747311	0.88 ± 0.0	0.02	0.02	0.07	10.6	109.3 ± 1.016
960767	149.848315	2.760829	0.7 ± 0.0	0.1	0.11	0.03	10.4	78.83 ± 1.575
964786	150.126928	2.7654	0.57 ± 0.0	0.0	0.0	0.05	10.6	56.32 ± 0.274
970636	150.408721	2.777253	0.84 ± 0.09	0.01	0.01	0.08	10.9	114.8 ± 26.57
978011	150.155692	2.787663	0.73 ± 0.0	0.0	0.01	0.0	10.4	18.89 ± 0.559
981123	150.399371	2.794152	0.82 ± 0.0	0.01	0.01	0.04	10.6	170.4 ± 3.618

Table A.1. Table columns: (1,2,3) Identification number, RA and DEC (in degree) from Laigle et al. (2016); (4) photometric redshift (or spectroscopic if available) from Jin et al. (2018); (5,6) clumpiness parameters (clumpiness is estimated as in equation 4, while in c' the flux of the clumps is divided by the total flux of the galaxy (including the nuclei) inside the segmentation map; (7) *merginess* parameter, estimated as in equation 3; (8) stellar mass from Laigle et al. (2016), with typical uncertainty of 0.1 dex; (9) SFR_{IR} from Jin et al. (2018).

Appendix B

Proposals

- **A. Calabrò**, E. Daddi et al. (2018) Grade B proposal at IRAM/NOEMA: *Confirming the discovery of an evolutionary sequence of merger stages at z=0.7*. This accepted proposal is presented below.
- co-investigator in other 8 accepted proposals at VLT/KMOS, Subaru/MOIRCS, Magellan/FIRE, HST, IRAM - Plateau de Bure Interferometer/NOEMA and ALMA.
- Pending proposal ALMA 2019: *Unveiling the nature of distant starbursts through spatially-resolved dust and gas maps* (PI: A. Calabrò)

IRAM

300, rue de la Piscine
38406 Saint-Martin-d'Hères (France)
Fax: (33/0) 476 42 54 69

Registration n°: **W18CX**
Date: **13-SEP-2018**

PROPOSAL FOR THE NOEMA INTERFEROMETER

Title: Confirming the discovery of an evolutionary sequence of merger stages at z=0.7

PIs: Antonello Calabro' (FR)
CoIs: Emanuele Daddi (FR), Shuowen JIN (CN), Annagrazia Puglisi (FR), Francesco Valentino (DK), Masato Onodera (US) (pending), Paolo Cassata (IT), Raphael Gobat (CL)

Proposal category: Standard
Scientific category: Luminous and Ultra-Luminous Infra-Red Galaxies (LIRG & ULIRG), Surveys of galaxies, Merging and interacting galaxies

Total requested time: 31.0 (PolyFiX)

Abstract:
Using our unique sample of 25 starburst (excess specific SFR) galaxies at z=0.5-1 with near-IR rest frame spectroscopy of Paschen lines, we have found that these objects are extremely obscured with Av ~ 9 mag, on average, towards their centers (as inferred from PaB/LIR luminosity ratios). We also discovered relatively tight correlations between total obscuration, emission line ionisation, and effective age (as traced by line EWs), all scaling with starburst core size as inferred from radio at 3GHz. We propose to use NOEMA to derive the CO[3-2] (and underlying continuum) luminosities and sizes for 8 targets spanning the full range of properties. These CO-based quantities (which are dust and AGN-free) will be crucially important to search for SFR evolutionary effects (due to the different timescales traced by CO, IR and radio) and thus to clarify whether the above correlations correspond to a time-evolutionary sequence. These new data would allow to study the entire sequence of the merger-triggered starbursts process, which is supposed to end with a strong, possibly AGN-driven SFR suppression.

Proposal history:
This is a resubmission of a previous NOEMA proposal (Registration number= P321988) on 14th September 2017, which was not approved. We took into consideration the previous comments and improved the scientific case of the project.

Sources:

Id	Epoch	RA	DEC	z (redshift)	Setups	
303305	J2000	10:01:55.932	01:44:52.658	0.53062778	1	edit/delete
578239	J2000	10:03:03.703	02:10:51.557	0.557843	5	edit/delete
685067	J2000	09:58:59.352	02:20:44.662	0.37345054	2	edit/delete
223715	J2000	09:59:03.689	01:37:01.263	0.51741	3	edit/delete
232171	J2000	10:00:14.479	01:37:57.687	0.52507	4	edit/delete
519651	J2000	10:01:43.247	02:05:12.777	0.6709	5	edit/delete
894779	J2000	10:01:42.503	02:39:23.180	0.550619	4	edit/delete
245158	J2000	10:00:45.250	01:39:17.919	0.5172	1	edit/delete

Confirming the discovery of an evolutionary sequence of merger stages at z=0.7

Scientific motivation

High-redshift starbursts: key objects to understand the formation of massive galaxies: starburst galaxies (SBs) at high redshift, identified as outliers from the Main Sequence (the tight correlation between SFR and stellar mass observed for the average star-forming galaxy population (Noeske et al.2007, Daddi et al.2007)), are generally thought to be progenitors of massive ellipticals through merger episodes, as suggested by galaxy simulations (Di Matteo et al. 2005; Hopkins et al. 2010). However, since these objects are in general highly dust-obscured, it is very difficult to derive their intrinsic physical properties, and their nature is indeed hotly debated in the community, with alternative works claiming they are anomalous gas rich systems (Scoville et al.2016).

A unique sample of SBs with near-IR spectra at z ~ 0.7 : If we want to test the merger-induced scenario and study the physical properties of these systems, we need to observe them at longer wavelengths, where the attenuation is lower compared to the optical range. With this intention, we have observed with Magellan-FIRE the near-IR rest-frame spectra of 25 starbursts at intermediate redshift, which were randomly selected among the 152 starbursts found in the whole COSMOS field (requiring $SFR_{IR} > 4\times SFR_{MS}$ at a stellar mass above 10^{10} $M_{\odot}$ and $0.5 < z < 0.9$). This constitutes a first statistical sample with near-IR rest-frame spectra at intermediate redshift, z ~ 0.9 being the maximum allowed to observe Paβ from current ground-based facilities.

A new picture of SB galaxies emerging : This unique sample in terms of spectral coverage has allowed us to find new results, of which we emphasize here the key points:

- the attenuation of Hα and that of Paβ is not in agreement with the Calzetti/Cardelli attenuation curves: the observed ratio between Paβ and Hα does not increase with total attenuation A_{IRX} (inferred from Paβ luminosity and bolometric LIR), but saturates at a constant value of $\simeq$ 0.17. Our galaxies follow very tightly the predictions of an optically thick 'mixed model' geometry in which gas and stars are homogeneously distributed inside a volume (Fig.2-left), producing a very strong attenuation towards the core and allowing only optical light from the skin to escape (see Calabrò et al. 2018a for more details).
- high redshift starbursts are not a single monolithic sample, but they show a wide range of different properties (total obscuration, size, line equivalent width (EW)). In particular, we found total A_V towards the center (derived from A_{IRX} and assuming a mixed model) spanning from 1 to 30 magnitudes (~ 9 mag on average), while radio FWHM deconvolved sizes, obtained with GALFIT by fitting a gaussian profile to their VLA (3GHz, 0.75″ resolution) images, range within 0.7 and 10 kpc.
- the results of Calabrò et al. 2018a strengthen the starburst-merger connection at z~ 0.7: all the 25 starbursts are recognized as mergers from either their morphology or from their high dust obscuration, which becomes the only easy option to identify mergers at the coalescence, where low surface-brightness residual interacting features are nearly impossible to detect at high-z.
- we found intriguing correlations between the total dust attenuation of the mixed model and the radio FWHM size at $> 15\sigma$ level (Fig.2-right). The SB sizes and their obscurations are then tightly connected to other physical quantities, i.e., the N2 index (=log([N II]/Hα)), the EW of all Balmer and Paschen lines and the emission line velocity widths (a proxy for the velocity dispersions) (Fig.3).

Towards a time-evolutionary sequence of high-z mergers : We were surprised to find all the above correlations that not even ~40 years of studies on local ULIRGs have disclosed. The times are mature to study observationally and with statistical relevance the different phases of merger evolution as observed in simulations (Hopkins et al.2006, Toomre&Toomre 1972), from the first encounter to the compact starburst phase and AGN triggering, ending up with the AGN-driven blow-out (eventually passing through a QSO phase) and SFR suppression, which leaves a passively evolving remnant. Our findings indicate that we may be starting to see this evolutionary sequence at high redshift (Calabrò et al. 2018b in prep.): as the merger evolves, the starbursts become more compact and obscured, increasingly dominated by shocks (higher [N II]/Hα) and older stellar populations (lower equivalent width of Balmer/Paschen lines) in the outskirts, due to the withdrawal of the burst to deeper regions. The coalescing process also enhances the velocity dispersion of the system, probed by the line velocity width. Fig.3-bottom-right also shows that our 6 SBs that are also detected in X-rays are all found in the latest merger phase, lying below the Mass-size relation of ETGs at z~ 0.7. This is again consistent with a scenario in which the AGNs blow out gas and dust from the galaxy after the coalescence (leading eventually to a bright QSO), allowing them to be detected in X-ray surveys.

Problems and uncertainties : Despite of the clear results and relations that we found, our interpretation remains still an hypothesis. Using ancillary optical spectra, we surprisingly discovered that in some galaxies, while being starbursts forming stars at ~ 100$M_{\odot}$/yr (inferred from IR), Hδ, Hγ and Hβ are globally in absorption. The EW of Hδ reaches

−10Å, resembling that of post-starburst galaxies (Poggianti et al.2009), as if star-formation has been completely shut down (possibly because of AGN or supernova feedback, at least in the skin). This evidence suggests then the possibility that the dust attenuation pattern in Fig.2-left is mainly driven by the infrared luminosity tracing the SFR on longer timescales compared to the lines, thus discarding dust geometry effects.

Immediate objective

With this sample of z∼ 0.7 SB galaxies, we have the opportunity to understand the key phase of galaxy formation through merger induced starbursts, but our current results still leave the place for different interpretations. In this proposal we ask to observe with NOEMA (band 3) the CO lines and dust continuum of a representative subset of 8 SBs among our Magellan sample. The number of targets is determined by requiring a SNR of the CO lines of at least 10, to enable size measurements, and at the same time keep the proposal manageable with current sensitivity and resolution levels at a total observing time ∼ 30h. We remark that, even with this reduced number of galaxies, the selected SBs are distributed over the entire ranges of attenuation, radio size, velocity width, N2 and EW (see Fig. 3), thus they are representative of the whole correlation sequence and allow us to test all possible conditions/merger stages. We would like to use NOEMA on these 8 galaxies to address the following points:

(1) test SFR time variations: We will measure the CO luminosity (L'CO) for all the 8 targets and check whether they all obey the tight correlation known to exist with LIR (Liu et al. 2015). For the galaxies deviating below from such correlation, which may be candidates where the final blow-out phase has already started and their SFR has been experiencing a strong suppression, we can use their L'CO to derive a crude estimate of their instantaneous SFR. Given the 0.2 dex dispersion, we can select deviants at 2σ, corresponding to a suppression of a factor of ∼ 3 (models predict that abruptly decreasing SFRs by orders of magnitudes could apply), and statistically detect (by averaging) even finer departures. We will then use this instantaneous indicator in place of SFR_{IR} (which probes longer SF timescales of ∼ 100 Myr) to compute more realistic attenuations as $A_{CO,Pa\beta}$=2.5 × log_{10}(1+SFR_{CO}/$SFR_{Pa\beta,obs}$), redrawing Fig.2-left with this new quantity. This will clarify whether previously found large attenuations A_{IRX} were entirely caused by comparing SFRs (from LIR and from the lines) with different timescales, and whether the mixed model prediction is still valid.

(2) measure the CO and dust-continuum sizes, through which we directly probe the current physical extension of the SFR and gas reservoirs, respectively. Indeed, even though we will be guided by previous radio size estimates, these latter are hard to interpret, as radio synchrotron radiation can be powered by different physical mechanisms that are not yet fully understood (see Condon et al.1992 for a review). Furthermore, the radio sizes are tracing somewhat indirectly the distribution of SFR (Condon et al. 1991) on longer timescales (∼ 100-200 Myr) that are comparable to the merger/starburst duration (∼ 200-400 Myr, Di Matteo et al.2008). An additional problem affecting the radio sizes could be the presence of an AGN, which is ubiquitous in the coalescing merger phase. We remark the importance of having access to these instantaneous tracers: only by comparing CO-sizes and CO-based $A_{CO,Pa\beta}$ (addressed through the first point) we can clarify if the attenuation-size relation is real and is not driven by other (e.g., timescale) effects. Finally, if we find a systematic difference between the CO and continuum-based sizes would be again an evidence of evolution/compactification of the starburst core size during the merging process.

Observing plan

We propose spectral observations at frequencies between 200 and 230 GHz, targeting the CO[3-2] line for a total number of 8 starbursts. For this sample, we already have accurate redshift and SFR measurements (Fig.1) at < 0.1% and 1% errors, respectively. We first predict CO[5-4] fluxes from LIR using the linear correlations presented by Daddi et al. (2015) and Liu et al. (2015), and then conservatively scale these fluxes to CO[3-2] adopting a ULIRG CO SLED (Papadopoulos et al 2012, Daddi et al 2015). Continuum flux predictions around CO[3-2] are instead derived from SED fitting using our multi-wavelength SED including Herschel and SCUBA2 fluxes (Fig.1). For two pairs of galaxies with similar redshifts we share the same setup (minimizing the overheads), thus we have created 6 different instrumental setups. The integration times chosen for each target will allow to detect the CO[3-2] line (assuming a point-source equivalent case) at a minimum S/N of 10 (see techsheets), assuming a conservative velocity width of 500 km/s, consistent with our Paβ line profiles. Such high SNR will allow to derive size measurements with an accuracy of < 0.1″ (i.e., ∼ 0.7 kpc at z= 0.7) (the size error can be estimated as the ratio of the beam-size and the expected SNR, as done in Coogan et al. 2018), thus ideal for our purposes. At the same time, we will detect the continuum at minimum S/N of 5 (for 2 sources we will reach actually a S/N of 3 on the continuum, but we will be helped by doing our measurements at a fixed positions/shape, guided by the bright CO32 line and also previous radio estimates). By summing all the 6 setups for the 8 targets, we end up with a total NOEMA time of 31 hours, that we request for this scientific project. We choose configuration C, which provides an average beamsize of 0.9″ (at ∼ 230GHz) for several reasons: (1) allow the most extended objects (which are recognized as pre-coalescence starbursts from our Magellan spectra) to be still measurable and detected, given that their size can be at most comparable with the beam, and we

know their position extremely accurately from the radio; (2) C-conf is basically identical to the one in 3GHz radio, allowing to build matched PSF color images to search for radial gradients together with the CO and dust continuum maps. Finally, in case of extremely compact sources (actually only galaxy ID 303305 was not resolved in radio), C-conf will provide upper limits to the intrinsic sizes at the level of 0.2″ (we will analyse our data in the uv space with GILDAS), which is still acceptable for our goals.

Table 1: Main properties of the starburst galaxies targeted in this proposal

ID	z_{spec}	LIR	ν_{CO}	$f_{\nu_{CO}}$	F_{CO}
245158	0.5172	8.05E+11	227.9	622.7	6.6
303305	0.5306	9.24E+11	225.9	304.0	8.1
578239	0.5578	1.96E+12	222.0	581.0	11.4
685067	0.3735	9.71E+11	251.8	666.3	26.3
223715	0.5174	6.04E+11	227.9	411.8	14.3
232171	0.5251	5.09E+11	226.7	174.1	8.0
326384	0.8042	1.58E+12	255.5	540.9	6.2
519651	0.6709	1.41E+12	207.0	285.0	7.1
894779	0.5506	6.13E+11	223.0	186.7	13.0

Columns: (1,2) identification number and spectroscopic redshift from Calabrò et al.2018; (3) Total infrared luminosity ($L_{\odot}$) derived through SED fitting as shown in Jin et al.2018; (4) frequency (in GHz) of the targeted CO[3-2] line; (5) continuum flux predicted at ν_{CO} (in μJy) from SED fitting; (6) CO flux (in mJy) estimated as described in the text.

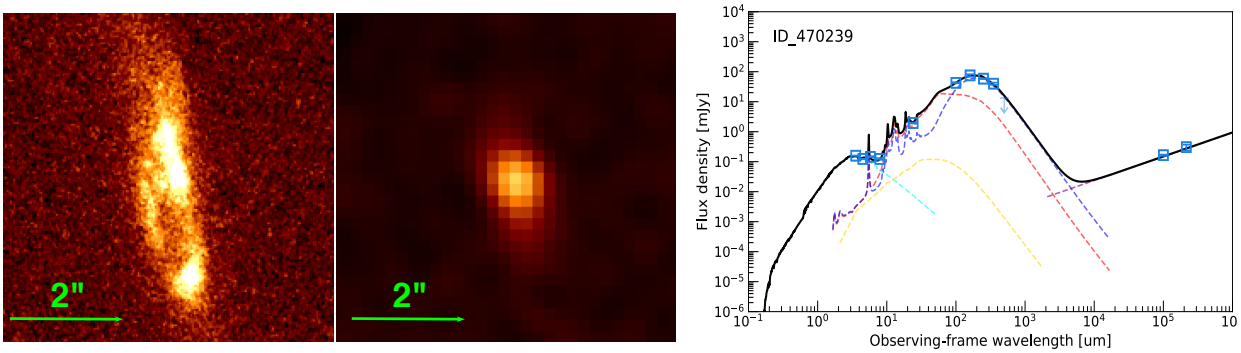

Figure 1: For one galaxy in the parent sample (ID 470239), we show for example purposes: i-band HST and radio VLA images and SED fitting with 5 components (stellar component (cyan), AGN (yellow), warm (red) and cold (blue) dust, and radio (violet)), yielding an estimation of AGN-decontaminated bolometric LIR integrated over 8-1000μm rest-frame. The current IR photometry constrains the dust mass M_{dust} accuracy to < 0.1 dex, however these measurements will soon improve.

References:

Calabrò, A., et al. 2018a, ApJ, 862, L22: *Near-infrared Emission Lines in Starburst Galaxies at 0.5 < z < 0.9: Discovery of a Merger Sequence of Extreme Obscurations*; **Calabrò, A.,** et al. 2017, A&A, 601, A95: *Characterization of star-forming dwarf galaxies at* $0.1 \lesssim z \lesssim 0.9$ *in VUDS: probing the low-mass end of the mass-metallicity relation*; **Daddi, E., Jin, S., Calabro, A., Valentino, F.,** et al. 2017, ApJ, 846, L31: *Radio selection of the most distant galaxy clusters*; **Cassata, P.,** et al. 2011 ApJ, 743 96:*The Relative Abundance of Compact and Normal Massive Early-type Galaxies and Its Evolution from Redshift z ~ 2 to the Present*; **Cassata, P.,** et al. 2013 ApJ, 775 106:*Constraining the Assembly of Normal and Compact Passively Evolving Galaxies from Redshift z = 3 to the Present with CANDELS*; **Onodera, M., Daddi, E.,** et al. 2012, ApJ, 755, 26: *Deep Near-infrared Spectroscopy of Passively Evolving Galaxies at z* > 1.4; **Puglisi, A., Daddi, Valentino, F., Calabro, A., Jin, S.,** et al. 2017, ApJ, 838, L18: *The Bright and Dark Sides of High-redshift Starburst Galaxies from Herschel and Subaru Observations*; **Valentino, F., Daddi, E., Onodera, M.,** et al. 2015, ApJ, 801, 132: *Metal deficiency in cluster star-forming galaxies at z=2*;

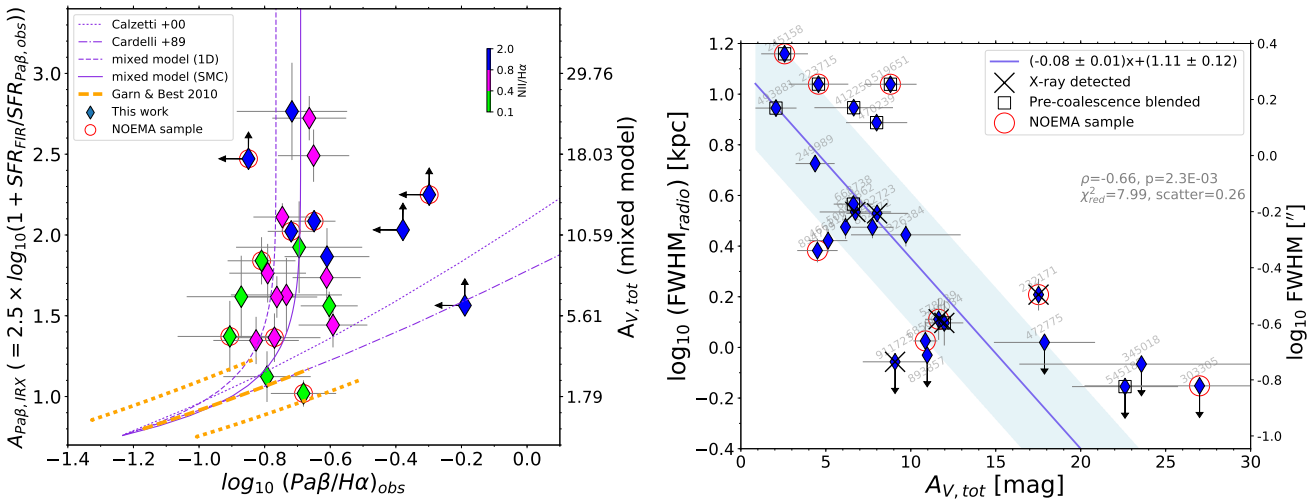

Figure 2: **Left:** Diagram showing that Paβ/Hα (for the complete Magellan/FIRE sample) do not follow the Cardelli and Calzetti relations (green lines), but saturate as predicted by a mixed geometry model. In such a model, the differential attenuation law has to be set. Here we consider a Cardelli-like (red dashed) and an SMC-like (red continuous line) local attenuations. We enclose with yellow lines the region ($\pm 1\sigma$) occupied by MS galaxies at varying stellar masses (Garn&Best 2010). **Right:** Correlation between the attenuation and radio major-axis sizes, expressed as FWHM in kpc. We display on the y-axis at the right the scale in arcseconds, assuming a median redshift of the sample ($z_{med} \simeq 0.7$), for a standard Λ-CDM cosmology with h= 0.7, Ω_m=0.3 and Ω_λ=0.7. The Pearson correlation coefficient ρ, p-value, residual χ^2 and the scatter of the relation are shown in light grey below the legend.

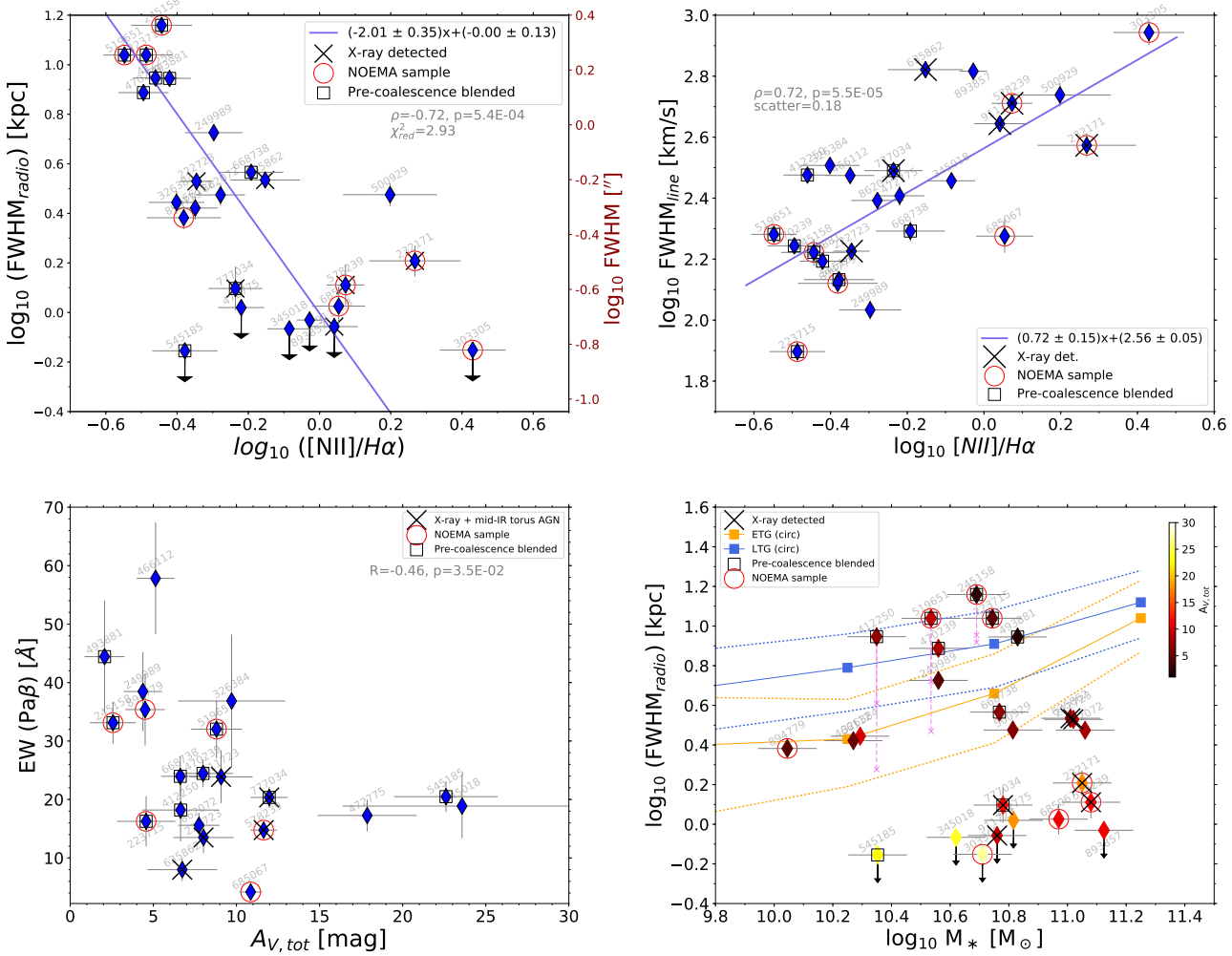

Figure 3: **In clockwise order : (1) and (2)** Correlation between [N II]/Hα and, respectively, the radio size FWHM$_{\rm radio}$ and the emission line velocity width FWHM$_{\rm line}$. **(3)** Stellar mass- radio size diagram for the Magellan sample, compared to the M$_*$-size relation of LTGs and ETGs of Van Der Wel et al. 2014. Three sources have been deblended, and the radio sizes of their single merger components are shown with violet crosses. **(4)** Correlation between the EW of Paβ and $A_{Paβ,IRX}$, which has been used also in Fig.2-left. Similar trends are found also when adopting the EW of Hδ, Hβ and Hα.

Liste des documents retirés

Fig. 1.1, page 3 de la thèse et 21 du pdf : image pris du livre Mo,Van Den Bosh,White (2010)